Eliminating Interface Losses in Perovskite Single Junctions for Efficient Tandem Solar Cells

vorgelegt von
M. Sc.
Amran Al-Ashouri
ORCID: 0000-0001-5512-8034

an der Fakultät IV – Elektrotechnik und Informatik
der Technischen Universität Berlin
zur Erlangung des akademischen Grades

Doktor der Naturwissenschaften
– Dr. rer. nat. –

genehmigte Dissertation

Promotionsausschuss:

Vorsitzender:	Prof. Dr. Bernd Szyszka
Gutachter:	Prof. Dr. Steve Albrecht
Gutachter:	Prof. Dr. Bernd Rech
Gutachterin:	Prof. Dr. Yana Vaynzof (TU Dresden)

Tag der wissenschaftlichen Aussprache: 29. Juni 2021

Berlin 2021

This is the electronic version of the cumulative thesis, in single-page format and containing clickable links to figures, references, article websites etc. (dark blue color). Articles and their supplementary materials that were the basis of this work are reprinted with permission in the appendix (two articles as published, one as accepted version).

Abstract

Perovskite-based tandem solar cells have the potential to surpass single junction efficiency limits at low costs and to further spur the expansion of solar energy. This thesis deals with the optimization of tandem-relevant perovskite solar cells (PSCs), by mitigation of interfacial power losses between perovskite and charge-selective layers. A key theme in this work is the establishment of hole-selective self-assembled monolayers (SAMs), which can functionalize oxide surfaces in a self-limiting process with precise control. This enabled a simple and robust PSC structure with power conversion efficiencies of over 21% with single junction cells, over 24% with perovskite/CIGSe tandem solar cells and over 29% with perovskite/silicon tandem solar cells. It furthermore enabled studies on device-relevant model systems to gain understanding about optimal charge-selective layer design, characterization of charge extraction and stability enhancement. The gains in efficiency were rationalized by photoluminescence studies, both with absolute calibration for quantifying the voltage gains at the interfaces and with time resolution to investigate the charge carrier dynamics. By employing a combination of photoluminescence, solar cell characteristics and measurements of the energetic alignment between hole-selective layer and perovskite, we identified the energetic offset between the hole-accepting energy level of the SAM and the perovskite valence band maximum as the critical parameter that determined the open-circuit voltage (V_{OC}) of the solar cell. One of the studied SAMs, a carbazole unit attached to ethylphosphonic acid (2PACz), has shown optimal energetic alignment and minimal non-radiative recombination losses, rendering a "lossless" interface and enabling a V_{OC} of 1.19 V at 1.63 eV bandgap, without interlayers, dopants or additives. By using the SAM on rough CIGSe as hole-selective layer for the perovskite top cell, we have shown a certified 23.3%-efficient, monolithic perovskite/CIGSe tandem solar cell with 1 cm^2 active area, which surpassed the previous record in size and efficiency (22.4% on 0.04 cm^2), demonstrating how SAMs can simplify cell fabrication. Further optimization with a focus on the fill factor, the only parameter where best perovskite solar cells still lack behind mature solar cell technologies, led to the finding that a methyl-substituted carbazole-based SAM (Me-4PACz) considerably enhanced the hole-extraction speed and thus the fill factor (up to 84%), while keeping the high-V_{OC} feature of 2PACz. By combining transient photoluminescence with photoconductivity measurements and solar cell data, we identified that the hole-selective interface was limiting the fill factor in *p-i-n* PSCs. Integrating Me-4PACz into perovskite/silicon tandem solar cells led to a certified record efficiency of 29.15% and to a cell retaining 95.5% of its initial efficiency after 300 h under continuous operation in ambient air. The results helped progressing perovskite tandem photovoltaics and might lay guides for future endeavors of industrial entry.

Zusammenfassung

Perowskit-basierte Tandemsolarzellen bergen das Potenzial, Einzelsolarzell-Effizienzen zu übertreffen und die Nutzung von Solarenergie auszuweiten. Die vorliegende Arbeit befasst sich mit der Optimierung von Tandem-relevanten Perowskitsolarzellen (PSZn) durch Reduktion von Leistungsverlusten an den Grenzflächen zwischen Perowskitschicht und den ladungsselektiven Schichten. Ein Hauptmotiv dieser Arbeit ist die Etablierung von Loch-selektiven selbstorganisierten Monolagen (SAMs), die Oxidschichten selbstständig funktionalisieren können. Dies ermöglichte eine einfache und robuste PSZ-Struktur mit Leistungsumwandlungseffizienzen (PCEs) von über 21% mit Einzelsolarzellen, >24% mit Perowskit/CIGSe Tandemsolarzellen und >29% mit Perowskit/Silizium Tandemsolarzellen. Außerdem ermöglichte es Solarzell-relevante Modellsysteme für einen Verständnisgewinn über optimales Design von ladungsselektiven Schichten, Ladungsträgerextraktion und Erhöhung der Stabilität. Die Effizienzgewinne wurden mit Photolumineszenz-Studien erklärt, sowohl mit absoluter Kalibrierung zur Quantifizierung von Spannungsgewinnen an den Grenzflächen, als auch mit Zeitauflösung, um die Ladungsträgerdynamik genauer zu untersuchen. Mit einer Kombination von Photolumineszenz, Solarzell-Eigenschaften und der Messung von Energieniveaus wurde die Ausrichtung zwischen Loch-selektiver Schicht und der Perowskit-Valenzbandkante als entscheidender Parameter für die Leerlaufspannung (V_{OC}) der Solarzelle identifiziert. Einer der untersuchten SAMs, eine Carbazol-Einheit verbunden mit Ethanphosphonsäure (2PACz), zeigte optimale energetische Ausrichtung und minimale nichtstrahlende Verluste, was eine "verlustfreie" Grenzfläche ermöglichte und zu hohen V_{OC}-Werten von bis zu 1,19 V bei 1,63 eV-Bandlücke führte, ohne Zwischenschichten, Dotierung oder Additiven. Durch einen SAM auf rauer CIGSe-Oberfläche als Loch-selektive Schicht für die Perowskit-Topzelle, wurde eine monolithische Perowskit/CIGSe Tandemzelle realisiert mit zertifizierter Effizienz von 23,3% auf einer Fläche von 1 cm^2, was den vorigen Rekord in Fläche und Effizienz übertraf (22,4% auf 0,04 cm^2). Weitere Optimierung mit Fokus auf den Füllfaktor der Solarzellen, den einzigen Parameter bei dem beste PSZn noch nicht die Werte von ausgereiften Solarzell-Technologien erreicht haben, führte zu der Erkenntnis, dass eine Methyl-substituierte Carbazol-SAM (Me-4PACz) die Loch-Extraktion deutlich beschleunigte und damit den Füllfaktor erhöhte (bis auf 84%), unter Beibehaltung der hohen V_{OC} von 2PACz. Durch transiente Photolumineszenz, Photo-Leitfähigkeitsmessungen und Solarzell-Daten ergab sich, dass die Loch-selektive Grenzfläche in *p-i-n* PSZn den Füllfaktor limitierte. Der Einsatz von Me-4PACz in Perowskit/Silizium-Tandemsolarzellen führte zu einer zertifizierten Rekordeffizienz von 29,15% und zu einer Zelle, die 95,5% ihrer Initialeffizienz nach 300 h unter dauerhaftem Betrieb an Luft behielt.

Contents

Chapter 1

Introduction

"...the beginning of a new era, leading eventually to the realization of one of mankind's most cherished dreams–the harnessing of the almost limitless energy of the sun for the uses of civilization."

New York Times (front page), April 26, 1954.

Life on earth in its current form would not have been possible without the enormous amount of energy that our sun has been providing as a major driving force for a variety of life cycles on planet earth. Today and in future, the sunlight hitting earth's surface carries enough power to match our growing demand for electricity. In fact, the potential lying within the harvest of solar energy outclasses all other existing, scalable possibilities [1–3]. Compared to other forms of energy, it is furthermore more equally distributed across the nations. Together with appropriate, responsive energy storage, i. e. electrochemical, mechanical or in the form of chemical bonds, solar energy will be part of a global, decentralized solution to sustainably power civilizations.

The enormous challenge posed by anthropogenic climate change and the burning of coal, natural gas and oil are interwoven: The CO_2-equivalent footprint[1] of every individual can be roughly divided into consumption of goods, diet, travel and housing (including electricity and heating), with similar weights [4]. The energy consumption of industrial production, travel, electricity and heating can be covered by renewable energies, which could reduce the footprint of three of the four points. Thus, besides the practices of sufficiency and dietary optimization [5, 6], the scale-up of renewable energies is an obvious path for reducing the average CO_2-equivalent footprint per person from now 11 t in Germany towards climate neutrality. This is critical to keep the global average temperature rise below the threshold of $1.5 - 2\,^{\circ}C$, above which spirals of self-reinforcing tipping points are expected to lead to unstoppable climate catastrophes

[1] The "equivalent" figure accounts for other greenhouse gases as well, e. g., methane with a 25-times higher climate effectivity than CO2.

[7]. Today, the energy needs of our civilizations largely rely on the exploitation of fossil resources that needed hundreds of thousands of years to form (Fig. 1.1). Considering that energy consumption scales with level of civilization and that developing countries will follow the economic pathways of industrial nations, the fossil reserves are not likely to last until later than 2100 [8], with oil and gas reserves estimated to deplete in even less than 50 years.

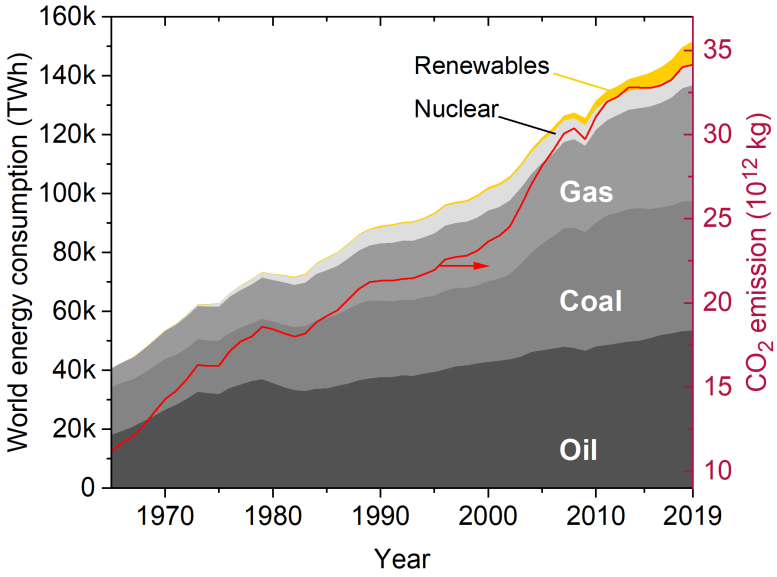

Figure 1.1: Energy consumption of humankind (left axis) in a stacked plot itemizing the sources by color. The right axis (red curve) shows the accumulated CO_2 emission. Data from ref. [8].

In the light of this perspective, the share of renewable energies should rise at a much faster pace than currently observed (see Fig. 1.1). For the world's energy needs to be covered half by solar power, the global capacity of installed modules has to rise by a factor of 30-40 [1]. The needed speed growth must be driven by economy, which itself is guided by price differences between available options. Currently, solar electricity is the cheapest form of energy and its installation growth is experiencing positive acceleration [1]. To be precise, the growth is so large that the International Agency of Energy (IEA) had to correct their (optimistic) predictions upwards several times [9], with total installed capacity now being >500 GW, which was not expected to be reached until 2030. Nevertheless, e. g., in Germany throughout the year 2020, photovoltaics made only 10.5% of the electricity mix, which was lower than the declining nuclear energy (12.5%) [10]. Hence, there is hope that a further decrease of the levelized cost of electricity, by increase of power conversion efficiency and decrease of fabrication cost, solar energy will gain even more popularity, availability and ubiquity.

1.1 Generations of solar cells

Today, the largest share of the solar market is held by silicon wafer technology. The large abundance of silicon, excellent stability and over half a century of research & development make it an advantageous technology that has proven its scalability. Silicon solar cells are regarded as the 'first generation' of solar technology [11]. A downside of solar cell production from silicon wafers is the high amount of energy needed for wafer purification and fabrication. At some point, the decrease of total module cost is limited by the material and fabrication costs, making it necessary for other technologies to emerge. The 'second generation' photovoltaics therefore consists of materials that are easier to produce under a lower material and energy consumption. Mostly it is based on thin-film technologies like, e. g., cadmium telluride (CdTe) and copper indium gallium selenide (CIGSe), which already experienced market entry. The energy payback time, i. e., the time of solar cell operation needed to offset the embedded energy from production, is 2-3 times lower than that of silicon solar cells [12]. Still, the price of silicon solar cells is lower than that of thin-film technologies, presumably due to a combination of their larger market scale, government incentives and possibly more conservative processing methods.

Finally, 'third generation' photovoltaics means more advanced technologies, such as organic solar cells, and new concepts of solar-to-electricity conversion for overcoming the theoretical efficiency limit of single solar cells. Examples are multilayer solar cells consisting of stacked absorber materials with different absorption thresholds (bandgaps) to more effectively capture solar radiation and lose less energy through heat in the conversion process. More sophisticated methods include the capture of "hot charge carriers" and the down-conversion of high-energy light into low-energy light of higher intensity. However, to date only the multijunction approach, including tandem solar cells, has experimentally proven that it can surpass single cell efficiency limits [13, 14].

1.1.1 Perovskite solar cells

The solar cell research communities experienced a disrupting shake in recent years since the rapid surge of perovskite solar cells gathered pace after 2009 [15]. They expanded the choice of thin-film photovoltaic materials by a high-efficiency technology that is capable of low-energy fabrication with low material consumption. Perovskite solar cells are called after their crystal structure and often consist of hybrid organic/inorganic metal halide materials. Due to their rare combination of favorable properties, they might in near future belong to high-efficiency second-generation photovoltaics and be a catalyst for the rise of affordable third-generation solar cells. One reason is that the absorber bandgap can be tuned across a wide range, similar to CIGSe, either for making highly efficient single junction cells (currently >25% efficiency [13]) or for optimized operation in tandem with a lower bandgap material (currently >29% in conjunction

with silicon). Across the wide bandgap range, the perovskite solar cells remain efficient and can be fabricated either via solution-processing (leading to the vision of super-lightweight, flexible and/or semi-transparent solar cells being roll-to-roll printed like newspaper) or via evaporation from dry sources, similar to CdTe or CIGSe. A more detailed background of perovskite solar cell research is given in section 2.4.

There are several philosophies concerning the market entry of perovskite-based photovoltaics [16, 17]. Low-cost fabrication can be realized most effectively if the solar cells are solely based on perovskite, either in single or multijunction configuration. However, they would have to face the dominating silicon solar cells which filled the market with very competitive prices. New companies would need to gain returns on their investments of new equipment, which requires higher pricing in the beginning, leading to a disadvantage compared to the established and trusted silicon technology with highly optimized supply and mass production chains. Therefore, an often considered market entry path of perovskite photovoltaics is as an expansion of existing silicon production lines. As such, perovskite-based devices would act as a top cell in perovskite/silicon tandem solar cells [18, 19]. Due to their combination of low cost, tunability and high efficiency, they can potentially lower the levelized cost of electricity (LCOE) across the lifespan of the solar modules. This would also be an attractive progression for the silicon industry, because commercial silicon solar modules are approaching their practical efficiency limits [20, 21].

This thesis is dedicated to contribute to the progress of perovskite solar cells for tandem applications. Throughout this work, tandem-relevant single junction devices have been fabricated, optimized and analyzed to find design guidelines for surpassing a tandem power conversion efficiency of 30% in perovskite/silicon tandem solar cells and >25%-efficient perovskite/CIGSe tandem solar cells. As detailed in section 2.4, state-of-the-art perovskite solar cells that are most suitable for tandem cells are currently limited by power losses at their interfaces to the charge-selective contacts. Key themes of this work are the introduction, application and development of new materials that can act as surprisingly efficient charge-selective layers by forming a molecular self-assembled monolayer (SAM) on the electrode. This progress was developed in close collaboration with the group of Prof. Vytautas Getautis and especially Artiom Magomedov from Kaunas University of Technology, who initially suggested this possibility and synthesized most of the molecules. Importantly, while the SAMs help to improve perovskite solar cell performance and simultaneously simplify the fabrication, they are ideal for constructing model systems for deepening the physical understanding of loss mechanisms and charge carrier dynamics in devices, as detailed in the results chapters.

After an introduction to the general concepts of solar cell physics, a brief summary of perovskite solar cell research and the history as well as advantages of SAMs in chapter 2, the following chapters chronologically present the peer-reviewed and published

reports of this thesis. The experimental methods, sample fabrication protocols, solar cell measurement conditions and explanations of more advanced material analysis methods are summarized in the appendix. The respective publications that form the basis of the chapters are reprinted in the appendix as well, along with the supporting information of the publications.

Chapter 3 is dedicated to the first publication of this thesis, introducing a hole-selective SAM (V1036) applied as the sole hole-selective layer in perovskite solar cells for the first time. The chapter furthermore explains why SAMs can fill an urgent gap of tandem-relevant perovskite solar cell architectures and discusses first hints on what hole-selective layers have to fulfill in order to work efficiently in perovskite solar cells.

Chapter 4 presents a follow-up study that emerged from searching for SAMs that work more efficiently than V1036. The new SAMs from this second generation (2PACz and MeO-2PACz) enable solar cell efficiencies surpassing state-of-the-art cells and help understanding how to mitigate open-circuit voltage losses more easily. Furthermore, a monolithic perovskite/CIGSe tandem solar cell with a record efficiency of 23.3% at 1 cm^2 active area is presented. With this, it was demonstrated that SAMs can conformally cover rough surfaces with high aspect ratios such as with CIGSe bottom cells, overcoming the challenge of voltage losses at such rough interfaces.

Chapter 5 presents the application of high-efficiency SAMs in perovskite/silicon tandem solar cells that enable a record power conversion efficiency of 29.2% with an optimized SAM (Me-4PACz). While in the previous paper the aim was to decrease voltage losses, the purpose in this work was to decrease transport losses in perovskite single junction and tandem solar cells. It was shown that while the electron-selective interface usually limits the open-circuit voltage, the hole-selective interface limited charge extraction speed.

Finally, the chapter closes with further results of ongoing work that is dedicated to revealing more details about charge extraction speed in order to understand what makes the charge-selective interfaces either perform well or limiting further gains.

Chapter 2

Fundamentals

2.1 Basic principles of solar cells

Solar cells are devices designed to transform the power carried by light into electrical power. An intermediate step is the conversion of the energy carried by light into energy carried by excited charge carriers (chemical energy), which implies strong light-matter interaction and the possibility to harness the electrical power via conducting terminals – the contacts. The purpose of this section is to briefly introduce the physics that describes this conversion process and operational behavior of solar cells.

Semiconductor physics, with a focus on describing charged quanta (charge carriers) in a crystalline environment, is the framework in which most models describe how, and how well solar cells work. Alternatively, a solar cell can be seen as a thermodynamic machine that converts heat of the sun into extractable work. Throughout the developments of models for describing solar cells, inputs from both disciplines, thermodynamics and semiconductor physics, have been used [22–27]. This chapter gives a brief summary of the "microscopic" view on solar cells (charge carrier dynamics inside the semiconductor) with relevant recalls on thermodynamic principles that form the basis of solar cell physics and which have proven useful in analyzing them.

The history of the photoelectric effect, an underlying physical law of every solar cell, is an example of how fundamental research led to a widespread, finely engineered technology. It is furthermore deeply interconnected to the birth of quantum mechanics, now considered to be the most advanced picture of nature developed by modern humanity. In 1839, A. E. Becquerel reported an electrical current flowing between two electrodes in an electrolyte when exposing the electrodes to sunlight [28, 29]. A series of further experiments involving prominent scientists of the 19th and 20th century followed this discovery of a photovoltaic effect. After J. J. Thomson found that electrons are emitted from metal surfaces into vacuum when ultraviolet light is shone onto them. Philipp Lenard published in 1902 that the energy of these electrons depends on the frequency of the impinging light [30]. At that time, this observation

seemed contradictory to the Maxwell theory of light, which rather predicted that the energy of ejected electrons would depend on the intensity of incident light. The modern explanation of the photoelectric effect led to the Nobel prize of Albert Einstein. In 1905 Einstein followed Max Planck's suggestion that light can carry energy only in discrete packets (later called "photons"), and deduced that the energy of light, $E = h\nu = \hbar\omega$, which is the wave frequency ν times the Planck constant $h \approx 6.6 \times 10^{-34}$ J s, has to be above a certain threshold to eject an electron out of a material [31]. The photon transfers its energy to a single electron, solving the riddle why under some circumstances light with high energy photons at low intensity can lead to free electrons out of metals, while light with low energy photons at high-intensity cannot.

The first solar cell to make use of the photoelectric effect was published in 1883 by Fritts [32] (using Selenium) and it took over 70 years more for the first practically viable solar cell to be published by Chapin [33], using crystalline silicon as the semiconducting absorber. Several decades of research & development later, solar cells now power, among other things, homes, ships, backpack batteries and mars rovers.

2.1.1 Absorption of light and charge carrier generation

Semiconductors are ubiquitous in our modern world, since their material properties can be dynamically adjusted to fit the intended applications, which has been most prominently mastered in electronics. A typical semiconductor is a material with electrical conductivities and bandgaps between those of insulators and metals. Different to insulators, they can conduct small currents at room temperature, and the conductivities can be tuned by multiple orders of magnitude by the introduction of impurities ("doping"). Common semiconductors absorb light above a certain energetic threshold that lies in the visible to infrared range, depending on the band diagram of the material. The band diagram of a solid gives the distribution of states that electrons can occupy. It is determined by the crystalline structure and can be calculated using quantum mechanics if the crystal atoms and their ordering are known. The bandgap of a solid state semiconductor determines the absorption threshold and is a characteristic feature that also determines its usability for photovoltaics. It is defined by the energetic difference between the valence band maximum (VBM) and the conduction band minimum (CBM) and marks the minimum energy photons must have for being absorbed by the material.

When a photon of higher energy than the bandgap hits the semiconductor, it is absorbed with a certain probability that follows from the band structure. This leads to an electron from the valence band to occupy a higher-energy state in the conduction band, leaving a vacancy in the valence band, which can conveniently be treated as a quasi-particle – a 'hole'. The task in building solar cells is to optimize the light incoupling and the continuous collection of electrons and holes at two different electric terminals to be as efficient as possible, i. e. under minimal loss of the excited charge carriers on their way to the terminals.

The spectrally resolved absorption characteristics (absorptivity $a(E)$) of materials contain information about the position and type of bandgap, the photon absorption probability per thickness of the material and the electronic disorder. If the electrons and holes can be separated by each other, say by two 'semi-permeable membranes' that only let through one type of charge carrier [24, 34], and are subsequently led to conductive terminals, a simple solar cell is already built. The light thereby leads to electrical current that can be extracted, which depends only on the absorptivity of the material and spectrum ϕ_{sun} of the incoming light. When externally shorting the two terminals, the flowing short circuit current density J_{SC} is:

$$J_{\text{SC}} = e \int_0^\infty a(E)\phi_{\text{sun}}(E)\mathrm{d}E \tag{2.1}$$

2.2 Charge carrier extraction and recombination

In a solar cell, the absorbed light can be considered as the driving force for the creation of free charge carriers, bringing the material into a non-equilibrium state, while all other concurrent processes of the carriers drive towards their relaxation back to thermal equilibrium. For extracting the charge carriers at different terminals, their separation and opposite flow is necessary. In general, the charge currents for electrons (j_e) and holes (j_h) are analogous to Fick's law of particle diffusion and are given by the gradient of their electrochemical potentials $\eta_{e,h}$ (which is the sum of chemical potential and electrical potential = quasi-Fermi levels ϵ_F) [35]. The total charge current is then

$$j = \frac{\sigma_e}{e}\mathrm{grad}\eta_e - \frac{\sigma_h}{h}\mathrm{grad}\eta_h \tag{2.2}$$

$$= \frac{\sigma_e}{e}\mathrm{grad}\epsilon_{F,e} + \frac{\sigma_h}{h}\mathrm{grad}\epsilon_{F,h}, \tag{2.3}$$

which holds true with and without the presence of electric fields in the absorber. $\sigma_{e,h}$ is the conductivity for electrons/holes, e is the elementary charge, $\epsilon_{F,e}$ is the quasi-Fermi level for electrons and $\epsilon_{F,h} = -\eta_h$ the quasi-Fermi level for holes. The generation of charge carriers is given by eq. (2.1) and their charge flow (current) by eq. (2.3). If the concentrations of electrons and holes are spatially uniform, the electric field can be the only driving force on the charge carriers – then the 'diffusion' current is zero and the flowing current is solely a 'drift' current [35]. Besides charge flow into terminals, another rate that reduces the amount of excited charge carriers after absorption is recombination, as discussed in the following.

The description of how a device based on the studied semiconductor behaves can be captured by rate equations, for establishing simple pictures of charge carrier dynamics. This section describes the usually considered recombination mechanisms that are part

of the rate equations. Once free electrons and holes are created inside the semiconductor after optical absorption with a generation rate G, their energy seeks to be minimized. An electron in the conduction band carrying the energy $h\nu - E_g$ will firstly dissipate it to the surrounding crystal by creating lattice vibrations (heat), until its energy reaches values close to E_g. This process is called 'thermalization' and is considered to take place within a several orders of magnitude shorter time than the recombination processes following afterwards, as detailed next. If the electron subsequently occupies a hole in the valence band by skipping the bandgap ('band-to-band recombination'), it releases a photon with an energy near E_g. This process is called 'radiative recombination' and its rate is a material parameter (bimolecular recombination coefficient) which determines how bright the material luminesces upon excitation of charge carriers. In light-emitting diodes (LEDs), this rate is the main figure of merit for their brightness. As elaborated below, it also determines how efficient a solar cell can be. Since both charge carriers are involved, the rate scales with the product of electron density n and hole density p (thus, in intrinsic semiconductors with $\propto n^2$). This type of recombination is also referred to as bimolecular, direct or second-order.

If there are energetic states inside the bandgap that electrons or holes can occupy ('defects'), the radiative recombination rate is reduced by 'non-radiative', or 'Shockley-Read-Hall' (SRH) recombination [36] (sometimes also called monomolecular, trap-assisted or first-order recombination). This non-radiative recombination rate generally reduces solar cell performance and depends on the number and energetic position of the defects, as well as their capture cross sections. Since electrons and holes can be captured by defects with the same rate if the defect lies in the exact middle of the bandgap, such a 'midgap defect' leads to the strongest loss of free charge carriers. Contrary, a charge carrier can easily escape a 'shallow trap' state that is close to a band edge, when it carries a certain thermal energy. The SRH recombination rate scales proportionally to the carrier density ($\propto n$). The proportionality factor is a figure of merit for strength of non-radiative losses, either expressed as a rate at which this recombination process is happening, or as a lifetime value, the inverse of the rate. Another rate competing to radiative recombination is surface recombination R_{surf}, that is described by a surface recombination velocity S_{surf} in units of cm/s: $R_{surf} = S_{surf}(n - n_0)$, where n_0 accounts for the equilibrium charge carrier density in the dark (in cm^{-3}). R_{surf} is a value for charge extraction across an interface[1]. High surface recombination rates are the major challenge for high-efficiency PSCs, as discussed in section 2.4.2 and chapter 4.

Another form of non-radiative recombination occurs when the band-to-band energy is transferred to a third charge carrier instead of emitted via a photon (Auger recombination). The rate of this process scales with n^3. For silicon cells, Auger recombination is of special importance, because it limits the maximum achievable efficiency [20], whereas

[1] If considered for minority carriers, it represents a loss channel, while it can also be referred to the extraction 'speed' of majority carriers for which a high value is desirable.

for perovskite solar cells (PSCs), Auger recombination does not play a role for operation under non-concentrator, terrestrial application.

In summary, the density of free charge carriers can be described by the following rate equation for the time derivative, which is often useful in describing transient experiments:

$$\partial_t n(t) = G - R \tag{2.4}$$

$$= G - \frac{1}{\tau} n - \beta n^2 - C n^3 - S_{\text{surf}}(n - n_0). \tag{2.5}$$

G is the generation rate of free carriers, τ the SRH lifetime, β the bimolecular recombination coefficient and C the Auger coefficient. While Auger and SRH recombination are in principle avoidable, radiative recombination is thermodynamically required and dominates in good solar cells. C and β are material constants and can determine how well a material is potentially suited for making a solar cell. τ is a measure for the amount of non-radiative recombination that takes place in the material, which usually depends on the amount of defects in the material and nature of the surfaces. If charge flow needs to be considered as well, eq. (2.5) can be subtracted by the divergence of eq. (2.3), such that for one carrier type: $\partial_t n_e(t) = G_e - R_e - \text{div} j_e$. Typical values for metal halide perovskites used for solar cells are 100-1000 ns for τ, 3-6 $\times 10^{-11}$ cm^{3}s^{-1} for β and roughly 1×10^{-28} cm^{6}s^{-1} for C [37, 38].

2.2.1 Photoluminescence and radiative efficiency

In equilibrium, the charge carrier distribution of an intrinsic semiconductor is sufficiently described with one value for the Fermi energy level. However, under illumination, the electron density increases in the conduction band and likewise the hole density in the valence band. Both distributions follow two separate Fermi-Dirac statistics with two different 'quasi' Fermi levels. By the photoelectric effect, this creates an internal voltage equal to the difference between both Fermi levels (or chemical potentials) divided by the elementary charge. This value determines the maximum voltage that could be externally measured in a device at the given illumination intensity and indicates the relation of recombination rates. Radiative recombination and the corresponding luminescence (or "non-thermal radiation") can be a useful measure to draw conclusions about the quality of the material and its usability in solar cell devices, as used throughout this thesis. Hence, the fundamentals of photoluminescence (PL) are important for solar cells and thus covered below.

Every solid material of non-zero temperature emits electromagnetic radiation. Planck's law of thermal radiation describes the spectral intensity of a blackbody with absolute temperature T by [35, 39]

$$\phi_{\mathrm{BB}}(E) = \frac{2n_0^2E^2}{h^3c^2}\left[\exp\left(\frac{E}{kT}\right) - 1\right]^{-1} \approx \frac{2E^2}{h^3c^2}\exp\left(-\frac{E}{kT}\right), \tag{2.6}$$

where k is the Boltzmann constant, n_0 the refractive index of the medium, E the photon energy and ϕ_{BB} the number of photons per unit time, area and energy interval into a solid angle ($\pi \cdot \phi_{\mathrm{BB}}$ gives the photon flux as Lambertian emission, $4\,\pi \cdot \phi_{\mathrm{BB}}$ the emission into all directions). The approximate expression on the right is called the Boltzmann approximation, which holds if the exponential term dominates in the denominator ($kT << E$).

Kirchhoff has derived the equivalence at each wavelength between emission and absorption of black body radiation [40]. This means that a photon of certain wavelength λ can only be absorbed if it can also be emitted with the same λ. In fact, this "Principle of Detailed Balancing" has proven useful in theoretical thermodynamics [41] and says that a microscopic process or energetic transition is only possible if its reverse process is given as well. The principle follows from the conservation of energy [42] and was utilized by Shockley and Queisser to elegantly calculate the maximum efficiency potential of solar cells. The theory was later extended to not only cover thermal radiation, but also luminescence [23]. P. Würfel has thereby connected an internal property of the semiconductor, namely the splitting between electron and hole quasi Fermi levels (Quasi Fermi level splitting, QFLS) with an externally accessible measure, the intensity of luminescence.

On the basis of Planck's law of thermal radiation, Würfel studied light-matter interaction and derived a generalized formula (describing both thermal and luminescent radiation) for the flux[2] of photons emitted by a material with QFLS μ depending on the photon energy E:

$$\phi(E) = \frac{E^2a(E)}{4\pi^2\hbar^3c^2}\left[\exp\left(\frac{E-\mu}{kT}\right) - 1\right]^{-1}. \tag{2.7}$$

Here, $a(E)$ is the absorptivity of the material and T is its temperature. The emission of only black body radiation is a special case of this equation, with $a(E) = 1$ and the μ set to zero, describing a system without two separate states that form an optical transition [23]. In the derivation, the photons were assigned a chemical potential equal to the QFLS. If it is an external voltage V that creates a QFLS instead of optical excitation, the term μ can be replaced by eV. When the absolute intensity of the emitted photons is known, the QFLS can be calculated. The QFLS is the upper limit of energy in a material (or solar cell) from which work can be extracted.

Using the detailed balance principle (implying the reciprocity of emission and absorp-

[2] This formula is in units of number of photons per energy, area and time at Lambertian emission. R. Ross has arrived to a comparable expression between QFLS and photon emission flux already in 1967 [22], albeit with a much shorter discussion of the implications.

tion [43]) and Planck's law of thermal radiation, R. T. Ross has derived a relationship between the ratio of emitted to absorbed photons (external photoluminescence quantum yield, PLQY) and the QFLS [22]:

$$\mathrm{QFLS} = \mathrm{QFLS}_{\mathrm{max}} + kT \ln(\mathrm{PLQY}), \tag{2.8}$$

$$\text{where } \mathrm{QFLS}_{\mathrm{max}} = kT \ln(J_{\mathrm{SC}}/J_0), \tag{2.9}$$

$$\text{and } J_0 = e \int_0^\infty a(E)\phi_{\mathrm{BB}}(E)\mathrm{d}E. \tag{2.10}$$

This relationship was derived from a basic thermodynamic consideration and is thus valid for every system that involves the interaction of radiation with an optical transition in matter (be it organic molecules or crystalline semiconductors), in equilibrium. Equation (2.8) is experimentally useful, because the measurement of PLQY only requires a setup that is calibrated with regard to its spectral sensitivity, as then the PLQY follows as a ratio between the PL counts of emitted to absorbed light. In contrast, calculating the QFLS with eq. (2.7) requires a system calibrated to absolute photon numbers.

Relevance for solar cells

$\mathrm{QFLS}_{\mathrm{max}}$ (eq. (2.9)) corresponds to the highest free energy that the material can hold. It rises with decreasing temperature and for a semiconductor of given bandgap E_{g}, $\mathrm{QFLS}_{\mathrm{max}}$ is largest when the absorptivity is a step-like function at E_{g}, as then J_0 is smallest. If the absorption onset deviates from a step-like function through, e. g., defect states in the bandgap or electronic disorder (higher Urbach energy), $\mathrm{QFLS}_{\mathrm{max}}$ reduces. The corresponding voltage $\mathrm{QFLS}_{\mathrm{max}}/e$ in a solar cell could only be reached if radiative recombination is the only relaxation process. The PLQY is a number between 0 and 1, therefore the QFLS is always smaller than $\mathrm{QFLS}_{\mathrm{max}}$. In non-perfect materials that contain trap states for charge carriers, non-radiative recombination lowers the PLQY (lower τ and thus lower ratio between second-order recombination and the sum of all recombination processes, eq. (2.5)). With the measured PLQY of a material or photovoltaic device, QFLS/e is an upper bound for the open-circuit voltage (V_{OC}) it can reach. The V_{OC} is the voltage the device reaches without any load, where charge carrier generation is in equilibrium with recombination. This makes the measurement of PLQY a convenient tool for quantifying the degree of non-radiative recombination and to determine the maximum potential of a solar cell. Typical PLQY values under 1-sun equivalent charge carrier densities of good metal-halide perovskite solar cells (around 20% power conversion efficiency) reach from 0.01% to almost 10% [37, 44].

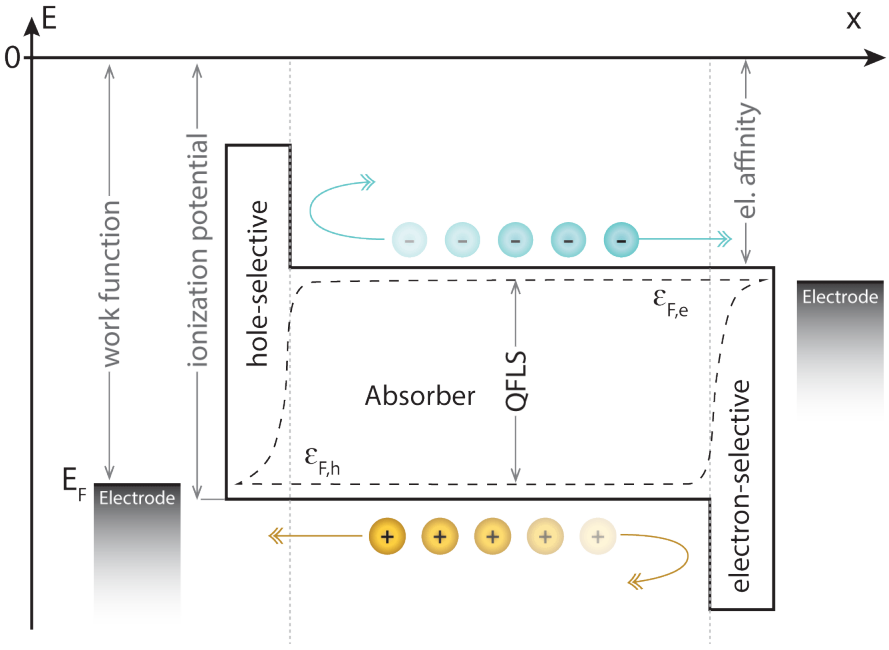

Figure 2.1: Energy-space scheme of an idealized heterostructure cell with labels of parameters that are typically used in discussions about charge-selective layers and solar cells. The larger bandgap semiconductors on each side of the absorber ideally are resistive to minority carriers and conductive for majority carriers. The energetic offset ensures that the minority carrier density in the charge-selective layers is small. This keeps the minority current density low despite the large gradient of their quasi Fermi levels (ϵ_F).

2.2.2 Charge separation

The conversion of the chemical energy that the electron-hole pairs carry into electrical energy requires the spatial separation of electrons and holes onto two different terminals before they recombine. This is possible via a strong enough gradient of the carrier density or electric field (or in summary, the quasi-Fermi levels), ideally via charge-selective layers interfacing the absorber. In general, charge selective layers[3] are materials that only let one type of charge carrier pass through, while being resistive to the other. Such layers were coined 'semi-permeable membranes' by Würfel [24] and earlier by Shockley [34]. In the general notion they are imagined by having a large conductivity for one carrier type and low conductivity for the other carrier type. For instance, a p-doped semiconductor would be considered a hole-selective layer if

[3]The term 'charge-selective layer contact' means the layer responsible for carrier separation at the interface. A 'charge selective contact' includes an interfacing metal-like material (electrode) that constitutes the electrical terminal and is covered by the charge-selective layer.

adjacent to its intrinsic version, if there is no energetic barrier for the holes to reach the p-type layer.

The typical way to let electrons and holes flow into different directions is by a gradient of their electrochemical potentials (quasi-Fermi levels) into correct directions, e. g., by forming a junction between strongly p- and n doped semiconductor material ('homojunction' if the same material is used for p and n). However, for a solar cell, this approach is not ideal, because it comes with two contradicting requirements for good cell operation [35]: 1) High minority carrier concentration under illumination (electrons in the p-doped region and vice versa) in order to achieve a high QFLS. 2) Low conductivity for minority carriers (and thus low minority carrier concentration), in order to be selective. One ideal cell design thus features two selective layers at each of the absorber interfaces, each being selective to a different charge carrier type. Such a 'heterostructure' architecture consists of three different semiconductor materials, with the charge-selective layers having a larger bandgap than the absorber layer, which also ensures that parasitic absorption is suppressed. To prevent charge carriers entering the wrong layer, an energetic barrier works efficiently by deflecting minority carriers, as depicted in Fig. 2.1. This way, the minority carrier concentration in the charge-selective layers is kept low (low specific conductivity), and thus, despite of the larger gradient for minority carriers inside the charge-selective layers, their current density is low [35]. The electrodes are ideally metallic and fix the Fermi levels at the surface, where both quasi Fermi levels ($\epsilon_{F,e}$ and $\epsilon_{F,h}$) meet.

2.3 Performance metrics and maximum efficiency of solar cells

Assuming that a device with photovoltaic material manages to separate holes from electrons, a diode model can describe the voltage-dependent behavior of solar cells well and it comes with the convenience of delivering intuitive pictures. A diode is a semiconductor element allowing for a charge carrier current to flow in only one direction. The current density J flowing through is

$$J = J_0 \exp\left(V/V_{\mathrm{th}}\right), \tag{2.11}$$

with J_0 being the reverse saturation current and V_{th} the thermal voltage, $V_{\mathrm{th}} = k_{\mathrm{B}}T/e$. In the diode picture, J_0 is the current density that flows in reverse direction, due to charge carriers that were thermally excited. In thermal equilibrium, these charge carriers are generated by the black body radiation of the surrounding with temperature T. Thus, J_0 also depends on absorption characteristics of the material, as given by eq. (2.10).

Under the considerations of detailed balance that recombination must equal genera-

tion, Shockley and Queisser calculated current-voltage curves of solar cells that almost fit to the experimentally measured ones [34, 45]:

$$J(V) = J_{SC} - J_0 \left(\exp\left(\frac{eV}{kT} \right) - 1 \right). \tag{2.12}$$

This formula only includes radiative recombination as the only carrier relaxation mechanism. To describe non-ideal solar cells more closely, J_0 also includes non-radiative recombination losses when the real absorptivity or external quantum efficiency is used in eq. (2.10). Resistive losses can be accounted for by extending the formula to:

$$J(V) = J_{SC} - J_0 \left(\exp\left(\frac{e(V - JR_s)}{n_{id} kT} \right) - 1 \right) - \frac{V - JR_s}{R_p}. \tag{2.13}$$

n_{id} is the diode ideality factor that corrects the exponential slope of the ideal model. It is $n_{id} = 1$ in the "ideal" case, when radiative recombination largely dominates. For only trap-assisted recombination, it is $n_{id} = 2$ and for only Auger recombination, the ideality factor takes the value 2/3 [35]. Realistic solar cells show values between 1 and 2. Most perovskite solar cells with high efficiencies show ideality factors of $1.4 - 2$ and the exact interpretation is often not straight-forward; only in special cases conclusions about the underlying recombination mechanisms are possible [46–48]. R_s is the series resistance, at which part of the applied voltage drops, which becomes more severe the higher the current density J is. R_p denotes the parallel resistance (or also called shunt resistance) and refers to a hypothetical resistance connected in parallel to the diode. The higher R_p, the more resilient the device is to currents flowing through shunts instead of delivering electrical power.

Solving eq. (2.12) after V, for the case of zero net current, where total recombination current density equals the generation current density J_{SC}, one obtains the open-circuit voltage V_{OC}:

$$V_{OC} = \frac{kT}{e} \ln\left(\frac{J_{SC}}{J_0} + 1 \right). \tag{2.14}$$

For very good solar cells, the V_{OC} value is a few 10 mV below QFLS_{max}/e, which in turn usually lies 200-350 mV below E_g/e, at room temperature. These regimes have been achieved with perovskite solar cells already, showing deficits of only 60-70 meV [44, 49].

The power conversion efficiency (PCE) of a solar cell is defined as the ratio between output electrical power and incoming radiation power density P_{in} and reads:

$$\mathrm{PCE} = \frac{|\max(J \cdot V)|}{P_{in}} = \frac{J_{SC} V_{OC} FF}{P_{in}}, \tag{2.15}$$

where FF is a unit-less geometrical factor of the $J-V$ curve, expressed by

$$FF = P_{\mathrm{max}}/(J_{\mathrm{SC}}V_{\mathrm{OC}})),$$

where P_{max} is the maximum extractable power density of the cell, being the product of current density J_{MPP} and voltage V_{MPP} at the cell's maximum power point (MPP). The FF indicates how closely the curve resembles a rectangular shape. For good solar cells, the value lies between 0.8 and 0.9. For silicon ($E_{\mathrm{g}} = 1.12\,eV$), the detailed balance FF limit[4] is 87%, with the best Si solar cell already achieving up to 84.9% [14]. The highest experimental FF (at 1-sun equivalent illumination) has been achieved with epitaxially grown GaInP, with a value of 90.2% at a detailed balance limit of 91.9%. With PSCs, high values were only recently achieved, with a maximum FF of 84.8% in the current record device [14], while the theoretical maximum lies at 90.2% (at 1.55 eV bandgap, it generally increases with the bandgap).

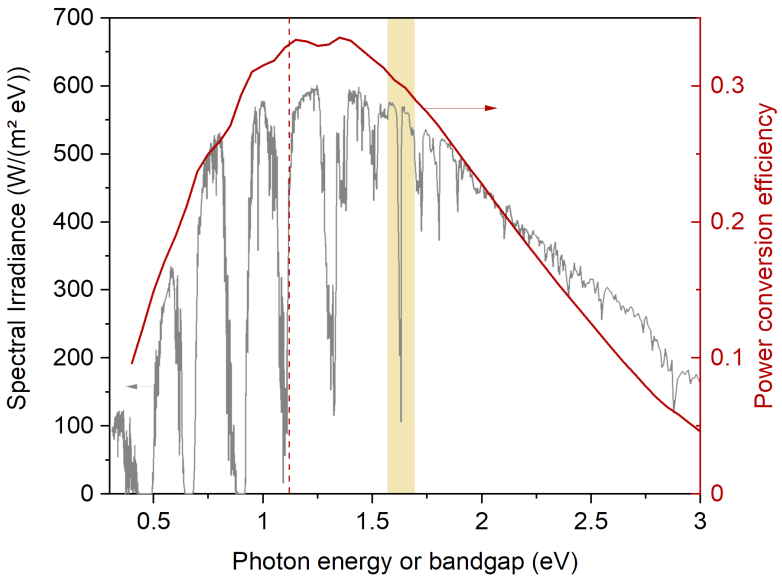

Figure 2.2: Solar irradiance spectrum AM1.5G versus photon energy (left axis, gray line) and maximum solar cell efficiency versus material bandgap (right axis, red line) calculated via the detailed balance limit with the AM1.5G spectrum at a cell temperature of 300 K. The dashed line marks the bandgap of silicon and the yellow rectangle marks the range of bandgaps for perovskite solar cells used in this work. The spectrum data is from the National Institute of Standards and Technology (NIST).

The above considerations allow for an estimation of the maximum efficiency a solar cell featuring a material of bandgap E_{g} can achieve. It strongly depends on

[4] The high Auger recombination rate in silicon sets the lowest possible ideality factor to below 1, which leads to a maximum FF of 89.3%, higher than the detailed balance limit.

the spectrum of illumination and bandgap of the semiconductor material. It also changes with the cell temperature, solid angle of the illumination source and material properties such as Auger and bimolecular recombination coefficient. In terrestrial solar cell testing, the standardized solar illumination spectrum (AM1.5G) is taken as the reference, with ~100 mW/cm² incident irradiance. In an idealized scenario where only radiative recombination occurs, the maximum efficiency, the so called detailed balance limit for the PCE (or Shockley-Queisser[5] limit [45], or radiative limit) can be calculated. Both the standard terrestrial solar spectrum and detailed balance limit versus energy are shown in Fig. 2.2.

The maximum possible single-cell efficiency is thus 33.5%. For the Si bandgap, it is 33.4%, however, the Auger recombination rate in Si is limiting the possible PCE maximum to 29.4% [20]. In metal-halide perovskites, the Auger recombination rate is high as well, but partly compensated by the high radiative recombination rate, leading to a maximum possible PCE of 30.5% at 1.55-1.6 eV bandgap [50].

2.3.1 Current-voltage characteristics

The *J-V* curve reflects the above discussed cell parameters in its shape. Figure 2.3 shows simulated *J-V* curves with isolated variations of R_p, R_s and n_{ID}. The influence of R_p is most strongly visible near 0 V, where the slope of the curve can be used to estimate the value of it. R_s can be estimated by the slope at V_{OC}. The ideality factor determines the curvature around the maximum power point (The MPP is exemplary indicated in Fig. 2.3b), thus having a strong effect on the fill factor as well (see inset in Fig. 2.3c).

Low R_p values usually indicate a shunt or shortening between the contacts, where the generated current can flow through with a lower resistance than through the load. In thin-film solar cells, the shunt resistance is often a parameter that needs optimization, because a speck of dust can be enough to cause a spot in the active area which the absorber is not covering, thus creating a possibility of the electrodes touching each other. The more conducting the contact materials and the absorber are, the higher the shunt current and power loss can be. Loss of power also occurs through voltage drops across series resistances, which include contact resistances at interfaces, "internal" resistance of the absorber material and resistance coming from the conductivities of the electrodes.

The ideality factor can be determined by measuring the V_{OC} at different intensities, as it determines the slope via:

$$V_{OC} = \frac{n_{ID} kT}{e} \ln\left(\frac{J_{SC}}{J_0}\right). \tag{2.16}$$

[5] It is increasingly called 'detailed balance limit' due to Shockley's propagations and works on racial genetics.

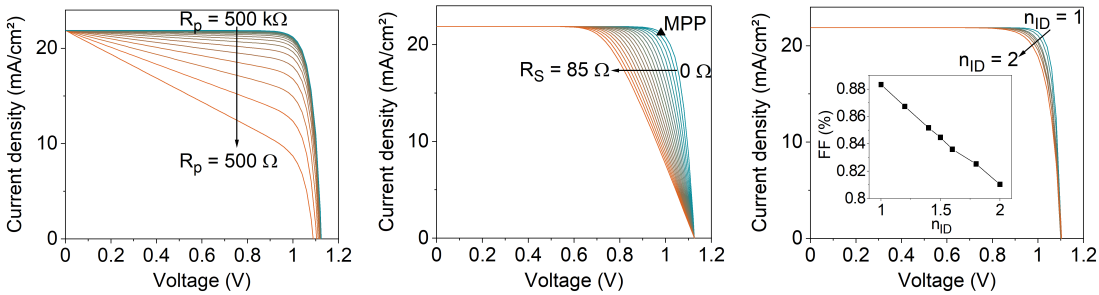

Figure 2.3: Solar cell JV curves calculated from eq. (2.13), showing the influence of parallel resistance (a), series resistance (b) and ideality factor (c). For (a) and (b), an ideality factor of 1.4 was used. In (b), the triangle marks the maximum power point for the 0 Ω curve. In (c), J_0 was tailored for each n_{id} such that the V_{OC} stays the same. The inset shows the fill factor of the displayed curves. The cell parameters were derived from a standard *p-i-n* PSC (see section 2.4) with 1.63 eV bandgap.

Additionally, n_{ID} determines the linear slope n_{ID}/V_{th} of the J-V curve obtained under dark condition, near V_{MPP}. If R_p is high enough and R_S low enough to not mask the slope given by n_{ID}, its value follows from the dark current J_D via

$$n_{ID} = \frac{e}{kT}\frac{dV}{dJ_D(V)}. \tag{2.17}$$

Near $V = 0$ V, the dark J-V curve is mostly influenced by the shunt resistance, whereas for low series resistances, R_s reduces the J-V slope above V_{MPP}. For higher R_s, the slope is already influenced below V_{MPP}, which makes the determination of n_{id} via intensity-dependent V_{OC} the more accurate method.

2.3.2 Tandem solar cells

According to Fig. 2.2, the maximum efficiency limit of a solar cell under AM1.5G illumination is 33.5% at a bandgap of $E_g = 1.35$ eV. The remaining power is lost due to a combination of transmission of photons that carry not enough energy and due to thermalization losses, i. e., energy lost as lattice vibrations from thermalizing electrons excited above the conduction band edge. Real solar cells additionally suffer losses coming from non-radiative and Auger recombination and non-perfect collection of the charge carriers [51].

One way to reduce the thermalization losses and use the solar spectrum more efficiently is to stack solar cells consisting of materials with different bandgaps. For of a cell made out of two stacked subcells, a tandem solar cell, the detailed balance limit calculation [52, 53] under AM1.5G spectrum yields a maximum of around 45% when

combining a 0.94 eV-bandgap bottom cell with a 1.61 eV top cell. This way, the absorbed spectrum is divided into the subcells that each deliver their power. Under direct series connection (monolithic configuration), the voltage of the subcells add up, while the current density is set by the smaller value. Thereby, under setting of optimal bandgap combinations, the single junction detailed balance limit can be overcome. Relying on Si for the bottom cell, the ideal partnering top cell needs a bandgap of ~1.72 eV [54, 55], which results in a maximum possible tandem cell efficiency of around 44 % under standard test conditions. Notably, this value assumes that the subcells fully absorb the light with energies above the step-like absorption onsets. If, e. g., the top cell absorber is not thick enough, the optimal bandgap shifts to lower values: For typical perovskite absorbers, the optimal value is near 1.68 eV and even lower when considering that solar cells experience elevated temperatures of >60 °C ([56, 57]).

Two subcells can either be independently completed and stacked mechanically on top of each other, or the top cell can be processed on top of the topmost layer of the bottom cell, such that both cells share a common contact (monolithic). In the first approach, both subcells can be independently adjusted (usually called "4-terminal" cell) and thus dynamically optimized for maximum yield over the course of the day, depending on the light spectrum. For characterization, both subcells have to be measured, with the top cell simply acting as a filter for the bottom cell, and their efficiencies add up. In the monolithic case ("2-terminal"), the subcells are connected in series, hence their voltages add up, but they share the same current flow – the tandem current density is given by the limiting cell, i. e. the one with the lower current density. Thus, for maximum efficiency, in the monolithic tandem cell, 'current matching' is of critical importance for efficient operation. It is, however, noteworthy that under current mismatch due to changing solar spectrum (over the course of the day), the tandem *FF* increases, dampening losses in total energy yield [58, 59]. Compared to the 4-terminal approach, monolithic tandem cells need one less transparent contact and one less inverter, thus the balance of system costs are considered to be lower. In an intermediate case, the subcells share one contact which can independently be voltage-controlled as an electrode ("3-terminal"). This approach can combine both advantages, lower complexity and lower sensitivity on spectral changes. However, experimental demonstrations are still in the proof-of-concept phase [60, 61].

Experimentally, combinations of III-V semiconductors have already proven that multi-junction solar cells can surpass the single junction detailed balance limit, with a maximum value of 38.8% for a 5-junction cell [62] and 32.8% for the best 2-junction cell consisting of GaInP and GaAs [14]. However, the material costs and need for their slow, ultra-clean deposition via epitaxy of such systems prevents them from being economically relevant in large scale. Additionally, the global market and industry are already interspersed by silicon cell technology, which itself comes with a large abundance and already available engineering specialization for large scale. Thus, it is wise to search for

a material that can work in tandem with silicon while bringing economic benefit to the levelized cost of electricity. This is where metal-halide perovskite solar cells fill the gap.

2.4 Metal-halide perovskites

Perovskite denotes the generalization of the crystal structure of CaTiO3, which contains three different constituents in the formula ABX_3. For the class of metal-halide perovskites (MHPs), X stands for a halide, B for a divalent metal ion and A for a monovalent cation. A can be either an organic molecule or inorganic element, or a mixture of both, thus the material class is often called 'organic-inorganic metal-halide perovskite'. B sits inside an octahedron spanned by X_6, and A sits inside a cube made out of eight octahedra, as depicted in Fig. 2.4. Both X and B can also be a mixture of different elements. Often used constituents for A are Cs, K, methylammonium ($CH_3NH_3^+$) and formamidinium ($(NH_2)_2CH^+$). B is usually Pb^{2+}, Sn^{2+} or Ge^{2+} and X is often I^-, Br^- or Cl^-.

The original perovskite was first discovered by Gustav Rose in 1840 [63] and the first publication featuring an organic cation appeared in 1978 by Weber [64]. After a description of the semiconducting properties of a halide perovskite by Mitzi in 1994 [65], it took until 2009 when the first use of a MHP as a solar cell was published by the group of Miyasaka [15]. After this birth of PSCs, an unparalleled technological development followed with around 4000 publications in 2020 alone [66], and record PCEs rising from 3.8% in 2009 to 25.5% in 2020 [67], a faster development than for any other solar technology [13]. This speed was certainly nourished by the knowledge gained in mature technologies (Si, GaAs, CIGSe, CdTe) and the organic photovoltaics community concerning the available choice of charge-selective materials. In addition, it was accelerated by the favorable material properties of MHPs, as are discussed below.

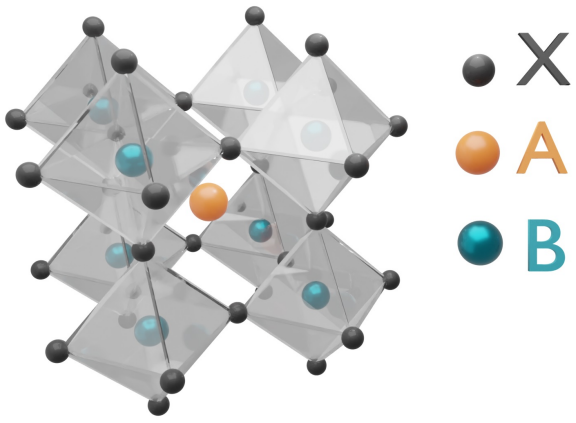

Figure 2.4: Schematic picture of the general perovskite crystal structure with composition ABX_3.

The versatility of compositions make MHPs a highly adaptable material class [68].

Importantly, by compositional tuning of the crystal elements, the bandgap is adjustable, mostly by tuning the X part [69, 70], while there is also an effect on the crystal unit size via compositional change at the A site [71]. Additionally, MHPs feature a series of desirable properties for both, efficient solar cell operation and potential low-cost scalability. Hence, they can be adjusted to work well as the top cell in tandem architectures with established, low-bandgap solar cell technologies like silicon or copper indium gallium Selenide (CIGSe). MHPs are ionic materials, thus the mobile species can lead to transient effects like current-voltage hysteresis [72] and descriptions resembling that of electrolyte cells or ionic conductors can be necessary [73, 74]. Nevertheless, with stable compositions and under low stress, MHPs can be described with basic semiconductor physics as intrinsic semiconductors with a direct bandgap[6].

2.4.1 Suitability for solar cells

MHPs combine several advantages for solar cell operation: High absorption coefficient, steep absorption onset [75] (indicating good crystal quality), tunability [68] and defect tolerance [76, 77]. The latter meaning that detrimental traps are less likely to form [77] and even at the presence of non-radiative recombination centers (traps, defects), the non-radiative recombination rate remains low [78]. In other high-performance solar cell materials such as GaAs and Si, the presence of small defect concentrations significantly deteriorate the device performance, which makes it necessary to fabricate them with high-temperature processes in ultra-clean environments and with high material purities. By contrast, MHPs require comparatively low temperatures for a sufficient crystal quality (~100 °C), can be processed from solution and due to their strong absorption only require small thicknesses (up to 1 µm, commonly 500 nm) to capture the full sunlight above the absorption threshold. This makes PSCs a high-efficiency thin-film technology, bringing the potential of resource-efficient fabrication and mechanically flexible modules.

Another prerequisite for good solar cells is a sufficient lifetime of the charge carriers after photo-excitation, so that they are able to reach the charge-selective contacts before they recombine again. In this regard, the thin-film character is beneficial, since the absorber thickness is smaller than the usual carrier diffusion length of around 1 µm [79, 80]. The combination of these properties led to record V_{OC} values just 70 meV short of the detailed balance limit [44, 49] and optical efficiency values ($J_{SC}/J_{SC,max}$) rivaling those reached with Si and GaAs [51].

[6] 'Direct' meaning that both the conduction band minimum and valence band maximum lie at the same momentum in the energy-momentum diagram. This is favorable for photoactive materials because of a possible large radiative recombination coefficient and strong absorption.

2.4.2 Perovskite solar cells: state of the art

Perovskite solar cells started with absorbers in liquid form [15], by applying typical device architectures of dye-sensitized solar cells, however, in this form suffered from severe instabilities. In 2012, the groups of Snaith and Grätzel have shown that efficient PSCs (~10%) can be processed with thin, solid perovskite films, using a Methylammonium (MA) lead iodide ($MAPbI_3$) composition in an architecture resembling a heterostructure [81, 82]. $MAPbI_3$ is still a widely used composition due to its simplicity. It was also found that it is possible to deposit the perovskite via co-evaporation using two evaporation sources that contain MAI and PbI_2 powders; such that the perovskite film forms from the gas phase on the substrate [83]. In 2014 and 2015, spray coating and slot die coating the perovskite precursor have shown to be a viable technique for upscaling as well [84, 85]. During that time and henceforth, emphasis was laid on tailoring of the precursor solution, leading to the discovery that higher-quality films can be formed with the usage of mixed solvents [86, 87] that encourage intermediate crystallization steps during film formation. Within this development, Jeon et al. found that the use of an anti-solvent to drive out the main solvents from the thin film leads to quick coordination and pre-crystallization during the spin-coating step, resulting in high crystal quality. Another key step was the insight that PSCs can work efficiently with thin organic layers at both absorber interfaces [88, 89]. Until then, PSCs relied on metal oxides as electron-selective layers, which needed high-temperature processing and/or delicate fabrication.

The combination of a number of optimized deposition and solvent engineering techniques called for developmental milestones in the crystal composition of the perovskite absorber. After the introduction of mixed cations and halides [90–92], in 2016 Saliba et al. found an enhanced device performance and reproducibility upon the addition of Cs into a mixed MA/FA perovskite composition [93]. This composition was termed "triple-cation" perovskite and gained strong popularity. In another step, "quadruple-cation" compositions (containing MA, FA, Cs and Rb) showed increased efficiency and that perovskite thin-films can be highly customizable and complex [94]. Because of its high reproducibility and decent performance in PSCs, the triple-cation recipe is what forms the basis of PSC fabrication in this thesis (see chapter 7 for experimental details). Highest efficiencies have been reached with mostly the $FAPbI_3$ composition (with only a small amount of MA used as an additive) due to its lower bandgap (1.5-1.55 eV) [49, 95], while the triple-cation compositions were used for tandem-applications due to their simple tunability at higher bandgaps. In chapter 4, solar cells based on three different compositions are shown: 1.63 eV triple-cation "CsMAFA", 1.55 eV double cation "MAFA" and single cation $MAPbI_3$. In chapter 5, the tandem-optimal bandgap of 1.68 eV is explored with CsMAFA containing a higher MA and Br loading.

Currently, several perovskite deposition techniques are being used, of which spin-coating is most widely adapted for fast compositional optimization. At the same time,

co-evaporation techniques and wet-chemical processing like slot-die-coating are being rapidly refined for upscaling PSC fabrication or for conformally depositing perovskite films on rough or textured substrates [96–98]. Increasingly, the operational stability of PSCs is in the focus of research, now that high efficiencies are established and PCEs of >20% are considered standard in many laboratories. For stability testing, a number of different protocols were used in literature, with a consensus on how to unambiguously quantify stability only recently forming [99]. This includes the continuous measurement of the maximum power output (MPP tracking) either under controlled temperature (25° for standard condition, 60° or 85° for accelerated aging) and atmosphere or in ambient air with humidity tracking. Importantly, the spectrum of the lamp used for aging should be known, because different transport layers and perovskite compositions react differently depending on the wavelengths of light illuminating them.

Architectures

During the developments of PSC technology, two general architectures were established: The "regular" *n-i-p*, and "inverted" *p-i-n* configuration (see Fig. 2.5). The first letter in the heterojunction denotation refers to the type of charge-selective semiconductor layer on which the perovskite film is deposited, with *p* meaning hole-selective and *n* electron-selective. The *n-i-p* architecture was employed in the first thin-film PSC [81], relying on TiO_2 as the electron-selective layer, and is still the more popular choice among laboratories, possibly due to the PCE records being achieved in *n-i-p*.

Considering tandem solar cells, the *p-i-n* architecture is the more frequent and rational choice [56, 100], because of lower parasitic absorption losses and low-temperature processing of high-efficiency devices (>20%). While the first perovskite/silicon tandem solar cells were fabricated with *n-i-p* PSCs [18, 101], the surge in their efficiency to >23% came with the switch to *p-i-n* top cells [100, 102]. *p-i-n* top cells are still the standard in high-efficiency tandems at >29% PCE. To this day, the single-cell efficiency record with silicon could only be surpassed with *p-i-n* perovskite top cells. Furthermore, the *p-i-n* PSC architecture comes with less complicated, low-temperature processing, less transient effects in their operation [103, 104], superior long-term stability due to the absence of dopants in the charge-selective layers [105–107] and compatibility to flexible substrates [108, 109]. As standard charge-selective layers, the polymer poly(bis4-phenyl2,4,6-trimethylphenylamine) (PTAA) acts as the hole-selective layer (typical thickness 5-15 nm) and fullerene based layers (such as C_{60} and $PC_{61}BM$ (Phenyl-C61-butyric acid methyl ester)) topped by a buffer layer and metals (Cu, Ag) form the electron-selective contact [88, 103].

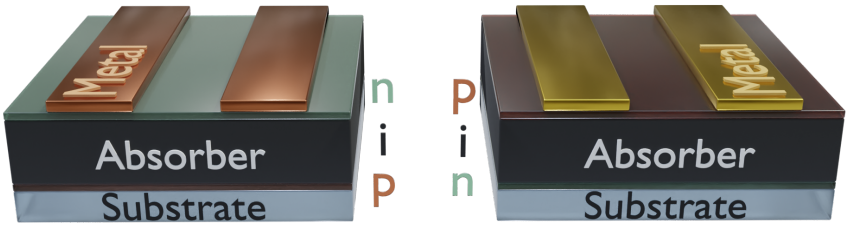

Figure 2.5: Schematic drawing of the two main perovskite heterojunction cell configurations, *p-i-n* (or "inverted") on the left and *n-i-p* ("regular") on the right. The sunlight enters the cell through the bottom.

Operational stability

Some of the ionic constituents of halide perovskites are mobile at room temperature and have low activation energies for movement [110] (in the order of 0.5 eV). In particular, iodine I^- is a highly mobile species and was often subject to investigation regarding its role in hysteresis phenomena and defect migration [111–113]. Since ions carry charge, their movement is influenced by electrical biasing, and in turn their migration and accumulation can affect the electrical potentials throughout the device. Even without electrical biasing, light or excited charge carriers are a driving force for ion migration and decomposition as well [114–116]. This can lead to dynamic behavior of the material, generally causing transient electric effects and instabilities in device operation [73]. A prominent consequence is current-voltage hysteresis [72], meaning that the value of measured current upon voltage bias scanning depends on the scan direction. This is more pronounced in *n-i-p* cells than in *p-i-n* cells, but can be tackled with additives or passivation of the charge-selective interfaces [117].

The magnitude of these issues rises with temperature [118], which, considering that solar cells can reach operating temperatures of over 80 °C in summer weather, is a serious challenge that is being increasingly addressed in literature. Several strategies have been suggested to overcome thermal instabilities, the main one being changes in the absorber composition to reduce the volatile MA content [119] or to entirely avoid organic components [120]. Other sources of instability concern the perovskite's sensitivity to humid air and that it can be dissolved by water. Upon contact with water, the absorber decomposes into PbI_2 and loses its photoactive properties [121]. Oxygen can also promote a faster degradation [122]. To overcome these sensitivities, considerable effort was invested into barrier design [123, 124] or how to make the perovskite absorber contain an intrinsic barrier by additives in the precursor solution [125, 126]. However, a noteworthy insight is that $MAPbI_3$ powder in the photoactive black phase can behave intrinsically stable in air and under high temperatures (> 200 °C) if synthesized mechano-chemically [127]. Once the powder is dissolved for

spin-coating thin-film devices, the absorber behaves unstable again. This difference might be explainable by the influence of strain in the film or crystals [128, 129], or remaining residues of solvent phases.

Despite these culprits, state-of-the-art perovskite compositions like the multiple cation recipes or low-bandgap compositions containing a high FA amount already show acceptable stability for laboratory stress tests [49, 93, 94, 130]. In their case, it became clear that the interfaces between perovskite and charge-selective layers also influence the device stability [131–136]. Importantly, strain at the interfaces can also be influenced by the choice of charge-selective layers [137]. Combining these insights even led to demonstrations of PSCs passing industrial standard stability tests (85 °C at 85% humidity for 1000 hours) [125, 138].

Nevertheless, the mitigation of instabilities, particularly under continuous operation, is still a major challenge for the commercialization of PSCs. And since the community increasingly shifts their focus from pushing efficiency to enhancing and understanding stability, major progress is expected in the coming years to improve operational stability towards the standards of commercial application. Especially larger-bandgap compositions that often contain an increased ratio of bromide to iodide tend to form separate phases, resulting in the perovskite having iodide- and bromide-rich film domains – a phenomenon known as phase segregation [139, 140]. This process implies the migration of ions, which can only happen in the presence of defects (or its inverse movement, the migration of ionic vacancies) [141, 142]. Since grain boundaries of the (poly-crystalline) perovskite film commonly are defective, phase segregation especially happens or begins there [143]. Thus, the nanostructural properties, film morphology and their impact on phase stability is a dedicated field of study [120, 144]. Interestingly, the interfaces to charge-selective layers can dictate the phase stability as well, as found in the results to chapter 5 and reported by others [116, 118, 145].

The usage of lead

The solar cell-relevant perovskite compositions are water-soluble and a perovskite solar module would contain up to 1 g of lead per square meter [146]. Although seeming like a small amount, dissolution into the environment through, e. g., flooding or extreme weather events must be prevented, considering the toxicity of some perovskite compounds and that lead accumulates in living beings and plants [146]. Several suggestions to mitigate this problem have been proposed and an entire research branch is actively researching on the replacement of lead through tin. Tin-based PSCs significantly lack behind their lead counterparts in stability and efficiency, and it is yet under debate whether the usage of tin can truly offset the environmental impact when considering the complete life cycle of PSCs [147, 148]. Meanwhile, a popular option is to stay with lead-based PSCs due to their yet unique optoelectronic quality and to further

invest efforts into techniques that capture lead in the case of leakage, either via special encapsulation [149] or design of the charge-selective layers [150].

The role of interfaces

The best demonstrated optoelectronic qualities of halide perovskite thin films and single crystals have reached levels comparable to ultra-clean samples of established semiconductor technologies like GaAs. This manifested itself in PLQY values approaching radiative limits [151, 152] and charge carrier lifetimes commonly reaching several µs. However, these properties were only measured in bare films and not full devices. This discrepancy led to studying the impact of interface recombination on the difference between maximum possible V_{OC} derived from the absorber alone and experimental V_{OC} values. Sarritzu et al. therefore decoupled recombination currents from interfaces and the absorber bulk by intensity-dependent, calibrated photoluminescence (PL) measurements to measure the impact of each on the QFLS [153] (see Fig. 2.6). They concluded that while the QFLS in the bulk is dictated by trap-assisted recombination, non-radiative recombination at the interfaces to charge-selective layers limits the QFLS of the full solar cell stack.

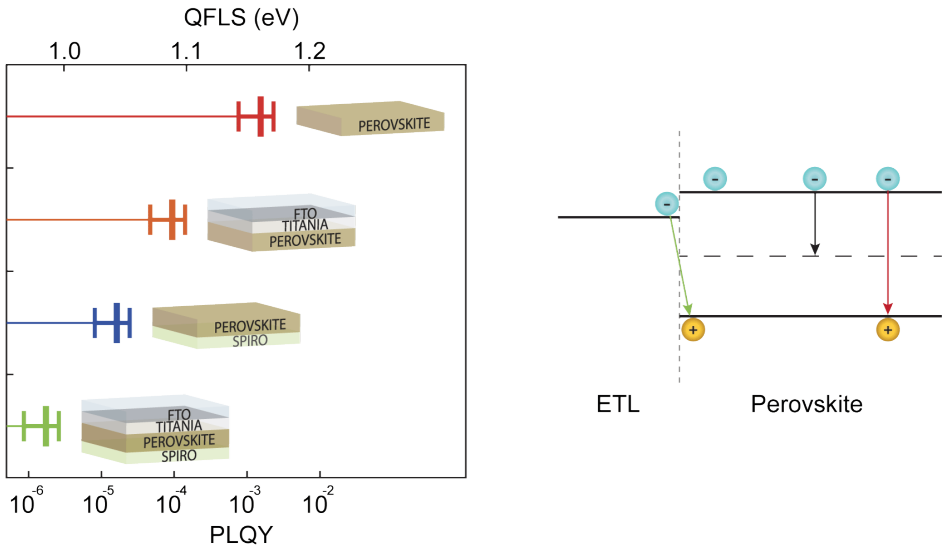

Figure 2.6: QFLS and PLQY values for perovskite/charge-selective layer stacks, showing that the charge-selective reduce the free energy by non-radiative recombination (left). The drawing on the right shows recombination processes in the heterojunction between perovskite and electron-selective layer (ETL): radiative recombination as the origin of PL (red arrow), bulk SRH recombination (black arrow) and interfacial recombination (green arrow). Reprinted with modifications from ref. [153] and CC BY - published by Springer Nature.

In principle, these losses are avoidable upon reduction of the minority carrier concentration at the interfaces. Building on this, Stolterfoht et al. studied *p-i-n* PSCs with absolute PL and confirmed the method's validity by V_{OC} measurements of full devices [154]. The interface losses could be reduced by the insertion of thin ($\approx$ 1 nm) layers between PTAA/C_{60} and perovskite, leading to >21%-efficient devices with V_{OC}s (1.17 V) approaching the QFLS of the bare perovskite (1.22 eV). The same group later generalized the insight that PSCs are limited by interfacial recombination with a study comprising both architectures, different perovskite compositions and ten different charge-selective layers that are commonly used in research [155]. All studied layers introduced losses compared to the bare perovskite. The standard hole-selective layer since its introduction in *n-i-p* cells, Spiro-OMeTAD, showed notably low losses, which might explain why *n-i-p* cells had higher V_{OC} values throughout the PSC developments [46]. The search for lossless charge-selective layers for PSCs is thus an important quest for the perovskite community. In chapter 4, this thesis introduces a hole-selective layer (2PACz) for *p-i-n* PSCs with these desirable properties.

Passivating layers

The benchmarks in PLQY measurements were only reached upon passivation of the perovskite film surface, with the most effective method being covering the surface with trioctylphosphine oxide (TOPO) [152]. Originally used as ligands for the synthesis of InP quantum dots [156], the TOPO molecules are believed to bond with the perovskite surface at halide vacancies that otherwise act as non-radiative recombination centers [157, 158]. Unfortunately, TOPO is not conductive or charge-selective, thus it does not function as a replacement for common charge-selective layers (which all introduce non-radiative recombination). In fact, materials that passivate an interface and do not hinder charge transport at the same time are rare. If processed as a very thin layer (a few nm), poly(methyl methacrylate) (PMMA) has shown to work as such a layer in PSCs [119, 159, 160]. The authors explain the improved performance by retarded crystallization of the perovskite layer through formation of intermediate compounds, or by the PMMA doing an electronic passivation of Pb^{2+} ions at the surface.

However, the PMMA layer was processed from solution by spin-coating. Considering the small thickness needed to not increase series resistance, this delicacy is hard to scale up. Evaporation of passivating interlayers is more promising in this regard, and of the commonly known interlayer materials in PSC literature, LiF seems to be most effective in reducing non-radiative recombination while keeping a high *FF* [154, 161, 162]. The exact mechanism of how LiF functions as a voltage-enhancing layer is still under debate. Recent studies presume that it might induce a dipole-like energetic barrier at the perovskite surface adjacent to the electron-selective layer, which hinders holes from entering the layer where they would otherwise be lost upon recombination with electrons [163, 164].

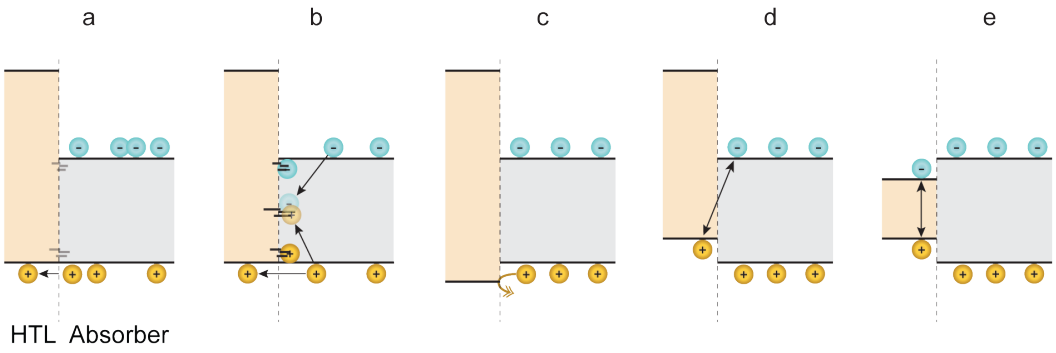

Figure 2.7: Schematic representation of absorber/hole-selective layer (HTL) interfaces, to illustrate different examples of unfavorable situations that reduce the V_{OC}, compared to the ideal situation. (a): high defect density at the interface (b), barrier for the majority carriers (c), offset for majority carriers, reducing the maximum possible QFLS (d), low selectivity due to the HTL also accepting electrons (e). Another dimension to consider (except for very thin layers of roughly <5 nm) is the specific conductivity of the hole-selective layer material, which can cause losses as well if it reduces permeability for majority carriers or is not resistive enough for minority carriers. The role of the Fermi level of the electrode (on which the HTL is on, not shown here) is discussed in section 2.5 and chapter 4.

Overall, the perfect charge-selective layer would be 1) impermeable by minority carriers, 2) without inducing resistance to majority carriers, while 3) having a passivation function at the absorber interface (or least not introducing any interface traps). Point 1 can be realized by an energetic barrier for minority carriers coming from the valence or conduction band of the absorber, with the bandgap of charge-selective layers usually having higher E_g than the absorber. With organic charge-selective layers, an asymmetry of electron and hole mobility can be realized with materials where the orbital overlaps differ in the HOMO and LUMO (highest occupied molecular orbital and lowest unoccupied molecular orbital, respectively) [165], as detailed further in the section below. Both effects keep the minority carrier density low in the contact, which ensures low non-radiative recombination losses. Point 2 is feasible by making the layer either highly conductive for one carrier type by doping, or by making the extracting layer very thin, such that conductivity does not play a role anymore. However, doping of charge-selective layers has been shown to induce instabilities in perovskite cells [105, 106, 166, 167] and it requires highly optimized processing, which together with the additional savings of trimming material usage favors the strategy of making the layers as thin as possible. For the third point there exists no fundamental guideline, because the exact defect formation mechanism at interfaces is intrinsically hard to probe and it is yet unclear how the interaction between the perovskite interface and charge-selective materials influences non-radiative recombination losses. In addition, it is generally ad-

vantageous when the majority carrier-accepting energy level (conduction/valence band onset, or HOMO/LUMO) is with minimal offset to the respective valence or conduction band edge of the absorber. If there is an offset towards higher energy for majority carriers, they experience a barrier; and if the offset is towards lower energies (i. e. step upwards for holes and step downwards for electrons), it might increase carrier collection speed, but decrease the maximum possible V_{OC} by that offset. This has partly held true for PSCs as well [155, 168, 169]. For fulfilling points 1 and 2 and for systematically exploring point 3, charge-selective layers made from self-assembled monolayers are a favorable choice, as explained below. In this thesis, several hole-selective monolayers were studied which were key for reaching highly efficient *p-i-n* PSCs and tandem cells.

2.5 Self-assembled monolayers

A self-assembled monolayer (SAM) is a layer made of organized molecules that bonded to a surface autonomously by self-assembly. The elegance of this approach for functionalizing surfaces lies within the idea to encode the function of the macroscopic layer into the design of a single molecule. The macroscopic layer then forms in a self-limiting process [170]: Once all bonding sites on the surface are occupied, the formation of the SAM is complete, yielding a reproducible layer with a thickness of only a molecule. The first report of a SAM appeared in 1946 by Bigelow et al., investigating the adsorption on a metal surface [171]. After the pioneering study of Aviram and Ratner in 1974 that showed how organic molecules can rectify current flow for eventual use in electronics [172], several studies followed studying the electronic properties of organic monolayers [173, 174]. It took until 2004 when the impressive demonstration of SAM-based electronics revived hopes that organic electronics may become an alternative path to the efforts of down-scaling silicon electronics into quantum-mechanical regimes [175]: Halik et al. built thin-film transistors featuring a SAM as the gate dielectric, which despite its thickness of only 2 nm led to leakage currents as low as in mature Si-based devices. In a further study, SAM-based inverters and logic gates were demonstrated as well [176].

The rectification in single organic molecules was studied and published in several reports with some intriguing results. Organic molecules that are conjugated (i.e., alternating single and double hydrocarbon bonds creating delocalized states for excited charge carriers) behave as semiconductors where the 'highest occupied molecular orbital' (HOMO) is roughly equivalent to the valence band maximum in inorganic semiconductors and the lowest unoccupied molecular orbital (LUMO) to the conduction band minimum. The delocalization of electrons in the molecules and the engineering of energy levels makes molecular electronics possible [174]. Briefly, one can exploit fundamental asymmetries of the molecule itself, the energetic offsets between orbitals of adjacent molecules or the offset between molecular orbitals and band edges of adjacent

semiconductors. When interfacing a metal instead of a semiconductor, the energetic offset between the orbitals and the metal's Fermi level is the determining parameter. In addition, molecules can carry a dipole, which shifts the work function of the substrate [174, 177] – a powerful tool for modifying the functionality and suitability of metallic or semiconducting surfaces.

Some of the insights of organic molecular electronics have implications for how to interpret parts of the results of this thesis. Strikingly, by favorable offsets between HOMO/LUMO and the Fermi level of the adjacent metal or semiconductor, a resistance of several megaohms for flowing electrons has been demonstrated through a single molecule [178, 179] of roughly 1 nm size. An inorganic layer of that thickness would be considered an easily permeable barrier for tunneling electrons. This underlines the potential for charge selectivity, considering the following scenario: If alignment can be ensured between, e.g., the HOMO level of the molecule and the Fermi level of the adjacent metal, charge selectivity becomes possible through "resonant" transport [180, 181]. If from a charge reservoir (consider a free charge-creating photovoltaic absorber) holes can enter the molecule through the HOMO and electrons through the LUMO, the holes might further translate or recombine, while electrons would experience a high resistance. Thus, a layer of specifically tuned organic molecules can act as a semi-permeable membrane for charges. This type of membrane or functional layer is not only scientifically interesting, but is economically attractive as well, due to the minimal material usage of a SAM and manifold compatibility to substrates, absorbers and functions, depending on the chemical design.

2.5.1 General structure and formation mechanism

A molecule for self-assembly can be divided into three fragments: Anchor, spacer and head (or functional group). The anchor defines to which bonding sites the molecule can bond to - the most common choices there are phosphonic or carboxylic acids (bonding to or adsorbing on oxides), thiols (bonding to gold) and silanes (bonding to Si and some oxides). In this thesis, phosphonic acids were used due to their high versatility and very stable bonds [182]. The spacer fulfills several functions, albeit not necessary for forming a SAM: During SAM formation, van-der-Waals forces between the molecules stabilize the layer formation, promote an upward orientation, ordered assembly and high molecule density [174, 182]. Additionally, the spacer can be regarded as an electronic decoupler from the substrate, because it is usually made of a hydrocarbon (alkyl) chain that is isolating. The head group, 'functional fragment' or 'termination' gives the SAM most of its functionality, as it becomes the new surface of the substrate, with the functional groups facing upwards. The molecularly given functionalities range from stent coatings in medical applications to ion sensing, implants, patterning and even charge storage [183–185].

The traditional way of processing SAMs on surfaces is via immersion of the substrate

into a solution that contains the molecules. The film forming process can then be imagined as the condensation of material from a gas phase [186]: First, the molecules physically adsorb onto the surface and form isolated, disordered islands of low density. These nucleates grow in size until the layer covers the whole substrate. At this stage, densification of the layer and ordering/orientation of the molecules takes place. In the case of phosphonic acids, the bonding occurs via deprotonation of the phosphate group and OH groups on the surface, such that P-O-metal links remains. The bond can be either mono-, bi- or tri-dentate, meaning the number of P-O bonds involved from the phosphonic acid group [187] (see Fig. 2.8).

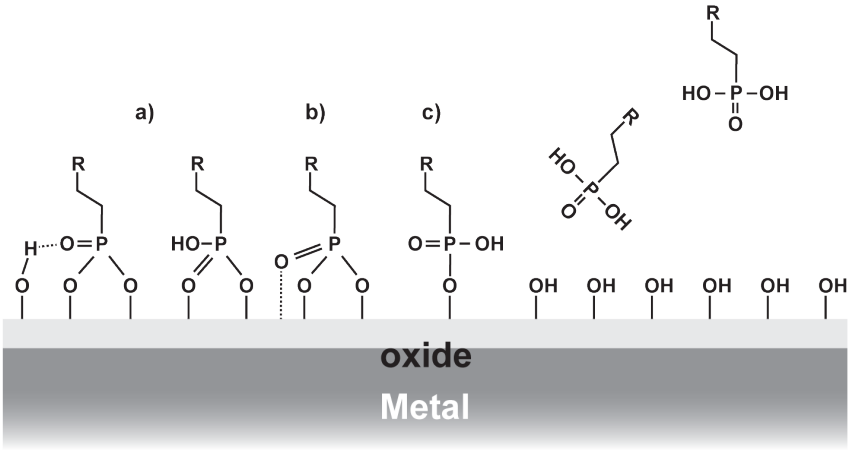

Figure 2.8: Illustration of phosphonic acid molecules attaching to a metal oxide surface, showing examples of different bonding modes (a) bidentate, b) tridentate and c) monodentate. R denotes a rest of the molecule, the "head" group that gives the surface its intended function. After references [188] and [189].

Hole-selectivity and carbazole

It is still under debate what exactly determines the charge-selectivity of organic compounds, although several theories exist that successfully model charge transport across conjugated molecules and transport layers [190, 191]. One major design guideline to render a material either electron- or hole-selective is the alignment of the HOMO/LUMO to the electrode's work function [192]: If the ionization energy is aligned, the material is considered as a hole transporter, whereas it is an electron transporter if the electron affinity matches the Fermi level of the electrode's material. Although in early organic semiconductor devices, conjugated polymers were usually used as hole transporters [193], it has been shown that with a suitable electron affinity, such materials can be 'n-type' as well [192]. Charge selectivity is also governed by differences between hole

and electron mobility. The fact that most conjugated polymers have lower electron than hole mobility can be explained by the presence of electron traps in such materials, which can capture electrons that then contribute to increased Coulomb scattering, or by instabilities of the molecules upon accepting electrons. Upon filling or avoiding these traps, the materials show enhanced electron mobility [194, 195]. However, there was also evidence that the molecule itself can have an intrinsic asymmetry between the electron and hole mobility [190], e. g., depending on the density of states in the LUMO and HOMO: while electrons travel through unoccupied states in the LUMO, holes travel through occupied states in the HOMO [196]. Additionally, the orbitals can be formed such that one carrier type is localized while the other is delocalized across the material.

Considering a standard electrode material that is commonly used in solar cells and light-emitting diodes, indium tin oxide (ITO), a material with a HOMO level that is well-aligned to the ITO's Fermi level is *carbazole*, making it favorable for electron injection from the ITO into the molecule (i.e., hole extraction) [197]. Furthermore, the nitrogen atom in its molecular structure induces an asymmetry for charges, such that holes stay delocalized in the conjugated structure while electrons see a preferred localization. With carbazole as the functional group, the easiest possible hole-selective SAM consists of a carbazole core, linked to an anchor (phosphonic acid) by an aliphatic chain.

2.5.2 Application in perovskite solar cells

After field-effect transistors, the next electronic devices in which SAMs were beneficially deployed were light-emitting diodes (LEDs) and dye-sensitized solar cells [198, 199]. A SAM with a hole-selective moiety was used by Bardecker et al. to improve the hole injection from the ITO in organic LEDs [200], with the molecule consisting of a triarylamine head and phosphonic acid anchor. In their case, the SAM acted as the hole-selective layer, introducing states with energies between the ITO Fermi level and HOMO level of the emitter material. In perovskite literature, SAMs found their appearance as interface modifiers (silanes) to alter the wettability and surface energetics of the electron transport layer (TiO_2) in *n-i-p* PSCs [201, 202]. In a more recent work, the electron-selective layer was replaced with a C_{60}-based phosphonic acid SAM on ITO, leading to devices with high stability, and, if paired with common electron-selective layers on top of the SAM, high PCE of >21% [203]. It was also shown that the C_{60} SAM can suppress hysteresis by passivating defects that would otherwise act as migration sites for ions [204]. Earlier, another fullerene-based SAM (phenyl-C_{61}-butyric acid with carboxyl group anchor) was used to render the TiO_2 surface such that high V_{OC} values were achieved [205]. In another approach, passivating SAMs were used in *p-i-n* perovskite solar cells between the perovskite and C_{60} layer, attaching to the perovskite surface via halogen-type bonding and making the perovskite surface hydrophobic [206].

The introduction and establishment of hole-selective SAMs into the *p-i-n* architec-

ture was part of this thesis. In close collaboration with Artiom Magomedov (Kaunas University of Technology), who first suggested the possibility of SAM-based devices ("hole transport layer-free") and who's group synthesized phosphonic acid SAMs with carbazole head group, the first SAM-based *p-i-n* PSCs were realized. In the first generation, a SAM molecule termed **V1036** showed the potential in devices with 18%-efficient PSCs that otherwise did not contain any hole-selective layer between the electrode and perovskite [207]. This work is subject of chapter 3. The design of the hole transporting moiety was inspired by the popular hole transport material spiro-OMeTAD of the *n-i-p* architecture. In further optimization, while testing the dependence of the molecule size on device performance, one of the simplest hole-selective SAM designs thinkable (carbazole core + 2-hydrocarbon chain + phosphonic acid), named **2PACz**, proved its outstanding potential by being superior to all other known hole-selective materials for *p-i-n* PSCs [208], as judged from the device performance and an analysis of the practically lossless hole-selective interface. Chapter 4 is devoted to that work with discussions on the possible reasons. Having established efficient single junction solar cells with SAMs and well-working perovskite/CIGSe tandem solar cells, we desired to deploy SAMs for efficient perovskite/silicon tandem solar cells as well. Thus, the search for even better SAMs continued, having noticed that although the efficiency was high with 2PACz, in early tries it has led to low fill factors in the tandem structure, presumably due to a low hole extraction rate compared to common hole-selective layers. An optimized SAM based on the insights from the publication finally confirmed that *p-i-n* PSCs strongly benefit from accelerated hole extraction at the hole-selective interface. The molecule **Me-4PACz** then was key to realizing a perovskite/silicon tandem cell with 29.2% efficiency [209]. This value was the world record from January to December 2020. Chapter 5 presents this work and deepens the explanations to the analytical techniques used for characterizing the hole extraction speed.

Chapter 3

Introducing Hole-selective Self-assembled Monolayers for Perovskite Solar Cells

This chapter is based on:

A. Magomedov*, A. Al-Ashouri*, E. Kasparavičius, S. Strazdaite, G. Niaura, M. Jošt, T. Malinauskas, S. Albrecht and V. Getautis.
"**Self-Assembled Hole Transporting Monolayer for Highly Efficient Perovskite Solar Cells**".
Advanced Energy Materials 8, 1801892 (2018). Doi: 10.1002/aenm.201801892

*equal contribution

Contributions of A.A.A: Assistance in the realization of first SAM-based cells and concept development, optimization of SAM deposition parameters, solar cell fabrication (baseline-establishment and SAM-based solar cells) and characterization, and co-writing of the manuscript.

Synthesis, chemical design and initial idea of the SAMs were by A.M., E.K., T.M. and V.G.

The paper is reprinted in section 7.3 of the appendix with permission from John Wiley and Sons (lic. no. 4984111482075) [207]. This publication was featured on the cover page of *Advanced Energy Materials*, see Fig. 7.5 in the appendix.

3.1 The need for alternative charge-selective layers

Inverted (p-i-n) perovskite solar cells, where the perovskite layer is deposited on the hole-selective layer, have a number of advantages compared to their regular (n-i-p) counterparts, as summarized in section 2.4.2. Most importantly for the progression of this work is their superior suitability for tandem solar cells. Economically, with the aspect of large-scale cell production, high-efficiency p-i-n PSCs come with the convenience of low-temperature processing, meaning that the substrate does not need high temperature treatment throughout all fabrication steps. In particular, state-of-the-art p-i-n PSCs (at the time of this publication) that included polymers as the hole-selective layer only needed substrate heating up to 100 °C.

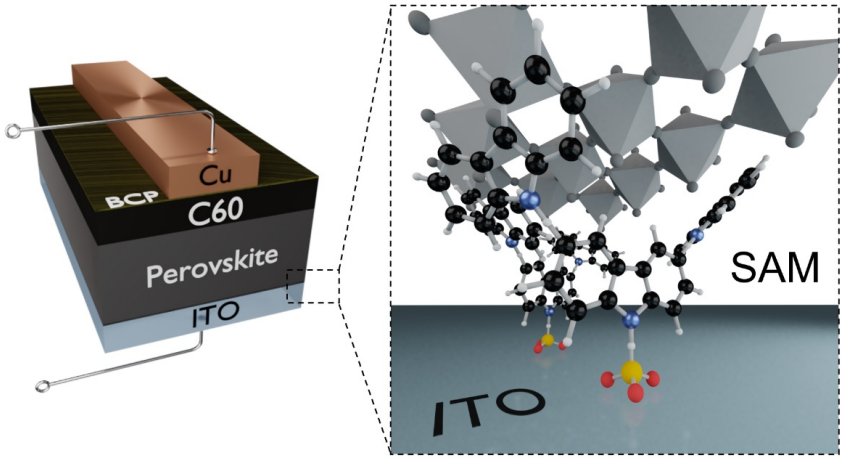

Figure 3.1: Illustration of a p-i-n perovskite solar cell with a C_{60}/BCP/Cu top contact and a zoom-in showing the V1036 SAM molecules between a indium tin oxide (ITO) electrode and the perovskite layer.

The often-used electron-selective layer, fullerene C_{60}, is deposited via evaporation, which is a industrially scalable technique. In contrast, the deposition of hole-selective polymers mostly involved spin-coating a dilute solution to obtain a 5- 15 nm thick layer between the perovskite and the electrode. The high material waste of spin-coating can be overcome by other solution-processing techniques. However, solution processing of thin polymer layers comes with the need of microscopically flat substrates, in order to avoid blank electrode spots. This is a big disadvantage that would render the integration of perovskite cells on top of usually rough or textured industrial silicon solar cells a too difficult task. Additionally, the highest-efficiency materials (PTAA and polyTPD) still induce non-radiative recombination losses that reduce the maximum possible V_{OC} [154], and some, albeit small, parasitic absorption (~1% of the total J_{SC} in the blue region, which increases upon doping the layer [210]). An often-used alternative hole-selective

layer is nickel oxide (NiOx), which can be prepared by, e. g., evaporation, atomic layer deposition and sputtering for conformally covering rough surfaces. Unfortunately, the processing of NiOx is highly delicate and usually additional passivation is needed to enable similar efficiency as with organic hole-selective layers, which was traced back to redox reactions and the formation of PbI_2 at the NiOx/perovskite interface [211].

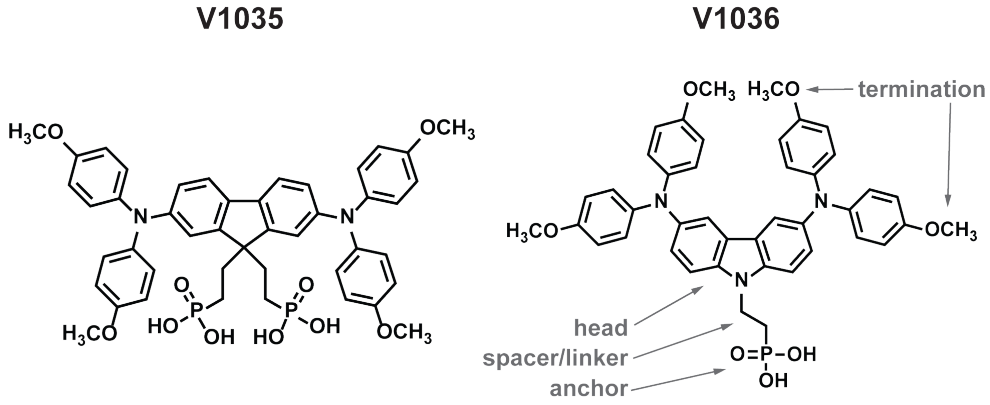

Figure 3.2: Molecular structures of the first hole-selective SAMs that were included into p-i-n perovskite cells to replace the polymeric hole-selective layer. The hole-selective fragments roughly resemble the structure of the popular hole transport material Spiro-OMeTAD. Structure files adapted from Artiom Magomedov (Kaunas University).

In this work, the aim was to enlarge the choice of hole-selective layers that are scalable and that keep the advantages of *p-i-n* solar cells. Furthermore, since the perovskite crystallizes on the hole-selective layer, it is plausible that the crystallization and thus the perovskite interface quality is influenced by the hole-selective material. That interface, however, is challenging to investigate, because it is 'buried'. A systematic, phenomenological investigation of the interface requires microscopic adjustments of the atomic interface composition. As summarized in section 2.5, SAMs offer a great potential to experimentally achieve this, since the atoms that interface with the perovskite can be tailored by engineering the SAM molecule termination (functional group). SAMs have been used in perovskite solar cells since 2013, however, only for slight modifications of electrodes or interfaces. To make SAMs an integral part of cell development, they should completely replace the archetypal charge-selective layer of heterostructure solar cells [212].

In 2017, Lin et al. used two different SAMs to create an asymmetry between the work functions of electrodes in back-contacted PSCs [213]. The molecules only served as work function modifiers through their embedded dipoles, however, they were not designed to be selective to either charge carrier type. Hole-selective SAMs have not been used in perovskite solar cells up to this publication. We aimed to show that a SAM, called **V1036** ((2-{3,6- bis[bis(4-methoxyphenyl)amino]-9H-carbazol-9-yl}ethyl)phosphonic

acid), can be the fully functional hole-selective layer (see 3.1). The SAM-based p-i-n devices have shown a maximum PCE of 17.8%, which was still lower compared to state-of-the-art PTAA-based cells (19.2%), but decent nonetheless considering that this is a single molecular layer compared to a roughly 10 nm-thick polymer. The solar cells have thereby proven that a SAM can be selective and dense enough for enabling efficient operation with low leakage current (see also Fig. 3.4). The shortcoming in comparison to PTAA was the V_{OC}, indicating increased non-radiative recombination losses. It was unclear whether this stemmed from a reduced perovskite quality at the interface, incomplete coverage or due to unfavorable energetic alignment with the indium-doped tin oxide (ITO), which served as transparent conductive oxide electrode. This and a further optimization of the SAM was subject of the next publication, as summarized in chapter 4.

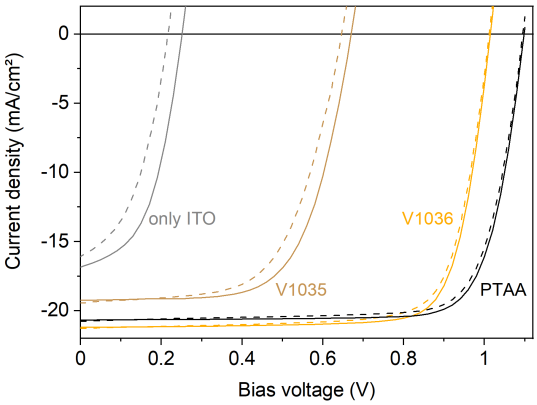

	ITO	V1035	V1036	PTAA
J_{SC} (mA/cm^2)	16.8	19.3	21.2	20.7
V_{OC} (V)	0.252	0.670	1.015	1.098
FF (%)	49.4	65.5	79.0	79.4
PCE (%)	2.1	8.45	17.0	18.0

Figure 3.3: *J-V* curves of early SAM-based solar cells (V1035 and V1036), in comparison to representative *J-V* curves of a PTAA-based and hole-selective-layer-free (only ITO) perovskite solar cell. The table shows the respective performance parameters. For more suitable comparison, this figure and table show cells from similar batches fabricated in early optimization times (2017). Champion cells of the publication (fabricated later) have shown a PCE of 17.8% and 19.2% for V1036 and PTAA, respectively.

A first confirmation for how the molecular structure determines device performance was a comparison between the compounds V1035 and V1036. Both structures are depicted in Fig. 3.2 and representative solar cell *J-V* curves under 1-sun illumination are shown in Fig. 3.3. In comparison to bare ITO, the V1035 SAM seems to have reduced non-radiative interface recombination losses, showing its selectivity and thus allowing for a substantially higher V_{OC}. However, despite both SAMs sharing the same termination (methoxy group OCH_3), V1036 allowed for substantially more efficient cell operation with increased fill factor (79% vs. 65%) and much higher V_{OC} (345 mV more). The commonly used standard hole transporter poly(triaryl amine) (PTAA) still led to

significantly higher PCEs (over 1% more in average) due to a >90 mV higher average V_{OC}.

Interestingly, the *FF*s were similar between V1036 and PTAA, with a slight advantage in average values for the SAM (fig. S14 in the SI of the publication, see appendix 7.3). This was a motivating result, since it is not self-evident that a monolayer can ensure a high shunt resistance. In fact, as depicted in Fig. 3.4, SAM-based cells usually led to a higher shunt resistance than good PTAA cells, while still enabling a similarly good injection. The question about the conditions for efficient rectification by a SAM was a recurring theme in subsequent studies. In the works that followed, we phenomenologically studied the relationship between molecular structure and device efficiency. While the termination (and thus dipole) acted as a tuning knob for mostly the V_{OC}, all SAM-based devices had a high shunt resistance in common, with similar shapes of the dark *J-V* curves.

The first SAM functionalizations of the ITO substrates were done following common recipes in the literature of phosphonic acids (overnight dipping of the UV-ozone-treated substrates in a dilute alcohol solution of the compound, with subsequent substrate drying, heating and rinsing). Finding the optimal processing conditions for V1036 was the task that followed on the way to study the potential of SAM-based PSCs.

3.2 Optimization and analysis of monolayer deposition

A first speculation regarding the V_{OC} gap between V1036 and PTAA was that the SAM is either not complete or not ordered well enough. Hence, we first optimized the SAM deposition in terms of used solvents, dipping times and modes (i. e. single vs. double dipping), concentrations and temperatures, with the results suggesting that the functionalization itself is insensitive to the varied conditions. Thus, inspired by a publication that the SAM ordering can be improved by mixing the functional molecules with small "filler" molecules [214], we mixed V1036 solutions with aliphatic phosphonic acids (C2, C4, C6, C10, C3-NH2), of which C4 (4 hydrocarbons on a phosphonic acid group) has shown the largest effect on V_{OC}, as shown in fig. 5 of the publication (appendix 7.3). At an optimal nominal concentration of 10% V1036 and 90% C4 (molar) of the dipping solution, the devices reached up to 1.09 V V_{OC}, only 40 mV short of the best PTAA cell.

A probable working mechanism for this enhancement by including C4 is that it acted as gap filler between the V1036 molecules that would otherwise be exposed ITO spots that induce non-radiative recombination losses. Another mechanism that could be considered is the degree of order of the SAM layer, since higher orderings have been connected to a better interface quality [182, 201]. However, using vibrational

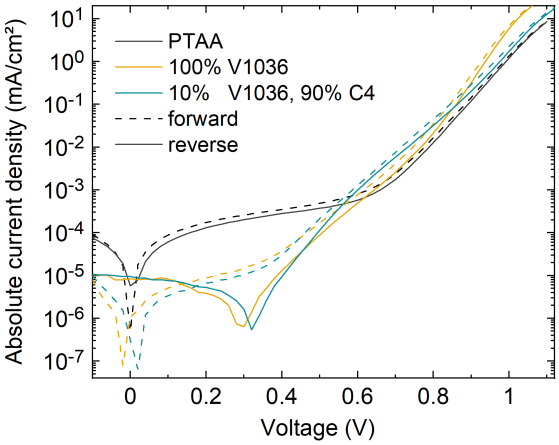

Figure 3.4: *J-V* curves measured in the dark, comparing representative SAM cells with a PTAA solar cell. Interestingly, SAM cells showed a higher shunt resistance than PTAA-based cells.

Table 3.1: Ionization potentials for bare ITO and the respective hole-selective layers on ITO, measured by photoelectron spectroscopy in air [207] and champion V_{OC} values (after some minutes of light-soaking). The max. V_{OC} value for ITO (not shown in the paper) was taken from the batches of the time of publication; values can - within a large variation - also exceed 0.5 V.

	ITO	100% V1036 SAM	10%/90% V1036/C4	PTAA	perovskite
Ionization potential (eV)	4.6	5.0	5.1	5.2	5.6
Max. V_{OC} (V)	0.3	1.02	1.09	1.13	

sum frequency generation (VSFG) spectroscopy on the substrates, which is a highly interface-sensitive Fourier transform infrared (FTIR) spectroscopy method, the ordering was actually found to be reduced for the mixed SAM compared to the pure V1036 SAM (fig. S5 of the publication's SI). Notably, we measured a trend between the ionization potential of the substrate and the obtained V_{OC}, as table 3.1 shows. Despite the ongoing debate whether the alignment between the ionization energies of perovskite and hole-selective layer plays a major role in the device performance [215–217], it later turned out to be the important parameter that differentiated the SAM designs that followed (see chapter 4).

The fact that the SAM indeed consisted of a mixture of molecules was confirmed by contact angle measurements of perovskite solution drops on the functionalized ITO. The aliphatic chain is hydrophobic, thus increasing the contact angle, while V1036 is less hydrophobic, resulting in a low contact angle of 26.3° on 100% V1036-functionalized substrates, while 100% C4 led to a contact angle of 60.5° (see fig. 2 of the publication). With these differences in wettability, we observed a difference in perovskite grain morphology as well (fig. S19 in the SI of the publication), with higher contact angles leading to slightly larger grains. With the optimal mixing ratio,

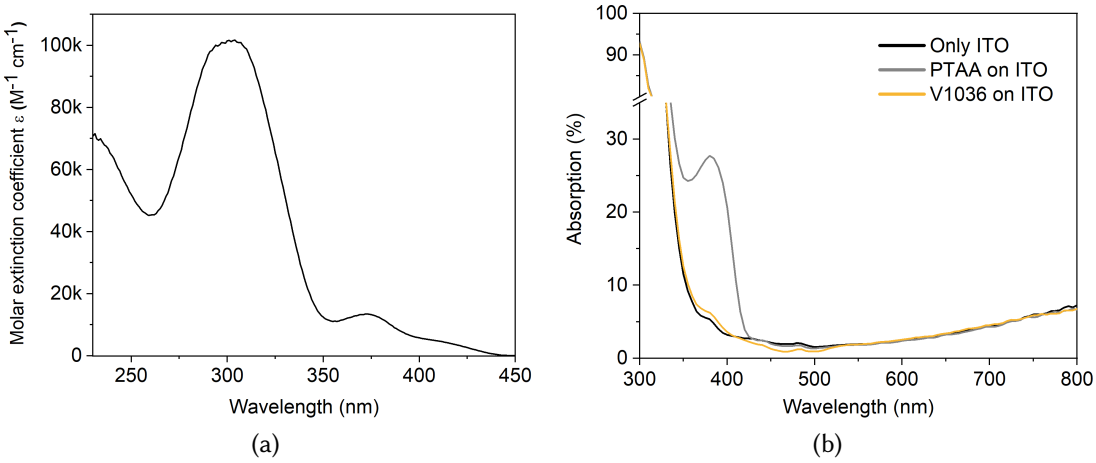

Figure 3.5: Molar extinction coefficient of V1036 solution (0.1 mmol/l in tetrahydrofuran) (a), and reflection-corrected optical absorption of glass/ITO substrates either covered by PTAA or V1036 (b).

no significant differences were noticeable by scanning electron microscopy between V1036/C4 and PTAA (fig. 4 of the publication). A confirmation of the actual V1036 molecule on the substrate was given by FTIR measurements (fig. 3 of the publication, see appendix). The absorbance spectrum showed the same features as the bulk compound itself. Note that the substrate processing included washing with the same solvent that was used to dissolve the molecules, to remove any multilayers or non-bonded species from the surface. If the molecules would not have a strong bond to the substrate, they would not form a functioning layer for solar cell operation and would likely not be detectable by FTIR.

To confirm that there were no multilayers present, we estimated the thickness of the layer by optical UV-vis absorption spectroscopy, since the molecule itself shows a noticeable absorption at 303 nm (fig. 1 in the publication), with a molar extinction coefficient of $\epsilon \approx 10^5\,\mathrm{M}^{-1}\,\mathrm{cm}^{-1}$ measured from solution (Fig. 3.5 (a)). With a known concentration of the solution the absorption coefficient α is known as well, however, the concentration is different on the ITO substrate compared to the solution. Treating the SAM as a volume cuboid and assuming that one V1036 molecule occupies $1\,\mathrm{nm}^2$ ITO area, we arrive at a concentration of 10^{24} molecules per liter, or $M_{\mathrm{SAM}} \approx 1.7\,\mathrm{mol}/l$. With $\alpha = \epsilon M_{\mathrm{SAM}}$ and from the Beer-Lambert law of absorption, $\alpha = A/d$, where d is the thickness of the absorbing layer and A is the absorbance, we get $d = A/(\epsilon M_{\mathrm{SAM}})$. Comparing the absorbance spectrum of bare ITO with V1036 SAM-covered ITO, there is no significant difference within the measurement error of roughly 1% (see Fig. 3.5). For an absorption of 1% the layer thickness has to be $d = 0.01/(10^5 \cdot 1.7\mathrm{cm}^{-1}) \approx 0.6\,\mathrm{nm}$, or 2.4 nm if assuming an occupation of $2\,\mathrm{nm}^2$ per molecule. The vertical molecule

size (1.5 nm, see fig. S20 & S21 in the SI) lays in between these two values, from which we concluded that the analyzed layer had only monolayer thickness. In another approach, using 0.7 nm^2 per molecule as reported for a molecule of similar size [200] and calculating the extinction coefficient $k = M_{SAM}\epsilon\lambda/(4\pi)$ at every wavelength, we used the optical simulation software `GenPro4` to compute that the layer must be thinner than 2 nm to absorb less than 1% of the light (SI of the publication, fig. S17 & S18), which led to the same conclusion.

Chapter 4

Surpassing Standard Hole-selective Layers with Self-assembled Monolayers

This chapter is based on:

A. Al-Ashouri, A. Magomedov, M. Roß, M. Jošt, M. Talaikis, G. Chistiakova, T. Bertram, J. A. Márquez, E. Köhnen, E. Kasparavičius, S. Levcenco, L. Gil-Escrig, C. J. Hages, R. Schlatmann, B. Rech, T. Malinauskas, T. Unold, C. A. Kaufmann, L. Korte, G. Niaura, V. Getautis and S. Albrecht.
"**Conformal monolayer contacts with lossless interfaces for perovskite single junction and monolithic tandem solar cells**".
Energy & Environmental Science 12, 3356–3369 (2019). Doi: 10.1039/C9EE02268F

Contributions of A.A.A.: Project coordination and experimental plan, optimization of SAM deposition, sample and solar cell fabrication/characterization (single junctions and tandems), PL measurements, data analysis, figures and manuscript writing.

The SAM molecules were designed and synthesized by A.M., Er.K. and T.M. The co-evaporated solar cell was fabricated by M.R. and L.G.E. The CIGSe bottom cell was fabricated by T.B. and C.K.

4.1 Enabling simple, high-efficiency solar cells

In the previous chapter it was shown that SAMs can be a viable replacement of the hole-selective layer in perovskite solar cells. V1036-based cells have already reached a high fill factor, however, suffered from limited V_{OC}. The next task was to overcome this limitation by an adaptation of the molecular design and to correlate the chemical nature of the SAM molecules with solar cell device characteristics. In chapter 3 we have seen the indication that the V_{OC} might correlate with the ionization potential of the substrate covered by the hole-selective layer. In this chapter, this correlation is studied and further confirmed across a larger window of ionization potentials and hole-selective materials. Fig. 4.1 depicts the involved energy levels and variation, where the Fermi level of the ITO bulk and ITO/SAM interface are drawn separately (see discussions in section 2.5.1). For a systematic study, this publication introduced two new SAMs,

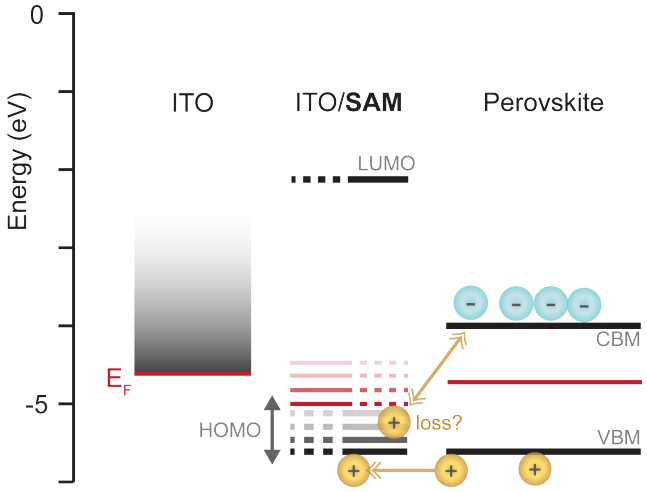

Figure 4.1: Schematic of the energy level alignment between ITO electrode, hole-selective SAM and perovskite, pointing to the question which influence the offsets between electrode Fermi level, HOMO level of the hole-selective layer and valence band maximum of the perovskite. The dashed lines in the HOMO/LUMO and Fermi level of the ITO/SAM indicate that it is yet unclear how the energetic levels of the ITO and SAM material influence and impinge each other. Thus, the ITO itself is drawn here separately since its bulk Fermi level alignment to the SAM HOMO has an influence on the hole-selectivity, as discussed in section 2.5.1.

MeO-2PACz ([2-(3,6-dimethoxy-9H-carbazol-9-yl)ethyl]phosphonic acid) and **2PACz** ([2-(9H-carbazol-9-yl)ethyl]phosphonic acid), which are simplifications of V1036 but follow the same concept (see Fig. 4.2): carbazole as the fragment that constitutes hole-selectivity and phosphonic acid as the anchoring fragment, both connected through a hydrocarbon chain.

4.1.1 Monolayer identification and properties

The classical method to coat surfaces with SAMs is the immersion into a dilute solution that contains the molecules, as also optimized for V1036 in the previous chapter. However, for higher throughput adjustment in laboratory workflows, spin-coating the solution is more practical, which is why this was tried as well. Interestingly, no significant difference was observed for both methods with regard to device performance. SAM deposition by spin-coating is not new, as it was explored by Nie et al. in 2006 for other phosphonic acids on silicon oxide [218]. The authors argued that by using a non-polar solvent that carries the molecules, the hydrophilic phosphonic acid groups tend to orient outwards to the solvent/air interface. Thereby, they come in direct contact with the oxide surface in an oriented manner. For this to efficiently work, the oxide surface has to be hydrophilic as well, which was achieved by UV-O_3 treatment of the surface just before SAM deposition [219]. The UV-O_3 removes organic contamination and renders the surface hydrophilic by oxidation.

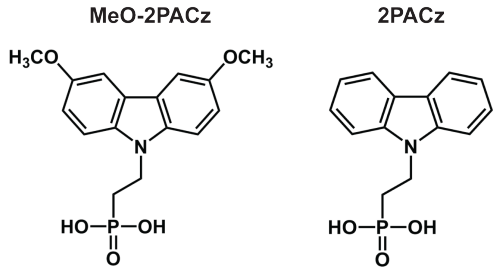

Figure 4.2: Molecular structure of the herein introduced molecules that form SAMs: MeO-2PACz ([2-(3,6-dimethoxy-9H-carbazol-9-yl)ethyl]phosphonic acid) and 2PACz ([2-(9H-carbazol-9-yl)ethyl]phosphonic acid).

Using RAIRS, we compared SAMs formed by both methods and cross-checked such samples by x-ray photoelectron spectroscopy (XPS) to determine the atomic composition of the SAMs on the surface. RAIRS is also referred to as a method of 'vibrational surface spectroscopy', as IR photons of varying frequency are sent to the surface within a shallow angle to excite molecule-specific vibrational modes in the molecules. By comparing the reflected beams from a SAM-covered ITO substrate to a bare ITO substrate, the "fingerprints" of attached molecules can be identified with sub-monolayer sensitivity [220]. The signal depends on the oscillation (absorption) strength of the molecules and their orientation, however, not necessarily on their density. The ratio of reflection (times -1) from the SAM-covered ITO to bare ITO, as plotted in Fig. 4.3, is in this case a measure for absorption of the IR photons. The spectra show many vibrational modes of the molecules, but characteristically, the C-N stretching vibrations near 1330 cm^{-1} and carbazole ring stretching vibrations near 1490 cm^{-1} could be identified

by comparison with literature[221, 222]. Importantly, evidence of deprotonation of the phosphonic acid group, which happens upon bonding to the oxide, can be seen in the spectra: The P-OH peak at 941 cm^{-1} from the powder spectrum is not visible anymore in the SAM spectrum, and instead, a peak associated to P-O(-metal) bonding was detected near 1014 cm^{-1}.

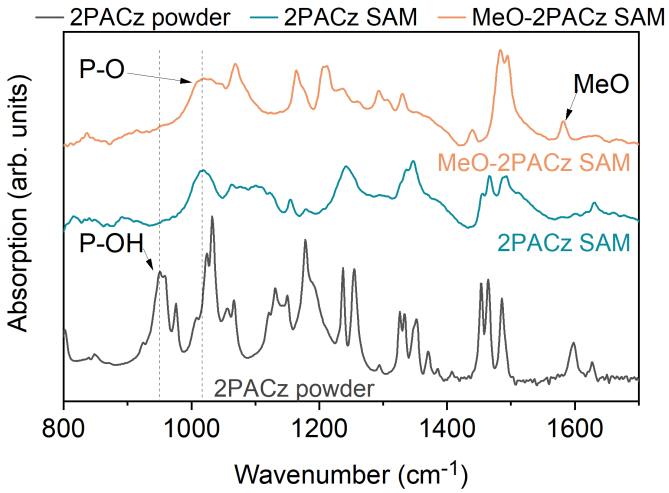

Figure 4.3: Reflection-absorption infrared spectroscopy (RAIRS) on glass/ITO substrates covered with the SAMs 2PACz and MeO-2PACz in comparison to the FTIR signal of 2PACz powder (gray line). Importantly, the peak corresponding to free P-OH groups (at 950 cm^{-1}) in the bulk spectrum is not visible anymore in the SAM spectra. Instead, the peak corresponding to bound P-O species emerged .

With XPS, the presence of the atoms as expected from the molecule structures (Fig. 4.2) were confirmed. In the paper (fig. 2d, see appendix 7.4), the XPS data from the C1s region was evaluated. Based on published data of XPS on carbazole and carbon [223–225], the assignment of atomic species based on their relative energetic positions was performed, after a global, simultaneous fit of three spectra (V1036, MeO-2PACz, 2PACz). With this, the ratios of relative peak areas were in line with the counts of the atom bonds derived from the structure. Nevertheless, considering the large spread of data in literature about fitting XPS data of carbon compounds, not all peaks could be unambiguously assigned. However, relative differences between the spectra can be used to find differences in composition. Thereby, the C-O-C bonds could be identified in the spectra of V1036 and MeO-2PACz, which both feature methoxy groups, in contrast to 2PACz. This also emerged from the comparison of XPS data in the O1s region, as shown in Fig. 4.4.

Interestingly, in an adaptation by Lin et al. [229], 2PACz has been shown to work efficiently as hole-selective layer in organic photovoltaics as well. It enabled an efficiency of up to 18% with increased *FF* and J_{SC} compared to the commonly used hole conductor

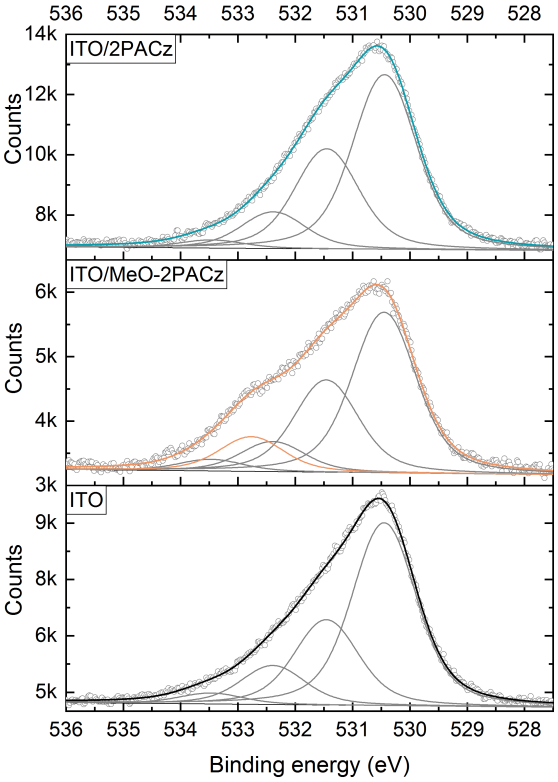

Figure 4.4: XPS data (circles) and fits to the spectra (solid lines) on glass/ITO/SAMs samlples. The ITO was UV-O_3 cleaned just before the measurement. The differences between the peaks were locked to the same values as determined from the bare ITO fit. The peaks of bare ITO show the expected positions of bulk oxygen (530.5 eV from In_2O_3, Sn-O bonds coincide here) and hydroxide specie [226–228]. The hydroxide peak at 531.5 eV increased in relative peak area after SAM treatment, which might indicate that less signal from the ITO bulk/surface was collected. The fit of MeO-2PACz required an additional peak. The fit of MeO-2PACz numerically required an additional peak (orange line), which can be assigned to the C-O-C bonds [226]. Plot as published in the the supporting information of ref. [208] by The Royal Society of Chemistry.

PEDOT:PSS, and an enhanced stability under continuous operation. The authors used spin-coating for SAM deposition following the results of the herein presented publication, and have also used XPS for characterization. From the XPS results, they estimated a molecule surface coverage of 4×10^{14} molecules/cm^2, which fits to other published values for a saturated surface by phosphonic acid molecules [230]. Thus, it can be stated that 2PACz forms a dense layer, as can also be supposed here from the PL measurements (fig. 4b of the publication). This is a notable fact when considering the short amount of time the molecules have for arrangement and orientation during spin-coating. With the flat molecule form, we speculate that it is mainly the interaction between two carbazole moieties (π-π stacking) that stabilize SAM formation (see section 2.5.1 for a summary on SAM formation), rather than the usually considered van der Waals interaction between hydrocarbon chains [231, 232].

4.1.2 Device performance

Fig. 4.5 displays a comparison of the J-V device performance metrics between the hole-selective layers, including the standard PTAA and the first-generation SAM V1036 that was introduced in the previous chapter. All devices were fabricated without interlayers or dopants, to simplify the understanding of the intrinsic interface behavior and increase

stability. The PTAA devices reached V_{OC}s of max. 1.13 V and PCEs of >19%, which is state of the art for interlayer-free PTAA devices with 1.63 eV bandgap absorber [154, 233]. Both MeO-2PACz and 2PACz surpassed the PTAA control cells in terms of V_{OC} and J_{SC}, while the *FF* remained similar across all layers. The highest PCE was achieved with 2PACz at a stabilized MPP value of 20.8%. As also noticed in the previous chapter, the dark curves indicated a smaller leakage current with all SAMs compared to PTAA (fig. 3d in the publication).

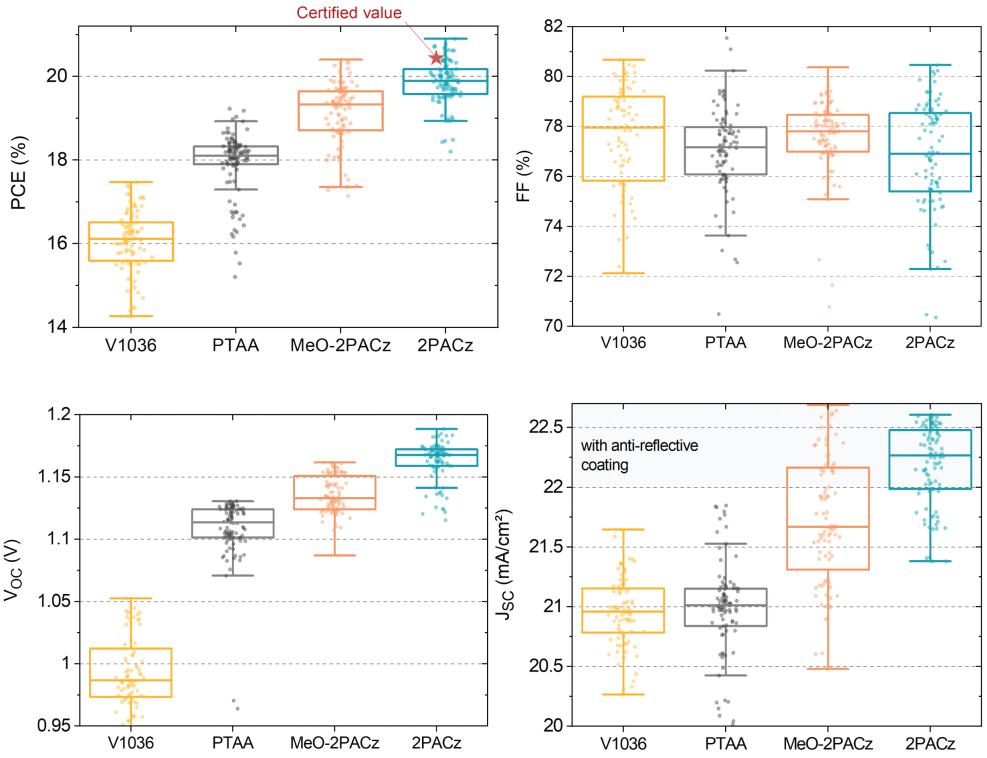

Figure 4.5: Device performance metrics of solar cells employing the studied hole-selective layers. For each layer, data of 40-50 solar cells are displayed (cell area: 0.16 cm^2).

In literature, lower bandgap compositions have shown a higher efficiency, as expected from the detailed balance theory (see Fig. 2.2). Thus, the compatibility of a 1.55 eV bandgap composition to a SAM was tested and it indeed led to a champion PCE of 21.1%. For tandem cells however, a slightly higher bandgap is favorable (section 2.3.2). Optimally, the bandgap in conjunction with the herein presented perovskite/CIGSe tandem solar cells should be around 1.68 eV. However, without detailed optimization of the CIGSe roughness and processing for preventing shunting, we opted to stay with 1.63 eV and limit the perovskite thickness to ensure enough transmission into the CIGSe for current matching. Perovskite/CIGSe tandem solar cells as all-thin-film devices pose an interesting technology for niche markets where low weight is needed (e.g., boats,

wearables, space applications [234]) or for larger markets where curved surfaces are to be covered with flexible solar cells, see Fig. 7.1 (e. g., car roofs and building facades).

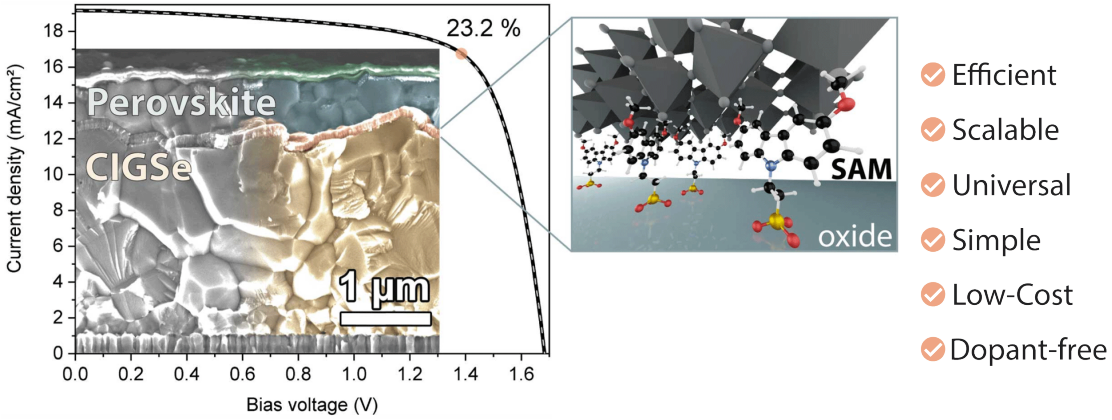

Figure 4.6: Cross-sectional scanning electron microcscope image of a monolithic perovskite/CIGSe tandem solar cell and *J-V* curve of the record tandem cell as certified by Fraunhofer ISE (dashed line = forward scan, solid line = reverse scan direction). The right zoom-in image depicts the perovskite/electrode interface which is covered by a 3D model of the MeO-2PACz SAM. The checkpoints on the right summarize the technological advantages of these SAM-based perovskite solar cells.

Up until this publication, the highest efficiency of perovskite/CIGSe tandem cells was 22.4% at an active area of 0.04 cm^2, published in 2018 [235]. In their work, Han et al. used a polished CIGSe surface to overcome the problem of the rough CIGSe grains (see Fig. 4.6) that could cause shunting in the perovskite top cell. However, polishing is energy- and material-demanding, therefore expensive for upscaling and not viable for market application. With a more viable method, Jošt et al. have shown how a bi-layer of nickel oxide, which conformally covered the rough surface, and PTAA, which improved the interface to the perovskite, could prevent shunting and enable decent V_{OC} [236], reaching 21.6% at an active area of 0.8 cm^2. As a new approach in this publication, we have used the SAM directly on the transparent conductive oxide (Al-doped zinc oxide, AZO), combining both benefits of the bi-layer used before. The SAM conformally covered the rough CIGSe surface and kept the favorable interface properties as seen in the single junction cells, thus simplifying the fabrication process. This enabled an efficient perovskite top cell for a certified tandem efficiency of 23.3% on 1 cm^2 active area (fig. 6b in the publication and Fig. 4.6 here), which at the time was the highest PCE for this technology at the largest area. The bottom cell has shown PCEs of 15-16%. After optimization at a later stage, we realized a SAM-based perovskite/CIGSe tandem cell with 24.2% certified efficiency. This value surpassed the record CIGSe single cell value and to this date is still the highest value [14].

From a device processing perspective, the SAMs significantly help to simplify the fabrication of high-efficiency solar cells. In addition, the interesting scientific question is why MeO-2PACz and 2PACz enabled to overcome the V_{OC} limitation that was simulated and measured to be set by the C_{60} layer at ~1.13 V for this perovskite composition [154] (as discussed in section 2.4.2).

4.1.3 Minimized interface losses

A good indication of whether a charge-selective layer introduces non-radiative recombination losses can be obtained by comparing the PL of bare perovskite film deposited on the layer *versus* deposited on quartz glass. Quartz glass is considered to be chemically inert, passive and free of interface defects [151, 152, 154]. Hence, the obtained PLQY values of the deposited perovskite layer thereon serves as an estimate of the bulk crystal quality. Usually, charge-selective layers are "quenchers" of the PL intensity – meaning a reduction of radiative recombination, which in literature is often incorrectly interpreted as a consequence of charge extraction [237]. Instead, the origin of this PLQY reduction is almost always an increased non-radiative recombination rate as the majority of available charge-selective layers creates defective interfaces [155] (see also section 2.4.2).

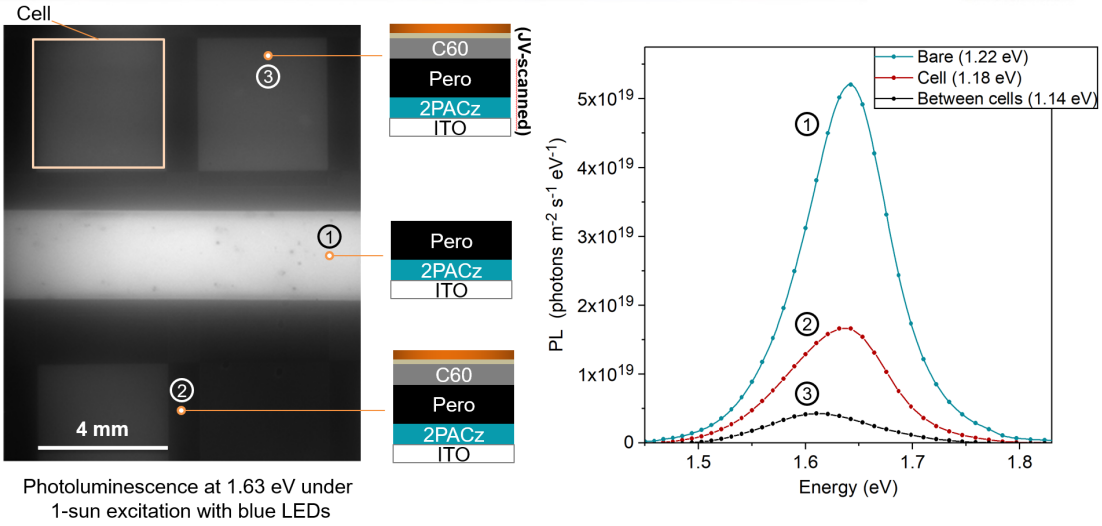

Figure 4.7: Absolute PL imaging on a solar cell device sample that featured a stripe that was not covered with C_{60}. From a spectrally resolved series of PL images and calibration of the setup to absolute photon numbers, the spectra on the right were computed. The values in brackets show the QLFS values calculated with the high energy tail fit method [238]. The image shows how the *J-V* scanned area ("activated") of the electrode-covered part had a brighter PL than between the solar cell pixels, where the C_{60} reduced the QFLS to 1.14 eV (see also section 5.1.3).

Strikingly, the interface of 2PACz/perovskite seemed to not induce any non-radiative losses although it works as an efficient hole-selective layer, as seen in the decent *FF* values. Comparing the PLQYs or resulting QFLS values (fig. 4b in the publication), the bare perovskite absorber deposited on ITO/2PACz enabled a similar value as deposited on quartz glass (1.22 eV, Fig. 4.7). A PL image is shown in Fig. 4.7, capturing multiple areas on a sample to study three variations: A stripe without the C_{60} layer (bare perovskite on 2PACz, 1.22 eV QFLS), the solar cell area after *J-V* scanning (1.18 eV QFLS, fitting to the obtained V_{OC}) and a solar cell area which did not experience *J-V* scanning (1.14 eV QFLS), showing the limitation by the C_{60} layer as measured before in another work [154] and hinting to an 'activation' mechanism that overcame this limitation (see also chapter 5). As a cross-check to absolute PL, transient photoluminescence (TrPL) led to a similar conclusion that 2PACz does not introduce any additional losses, with mono-exponential decay times being 2 µs with 2PACz and 0.86 µs with quartz glass. These results suggest that the hole-selective interface must be free of midgap levels that can act as trap states (see section 2.2), which would reduce the TrPL decay time. Fundamentally, the high V_{OC} means that the flow of electrons through the SAM must be minimal (see explanations to Fig. 2.1), despite the large gradient of the electron quasi Fermi level $\epsilon_{F,e}$ towards the ITO contact, where both Fermi levels must meet. Classically, in a heterostructure cell featuring selective layers of thicknesses >10 nm, a good selectivity would be explained by a large resistance for the minority carriers. But considering the small thickness of the SAM and the fact that the ITO has a large conductivity for electrons, the real reason for the high selectivity and simultaneous absence of defects must be more complex.

As summarized in section 2.5.1, when arguing about hole selectivity in a system of metal electrode and organic layer, one must consider both, the alignment between electrode work function and HOMO level of the organic layer and between HOMO level and valence band onset of the absorber. Additionally, for oriented layers as in the case of SAMs, the dipole moment of the material modifies this alignment, especially as a shift of the electrode work function. The hole-transporting fragments of the herein compared molecules carry an intrinsic dipole moment, as calculated from density functional theory (SI of ref. [208]). The dipole moment of V1036 is −2.4 D, MeO-2PACz carries a dipole moment of +0.2 D and 2PACz carries a dipole moment of +2 D. The bare ITO work function was measured with UPS to a value of 4.6 eV. In line with what to expect from the trend in dipole moments, the SAM-covered ITO substrates showed work functions of 4.4 eV, 4.6 eV and 5.0 eV for V1036, MeO-2PACz and 2PACz, respectively.

As discussed at the end of section 2.4.2, an ideal hole-selective contact would pose no energetic offset between the hole-"accepting" energy level (the HOMO) and the valence band edge of the absorber. And indeed, as depicted in fig. 4a of the publication, the trend in rising V_{OC} follows the trend of sinking energetic offset between the HOMO of the hole-selective layer and perovskite valence band onset. This is in line with several

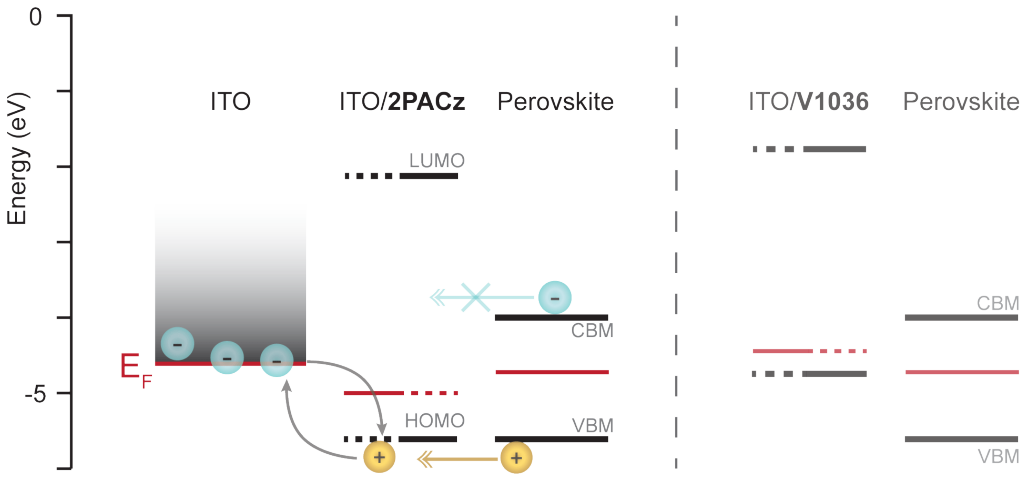

Figure 4.8: Schematic of the energy level alignment between the ITO electrode, 2PACz and perovskite, showing how 2PACz acts as an ideal hole-selective layer. On the right side, the alignment of V1036 (low V_{OC}, chapter 3) is shown for comparison. Data taken from fig. 4 of the publication [208].

other reports where in most cases the ionization potential of the hole-selective layer dictated the device V_{OC}, as summarized by Schulz et al. in a meta study [239]. Because of this phenomenological insight, we decided to follow vacuum level alignment when discussing energetic offsets between (undoped) organic charge-selective layers and the perovskite absorber [240]. Under this paradigm, as depicted in Fig. 4.8, where the vacuum level is referenced at 0 eV for all materials, 2PACz showed no offset between its HOMO level and the valence band edge of the perovskite. Since a hole-selective contact implies recombination with an electron of the electrode, the ITO work function (here E_F) favorably lies slightly above the HOMO level, such that electrons from the large reservoir in the ITO can lower their energy by recombining with the extracted holes. For comparison, the figure also shows the alignment in the case of V1036. The Fermi level of the ITO is shifted such that it lies closer to the conduction band edge of the perovskite. Additionally, there is a large offset between the valence band edge and the HOMO level of V1036, lying in the middle of the perovskite bandgap. This situation is unfavorable for charge selectivity since both electrons and holes have similar offsets to the HOMO level and modified work function. The fact that V1036-based devices still reached a higher V_{OC} than with bare ITO might stem from the intrinsic hole selectivity of the material and especially the low offset for holes between HOMO level and ITO work function (see chapter 3 and section 2.5.1). As speculated in the previous chapter, the beneficial V_{OC} effect of creating a mixed SAM containing the isolating C4 could be a further prevention of electrons entering the ITO.

It is, however, important to note that this way of aligning energy levels of semiconductor layers is different to what is done in established technologies like silicon devices, where two adjacent layers usually align along their Fermi levels (as expected from equilibrating charge reservoirs). This discrepancy for organic semiconductors is still subject to debate, although many works were dedicated to physically explain and simulate the electrostatics of metal/organic interfaces [240–242]. In general, as long as the metal Fermi level lies within the bandgap of the organic layer and if the organic layer has a sufficiently low density of midgap states, not enough charge transfer can happen to equilibrate the Fermi levels as, e. g., in metal/metal contacts (Mott-Schottky limit, or "common vacuum level" approximation [243]). The inhibition of charge rearrangement can also come from the organic layer being charge localizing or from the formation of an energetic barrier at the interface through polarization of the metal surface or mirror charges [244, 245]. Therefore, in most cases of metal/organic interfaces, vacuum level alignment is appropriate [241]. However, the influence of the intrinsic dipole moment of the hole-selective layer on the electrostatic environment in the perovskite remains an open question. Likewise the extent to which the vacuum level would have to be shifted compared to the bare ITO due to the molecular dipole. In the interpretations herein, the effect of the dipole is treated only as the reason for the work function shift of the ITO.

Independent of the exact physics under theoretical considerations, it is worth noting that the "real" picture is hard to capture also due to experimental complications, which are device-relevant but can obscure access to the parameters needed for accurate modeling:

1. The intrinsic dipole of the molecules can change the charge state in the electrode and absorber under operation.

2. During solar cell operation, charge flows through the monolayer, which can alter the energetics compared to the isolated measurement.

3. The ultraviolet photoelectron measurement excites electrons from a depth that is comparable to the thickness of the SAM (~1 nm), complicating the distinction between contributions from the SAM layer itself and the modified ITO.

4. After perovskite deposition, the interface is likely to change. This change cannot be probed directly, because it is a buried interface.

Taking these thoughts into account, it is not self-evident that the correlation between V_{OC} and measured energetic offset between perovskite valence band edge and HOMO of the ITO/SAMs could be found. As mentioned in the paper, the perovskite crystal quality itself was not found to alter between the studied hole-selective layers (estimated by x-ray diffraction and scanning electron microscopy), despite the perovskite crystallizing

on the respective layers. This makes the ITO/SAM/perovskite stack together with the *p-i-n* solar cells a convenient model system for studying the influence of interface modifications on device operation. Importantly, through the combination of optimal energetic alignment and apparent absence of interfacial defects, with 2PACz we have found a "lossless" hole-selective layer that also allows for high *FF* values. The optimal interface and the nature of a SAM was also beneficial for the stability of the devices under continuous illumination (fig. 5 in the publication). As argued in section 2.4.2, this combination extends the choice of available charge-selective contacts by a rare and valuable entry.

To conclude, both new SAMs enabled to surpass state-of-the-art PTAA-based cells, with 2PACz leading to high V_{OC} values of up to 1.19 V, 60 mV more than best PTAA-based cells, and a 10-times higher PLQY (see eq. (2.8)). Best SAM-based cells reached a PCE of >21% and a triple-cation, 2PACz-based cell was certified to a stabilized MPP value of 20.4%. Importantly, we could show that the SAMs work well with three different perovskite compositions, which suggests universality: single-cation $MAPbI_3$ prepared by co-evaporation (E_g = 1.6 eV), double cation $FA_{0.95}MA_{0.05}Pb(Br_{0.05}I_{0.95})_3$ (E_g = 1.55 eV) and triple-cation $Cs_5(MA_{17}FA_{83})_{95}Pb(I_{83}Br_{17})_3$ (E_g = 1.63 eV), both prepared by spin-coating[1]. Furthermore, we have proven the applicability of SAMs in complex tandem solar cells by realizing a monolithic 23.26%-efficient perovskite/CIGSe tandem solar cell with rough, as-deposited CIGSe surface and an active area of 1 cm^2. The fact that the SAM effectively covered the microscopically rough CIGSe surface (see Fig. 4.6) confirmed the advantage of SAMs to cover surfaces conformally, which led to a record PCE value for perovskite/CIGSe tandems. The jump in V_{OC} in the single junction devices was surprising, since *p-i-n* cells were thought to be limited by non-radiative recombination at the perovskite/C_{60} interface, as simulated and measured before [154] (see 2.4.2 for a summary on state of the art). Thus, no gains were expected by improvements at the hole-selective interface. While to date, the reasons for improved V_{OC} despite the usage of C_{60} could still not be fully resolved, this publication gives indications for possible reasons by absolute photoluminescence and ultra-violet photoelectron spectroscopy (UPS). The film properties of the SAMs were investigated by highly interface-sensitive, reflection-absorption Fourier-transform infrared spectroscopy (RAIRS), comparing SAMs formed by dipping vs. spin-coating, where both methods yielded similar device performance. The latter is more suitable for laboratory-based screening of processing parameters for optimization, while the possibility of dipping ensures potential scalability. Further, RAIRS helped to confirm that indeed covalent bonds were formed by the phosphonic acid on the oxide, by detection of deprotonation of the phosphonic acid group, upon comparison of the bulk material to the final SAM on the substrate (see also section 2.5.1 for the SAM formation mechanism).

[1] In a recent work, 2PACz has proven to work effectively with slot-die-coated perovskite as well [246].

Chapter 5

Over 29%-efficient Perovskite/Silicon Tandem Solar Cell by Enhanced Hole Extraction

This chapter is based on:

A. Al-Ashouri*, E. Köhnen*, B. Li, A. Magomedov, H. Hempel, P. Caprioglio, J. A. Márquez, A. B. Vilches, E. Kasparavicius, J. A. Smith, N. Phung, D. Menzel, M. Grischek, L. Kegelmann, D. Skroblin, C. Gollwitzer, T. Malinauskas, M. Jošt, G. Matič, B. Rech, R. Schlatmann, M. Topič, L. Korte, A. Abate, B. Stannowski, D. Neher, M. Stolterfoht, T. Unold, V. Getautis and S. Albrecht. "**Monolithic perovskite/silicon tandem solar cell with >29% efficiency by enhanced hole extraction**".
Science 370 (6522), 1300–1309 (2020). Doi: 10.1126/science.abd4016
*equal contribution

Contributions of A.A.A.: Planning and coordination of the work, processing of single-junction solar cells and PL samples, optimization of SAM deposition (for single junctions and tandems), PL/TrPL analysis, interpretation of TrPL, THz, EL, pseudo-FF data, initial figures and manuscript writing (with Ei.K.).

Er.K., A.M., and T.M. designed and synthesized the Me-4PACz SAM and the (Me-)nPACz series; Ei.K. and B.L. processed the tandem cells (bottom cells by A.B.V. and B.S.); G.M., M.J., B.L., and Ei.K. built the tandem aging setup and recorded long-term MPP tracks.

The *accepted version* of the paper text and published versions of the figures are reprinted in section 7.5 of the appendix with permission (lic. no. 4984121212048) – Published by The AAAS [209] (formatted and edited version by *Science* available online). The chapter also contains results from a yet unpublished project (section 5.2).

5.1 Tackling charge extraction speed

With the SAMs MeO-2PACz and 2PACz, we have learned about the importance of energy level alignment at the hole-selective interface for reaching high V_{OC} values. By minimal energetic offset and defect density, 2PACz thereby enabled a "lossless" interface, acting like a passivated surface such as quartz glass, while still allowing for effective charge transport for efficient solar cell performance. Both new SAMs surpassed all other available hole-selective materials for the *p-i-n* architecture and strongly simplified us to reach a robust 20%-efficient *p-i-n* solar cell baseline, without the need of exhaustively fine-tuning passivating interlayers between perovskite and charge-selective layers or chemical additives for the perovskite precursor.

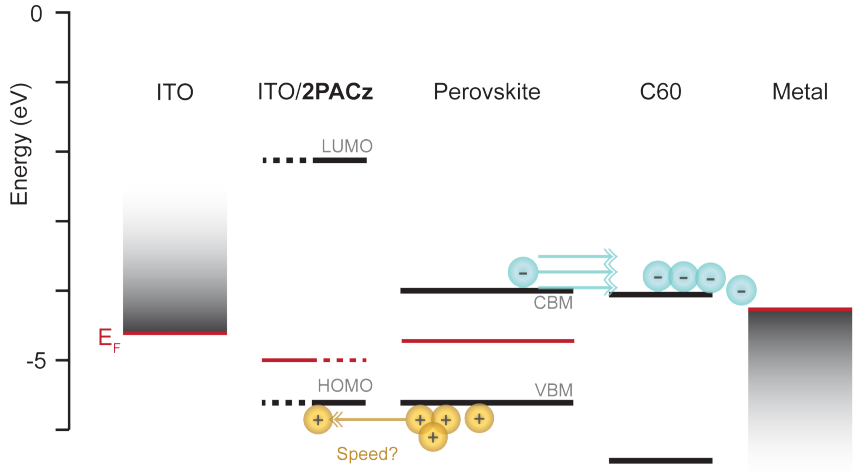

Figure 5.1: Schematic of the energetic alignment of a 2PACz-based *p-i-n* cell, hinting the question of how to quantify charge extraction speed. In this publication, we found that our used hole-selective layers extracted holes around 100-times slower than C_{60} extracted electrons. Data from refs. [208] and [169].

However, while the V_{OC} values were high, the maximum fill factors of around 81% are still far short of the maximum potential of perovskite solar cells. Without resistive losses at an ideality factor of 1 and at a V_{OC} near 1.2 V, a *FF* of almost 89% should be possible (from eq. (2.13)). Both the V_{OC} of 1.2 V and the often reached *FF*s of 80%-81% represent around 90% of the radiative limit for a 1.63 eV perovskite absorber. Though for the V_{OC}, strategies for enhancing it were already largely explored and just require experimental tuning, such as different perovskite precursor routes and additives that enhance the PLQY. Thereby, V_{OC} values surpassing 95% of the radiative limit have already been demonstrated both in *p-i-n* and *n-i-p* configuration [44, 49]. In contrast, the *FF* is rarely subject to optimization and 80% is already considered a decent value. Surely a large contribution of the experimental *FF* loss comes from the series resistance, however,

even with small device areas of 0.06 cm^2 and very thin PTAA thickness, Stolterfoht et al. have shown a maximum device *FF* of 84% at the expense of strongly reduced V_{OC} [247]. The combination of high V_{OC} and high *FF* is still a rare case in the perovskite community, although it is needed towards surpassing the PCEs of Si and GaAs solar cells. In fact, the *FF* is the only parameter left in which perovskite solar cells have not reached the realms of mature solar cell technologies [51]; Fig. 5.2 shows at which extent. As identified by Green and Baille, this can be traced back to a predominantly higher ideality factor n_{ID}, which usually lies between 1.4 and 2 for highly efficient perovskite solar cells, while it is near 1.1 for Si and GaAs cells [248]. There are some cases with lower n_{ID} in perovskite cells as well, where, e. g., PEDOT:PSS is used as hole-selective layer in *p-i-n* configuration, however, such cells come with strongly reduced V_{OC} due to strong interfacial recombination at the PEDOT interface. The combination of high V_{OC} with low n_{ID} (and high *FF*) is needed and an important goal to strive for [48].

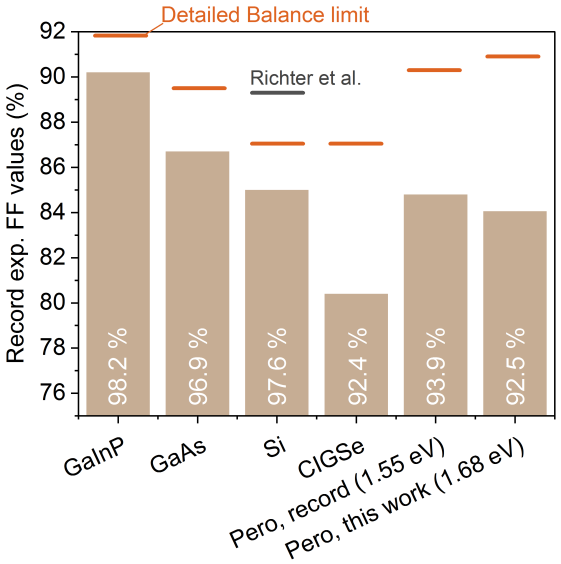

Figure 5.2: Comparison between solar cell technologies in experimentally achieved *FF* values [14]. The percentages inside the bars give the portion of experimentally achieved *FF*s to the detailed balance limit (orange lines). The gray line indicates the Auger limit for Si [20].

The lack in *FF* optimization is even more severe with higher bandgap perovskite compositions, probably due to the smaller amount of research laboratories actively optimizing tandem solar cells. Furthermore, higher bandgap perovskite compositions come with the additional complication of being less stable under illumination, showing phase segregation into iodide and bromide-rich regions [114, 249], with iodide being the most mobile ion in the film [142]. In the herein presented publication, both issues were addressed by studying and enhancing the speed of charge extraction in a tandem-relevant perovskite composition with 1.68 eV bandgap. This was achieved with a new

SAM, **Me-4PACz** ([4-(3,6-dimethyl-9H-carbazol-9-yl)butyl]phosphonic acid), which was designed to have a similar dipole moment as 2PACz for an advantageous energetic alignment (see chapter 4), but with methyl group termination, which is common in hole-selective materials for *p-i-n* PSCs. The accelerated hole extraction speed with Me-4PACz lead to high *FF* values of up to 84% while simultaneously enabling high V_{OC} values of up to 1.23 V. Furthermore, the enhanced extraction speed went along with a suppressed phase segregation speed and lower ideality factor (1.26). The lower segregation speed did not come at a surprise, since earlier works reported a connection between reduced charge carrier accumulation and higher activation energy for ion movement [116, 118]. It is, however, valuable to know that PTAA, MeO-2PACz and 2PACz were apparently not extracting holes fast enough to prevent phase segregation (Fig. 5.1). Furthermore, it is a new insight that the hole-selective interface limited the *FF*, while it was known before that the C_{60} interface limited the V_{OC} [154].

After demonstrating the effects of high hole extraction speed on the PL stability of perovskite films, the paper presents a method for quantifying differences in the extraction speeds using TrPL. As a further confirmation that Me-4PACz features the fastest hole extraction speed, single junction cells are presented, demonstrating how it transferred into higher *FF* and lower n_{ID} values. These benefits also transferred into the tandem structure, showing up to 29.3%-efficient perovskite/silicon tandem solar cells. The certified value of 29.15% surpassed the previously certified record value of 28%, scientifically published highest certified value of 26.2% [250] and is on par with the best GaAs cell at the same active area [14]. Finally, by intensity-dependent electroluminescence (EL), we estimated the maximum possible *FF* of this cell design, in the absence of resistive losses (pseudo-*FF*). Assuming also perfect current matching between the two subcells, we calculated an efficiency potential exceeding 32% with the presented device stack and non-optimized perovskite absorber.

5.1.1 Suppression of halide segregation

Since it was first described that mixed-halide perovskite compositions show the instability of phase segregation, with lower bandgap, iodide-rich regions forming in the film [114, 139], considerable effort was dedicated to understanding the impact on device performance and stability [140, 251–253]. Among these, the insight emerged that an improved crystal quality inhibits ion movement [254, 255]. This is likely because ion movement needs defect migration as its inverse process [142, 256]. Additionally, if defects are populated by charge, mobile ions will be inclined to compensate the resulting field by migration to the surfaces [257]. Because grain boundaries and surfaces are more defective than the interior or bulk, recent works have shown that the segregated phases predominantly form at the grain boundaries [143, 258]. Thus, passivation techniques that target the film surfaces are one way to overcome halide segregation. Chemical tailoring of the perovskite precursor by additive and compositional engineering has

also shown promising results [125, 259, 260]. However, a different approach with a potentially larger flexibility is the stabilization via the charge-selective layers, that ultimately contact the perovskite surfaces. There already have been several hints to a sensitivity of the phase stability to the layer either below or on top of the perovskite absorber [116, 145, 257].

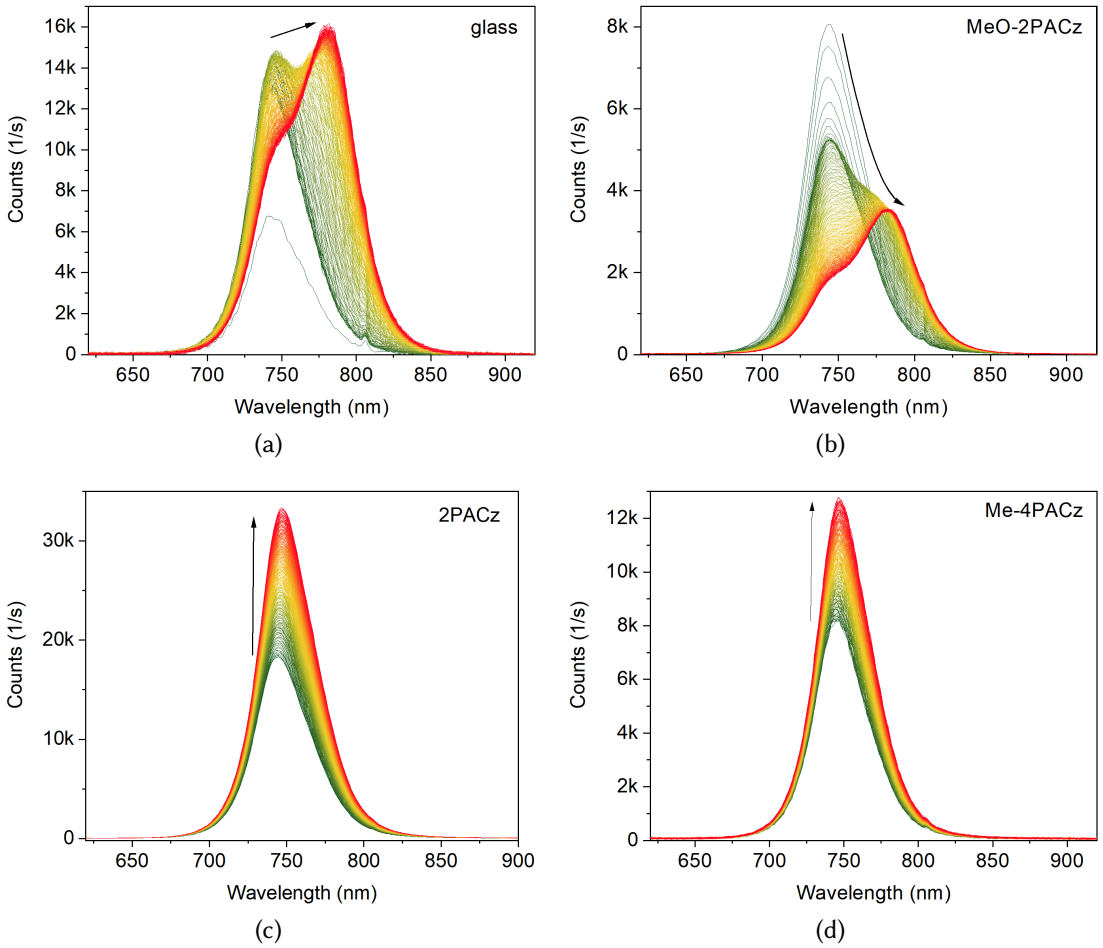

Figure 5.3: Time evolution (10 min) of PL spectra of 1.68 eV-bandgap perovskite on a glass substrate and on ITO substrates covered by SAMs. Phase segregation into lower-bandgap iodide-rich domains lead to the emergence of the new peak at 780 nm. Reprinted from supplementary materials of the paper [209] – published by the AAAS.

Here, we investigated the influence of the hole-selective layer on the phase stability by time-dependent PL. A phase-segregated film typically shows a double-peak signature in the PL spectrum, which makes it possible to estimate the extent of segregation. The excitation source was a laser spot (0.12 cm^2) adjusted to either 1-sun or 30-sun equivalent

photon flux for accelerated testing. Spot illumination by itself already poses an acceleration for phase segregation, because it creates a driving force for ions outwards of the illuminated area [256, 261]. The herein used perovskite precursor composition differed from the one in previous chapters only by a higher Br and methylammonium amount, to slightly increase the bandgap from 1.63 eV to 1.68 eV: $Cs_5(MA_{22}FA_{78})_{95}Pb(I_{78}Br_{22})_3$. As apparent from the double peak formation in Fig. 5.3 on both substrates, glass and ITO/MeO-2PACz, the perovskite itself is not phase-stable under illumination. The initial peak of the pristine, mixed phase emitted at 740 nm and upon formation of the iodide-rich phases, their emission at 780 nm became apparent. Because of their lower bandgap, these domains likely serve as charge carrier "sinks", which enhances the radiative recombination rate inside them and thus their PLQY, making them appear brighter than the surrounding material [258, 262, 263]. Interestingly, with 2PACz and the new SAM Me-4PACz, no such double-peak formation was observed (see fig. 1 in the publication and Fig. 5.3c-d here). As discussed above, ion movement can be promoted

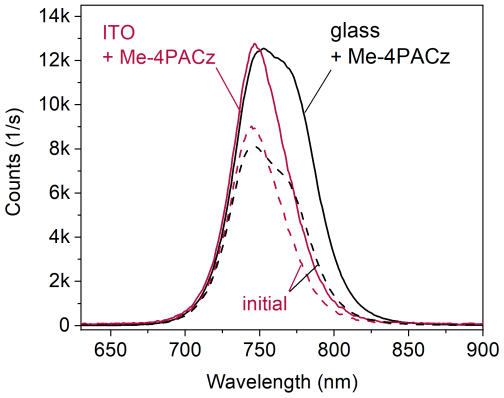

Figure 5.4: PL spectra from the beginning (dashed) and end of a 10 min long exposure to spot illumination of 1-sun equivalent photon flux, probing the influence of the substrate on which Me-4PACz and perovskite were deposited. Only the combination of passivation by the SAM and conductive substrate (ITO) for hole transfer prevented double-peak formation that indicates phase segregation.

by defects at a surface and by charge accumulation. Both on 2PACz and Me-4PACz, the perovskite film has shown a QFLS of 1.25 eV, the same value as on quartz glass (fig. 1B in the publication). As also argued in chapter 4, the SAM/perovskite interface can therefore by regarded as virtually free of non-radiative recombination, which implies minimal defect density. However, upon a 30-fold increase of the illumination intensity, only the perovskite on Me-4PACz held its initial PL shape, while on 2PACz, the double peak feature clearly appeared (fig. 1H of the publication). In addition, the PL shape of the perovskite on quartz glass was also considerably broadened and double-peaked. To this end, the roles of passivation and charge extraction were not clear. Thus, we isolated passivation and charge extraction from each other by comparing a glass substrate covered by Me-4PACz with a conductive ITO substrate covered by Me-4PACz (Fig. 5.4). This comparison has shown that charge extraction out of the perovskite bulk into the underlying ITO electrode is explicitly required to prevent phase segregation. The result can be interpreted in mainly two ways: Either the segregated phases have formed already and instead of holes funneling into the iodide-rich domains, they were

extracted into the ITO where they recombined with electrons from the large electron reservoir [145], or – more likely – the prevention of charge accumulation suppressed the formation of iodide-rich phases [116, 118]. For clearing this remaining question, microscopic techniques might be helpful that can picture and quantify the amount of segregation domains, resolved in time [258]. From a crystallographic view, we did not observe any notable differences in crystal orientation or quality in the x-ray diffraction data of perovskites deposited on all studied hole-selective layers (see Fig. S13-S15 in the SI of the publication), with the exception of PTAA. On PTAA, the (200) perovskite scattering peak was broader than on all SAM samples, however, we could not exclude that the perovskite on PTAA has already slightly degraded before the measurement (larger PbI_2 peak). On fresh samples and in scanning electron microscopy images, no such differences could be observed. Thus, we assumed that the different hole-selective layers did not considerably alter the perovskite crystal growth.

5.1.2 Quantifying charge extraction

While PL and EL have been established as standard methods for assessing voltage losses (for understanding V_{OC} optimization), there is no such standard method for the quantification of charge extraction (for understanding *FF* optimization). In a work by Krogmeier et al., it was shown that TrPL is sensitive to charge extraction if the transient can be sufficiently resolved [264]. With the SAMs 2PACz and Me-4PACz, the non-radiative recombination rate is low enough and thus decay transient long enough to experimentally allow for such observations (see Fig. 5.5). Reassuringly, the simulated differential lifetime[1] plots of ref. [264] had a similar shape as the experimental results obtained here. Also the change in shape upon higher excitation intensity of the differential lifetime curve (Fig. 5.5 (b)) was similar between simulation and experiment. Thus, we interpreted the steep rise at early times as a signature of hole extraction and the plateau as the lifetime in the limit that is dominated by non-radiative interface recombination. With this, we concluded that Me-4PACz extracts holes faster than 2PACz which featured a less steep initial slope (fig. 2 in the publication). This was established further with evaluation of the intensity-dependent data, as detailed below.

As a further confirmation of the steep initial slope being connected to hole extraction, we prepared a sample where the ITO was etched away from one part of the glass, the SAM covered the complete substrate afterwards. Thereby, we could compare the same perovskite on two different undergrounds, of which only the ITO side would allow for charge transfer out of the perovskite bulk. As expected, with the ITO substrate, the PL intensity sharply dropped at first, with a mono-exponential decay at later time (see Fig. 5.6). Interestingly, the time constant is higher for the case with ITO (1.1 µs vs 0.6 µs), as

[1] The differential lifetime is an evaluation of the transient to read the mono-exponential decay time at every position, instead of extracting the decay time from a single fit: $\tau = -[\mathrm{d}\ln(\phi(t))/\mathrm{d}t]^{-1}$. The transients were fitted before derivation with triple-exponential functions to avoid noise [38, 264].

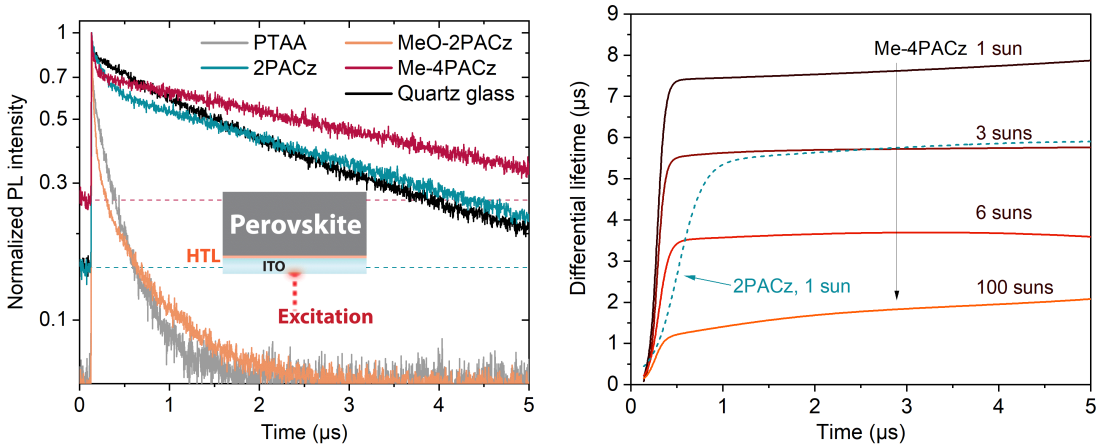

Figure 5.5: (a) Transient photoluminescence measurements, comparing the studied hole-selective layers (HTL). The excitation intensity was set to mimic charge carrier density equivalent to 1-sun illumination. Reprinted with from the paper [209] – published by the AAAS. (b) Differential lifetimes of the Me-4PACz sample at different excitation intensities. The transition in shape from low to high intensity resembles simulated curves by Krogmeier et al. [264]. For comparison, the differential lifetime curve of the 2PACz sample is included (dashed line), showing how the initial rise (charge extraction regime) is slower.

a consequence of lower charge carrier density with the extracting ITO electrode. This raises that caution should be maintained when using decay times as estimates for the bulk perovskite quality.

In the TrPL transients of perovskite on 2PACz and Me-4PACz, non-radiative decay (scaling with n, see eq. (2.5) in chapter 2), which dominates the transient at longer times (at lower carrier concentrations), had a time constant that differs sufficiently from the characteristic charge transfer times, such that both processes are visible within the same transient. We exploited this circumstance and recorded TrPL transients at different excitation densities, with charge carrier densities ranging roughly from equivalent 1 sun to 100 suns intensity. The idea of the analysis was that charge accumulation leads to a higher bulk carrier concentration, which promotes radiative recombination (scaling with n^2, eq. 2.5), leading to the transient to differ more from mono-exponential decay with slower charge extraction. By "dissecting" the transient into parts of single order (mono-exponential fit to longer times) and higher order (transient minus mono-exponential fit), we had a figure of merit for the speed of hole extraction (see fig. 2C in the publication). We thereby estimated that the hole transfer flux of Me-4PACz is 10 times higher than of 2PACz, because the TrPL transient shape with Me-4PACz showed a signature of radiative recombination similar to the 2PACz sample only at a 10 times higher excitation intensity.

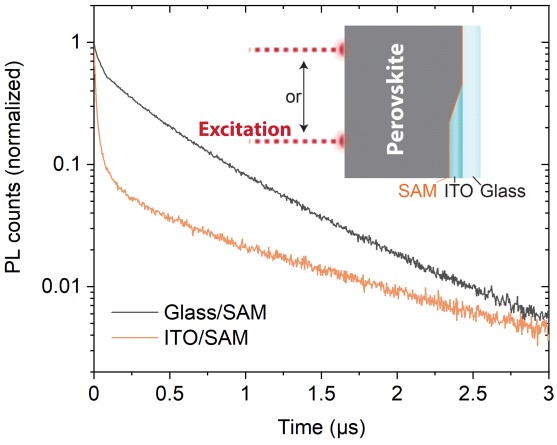

Figure 5.6: TrPL transients of perovskite deposited on glass/ITO/MeO-2PACz (orange line) and glass/MeO-2PACz (black line) within the same glass substrate. This demonstrates how the possibility of hole-extraction induces the steep drop in PL intensity (corresponding to a steep rise in differential lifetime). Sample prepared by Philipp Tockhorn.

Electron extraction into the C_{60}

One important result of this work was that we learned that the *FF* in state-of-the-art *p-i-n* devices was limited by the hole extraction speed at the hole-selective interface, rather than by the electron extraction speed at the C_{60} interface. This became evident from a transient measurement on a glass/perovskite/C_{60} sample, using optical pump, terahertz probe measurements, which feature a higher time resolution than TrPL. As shown in Fig. 5.7 (a), the TrPL signal quickly drops to noise level already after 100 ns. To differentiate whether the initial drop is due to charge transfer or non-radiative recombination at the interface, a comparison between the THz conductivity signal and the TrPL transient is useful, as shown in Fig. 5.7 (b).

The mono-exponential part of the TrPL transient stems from the reduction in photoemission governed by trap-assisted, non-radiative recombination with a time constant of roughly 40 ns (see section 2.2). This time constant approximately fits to the one needed for the usual V_{OC} values reached in *p-i-n* cells [265], thus it can be assumed that this process is the limiting one in trap-assisted recombination (determining V_{OC}). In the THz conductivity transients (Fig. 5.7), a ~20-times faster process is visible that, by comparison of the two optical excitation directions using blue laser light that is predominantly absorbed near the surface, seems to occur at the C_{60} interface. With the V_{OC}-limiting process being identified in the TrPL transient (shown as dashed line in Fig. 5.7 (b)), this fast process is likely a signature of the fast charge transfer into the C_{60} (lower transient in Fig. 5.7 (b)). With the time constant of this THz transient (1-2 ns), we can estimate a roughly 100-times faster electron transfer rate into the C_{60} than hole transfer rate into the SAM/ITO contact. It remains open whether only electrons or also holes transfer into the C_{60}, and whether the fast process is an entanglement of several non-radiative recombination pathways with carrier density-dependent activation of certain trap levels. However, the main conclusion that charge transfer in *p-i-n* cells is

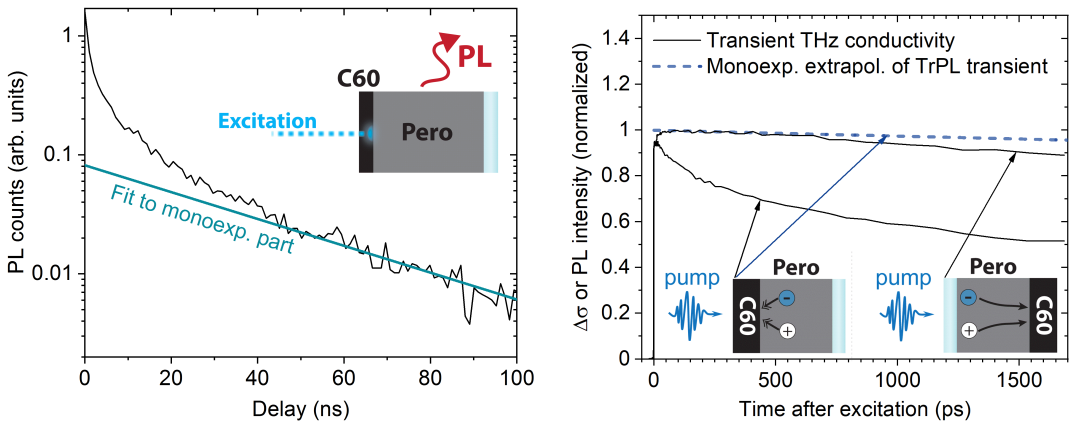

Figure 5.7: Fast charge extraction into the C_{60} layer. (a) TrPL measurements on a glass/perovskite/C_{60} sample, excited with blue laser light from the C_{60} side. The blue line is a linear fit to the mono-exponential part of the transient. (b) THz conductivity transients collected from both sides of the sample, showing that a fast process happens at the C_{60} interface and that the carriers need around 1-2 ns to travel through the perovskite layer. The dashed line is an extrapolation from the linear fit in (a). Reprinted and modified from the SI of the publication [209] – published by the AAAS.

unbalanced and limited by the hole-selective interface is being confirmed by the fact that a faster hole-extracting layer led to higher *FF* values in the solar cells.

5.1.3 Effect on solar cell performance

As visible in fig. 3 of the publication, the maximum fill factor is substantially increased by Me-4PACz in cells comprised of ITO/SAM/perovskite/C_{60}/SnO_2/Ag. While both MeO-2PACz and 2PACz led to 82%, with Me-4PACz the maximum value was 84% (compared within the same batch of perovskite solution, day and contact evaporation runs). Interestingly, champion Me-4PACz devices had a reduced ideality factor of 1.2-1.3, instead of the usual values of 1.4-1.6, despite keeping high V_{OC} values close to the ones obtained with 2PACz, which is a rare case for perovskite solar cells [48]. The reduced n_{ID} is the reason for the *FF* advantage of Me-4PACz in comparison to 2PACz (both had similar shunt and series resistances). As discussed in the case of limiting surface recombination by Caprioglio et al. [48] and summarized by Wolff et al. [46], discussing the underlying reason of the ideality factor in perovskite solar cells requires caution, and conclusions about the charge carrier dynamics are generally not obvious. To theorize with one possible explanation, we could start from the premise that no strong surface recombination or other process saturates the V_{OC} and could take the considerations of Sarritzu et al. as a basis [153]: Assuming that the ideality factor is dictated by the dominating recombination order in the device [35] and that electrons and holes have two different recombination orders, the ideality factor is $n_{ID} = n_{ID,e}/2 + n_{ID,h}/2$. Knowing that electron extraction is fast enough to keep the electron density in the perovskite bulk low, such that trap-assisted recombination is the dominant process (order 1, see section 2.2), the "electron ideality factor" is 1. Under accumulation of holes, radiative recombination is the dominant process[2] (order 2), which would leave us with $n_{ID} = 1/2 + 2/2 = 1.5$, a typical value for *p-i-n* cells. Upon faster extraction of holes, the recombination process is mainly mono-exponential as indicated by the TrPL transients (order 1). The closer $n_{ID,h}$ is to 1, the closer the total ideality factor shifts towards 1. Thus, this would be a connection between hole extraction speed and n_{ID}.

By intensity-dependent absolute PL we reconstructed the potential *J-V* curves of ITO/SAM/perovskite stacks to evaluate the maximum attainable *FF* (pseudo-*FF*) depending on the hole-selective layer (Table 1 in the publication). In this method, the intensity or photon flux corresponds to a generated current density and the QFLS corresponds to a voltage [266]. With these value pairs, the pseudo-*J-V*s were constructed. Both 2PACz and Me-4PACz have shown a pseudo-*FF* of 88%, which is 97% of the radiative limit. In contrast, PTAA allowed for 85.6% because of the reduced V_{OC}. Notably, with a C_{60} layer on top of the perovskite films, the pseudo-*FF* was the same with all hole-selective layers (85.3%). Also the QFLS was the same across all layers at around 1.13 V. This is the C_{60} layer limitation that was also discussed in chapter 4 and 2 (2.4.2). However, there is an obvious advantage for SAM-based cells in both *FF* and V_{OC} (with values 20-60 mV above

[2] Alternatively, knowing that the C_{60} causes strong non-radiative recombination, electrons could be thought of populating traps, where then holes recombine with the electrons in a bimolecular fashion (recomb. order 1 for electrons, and 2 for holes) [46].

the C_{60} limitation, without LiF interlayer). In addition, pseudo-*J-V* curves reconstructed from full cells with intensity-dependent V_{OC} measurements (suns-V_{OC}) also revealed pseudo-*FF*s of 87% and 88% for 2PACz and Me-4PACz, respectively. We explained this overcoming of the C_{60} limitation in full cells by an enhanced built-in field through the positive dipoles at the ITO, which is only well-defined in the presence of both electrodes at each side [164, 168, 267].

Influence of the alkyl chain length

We tested the influence of the number of hydrocarbons in the linking chain (n) of both the hydrogen- and methyl-terminated SAMs (see Fig. 5.8). n = 4 gave the highest fill factor and PCE in case of methyl termination and n = 2 was optimal in the case of hydrogen-termination (bare carbazole). Compared within the same batch (with bathocuproine as buffer layer instead of SnO_2), the average fill factors were slightly below 82%, 82% (max. 84%), 64% with Me-termination, and 81.5% (max. 83%), 80%, 65% with H-termination, for n = 2, 4, 6 respectively (see fig. S23 in the SI of the publication for box plots). Methoxy termination (as in MeO-2PACz) also has shown optimal *FF* values at n = 4 (not shown here), albeit with around 2%abs lower values than with methyl termination. V_{OC} values remained similar between 1.14-1.17 V across

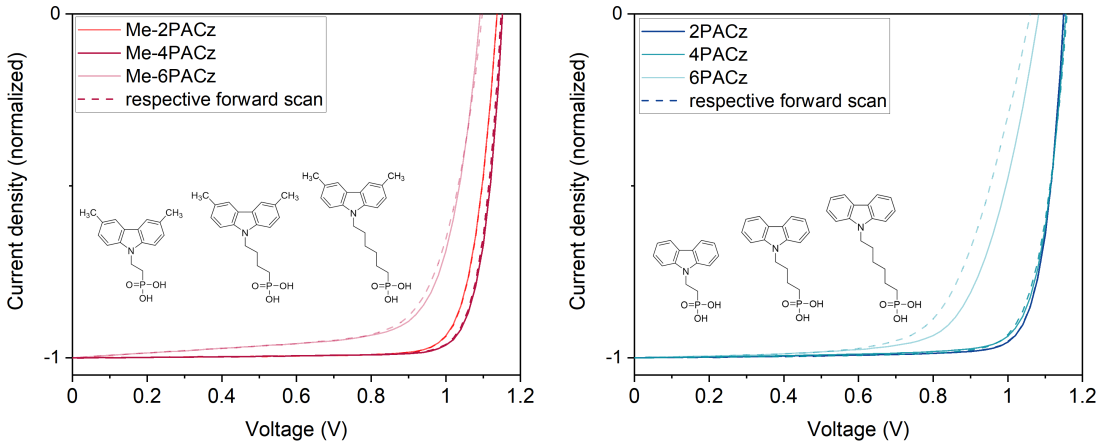

Figure 5.8: Optimal chain length determination for SAMs with hydrogen and methyl termination: *J-V* curves under illumination for a) Me-nPACz and b) nPACz as a function of chain length – n=2, 4, 6. From figure S23 of the publication [209] – published by the AAAS.

all SAMs, except for Me-6PACz. Interestingly, in both cases n = 6 lead to current-voltage hysteresis, indicating that the isolating chain might have caused strong hole accumulation. The difference in optimal chain length depending on the termination

might be explainable by different layer formation kinetics: while a shorter chain is beneficial for fast charge transfer, with a bulkier termination an interplay between steric hindrance and stabilization by van der Waals forces takes place [200, 268, 269].

5.1.4 Integration into silicon tandem cells

To test the higher *FF* potential with Me-4PACz, monolithic perovskite/silicon tandem solar cells were fabricated. The interconnecting layer between the two subcells in our perovskite/silicon tandem solar cells is sputtered ITO, which was also activated via UV-O_3 to create a bonding surface for the SAMs. This way, the SAMs MeO-2PACz, 2PACz and Me-4PACz also enabled highly efficient tandem cells which surpassed PTAA-based cells (see fig. 4 in the publication). As for the single junction cells, maximum fill factors (>80%) were achieved with Me-4PACz, while the V_{OC} values were similar between Me-4PACz and 2PACz. The maximum efficiency of 29.15% was certified by Fraunhofer ISE and marked the highest value achieved for both 2-terminal and 4-terminal perovskite/silicon solar cells from January to December 2020. The certified cell operated under current limitation by the perovskite subcell, with 19.4 mA/cm² from the perovskite cell and 20.2 mA/cm² from the silicon cell. Despite the fact that the limiting subcell dictated the shunt resistance of the tandem [270], and usually the perovskite shunt resistance is not optimal at these areas (1 cm²), the reached *FF*s were on a high level near 80%. A possible short-term step for improving the PCE further would be to reach silicon cell limitation by, e.g., increasing the thickness of the perovskite layer. This way, the tandem shunt resistance would be enhanced and thereby the *FF* could be enhanced even further.

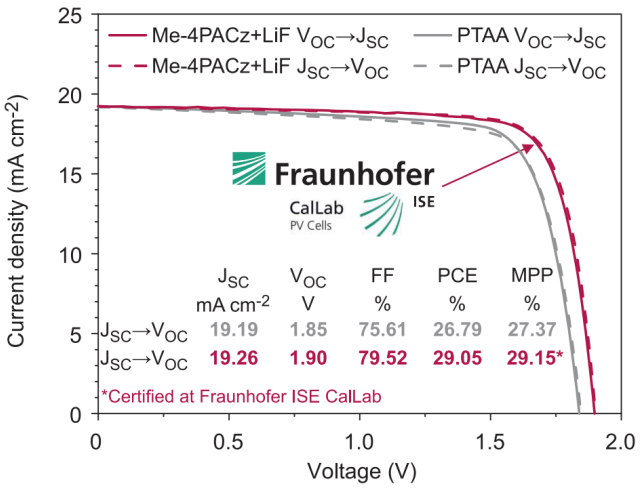

Figure 5.9: Certified Me-4PACz-based perovskite/silicon tandem solar cell (red curve), in comparison to the champion PTAA-based tandem cell.

The devices were MPP-tracked in ambient air, without encapsulation, in a custom-built aging setup that consisted of blue and infrared LED arrays which could be adjusted

such that the current densities in both subcells matched those obtained under AM1.5G-equivalent illumination. A Me-4PACz-based tandem cell retained 95.5% of its initial efficiency after 300 h of operation, similar to a 2PACz-based cell with 87.6%. With the interlayer LiF between perovskite and C_{60}, which increased the V_{OC} by up to 50 meV (see fig. S20 and S26 in the SI of the publication), we noticed a less stable behavior, with only 76% of the initial efficiency kept after 300 h of constant operation at MPP load. LiF-containing cells were generally less stable under repeated *J-V* measurements as well, loosing in *FF* and J_{SC}. The origin might lie within the high mobility of Li ions that could migrate through the perovskite and deteriorate the electrodes or alter the selective-contacts [271–274]. Thus, finding alternative interlayers to reduce V_{OC} losses at the C_{60} interface is a next rational task.

Maximum possible efficiency

To evaluate the maximum efficiency this tandem device stack (shown in fig. 4A in the publication) could deliver, we reconstructed the pseudo *J-V* curves with EL instead of PL. This way, the current density is the injected current and from the EL quantum yield (instead of PLQY), the QFLS at each injection level could be calculated for both perovskite and silicon subcell independently [275, 276]. Together, these pairs of current density and implied voltage make the implied *J-V* curve, similar to as presented above. The reconstructed subcell and tandem *J-V* curves are shown in Fig. 5.10. Similar to the value obtained in the single junction cells, the perovskite subcell showed a pseudo *FF* of 87%, while the silicon cell gave 84.8%. The *J-V* curve of the tandem featured a pseudo-*FF* of 87.8%, with which the PCE would be 31.7%. Assuming current matching between both subcells (both generating 19.6 mA/cm²), the maximum attainable PCE would be 32.4%. Note that this value marks the maximum PCE if resistive losses could be fully mitigated, with this standard perovskite composition that did not feature any bulk passivation. In fact, the perovskite subcell in this EL experiment has shown a poor PLQY of 0.02% (still 1.18 V V_{OC} because of a higher bandgap in this particular sample, 1.72 eV instead of 1.68 eV), while the silicon cell had a PLQY of 1.5%. Usually, the bare perovskite films show a PLQY of around 1%. Thus, an even higher maximum PCE is to be expected upon increase of the PLQY and further mitigation of interface losses at the electron-selective side. Taking the highest reported PLQY of a full *p-i-n* solar cell (8.4%) [44], it would correspond to a V_{OC} of 1.295 V for the 1.68 eV-bandgap perovskite composition and a tandem V_{OC} of 2.016 V, which would yield a maximum tandem PCE of 34.7% when keeping the same pseudo-*FF* of 87.8%. In the radiative limit for the perovskite (V_{OC} = 1.36 V), at the same pseudo-*FF* the tandem V_{OC} of 2.08 V would yield a PCE of 35.8%, and almost 37% when considering that the pseudo-*FF* would rise to above 90% for such a high V_{OC}.

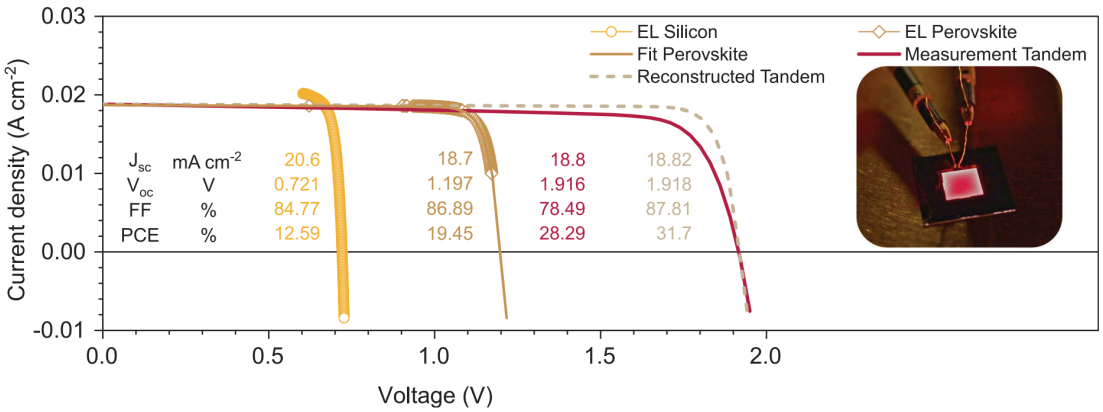

Figure 5.10: Reconstruction of pseudo *J-V* curves of the subcells from a Me-4PACz-based perovskite/silicon tandem solar cell, by intensity-dependent electroluminescence (EL). The inset shows a photograph of the tandem cell operating as an LED (charge injection under forward bias voltage, long exposure photo). Reprinted from ref. [209] – published by the AAAS.

5.2 Measuring charge extraction via surface photovoltage

As stated above, for the quantification of charge extraction that is relevant for solar cell operation there exists no standard in the perovskite community yet, while for quantification of voltage losses, PL is an established method. To extent the choice of experimental methods for this and to cross-check our TrPL results, we explored time-resolved surface photovoltage (trSPV) as a complementary method to TrPL, as it captures the essence of charge extraction and solar cell operation: the separation of holes and electrons [277–279]. Compared to TrPL, it comes with the advantage that no radiative recombination is needed, because it is only sensitive to the photovoltage between the two electrodes, which scales with the amount of separated charges and their distance to each other. Using an oscilloscope for detecting the voltage evolution, the time resolution can range from 1 ns to 1 s within one transient, which covers the time domains of charge transfer up to capacitive effects. And recently, it was shown that trSPV can be used for quantifying differences of perovskite solar cells depending on the hole-selective layer [280].

Fig. 5.11 shows SPV transients collected on perovskite-coated ITO substrates that either contained a hole-selective layer or not. Without a hole-selective layer, which separates charges by transferring holes into the ITO, such that a majority of electrons remains in the perovskite layer (negative SPV signal), there was a slight tendency for holes to accumulate at the perovskite surface, as seen by the positive SPV signal

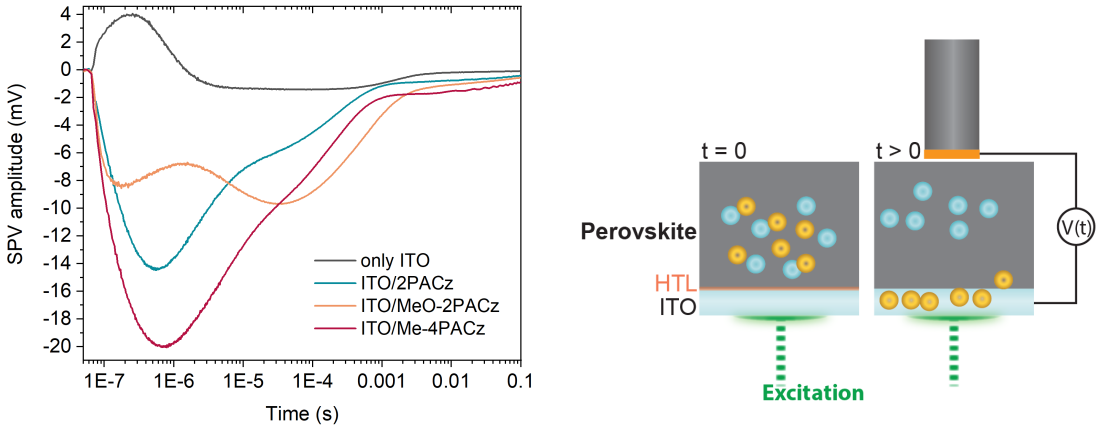

Figure 5.11: Detecting charge extraction with transient surface photovoltage (SPV). (a) shows transients of the SPV amplitude collected on ITO/SAM/perovskite samples, compared to an ITO sample which was not covered by a SAM. (b) displays a sketch of photo-excited charge carriers in the sample at the time of laser pulse arrival ($t = 0$) and upon charge separation by the hole-selective layer ($t > 0$), collecting holes (orange disks) in the ITO. This situation leads to a negative photovoltage. The SPV signal arises from charge build-up in the capacitor that forms between the F-doped SnO_2 electrode and ITO electrode (measured with an oscilloscope [281]). A pulsed laser (5 ns pulse width, 600 nm wavelength) was the excitation source. Data measured by Igal Levine and Thomas Dittrich.

(black line). This might indicate either a slight *p* doping of the surface, a hole-repelling downward band bending at the ITO interface, or the presence of electron traps at the ITO surface, leading to a more electron-rich surface at the ITO interface. However, the SPV signal is generally small, as expected from an intrinsic semiconductor. In line with the interpretations made from the TrPL data (Fig. 5.5 (b)), the initial rise of the SPV is faster (~factor 2 higher in max. slope) with Me-4PACz compared to 2PACz (see Fig. 5.11 (a)). This transient regime holds until a few hundred ns, similar to as observed with TrPL. With MeO-2PACz, the initial slope resembles that of the Me-4PACz transient first, however, another process forces the transient to invert its slope, until another rise occurs before it can slowly decay. The emergence of a second peak in the 100 µs regime might be connected to a release of trapped charges and is still subject to further investigation. This could potentially explain the lower QFLS and V_{OC} values obtained on MeO-2PACz (see chapter 4), if it is indeed connected to trap states that have not been passivated by the SAM in contrast to 2PACz and Me-4PACz.

As a further confirmation that trSPV is indeed suited for examining charge extraction speeds that are device-relevant; Fig. 5.11 shows SPV transients collected on the nPACz SAM series of which solar cell data was shown in Fig. 5.8. In this model system, we know that with a longer aliphatic chain (isolating), the *FF* in solar cells dropped, presumably

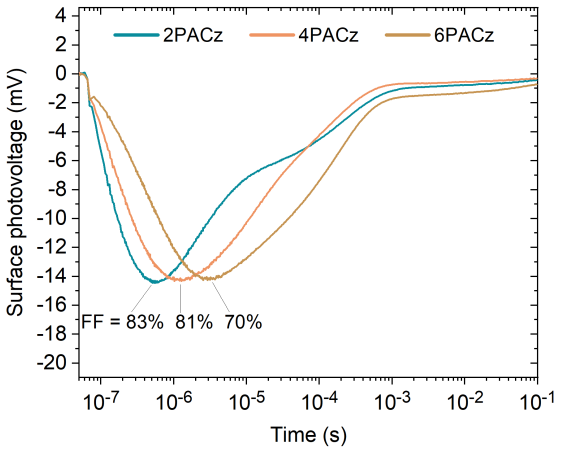

Figure 5.12: SPV transients comparing the nPACz series on ITO/SAM/perovskite samples (full solar cells based on these SAMs are shown in Fig. 5.8 (b)). The *FF* number labels are maximum fill factors reached with the respective SAM.

due to a slower extraction of holes into the ITO. In line with this experimental results, the initial rise of SPV was slower with longer chain. Interestingly, the maximum SPV signal was similar among all SAMs, meaning that the second process that lets the signal decay had a slower rate as well, the slower the charge extraction in the beginning. The measured V_{OC}s of the respective solar cells have also shown similar values.

Chapter 6

Conclusion and Outlook

This thesis was dedicated to contributing to the applicability of perovskite solar cells for tandem solar cells that have the potential to promote leaps in efficiency by deeper understanding and thus larger adaptation in the solar cell industry. The experimental work has thus revolved around the optimization of tandem-relevant *p-i-n*-type solar cells and the investigation of power losses at their interfaces to the charge-selective layers. As a general theme, the work was dealing with the replacement of the traditional hole-selective layer by self-assembled monolayers (SAMs) that can conformally cover the transparent conductive oxides which are one of the electrodes. This method has proved to be advantageous for studying the role of the hole-selective interface in solar cell operation and for optimizing it rationally. The idea of using hole-selective SAMs in perovskite solar cells was patented, with a series of possible molecule designs, and the SAMs are now commercially available from different suppliers.

We demonstrated the first efficiently working hole-selective SAM with the molecule V1036, which consisted of a carbazole core with diphenylamine substitution, terminated by methoxy groups. This hole-selective fragment was paired with a phosphonic acid group which bonds to oxide surfaces. By immersion of the ITO substrates in a dilute V1036-containing solution, the substrates were covered by the molecules with a density high enough to enable remarkably low leakage currents. The solar cells based on V1036 had a power conversion efficiency of max. 18%, while with the standard material for *p-i-n* solar cells, poly(triarylamine), the maximum efficiency was at around 19%. The fill factors of the SAM cells were decent, however, they have shown deficits in the open-circuit voltage (V_{OC}). By mixing the V1036 with a non-conjugated "filler molecule" in the SAM solution with the same anchoring group, butyl-phosphonic acid, the open circuit voltage could be enhanced by roughly 80 meV. We identified that it was not the ordering of the SAM layer that improved upon mixing, but measured a correlation between the ionization potential of the functionalized substrate and the V_{OC}. The energetic alignment between valence band maximum of the perovskite and hole-accepting level of the hole-selective layer was then further confirmed as the determining parameter for device performance in the work that followed after.

In search of more efficient SAMs, we explored other molecule designs of which the simplest and smallest, a carbazole fragment linked to an ethyl-phosphonic acid group (2PACz), has shown the most promising results. In this project, we published two new SAM materials, 2PACz and its methoxy-substituted variant MeO-2PACz, which enabled to surpass state-of-the-art *p-i-n* solar cells. Using reflection-absorption infrared spectroscopy, we identified monolayer formation and found that similar layers can be processed both by the classical dipping method and by spin-coating a SAM solution of appropriate concentration, in line with the results on solar cell level. Without the use of interlayers, dopants or additives, the solar cells reached a power conversion efficiency of up to 21.2%. Furthermore, we have shown that SAMs can cover arbitrarily formed surfaces by demonstrating a monolithic perovskite/CIGSe tandem solar cell with 23.3% certified efficiency on 1 cm^2 active area. This surpassed the previous record (22.4% on 0.04 cm^2) in both efficiency and size and served as a confirmation that SAMs enable applications that were not straight-forward to realize without them. With a combination of photoluminescence and photoelectron spectroscopy, we analyzed the reasons behind the improved performance. With 2PACz, we found that its interface to the perovskite was practically "lossless", meaning there was no measurable loss of potential due to non-radiative recombination. Furthermore, the three SAMs were studied regarding their energetic alignment to the perovskite's valence band onset and we found that the smaller the offset, the higher the V_{OC} was. The different offsets could be explained by the different intrinsic dipole moments that the molecules carried, rendering it as a tool for tailoring the perfect hole-selective contact with regard to energetic alignment depending on the perovskite composition.

Finally, knowing about the importance of minimal energetic offset for realizing ideal interfaces for high V_{OC}s, we continued optimization by focusing on the fill factor, which is a parameter that also for the best perovskite solar cells still lacks behind compared to mature solar cell technologies. By testing another SAM design, similar to 2PACz but with methyl group termination and four hydrocarbons in the linking chain (Me-4PACz), we found a hole-selective layer that surpassed all other available ones in fill factor, while keeping the high V_{OC} of 2PACz-based cells. The distinct difference lied within the ideality factor of the current-voltage characteristics, where Me-4PACz led to a value of 1.26, while usual values of *p-i-n* cells are measured at around 1.4 to 1.5. Single junction devices based on Me-4PACz reached fill factors of up to 84% and V_{OC}s of up to 1.234 V (compared to 82% with 2PACz with similar V_{OC}). The combination of high V_{OC} and low ideality factor is a rare case in the perovskite research field and the presented cells might help to extend the understanding on limitations set by the usually high ideality factors. Using intensity-dependent transient photoluminescence measurements, we found a way to quantify hole extraction, which was not yet focused on in literature and thus no standards for the quantification of charge extraction efficiencies existed. This has partly to do with the complication of several processes overlapping with charge

extraction, making it challenging to isolate from each other. However, as in the case for studying V_{OC} losses, the SAMs have shown their potential for building model systems here as well. We estimated an approximately 10-times higher hole extraction flux with Me-4PACz compared to 2PACz and assumed that this enhanced extraction reduced the ideality factor. By transient surface photovoltage measurements, we found more evidence for our interpretations and have shown that this method is also helpful for potentially modeling charge carrier dynamics within a wide time frame (ns to ms). The enhanced hole extraction also stabilized the mixed perovskite phase of a tandem-relevant composition with 1.68 eV bandgap by preventing charge accumulation. By integrating the SAM into monolithic perovskite/silicon tandem solar cells, the benefit transferred into higher fill factors here as well and stable operation under continuous illumination. A Me-4PACz tandem cell was certified to a power conversion efficiency of 29.15%, marking a new record at the time and significantly surpassing previously published values. With injection-dependent electroluminescence spectroscopy, we reconstructed the subcell current-voltage characteristics without the influence of resistive losses to estimate the maximum performance possible for the used device stack. Thereby, we calculated implied efficiencies of over 32% in the investigated device, and over 34% if the perovskite quality (photoluminescence quantum yield and with that the V_{OC}) could be improved to levels that have already been reached in literature of record cells.

Outlook

Record power conversion efficiencies of perovskite solar cells will continue to rise. Presumably, as best V_{OC} values are already near their theoretical maximum, the focus of development will further shift towards reaching higher stability and the mitigation of fill factor losses, with parallel development of technologies for upscaled fabrication. Further research will tell whether the higher stability and fill factors will be reached through interfacial engineering or by completely replacing the used perovskite compositions by alternatives. Current approaches often use additives to the perovskite solution that enhance the complexity of the fabrication process, which is detrimental to adaptation and reproducibility in other laboratories. Promising approaches seem to be those that enable high solar cell performance with high simplicity and robustness.

For the tandem-relevant *p-i-n* type solar cells, the reduction of V_{OC} losses will likely remain a focus of research in the coming years. Having identified that for most solar cells, the dominating losses happen at the electron-selective interface, further progress will need the exploration of alternative electron-selective materials to replace the fullerenes or the reliable formation of a selectivity-enhancing interlayer other than lithium fluoride. The challenge here is to find a combination of layers and perovskite

compositions that combine all promises of perovskite solar technology – high efficiency, low fabrication costs, high simplicity & flexibility – with stability and scalability into one design, instead of demonstrating only few of these aspects within one functioning solar cell. Suitable SAMs intrinsically come with the combination of scalability, simplicity, low costs and stability and might thus be an appropriate pathway for exploring alternative electron-selective layers or interlayers as well. And since "often, [...] the interface is the device" (H. Kroemer), they offer the possibility to sensitively study the interfacial chemistry and charge carrier dynamics, which also for perovskites have been identified to play a key role in solar cell performance and stability. A disruptive approach would be a perovskite solar cell sandwiched by two SAMs, abandoning dedicated charge-selective layers entirely, which would need the exploration of suitable electron-selective fragments and anchoring groups that reliably bond to the complex perovskite surface. Within another approach, the research field might explore perovskite compositions that are intrinsically compatible with the (valuably stable) fullerene-based electron-selective layers or to inorganic charge-selective layers, while providing enhanced stability. In the pursuit of these goals, advanced characterization methods targeting to further understand the interfacial charge carrier dynamics and molecular interaction between the perovskite and charge-selective layers could provide valuable input for design guidelines. Building on the results of this thesis, especially investigating the "lossless" feature of the 2PACz/perovskite interface might unfold hints on how to design more of such materials. However, as this interface is buried, challenges arise from accessing the device-relevant physics nondestructively. Interesting strategies might employ interface-selective techniques like sum frequency generation vibrational spectroscopy, paired with photoelectron spectroscopy for studying the energetic alignment and x-ray techniques for monitoring the crystal formation kinetics at the interface. Using such methods during solar cell operation to monitor whether under load and charge flow the guidelines for ideal contacts change compared to the evaluations done on the individual layers without illumination or charge flow could lead to new knowledge as well.

Within the next few years, we might witness the interesting step of perovskite solar cells entering industrial production, with perovskite/silicon tandem solar cells looming to be a first entry point. With rapidly sinking prices of conventional silicon solar modules, the time frame within which the addition of a perovskite top cell can disruptively lower the levelized cost of electricity is narrow. However, once modules with >400 W peak power are demonstrated, their momentum will also be beneficial to perovskite solar cell research. Hence, photovoltaics will further undercut the price of every other form of electricity generation. There is hope and the feasibility that it will eventually surpass all other sources in ubiquity as well, such that humankind takes advantage of the rich amount of energy our sun gifts us every day for the next billions of years.

Bibliography

[1] IRENA. *Future of Solar Photovoltaic: Deployment, investment, technology, grid integration and socio-economic aspects (A Global Energy Transformation: paper), Abu Dhabi.* 2019.

[2] N. S. Lewis and D. G. Nocera. "Powering the planet: Chemical challenges in solar energy utilization". In: *Proceedings of the National Academy of Sciences* 103.43 (2006), pp. 15729–15735. DOI: 10.1073/pnas.0603395103.

[3] J. Jean et al. "Pathways for solar photovoltaics". In: *Energy and Environmental Science* 8.4 (2015), pp. 1200–1219. DOI: 10.1039/c4ee04073b.

[4] Umweltbundesamt. *CO2 calculator of the german Federal Environment Agency.* 2021. URL: https://uba.co2-rechner.de (visited on 02/02/2021).

[5] E. Stehfest et al. "Climate benefits of changing diet". In: *Climatic Change* 95.1-2 (2009), pp. 83–102. DOI: 10.1007/s10584-008-9534-6.

[6] A. D. González, B. Frostell, and A. Carlsson-Kanyama. "Protein efficiency per unit energy and per unit greenhouse gas emissions: Potential contribution of diet choices to climate change mitigation". In: *Food Policy* 36.5 (2011), pp. 562–570. DOI: 10.1016/j.foodpol.2011.07.003.

[7] W. Steffen et al. "Trajectories of the Earth System in the Anthropocene". In: *Proceedings of the National Academy of Sciences* 115.33 (2018), pp. 8252–8259. DOI: 10.1073/pnas.1810141115.

[8] *bp Statistical Review of World Energy 2020.* URL: https://www.bp.com/en/global/corporate/energy-economics/statistical-review-of-world-energy/downloads.html (visited on 02/02/2021).

[9] J. Jean and P. R. Brown. *Emerging Photovoltaic Technologies.* IOP Publishing, 2020.

[10] *Press Release by Fraunhofer ISE: Nettostromerzeugung in Deutschland 2020: erneuerbare Energien erstmals über 50 Prozent.* URL: https://www.ise.fraunhofer.de/de/presse-und-medien/news/2020/nettostromerzeugung-in-deutschland-2021-erneuerbare-energien-erstmals-ueber-50-prozent.html (visited on 02/22/2021).

[11] M. A. Green. "Third generation photovoltaics: solar cells for 2020 and beyond". In: *Physica E: Low-dimensional Systems and Nanostructures* 14.1-2 (2002), pp. 65–70. DOI: 10.1016/S1386-9477(02)00361-2.

[12] K. P. Bhandari et al. “Energy payback time (EPBT) and energy return on energy invested (EROI) of solar photovoltaic systems: A systematic review and meta-analysis”. In: *Renewable and Sustainable Energy Reviews* 47 (2015), pp. 133–141. DOI: 10.1016/j.rser.2015.02.057.

[13] *National Renewable Energy Laboratory, "Best Research-Cell Efficiency Chart"*. 2020. URL: www.nrel.gov/pv/cell-efficiency.html (visited on 06/04/2020).

[14] M. A. Green et al. “Solar cell efficiency tables (version 56)”. In: *Progress in Photovoltaics: Research and Applications* 28.7 (2020), pp. 629–638. DOI: 10.1002/pip.3303.

[15] A. Kojima et al. “Organometal halide perovskites as visible-light sensitizers for photovoltaic cells”. In: *Journal of the American Chemical Society* 131.17 (2009), pp. 6050–6051. DOI: 10.1021/ja809598r.

[16] Y. Rong et al. “Challenges for commercializing perovskite solar cells”. In: *Science* 361.6408 (2018), eaat8235. DOI: 10.1126/science.aat8235.

[17] G. E. Eperon, M. T. Hörantner, and H. J. Snaith. “Metal halide perovskite tandem and multiple-junction photovoltaics”. In: *Nature Reviews Chemistry* 1.12 (2017), p. 0095. DOI: 10.1038/s41570-017-0095.

[18] J. P. Mailoa et al. “A 2-terminal perovskite/silicon multijunction solar cell enabled by a silicon tunnel junction”. In: *Applied Physics Letters* 106.12 (2015), pp. 30–33. DOI: 10.1063/1.4914179.

[19] S. Albrecht and B. Rech. “Perovskite solar cells: On top of commercial photovoltaics”. In: *Nature Energy* 2.1 (2017). DOI: 10.1038/nenergy.2016.196.

[20] A. Richter, M. Hermle, and S. W. Glunz. “Reassessment of the limiting efficiency for crystalline silicon solar cells”. In: *IEEE Journal of Photovoltaics* 3.4 (2013), pp. 1184–1191. DOI: 10.1109/JPHOTOV.2013.2270351.

[21] K. Yoshikawa et al. “Silicon heterojunction solar cell with interdigitated back contacts for a photoconversion efficiency over 26%”. In: *Nature Energy* 2.5 (2017), p. 17032. DOI: 10.1038/nenergy.2017.32.

[22] R. T. Ross. “Some Thermodynamics of Photochemical Systems”. In: *The Journal of Chemical Physics* 46.12 (1967), pp. 4590–4593. DOI: 10.1063/1.1840606.

[23] P. Würfel. “The chemical potential of radiation”. In: *Journal of Physics C: Solid State Physics* 15.18 (1982), pp. 3967–3985. DOI: 10.1088/0022-3719/15/18/012.

[24] P. Würfel. *Physics of Solar Cells*. Wiley-VCH Verlag GmbH & Co, Weinheim, 2005.

[25] J. Melskens et al. “Concepts and prospects of passivating contacts for crystalline silicon solar cells”. In: *2015 IEEE 42nd Photovoltaic Specialist Conference, PVSC 2015* (2015). DOI: 10.1109/PVSC.2015.7355646.

[26] U. Rau. "Reciprocity relation between photovoltaic quantum efficiency and electroluminescent emission of solar cells". In: *Physical Review B* 76.8 (2007), p. 085303. DOI: 10.1103/PhysRevB.76.085303.

[27] S. Smit. "Passivating selective contacts for silicon photovoltaics". PhD thesis. Eindhoven University of Technology, 2016.

[28] A.-E. Becquerel. "On Electron Effects under the Influence of Solar Radiation". In: *Comptes Rendus de l'Academie Sciences Paris* 9 (1839), pp. 561–567.

[29] R. Williams. "Becquerel photovoltaic effect in binary compounds". In: *The Journal of Chemical Physics* 32.5 (1960), pp. 1505–1514. DOI: 10.1063/1.1730950.

[30] P. Lenard. "Über die lichtelektrische Wirkung". In: *Annalen der Physik* 313.5 (1902), pp. 149–198.

[31] A. Einstein. "Über einen die Erzeugung und Verwandlung des Lichtes betreffenden heuristischen Gesichtspunkt". In: *Annalen der Physik* 322.6 (1905), pp. 132–148. DOI: 10.1002/andp.19053220607.

[32] C. E. Fritts. "On a new form of selenium cell, and some electrical discoveries made by its use". In: *American Journal of Science* s3-26.156 (1883), pp. 465–472. DOI: 10.2475/ajs.s3-26.156.465.

[33] D. M. Chapin, C. S. Fuller, and G. L. Pearson. "A new silicon p-n junction photocell for converting solar radiation into electrical power [3]". In: *Journal of Applied Physics* 25.5 (1954), pp. 676–677. DOI: 10.1063/1.1721711.

[34] W. Shockley. "The Theory of p-n Junctions in Semiconductors and p-n Junction Transistors". In: *Bell System Technical Journal* 28.3 (1949), pp. 435–489. DOI: 10.1002/j.1538-7305.1949.tb03645.x.

[35] P. Würfel and U. Würfel. *Physics of solar cells: from basic principles to advanced concepts*. John Wiley & Sons, 2016.

[36] W. Shockley and W. T. Read. "Statistics of the Recombinations of Holes and Electrons". In: *Physical Review* 87.5 (1952), pp. 835–842. DOI: 10.1103/PhysRev.87.835.

[37] T. Kirchartz et al. "Photoluminescence-Based Characterization of Halide Perovskites for Photovoltaics". In: *Advanced Energy Materials* 10.26 (2020), p. 1904134. DOI: 10.1002/aenm.201904134.

[38] F. Staub et al. "Beyond Bulk Lifetimes: Insights into Lead Halide Perovskite Films from Time-Resolved Photoluminescence". In: *Physical Review Applied* 6.4 (2016), p. 044017. DOI: 10.1103/PhysRevApplied.6.044017.

[39] M. Planck. "Zur Theorie der Wärmestrahlung". In: *Annalen der Physik* 336.4 (1910), pp. 758–768. DOI: 10.1002/andp.19103360406.

[40] G Kirchhoff. "Ueber das Verhältniss zwischen dem Emissionsvermögen und dem Absorptionsvermögen der Körper für Wärme und Licht". In: *Annalen der Physik und Chemie* 185.2 (1860), pp. 275–301. DOI: 10.1002/andp.18601850205.

[41] L. Onsager. "Reciprocal Relations in Irreversible Processes. I." In: *Physical Review* 37.4 (1931), pp. 405–426. DOI: 10.1103/PhysRev.37.405.

[42] P. W. Bridgman. "Note on the Principle of Detailed Balancing". In: *Physical Review* 31.1 (1928), pp. 101–102. DOI: 10.1103/PhysRev.31.101.

[43] E. H. Kennard. "On The Thermodynamics of Fluorescence". In: *Physical Review* 11.1 (1918), pp. 29–38. DOI: 10.1103/PhysRev.11.29.

[44] Z. Liu et al. "Open-Circuit Voltages Exceeding 1.26 V in Planar Methylammonium Lead Iodide Perovskite Solar Cells". In: *ACS Energy Letters* 4.1 (2019), pp. 110–117. DOI: 10.1021/acsenergylett.8b01906.

[45] W. Shockley and H. J. Queisser. "Detailed Balance Limit of Efficiency of p-n Junction Solar Cells". In: *Journal of Applied Physics* 32.3 (1961), pp. 510–519. DOI: 10.1063/1.1736034.

[46] C. M. Wolff et al. "Nonradiative Recombination in Perovskite Solar Cells: The Role of Interfaces". In: *Advanced Materials* 31.52 (2019), p. 1902762. DOI: 10.1002/adma.201902762.

[47] T. Kirchartz et al. "Recombination via tail states in polythiophene:fullerene solar cells". In: *Physical Review B - Condensed Matter and Materials Physics* 83.11 (2011), pp. 1–13. DOI: 10.1103/PhysRevB.83.115209.

[48] P. Caprioglio et al. "On the Origin of the Ideality Factor in Perovskite Solar Cells". In: *Advanced Energy Materials* 10.27 (2020), p. 2000502. DOI: 10.1002/aenm.202000502.

[49] Q. Jiang et al. "Surface passivation of perovskite film for efficient solar cells". In: *Nature Photonics* 13.7 (2019), pp. 460–466. DOI: 10.1038/s41566-019-0398-2.

[50] L. M. Pazos-Outón, T. P. Xiao, and E. Yablonovitch. "Fundamental Efficiency Limit of Lead Iodide Perovskite Solar Cells". In: *The Journal of Physical Chemistry Letters* (2018), pp. 1703–1711. DOI: 10.1021/acs.jpclett.7b03054.

[51] J.-F. Guillemoles et al. "Guide for the perplexed to the Shockley–Queisser model for solar cells". In: *Nature Photonics* 13.8 (2019), pp. 501–505. DOI: 10.1038/s41566-019-0479-2.

[52] A. D. Vos. "Detailed balance limit of the efficiency of tandem solar cells". In: *Journal of Physics D: Applied Physics* 13.5 (1980), pp. 839–846. DOI: 10.1088/0022-3727/13/5/018.

[53] A. S. Brown and M. A. Green. "Detailed balance limit for the series constrained two terminal tandem solar cell". In: *Physica E: Low-dimensional Systems and Nanostructures* 14.1-2 (2002), pp. 96–100. DOI: 10.1016/S1386-9477(02)00364-8.

[54] M. H. Futscher and B. Ehrler. "Efficiency Limit of Perovskite/Si Tandem Solar Cells". In: *ACS Energy Letters* 1.4 (2016), pp. 863–868. DOI: 10.1021/acsenergylett.6b00405.

[55] T. Leijtens et al. "Opportunities and challenges for tandem solar cells using metal halide perovskite semiconductors". In: *Nature Energy* 3.10 (2018), pp. 828–838. DOI: 10.1038/s41560-018-0190-4.

[56] K. Jäger et al. "Numerical optical optimization of monolithic planar perovskite-silicon tandem solar cells with regular and inverted device architectures". In: *Optics Express* 25.12 (2017), A473. DOI: 10.1364/OE.25.00A473.

[57] E. Aydin et al. "Interplay between temperature and bandgap energies on the outdoor performance of perovskite/silicon tandem solar cells". In: *Nature Energy* (2020). DOI: 10.1038/s41560-020-00687-4.

[58] C. Ulbrich et al. "Matching of silicon thin-film tandem solar cells for maximum power output". In: *International Journal of Photoenergy* 2013 (2013). DOI: 10.1155/2013/314097.

[59] E. Köhnen et al. "Highly efficient monolithic perovskite silicon tandem solar cells: analyzing the influence of current mismatch on device performance". In: *Sustainable Energy & Fuels* 3.8 (2019), pp. 1995–2005. DOI: 10.1039/C9SE00120D.

[60] P. Tockhorn et al. "Three-Terminal Perovskite/Silicon Tandem Solar Cells with Top and Interdigitated Rear Contacts". In: *ACS Applied Energy Materials* 3.2 (2020), pp. 1381–1392. DOI: 10.1021/acsaem.9b01800.

[61] M. A. Steiner et al. "A monolithic three-terminal GaInAsP/GaInAs tandem solar cell". In: *Progress in Photovoltaics: Research and Applications* 17.8 (2009), pp. 587–593. DOI: 10.1002/pip.913.

[62] P. Chiu et al. "35.8% space and 38.8% terrestrial 5J direct bonded cells". In: *2014 IEEE 40th Photovoltaic Specialist Conference (PVSC)*. IEEE, 2014, pp. 0011–0013. DOI: 10.1109/PVSC.2014.6924957.

[63] G. Rose. "Ueber einige neue Mineralien des Urals". In: *Journal für Praktische Chemie* 19.1 (1840), pp. 459–468. DOI: 10.1002/prac.18400190179.

[64] D. Weber. "CH3NH3PbX3, ein Pb (II)-System mit kubischer Perowskitstruktur/CH3NH3PbX3, a Pb (II)-System with Cubic Perovskite Structure". In: *Zeitschrift für Naturforschung B* 33.12 (1978), pp. 1443–1445. DOI: 10.1515/znb-1978-0809.

[65] D. B. Mitzi et al. "Conducting tin halides with a layered organic-based perovskite structure". In: *Nature* 369.6480 (1994), pp. 467–469. DOI: 10.1038/369467a0.

[66] *Search for "perovskite solar" as topics in Web of Science.* 2021. (Visited on 01/04/2021).

[67] M. A. Green et al. "Solar cell efficiency tables (Version 55)". In: *Progress in Photovoltaics: Research and Applications* 28.1 (2020), pp. 3–15. DOI: 10.1002/pip.3228.

[68] T. Jesper Jacobsson et al. "Exploration of the compositional space for mixed lead halogen perovskites for high efficiency solar cells". In: *Energy and Environmental Science* 9.5 (2016), pp. 1706–1724. DOI: 10.1039/c6ee00030d.

[69] E. L. Unger et al. "Roadmap and roadblocks for the band gap tunability of metal halide perovskites". In: *J. Mater. Chem. A* 5.23 (2017), pp. 11401–11409. DOI: 10.1039/C7TA00404D.

[70] J. H. Noh et al. "Chemical management for colorful, efficient, and stable inorganic-organic hybrid nanostructured solar cells". In: *Nano Letters* 13.4 (2013), pp. 1764–1769. DOI: 10.1021/nl400349b.

[71] K. A. Bush et al. "Compositional Engineering for Efficient Wide Band Gap Perovskites with Improved Stability to Photoinduced Phase Segregation". In: *ACS Energy Letters* 3.2 (2018), pp. 428–435. DOI: 10.1021/acsenergylett.7b01255.

[72] H. J. Snaith et al. "Anomalous hysteresis in perovskite solar cells". In: *Journal of Physical Chemistry Letters* 5.9 (2014), pp. 1511–1515. DOI: 10.1021/jz500113x.

[73] E. L. Unger et al. "Hysteresis and transient behavior in current-voltage measurements of hybrid-perovskite absorber solar cells". In: *Energy and Environmental Science* 7.11 (2014), pp. 3690–3698. DOI: 10.1039/c4ee02465f.

[74] J. Bisquert et al. "Theory of impedance and capacitance spectroscopy of solar cells with dielectric relaxation, drift-diffusion transport, and recombination". In: *Journal of Physical Chemistry C* 118.33 (2014), pp. 18983–18991. DOI: 10.1021/jp5062144.

[75] S. De Wolf et al. "Organometallic Halide Perovskites: Sharp Optical Absorption Edge and Its Relation to Photovoltaic Performance". In: *The Journal of Physical Chemistry Letters* 5.6 (2014), pp. 1035–1039. DOI: 10.1021/jz500279b.

[76] W. J. Yin, T. Shi, and Y. Yan. "Unusual defect physics in CH3NH3PbI3 perovskite solar cell absorber". In: *Applied Physics Letters* 104.6 (2014), pp. 10–14. DOI: 10.1063/1.4864778.

[77] K. X. Steirer et al. "Defect Tolerance in Methylammonium Lead Triiodide Perovskite". In: *ACS Energy Letters* 1.2 (2016), pp. 360–366. DOI: 10.1021/acsenergylett.6b00196.

[78] D. Meggiolaro et al. "Iodine chemistry determines the defect tolerance of lead-halide perovskites". In: *Energy and Environmental Science* 11.3 (2018), pp. 702–713. DOI: 10.1039/c8ee00124c.

[79] I. Levine et al. "Can we use time-resolved measurements to get steady-state transport data for halide perovskites?" In: *Journal of Applied Physics* 124.10 (2018). DOI: 10.1063/1.5037637.

[80] S. D. Stranks et al. "Electron-Hole Diffusion Lengths Exceeding 1 Micrometer in an Organometal Trihalide Perovskite Absorber". In: *Science* 342.6156 (2013), pp. 341–344. DOI: 10.1126/science.1243982.

[81] M. M. Lee et al. "Efficient Hybrid Solar Cells Based on Meso-Superstructured Organometal Halide Perovskites". In: *Science* 338.6107 (2012), pp. 643–647. DOI: 10.1126/science.1228604.

[82] H.-S. Kim et al. "Lead Iodide Perovskite Sensitized All-Solid-State Submicron Thin Film Mesoscopic Solar Cell with Efficiency Exceeding 9%". In: *Scientific Reports* 2.1 (2012), p. 591. DOI: 10.1038/srep00591.

[83] M. Liu, M. B. Johnston, and H. J. Snaith. "Efficient planar heterojunction perovskite solar cells by vapour deposition". In: *Nature* 501.7467 (2013), pp. 395–398. DOI: 10.1038/nature12509.

[84] A. T. Barrows et al. "Efficient planar heterojunction mixed-halide perovskite solar cells deposited via spray-deposition". In: *Energy and Environmental Science* 7.9 (2014), pp. 2944–2950. DOI: 10.1039/c4ee01546k.

[85] K. Hwang et al. "Toward large scale roll-to-roll production of fully printed perovskite solar cells". In: *Advanced Materials* 27.7 (2015), pp. 1241–1247. DOI: 10.1002/adma.201404598.

[86] N. Ahn et al. "Highly Reproducible Perovskite Solar Cells with Average Efficiency of 18.3% and Best Efficiency of 19.7% Fabricated via Lewis Base Adduct of Lead(II) Iodide". In: *Journal of the American Chemical Society* 137.27 (2015), pp. 8696–8699. DOI: 10.1021/jacs.5b04930.

[87] N. J. Jeon et al. "Solvent engineering for high-performance inorganic–organic hybrid perovskite solar cells". In: *Nature Materials* 13.9 (2014), pp. 897–903. DOI: 10.1038/nmat4014.

[88] O. Malinkiewicz et al. "Perovskite solar cells employing organic charge-transport layers". In: *Nature Photonics* 8.2 (2014), pp. 128–132. DOI: 10.1038/nphoton.2013.341.

[89] J. Y. Jeng et al. "CH3NH3PbI3 perovskite/fullerene planar-heterojunction hybrid solar cells". In: *Advanced Materials* 25.27 (2013), pp. 3727–3732. DOI: 10.1002/adma.201301327.

[90] N. Pellet et al. "Mixed-organic-cation perovskite photovoltaics for enhanced solar-light harvesting". In: *Angewandte Chemie - International Edition* 53.12 (2014), pp. 3151–3157. DOI: 10.1002/anie.201309361.

[91] G. E. Eperon et al. "Formamidinium lead trihalide: a broadly tunable perovskite for efficient planar heterojunction solar cells". In: *Energy & Environmental Science* 7.3 (2014), p. 982. DOI: 10.1039/c3ee43822h.

[92] D. P. McMeekin et al. "A mixed-cation lead mixed-halide perovskite absorber for tandem solar cells". In: *Science* 351.6269 (2016), pp. 151–155. DOI: 10.1126/science.aad5845.

[93] M. Saliba et al. "Cesium-containing triple cation perovskite solar cells: improved stability, reproducibility and high efficiency". In: *Energy Environ. Sci.* 9.6 (2016), pp. 1989–1997. DOI: 10.1039/C5EE03874J.

[94] M. Saliba et al. "Incorporation of rubidium cations into perovskite solar cells improves photovoltaic performance". In: *Science* 354.6309 (2016), pp. 206–209. DOI: 10.1126/science.aah5557.

[95] H. Min et al. "Efficient, stable solar cells by using inherent bandgap of a-phase formamidinium lead iodide". In: *Science* 366.6466 (2019), pp. 749–753. DOI: 10.1126/science.aay7044.

[96] Y. Hou et al. "Efficient tandem solar cells with solution-processed perovskite on textured crystalline silicon". In: *Science* 367.6482 (2020), pp. 1135–1140. DOI: 10.1126/science.aaz3691.

[97] L. Gil-Escrig et al. "Fully Vacuum-Processed Perovskite Solar Cells on Pyramidal Microtextures". In: *Solar RRL* 2000553.December (2020), pp. 1–9. DOI: 10.1002/solr.202000553.

[98] B. Chen et al. "Blade-Coated Perovskites on Textured Silicon for 26%-Efficient Monolithic Perovskite/Silicon Tandem Solar Cells". In: *Joule* 4.4 (2020), pp. 850–864. DOI: 10.1016/j.joule.2020.01.008.

[99] M. V. Khenkin et al. "Consensus statement for stability assessment and reporting for perovskite photovoltaics based on ISOS procedures". In: *Nature Energy* 5.1 (2020), pp. 35–49. DOI: 10.1038/s41560-019-0529-5.

[100] K. A. Bush et al. "23.6%-efficient monolithic perovskite/silicon tandem solar cells with improved stability". In: *Nature Energy* 2.4 (2017), p. 17009. DOI: 10.1038/nenergy.2017.9.

[101] S. Albrecht et al. "Monolithic perovskite/silicon-heterojunction tandem solar cells processed at low temperature". In: *Energy Environ. Sci.* 9.1 (2016), pp. 81–88. DOI: 10.1039/C5EE02965A.

[102] F. Sahli et al. "Improved Optics in Monolithic Perovskite/Silicon Tandem Solar Cells with a Nanocrystalline Silicon Recombination Junction". In: *Advanced Energy Materials* 1701609 (2017), pp. 1–8. DOI: 10.1002/aenm.201701609.

[103] J. H. Heo et al. "Hysteresis-less inverted CH3NH3PbI3 planar perovskite hybrid solar cells with 18.1% power conversion efficiency". In: *Energy and Environmental Science* 8.5 (2015), pp. 1602–1608. DOI: 10.1039/c5ee00120j.

[104] C.-G. Wu et al. "High efficiency stable inverted perovskite solar cells without current hysteresis". In: *Energy Environ. Sci.* 8.9 (2015), pp. 2725–2733. DOI: 10.1039/C5EE00645G.

[105] A. Magomedov et al. "Pyridination of hole transporting material in perovskite solar cells questions the long-term stability". In: *Journal of Materials Chemistry C* 6.33 (2018), pp. 8874–8878. DOI: 10.1039/c8tc02242a.

[106] E. Kasparavicius et al. "Long-Term Stability of the Oxidized Hole-Transporting Materials used in Perovskite Solar Cells". In: *Chemistry - A European Journal* 24.39 (2018), pp. 9910–9918. DOI: 10.1002/chem.201801441.

[107] F. Lamberti et al. "Evidence of Spiro-OMeTAD De-doping by tert-Butylpyridine Additive in Hole-Transporting Layers for Perovskite Solar Cells". In: *Chem* (2019), pp. 1–12. DOI: 10.1016/j.chempr.2019.04.003.

[108] P. Docampo et al. "Efficient organometal trihalide perovskite planar-heterojunction solar cells on flexible polymer substrates". In: *Nature Communications* 4 (2013), pp. 1–6. DOI: 10.1038/ncomms3761.

[109] M. Kaltenbrunner et al. "Flexible high power-per-weight perovskite solar cells with chromium oxide-metal contacts for improved stability in air". In: *Nature Materials* 14.10 (2015), pp. 1032–1039. DOI: 10.1038/nmat4388.

[110] C. Eames et al. "Ionic transport in hybrid lead iodide perovskite solar cells". In: *Nature Communications* 6.1 (2015), p. 7497. DOI: 10.1038/ncomms8497.

[111] D. W. DeQuilettes et al. "Photo-induced halide redistribution in organic–inorganic perovskite films". In: *Nature Communications* 7.May (2016), p. 11683. DOI: 10.1038/ncomms11683.

[112] J. F. Galisteo-López, Y. Li, and H. Míguez. "Three-Dimensional Optical Tomography and Correlated Elemental Analysis of Hybrid Perovskite Microstructures: An Insight into Defect-Related Lattice Distortion and Photoinduced Ion Migration". In: *Journal of Physical Chemistry Letters* 7.24 (2016), pp. 5227–5234. DOI: 10.1021/acs.jpclett.6b02456.

[113] A. Merdasa et al. "Impact of Excess Lead Iodide on the Recombination Kinetics in Metal Halide Perovskites". In: *ACS Energy Letters* 4.6 (2019), pp. 1370–1378. DOI: 10.1021/acsenergylett.9b00774.

[114] D. J. Slotcavage, H. I. Karunadasa, and M. D. McGehee. "Light-Induced Phase Segregation in Halide-Perovskite Absorbers". In: *ACS Energy Letters* 1.6 (2016), pp. 1199–1205. DOI: 10.1021/acsenergylett.6b00495.

[115] N. H. Nickel et al. "Unraveling the Light-Induced Degradation Mechanisms of CH3NH3PbI3 Perovskite Films". In: *Advanced Electronic Materials* 3.12 (2017), pp. 1–9. DOI: 10.1002/aelm.201700158.

[116] Y. Lin et al. "Excess charge-carrier induced instability of hybrid perovskites". In: *Nature Communications* 9.1 (2018), p. 4981. DOI: 10.1038/s41467-018-07438-w.

[117] Z. Tang et al. "Hysteresis-free perovskite solar cells made of potassium-doped organometal halide perovskite". In: *Scientific Reports* 7.1 (2017), pp. 1–7. DOI: 10.1038/s41598-017-12436-x.

[118] B. Chen et al. "Synergistic Effect of Elevated Device Temperature and Excess Charge Carriers on the Rapid Light-Induced Degradation of Perovskite Solar Cells". In: *Advanced Materials* 31.35 (2019), p. 1902413. DOI: 10.1002/adma.201902413.

[119] S.-H. Turren-Cruz, A. Hagfeldt, and M. Saliba. "Methylammonium-free, high-performance and stable perovskite solar cells on a planar architecture". In: *Science* (2018). DOI: 10.1126/science.aat3583.

[120] Q. Wang et al. "Enhancement in lifespan of halide perovskite solar cells". In: *Energy & Environmental Science* 12.3 (2019), pp. 865–886. DOI: 10.1039/C8EE02852D.

[121] J. S. Yun et al. "Humidity-Induced Degradation via Grain Boundaries of HC(NH 2) 2 PbI 3 Planar Perovskite Solar Cells". In: *Advanced Functional Materials* 28.11 (2018), p. 1705363. DOI: 10.1002/adfm.201705363.

[122] N. Aristidou et al. "Fast oxygen diffusion and iodide defects mediate oxygen-induced degradation of perovskite solar cells". In: *Nature Communications* 8.1 (2017), p. 15218. DOI: 10.1038/ncomms15218.

[123] R. Cheacharoen et al. "Design and understanding of encapsulated perovskite solar cells to withstand temperature cycling". In: *Energy & Environmental Science* 11.1 (2018), pp. 144–150. DOI: 10.1039/C7EE02564E.

[124] C. C. Boyd et al. "Understanding Degradation Mechanisms and Improving Stability of Perovskite Photovoltaics". In: *Chemical Reviews* 119 (2018), pp. 3418–3451. DOI: 10.1021/acs.chemrev.8b00336.

[125] Y.-H. Lin et al. "A piperidinium salt stabilizes efficient metal-halide perovskite solar cells". In: *Science* 369.6499 (2020), pp. 96–102. DOI: 10.1126/science.aba1628.

[126] Y. Bai et al. "Oligomeric Silica-Wrapped Perovskites Enable Synchronous Defect Passivation and Grain Stabilization for Efficient and Stable Perovskite Photovoltaics". In: *ACS Energy Letters* (2019), pp. 1231–1240. DOI: 10.1021/acsenergylett.9b00608.

[127] N. Leupold et al. "High Versatility and Stability of Mechanochemically Synthesized Halide Perovskite Powders for Optoelectronic Devices". In: *ACS Applied Materials & Interfaces* 11.33 (2019), pp. 30259–30268. DOI: 10.1021/acsami.9b09160.

[128] J. Zhao et al. "Strained hybrid perovskite thin films and their impact on the intrinsic stability of perovskite solar cells". In: *Science Advances* 3.11 (2017). DOI: 10.1126/sciadv.aao5616.

[129] X. Li et al. "Residual Nanoscale Strain in Cesium Lead Bromide Perovskite Reduces Stability and Shifts Local Luminescence". In: *Chemistry of Materials* 31.8 (2019), pp. 2778–2785. DOI: 10.1021/acs.chemmater.8b04937.

[130] N. J. Jeon et al. "A fluorene-terminated hole-transporting material for highly efficient and stable perovskite solar cells". In: *Nature Energy* (2018). DOI: 10.1038/s41560-018-0200-6.

[131] B. Roose, Q. Wang, and A. Abate. "The Role of Charge Selective Contacts in Perovskite Solar Cell Stability". In: *Advanced Energy Materials* 9.5 (2019), pp. 1–20. DOI: 10.1002/aenm.201803140.

[132] Y. Hou et al. "A generic interface to reduce the efficiency-stability-cost gap of perovskite solar cells". In: *Science* 358.6367 (2017), pp. 1192–1197. DOI: 10.1126/science.aao5561.

[133] J. A. Christians et al. "Tailored interfaces of unencapsulated perovskite solar cells for >1,000 hour operational stability". In: *Nature Energy* 3.1 (2018), pp. 68–74. DOI: 10.1038/s41560-017-0067-y.

[134] G. Grancini et al. "One-Year stable perovskite solar cells by 2D/3D interface engineering". In: *Nature Communications* 8 (2017), pp. 1–8. DOI: 10.1038/ncomms15684.

[135] Z. Wang et al. "Efficient ambient-air-stable solar cells with 2D–3D heterostructured butylammonium-caesium-formamidinium lead halide perovskites". In: *Nature Energy* 2.9 (2017), p. 17135. DOI: 10.1038/nenergy.2017.135.

[136] S. Seo et al. "Perovskite Solar Cells with Inorganic Electron- and Hole-Transport Layers Exhibiting Long-Term (500 h) Stability at 85 °C under Continuous 1 Sun Illumination in Ambient Air". In: *Advanced Materials* 30.29 (2018), p. 1801010. DOI: 10.1002/adma.201801010.

[137] D.-j. Xue et al. "Regulating strain in perovskite thin films through charge-transport layers". In: *Nature Communications* 11.1 (2020), p. 1514. DOI: 10.1038/s41467-020-15338-1.

[138] T. Matsui et al. "Compositional Engineering for Thermally Stable, Highly Efficient Perovskite Solar Cells Exceeding 20% Power Conversion Efficiency with 85 °C/85% 1000 h Stability". In: *Advanced Materials* 31.10 (2019), p. 1806823. DOI: 10.1002/adma.201806823.

[139] E. T. Hoke et al. "Reversible photo-induced trap formation in mixed-halide hybrid perovskites for photovoltaics". In: *Chemical Science* 6.1 (2015), pp. 613–617. DOI: 10.1039/c4sc03141e.

[140] C. G. Bischak et al. "Origin of Reversible Photoinduced Phase Separation in Hybrid Perovskites". In: *Nano Letters* 17.2 (2017), pp. 1028–1033. DOI: 10.1021/acs.nanolett.6b04453.

[141] S. J. Yoon, M. Kuno, and P. V. Kamat. "Shift Happens . How Halide Ion Defects Influence Photoinduced Segregation in Mixed Halide Perovskites". In: *ACS Energy Letters* 2.7 (2017), pp. 1507–1514. DOI: 10.1021/acsenergylett.7b00357.

[142] S. Meloni et al. "Ionic polarization-induced current-voltage hysteresis in CH3NH3PbX3 perovskite solar cells". In: *Nature Communications* 7.1 (2016), p. 10334. DOI: 10.1038/ncomms10334.

[143] X. Tang et al. "Local Observation of Phase Segregation in Mixed-Halide Perovskite". In: *Nano Letters* 18.3 (2018), pp. 2172–2178. DOI: 10.1021/acs.nanolett.8b00505.

[144] N. Phung and A. Abate. "The Impact of Nano- and Microstructure on the Stability of Perovskite Solar Cells". In: *Small* 14.46 (2018), pp. 1–11. DOI: 10.1002/smll.201802573.

[145] J. T. Dubose and P. V. Kamat. "TiO2-Assisted Halide Ion Segregation in Mixed Halide Perovskite Films". In: *Journal of the American Chemical Society* 142.11 (2020), pp. 5362–5370. DOI: 10.1021/jacs.0c00434.

[146] J. Li et al. "Biological impact of lead from halide perovskites reveals the risk of introducing a safe threshold". In: *Nature Communications* 11.1 (2020), p. 310. DOI: 10.1038/s41467-019-13910-y.

[147] L. Serrano-Lujan et al. "Tin- and lead-based perovskite solar cells under scrutiny: An environmental perspective". In: *Advanced Energy Materials* 5.20 (2015), pp. 1–5. DOI: 10.1002/aenm.201501119.

[148] G. Schileo and G. Grancini. "Lead or No Lead? Availability, Toxicity, Sustainability and Environmental Impact of Lead-Free Perovskites Solar Cells". In: *Journal of Materials Chemistry C* (2020). DOI: 10.1039/d0tc04552g.

[149] S. Chen et al. "Trapping lead in perovskite solar modules with abundant and low-cost cation-exchange resins". In: *Nature Energy* (2020). DOI: 10.1038/s41560-020-00716-2.

[150] S. Wu et al. "2D metal–organic framework for stable perovskite solar cells with minimized lead leakage". In: *Nature Nanotechnology* (2020). DOI: 10.1038/s41565-020-0765-7.

[151] I. L. Braly et al. "Hybrid perovskite films approaching the radiative limit with over 90% photoluminescence quantum efficiency". In: *Nature Photonics* 12.6 (2018), pp. 355–361. DOI: 10.1038/s41566-018-0154-z.

[152] D. W. DeQuilettes et al. "Photoluminescence Lifetimes Exceeding 8 μs and Quantum Yields Exceeding 30% in Hybrid Perovskite Thin Films by Ligand Passivation". In: *ACS Energy Letters* 1.2 (2016), pp. 438–444. DOI: 10.1021/acsenergylett.6b00236.

[153] V. Sarritzu et al. "Optical determination of Shockley-Read-Hall and interface recombination currents in hybrid perovskites". In: *Scientific Reports* 7.1 (2017), p. 44629. DOI: 10.1038/srep44629.

[154] M. Stolterfoht et al. "Visualization and suppression of interfacial recombination for high-efficiency large-area pin perovskite solar cells". In: *Nature Energy* 3.10 (2018), pp. 847–854. DOI: 10.1038/s41560-018-0219-8.

[155] M. Stolterfoht et al. "The impact of energy alignment and interfacial recombination on the internal and external open-circuit voltage of perovskite solar cells". In: *Energy & Environmental Science* 12.9 (2019), pp. 2778–2788. DOI: 10.1039/C9EE02020A.

[156] O. I. Micic et al. "Synthesis and Characterization of InP Quantum Dots". In: *The Journal of Physical Chemistry* 98.19 (1994), pp. 4966–4969. DOI: 10.1021/j100070a004.

[157] X. Yang et al. "Efficient green light-emitting diodes based on quasi-two-dimensional composition and phase engineered perovskite with surface passivation". In: *Nature Communications* 9.1 (2018), pp. 2–9. DOI: 10.1038/s41467-018-02978-7.

[158] L. Na Quan et al. "Edge stabilization in reduced-dimensional perovskites". In: *Nature Communications* 11.1 (2020), p. 170. DOI: 10.1038/s41467-019-13944-2.

[159] D. Bi et al. "Polymer-templated nucleation and crystal growth of perovskite films for solar cells with efficiency greater than 21%". In: *Nature Energy* 1.10 (2016), pp. 1–5. DOI: 10.1038/nenergy.2016.142.

[160] J. Peng et al. "A Universal Double-Side Passivation for High Open-Circuit Voltage in Perovskite Solar Cells: Role of Carbonyl Groups in Poly(methyl methacrylate)". In: *Advanced Energy Materials* 8.30 (2018), p. 1801208. DOI: 10.1002/aenm.201801208.

[161] J. Seo et al. "Benefits of very thin PCBM and LiF layers for solution-processed p-i-n perovskite solar cells". In: *Energy and Environmental Science* 7.8 (2014), pp. 2642–2646. DOI: 10.1039/c4ee01216j.

[162] Z. Sun et al. "Role of Thick-Lithium Fluoride Layer in Energy Level Alignment at Organic/Metal Interface: Unifying Effect on High Metallic Work Functions". In: *Advanced Materials Interfaces* 2.4 (2015), pp. 1–8. DOI: 10.1002/admi.201400527.

[163] F. Peña-Camargo et al. "Halide Segregation versus Interfacial Recombination in Bromide-Rich Wide-Gap Perovskite Solar Cells". In: *ACS Energy Letters* 5.8 (2020), pp. 2728–2736. DOI: 10.1021/acsenergylett.0c01104.

[164] Q. An et al. "Enhancing the Open-Circuit Voltage of Perovskite Solar Cells by up to 120 mV Using π-Extended Phosphoniumfluorene Electrolytes as Hole Blocking Layers". In: *Advanced Energy Materials* 9.33 (2019), p. 1901257. DOI: 10.1002/aenm.201901257.

[165] G. J. A. Wetzelaer et al. "Asymmetric electron and hole transport in a high-mobility n-type conjugated polymer". In: *Physical Review B - Condensed Matter and Materials Physics* 86.16 (2012), pp. 1–9. DOI: 10.1103/PhysRevB.86.165203.

[166] W. Zhou, Z. Wen, and P. Gao. "Less is More: Dopant-Free Hole Transporting Materials for High-Efficiency Perovskite Solar Cells". In: *Advanced Energy Materials* 8.9 (2018), pp. 1–28. DOI: 10.1002/aenm.201702512.

[167] J. Liu et al. "A dopant-free hole-transporting material for efficient and stable perovskite solar cells". In: *Energy and Environmental Science* 7.9 (2014), pp. 2963–2967. DOI: 10.1039/c4ee01589d.

[168] N. Tessler and Y. Vaynzof. "Insights from Device Modeling of Perovskite Solar Cells". In: *ACS Energy Letters* 5.4 (2020), pp. 1260–1270. DOI: 10.1021/acsenergylett.0c00172.

[169] P. Schulz et al. "Electronic Level Alignment in Inverted Organometal Perovskite Solar Cells". In: *Advanced Materials Interfaces* 2.7 (2015). DOI: 10.1002/admi.201400532.

[170] J. Sagiv. "Organized monolayers by adsorption. 1. Formation and structure of oleophobic mixed monolayers on solid surfaces". In: *Journal of the American Chemical Society* 102.1 (1980), pp. 92–98. DOI: 10.1021/ja00521a016.

[171] W. C. Bigelow, D. L. Pickett, and W. A. Zisman. "Oleophobic monolayers. I. Films adsorbed from solution in non-polar liquids". In: *Journal of Colloid Science* 1.6 (1946), pp. 513–538. DOI: 10.1016/0095-8522(46)90059-1.

[172] A. Aviram and M. A. Ratner. "Molecular rectifiers". In: *Chemical Physics Letters* 29.2 (1974), pp. 277–283. DOI: 10.1016/0009-2614(74)85031-1.

[173] E. E. Polymeropoulos and J. Sagiv. "Electrical conduction through adsorbed monolayers". In: *The Journal of Chemical Physics* 69.5 (1978), pp. 1836–1847. DOI: 10.1063/1.436844.

[174] A. Ulman. "Formation and Structure of Self-Assembled Monolayers". In: *Chemical Reviews* 96.4 (1996), pp. 1533–1554. DOI: 10.1021/cr9502357.

[175] M. Halik et al. "Low-voltage organic transistors with an amorphous molecular gate dielectric". In: *Nature* 431.7011 (2004), pp. 963–966. DOI: 10.1038/nature02987.

[176] H. Klauk et al. "Ultralow-power organic complementary circuits". In: *Nature* 445.7129 (2007), pp. 745–748. DOI: 10.1038/nature05533.

[177] B. De Boer et al. "Tuning of metal work functions with self-assembled monolayers". In: *Advanced Materials* 17.5 (2005), pp. 621–625. DOI: 10.1002/adma.200401216.

[178] M. A. Reed et al. "Conductance of a molecular junction". In: *Science* 278.5336 (1997), pp. 252–254. DOI: 10.1126/science.278.5336.252.

[179] J. Reichert et al. "Driving Current through Single Organic Molecules". In: *Physical Review Letters* 88.17 (2002), p. 4. DOI: 10.1103/PhysRevLett.88.176804.

[180] C. Krzeminski et al. "Theory of electrical rectification in a molecular monolayer". In: *Physical Review B* 64.8 (2001), p. 085405. DOI: 10.1103/PhysRevB.64.085405.

[181] I. I. Oleynik et al. "Rectification mechanism in diblock oligomer molecular diodes". In: *Physical Review Letters* 96.9 (2006), pp. 1–4. DOI: 10.1103/PhysRevLett.96.096803.

[182] A. Khassanov et al. "Structural investigations of self-assembled monolayers for organic electronics: Results from X-ray reflectivity". In: *Accounts of Chemical Research* 48.7 (2015), pp. 1901–1908. DOI: 10.1021/acs.accounts.5b00022.

[183] M. Burkhardt et al. "Concept of a molecular charge storage dielectric layer for organic thin-film memory transistors". In: *Advanced Materials* 22.23 (2010), pp. 2525–2528. DOI: 10.1002/adma.201000030.

[184] X. Han et al. "Formation of Highly Stable Self-Assembled Alkyl Phosphonic Acid Monolayers for the Functionalization of Titanium Surfaces and Protein Patterning". In: *Langmuir* 31.1 (2015), pp. 140–148. DOI: 10.1021/la504644q.

[185] R. M. Metzger. "Unimolecular electrical rectifiers". In: *Chemical Reviews* 103.9 (2003), pp. 3803–3834. DOI: 10.1021/cr020413d.

[186] D. K. Schwartz. "Mechanisms and Kinetics of Self-assembled Monolayer Formation". In: *Annual Review of Physical Chemistry* 52.1 (2001), pp. 107–137. DOI: 10.1146/annurev.physchem.52.1.107.

[187] S. A. Paniagua et al. "Phosphonic Acid Modification of Indium-Tin Oxide Electrodes: Combined XPS/UPS/Contact Angle Studies". In: *J. Phys. Chem. C* 112.21 (2008), pp. 7809–7817. DOI: 10.1021/jp710893k.

[188] P. J. Hotchkiss et al. "The Modification of Indium Tin Oxide with Phosphonic Acids: Mechanism of Binding, Tuning of Surface Properties, and Potential for Use in Organic Electronic Applications". In: *Accounts of Chemical Research* 45.3 (2012), pp. 337–346. DOI: 10.1021/ar200119g.

[189] F. Brodard-Severac et al. "High-Field 17 O MAS NMR Investigation of Phosphonic Acid Monolayers on Titania". In: *Chemistry of Materials* 20.16 (2008), pp. 5191–5196. DOI: 10.1021/cm8012683.

[190] G. Pace et al. "Intrinsically distinct hole and electron transport in conjugated polymers controlled by intra and intermolecular interactions". In: *Nature Communications* 10.1 (2019), p. 5226. DOI: 10.1038/s41467-019-13155-9.

[191] S. R. Saudari and C. R. Kagan. "Electron and hole transport in ambipolar, thin film pentacene transistors". In: *Journal of Applied Physics* 117.3 (2015), p. 035501. DOI: 10.1063/1.4906145.

[192] V. Coropceanu et al. "Charge Transport in Organic Semiconductors". In: *Chemical Reviews* 107.4 (2007), pp. 926–952. DOI: 10.1021/cr050140x.

[193] A. Dodabalapur. "Negatively successful". In: *Nature* 434.7030 (2005), pp. 151–152. DOI: 10.1038/434151a.

[194] M. Ahles, R. Schmechel, and H. Von Seggern. "N-type organic field-effect transistor based on interface-doped pentacene". In: *Applied Physics Letters* 85.19 (2004), pp. 4499–4501. DOI: 10.1063/1.1818737.

[195] L.-l. Chua et al. "General observation of n-type field-effect behaviour in organic semiconductors". In: *Nature* 434.7030 (2005), pp. 194–199. DOI: 10.1038/nature03376.

[196] E. C. Smits et al. "Ambipolar charge transport in organic field-effect transistors". In: *Physical Review B - Condensed Matter and Materials Physics* 73.20 (2006), pp. 1–9. DOI: 10.1103/PhysRevB.73.205316.

[197] A. van Dijken et al. "Carbazole Compounds as Host Materials for Triplet Emitters in Organic Light-Emitting Diodes: Polymer Hosts for High-Efficiency Light-Emitting Diodes". In: *Journal of the American Chemical Society* 126.24 (2004), pp. 7718–7727. DOI: 10.1021/ja049771j.

[198] S. A. Paniagua et al. "Phosphonic Acids for Interfacial Engineering of Transparent Conductive Oxides". In: *Chemical Reviews* 116.12 (2016), pp. 7117–7158. DOI: 10.1021/acs.chemrev.6b00061.

[199] P. Wang et al. "Amphiphilic Ruthenium Sensitizer with 4,4'-Diphosphonic Acid-2,2'-bipyridine as Anchoring Ligand for Nanocrystalline Dye Sensitized Solar Cells". In: *The Journal of Physical Chemistry B* 108.45 (2004), pp. 17553–17559. DOI: 10.1021/jp046932x.

[200] J. A. Bardecker et al. "Self-assembled Electroactive Phosphonic Acids on ITO: Maximizing Hole-Injection in Polymer Light-Emitting Diodes". In: *Advanced Functional Materials* 18.24 (2008), pp. 3964–3971. DOI: 10.1002/adfm.200800033.

[201] A. Abrusci et al. "High-Performance Perovskite-Polymer Hybrid Solar Cells via Electronic Coupling with Fullerene Monolayers". In: *Nano Letters* 13.7 (2013), pp. 3124–3128. DOI: 10.1021/nl401044q.

[202] L. Liu et al. "Fully printable mesoscopic perovskite solar cells with organic silane self-assembled monolayer". In: *Journal of the American Chemical Society* 137.5 (2015), pp. 1790–1793. DOI: 10.1021/ja5125594.

[203] Y Hou et al. "A generic interface to reduce the efficiency-stability-cost gap of perovskite solar cells". In: 5561.November (2017), pp. 1–10. DOI: 10.1126/science.aao5561.

[204] Y. Hou et al. "Suppression of Hysteresis Effects in Organohalide Perovskite Solar Cells". In: *Advanced Materials Interfaces* 4.11 (2017), pp. 1–9. DOI: 10.1002/admi.201700007.

[205] Y. Dong et al. "Highly Efficient Planar Perovskite Solar Cells Via Interfacial Modification with Fullerene Derivatives". In: *Small* 12.8 (2016), pp. 1098–1104. DOI: 10.1002/smll.201503361.

[206] C. M. Wolff et al. "Perfluorinated Self-Assembled Monolayers Enhance the Stability and Efficiency of Inverted Perovskite Solar Cells". In: *ACS Nano* 14.2 (2020), pp. 1445–1456. DOI: 10.1021/acsnano.9b03268.

[207] A. Magomedov et al. "Self-Assembled Hole Transporting Monolayer for Highly Efficient Perovskite Solar Cells". In: *Advanced Energy Materials* 8.32 (2018), p. 1801892. DOI: 10.1002/aenm.201801892.

[208] A. Al-Ashouri et al. "Conformal monolayer contacts with lossless interfaces for perovskite single junction and monolithic tandem solar cells". In: *Energy & Environmental Science* 12.11 (2019), pp. 3356–3369. DOI: 10.1039/C9EE02268F.

[209] A. Al-Ashouri et al. "Monolithic perovskite/silicon tandem solar cell with >29% efficiency by enhanced hole extraction". In: *Science* 370.6522 (2020), pp. 1300–1309. DOI: 10.1126/science.abd4016.

[210] Q. Wang, C. Bi, and J. Huang. "Doped hole transport layer for efficiency enhancement in planar heterojunction organolead trihalide perovskite solar cells". In: *Nano Energy* 15 (2015), pp. 275–280. DOI: 10.1016/j.nanoen.2015.04.029.

[211] C. C. Boyd et al. "Overcoming Redox Reactions at Perovskite-Nickel Oxide Interfaces to Boost Voltages in Perovskite Solar Cells". In: *Joule* 4.8 (2020), pp. 1759–1775. DOI: 10.1016/j.joule.2020.06.004.

[212] R. Qiao and L. Zuo. "Self-assembly monolayers boosting organic–inorganic halide perovskite solar cell performance". In: *Journal of Materials Research* 33.4 (2018), pp. 387–400. DOI: 10.1557/jmr.2017.477.

[213] X. Lin et al. "Dipole-field-assisted charge extraction in metal-perovskite-metal back-contact solar cells". In: *Nature Communications* 8.1 (2017). DOI: 10.1038/s41467-017-00588-3.

[214] A. Rumpel et al. "Tuning the Molecular Order of C 60 Functionalized Phosphonic Acid Monolayers". In: *Langmuir* 27.24 (2011), pp. 15016–15023. DOI: 10.1021/la203916h.

[215] J. P. Correa Baena et al. "Highly efficient planar perovskite solar cells through band alignment engineering". In: *Energy and Environmental Science* 8.10 (2015), pp. 2928–2934. DOI: 10.1039/c5ee02608c.

[216] R. A. Belisle et al. "Minimal Effect of the Hole-Transport Material Ionization Potential on the Open-Circuit Voltage of Perovskite Solar Cells". In: *ACS Energy Letters* 1.3 (2016), pp. 556–560. DOI: 10.1021/acsenergylett.6b00270.

[217] P. Schulz. "Interface Design for Metal Halide Perovskite Solar Cells". In: *ACS Energy Letters* 3 (2018), pp. 1287–1293. DOI: 10.1021/acsenergylett.8b00404.

[218] H. Y. Nie, M. J. Walzak, and N. S. McIntyre. "Delivering octadecylphosphonic acid self-assembled monolayers on a Si wafer and other oxide surfaces". In: *Journal of Physical Chemistry B* 110.42 (2006), pp. 21101–21108. DOI: 10.1021/jp062811g.

[219] L. Zazzera and J. F. Evans. "In situ internal reflection infrared study of aqueous hydrofluoric acid and ultraviolet/ozone treated silicon (100) surfaces". In: *Journal of Vacuum Science & Technology A: Vacuum, Surfaces, and Films* 11.4 (1993), pp. 934–939. DOI: 10.1116/1.578571.

[220] F. M. Hoffmann. "Infrared reflection-absorption spectroscopy of adsorbed molecules". In: *Surface Science Reports* 3.2-3 (1983), pp. 107–192. DOI: 10.1016/0167-5729(83)90001-8.

[221] O. I. Negru and M. Grigoras. "Electrochemically generated networks from poly(4,4-triphenylamine-co-9,9-dioctyl-2,7-fluorene) with grafts containing carbazole groups". In: *Journal of Polymer Research* 22.1 (2015), pp. 1–11. DOI: 10.1007/s10965-014-0637-7.

[222] I. Matulaitiene et al. "SERS of the Positive Charge Bearing Pyridinium Ring Terminated Self-Assembled Monolayers: Structure and Bonding Spectral Markers". In: *Journal of Physical Chemistry C* 119.47 (2015), pp. 26481–26492. DOI: 10.1021/acs.jpcc.5b07687.

[223] W Reppe and E Keyssner. "N-Vinyl Compounds". In: *DRP* 618 (1935), p. 120.

[224] J. F. Moulder et al. *Handbook of X-ray Photoelectron Spectroscopy*. 1992, p. 261.

[225] S. T. Jackson and R. G. Nuzzo. "Determining hybridization differences for amorphous carbon from the XPS C 1s envelope". In: *Applied Surface Science* 90.2 (1995), pp. 195–203. DOI: 10.1016/j.saa.2013.10.042.

[226] J. S. Kim et al. "X-ray photoelectron spectroscopy of surface-treated indium-tin oxide thin films". In: *Chemical Physics Letters* 315.5-6 (1999), pp. 307–312. DOI: 10.1016/S0009-2614(99)01233-6.

[227] C. Donley et al. "Characterization of indium-tin oxide interfaces using X-ray photoelectron spectroscopy and redox processes of a chemisorbed probe molecule: Effect of surface pretreatment conditions". In: *Langmuir* 18.2 (2002), pp. 450–457. DOI: 10.1021/la011101t.

[228] A. W. Lin, N. R. Armstrong, and T. Kuwana. "X-ray Photoelectron/Auger Electron Spectroscopic Studies of Tin and Indium Metal Foils and Oxides". In: *Analytical Chemistry* 49.8 (1977), pp. 1228–1235. DOI: 10.1021/ac50016a042.

[229] Y. Lin et al. "Self-Assembled Monolayer Enables Hole Transport Layer-Free Organic Solar Cells with 18% Efficiency and Improved Operational Stability". In: *ACS Energy Letters* 5 (2020), pp. 2935–2944. DOI: 10.1021/acsenergylett.0c01421.

[230] S. A. Paniagua, E. L. Li, and S. R. Marder. "Adsorption studies of a phosphonic acid on ITO: Film coverage, purity, and induced electronic structure changes". In: *Physical Chemistry Chemical Physics* 16.7 (2014), pp. 2874–2881. DOI: 10.1039/c3cp54637c.

[231] R.-F. Dou et al. "Self-Assembled Monolayers of Aromatic Thiols Stabilized by Parallel-Displaced π-π Stacking Interactions". In: *Langmuir* 22.7 (2006), pp. 3049–3056. DOI: 10.1021/la052987u.

[232] S. Casalini et al. "Self-assembled monolayers in organic electronics". In: *Chemical Society Reviews* 46.1 (2017), pp. 40–71. DOI: 10.1039/c6cs00509h.

[233] X. Zheng et al. "Defect passivation in hybrid perovskite solar cells using quaternary ammonium halide anions and cations". In: *Nature Energy* 2.7 (2017), p. 17102. DOI: 10.1038/nenergy.2017.102.

[234] F. Lang et al. "Proton Radiation Hardness of Perovskite Tandem Photovoltaics". In: *Joule* 4.5 (2020), pp. 1054–1069. DOI: 10.1016/j.joule.2020.03.006.

[235] Q. Han et al. "High-performance perovskite/Cu(In,Ga)Se ₂ monolithic tandem solar cells". In: *Science* 361.6405 (2018), pp. 904–908. DOI: 10.1126/science.aat5055.

[236] M. Jošt et al. "21.6%-Efficient Monolithic Perovskite/Cu(In,Ga)Se 2 Tandem Solar Cells with Thin Conformal Hole Transport Layers for Integration on Rough Bottom Cell Surfaces". In: *ACS Energy Letters* 4.2 (2019), pp. 583–590. DOI: 10.1021/acsenergylett.9b00135.

[237] E. M. Hutter et al. "Pitfalls and prospects of optical spectroscopy to characterize perovskite-transport layer interfaces". In: *Applied Physics Letters* 116.10 (2020). DOI: 10.1063/1.5143121.

[238] T. Unold and L. Gütay. "Photoluminescence Analysis of Thin-Film Solar Cells". In: *Advanced Characterization Techniques for Thin Film Solar Cells*. Weinheim, Germany: Wiley-VCH Verlag GmbH & Co. KGaA, 2011. Chap. 7, pp. 151–175. DOI: 10.1002/9783527636280.ch7.

[239] P. Schulz, D. Cahen, and A. Kahn. "Halide Perovskites: Is It All about the Interfaces?" In: *Chemical Reviews* 119.5 (2019), pp. 3349–3417. DOI: 10.1021/acs.chemrev.8b00558.

[240] H. Ishii et al. "Energy level alignment and interfacial electronic structures at organic/metal and organic/organic interfaces". In: *Advanced Materials* 11.8 (1999), pp. 605–625. DOI: 10.1002/(SICI)1521-4095(199906)11:8<605::AID-ADMA605>3.0.CO;2-Q.

[241] J. Hwang, A. Wan, and A. Kahn. "Energetics of metal-organic interfaces: New experiments and assessment of the field". In: *Materials Science and Engineering R: Reports* 64.1-2 (2009), pp. 1–31. DOI: 10.1016/j.mser.2008.12.001.

[242] A. Vilan and D. Cahen. "Chemical Modification of Semiconductor Surfaces for Molecular Electronics". In: *Chemical Reviews* 117.5 (2017), pp. 4624–4666. DOI: 10.1021/acs.chemrev.6b00746.

[243] N. F. Mott. "Note on the contact between a metal and an insulator or semiconductor". In: *Mathematical Proceedings of the Cambridge Philosophical Society* 34.4 (1938), pp. 568–572. DOI: 10.1017/S0305004100020570.

[244] G. Witte et al. "Vacuum level alignment at organic/metal junctions: "Cushion" effect and the interface dipole". In: *Applied Physics Letters* 87.26 (2005), p. 263502. DOI: 10.1063/1.2151253.

[245] M. Timpel et al. "Electrode Work Function Engineering with Phosphonic Acid Monolayers and Molecular Acceptors: Charge Redistribution Mechanisms". In: *Advanced Functional Materials* 28.8 (2018), pp. 1–12. DOI: 10.1002/adfm.201704438.

[246] J. Li et al. "20.8% Slot-Die Coated MAPbI 3 Perovskite Solar Cells by Optimal DMSO-Content and Age of 2-ME Based Precursor Inks". In: *Advanced Energy Materials* (2021), p. 2003460. DOI: 10.1002/aenm.202003460.

[247] M. Stolterfoht et al. "Approaching the fill factor Shockley–Queisser limit in stable, dopant-free triple cation perovskite solar cells". In: *Energy & Environmental Science* 10.6 (2017), pp. 1530–1539. DOI: 10.1039/C7EE00899F.

[248] M. A. Green and A. W. Ho-Baillie. "Pushing to the Limit: Radiative Efficiencies of Recent Mainstream and Emerging Solar Cells". In: *ACS Energy Letters* 4.7 (2019), pp. 1639–1644. DOI: 10.1021/acsenergylett.9b01128.

[249] E. T. Hoke et al. "Reversible photo-induced trap formation in mixed-halide hybrid perovskites for photovoltaics". In: *Chemical Science* 6.1 (2015), pp. 613–617. DOI: 10.1039/C4SC03141E.

[250] D. Kim et al. "Efficient, stable silicon tandem cells enabled by anion-engineered wide-bandgap perovskites". In: *Science* 368.6487 (2020), pp. 155–160. DOI: 10.1126/science.aba3433.

[251] A. Knight and L. M. Herz. "Preventing Phase Segregation in Mixed-Halide Perovskites: A Perspective". In: *Energy & Environmental Science* (2020). DOI: 10.1039/d0ee00788a.

[252] S. Draguta et al. "Rationalizing the light-induced phase separation of mixed halide organic-inorganic perovskites". In: *Nature Communications* 8.1 (2017). DOI: 10.1038/s41467-017-00284-2.

[253] B. Zhang et al. "Photoluminescence Study of the Photoinduced Phase Separation in Mixed-Halide Hybrid Perovskite CH3NH3Pb(BrxI1-x)3 Crystals Synthesized via a Solvothermal Method". In: *Scientific Reports* 7.1 (2017), pp. 1–8. DOI: 10.1038/s41598-017-18110-6.

[254] W. Rehman et al. "Photovoltaic mixed-cation lead mixed-halide perovskites: links between crystallinity, photo-stability and electronic properties". In: *Energy Environ. Sci.* (2017). DOI: 10.1039/C6EE03014A.

[255] M. Hu et al. "Stabilized wide bandgap MAPbBrxI3-x perovskite by enhanced grain size and improved crystallinity". In: *Advanced Science* 3.6 (2015), pp. 6–11. DOI: 10.1002/advs.201500301.

[256] N. Phung et al. "The Role of Grain Boundaries on Ionic Defect Migration in Metal Halide Perovskites". In: *Advanced Energy Materials* 10.20 (2020), p. 1903735. DOI: 10.1002/aenm.201903735.

[257] R. A. Belisle et al. "Impact of surfaces on photoinduced halide segregation in mixed-halide perovskites". In: *ACS Energy Letters* 3.11 (2018), pp. 2694–2700. DOI: 10.1021/acsenergylett.8b01562.

[258] P. Caprioglio et al. "Nano-emitting Heterostructures Violate Optical Reciprocity and Enable Efficient Photoluminescence in Halide-Segregated Methylammonium-Free Wide Bandgap Perovskites". In: *ACS Energy Letters* (2021), pp. 419–428. DOI: 10.1021/acsenergylett.0c02270.

[259] J. Xu et al. "Triple-halide wide-band gap perovskites with suppressed phase segregation for efficient tandems". In: *Science* 367.6482 (2020), pp. 1097–1104. DOI: 10.1126/science.aaz5074.

[260] H. X. Dang et al. "Multi-cation Synergy Suppresses Phase Segregation in Mixed-Halide Perovskites". In: *Joule* 3.7 (2019), pp. 1746–1764. DOI: 10.1016/j.joule.2019.05.016.

[261] Y. Luo et al. "Direct Observation of Halide Migration and its Effect on the Photoluminescence of Methylammonium Lead Bromide Perovskite Single Crystals". In: *Advanced Materials* 1703451 (2017), p. 1703451. DOI: 10.1002/adma.201703451.

[262] M. Yuan et al. "Perovskite energy funnels for efficient light-emitting diodes". In: *Nature Nanotechnology* 11.10 (2016), pp. 872–877. DOI: 10.1038/nnano.2016.110.

[263] S. Mahesh et al. "Revealing the origin of voltage loss in mixed-halide perovskite solar cells". In: *Energy and Environmental Science* 13.1 (2020), pp. 258–267. DOI: 10.1039/c9ee02162k.

[264] B. Krogmeier et al. "Quantitative analysis of the transient photoluminescence of CH 3 NH 3 PbI 3 /PC 61 BM heterojunctions by numerical simulations". In: *Sustainable Energy & Fuels* 2.5 (2018), pp. 1027–1034. DOI: 10.1039/C7SE00603A.

[265] C. M. Wolff et al. "Reduced Interface-Mediated Recombination for High Open-Circuit Voltages in CH3NH3PbI3Solar Cells". In: *Advanced Materials* 29.28 (2017). DOI: 10.1002/adma.201700159.

[266] M. Stolterfoht et al. "How To Quantify the Efficiency Potential of Neat Perovskite Films: Perovskite Semiconductors with an Implied Efficiency Exceeding 28%". In: *Advanced Materials* 32.17 (2020), p. 2000080. DOI: 10.1002/adma.202000080.

[267] W. Wang et al. "Synergistic Reinforcement of Built-In Electric Fields for Highly Efficient and Stable Perovskite Photovoltaics". In: *Advanced Functional Materials* 30.19 (2020), p. 1909755. DOI: 10.1002/adfm.201909755.

[268] P. N. Dickerson et al. "Hydrogen-Bonding versus van der Waals Interactions in Self-Assembled Monolayers of Substituted Isophthalic Acids". In: *Langmuir* 26.23 (2010), pp. 18155–18161. DOI: 10.1021/la103494g.

[269] N. Nerngchamnong et al. "The role of van der Waals forces in the performance of molecular diodes". In: *Nature Nanotechnology* 8.2 (2013), pp. 113–118. DOI: 10.1038/nnano.2012.238.

[270] M. Boccard and C. Ballif. "Influence of the Subcell Properties on the Fill Factor of Two-Terminal Perovskite–Silicon Tandem Solar Cells". In: *ACS Energy Letters* 5.4 (2020), pp. 1077–1082. DOI: 10.1021/acsenergylett.0c00156.

[271] R. Quintero-Bermudez et al. "Mechanisms of LiF Interlayer Enhancements of Perovskite Light-Emitting Diodes". In: *The Journal of Physical Chemistry Letters* 11.10 (2020), pp. 4213–4220. DOI: 10.1021/acs.jpclett.0c00757.

[272] Z. Li et al. "Extrinsic ion migration in perovskite solar cells". In: *Energy & Environmental Science* 10.5 (2017), pp. 1234–1242. DOI: 10.1039/C7EE00358G.

[273] S. N. Habisreutinger et al. "Carbon Nanotube/Polymer Composites as a Highly Stable Hole Collection Layer in Perovskite Solar Cells". In: *Nano Letters* 14.10 (2014), pp. 5561–5568. DOI: 10.1021/nl501982b.

[274] S.-M. Bang et al. "Defect-Tolerant Sodium-Based Dopant in Charge Transport Layers for Highly Efficient and Stable Perovskite Solar Cells". In: *ACS Energy Letters* 5.4 (2020), pp. 1198–1205. DOI: 10.1021/acsenergylett.0c00514.

[275] S. Chen et al. "Thorough subcells diagnosis in a multi-junction solar cell via absolute electroluminescence-efficiency measurements". In: *Scientific Reports* 5.1 (2015), p. 7836. DOI: 10.1038/srep07836.

[276] D. Hinken et al. "Series resistance imaging of solar cells by voltage dependent electroluminescence". In: *Applied Physics Letters* 91.18 (2007), p. 182104. DOI: 10.1063/1.2804562.

[277] T. Dittrich et al. "Charge Separation in Donor–Acceptor Spiro Compounds at Metal and Metal Oxide Surfaces Investigated by Surface Photovoltage". In: *Journal of Nanoscience and Nanotechnology* 13.7 (2013), pp. 5158–5163. DOI: 10.1166/jnn.2013.7506.

[278] P Zabel et al. "Charge Separation at Pd-Porphyrin/TiO 2 Interfaces". In: *The Journal of Physical Chemistry C* 113.50 (2009), pp. 21090–21096. DOI: 10.1021/jp905575j.

[279] L. Kronik. "Surface photovoltage phenomena: theory, experiment, and applications". In: *Surface Science Reports* 37.1-5 (1999), pp. 1–206. DOI: 10.1016/S0167-5729(99)00002-3.

[280] T. S. Ntia et al. "An Analytical Approach to CH 3 NH 3 PbI 3 Perovskite Solar Cells Based on Different Hole Transport Materials". In: *physica status solidi (a)* 216.14 (2019), p. 1900087. DOI: 10.1002/pssa.201900087.

[281] T. Dittrich et al. "High precision differential measurement of surface photovoltage transients on ultrathin CdS layers". In: *Review of Scientific Instruments* 79.11 (2008), p. 113903. DOI: 10.1063/1.3020757.

[282] A. Magomedov et al. “Cover picture: Hole Transporting Monolayers: Self-Assembled Hole Transporting Monolayer for Highly Efficient Perovskite Solar Cells (Adv. Energy Mater. 32/2018)”. In: *Advanced Energy Materials* 8.32 (2018), p. 1870139. DOI: 10.1002/aenm.201870139.

Chapter 7

Appendix

7.1 List of publications

- A. Magomedov*, A. Al-Ashouri*, E. Kasparavičius, S. Strazdaite, G. Niaura, M. Jošt, T. Malinauskas, S. Albrecht and V. Getautis.
"**Self-Assembled Hole Transporting Monolayer for Highly Efficient Perovskite Solar Cells**".
Advanced Energy Materials 8, 1801892 (2018). DOI: 10.1002/aenm.201801892
*equal contribution

- A. Al-Ashouri, A. Magomedov, M. Roß, M. Jošt, M. Talaikis, G. Chistiakova, T. Bertram, J. A. Márquez, E. Köhnen, E. Kasparavičius, S. Levcenco, L. Gil-Escrig, C. J. Hages, R. Schlatmann, B. Rech, T. Malinauskas, T. Unold, C. A. Kaufmann, L. Korte, G. Niaura, V. Getautis and S. Albrecht.
"**Conformal monolayer contacts with lossless interfaces for perovskite single junction and monolithic tandem solar cells**".
Energy & Environmental Science 12, 3356–3369 (2019). DOI: 10.1039/C9EE02268F

- A. Al-Ashouri*, E. Köhnen*, B. Li, A. Magomedov, H. Hempel, P. Caprioglio, J. A. Márquez, A. B. Vilches, E. Kasparavicius, J. A. Smith, N. Phung, D. Menzel, M. Grischek, L. Kegelmann, D. Skroblin, C. Gollwitzer, T. Malinauskas, M. Jošt, G. Matič, B. Rech, R. Schlatmann, M. Topič, L. Korte, A. Abate, B. Stannowski, D. Neher, M. Stolterfoht, T. Unold, V. Getautis and S. Albrecht.
"**Monolithic perovskite/silicon tandem solar cell with >29% efficiency by enhanced hole extraction**".
Science 370 (6522), 1300–1309 (2020). DOI: 10.1126/science.abd4016
*equal contribution

- E. Köhnen, M. Jošt, A. B. Morales-Vilches, P. Tockhorn, A. Al-Ashouri, B. Macco, L. Kegelmann, L. Korte, B. Rech, R. Schlatmann, B. Stannowski, S. Albrecht. "**Highly efficient monolithic perovskite silicon tandem solar cells: analyzing the influence of current mismatch on device performance**". *Sustainable Energy Fuels* 3, 1995–2005 (2019). DOI: 10.1039/C9SE00120D

- M. Jošt, T. Bertram, D. Koushik, J. A. Marquez, M. A. Verheijen, M. D. Heinemann, E. Köhnen, A. Al-Ashouri, S. Braunger, F. Lang, B. Rech, T. Unold, M. Creatore, I. Lauermann, C. A. Kaufmann, R. Schlatmann, S. Albrecht. "**21.6%-Efficient Monolithic Perovskite/Cu(In,Ga)Se 2 Tandem Solar Cells with Thin Conformal Hole Transport Layers for Integration on Rough Bottom Cell Surfaces**". *ACS Energy Letters* 4, 583–590 (2019). DOI: 10.1021/acsenergylett.9b00135

- P. Becker, J. A. Márquez, J. Just, A. Al-Ashouri, C. Hages, H. Hempel, M. Jošt, S. Albrecht, R. Frahm, T. Unold. "**Low Temperature Synthesis of Stable g-CsPbI 3 Perovskite Layers for Solar Cells Obtained by High Throughput Experimentation**". *Advanced Energy Materials* 9, 1900555 (2019). DOI: 10.1002/aenm.201900555

- D. Di Girolamo, N. Phung, M. Jošt, A. Al-Ashouri, G. Chistiakova, J. Li, J. A. Márquez, T. Unold, L. Korte, S. Albrecht, A. Di Carlo, D. Dini, A. Abate. "**From Bulk to Surface: Sodium Treatment Reduces Recombination at the Nickel Oxide/Perovskite Interface**". *Advanced Materials Interfaces* 6, 1900789 (2019). DOI: 10.1002/admi.201900789

- N. Phung, R. Félix, D. Meggiolaro, A. Al-Ashouri, G. Sousa e Silva, C. Hartmann, J. Hidalgo, H. Köbler, E. Mosconi, B. Lai, R. Gunder, M. Li, K.-L. Wang, Z.-K. Wang, K. Nie, E. Handick, R. G. Wilks, J. A. Marquez, B. Rech, T. Unold, J.-P. Correa-Baena, S. Albrecht, F. De Angelis, M. Bär, A. Abate. "**The Doping Mechanism of Halide Perovskite Unveiled by Alkaline Earth Metals**". *Journal of the American Chemical Society* 142, 2364–2374 (2020). DOI: 10.1021/jacs.9b11637

- N. Phung, A. Al-Ashouri, S. Meloni, A. Mattoni, S. Albrecht, E. L. Unger, A. Merdasa, A. Abate. "**The Role of Grain Boundaries on Ionic Defect Migration in Metal Halide Perovskites**". *Advanced Energy Materials* 10, 1903735 (2020). DOI: 10.1002/aenm.201903735

- F. Lang, M. Jošt, K. Frohna, E. Köhnen, A. Al-Ashouri, A. R. Bowman, T. Bertram, A. B. Morales-Vilches, D. Koushik, E. M. Tennyson, K. Galkowski, G. Landi, M. Creatore, B. Stannowski, C. A. Kaufmann, J. Bundesmann, J. Rappich, B. Rech,

A. Denker, S. Albrecht, H.-C. Neitzert, N. H. Nickel, S. D. Stranks. "**Proton Radiation Hardness of Perovskite Tandem Photovoltaics**".
Joule. 4, 1054–1069 (2020). DOI: 10.1016/j.joule.2020.03.006

- M. Jošt, B. Lipovšek, B. Glažar, A. Al-Ashouri, K. Brecl, G. Matič, A. Magomedov, V. Getautis, M. Topič, S. Albrecht.
"**Perovskite Solar Cells go Outdoors: Field Testing and Temperature Effects on Energy Yield**".
Advanced Energy Materials 10, 2000454 (2020). DOI: 10.1002/aenm.202000454

- M. Roß, L. Gil-Escrig, A. Al-Ashouri, P. Tockhorn, M. Jošt, B. Rech, S. Albrecht.
"**Co-Evaporated p-i-n Perovskite Solar Cells beyond 20% Efficiency: Impact of Substrate Temperature and Hole-Transport Layer**".
ACS Applied Materials Interfaces 12, 39261–39272 (2020). DOI: 10.1021/acsami.0c10898

- P. Tockhorn, J. Sutter, R. Colom, L. Kegelmann, A. Al-Ashouri, M. Roß, K. Jäger, T. Unold, S. Burger, S. Albrecht, C. Becker.
"**Improved Quantum Efficiency by Advanced Light Management in Nanotextured Solution-Processed Perovskite Solar Cells**".
ACS Photonics 7, 2589–2600 (2020). DOI: 10.1021/acsphotonics.0c00935

- J. Dagar, M. Fenske, A. Al-Ashouri, C, Schultz, B. Li, H. Köbler, R. Munir, G. Parmasivam, J. Li, I. Levine, A. Merdasa, L. Kegelmann, H. Näsström, J. A. Marquez, T. Unold, D. Többens, R. Schlatmann, B. Stegemann, A. Abate, S. Albrecht, E. Unger.
"**Compositional and Interfacial Engineering Yield High-Performance and Stable p-i-n Perovskite Solar Cells and Mini-Modules**".
ACS Appl. Mater. Interfaces 13, 13022–13033 (2021). DOI: 10.1021/acsami.0c17893

- L. Gil-Escrig, M. Roß, J. Sutter, A. Al-Ashouri, C. Becker, S. Albrecht.
"**Fully Vacuum-Processed Perovskite Solar Cells on Pyramidal Microtextures**".
Solar RRL 5, 2000553 (2021). DOI: 10.1002/solr.202000553

- D. Vaitukaitytė, A. Al-Ashouri, M. Daškevičienė, E. Kamarauskas, J. Nekrasovas, V. Jankauskas, A. Magomedov, S. Albrecht, V. Getautis.
"**Enamine-Based Cross-Linkable Hole-Transporting Materials for Perovskite Solar Cells**".
Solar RRL 5, 2000597 (2021). DOI: 10.1002/solr.202000597

7.1.1 Patents

- "Verbindung und Verfahren zur Bildung von selbstorganisierten Monolagen auf TCO-Substraten zur Verwendung in Perowskit-Solarzellen in invertierter Architektur".
  Artiom Magomedov, Amran Al-Ashouri, Ernestas Kasparavicius, Steve Albrecht, Vytautas Getautis, Marko Jošt, Tadas Malinauskas, Lukas Kegelmann, Eike Köhnen
  DE 10 2018 115 379 B3 2019.10.10.
  Applied 26.06.2018. Issued 10.10.2019.

  - International follow-up application of item above: "Hole-transporting Self-organised Monolayer for Perovskite Solar Cells".
    PCT/EP2019/060586, 25.04.2019, pending.

- "Perowskit-Mehrfachsolarzelle mit Multischichtsystem als Verbindungsschicht".
  Amran Al-Ashouri, Steve Albrecht, Eike Köhnen, Marcel Roß, Marko Jošt, Lukas Kegelmann, Artiom Magomedov, Vytautas Getautis, Tadas Malinauskas.
  DE 10 2019 116 851 B3 2020.11.05.
  Applied 21.06.2019. Issued 05.11.2020.

  - International follow-up application of item above: "Perovskite Multi-Junction Solar Cell Having Multi-Layer System as Connection Layer".
    PCT/EP2020/067252, 19.06.2020, pending.

7.2 Experimental methods

This section summarizes the techniques that were used for fabricating and analyzing the samples throughout this thesis. The fabrication ranged from simple thin-film preparations on given substrates to full solar cells including tandem architectures comprising CIGSe and Si bottom cells. Details regarding the respective experiments used in the publications (incl. UPS, FITR, RAIRS, XRD, THz conductivity, EL imaging etc.) can be round in their supporting information; the following sections expand some experimental details that were a focus during optimization runs.

The p-i-n (inverted) perovskite solar cells processed here had an inverted planar structure on ITO-covered glass (Automated Research GmbH, both 7 Ohm/sq and 15 Ohm/sq sheet conductivities were used in this work). Generally, the processing steps (except cleaning) were done in a N2-filled glovebox (MBRAUN). The hole-selective layers were deposited by either spin-coating or dip-coating (in the case of SAMs in early stages, as indicated in the publications, or for CIGSe bottom cells) and perovskite films were deposited by spin-coating in a one-step method (with antisolvent drip). The ITO substrates were purchased laser-patterned, such that individual solar cell pixels were electrically isolated from each other and from the contact patches where the ground contact is pressed on in the sample holder (see Fig. 7.1). The substrate cleaning should not be underestimated, since even microscopically small particles that are not visible by eye can cause shunting, and organic, very thin dirt can already be detrimental to device performance. The substrates were cleaned with Mucasol detergent (2% in DI-water, substrates were brushed), DI-water, acetone and isopropanol, each for 15 minutes in an ultrasonic bath at 40-55°C. Care needs to be taken to flush all residues of the soap after the first step and to not let Acetone dry out on the substrates upon switching liquids, since it leaves residues on the substrate that are hard to remove.

7.2.1 Perovskite films and compositions

Mainly three different perovskite compositions have been used in this work and, except for the co-evaporated solar cell, they were based on the stock solution method, where first, individual solutions of PbI_2 , $PbBr_2$ in a mixture of DMF/DMSO (4:1 volume ratio) (powders by TCI, >99% purity trace metals basis, solvents by Sigma Aldrich) and CsI (abcr GmbH) in DMSO were prepared 1-2 days before the actual mixing of needed perovskite precursor. The lead salt solutions (1.5 mol/l nominal concentration) were shaken over night in a thermo shaker (60°C), and let cool down to room temperature within 15-30 min, before they were used to dissolve the organic powders (FAI, MABr), which were previously weighed with 1 mg precision. The needed volume of lead salt

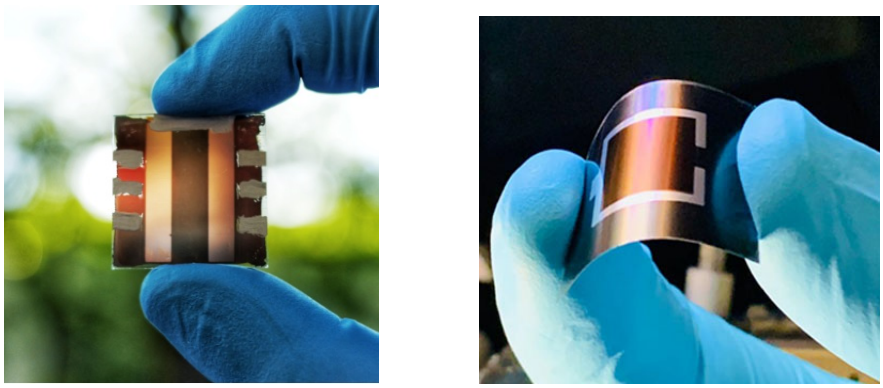

(a) (b)

Figure 7.1: Photographs of a sample with single junction cells (a) and a flexible perovskite/CIGSe tandem solar cell (b, steel substrate). The single junction device contains six individual pixels (each 0.16 cm^2), defined by the overlap of Cu top electrode and scribed ITO. The ground electrode is indicated by the silver paste stripe that connects both Cu stripes (the connection is not necessary).

solution was calculated such that the perovskite solutions of $FAPbI_3$ and $MAPbBr_3$ (1.24 mol/l nominal concentration) contained a 5-9%mol excess of $Pb(I,Br)_2$ for improved V_{OC}. The two perovskite solutions were mixed in an appropriate ratio for the aimed bandgap (i. e., 83:17 $FAPbI_3$:$MAPbBr_3$ for 1.63 eV bandgap, 78:22 for 1.68 eV, 95:5 for 1.55 eV [with addition of 5% of MACl/DMSO solution to aid crystallization]). Finally, 5 vol-% of the CsI solution was added just before spin-coating to the perovskite mixture to yield the triple cation compositions (not for the 1.55 eV perovskite). The final solution was yellow (see Fig. 7.2), which during spin-coating and drying turned slightly darker, upon antisolvent quenching it switched color to brown and during the first seconds after laying the sample on a 100°C hotplate turned to dark-brown/black. As the contact angle of perovskite solution on organic layers is high (preventing self-spreading across the sample surface), the solution (50-200 µl depending on the wettability) was spread across the substrate using a pipette tip, and upon reaching the substrate edge, the spinning program was immediately started.

As antisolvents, which drive out the initial solvents, ethyl acetate, chlorobenzene and di-ethyl ether have been used. Ethyl acetate (500 µl, 4000 rpm spin speed with 5s acceleration time, drip after 25 s after start of the program, 40 s total time, closed spin-coater lid) lead to thicker perovskite films (up to 700 nm), but a higher spread in *FF* values. Chlorobenzene (300 µl, 3000-3500 rpm spin speed with 5s acceleration time, drip after 35 s after start of the program, 40 s total time, open spin-coater lid) lead to higher average *FF* values, but due to its toxicity and narrow processing window (~1 s, with sensitiviy on how fast the dripping was done and at which angle), Anisole

has been used as the main antisolvent in later stages (end of chapter 4 and all single junction cells in 5), which had the same advantages of Chlorobenzene but with a larger processing window and no toxicity. With anisole, the spinning paramters were as for chlorobenzene, but the thickness could be controlled depending on the time of dripping and whether the spin-coater lid was open or closed, without considerable influence on the device performance or film QFLS. With chlorobenzene and anisole, the film thicknesses were generally lower (450-550 nm) and surfaces smoother/shinier. The perovskite layers have been annealed for 15-30 min on a 100°C hotplate.

Figure 7.2: Photograph of a 4 ml vial containing perovskite solution, enough for roughly 20-30 samples for spin-coating (on inch × inch substrates).

7.2.2 Processing of charge-selective contacts

As hole-selective contacts, PTAA has been used during baseline establishment (spin-coating a 1.5-2 mg/ml solution in toluene at 5000 rpm, closed lid). For the main publication, the SAMs were the standard (V1036, (Me- or MeO-)nPACz with n= 2, 4, 6), which reduced the spread compared to PTAA-based cells and later enabled higher PCEs. Critical for the SAMs to reliably bond to the electrode oxides was the UV-O3 treatment (in air) of the substrates (used machine: FHR UVOH 150 Lab) for 15 min. Subsequently, the samples were transferred into the glovebox where they were functionalized with the SAMs, either by spin-coating or dip-coating. For spin-coating, a 1 mmol/l solution in ethanol (methanol and isopropanol work similarly) has been used (roughly 0.5 mg/ml, 3000 rpm spin speed with 5 s acceleration for a total spinning time of 10-25 s without noticeable differences): dropping 100 µl solution onto the center of the substrate, letting it spread for 5 s and then starting the spinning. For dip-coating, a concentration of 0.1-0.5 mmol/l was used, letting the substrates rest in the solution usually over night, before removing the solution and letting them dry. With both methods, the substrates were subsequently heated at 100 °C for 1-10 min on a hotplate. The dipping solution can be reused and air exposure of the SAM-covered substrates did not lead to noticeable detrimental effects on device performance. After dipping and in some tests for spin-coated SAMs, the substrates have been washed after annealing with ethanol (2-3 × dynamic spin-coating) and then dried by N2 gun. The SAM powder have been synthesized at KTU as indicated in the author contributions (see supporting

informations for synthesis procedures) and for the paper in chapter 5, MeO-2PACz and 2PACz were bought from TCI.

After perovskite annealing, the electron-selective layer (C60, sublimed, 99.999%, CreaPhys GmbH) was deposited usually within the same day by thermal evaporation at a base pressure of 5E-5 to 1E-6 mbar, with a rate of 0.05-0.15 Å/s until a thickness of 18-23 nm. With longer waiting times for the perovskite vacuum until the C60 process started, lower V_{OC}s were observed – samples with C60 layer were vacuum-stable. Most single junction cells were then topped by a bathocuproine (BCP)/Cu contact, by thermal evaporation. Higher FFs have been noticed if the BCP and Cu were evaporated in the same vacuum run and if for the metal evaporation, lower pressures were used (2-5E-7 mbar seemed optimal). The C60 powder was heated to 355-380 °C and the BCP to 115-130 °C. Ag electrodes led to slightly lower series resistances than Cu, at the cost of slightly lower stability.

(a) (b)

Figure 7.3: Encapsulated and masked single junction cell that was sent for certification (chapter 4); the aperture area of the masked pixel was around 0.1 cm^2.

More air-stable single-junction cells could be fabricated with SnO_2 instead of BCP as the buffer layer between C60 and metal. The SnO_2 layer (20 nm) was deposited through atomic layer deposition (ALD, Arradiance GEMStar reactor). Tetrakis(dimethylamino)-tin(IV) (TDMASn) was used as the Sn precursor and was held at 60 °C in a stainless-steel container. Water was used as oxidant, and was delivered from a stainless-steel container without active heating, whereas the precursor delivery manifold was heated to 115 °C. For the deposition at 80 °C, the TDMASn/purge1/H2O/purge2 times were 1s/10s/0.2s/15s with corresponding nitrogen flows of 30sccm/90sccm/90sccm/90sccm. With this, 140 cycles lead to the 20 nm thick layer. We noticed a beneficial effect when letting the TDMASn bottle cool down to room temperature when not in use. Over time, the TDMASn seemed to lose in "quality", leading to a drop in V_{OC} and FF compared to BCP (higher series resistance). With fresh bottles, SnO2 and BCP cells had similar PCE.

For tests in air or, e. g., certification, the cells were encapsulated with cavity glass containing a getter foil for moisture absorption. The glass edges were then glued onto the sample, where the contact areas were scratched clean beforehand.

For highest-V_{OC} samples, a LiF layer has been used between perovskite and C60, by thermal evaporation at 0.5-1 nm thickness. NaF, CsF and KCl as evaporated interlayers were tried as well with limited success. PMMA as spin-coated interlayer (0.5-1 mg/ml in CBZ) also enabled high V_{OC}, however, lead to hysteresis in the J-V curve.

7.2.3 Tandem cell processing

Tandem solar cells with perovskite top cells on either CIGSe or Si bottom cells were processed similar to the single junction cells described above (with SnO2 on the C60 layer), but without immersion of the bottom cells into the cleaning solutions and without the usage of ultrasonic cleaning. The bottom cells were either blown clean with a nitrogen gun or cleaned with dynamic isopropanol or ethanol spin-coating, before UV-O3 treatment. Without the UV-O3 treatment, the SAMs cannot properly attach, thus leading to poor performance and low QLFS of the bare perovskite films. After

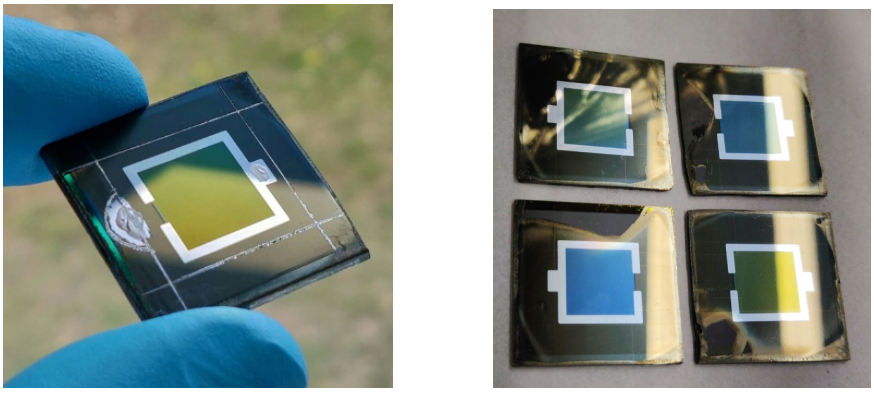

(a) (b)

Figure 7.4: Photographs of perovskite/CIGSe tandem solar cells (without antireflective coating on the active area – the color differences show slight variations in the thickness of the IZO). (a) shows an early sample where the active area was isolated from the sample edges by manual scribing – this also enhanced the V_{OC}, because the interconnecting AZO layer was sputtered on the full area (being otherwise dark area for the bottom cell). The molybdenum (silver color visible on the scribes) was contacted with a speck of silver paste, serving as the bottom electrode of the tandem. With this design, the two highest efficiencies were realized (23.3 and 24.2%). (b) later designs which where the molybdenum layer has been laser-scribed before CIGSe processing and the AZO layer sputtered through a mask to prevent shunting through handling outside of the active area and to reduce dark area.

SnO2 deposition, an IZO layer was deposited on top through a shadow mask, followed

by thermal evaporation of a 100 nm-thick silver ring (see Fig. 7.4) that overlapped with the IZO layer and contained a patch for contacting (ideally, there is no IZO below this patch to prevent shunting). For certification, another Ag evaporation run was done to obtain a closed ring (clearly defining the aperture area). Finally, a LiF antireflective layer was evaporated on the IZO (100 nm).

The CIGSe bottom cell was fabricated viaation on a glass substrate with sputtered Molybdenum, with RbF surface treatment on the CIGSe. The recombinatieated with UV-Ozone for 15 min, before submersing te CIGSe bottom cell into a 0.1 mmol/l MeO-PACz/Ethanol solution overnight. Spin-coating a 1 mmol/l MeO-PACz solution once or a 0.1 mmol/l solution three times also yielded >20%-efficient tandem cells as well. Subsequently, the bottom cells were heated at 100 °C for 10 min in a N2-filled glovebox, before proceeding the CsMAFA perovskite processing on top as described above.

7.2.4 Electrical characterization of solar cells

J-V and EQE measurement

J-V) characteristics under 1-sun equivalent illumination were recorded using a Wavelabs Sinus-70 LED class AAA sun simulator in air or in a glovebox with a Oriel halogen lamp, calibrated with a filtered KG3 Silicon reference solar cell certified by Fraunhofer ISE. J-V scans were performed in 2-point configuration with a Keithley 2400 SMU (4-point measurement with Keithley 2600 for the tandem cell), controlled by a measurement program written in LabView. The single junctions were not masked during measurement (due to small differences between J SC from integrated EQE and J-V). The voltage values were swept in 20 mV steps with an integration time of 40 ms per point and settling time of 20-40 ms after voltage application (maximum voltage sweep speed of 250 mV/s). The program first turned on the output of the SMU to 0 V, before switching the relais of the pixel switcher that established contact between solar cell and SMU, to avoid voltage spikes to damage the small cells. No spectral mismatch correction was applied due to the variation being within the measurement error. The cells were not preconditioned, however, the J-V curves sometimes tended to slightly improve upon multiple scanning

EQE spectra were recorded with an Oriel Instruments QEPVSI-b system with a Newport 300 W xenon arc lamp. The white light was filtered into monochromatic light by a Newport Cornerstone 260 monochromator with a 10 nm increment and chopped into a frequency of 78 Hz before being conducted to the solar cell surface via optical fibers. The system is calibrated using a Si reference cell with known spectral response before every measurement. The electrical response of the cell was measured with a Stanford Research SR830 Lock-In amplifier (time constant of 0.3 s) and evaluated in the proprietary software. The implied J_{SC} was calculated through integration of the interpolation of the EQE spectrum multiplied with the AM1.5G spectrum at every wavelength (1 nm step). The typical short-circuit current mismatch between integrated

external quantum efficiency (EQE) times AM1.5G irradiance and values from J-V scans is around 1%.

7.2.5 Material and interface analysis via photoluminescence

During optimization runs of perovskite film quality, for investigating interfacial recombination losses and tracking halide segregation, photoluminescence (PL) spectroscopy has been extensively used. Mostly, PL measurements (absolute and time-resolved) were conducted in the laboratories of Thomas Unold (HZB Wannsee).

Absolute photoluminescence

The absolute PL images and spectra as in chapter 4 were recorded in a custom hyperspectral imaging setup using excitation two 450 nm LEDs, calibrated to 1-sun equivalent fluence. PL emission was collected with a CCD camera coupled to a tunable liquid crystal filter for wavelength-selectivity The camera/filter column was calibrated to absolute photon numbers with light sources of known fluences, thus enabling to estimate the quasi fermi-level splitting from the generalized Planck law using the high-energy tail fit method. Alternatively, especially for samples that have shown double-peaks or not well-behaved spectral shapes, the PLQY was calculated to calculate the QFLS via the 'Ross method' (see eq. (2.8)). The samples were measured in air (encapsulation with, e.g., blufixx had an influence on the PL and was thus omitted) and often, a light-soaking effect was observed (rise of QFLS during the first few minutes of illumination, by roughly 10-30 meV).

Time-dependent steady state absolute photoluminescence measurements (for tracking halide segregation as in chapter 5) were performed with a home-built setup using an integrating sphere, where the samples were placed at the edge of the sphere. The PL was collected with a fiber connected to a CCD-array spectrometer (Ocean Optics). The samples were excited with a continuous-wave laser at 532 nm emission wavelength, a photon flux of 1.2E+16 photons/s and a spot size on the sample of 0.12 cm^2 (around 1-sun-equivalent excitation fluence, calibrated with a certified silicon reference cell). The 30-suns case was realized by a focusing lens to reduce the spot size to 0.4 mm^2. The spot size was measured by fitting a Gaussian curve to the beam profile extracted from CCD imaging the laser spot. The 1-sun 0.4 mm^2 case was realized by a focusing lens and appropriate ND filters. Non-absorbed laser light and emitted photoluminescence fluxes were simultaneously detected by the spectrometer, of which the spectral sensitivity was calibrated using a NIST-traceable halogen lamp. The spectral time evolutions of the perovskite films were recorded with an integration time of 300 ms and delay of 2-3 s between each integration. Measurements were carried out in air; the samples were measured promptly after they were taken out from the N2-filled glovebox.

Transient photoluminescence

Time-resolved photoluminescence (trPL) measurements were carried out in a home-built setup using excitation at a 660 nm wavelength from a pulsed supercontinuum laser light source (SuperK) with a spot size of 25-35 µm in diameter. The repetition rate was set to 125 or 304 kHz and the sample's PL emission was collected panchromatically through a photomultiplier. Utilizing a time-correlated single photon counting technique (TCSPC), the PL decay was recorded with a time resolution of approximately 4 ns. The excitation power was varied with a linear ND filter, tracked with a power meter and chosen as follows, for injecting approximately the amount of charge carriers that is relevant for device operation under 1-sun conditions: If at a 1-sun equivalent excess charge-carrier density Δn the PL decay is dominated by monomolecular recombination, the recombination rate R can be approximated by $\Delta n/\tau$, where τ is the trap-assisted recombination-limited lifetime. At quasi steady state, the generation rate G equals R. Thus, G is roughly the photon flux per penetration depth (approximated by the film thickness, approx. 500 nm) divided by the steady-state PL lifetime (we assume 500 ns). This G is compared to the expected G under 1-sun equivalent excitation for an absorber with 1.63 eV band gap, which is given by the respective integration of the AM1.5G irradiance spectrum (1.5E+21 m^{-2} s^{-1}). Under these estimations, a fluence of 10-30 nJ/cm^2 of pulsed excitation should create a 1-sun equivalent quasi-steady-state situation. The samples were excited from the glass side to avoid increased reflection stray light, however, no significant difference in decay times was observed between excitation from both sides.

Transient surface photovoltage

The SPV measurements were conducted by Igal Levine and Thomas Dittrich in fixed-capacitor configuration, where one electrode is below the substrate (connected to the ITO) and the other (a FTO-coated quartz cylinder) layed on top of the sample with a mica sheet in between. Excitation was performed with a pulsed laser (600 nm wavelength) at 2 Hz repetition rate and the SPV signal was recorded with an oscilloscope card (at 200 MS/s) with 100 averages per transient.

7.3 Publication to chapter 3

The paper is reprinted here with permission from John Wiley and Sons (lic. no. 4984111482075) [207].

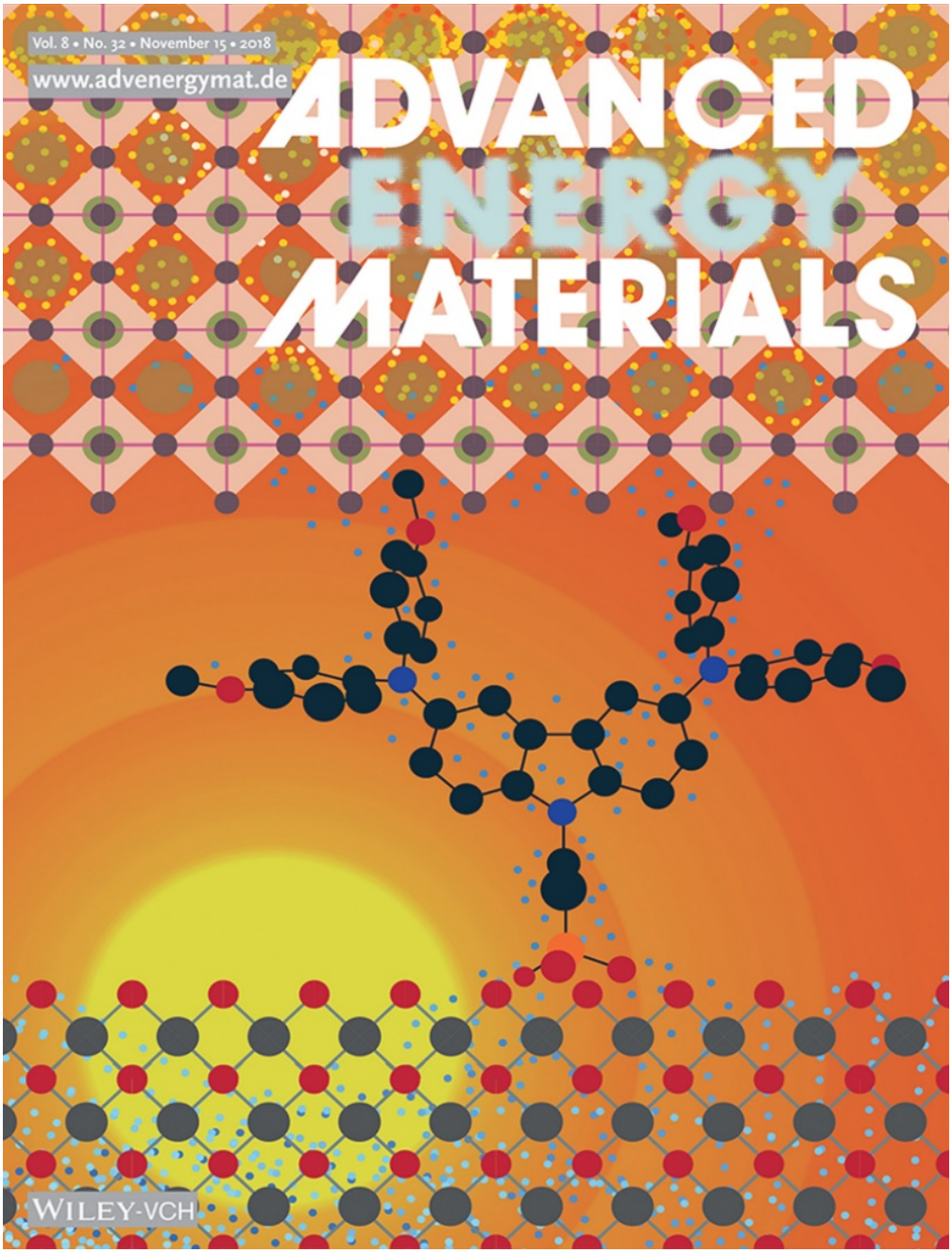

Figure 7.5: This publication was highlighted on the cover page of Advanced Energy Materials, depicting a self-assembled molecule between a bottom electrode and perovskite layer. Reprinted with permission by John Wiley and Sons (licence no. 5000461030985), [282]; artwork by Saule Magomedoviene.

ADVANCED ENERGY MATERIALS

www.advenergymat.de

Self-Assembled Hole Transporting Monolayer for Highly Efficient Perovskite Solar Cells

Artiom Magomedov, Amran Al-Ashouri, Ernestas Kasparavičius, Simona Strazdaite, Gediminas Niaura, Marko Jošt, Tadas Malinauskas, Steve Albrecht, and Vytautas Getautis**

The unprecedented emergence of perovskite-based solar cells (PSCs) has been accompanied by an intensive search of suitable materials for charge-selective contacts. For the first time a hole-transporting self-assembled monolayer (SAM) as the dopant-free hole-selective contact in p–i–n PSCs is used and a power conversion efficiency of up to 17.8% with average fill factor close to 80% and undetectable parasitic absorption is demonstrated. SAM formation is achieved by simply immersing the substrate into a solution of a novel molecule V1036 that binds to the indium tin oxide surface due to its phosphonic anchoring group. The SAM and its modifications are further characterized by Fourier-transform infrared and vibrational sum-frequency generation spectroscopy. In addition, photoelectron spectroscopy in air is used for measuring the ionization potential of the studied SAMs. This novel approach is also suitable for achieving a conformal coverage of large-area and/or textured substrates with minimal material consumption and can potentially be extended to serve as a model system for substrate-based perovskite nucleation and passivation control. Further gains in efficiency can be expected upon SAM optimization by means of molecular and compositional engineering.

1. Introduction

In a strikingly short period of time, solar cells with organic–inorganic perovskite absorbing layers have surpassed 20% power conversion efficiency (PCE), with a current record efficiency of 23.3%.[1] So far, the published record results for perovskite solar cells (PSCs)[2] were achieved in n-i-p configuration (in literature often referred to as "regular" PSCs) with a combination of a compact and mesoporous TiO_2 layer as an electron transporting material (ETL) deposited on a transparent conductive oxide (TCO) substrate. So called "planar" regular solar cells have also been reported using compact TiO_2, SnO_2, fullerene-based derivatives or a combination of these layers.[3–6] Recently, the p–i–n configuration (in literature often referred to as "inverted" PSCs), where first the hole transporting material (HTM) is deposited on the TCO, gained significant attention with reported efficiency over 20%.[7,8]

p–i–n PSCs have several advantages in comparison to the n–i–p architecture. First, high temperature annealing, which is required for the TiO_2 layer formation, is avoided. Second, they are known to have much less pronounced hysteresis, leading to virtually "hysteresis-free" devices,[9] even though it can still be detected under certain conditions.[10,11] Third, much cheaper copper can be used instead of gold as a metal contact layer.[7] Next, no doping is needed for the charge selective contacts which might improve the long-term stability, as dopants of spiro-OMeTAD are known to reduce device stability.[12] Finally, the p–i–n configuration was shown to enable higher tandem efficiency potential due to less parasitic absorption in the front contact[13,14] and thus p–i–n PSCs have a great potential for further development.

Currently, most popular hole transporting materials for p–i–n PSCs are p-type polymers (e.g., poly[bis(4-phenyl)(2,4,6-trimethylphenyl)amine] (PTAA),[8,15] Poly-TPD,[16,17] PEDOT:PSS[18,19]), or inorganic metal oxides (e.g., NiO_x[20]), which are deposited by a spin-coating technique. However, spin-coating is not suitable for large-scale production due to low throughput and large waste of materials. As an alternative, vacuum deposition technique can be utilized for the HTM formation (e.g., for TaTm[21]), yet its application is limited to small molecules, which are compatible with sublimation but usually not with solution-processed perovskites due to their low resistance to the used solvents.

In a recent work by Stolterfoht et al.[8] it was shown that reduction of the HTM film thickness leads to increase

A. Magomedov, E. Kasparavičius, Dr. T. Malinauskas, Prof. V. Getautis
Department of Organic Chemistry
Kaunas University of Technology
Radvilenu pl. 19, Kaunas LT-50254, Lithuania
E-mail: vytautas.getautis@ktu.lt

A. Magomedov, A. Al-Ashouri, Dr. M. Jošt, Dr. S. Albrecht
Institute for Silicon Photovoltaics
Helmholtz-Zentrum Berlin
Young Investigator Group for Perovskite Tandem Solar Cells
Kekuléstr. 5, Berlin D-12489, Germany
E-mail: steve.albrecht@helmholtz-berlin.de

Dr. S. Strazdaite, Prof. G. Niaura
Department of Organic Chemistry
Center for Physical Sciences and Technology
Sauletekio Ave. 3, Vilnius LT-10257, Lithuania

The ORCID identification number(s) for the author(s) of this article can be found under https://doi.org/10.1002/aenm.201801892.

DOI: 10.1002/aenm.201801892

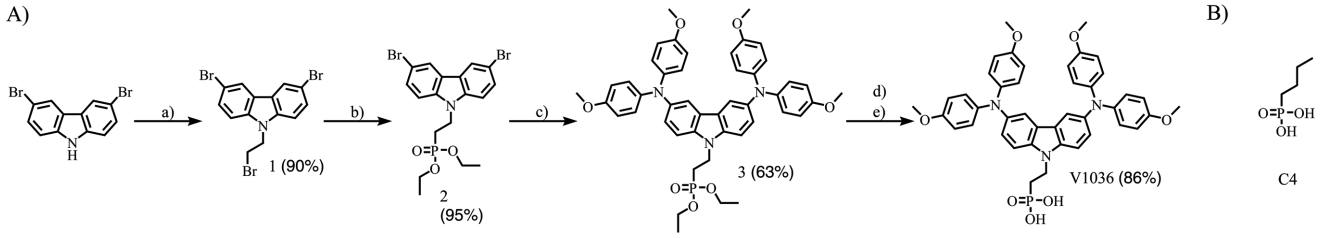

Scheme 1. A) Synthesis of the phosphonic acid functionalized carbazole derivative V1036. B) Chemical structure of C4, which was used in this study for the formation of mixed SAMs A-(a)1,2-dibromoethane (6.5 mL per equiv.), TBABr (0.3 equiv.), 50% KOH aqueous solution (15 equiv.), 72 h, 60 °C; A-(b) triethylphosphite (3.6 mL per /equiv.), 18 h, 165 °C; A-(c) 4,4′-dimethoxydiphenylamine (3 equiv.), $Pd(OAc)_2$ (0.3 equiv.), $P(t\text{-}Bu)_3{\cdot}BF_3$ (0.6 equiv.), NaO*t*-Bu (3 equiv.), anhydrous toluene (24.5 mL per equiv.), Ar, 5 h, reflux; A-(d) $BrSi(CH_3)_3$ (10 equiv.), anhydrous dioxane (29.4 mL per equiv.), Ar, 24 h, 25 °C; A-(e) MeOH (19.6 mL per equiv.), H_2O (19.6 mL per equiv.), 15 h, r.t.

in the FF (fill factor). However, as the films are getting thinner, the open-circuit voltage (V_{oc}) sharply drops, possibly due to the incomplete coverage of indium tin oxide (ITO), leading to a direct contact between perovskite and ITO and thereby enhancing the interface recombination.

The formation of a self-assembled monolayer (SAM) on TCO circumvents the disadvantages of spin-coating or vacuum deposition, while offering the benefits of uniformly formed layers with minimized thickness.[22,23] SAM HTMs would have minimal parasitic absorption, very low material consumption, would help to avoid doping procedures, and could be adopted for the large area production of solar cells. Moreover, due to the covalent linking to the substrate surface these layers are relatively tolerant against perovskite processing and could potentially ensure a conformal coverage of textured surfaces. Therefore, SAM HTMs would be perfect candidates for direct integration into monolithic perovskite/silicon solar cells on textured silicon or rough CIGS substrates.

Molecules with phosphonic acid anchoring groups are known to form densely packed, uniform monolayers on various oxides,[22,23] in particular on ITO by forming strong bidentate/tridentate bonds with the oxide surface,[24,25] which was shown to occur even at room temperatures.[26] They have been utilized for various applications, e.g., in dye-sensitized solar cells (DSSCs)[27] and in electrochromic devices.[28,29] However, up to date there are just several reports on the synthesis and application of hole transporting molecules, functionalized with phosphonic acid groups. Applications can be found in organic light-emitting diodes (OLEDs),[30] where HTM SAMs were used for better charge injection, or in SAM field-effect transistors (SAMFETs).[31,32]

Recently, several reports were published by Hou et al. on the use of a phosphonic acid-based mixed C_{60}/organic SAM as an ETL in n–i–p PSCs, replacing TiO_2.[33,34] Siloxane-functionalized C_{60} SAMs were used by Topolovsek et al. in a similar fashion.[35] In the work of Lin et al.[36] insulating SAMs on gold were used to achieve surface dipole assisted charge extraction. However, to the best of our knowledge, no hole-transporting SAMs for PSCs have been reported up to date.

In this work, a new hole transporting material **V1036**,[37] with a phosphonic acid anchoring group was synthesized and used for the formation of a self-assembled hole-transporting monolayer (SA-HTM) on ITO. For the first time, p–i–n PSCs with a SA-HTM were constructed and showed a very promising power conversion efficiency close to 18% using a mixed cation/mixed halide perovskite composition, the so called "triple cation" perovskite.[38] We believe that this strategy can be further developed by introducing other well-known HTM fragments, which eventually could lead to even higher efficiencies. Furthermore, use of the SAMs opens possibilities for the substrate-based perovskite nucleation and passivation control.

2. Results and Discussion

For this purpose, dimethoxydiphenylamine substituted carbazole **V1036**, functionalized with phosphonic acid, was synthesized. Dimethoxydiphenylamine substituted carbazole fragment can be found in several efficient HTMs[39–41] for regular perovskite solar cells, and reactive nitrogen in the 9-position of carbazole can be further used for the functionalization with a phosphonic acid anchoring group.

Synthesis was done in a 4-step synthetic procedure, starting from commercially available materials (**Scheme 1**A). 3,6-Dibromocarbazole was alkylated with 1,2-dibromoethane to give intermediate compound **1**. In the next step, by the means of Arbuzov reaction, aliphatic bromide was transformed into phosphonic acid ethyl ester **2**. Dimethoxydiphenylamine fragments were introduced to yield compound **3** via palladium-catalyzed Buchwald–Hartwig amination reaction. Finally, cleavage of the ester with bromotrimethylsilane resulted in phosphonic acid **V1036**. Structures of the synthesized compounds were confirmed by means of ^1H and ^{13}C NMR spectroscopy. A more detailed description of the synthetic procedures is available in the Supporting Information. A relatively high overall yield of 46% for the four-step synthesis is achieved due to the simplicity of most of the stages, making **V1036** a promising material for the practical application.

In an inverted PSC light first passes through the HTM layer when illuminated from the glass-substrate side, thus it is important to minimize parasitic absorption of this layer. Optical properties of **V1036** were investigated by means of UV–vis spectroscopy (**Figure 1**A). A strong π–π^* absorption band, with λ_{max} = 304 nm, as well as a weaker n–π^* band in the 350–450 nm region, which is characteristic for the dimethoxydiphenylamine 3,6-substituted carbazole chromophoric system,[39] can be observed. In comparison to PTAA (λ_{max} = 387 nm), **V1036** has an absorption maximum in a shorter wavelength range and weaker absorption in the visible range.

Additionally, UV–vis absorption of a PTAA layer and **V1036** SAM on ITO was measured as displayed in Figure 1B. The SAM is formed on the ITO substrate by immersing the

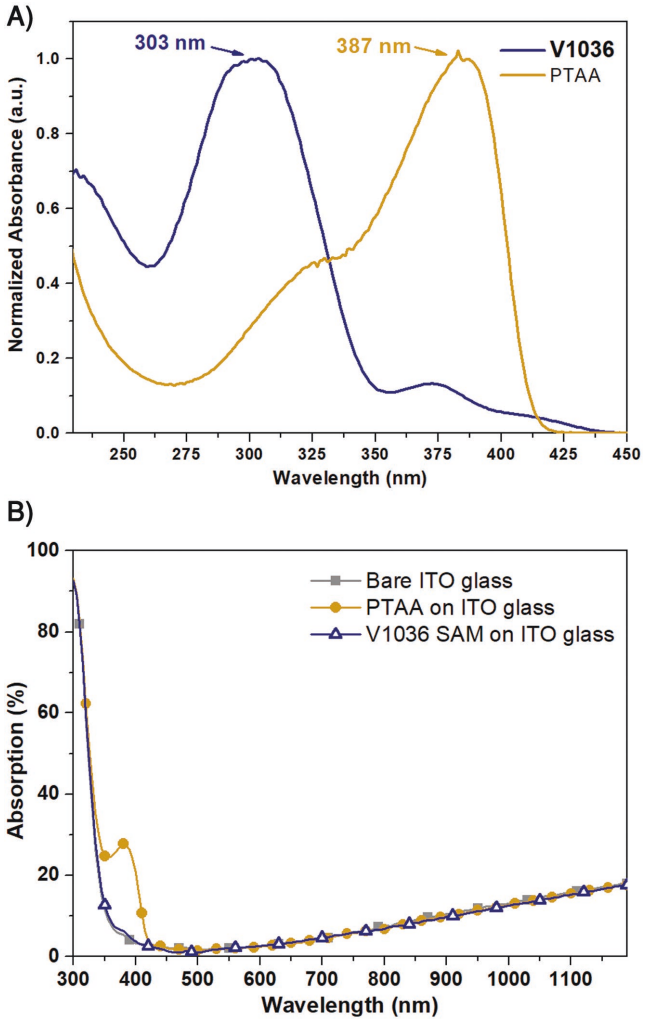

Figure 1. A) UV–vis absorption spectra for 10^{-4} M THF solution of **V1036** and PTAA; B) UV–vis absorption spectra of the bare ITO substrate, ITO with PTAA, and ITO with 100% **V1036** SAM.

substrate into a 1×10^{-3} M solution of **V1036** in isopropanol (see the Supporting Information for more details) for 20 h. Subsequently, the substrate is blown dry with nitrogen and then annealed for 1 h at 100 °C on a hotplate, before being washed with isopropanol and chlorobenzene. As can be seen from Figure 1B, the **V1036** SAM has a negligible influence on the absorption of ITO (<1%), therefore no parasitic absorption is expected. Under the given measurement uncertainty of ≈1% of the spectroscopy setup, the UV–vis spectra together with optical simulations allow us to estimate an upper bound for the thickness of the **V1036** layer on ITO (see the Supporting Information for more details). Assuming a previously reported surface packing density of 0.7 nm² per molecule for a similarly sized molecule,[30] the simulation reveals that the layer thickness must be below 2 nm in order to show an absorption of under 1% at 375 nm. The vertical size of the molecule (DFT calculations, Figures S20 and S21, Supporting Information) is ≈1.5 nm, pointing toward monolayer thickness.

Thermal decomposition of the **V1036** was investigated by means of thermogravimetric analysis (TGA). In Figure S1 (Supporting Information), a TGA heating curve of **V1036** is shown, from which the 95% weight loss temperature (T_{dec}) of 343 °C was determined. T_{dec} is high enough to make this material suitable for the practical applications in optoelectronic devices.

The first indication of a surface modification is the change of the contact angle of perovskite solution on the treated ITO substrates. In previous reports, SAM solutions mixed with smaller aliphatic molecules as fillers were used to improve the quality of the formed monolayers.[42,43] Following this insight, we mixed our SAM solution with butylphosphonic acid (**C4**) (Scheme 1B) in different ratios, as aliphatic phosphonic acids are known to form dense insulating monolayers on oxides,[44,45] and investigated the influence on contact angle and solar cell device performance. The total concentration of both phosphonic acids in the solutions was kept at 1×10^{-3} M, such that, e.g., a 50% **V1036** 50% **C4** SAM solution consists of 0.5×10^{-3} M **V1036** and 0.5×10^{-3} M **C4**. **Figure 2** shows contact angle measurements using "triple cation" perovskite solution in DMF:DMSO (4:1; v:v) as a probing liquid for different compositions of the immersion solution. As can be seen in Figure 2 and Table S1 (Supporting Information), for PTAA, 100% **V1036** SAM, and 100% **C4** SAM contact angles are 42.6°, 26.3°, and 60.5° respectively. For the mixed SAMs, the contact angle gradually changes with changing molar ratio between **C4** and **V1036**, confirming the presence of both species on the ITO surface. The smooth transition of the contact angle values confirms that the ratio of **C4** to **V1036** on the surface can be modified in a controllable fashion via composition of the immersion solution. Differences in contact angle correlate with the polarity of the material, giving the largest value for nonpolar aliphatic 100% **C4** SAM, and lowest value for 100% **V1036** SAM because of its polar methoxy functional groups.

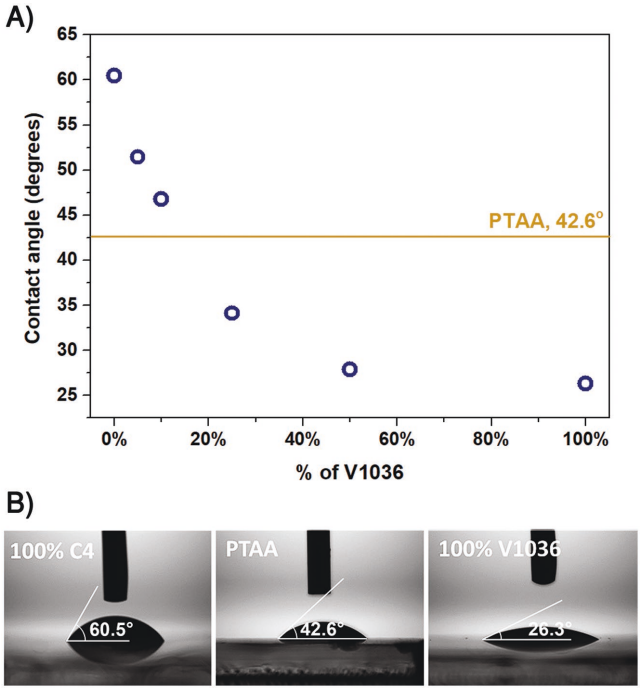

Figure 2. A) Contact angle dependence on the percentage of the **V1036** in the SAM composition; B) Equilibrium contact angle of perovskite solution on 100% **C4** SAM; PTAA; 100% **V1036** SAM.

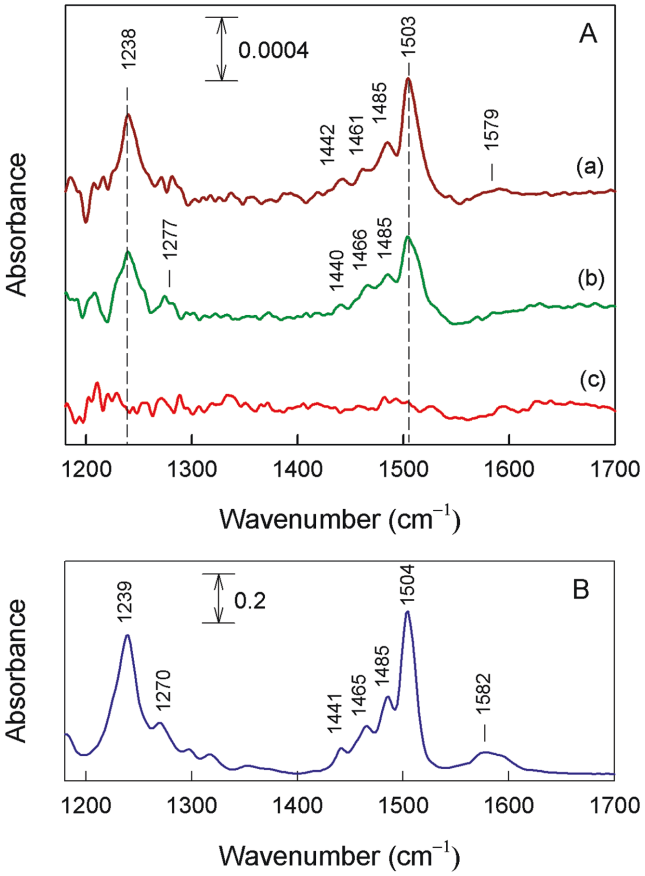

Figure 3. A) FTIR absorbance spectra of monolayers on ITO substrates prepared from (A-(a)) 1×10^{-3} M solution of **V1036**, (A-(b)) 1×10^{-3} M of mixed solution **V1036**:**C4** (1:9), and (A-(c)) 1×10^{-3} M solution of **C4**. B) FTIR spectrum of bulk **V1036** in KBr tablet.

To confirm that the surface modification is indeed induced by **V1036** molecules, Fourier-transform infrared (FTIR) spectra of the studied SAMs on ITO substrates were recorded (**Figure 3**A) and compared to the spectrum of bulk **V1036** compound dispersed in a potassium bromide (KBr) tablet (Figure 3B). The spectrum of a 100% **V1036** SAM exhibits two intense bands at 1238 and 1503 cm^{-1} along with lower intensity components near 1442, 1461, and 1485 cm^{-1} (Figure 3A-(a)). All observed features in the monolayer spectrum are close to the absorption bands visible in the infrared spectrum of bulk **V1036**, confirming its presence on the surface of the ITO substrate. The most intense band at 1503 cm^{-1} is associated with C=C in-plane stretching vibration of aromatic rings of the carbazole structure[46–48] with some contribution from C=C in-plane stretching vibration of *p*-methoxy-phenyl groups.[49] Stretching vibrations of C—N bonds[47,48] are visible as an intense band near 1238 cm^{-1}. Two medium intensity bands located in the vicinity of 1438–1442 and 1461–1466 cm^{-1} contain a high contribution from symmetric and asymmetric CH_3 deformation vibrations of the methoxy group.[49] The integrated absorbance intensity of the band near 1503 cm^{-1} was found to decrease for the SAM prepared from solution containing mixture of **V1036** (10%) and **C4** (90%) down to 0.62 of the relative intensity compared to the 100% **V1036** SAM (relative intensity 1.00), indicating a decrease in surface coverage by the **V1036** compound in the mixed SAM. Clearly, the decrease in surface coverage for the **V1036** compound is not as high as could be expected from the **C4** to **V1036** molar ratio (1:9) in the adsorption solution, which indicates a higher surface affinity for **V1036** compared to **C4**. 100% **V1036** monolayer showed no difference after the sample was kept for 25 days at ambient temperature in air (Figure S3, Supporting Information), suggesting good stability of the formed monolayer.

An additional argument for the absence of multilayers can be deducted from an analysis of FTIR spectra of samples prepared in adsorption solutions containing different concentrations of the **V1036** compound (Figure S2, Supporting Information). Vibrational bands of surface layers prepared from 0.1 and 1×10^{-3} M adsorption solutions are very similar both in peak positions and intensities. We found that the full width at half maximum (FWHM) of 1503 cm^{-1} band increases just slightly for the layer prepared from 1×10^{-3} M solution. The ratio of integrated absorbance intensity, was found to be A (0.1×10^{-3} M)/A (1×10^{-3} M) = 0.86 for the band near 1503 cm^{-1}. Small differences in FTIR spectra of **V1036** on ITO prepared from 0.1 and 1×10^{-3} M adsorption solutions suggest absence of multilayer material for our studied samples.

To further investigate SAMs on the ITO surface and assess differences in layer ordering, we performed vibrational sum-frequency generation spectroscopy (VSFG) on the same substrates as used for the FTIR spectra. Figure S4 in the Supporting Information shows the VSFG spectra of our SAMs in the spectral region 1150–1300 cm^{-1} (A) and 1400–1600 cm^{-1} (B). Two peaks at ≈1237 cm^{-1} (Figure S4A-(a), Supporting Information) and ≈1490 cm^{-1} (Figure S4B-(a) , Supporting Information) were identified in the spectra of the 100% **V1036** SAM substrate. Those two bands correspond to the two most intense vibrational bands seen in the FTIR spectra of the same monolayer (see Figure 3A-(a)). The shape of the resonance centered at ≈1490 cm^{-1} resembles an asymmetric Fano-like resonance curve and also appears to be shifted compared to its frequency in the FTIR spectra (≈1503 cm^{-1}). This can be explained by an interference between the resonant signal and a substantial nonresonant SFG signal from the ITO substrate, leading to spectral distortions as can be deduced from Equation S1 in the Supporting Information.[50]

No vibrational bands were identified in the VSFG spectrum of a 10% **V1036** 90% **C4** mixed SAM. The FTIR spectra showed that the surface coverage of **V1036** in the mixed SAM corresponds to ≈62% of the surface coverage of a pure **V1036** SAM. Thus, the VSFG signal of a monolayer with such surface coverage should be still detectable; however, no signal was registered. We conclude that a monolayer prepared from a mixed solution results in a more disordered structure compared to a monolayer from a pure **V1036** solution, since the measured VSFG signal is proportional to the molecular ordering of the probed molecules.[51]

Good matching of the energy levels between the absorber and charge selective contacts is an important requirement for efficient device operation. The work function of bare ITO was previously measured to be 4.6 eV[3] by means of ultraviolet photoelectron spectroscopy (UPS). The perovskite valence band edge and conduction band edge energies are measured to be in the range of 5.6–5.8 and 3.8–4.2 eV, respectively.[52–54] A good hole selective contact should have an ionization potential (I_p) close to the perovskite valence band edge energy and a large energetic

Table 1. I_p (W_f for ITO), E_g^{opt}, and EA values of the investigated substrates.

Material	I_p (W_f for ITO), [eV]	E_g^{opt}, [eV][a)]	*EA*, [eV][b)]
bulk **V1036**	5.04	2.75	2.29
100% **V1036** SAM	4.98	2.75[b)]	2.23
10% **V1036** 90% **C4** SAM	5.09	2.75[b)]	2.34
PTAA	5.18	2.96	2.22
ITO	4.6[3]	–	–

[a)]Optical band gap (E_g^{opt}) estimated from the edge of absorption spectra; [b)]For SAMs same E_g^{opt} value as for bulk **V1036** was used; [c)]EA calculated using the equation $EA = I_p - E_g^{opt}$.

offset between the electron affinity (EA) and the perovskite conduction band edge. In order to measure the I_p of the studied SAMs, we performed photoelectron spectroscopy in air (PESA) measurements on ITO/SAM samples and bulk **V1036** (**Table 1**; Table S2, Figures S5–S8, Supporting Information). For a PTAA film, spin-coated from a 2 mg mL^{-1} toluene solution on ITO, an I_p value of 5.18 eV was obtained, which is, within the measurement uncertainty of ≈0.03 eV, the same as a previously reported value of 5.16 eV.[55] Bulk **V1036** showed an I_p of 5.04 eV, which is a typical value for this chromophore.[39] For the 100% **V1036** SAM formed on ITO, I_p = 4.98 eV was obtained, which is in good agreement with the bulk material value. The mixed SAMs with a 10%–50% of **V1036** showed I_p in a range of 5.06–5.09 eV, with the highest value determined for the 10% **V1036** 90% **C4** composition. I_p values of these **V1036**:**C4** mixtures are more suitable for efficient hole extraction[12] than 100% **V1036**, or 5% **V1036** 95% **C4** SAMs (I_p = 5.01 eV). These results further suggest that the ionization potential might be potentially controllable by mixing different SAM molecules, opening up the possibility to easily adapt to different absorbers by choosing a suitable molar ratio between HTM SAM molecule and filler molecule. Electron affinity of the SAMs was calculated to be in a range of 2.23–2.34 eV (Table 1) which is close to that of PTAA (2.22 eV).

Next, to ensure that perovskite crystal formation on the SAM yields a homogenous film with reasonable grain size, we compare scanning electron microscopy (SEM) images of "triple cation" perovskite films on the SAMs and on a PTAA-coated substrate. As can be seen in **Figure 4** and Figure S19 (Supporting Information), the grain size of the perovskite is dependent on the monolayer composition. For the SAMs obtained from solutions containing 50% and 100% **V1036**, significantly smaller grains were obtained, which can be attributed to the better wetting of the perovskite solution.[15] On the other hand, 10% and 25% **V1036** SAMs demonstrated very similar morphology to that of the control film on PTAA.

The novelty of our approach lies within the usage of a hole transporting fragment as a monolayer building block, which acts as a hole contact in PSCs. To demonstrate the efficient hole extraction and transport of holes to the TCO, we fabricated p–i–n PSC devices in a ITO/HTM/Perovskite/C_{60}/BCP/Cu architecture,[8] using "triple cation" perovskite[38] as an absorbing layer. More details on device fabrication can be found in the Supporting Information.

The impact of the ratio between the charge transporting **V1036** and the electrically inactive filler molecule **C4** on the device performance was studied first. As can be seen in **Figure 5** and **Table 2**, the best PCE is achieved with the 10% **V1036** 90% **C4** mixed SAM. J_{sc} is almost the same for all SAM compositions, showing very small spread. FF values of the best performing devices are also very close, yet the results are more spread, and on average the best result is obtained for 10% **V1036** 90% **C4** and 25% **V1036** 75% **C4** SAMs. Out of all performance parameters, the most pronounced influence of the **C4**:**V1036** ratio was observed in the open-circuit voltage V_{oc}. The better performance of the mixed SAMs compared to the pure **V1036** SAMs can be rationalized based on the several aspects. First, with the addition of **C4**, the wettability of the perovskite solution was decreased, which was previously shown to potentially result in better device performance due to an improved film morphology.[15] This is in agreement with the SEM study of this work (Figure S19, Supporting Information). Second, mixing with **C4** resulted in slightly higher I_p, making it closer to the perovskite valence band, which is known to give higher V_{oc} in case of the dopant-free HTMs.[12] Indeed, in this work the highest V_{oc} is obtained by the SAM mixture with the highest I_p (10% **V1036** 90% **C4**). Third, it was shown by Moia et al.,[56] that hole transport between dye monolayer molecules in DSSCs accelerates recombination. By introducing insulating molecules in between, this process might be suppressed, thus giving higher V_{oc} values. Finally, small insulating **C4** molecules could reduce direct contact of the perovskite with ITO by filling potential gaps left by the larger

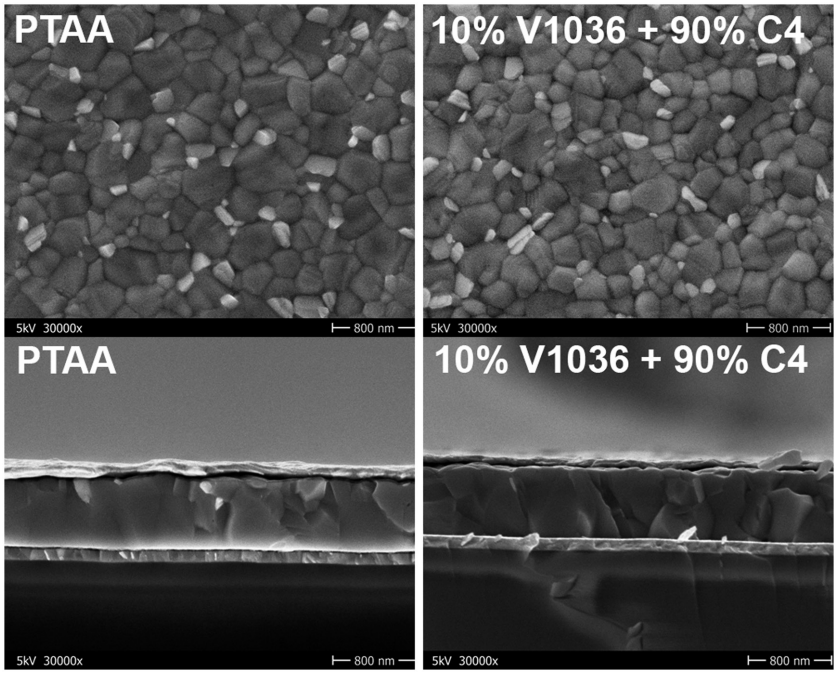

Figure 4. Top-view (top) and cross-sectional (bottom) SEM micrographs of perovskite film, deposited on PTAA and SAM-coated substrates.

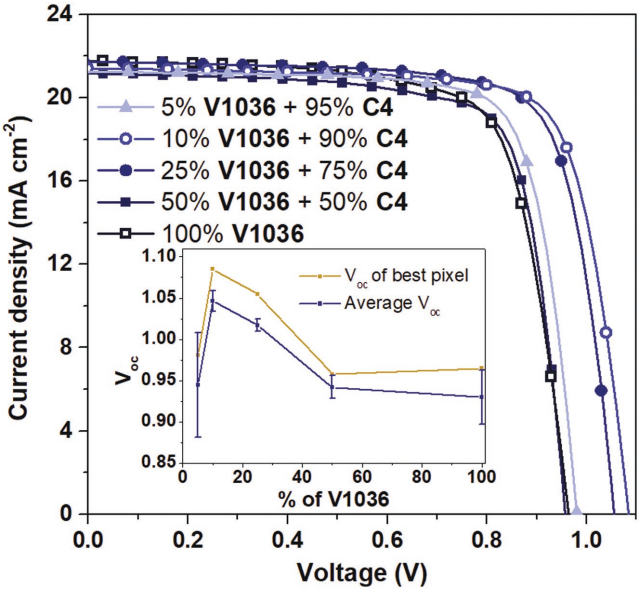

Figure 5. *J–V* characteristics of the best performing PSCs with mixed SA-HTMs. Inset: Average and best V_{oc} values obtained for different portions of **V1036** in the adsorption solution. Error bars are showing the standard error.

V1036 molecule, thus reducing interfacial recombination. This assumption is supported by the fact that HTM-free devices with bare ITO yield very low performance, mainly due to a strong reduction of V_{oc} (Figure S9, Supporting Information). Further reduction of the ratio from the 10/90 to 5% **V1036** and 95% **C4** SAM led to poor wetting by the perovskite solution and thus suboptimal film formation and device performance.

In principle, a variety of filler molecules can be used instead of **C4**. The length of the alkyl chain is known to have impact on the ordering of the SAM.[57] Thus, to study the influence of the length of aliphatic phosphonic acid on the overall device performance, we tested ethylphosphonic (**C2**), and *n*-hexylphosphonic (**C6**) acids as well. It was impossible to form a perovskite film on 10% **V1036** 90% **C6** SAM due to bad wetting. Devices with **C2** filler gave slightly lower performance compared to using **C4** as a filler molecule, due to a reduction in V_{oc} and J_{sc} (Figure S10, Supporting Information). Such behavior can be attributed to a reduction of electron-blocking properties upon reduction of the chain length of the filler molecule.[45]

To compare the SAM HTM performance to a well-established procedure in p–i–n PSC fabrication, solar cells with

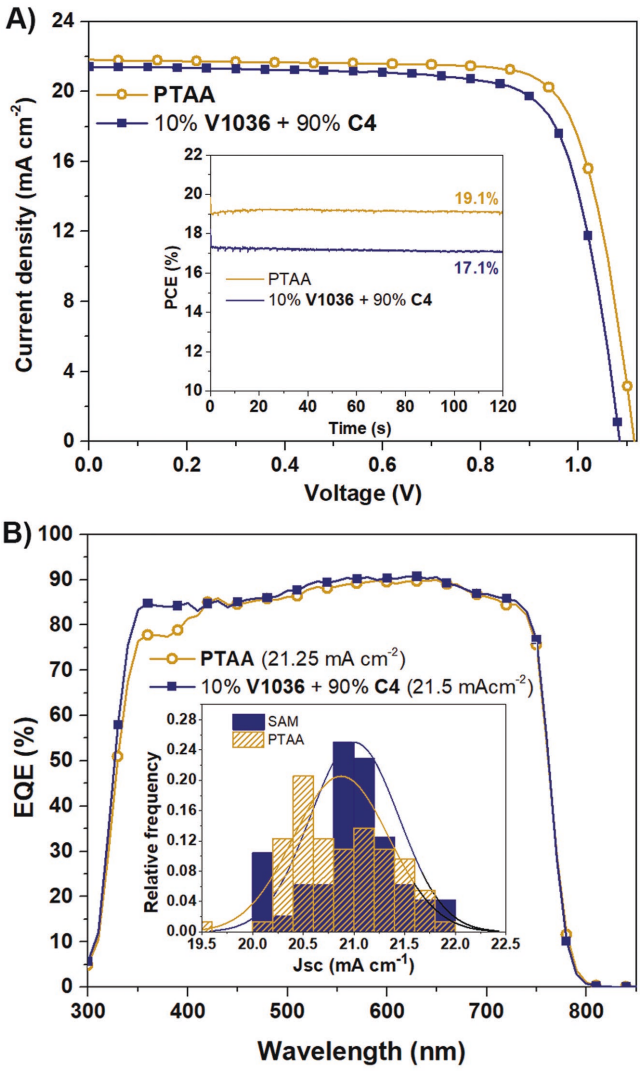

Figure 6. A) *J–V* characteristics of the best performing PSCs with 10% **V1036** 90% **C4** SAM and PTAA HTMs. The inset shows maximum power point (MPP) tracking of the best devices. B) EQE spectra of representative PTAA and mixed SA-HTM devices. The current values in parentheses are integrated J_{sc} values from the shown EQE spectra and the inset shows the statistical distribution of J_{sc} for both device types.

pristine PTAA[7,8] as a HTM were constructed. As can be seen from **Figure 6**A, best-performing SAM devices (10% **V1036** 90% **C4**) showed a reverse scan PCE of 17.8%, which is slightly

Table 2. Average PSC performance parameters[a] for different SA-HTM compositions.

SA-HTM	J_{sc}, [mA cm^{-2}]	V_{oc}, [V]	FF, [%]	PCE, [%]
5% **V1036** 95% **C4**	21.08 ± 0.27 (21.3)	0.95 ± 0.06 (0.98)	65.80 ± 2.11 (77.1)	13.05 ± 0.90 (16.1)
10% **V1036** 90% **C4**	21.19 ± 0.10 (21.4)	1.05 ± 0.01 (1.09)	70.87 ± 1.76 (76.5)	15.78 ± 0.55 (17.8)
25% **V1036** 75% **C4**	21.27 ± 0.19 (21.7)	1.02 ± 0.01 (1.06)	71.22 ± 1.56 (76.1)	15.43 ± 0.48 (17.5)
50% **V1036** 50% **C4**	20.91 ± 0.08 (21.2)	0.94 ± 0.01 (0.96)	67.17 ± 2.20 (76.0)	13.24 ± 0.51 (15.4)
100% **V1036**	21.22 ± 0.28 (21.8)	0.93 ± 0.03 (0.96)	66.48 ± 2.12 (72.8)	13.16 ± 0.83 (15.3)

[a]Data were extracted from *J–V* scans, including the standard errors and performance parameters of the best devices (in brackets). The statistics is based on 9–15 cells on different substrates for each SA-HTM composition.

Table 3. Average PSCs performance parameters[a] with 10% **V1036** 90% **C4** and PTAA HTMs.

HTM	J_{sc}, [mA cm^{-2}]	V_{oc}, [V]	FF, [%]	PCE, [%]
PTAA	20.87 ± 0.06 (21.8)	1.09 ± 0.002 (1.13)	77.82 ± 0.28 (81.0)	17.69 ± 0.08 (19.2)
10% **V1036** 90% **C4**	21.01 ± 0.06 (21.9)	1.00 ± 0.006 (1.09)	78.33 ± 0.46 (81.0)	16.46 ± 0.15 (17.8)

[a]Data, extracted from *J–V* scans, including the standard errors and the best performance parameters (in brackets). The statistics is based on 41 and 68 cells from several batches for 10% **V1036** 90% **C4** and PTAA respectively.

lower than that of the device with PTAA (19.2%) as the HTM. A stabilized efficiency from maximum power point tracking of 17.1% (Figure 6A, inset) and only a small difference between forward and reverse scans (Figure S11, Supporting Information) was measured at a high voltage sweep speed of 250 mV s^{-1}. Additionally, we performed a stability comparison. Both devices showed comparable shelf lifetime stability (Figure S16, Supporting Information), with ≈95% and ≈94% of the maximal performance for most stable PTAA and SAM-based devices respectively retained after 180 d of storage (N_2, dark, room temperature). Considering that we here compare a monolayer to a dense polymeric film, the insignificant difference in stability is a remarkable fact.

To have a conclusive comparison between PTAA and SAM device performance parameters, a statistical study was conducted. The results are presented in **Table 3** and Figures S12–S15 (Supporting Information). On average, J_{sc} values are ≈0.3 mA cm^{-2} higher for SAM devices. The reason behind the higher J_{sc} of the SA-HTM-based PSCs compared to PTAA-based PSCs can be directly elucidated by external quantum efficiency (EQE) measurements performed on full devices. Figure 6B shows that the gain in current stems from a higher EQE in the range from 350 to 400 nm. It can be attributed to the reduced absorption from the HTM, as already indicated by UV–vis absorption measurements (Figure 1B). J_{sc} values, obtained by integration of the EQE data, are in a close agreement with J_{sc} values obtained from *J–V* scans (within 1%–2%). FF values are on a high level for both device classes with a slight advantage for SAM devices, which is remarkable considering that only a single molecule layer yields sufficiently good selectivity, high charge extraction and shunt resistance needed for such high average FF values (close to 80%). Electrochemical impedance spectroscopy and dark *JV* measurements (Figures S22–S25, Supporting Information) further confirm the high charge extraction efficiencies of SAM-based devices. The PCE is mainly limited by V_{oc}, which will be the subject of further optimization and can be addressed by structurally more preferred hole transporting fragments.

3. Conclusion

In conclusion, a new promising HTM formation concept was presented in this work. For this purpose, a new molecule **V1036**, containing a hole transporting fragment and phosphonic acid group, was synthesized and used for the formation of self-assembled HTMs on ITO surfaces. The presence of **V1036** on the surface of the ITO was confirmed by FTIR, VSFG, contact angle, and I_p measurements. It was demonstrated that the addition of a small molecule, resulting in mixed SAMs, can have a positive impact on overall performance of SA-HTM-based devices, reaching a PCE of 17.8% for a 10% **V1036** 90% **C4** SAM-based device. The small amount of **V1036** needed for the mixed SAM formation can be attributed to its substantially higher surface affinity compared to **C4**. Due to the negligible parasitic absorption of SAMs, on average 0.3 mA cm^{-2} higher J_{sc} was measured compared to PTAA-based devices. Further studies will cope with generating an understanding of the charge extraction process by the monolayer. We believe that even higher efficiencies can be obtained upon further optimization by means of molecular and compositional engineering, e.g., by introducing active functional groups in the structure of the monolayer.

Supporting Information

Supporting Information is available from the Wiley Online Library or from the author.

Acknowledgements

A.M. and A.A.A. contributed equally to this work. A.M. acknowledges funding by the German Academic Exchange Service (DAAD). A.M., E.K., T.M., and V.G. acknowledge funding from the European Union's Horizon 2020 research and innovation programme under grant agreement No. 763977 of the PerTPV project. A.A.A., M.J., and S.A. acknowledge the German Federal Ministry of Education and Research (BMBF) for funding of the Young Investigator Group (Grant no. 03SF0540) within the project "Materialforschung für die Energiewende." The authors acknowledge E. Kamarauskas from Vilnius University for measurements of ionization potential and C. Klimm from Helmholtz-Center Berlin for SEM measurements. A.A.A. thanks Nga Phung for her help with impedance spectroscopy.

Conflict of Interest

The authors declare no conflict of interest.

Keywords

hole transporting materials, perovskite solar cells, self-assembled monolayers

Received: June 18, 2018
Revised: August 24, 2018
Published online:

[1] NREL efficiency chart. *NREL Effic. chart* **2018**.
[2] W. S. Yang, B.-W. Park, E. H. Jung, N. J. Jeon, Y. C. Kim, D. U. Lee, S. S. Shin, J. Seo, E. K. Kim, J. H. Noh, S. Il Seok, *Science* **2017**, *356*, 1376.

[3] L. Kegelmann, C. M. Wolff, C. Awino, F. Lang, E. L. Unger, L. Korte, T. Dittrich, D. Neher, B. Rech, S. Albrecht, *ACS Appl. Mater. Interfaces* **2017**, *9*, 17245.
[4] S.-H. Turren-Cruz, M. Saliba, M. T. Mayer, H. Juárez-Santiesteban, X. Mathew, L. Nienhaus, W. Tress, M. P. Erodici, M.-J. Sher, M. G. Bawendi, M. Grätzel, A. Abate, A. Hagfeldt, J.-P. Correa-Baena, *Energy Environ. Sci.* **2018**, *11*, 78.
[5] E. H. Anaraki, A. Kermanpur, L. Steier, K. Domanski, T. Matsui, W. Tress, M. Saliba, A. Abate, M. Grätzel, A. Hagfeldt, J.-P. Correa-Baena, *Energy Environ. Sci.* **2016**, *9*, 3128.
[6] D. Yang, X. Zhou, R. Yang, Z. Yang, W. Yu, X. Wang, C. Li, S. (Frank) Liu, R. P. H. Chang, *Energy Environ. Sci.* **2016**, *9*, 3071.
[7] J. Zhao, X. Zheng, Y. Deng, T. Li, Y. Shao, A. Gruverman, J. Shield, J. Huang, *Energy Environ. Sci.* **2016**, *9*, 3650.
[8] M. Stolterfoht, C. M. Wolff, Y. Amir, A. Paulke, L. Perdigón-Toro, P. Caprioglio, D. Neher, *Energy Environ. Sci.* **2017**, *10*, 1530.
[9] J. H. Heo, H. J. Han, D. Kim, T. K. Ahn, S. H. Im, *Energy Environ. Sci.* **2015**, *8*, 1602.
[10] D. Bryant, S. Wheeler, B. C. O'Regan, T. Watson, P. R. F. Barnes, D. Worsley, J. Durrant, *J. Phys. Chem. Lett.* **2015**, *6*, 3190.
[11] P. Calado, A. M. Telford, D. Bryant, X. Li, J. Nelson, B. C. O'Regan, P. R. F. Barnes, *Nat. Commun.* **2016**, *7*, 13831.
[12] W. Zhou, Z. Wen, P. Gao, *Adv. Energy Mater.* **2018**, *8*, 1702512.
[13] K. Jäger, L. Korte, B. Rech, S. Albrecht, *Opt. Express* **2017**, *25*, A473.
[14] K. A. Bush, A. F. Palmstrom, Z. J. Yu, M. Boccard, R. Cheacharoen, J. P. Mailoa, D. P. McMeekin, R. L. Z. Hoye, C. D. Bailie, T. Leijtens, I. M. Peters, M. C. Minichetti, N. Rolston, R. Prasanna, S. Sofia, D. Harwood, W. Ma, F. Moghadam, H. J. Snaith, T. Buonassisi, Z. C. Holman, S. F. Bent, M. D. McGehee, *Nat. Energy* **2017**, *2*, 17009.
[15] C. Bi, Q. Wang, Y. Shao, Y. Yuan, Z. Xiao, J. Huang, *Nat. Commun.* **2015**, *6*, 7747.
[16] O. Malinkiewicz, A. Yella, Y. H. Lee, G. M. Espallargas, M. Graetzel, M. K. Nazeeruddin, H. J. Bolink, *Nat. Photonics* **2014**, *8*, 128.
[17] J. T.-W. Wang, Z. Wang, S. Pathak, W. Zhang, D. W. deQuilettes, F. Wisnivesky-Rocca-Rivarola, J. Huang, P. K. Nayak, J. B. Patel, H. A. Mohd Yusof, Y. Vaynzof, R. Zhu, I. Ramirez, J. Zhang, C. Ducati, C. Grovenor, M. B. Johnston, D. S. Ginger, R. J. Nicholas, H. J. Snaith, *Energy Environ. Sci.* **2016**, *9*, 2892.
[18] P. Docampo, J. M. Ball, M. Darwich, G. E. Eperon, H. J. Snaith, *Nat. Commun.* **2013**, *4*, 2761.
[19] C.-G. Wu, C.-H. Chiang, Z.-L. Tseng, M. K. Nazeeruddin, A. Hagfeldt, M. Grätzel, *Energy Environ. Sci.* **2015**, *8*, 2725.
[20] W. Chen, Y. Wu, Y. Yue, J. Liu, W. Zhang, X. Yang, H. Chen, E. Bi, I. Ashraful, M. Grätzel, L. Han, *Science* **2015**, *350*, 944.
[21] C. Momblona, L. Gil-Escrig, E. Bandiello, E. M. Hutter, M. Sessolo, K. Lederer, J. Blochwitz-Nimoth, H. J. Bolink, *Energy Environ. Sci.* **2016**, *9*, 3456.
[22] P. J. Hotchkiss, S. C. Jones, S. A. Paniagua, A. Sharma, B. Kippelen, N. R. Armstrong, S. R. Marder, *Acc. Chem. Res.* **2012**, *45*, 337.
[23] S. A. Paniagua, A. J. Giordano, O. L. Smith, S. Barlow, H. Li, N. R. Armstrong, J. E. Pemberton, J. L. Brédas, D. Ginger, S. R. Marder, *Chem. Rev.* **2016**, *116*, 7117.
[24] P. B. Paramonov, S. A. Paniagua, P. J. Hotchkiss, S. C. Jones, N. R. Armstrong, S. R. Marder, J.-L. Brédas, *Chem. Mater.* **2008**, *20*, 5131.
[25] S. A. Paniagua, P. J. Hotchkiss, S. C. Jones, S. R. Marder, A. Mudalige, F. S. Marrikar, J. E. Pemberton, N. R. Armstrong, *J. Phys. Chem. C* **2008**, *112*, 7809.
[26] S. A. Paniagua, E. L. Li, S. R. Marder, *Phys. Chem. Chem. Phys.* **2014**, *16*, 2874.
[27] P. Wang, C. Klein, J.-E. Moser, R. Humphry-Baker, N.-L. Cevey-Ha, R. Charvet, P. Comte, A. Shaik, M. Zakeeruddin, M. Grätzel, *J. Phys. Chem. B* **2004**, *108*, 17553.
[28] R. Cinnsealach, G. Boschloo, S. Nagaraja Rao, D. Fitzmaurice, *Sol. Energy Mater. Sol. Cells* **1999**, *57*, 107.
[29] N. Vlachopoulos, J. Nissfolk, M. Möller, A. Briançon, D. Corr, C. Grave, N. Leyland, R. Mesmer, F. Pichot, M. Ryan, G. Boschloo, A. Hagfeldt, *Electrochim. Acta* **2008**, *53*, 4065.
[30] J. A. Bardecker, H. Ma, T. Kim, F. Huang, M. S. Liu, Y.-J. Cheng, G. Ting, A. K.-Y. Jen, *Adv. Funct. Mater.* **2008**, *18*, 3964.
[31] B. Gothe, T. de Roo, J. Will, T. Unruh, S. Mecking, M. Halik, *Nanoscale* **2017**, *9*, 18584.
[32] M. Novak, A. Ebel, T. Meyer-Friedrichsen, A. Jedaa, B. F. Vieweg, G. Yang, K. Voitchovsky, F. Stellacci, E. Spiecker, A. Hirsch, M. Halik, *Nano Lett.* **2011**, *11*, 156.
[33] Y. Hou, S. Scheiner, X. Tang, N. Gasparini, M. Richter, N. Li, P. Schweizer, S. Chen, H. Chen, C. O. R. Quiroz, X. Du, G. J. Matt, A. Osvet, E. Spiecker, R. H. Fink, A. Hirsch, M. Halik, C. J. Brabec, *Adv. Mater. Interfaces* **2017**, *4*, 1700007.
[34] Y. Hou, X. Du, S. Scheiner, D. P. McMeekin, Z. Wang, N. Li, M. S. Killian, H. Chen, M. Richter, I. Levchuk, N. Schrenker, E. Spiecker, T. Stubhan, N. A. Luechinger, A. Hirsch, P. Schmuki, H.-P. Steinrück, R. H. Fink, M. Halik, H. J. Snaith, C. J. Brabec, *Science* **2017**, *358*, 1192.
[35] P. Topolovsek, F. Lamberti, T. Gatti, A. Cito, J. M. Ball, E. Menna, C. Gadermaier, A. Petrozza, *J. Mater. Chem. A* **2017**, *5*, 11882.
[36] X. Lin, A. N. Jumabekov, N. N. Lal, A. R. Pascoe, D. E. Gómez, N. W. Duffy, A. S. R. Chesman, K. Sears, M. Fournier, Y. Zhang, Q. Bao, Y.-B. Cheng, L. Spiccia, U. Bach, *Nat. Commun.* **2017**, *8*, 613.
[37] A. Magomedov, A. Al-Ashouri, E. Kasparavičius, S. Albrecht, V. Getautis, M. Jost, T. Malinauskas, L. Kegelmann, E. Köhnen, Hole Transporting Self-Assembled Monolayer for Perovskite Solar Cells, *Patent pending DE 10 2018 115 379.1* **2018**.
[38] M. Saliba, T. Matsui, J.-Y. Seo, K. Domanski, J.-P. Correa-Baena, M. K. Nazeeruddin, S. M. Zakeeruddin, W. Tress, A. Abate, A. Hagfeldt, M. Grätzel, *Energy Environ. Sci.* **2016**, *9*, 1989.
[39] A. Magomedov, S. Paek, P. Gratia, E. Kasparavicius, M. Daskeviciene, E. Kamarauskas, A. Gruodis, V. Jankauskas, K. Kantminiene, K. T. Cho, K. Rakstys, T. Malinauskas, V. Getautis, M. K. Nazeeruddin, *Adv. Funct. Mater.* **2018**, *28*, 1704351.
[40] P. Gratia, A. Magomedov, T. Malinauskas, M. Daskeviciene, A. Abate, S. Ahmad, M. Grätzel, V. Getautis, M. K. Nazeeruddin, *Angew. Chem., Int. Ed.* **2015**, *54*, 11409.
[41] S. Do Sung, M. S. Kang, I. T. Choi, H. M. Kim, H. Kim, M. Hong, H. K. Kim, W. I. Lee, *Chem. Commun.* **2014**, *50*, 14161.
[42] A. Khassanov, H.-G. Steinrück, T. Schmaltz, A. Magerl, M. Halik, *Acc. Chem. Res.* **2015**, *48*, 1901.
[43] A. Rumpel, M. Novak, J. Walter, B. Braunschweig, M. Halik, W. Peukert, *Langmuir* **2011**, *27*, 15016.
[44] K. Jo, H. Yang, *J. Electroanal. Chem.* **2014**, *712*, 8.
[45] N. Metoki, L. Liu, E. Beilis, N. Eliaz, D. Mandler, *Langmuir* **2014**, *30*, 6791.
[46] S. Schneider, M. Füser, M. Bolte, A. Terfort, *Electrochim. Acta* **2017**, *246*, 853.
[47] O. I. Negru, M. Grigoras, *J. Polym. Res.* **2015**, *22*, 637.
[48] A. Botta, S. Pragliola, V. Venditto, A. Rubino, S. Aprano, A. De Girolamo Del Mauro, M. Grazia Maglione, C. Minarini, *Polym. Compos.* **2015**, *36*, 1110.
[49] O. Abbas, G. Compère, Y. Larondelle, D. Pompeu, H. Rogez, V. Baeten, *Vib. Spectrosc.* **2017**, *92*, 111.
[50] S. Ye, M. Osawa, *Chem. Lett.* **2009**, *38*, 386.

[51] Y. R. Shen, *Nature* **1989**, *337*, 519.
[52] Z. Tang, S. Uchida, T. Bessho, T. Kinoshita, H. Wang, F. Awai, R. Jono, M. M. Maitani, J. Nakazaki, T. Kubo, H. Segawa, *Nano Energy* **2018**, *45*, 184.
[53] C. Wang, C. Zhang, S. Wang, G. Liu, H. Xia, S. Tong, J. He, D. Niu, C. Zhou, K. Ding, Y. Gao, J. Yang, *Sol. RRL* **2018**, *2*, 1700209.
[54] M. Deepa, M. Salado, L. Calio, S. Kazim, S. M. Shivaprasad, S. Ahmad, *Phys. Chem. Chem. Phys.* **2017**, *19*, 4069.
[55] T. Matsui, I. Petrikyte, T. Malinauskas, K. Domanski, M. Daskeviciene, M. Steponaitis, P. Gratia, W. Tress, J.-P. Correa-Baena, A. Abate, A. Hagfeldt, M. Grätzel, M. K. Nazeeruddin, V. Getautis, M. Saliba, *ChemSusChem* **2016**, *9*, 2567.
[56] D. Moia, A. Szumska, V. Vaissier, M. Planells, N. Robertson, B. C. O'Regan, J. Nelson, P. R. F. Barnes, *J. Am. Chem. Soc.* **2016**, *138*, 13197.
[57] M. D. Losego, J. T. Guske, A. Efremenko, J.-P. Maria, S. Franzen, *Langmuir* **2011**, *27*, 11883.

ADVANCED ENERGY MATERIALS

Supporting Information

for *Adv. Energy Mater.,* DOI: 10.1002/aenm.201801892

Self-Assembled Hole Transporting Monolayer for Highly Efficient Perovskite Solar Cells

Artiom Magomedov, Amran Al-Ashouri, Ernestas Kasparavičiius, Simona Strazdaite, Gediminas Niaura, Marko Jošt, Tadas Malinauskas, Steve Albrecht, and Vytautas Getautis**

Supporting Information

Self-Assembled Hole Transporting Monolayer for Perovskite Solar Cells

Artiom Magomedov, Amran Al-Ashouri, Ernestas Kasparavičius, Simona Strazdaite, Gediminas Niaura, Marko Jošt, Tadas Malinauskas, Steve Albrecht and Vytautas Getautis**

General methods

Chemicals, unless stated otherwise, were purchased from Sigma-Aldrich and TCI Europe and used as received without further purification. The ^{1}H and ^{13}C NMR spectra were taken on Bruker Avance III (400 MHz) spectrometer at RT. All the data are given as chemical shifts in δ (ppm). The course of the reactions products was monitored by TLC on ALUGRAM SIL G/UV254 plates and developed with UV light. Silica gel (grade 9385, 230–400 mesh, 60 Å, Aldrich) was used for column chromatography. Elemental analysis was performed with an Exeter Analytical CE-440 elemental analyser, Model 440 C/H/N/. Electrothermal MEL-TEMP capillary melting point apparatus was used for determination of melting points. UV/Vis spectra were recorded on a PerkinElmer Lambda 35 spectrometer.

Formation of the SAMs

V1036, as well as mixed **V1036** and *n*-butylphosphonic acid (**C4**) SAMs were formed by immersing UV-ozone treated ITO substrates into 1 mM solution of phosphonic acid molecules, dissolved in isopropanol, for 20 h, followed by annealing at 100 °C for 1 h and subsequent washing with isopropanol and chlorobenzene. To exclude any possible negative impact of atmospheric oxygen all procedures were done in a nitrogen-filled glovebox. Used notation: e.g. 10% **V1036** 90% **C4** SAM means that monolayer was formed using a solution

containing 0.1 mM of **V1036** and 0.9 mM of **C4**. Sometimes a shortened notation was used, showing only percentage p of **V1036** in the solution (implying a percentage of 1-p for C4).

TGA

Thermogravimetric analysis (TGA) was performed on a Q50 thermogravimetric analyser (TA Instruments) at a scan rate of 10 K min^{-1} under nitrogen atmosphere.

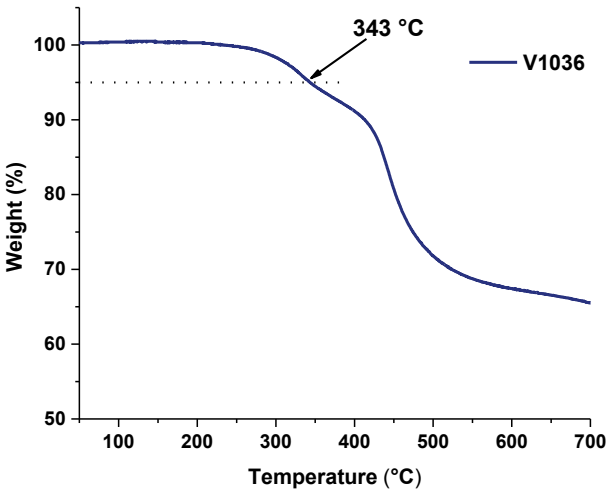

Figure S1. TGA heating curve **V1036**. Heating rate 10°C min^{-1}.

FTIR measurements

For the FTIR and VSFG measurements, 30 nm ITO was deposited on 625 µm thick Silicon substrates with DC magnetron sputter deposition in a Roth & Rau sputter tool at room temperature. SAMs were formed on these substrates according to the above mentioned procedure.

FTIR spectra of monolayers were recorded in transmission mode by using FTIR spectrometer Vertex 80v (Bruker, Inc., Germany), equipped with a liquid-nitrogen cooled MCT narrow band detector. Spectra were acquired from 512 interferogram scans with 4 cm^{-1} resolution; final spectrum was obtained by averaging two spectra. A blank Si substrate with 30 nm thick

ITO layer was used as a reference sample. The sample chamber and the spectrometer were evacuated during the measurements. Spectra were corrected by polynomial function background subtraction. No smoothing procedures were applied to the experimental data. Parameters of the bands were determined by fitting the experimental contour to Gaussian-Lorentzian shape components using GRAMS/AI 8.0 (Thermo Electron Corp.) software. The infrared spectrum of bulk **V1036** sample was recorded in transmission mode on an ALPHA FTIR spectrometer (Bruker, Inc., Germany), equipped with a room temperature detector DLATGS. The spectral resolution was set at 4 cm^{-1}. The spectrum was acquired from 124 interferogram scans. The sample solution was dispersed in a KBr tablet.

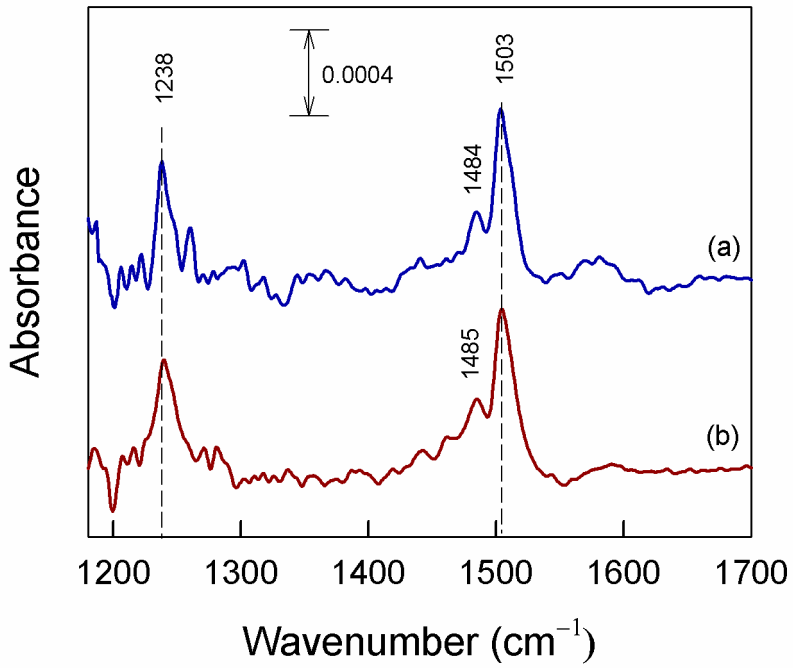

Figure S2. FTIR absorbance spectra of **V1036** monolayers prepared from (a) 0.1 mM and (b) 1 mM adsorption solutions.

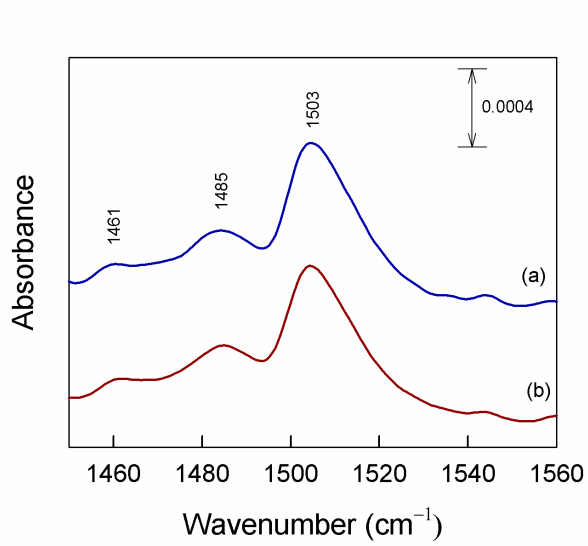

Figure S3. FTIR absorbance spectra of 100% **V1036** monolayer in the spectral range of 1503 cm^{-1} band recorded (a) initially and (b) after 25 days.

Vibrational Sum frequency generation (VSFG) measurements

VSFG spectra were recorded using a commercially available VSFG system (Ekspla PL2143A20). The method was described in detail in previous work.[1] In short, a Nd:YAG laser generates pulses at 1064 nm with a pulse length of ~28 ps and 20 kHz repetition rate. Part of the laser output is used to pump optical parametric generator (EKSPLA PG401VIR/DFG) to produce infrared pulses (ω_{IR}), which can be tuned in the range between 1000 cm^{-1} and 4000 cm^{-1} with typical energies of 60 – 200 μJ, respectively. The second harmonic of the laser output (532 nm) is used as a visible beam (ω_{VIS}) for sum-frequency generation (ω_{SF}). Sum-frequency is generated when infrared and visible pulses overlap in time and space on the sample surface. All spectra in this work were recorded with a polarization combination ssp (s – SFG, s – VIS, p - IR). The intensity of the visible beam was attenuated to avoid damage of the samples (~30 μJ). The generated sum-frequency light is filtered with a monochromator and detected with a photomultiplier tube (PMT).

The measured VSFG intensity is proportional to

$$I_{VSFG} \propto \left| A_{NR} e^{i\phi} + \sum_q \frac{A_{Rq}}{\omega_{IR} - \omega_q + i\Gamma_q} \right|^2, \quad \text{(S1)}$$

where A_{NR} is the non-resonant amplitude, A_{Rq} is the resonant amplitude of the q-th vibration, ϕ is the phase between resonant and non-resonant contributions. ω_q and Γ_q are frequency and width of the q-th vibration, respectively.

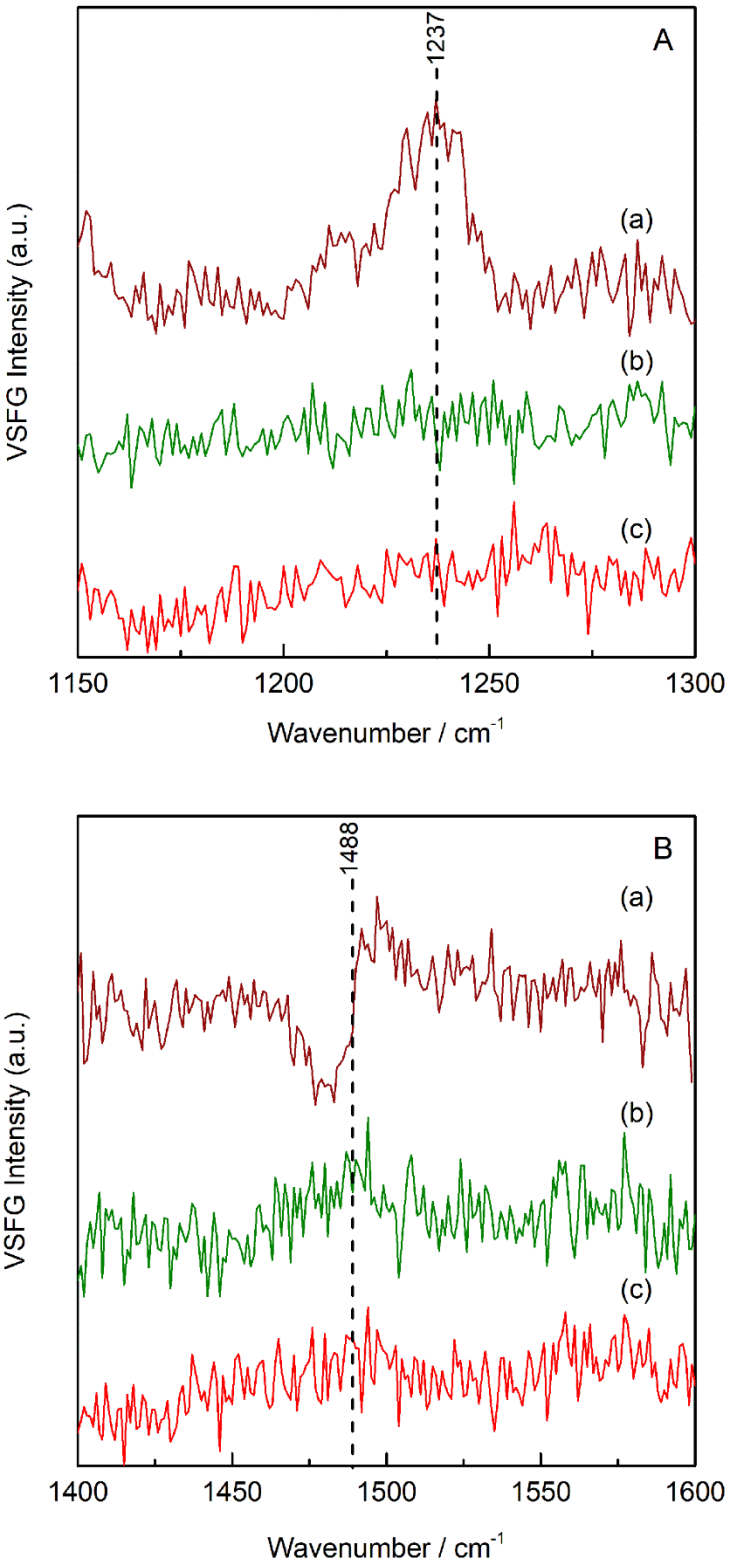

Figure S4. A) VSFG spectra of monolayers on Si/ITO substrate prepared from (a) 1 mM solution of **V1036**, (b) 1 mM of mixed solution **V1036**:**C4** (1:9), and (c) 1 mM solution of **C4** in the spectral region 1150 – 1300 cm^{-1} and B) in the spectral region 1400 – 1600 cm^{-1}.

Contact angle

Contact angle measurements were performed with a Kruss Drop Shape Analysis System DSA25.

Table S1. Values of the equilibrium contact angles for various substrates.

Substrate	Contact angle, degrees
PTAA	42.59
ITO	50.02
100% **C4**	60.47
5% **V1036** 95% **C4**	51.43
10% **V1036** 90% **C4**	46.75
25% **V1036** 75% **C4**	34.1
50% **V1036** 50% **C4**	27.84
100% **V1036**	26.28

Ionization potential measurements

The solid state ionization potential (I_p) of the **V1036**, PTAA on ITO, and SA-HTMs on ITO was measured by the electron photoemission in air method.[2-4] The sample for the ionization potential measurement of bulk **V1036** was prepared by dissolving the material in THF and coating it on an Al plate, pre-coated with a ~0.5 μm thick methylmethacrylate and methacrylic acid copolymer adhesive layer. The thickness of the layer was ~0.5-1 μm. PTAA layer on ITO was formed by spin-coating, in a similar manner to the procedure used for the PSC formation. SA-HTMs were formed by the above mentioned procedure.

Usually, photoemission experiments are carried out in vacuum and high vacuum is one of the main requirements for these measurements. If the vacuum is not high enough the sample surface oxidation and gas adsorption are influencing the measurement results. In our case, however, the organic materials investigated are stable enough towards oxygen, so that the measurements could be carried out in air. The samples were illuminated with monochromatic

light from a quartz monochromator with a deuterium lamp. The power of the incident light beam was $(2\text{-}5)\cdot10^{-8}$ W. A negative voltage of –300 V was supplied to the sample substrate with respect to the counter electrode, which contained a 4.5×15 mm^2 slit for illumination and was placed at 8 mm distance from the sample surface. The counter-electrode was connected to the input of the BK2-16 type electrometer, working in the open input regime, for the photocurrent measurement. The 10^{-15} – 10^{-12} A strong photocurrent was flowing in the circuit under illumination. The photocurrent I is strongly dependent on the incident light photon energy hν. The $I^{0.5}=f(h\nu)$ dependence was plotted. Usually the dependence of the photocurrent on incident light quanta energy is well described by a linear relationship between $I^{0.5}$ and $h\nu$ near the threshold. The linear part of this dependence was extrapolated to the hν axis and I_p value was determined as the photon energy at the interception point.

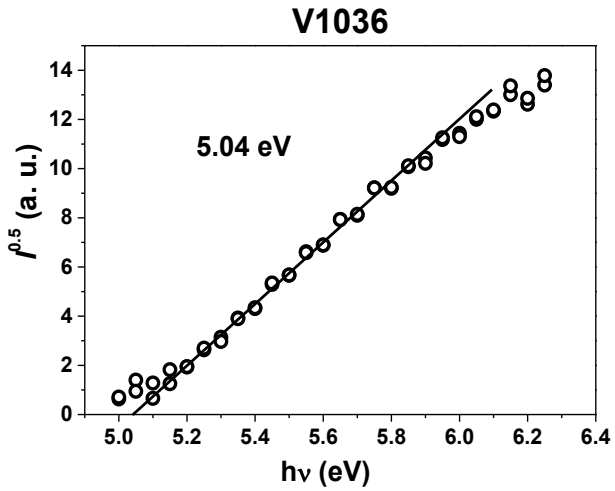

Figure S5. Photoemission in air spectra of the bulk **V1036**.

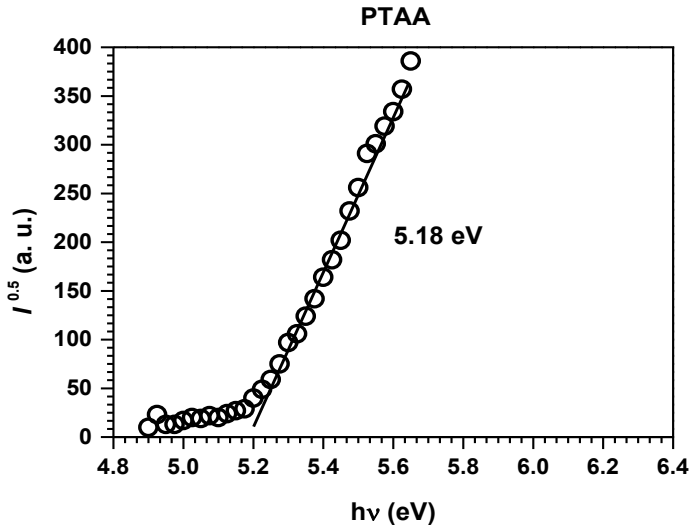

Figure S6. Photoemission in air spectra of the PTAA film on ITO.

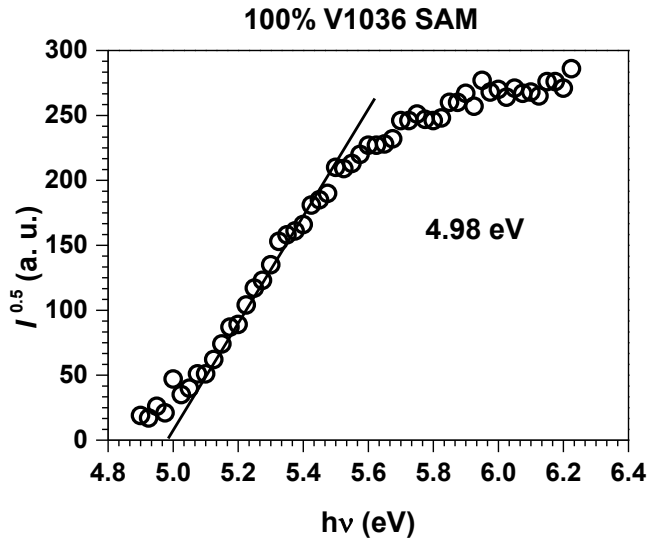

Figure S7. Photoemission in air spectra of the 100% **V1036** SAM.

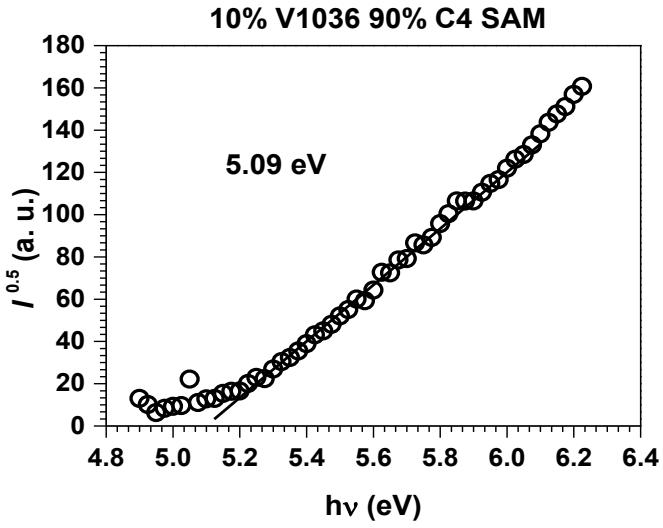

Figure S8. Photoemission in air spectra of the 10% **V1036** 90% **C4** SAM.

Table S2. I_p values for various substrates.

Substrate	5% **V1036** 95% **C4**	10% **V1036** 90% **C4**	25% **V1036** 75% **C4**	50% **V1036** 50% **C4**	100% **V1036**
I_p, eV	5.01	5.09	5.06	5.07	4.98

Device fabrication

Patterned indium tin oxide (ITO) glass substrates (25x25 mm, 15 Ω sq^{-1}, patterned by Automatic Research GmbH) were cleaned sequentially for 15 min with Mucasol 2% solution in water (Schülke), Acetone, and Isopropanol in an ultrasonic bath. After that, directly before HTM deposition, substrates were treated in an UV-ozone cleaner for 15 min.

All subsequent procedures were done in a nitrogen-filled glovebox.

SA-HTMs were deposited as specified above.

For the PTAA control devices, PTAA (Sigma Aldrich) was spin-coated from a 2 mg ml^{-1} solution in anhydrous toluene at 4000 rpm (5 s acceleration) for 30 s and annealed on a hot plate at 100°C for 10 min.

Triple-cation $Cs_{0.05}(MA_{0.17}FA_{0.83})_{0.95}Pb(I_{0.83}Br_{0.17})_3$ perovskite film was formed according to a slightly modified previously reported procedure.[5] First, $PbBr_2$ and PbI_2 were dissolved in a

mixture of anhydrous DMF:DMSO (4:1 volume ratio), to a nominal concentration of 1.5 M, by shaking overnight at 60°C. Next, the $PbBr_2$ and PbI_2 stock solutions were added to MABr and FAI powders respectively, to obtain $MAPbBr_3$ and $FAPbI_3$ solutions with a final concentration of 1.24 M. The molar ratio between lead and the respective cations was 1.09:1.00 (9% lead excess) for both solutions. $MAPbBr_3$ and $FAPbI_3$ solutions were then mixed in a 1:5 volume ratio. Finally, the Cesium cation was added from a 1.5 M CsI solution in DMSO in a 5:95 volume ratio. This final Perovskite solution was slightly diluted by adding DMF:DMSO (4:1) in a 5:95 volume ratio for substrates with suboptimal wettability properties. The Perovskite solution was deposited on top of the HTM layer by spin-coating using the following program: 4000 rpm (5 s acceleration) for 35 s (total time – 40 s). After 25 s, 500 µl of Ethyl Acetate was poured on the spinning substrate. After the spin-coating program, the perovskite-coated sample is annealed at 100°C for 60 min on a hotplate.

On top of the perovskite, 23 nm of C60 and 8 nm of BCP were deposited by thermal evaporation (Mbraun ProVap 3G) with evaporation rates of ca. 0.1-0.3 Å/s at a base presurre of under 1E-6 mbar. Finally, 80-100 nm of Cu was evaporated at a rate of 0.3-1 Å/s to complete the device structure. The active area is defined by the overlap of ITO and the metal electrode, which is 0.16 cm^2.

Device characterization

Current-voltage characteristics under 1 sun equivalent illumination were recorded using an Oriel LCS-100 class ABB solar simulator in a N_2-filled glovebox, calibrated with a Silicon reference cell from Fraunhofer ISE. Cross-checks were performed by measuring some samples in a Wavelabs Sinus-70 LED class AAA solar simulator in air to ensure correct current values. To further reduce possible overestimations, the precise electrode area was determined by microscope imaging using a Nikon Eclipse optical microscope. The average

short-circuit mismatch between integrated external quantum efficiency (EQE) values and values from J-V scans is 1-2%. J-V scans were performed with a Keithley 2400 SMU, controlled by a measurement control program written in LabView. The voltage values are swept in 20 mV steps with a integration time of 40 ms per point and settling time of 40 mV after voltage application, corresponding to a scan speed of 250 mV/s. This fast scan speed is chosen to emphasize possible current-voltage hysteresis. Forward and reverse scan are swept subsequently without interruption.

EQE spectra were recorded with an Oriel Instruments QEPVSI-b system with a Newport 300 W xenon arc lamp, controlled by TracQ-Basic software. The white light is split into monochromatic light by a Newport Cornerstone 260 monochromator and chopped at a frequency of 78 Hz before being conducted to the PSC surface via optical fibers. The system is calibrated using a Si reference cell with known spectral response before every measurement and cross-checked with an EQE system at the facilities of the Competence Centre Thin-Film- and Nanotechnology for Photo- voltaics Berlin (PVcomB). The electical response of the device under test is measured with a Stanford Research SR830 Lock-In amplifier and evaluated in TracQ.

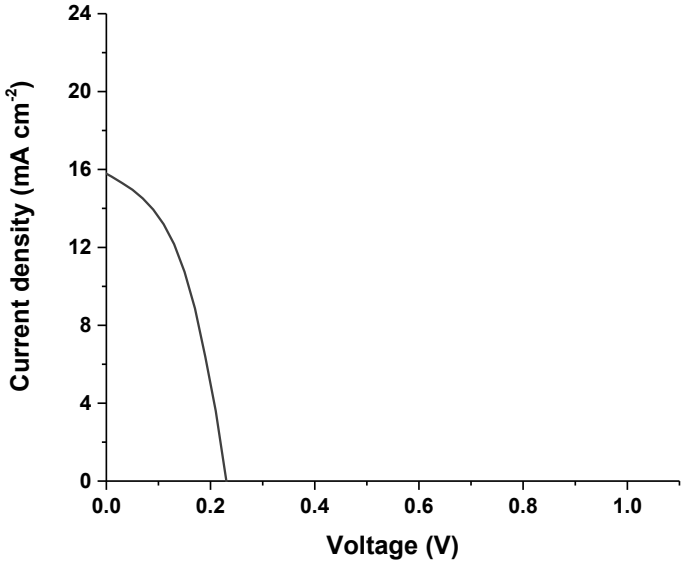

Figure S9. Representative J-V characteristics of HTM-free PSCs (Perovskite directly on ITO). J_{sc}=16.45 mA·cm^{-2}; V_{oc}=0.25 V; *FF*=50.15%; PCE=2.1%.

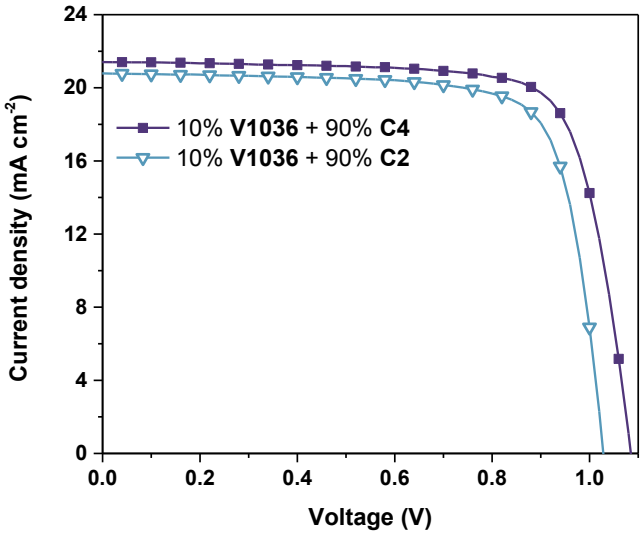

Figure S10. J-V characteristics of the PSCs with **C4** and **C2** aliphatic phosphonic acids.

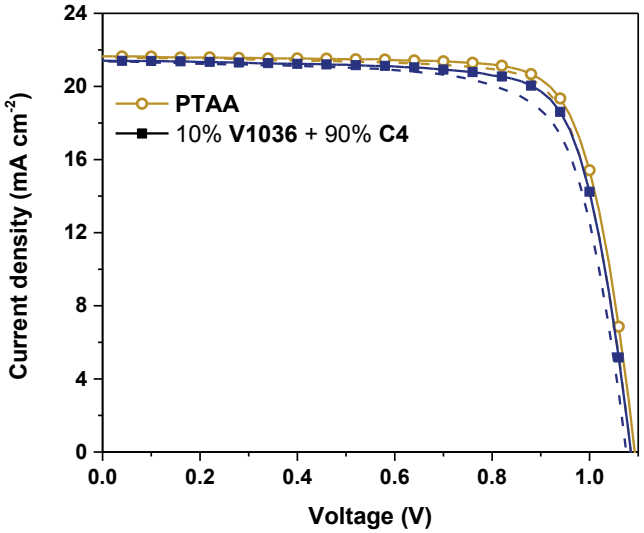

Figure S11. J-V characteristics from forward scan and reverse scan of the best performing PSCs with PTAA and 10% **V1036** 90% **C4** SAM HTMs.

Statistical distribution

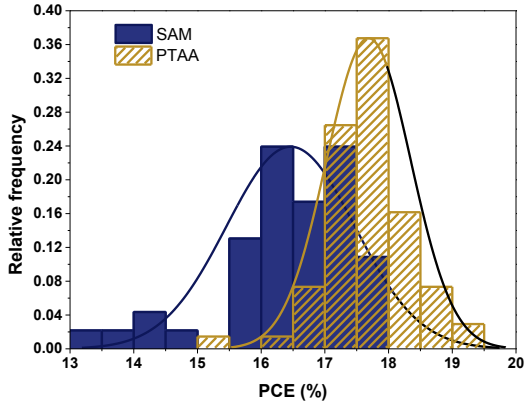

Figure S12. Histogram of PCEs of 41 and 68 cells from several batches for 10% **V1036** 90% **C4** and PTAA respectively.

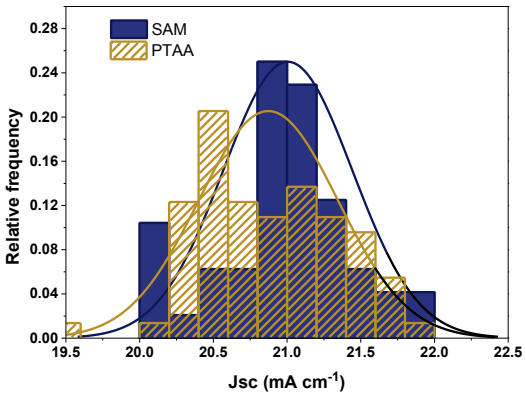

Figure S13. Histogram of J_{sc} of 41 and 68 cells from several batches for 10% **V1036** 90% **C4** and PTAA respectively.

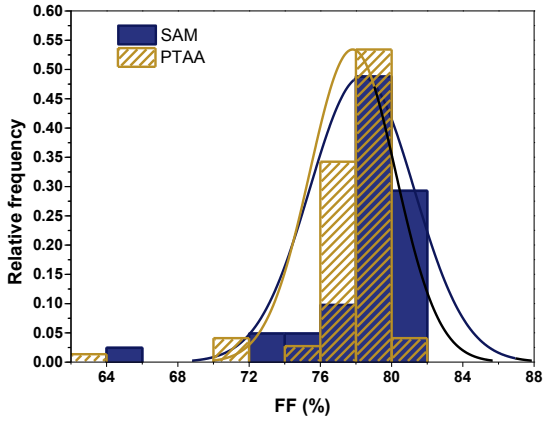

Figure S14. Histogram of *FF* of 41 and 68 cells from several batches for 10% **V1036** 90% **C4** and PTAA respectively.

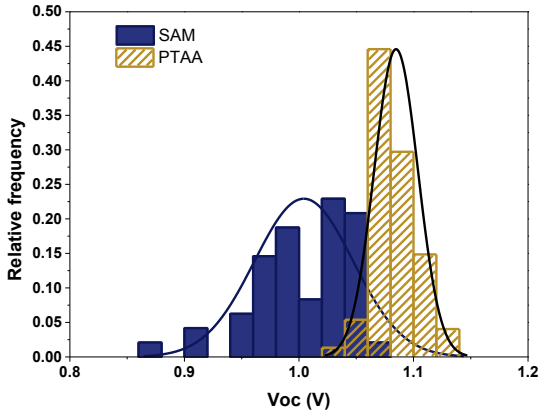

Figure S15. Histogram of V_{oc} of 41 and 68 cells from several batches for 10% **V1036** 90% **C4** and PTAA respectively.

Stability measurement

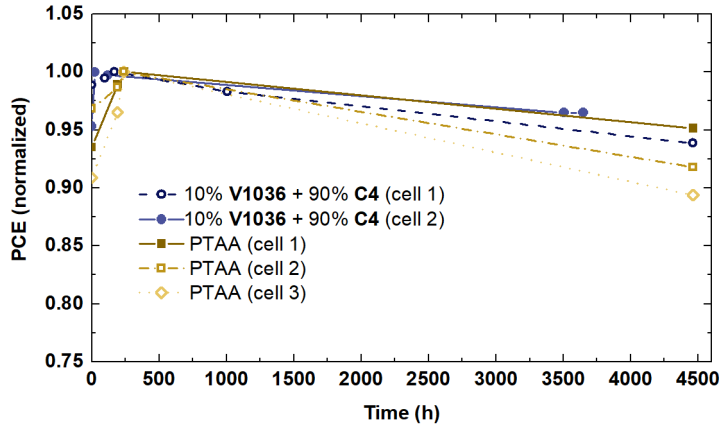

Figure S16. Shelf lifetime of representative PTAA (cell 1 max. PCE=18.5%) and 10% **V1036** 90% **C4** SAM (cell 1 max. PCE=17.8%) based devices. The devices were kept in a nitrogen-filled glovebox, dark, 20-26 °C. Within the measurement uncertainty and cell-to-cell spread, the stability of cells with either PTAA or SAM HTM is very similar.

Optical simulation of V1036 absorption

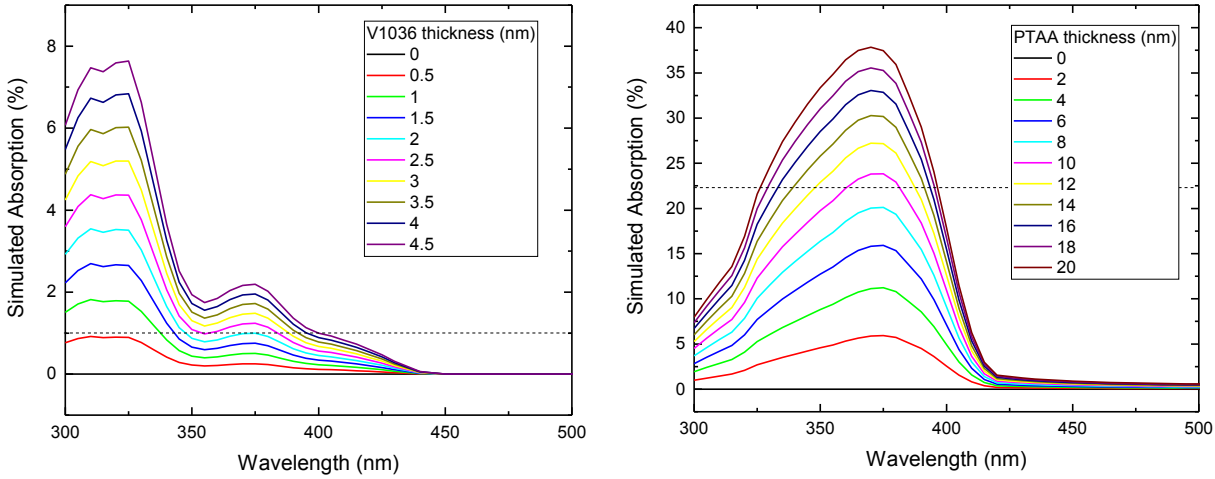

Figure S17. Coherent simulation of the absorption for the monolayer material and for PTAA in a stack of Air/Glass(1mm)/ITO(12nm)/HTM/Air with light entering from the glass side. The dashed line in the left plot shows the highest estimated absorption value that could be extracted from the UV/vis measurement shown in the main text. A layer thickness of 2 nm would be needed to detect 1% absorption. The dashed line in the right plot shows the measured absorption by the PTAA film. The concluded 8-10 nm PTAA thickness is in close agreement with other reported values for the used PTAA spin-coating procedure.[6]

The optical simulation was performed with GenPro4[7] developed at Delft University of Technology. k data for **V1036** was calculated from the molar extinction coefficient (ε) measurement shown in **Figure S17**, using a surface packing density of 0.7 nm² per molecule and $k = \frac{\alpha \cdot \lambda}{4\pi}$, where lambda is the wavelength and alpha the absorption coefficient (molar extinction coefficient multiplied with the molar SAM concentration on the surface). Since the measured absorption in **Figure 1B** is zero within the measurement uncertainty of 1%, we can conclude that if there is any absorption by the **V1036** layer, the layer thickness must be between 0 and 2 nm thick. Next to the previous knowledge in literature that such molecules as used here form monolayers on oxides, and with the aspects that we wash the SAM substrates with solvents after annealing, observe a controllable change in contact angle and measure a control of ionization potential, this simulation result together with the absorption measurement further confirms the presence of a single monolayer.

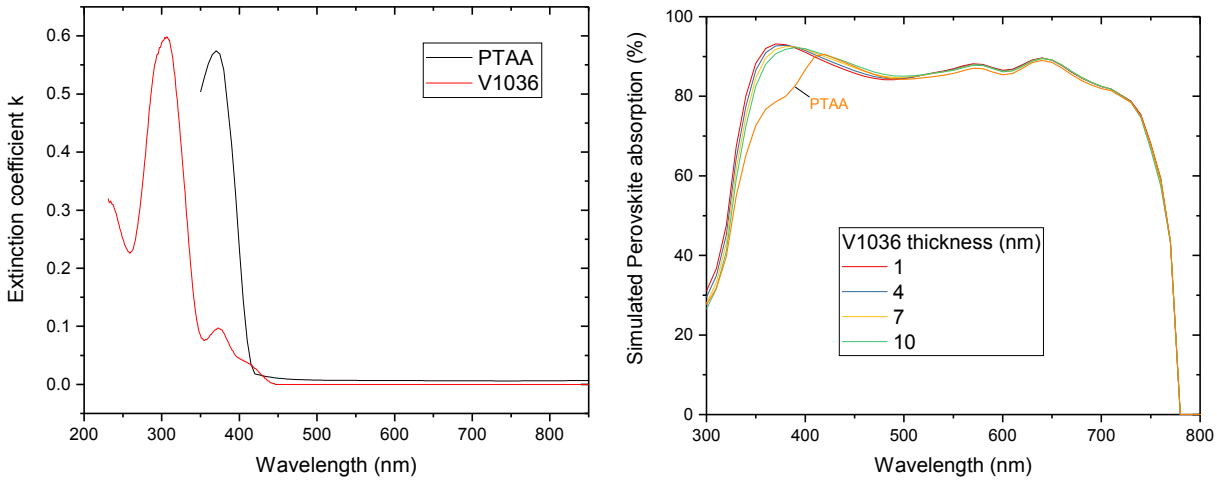

Figure S18. Left: Used extinction coefficients for the simulation. Right: Simulated absorption of the Perovskite layer in the stack Air/Glass(1mm)/ITO(120nm)/HTM(10 nm for PTAA)/Perovskite(650nm)/C60(23nm)/Cu(100nm). This plot shows that in EQE, **V1036** would not be detectable.

Scanning electron microscopy

Scanning electron microscope pictures were recorded with a Hitachi S-4100 at an acceleration voltage of 5 kV.

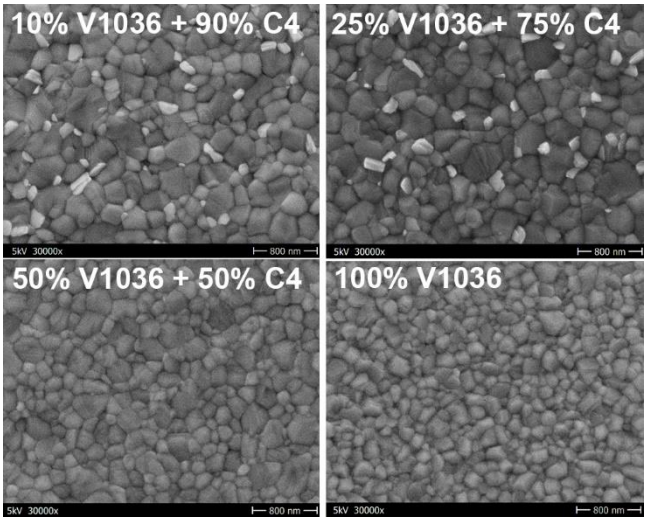

Figure S19. Top-view SEM micrographs of perovskite film, deposited on different SAM-coated substrates.

Computational details

Geometry optimization was performed using TURBOMOLE version 7.0 software,[8] with Becke's three parameter functional, B3LYP,[9,10] and def2-SVP[11,12] basis set in vacuum. Optimized structures and molecular orbitals were visualized with Avogadro: an open-source molecular builder and visualization tool. Version 1.1.1.[13]

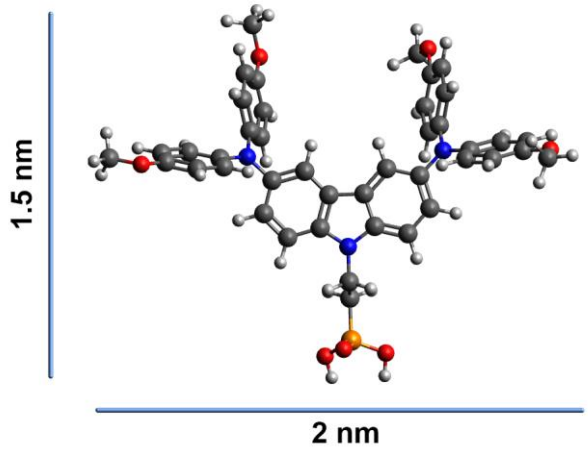

Figure S20. Side-view of the **V1036** optimized geometry.

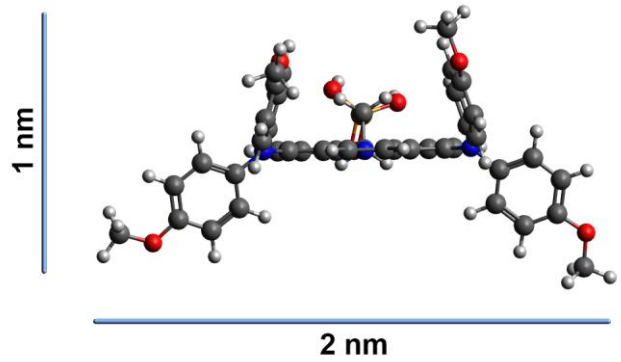

Figure S21. Top-view of the **V1036** optimized geometry.

Further electrical characterization

Figure S22 shows electrochemical impedance (EIS) measurements on two devices comprising a **V1036** SAM or PTAA layer respectively, with the rest of the device being equal. For the measurements a FRA-equipped Solarlab XM Potentiostat was used, with a Thorlabs DC2200 LED driver for controlling the LED intensity. These measurements can be used to e.g. characterize interface charge accumulation via fitting with an equivalent circuit model to extract device capacitances and resistances.

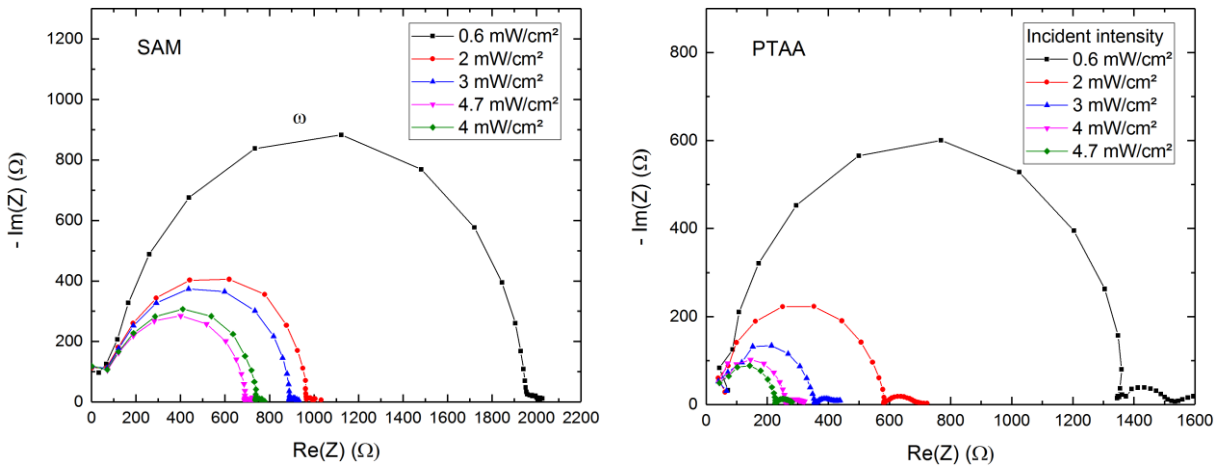

Figure S22. Nyquist plots of electrochemical impedance measurements on a device with a **V1036** SAM as the p-layer (left) and PTAA as a p-layer (right). The impedance was measured at open circuit condition for different illumination intensities (orange LED light) with a 10 mV voltage modulation in a frequency range of 0.1 Hz to 0.5 MHz.

The equivalent circuit used as a model is shown in **Figure S23** and consists of a series resistance R_S accounting for cable and contact resistances, a Voigt element C_g-R_{rec} describing the high frequency device response and another capacitance C_1 for the slower relaxation processes in the device.[14-16] C_g is being treated as a constant phase element (CPE) with impedance Q^{-1} $(Iw)^{-n}$, where n is the CPE index describing the ideality of the capacitor and Q the CPE prefactor, in order to account for the slight depression of the semicircles.[17] **Figure S23** shows an exemplary fit to the data displayed as a Bode plot. Special attention has been paid to the high frequency part of the measurements since this is typically connected to interface charge transfer. For every intensity, R_S was held constant at 65 W, R_C at 11 W, and n was fixed to 0.9. The extracted parameters are plotted in **Figure S24**. The CPE capacitance is calculated from R_{rec} and Q and n via $(R_{rec}\ Q)^{1/n}/R_{rec}$.

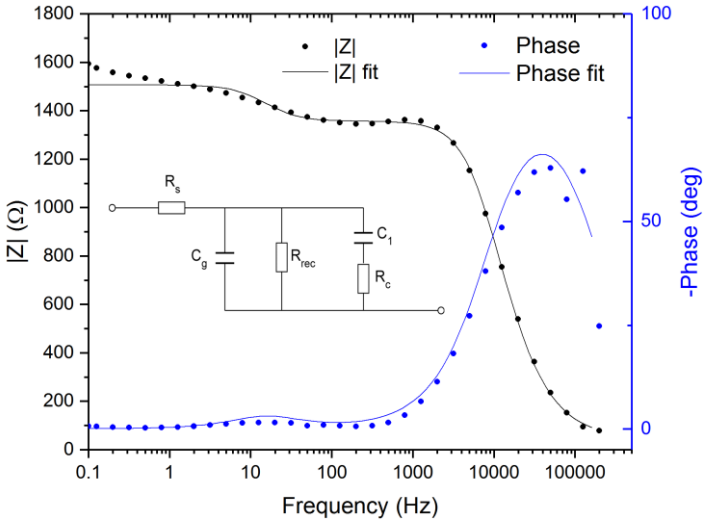

Figure S23. Exemplary fitting result of one EIS curve (PTAA device, 0.6 mW/cm² illumination) with using the equivalent circuit shown as an inset.

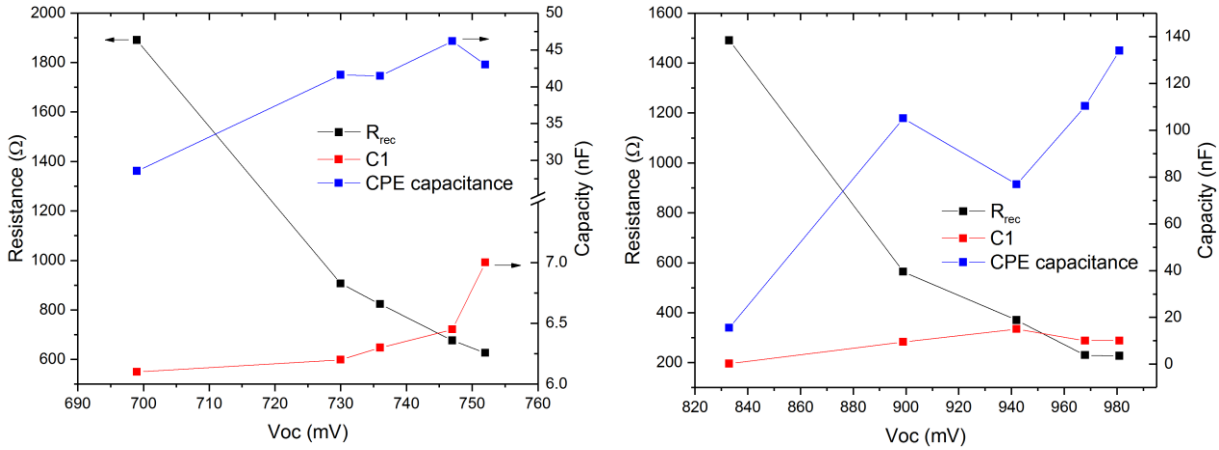

Figure S24. Parameters extracted from fitting the EIS curves with the equivalent circuit shown in Figure S23. Note that the low V_{OC} values stem from low illumination intensities (0.01-0.05 suns). Left: 100% **V1036** SAM, right: PTAA.

It is evident from **Figure S24** that both solar cell types show the expected behavior of a rising capacitance and falling recombination resistance with illumination intensity. It can be concluded from the similar (and even lower) CPE capacitance that no charge extraction limitation by charge accumulation is promoted by the SAM. This argument is underlined by the comparison of dark currents shown in **Figure S25**. SAM-based cells show a significantly lower dark current around short-circuit condition and similarly high injection as PTAA-based devices for applied voltages higher than V_{OC}. Note that the lower currents make the SAM-based devices more sensitive to hysteretic phenomena in the dark, which explains the shown slight hysteresis for some of the SAM devices.

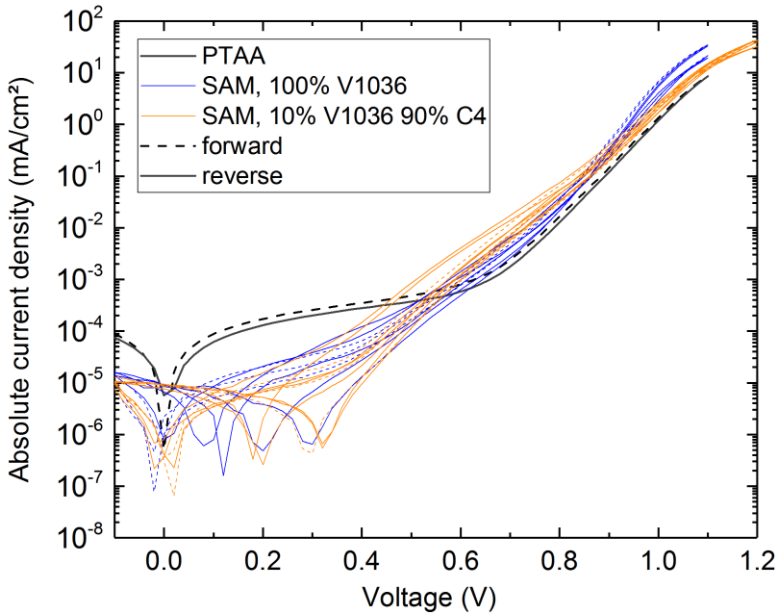

Figure S25. Dark JV measurements comparing a typical curve of a PTAA-based device with several SAM-based cells. Notably, the shunt resistance of the SAM-based devices is higher while showing a similarly high injection efficiency at high forward bias.

Synthesis

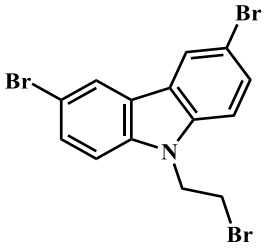

3,6-dibromo-9-(2-bromoethyl)-9*H*-carbazole (1)

3,6-dibromocarbazole (2 g, 6.15 mmol) was dissolved in 1,2-dibromoethane (40 ml), and tetrabuthylammonium bromide (0.198 g, 0.62 mmol) with 50% KOH aqueous solution (1.72 ml, 30.77 mmol) were added subsequently. Reaction was stirred at 60°C for three days (TLC, acetone:*n*-hexane, 1:24, v:v) after each 24 h adding 0.198 g of tetrabuthylammonium bromide and 1.72 ml of 50% aqueous KOH solution. After completion of the reaction, extraction was done with dichloromethane. The organic layer was dried over anhydrous Na_2SO_4 and the solvent was distilled off under reduced pressure. The crude product was

purified by column chromatography using acetone:*n*-hexane, 3:22, v:v as eluent to give 2.4 g (90 %) of white crystalline material (T_m=153-155^{o}C).

Anal. calcd for $C_{14}H_{10}NBr_3$, %: C 38.93; H 2.33; N 3.24; found, %: C 38.78; H 2.42; N 3.11.

^{1}H NMR (400 MHz, $CDCl_3$) δ 8.07 (d, J = 1.8 Hz, 2H); 7.54 (dd, J = 8.7, 1.9 Hz, 2H), 7.25 (d, J = 8.7 Hz, 2H); 4.59 (t, J = 7.2 Hz, 2H); 3.62 (t, J = 7.2 Hz, 2H).

^{13}C NMR (100 MHz, $CDCl_3$) δ 138.83; 129.28; 123.65; 123.38; 112.71; 110.16; 44.75; 27.94.

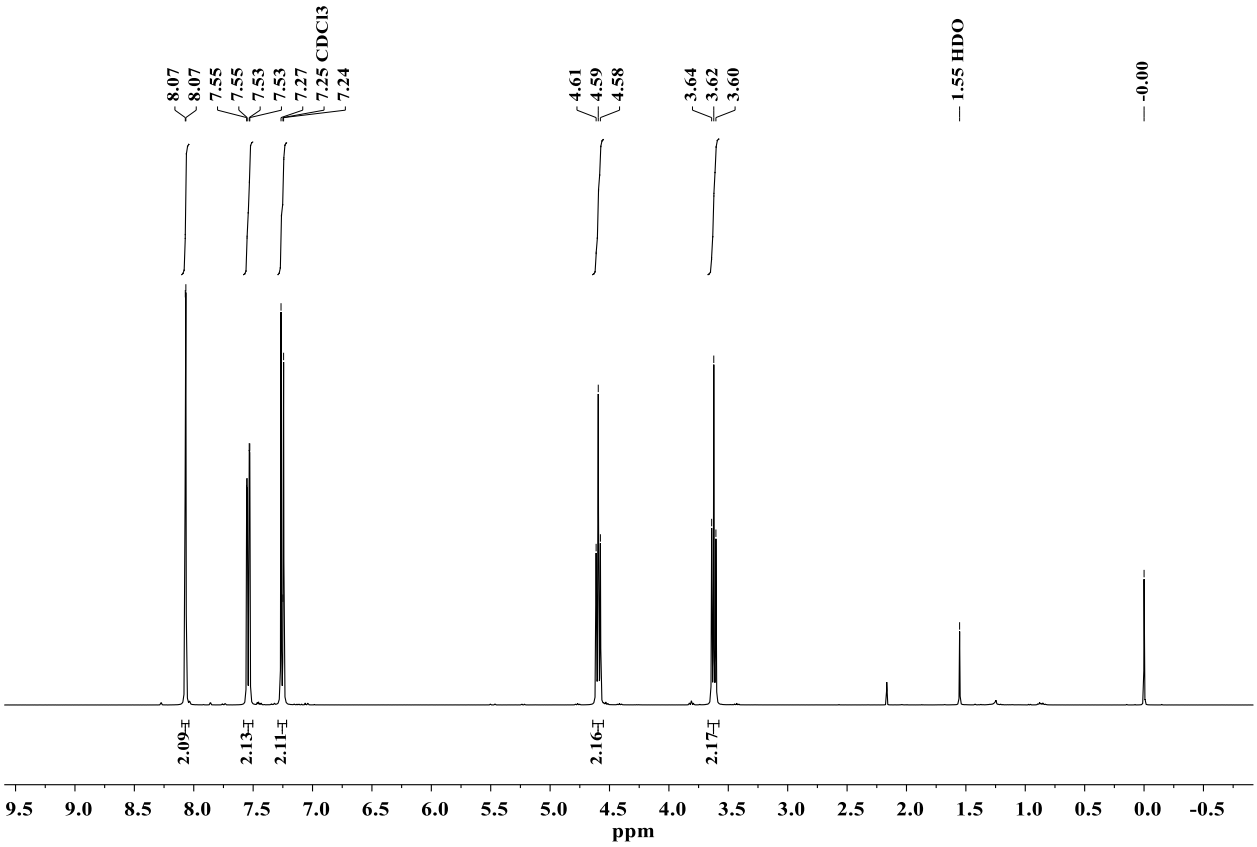

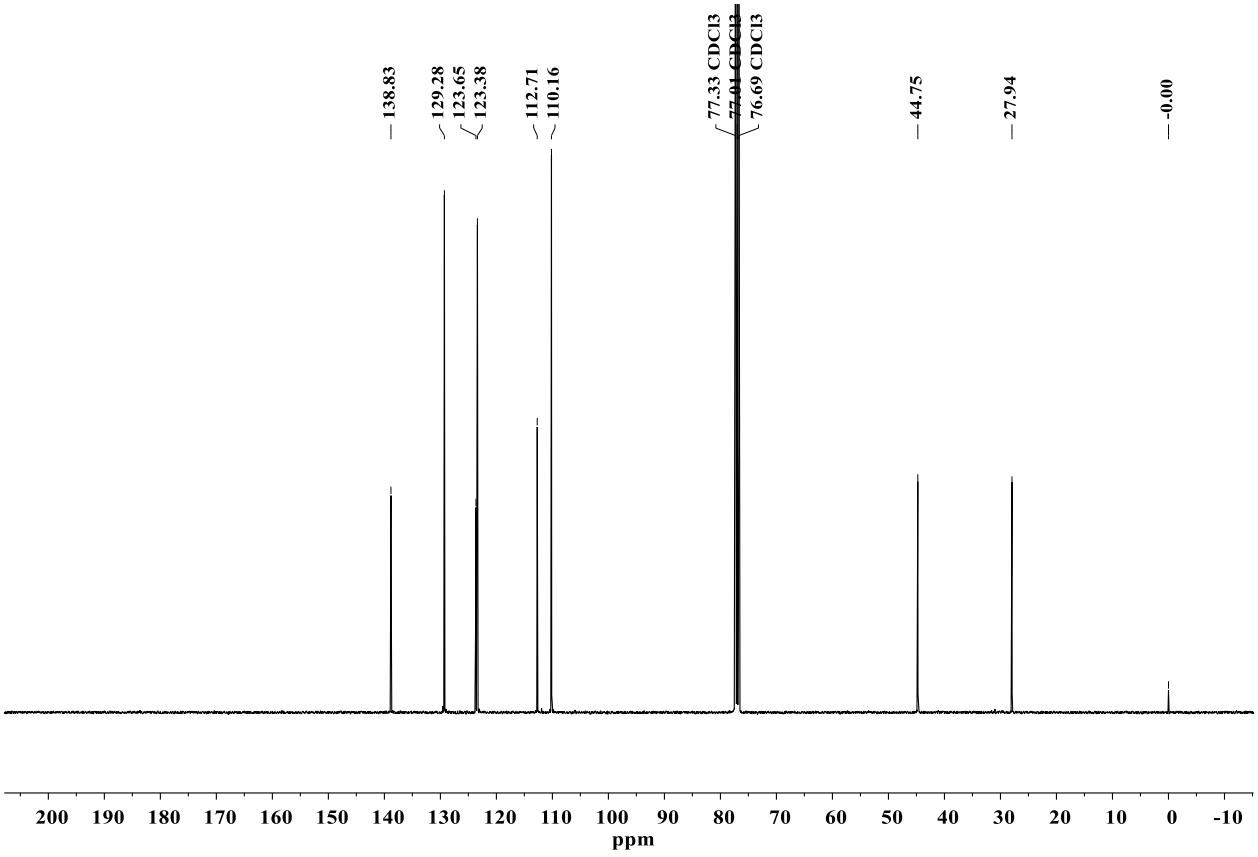

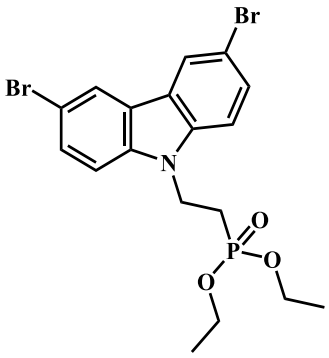

diethyl [2-(3,6-dibromo-9*H*-carbazol-9-yl)ethyl]phosphonate (2)

Compound **1** (2.4 g, 5.55 mmol) was dissolved in triethylphosphite (20 ml) and the reaction mixture was heated at reflux for 18 h. After reaction completion (TLC, acetone:*n*-hexane, 2:3, v:v) the solvent was distilled off under reduced pressure. The crude product was purified by column chromatography using acetone:*n*-hexane, 7:18, v:v as eluent to give 2.56 g (95%) of white crystalline material (T_m=118-119ºC)

Anal. calcd for $C_{18}H_{20}NBr_2O_3P$, %: C 44.20; H 4.12; N 2.86; found, %: C 44.09; H 4.26; N 3.02.

^{1}H NMR (400 MHz, $CDCl_3$) δ 8.11 (d, J = 1.8 Hz, 2H); 7.56 (dd, J = 8.7, 1.9 Hz, 2H); 7.30 (d, J = 8.7 Hz, 2H); 4.60 – 4.49 (m, 2H); 4.04 (dq, J = 14.2, 7.1 Hz, 4H); 2.28 – 2.16 (m, 2H); 1.24 (t, J = 7.1 Hz, 6H).

^{13}C NMR (100 MHz, $CDCl_3$) δ 138.65; 129.25; 123.71; 123.37; 112.50; 110.30; 62.01; 61.94; 37.26; 37.24; 25.88; 24.50; 16.37; 16.31.

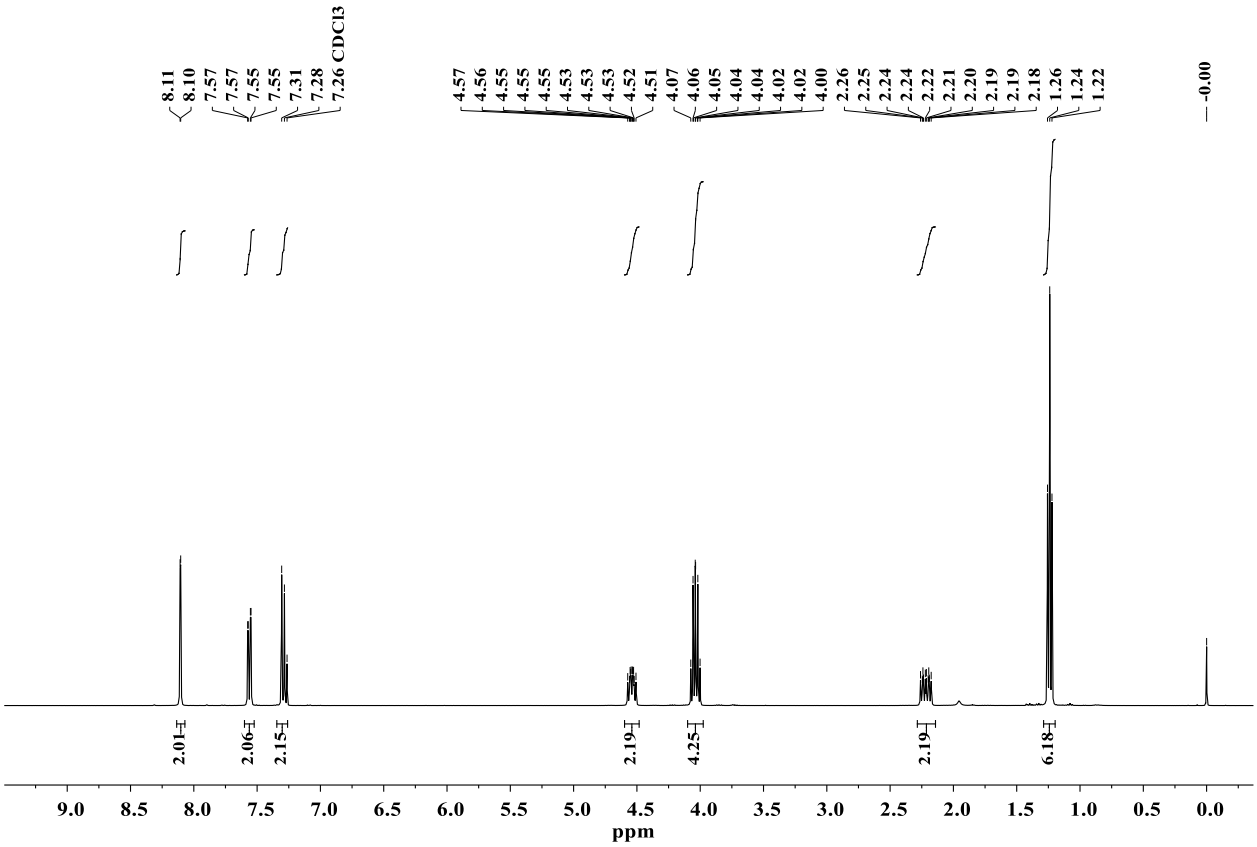

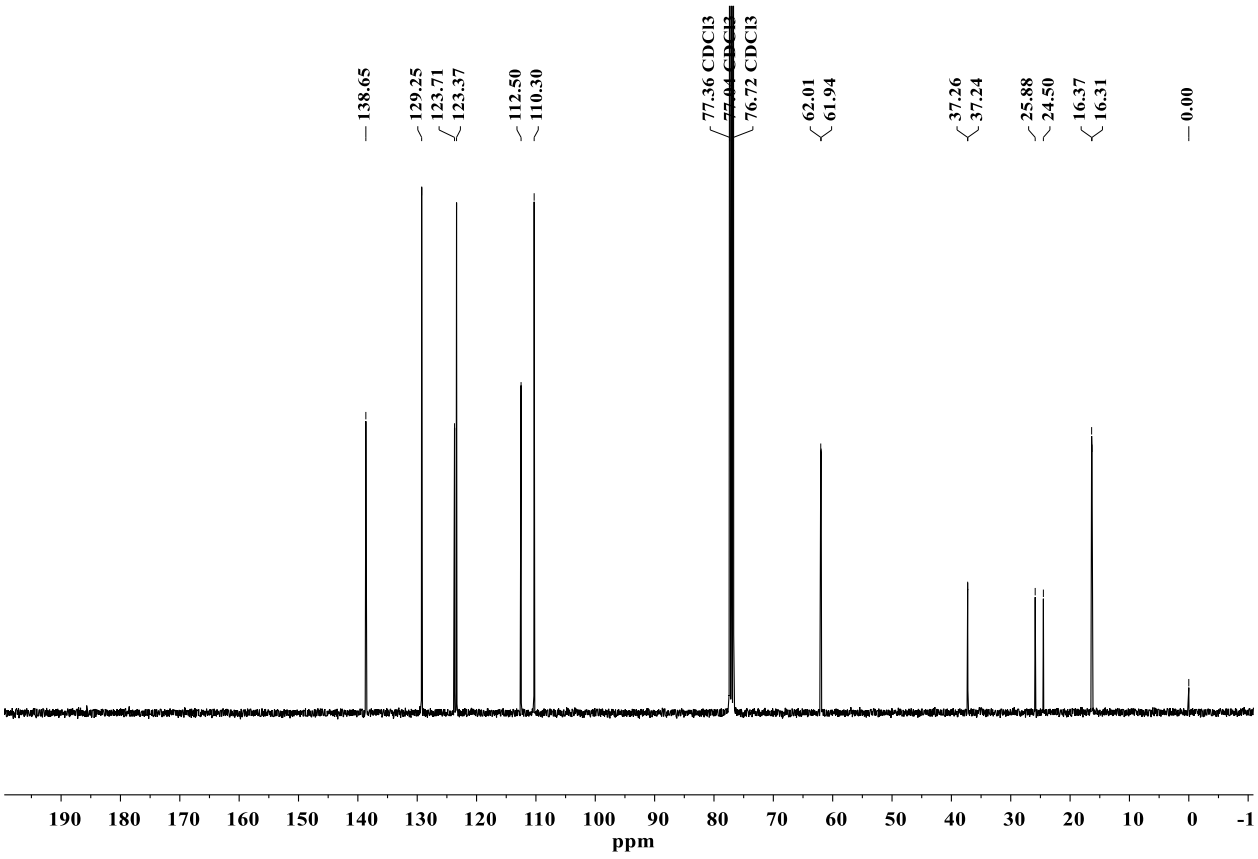

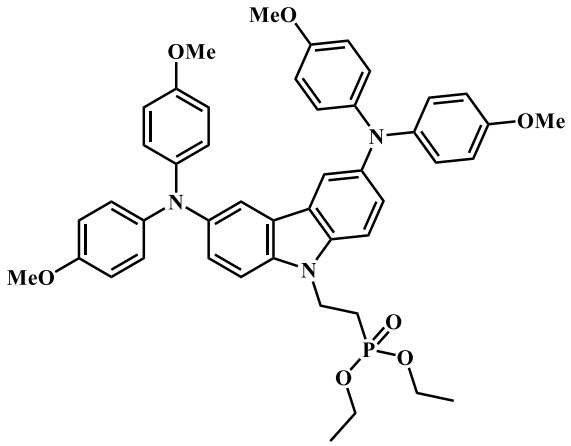

diethyl (2-{3,6-bis[bis(4-methoxyphenyl)amino]-9*H*-carbazol-9-yl}ethyl)phosphonate (3)

A solution of 2 (1 g, 2.04 mmol) and 4,4'-dimethoxydiphenylamine (1.37 g, 6.13 mmol) in anhydrous toluene (50 mL) was purged with argon for 20 min. Afterward, palladium(II) acetate (0.137 g, 0.613 mmol), tri-tert-butylphosphonium tetrafluoroborate (0.35 g, 1.23 mmol), and sodium tert-butoxide (0.59 g, 6.13 mmol) were added and the solution was refluxed under argon atmosphere for 5 h. After completion (TLC, acetone:*n*-hexane, 2:3, v:v) reaction mixture was filtered through Celite. The solvent was removed under reduced pressure

and the crude product was purified by column chromatography using acetone:*n*-hexane, 7:18, v:v as eluent to give 1 g (62.5%) of greenish powder.

Anal. calcd for $C_{46}H_{48}N_3O_7P$, %: C 70.30; H 6.16; N 5.35, found, %: C 70.14; H 6.29; N 5.56.

^{1}H NMR (400 MHz, DMSO-d_6) δ 7.64 (d, J = 2.2 Hz, 2H), 7.46 (d, J = 8.7 Hz, 2H), 7.11 (dd, J = 8.7, 2.2 Hz, 2H), 6.86 – 6.74 (m, 16H), 4.50 (dt, J = 13.8, 7.3 Hz, 2H), 3.92 (p, J = 7.2 Hz, 4H), 3.67 (s, 12H), 2.26 (dt, J = 18.2, 7.3 Hz, 2H), 1.12 (t, J = 7.0 Hz, 6H).

^{13}C NMR (101 MHz, DMSO) δ 154.16, 142.08, 140.25, 136.67, 124.39, 123.67, 122.90, 116.94, 114.60, 110.28, 61.20, 61.14, 55.15, 28.62, 16.13, 16.07.

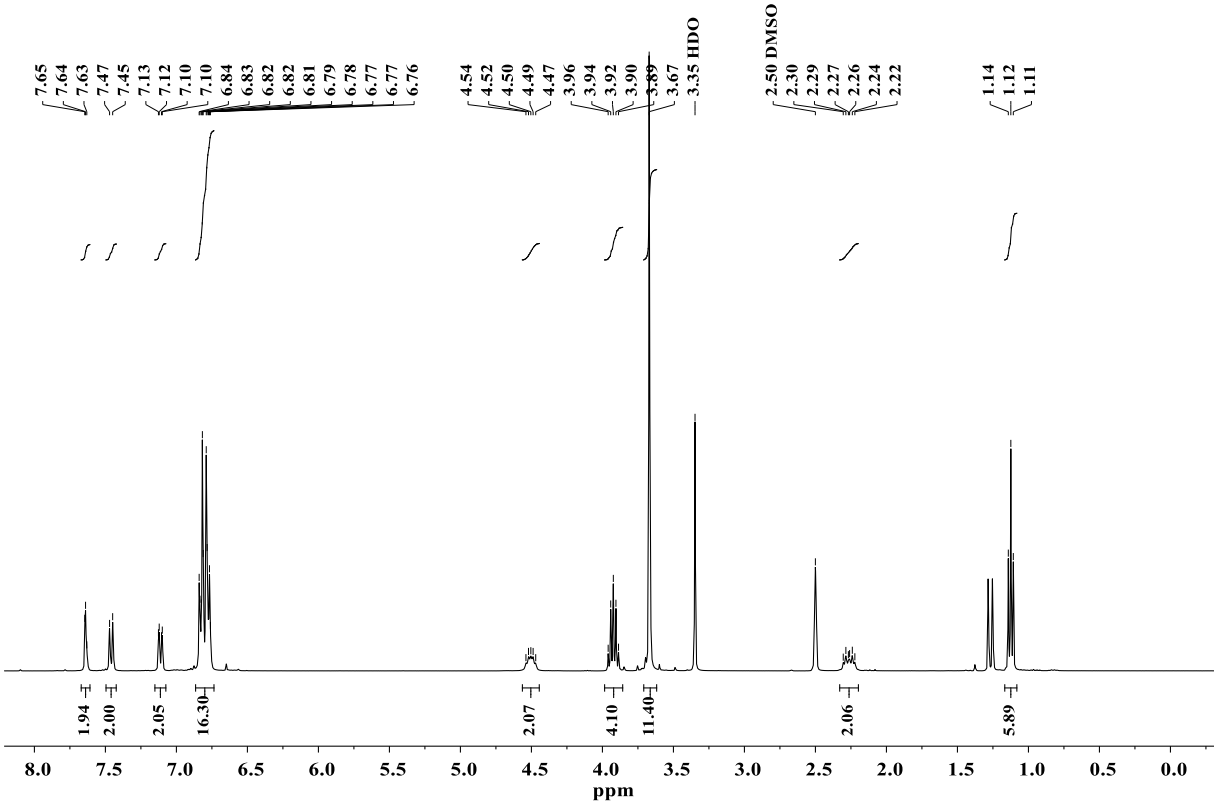

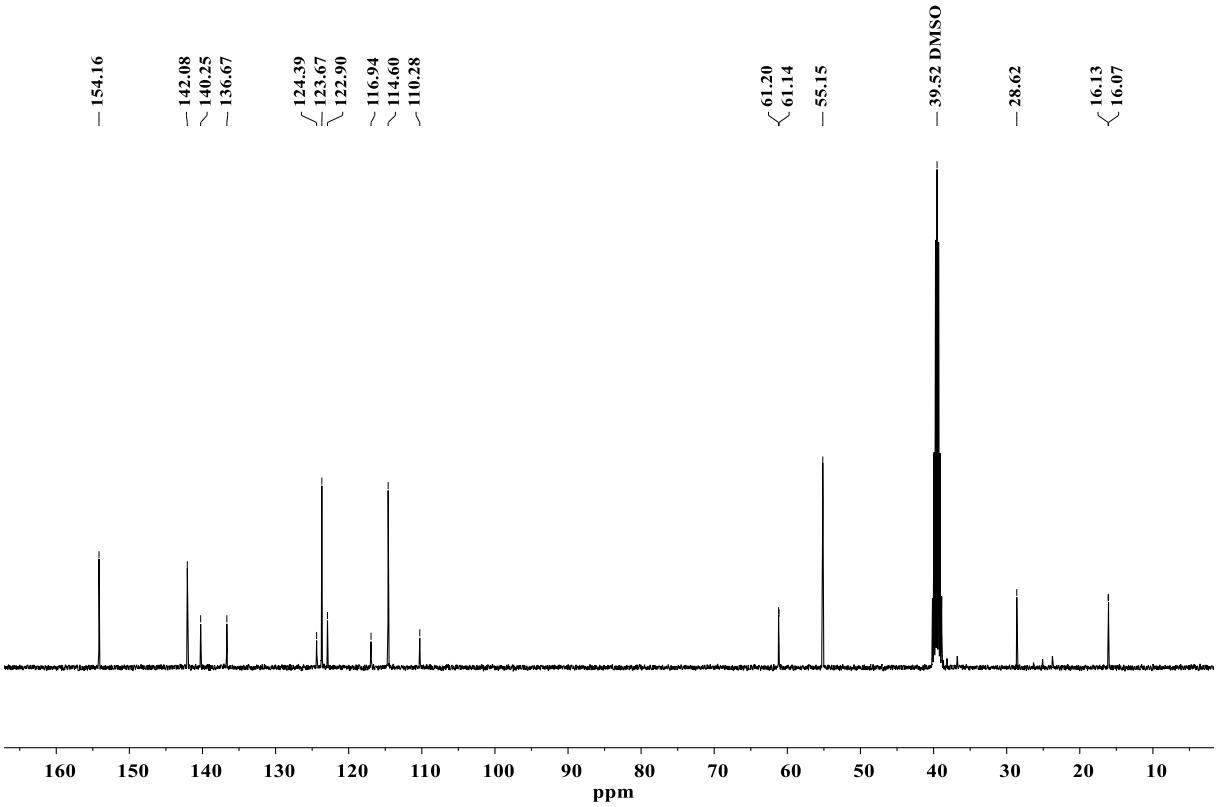

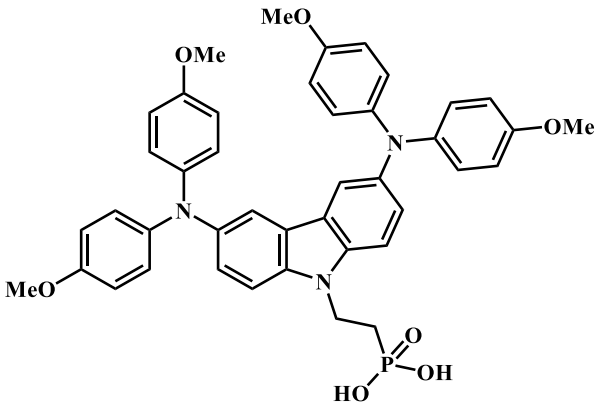

(2-{3,6-bis[bis(4-methoxyphenyl)amino]-9*H*-carbazol-9-yl}ethyl)phosphonic acid

3 (0.4 g, 0.51 mmol) was dissolved in dry 1,4-dioxane (15 ml) under argon. Afterwards, bromotrimethylsilane (0.67 ml, 5.08 mmol) was added dropwise. Reaction was kept for 24 h at 25^{o}C under argon atmosphere. Afterwards solvent was distilled off under reduced pressure, solid residue was dissolved in methanol (10 ml) and distilled water was added dropwise (10 ml), until solution became opaque, and was stirred for 15 h. Product was filtered off and washed with water to give 0.321 g (86 %) of greenish powder.

Anal. calcd for $C_{42}H_{40}N_3O_7P$, %: C 69.13; H 5.52; N 5.76, found, %: C 68.89; H 5.38; N 5.53.

^{1}H NMR (400 MHz, DMSO-d_6) δ 7.64 (s, 2H), 7.42 (d, J = 8.8 Hz, 2H), 7.15 – 7.07 (m, 2H), 6.87 – 6.74 (m, 16H), 4.50 – 4.44 (m, 2H), 3.67 (s, 12H), 2.02 (dt, J = 17.3, 8.0 Hz, 2H).

^{13}C NMR (100 MHz, DMSO-d6) δ 154.16; 142.09; 140.22; 1366; 124.60; 123.66; 122.88; 117.15; 114.63; 110.01; 66.36; 55.16.

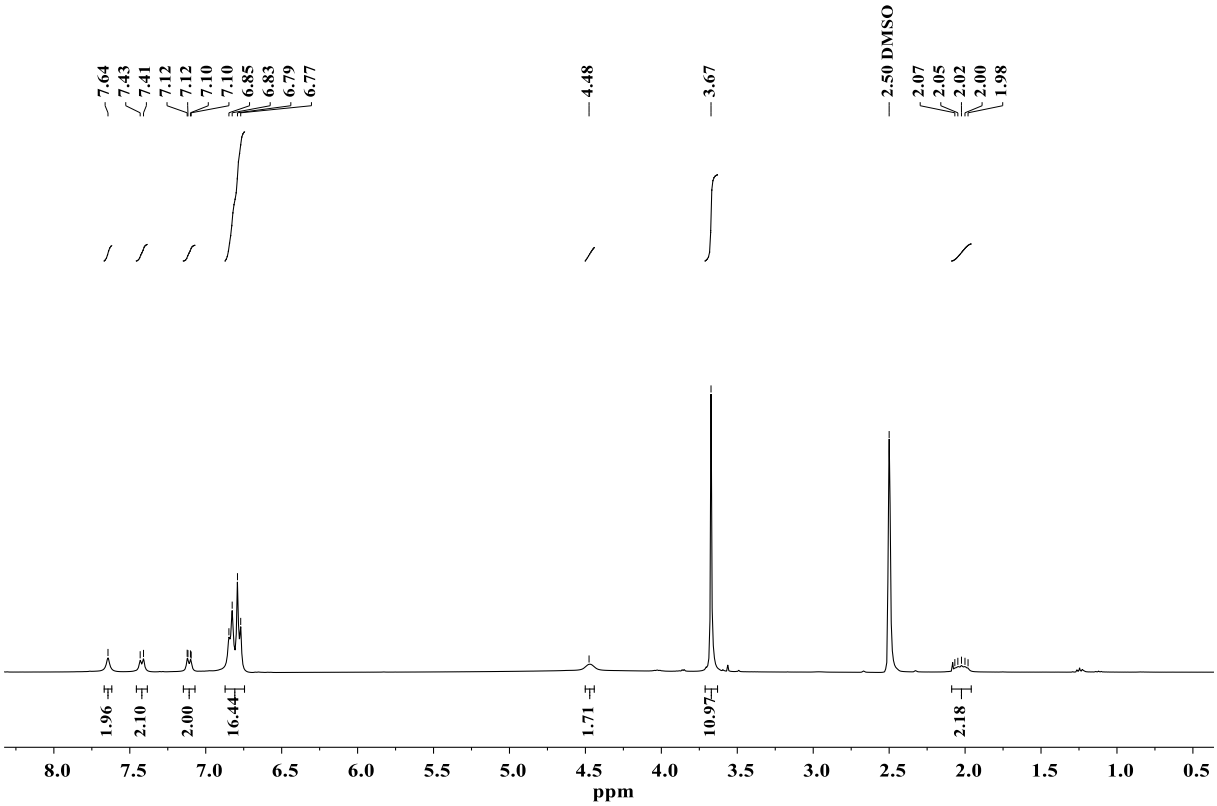

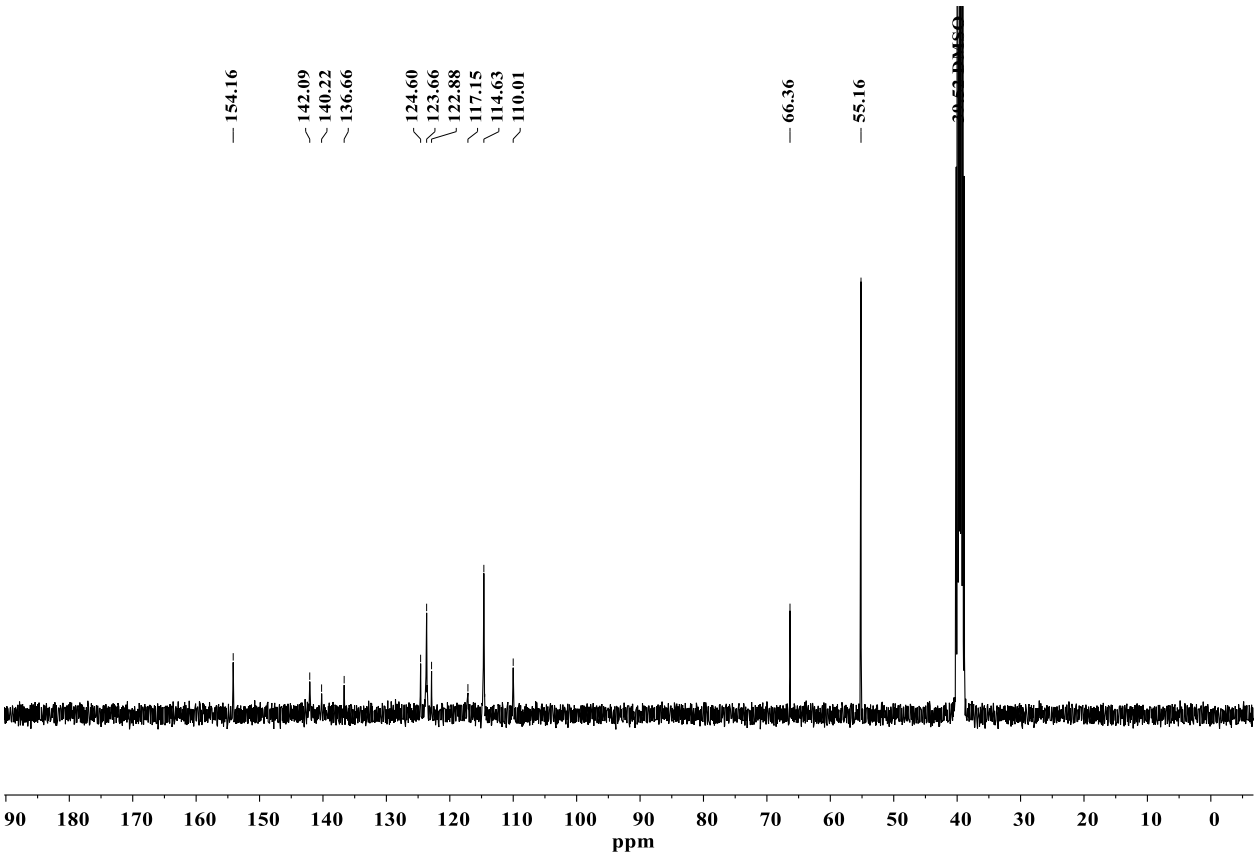
154.16
142.09
140.22
136.66
124.60
123.66
122.88
117.15
114.63
110.01
66.36
55.16
90 180 170 160 150 140 130 120 110 100 90 80 70 60 50 40 30 20 10 0
ppm

Literature

[1] G. Niaura, Z. Kuprionis, I. Ignatjev, M. Kažemėkaitė, G. Valincius, Z. Talaikytė, V. Razumas, A. Svendsen, *J. Phys. Chem. B* **2008**, *112*, 4094.
[2] M. Cordona, L. Ley, *Top. Appl. Phys.* **1978**, *26*, 1.
[3] E. Miyamoto, Y. Yamaguchi, M. Yokoyama, *Electrophotography* **1989**, *28*, 364.
[4] M. Kirkus, M.-H. Tsai, J. V. Grazulevicius, C.-C. Wu, L.-C. Chi, K.-T. Wong, *Synth. Met.* **2009**, *159*, 729.
[5] M. Saliba, T. Matsui, J.-Y. Seo, K. Domanski, J.-P. Correa-Baena, M. K. Nazeeruddin, S. M. Zakeeruddin, W. Tress, A. Abate, A. Hagfeldt, M. Grätzel, *Energy Environ. Sci.* **2016**, *9*, 1989.
[6] M. Stolterfoht, C. M. Wolff, Y. Amir, A. Paulke, L. Perdigón-Toro, P. Caprioglio, D. Neher, *Energy Environ. Sci.* **2017**, *10*, 1530–1539.
[7] R. Santbergen, T. Meguro, T. Suezaki, G. Koizumi, K. Yamamoto, M. Zeman, *IEEE J. Photovoltaics* **2017**, *7*, 919–926.
[8] R. Ahlrichs, M. Bär, M. Häser, H. Horn, C. Kölmel, *Chem. Phys. Lett.* **1989**, *162*, 165–169.
[9] C. Lee, W. Yang, R. G. Parr, *Phys. Rev. B* **1988**, *37*, 785–789.
[10] A. D. Becke, *J. Chem. Phys.* **1993**, *98*, 5648–5652.
[11] A. Schäfer, H. Horn, R. Ahlrichs, *J. Chem. Phys.* **1992**, *97*, 2571–2577.
[12] F. Weigend, R. Ahlrichs, K. A. Peterson, T. H. Dunning, R. M. Pitzer, A. Bergner, *Phys. Chem. Chem. Phys.* **2005**, *7*, 3297.
[13] M. D. Hanwell, D. E. Curtis, D. C. Lonie, T. Vandermeersch, E. Zurek, G. R. Hutchison, *J. Cheminform.* **2012**, *4*, 17.
[14] E. Ghahremanirad, A. Bou, S. Olyaee, J. Bisquert, J. Phys. Chem. Lett. 2017, 8, 1402–1406.
[15] A. Pockett, G. E. Eperon, T. Peltola, H. J. Snaith, A. Walker, L. M. Peter, P. J. Cameron, J. Phys. Chem. C 2015, 119, 3456–3465.
[16] I. Zarazúa, S. Sidhik, T. Lopéz-Luke, D. Esparza, E. De la Rosa, J. Reyes-Gomez, I. Mora-Seró, G. Garcia-Belmonte, J. Phys. Chem. Lett. 2017, 8, 6073–6079.
[17] J. Bisquert, F. Fabregat-Santiago, in Dye-Sensitized Solar Cells, (Ed: K. Kalyanasundaram), EPFL press, Lausanne, Switzerland 2010, pp. 457-555.

7.4 Publication to chapter 4

The paper is open-access and reprinted here under the Creative Commons BY 3.0 license – Published by The Royal Society of Chemistry [208]

Energy & Environmental Science

PAPER

View Article Online
View Journal | View Issue

Cite this: *Energy Environ. Sci.*, 2019, **12**, 3356

Conformal monolayer contacts with lossless interfaces for perovskite single junction and monolithic tandem solar cells†

Amran Al-Ashouri,[a]* Artiom Magomedov,[b]* Marcel Roß,[a] Marko Jošt,[a] Martynas Talaikis,[c] Ganna Chistiakova,[d] Tobias Bertram,[e] José A. Márquez,[f] Eike Köhnen,[a] Ernestas Kasparavičius,[b] Sergiu Levcenco,[f] Lidón Gil-Escrig,[a] Charles J. Hages,[f] Rutger Schlatmann,[e] Bernd Rech,[dg] Tadas Malinauskas,[b] Thomas Unold,[f] Christian A. Kaufmann,[e] Lars Korte,[d] Gediminas Niaura,[c] Vytautas Getautis[b] and Steve Albrecht*[ag]

The rapid rise of perovskite solar cells (PSCs) is increasingly limited by the available charge-selective contacts. This work introduces two new hole-selective contacts for p–i–n PSCs that outperform all typical p-contacts in versatility, scalability and PSC power-conversion efficiency (PCE). The molecules are based on carbazole bodies with phosphonic acid anchoring groups and can form self-assembled monolayers (SAMs) on various oxides. Besides minimal material consumption and parasitic absorption, the self-assembly process enables conformal coverage of arbitrarily formed oxide surfaces with simple process control. The SAMs are designed to create an energetically aligned interface to the perovskite absorber without non-radiative losses. For three different perovskite compositions, one of which is prepared by co-evaporation, we show dopant-, additive- and interlayer-free PSCs with stabilized PCEs of up to 21.1%. Further, the conformal coverage allows to realize a monolithic CIGSe/perovskite tandem solar cell with as-deposited, rough CIGSe surface and certified efficiency of 23.26% on an active area of 1 cm^2. The simplicity and diverse substrate compatibility of the SAMs might help to further progress perovskite photovoltaics towards a low-cost, widely adopted solar technology.

Received 17th July 2019,
Accepted 23rd September 2019

DOI: 10.1039/c9ee02268f

rsc.li/ees

Broader context

Perovskite-based photovoltaics promises three main benefits: low cost, high efficiency and large versatility. However, combining all three factors into one solar cell design is still a difficult endeavor. In particular, one of the main bottlenecks towards large-scale production is the available choice of hole-selective contacts. The best standards in both polarities, n–i–p (Spiro-OMeTAD) and p–i–n (PTAA), are highly unsuitable for commercial production due to their very high prices and limited processing versatility. Thus, with this work, we present a new generation of self-assembled monolayers (SAMs) as hole-selective contacts that are intrinsically scalable, simple to process, dopant-free and cheap. In addition, they enable highly efficient p–i–n perovskite solar cells and a record-efficiency monolithic perovskite/CIGSe tandem device. While self-assembly offers the crucial advantage of conformally covering rough surfaces within a self-limiting process, one of the herein used SAMs creates an energetically well-aligned interface to the perovskite absorber with minimal non-radiative recombination. Our model system further provides insights into the influence of molecular design on surface passivation and open-circuit voltage, beneficially adding to future prospects of rationally engineering perfect charge-selective contacts.

[a] *Young Investigator Group Perovskite Tandem Solar Cells, Helmholtz-Zentrum Berlin, Kekuléstraße 5, 12489 Berlin, Germany. E-mail: amran.al-ashouri@helmholtz-berlin.de, steve.albrecht@helmholtz-berlin.de*
[b] *Department of Organic Chemistry, Kaunas University of Technology, Radvilenu pl. 19, Kaunas LT-50254, Lithuania. E-mail: artiom.magomedov@ktu.lt*
[c] *Department of Organic Chemistry, Center for Physical Sciences and Technology, Sauletekio Ave. 3, Vilnius LT-10257, Lithuania*
[d] *Institute for Silicon Photovoltaics, Helmholtz-Zentrum Berlin, Kekuléstraße 5, 12489 Berlin, Germany*
[e] *PVcomB, Helmholtz Zentrum Berlin, Schwarzschildstr. 3, 12489 Berlin, Germany*
[f] *Department of Structure and Dynamics of Energy Materials, Helmholtz-Zentrum-Berlin für Materialien und Energie GmbH, Hahn-Meitner Platz 1, 14109 Berlin, Germany*
[g] *Faculty of Electrical Engineering and Computer Science, Technical University Berlin, Marchstraße 23, 10587 Berlin, Germany*

† Electronic supplementary information (ESI) available. See DOI: 10.1039/c9ee02268f

Introduction

Metal-halide perovskites triggered intensive research activities throughout the last 5 years with over 3000 published papers on perovskite solar cells (PSCs) only in 2018.[1] Typical metal-halide perovskite absorbers are composed of a mixture of different cations (methylammonium MA, formamidinium FA, Cs, Rb *etc.*) and anions (I^-, Br^-, Cl^-). These compositions have attracted attention due to their outstanding optoelectronic properties including a steep absorption onset together with strong solar absorption[2] and high defect tolerance.[3,4] Furthermore, the low non-radiative recombination rates enabled voltage deficits that are only $\sim$65 mV below the radiative limit,[5] which is striking for a material processed at low temperatures of around 100 °C. The perovskite layers can be fabricated through a variety of techniques, including vacuum deposition by co-evaporation[6] and versatile solution processing methods like spin coating or printing.[7] The relatively high band gap of 1.6–1.7 eV, together with the ability of band gap tuning by compositional engineering,[8] also renders these materials suitable for integration into tandem solar cell architectures to overcome the efficiency limit of single solar cells.[9] In efficient tandem devices, the PSC is used as the top cell absorber with either crystalline silicon,[10,11] Cu(In,Ga)Se_2 (CIGSe)[12,13] or a Sn-based perovskite forming the lower band gap bottom cell.[14]

Although highest reported power conversion efficiencies (PCEs) of over 23% are demonstrated for PSCs with the "regular" n–i–p device architecture,[15] the p–i–n (so called "inverted") architecture is gaining increasing popularity due to its ease of processing and superior suitability for perovskite-based tandem solar cells.[16–19] Moreover, p–i–n PSCs carry the promise of low-temperature fabrication, high stability[20] without the use of dopants that cause degradation,[21–23] low current–voltage hysteresis[24] and compatibility to flexible substrates.[25,26] However, compared to their n–i–p single junction counterparts, p–i–n PSCs still lack behind in maximum power-conversion efficiency. This is predominantly due to a higher loss in potential, *i.e.*, energetic difference between open-circuit potential (eV_{OC}, with elementary charge e) and band gap. This loss was identified to be dominated by the interfaces to charge-selective contacts.[27] Thus, recent efforts were dedicated to reduce these losses through surface passivation, mostly by processing nanometer-thick interfacial layers between absorber and charge-selective contacts.[28–34] Recently, changes of the perovskite precursor (*e.g.*, addition of Sr[35] or an organic molecule with passivating functional groups,[36] or a substitution[5] of PbI_2) led to open-circuit voltages of well over 1.20 V with comparable loss-in-potential values as obtained in best n–i–p PSCs. However, the mentioned strategies often require finely tuned processing that might be complicated to implement on a large scale. Additionally, for most high-V_{OC} approaches, acceptable stability of the PSCs has yet to be shown.

In the scope of future high-throughput commercialization, it is crucial to keep the simplicity and robustness that p–i–n PSCs exhibit even at high PCEs > 20%. Additionally, it is desirable to minimize parasitic absorption and to use low-cost materials that are suitable for a variety of substrates with arbitrary surfaces and large areas, in order to expand the fields of PSC applications. These ambitions could be realized by using self-assembled monolayers (SAMs) as charge-selective contacts: the required material quantities are minimal; the substrate compatibility is manifold and process control is simple, with the molecules autonomously forming a functional layer in a self-limiting process by design. Functionalization of surfaces with SAMs already has a rich history in surface chemistry.[37–39] With the rise of miniaturized electronics, *e.g.*, SAM-based field-effect transistors were built.[40,41] After first occurrences in PSCs as electrode modifications,[42,43] the first hole-selective SAMs were introduced in 2018.[44,45] These molecules covalently bind to the transparent conductive oxide (TCO), *e.g.*, indium tin oxide (ITO), on which the perovskite absorber crystallizes. Due to their hole-selectivity, the SAMs can replace the classical hole-transporting layer. To date, however, the SAMs in PSCs did not enable high PCEs of over 20% that would surpass those reached with the typically used polymeric hole contact material PTAA (poly[bis(4-phenyl)(2,4,6-trime-thylphenyl)amine]). Here, we reach this important objective by using a new generation of SAMs in which the molecules are based on carbazole bodies with phosphonic acid anchoring groups.

We show that the SAMs act as simple hole-selective contacts that can be prepared by classical dip-coating or spin-coating within wide processing windows. By replacing PTAA with a SAM, we demonstrate a maximum PCE of over 21%, which is comparable to current record-efficiencies in the p–i–n architecture.[27,34,36] Notably, this PCE is achieved without any perovskite post-treatments, additives, dopants or interlayers that are usually used for high PCEs after delicate fine-tuning. Ultraviolet photoelectron spectroscopy reveals that both new SAMs show a stronger hole-selectivity than PTAA, and photoluminescence (PL) studies show that the SAM/perovskite interface does not introduce non-radiative losses. This enables a V_{OC} of up to 1.19 V and a PL decay time of $\sim$2 μs. The investigated SAMs work efficiently for three different perovskite compositions, including a 19.6%-efficient PSC which is fabricated by co-evaporation, assuring that hole-extraction by SAMs is a universal approach. We further demonstrate that self-assembly leads to conformal coverage of rough surfaces like as-deposited CIGSe. By integrating a SAM into a tandem architecture, we realize a 23.26%-efficient monolithic CIGSe/perovskite tandem solar cell (certified) with an active area of 1.03 cm^2, embodying a low-cost, facile way of realizing all-thin-film tandem solar cells, which has proven to be a hard endeavor in the past.[46,47]

Results

A schematic representation of the used p–i–n device structure is displayed in Fig. 1a. The glass/ITO serves as a substrate for covalent bonding of the molecules to the ITO, forming a SAM. Afterwards, the perovskite is deposited on top of the SAM. As the electron-selective contact, C_{60} is thermally evaporated on top of the perovskite absorber. The device is completed by thermal evaporation of a bathocuproine (BCP)/Cu electrode.

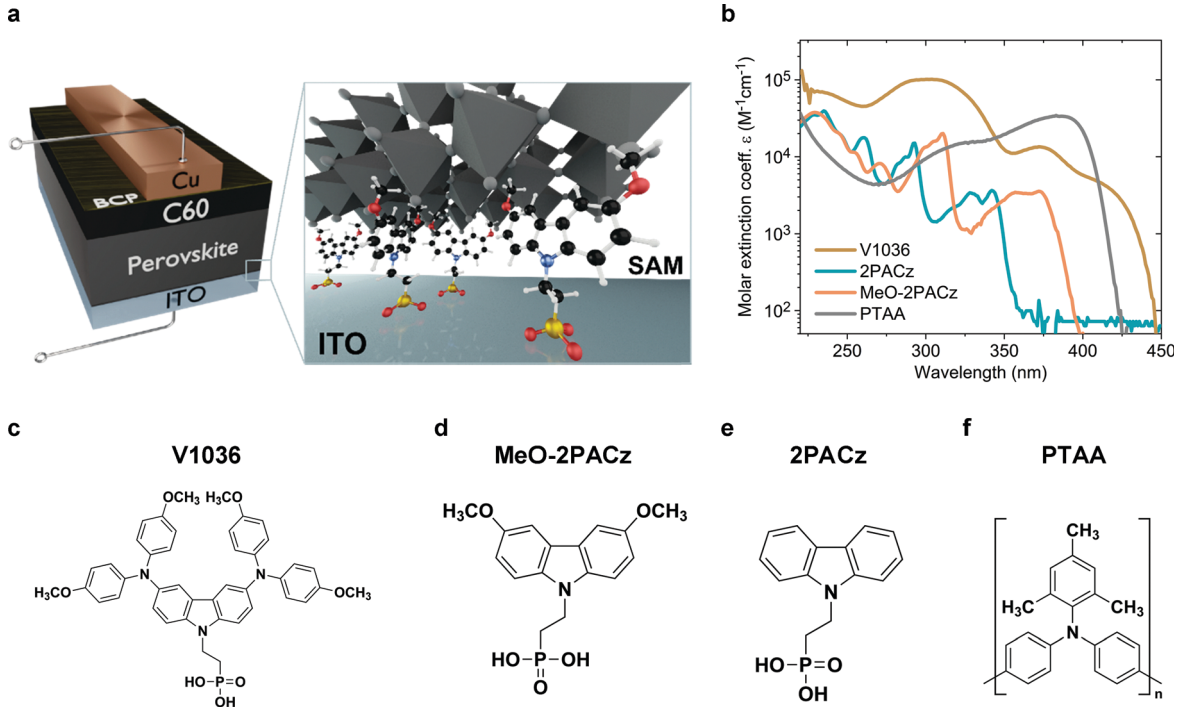

Fig. 1 Solar cell device architecture and molecule structures investigated in this work. (a) Schematic of the investigated device structure. The zoom-in visualizes how the SAM molecules attach to the ITO surface and therefore enable the hole selective contact to the perovskite above. (b) Molar extinction coefficient of solutions in tetrahydrofuran containing the different hole-selective contact materials at a concentration of 0.1 mmol l^{-1}. (c) Chemical structure of the SAM molecules **V1036**,[44] **MeO-2PACz** (d) and **2PACz** (e). (f) Chemical structure of the typically used polymer PTAA.

More details on sample fabrication and methods are provided in the supporting information. Fig. 1c–e displays the molecular structures of the molecules that form the SAMs. Fig. 1f shows the molecule structure of PTAA, which is currently used in the highest performing p–i–n PSCs in literature.[27,34,36] PSCs with **V1036** ((2-{3,6-bis[bis(4-methoxyphenyl)amino]-9*H*-carbazol-9-yl}ethyl)phosphonic acid) were already investigated in our previous work.[44] **MeO-2PACz** ([2-(3,6-dimethoxy-9*H*-carbazol-9-yl)ethyl]phosphonic acid) and **2PACz** ([2-(9*H*-carbazol-9-yl)ethyl]phosphonic acid) are new molecules based on a carbazole moiety.

Carbazole derivatives have been studied, *e.g.*, for their electron-localizing and thus hole-selective properties,[48] starting from first applications in electro-photographic devices. Since then, a huge variety of carbazole-based conductive polymers and molecular glasses has been synthesized and characterized.[49] Currently, the carbazole fragment is widely adapted in the synthesis of new materials used in organic light-emitting diodes,[50] and, more recently, in PSCs.[51] Organic phosphonic acids (PA) are known to form strong and stable bonds on, *e.g.*, ITO surfaces,[52–54] enable reliable work function modifications and can principally form bonds to any oxide surface.[55–57] In particular, it was calculated for the case of TiO_2 that PA has the strongest binding energy among all studied anchoring groups.[58] Strong bonds like these enable exceptional stability of the formed monolayers.[59] In the frame of perovskite photovoltaics, it has been shown that organic PAs on ITO are stable under continuous solar cell operation for at least 1000 h.[60] Fig. 1b presents the absorption spectra of all used molecules in a tetrahydrofuran solution. The new SAMs **2PACz** and **MeO-2PACz** show reduced absorption in the visible wavelength regime as compared to PTAA or **V1036**. The synthesis of these carbazole derivatives was conducted following a simplified version of the previously published synthesis procedure used for **V1036** (see Fig. S1 in the ESI†).[44] In comparison to **V1036**, the reaction scheme is one step shorter, no metal-based catalysis was required, and inexpensive, commercially available starting materials were used.

The classic method to coat oxide surfaces with a SAM is to immerse the substrates for several hours into a solution containing the material, optionally under heating of the solution to accelerate binding to the surface. Some molecules, such as the ones used in this work, can also form a dense monolayer simply by spin-coating the solution with a suitable concentration, as was previously described by Nie *et al.*[61] The process is intrinsically self-limiting, since the PA groups only attach to sites on the surface where there is still blank oxide. Following previous studies, we assume that the self-assembly is ordered and stabilized by π–π interactions between adjacent carbazole fragments, in contrast to an ordering that is dominated by van der Waals forces in long-chain aliphatic monolayers.[62–64] We investigated solar cells with SAMs formed both by classical dip-coating and spin-coating and did not observe significant differences in solar cell performance between both methods (Fig. S2 in the ESI†). This indicates SAMs of similar surface coverage in both cases. Dip-coating is more suitable for large-area application and conformal coating of textured or rough substrates, while spin-coating is useful for high-throughput optimization in laboratory workflows.

The SAM films obtained from both methods show similar properties in reflection–absorption infrared spectra (RAIRS) measured on ITO substrates as presented in Fig. 2. RAIRS is a molecule-specific, surface-sensitive technique, which allows for probing the structure and bonding of adsorbed molecules on metallic substrates with sub-monolayer sensitivity.[65] Here we use the reflection signal (R), normalized to the signal of a bare ITO substrate (R_0), to detect the absorption bands of the molecular vibrational modes of the SAM components. By comparing to density functional theory (DFT) calculations (see Fig. S4 and S5, ESI†) and previous reports,[66–70] we assign the individual absorption bands to the specific molecular bonds. In general, the observed bands fit to the ones expected from the molecular structure of the SAM molecules. For instance, in the **V1036** spectrum in Fig. 2a, the strong band near 1511 cm^{-1} can be assigned to C=C in-plane stretching vibrations of aromatic rings of the carbazole structure with some contribution from C=C in-plane stretching vibrations of *p*-methoxy-phenyl groups.[66–68,70] The second strongest band of **V1036** near 1246 cm^{-1} can be associated with C–N stretching vibrations.[67,68] Both **MeO-2PACz** and **2PACz** exhibit two bands located near 1490–1494 cm^{-1} and 1466–1483 cm^{-1} which are associated with carbazole ring stretching vibrations. Characteristically, **2PACz** exhibits two carbazole ring stretching modes at 1242 and 1347 cm^{-1} and **MeO-2PACz** a frequency mode at 1582 cm^{-1} that is associated with the asymmetric stretching vibration of rings with adjacent methoxy groups.[69]

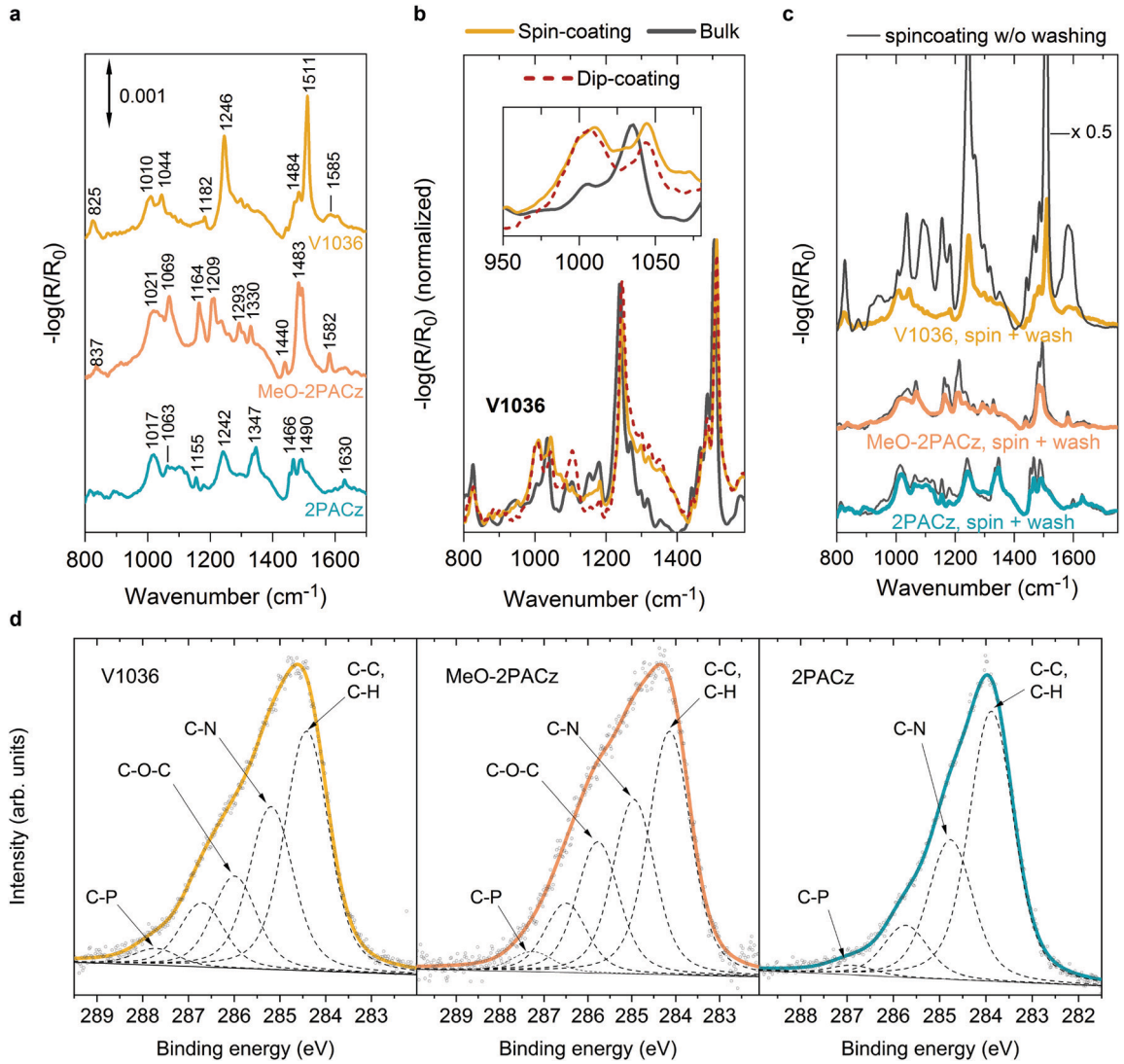

Fig. 2 Infrared and X-ray spectroscopic characterizations of SAM-coated ITO substrates. (a–c) FTIR spectrum of the SAM molecule bulk material and reflection–absorption infrared spectra (RAIRS) of monolayers on Si/ITO substrates. (a) Spectra of **V1036**, **MeO-2PACz** and **2PACz** from spin-coating on Si/ITO substrates, after washing with ethanol and chlorobenzene. (b) Comparison between **V1036** bulk material *vs.* SAM formation from spin-coating and dip-coating. Inset: Detail spectrum in which the monolayer fingerprint (P–O to metal bond) is visible as a broad peak at 1010 cm^{-1}. (c) Effect of the washing step on the RAIRS spectra on spin-coated SAMs. **MeO-2PACz** and **2PACz** already show the monolayer fingerprint without washing. (d) X-ray photoelectron spectroscopy (XPS) spectra of the C1s region, in which the solid line shows the fit to the data and the dotted lines show the components thereof. The additional methoxy group that defines **MeO-2PACz** in comparison to **2PACz** is visible as an additional peak near 286 eV that is assigned to carbon species in C–O–C bonds.

Importantly, the RAIR spectra show a signature of monolayer formation by detection of the bound PA functional group, which is the covalent link between hole-transporting fragment and metal oxide. In our previous work, we concluded the absence of multilayers by comparing absorption measurements to optical simulations.[44] This conclusion is further supported by the shown RAIRS analysis. Fig. 2b presents the RAIR spectra for molecules of **V1036**, comparing monolayers on ITO that are derived from spin- and dip-coating, *versus* the bulk Fourier-transform infrared (FTIR) spectrum obtained from the powder pressed into a KBr tablet. While the main spectral features are the same for all three materials, the monolayers, in contrast to the bulk material, exhibit a broad feature in the RAIR spectrum at 1010 cm^{-1} (see inset in Fig. 2b). Both monolayers formed from spin- and dip-coating of **V1036** show this band, while the bulk material of **V1036** only shows a small shoulder and a slightly shifted spectrum compared to the monolayer spectrum. In conjunction with previous reports,[71–74] we can assign the peak at 1010 cm^{-1} to P–O species bound to ITO. The appearance of this peak, together with the disappearance of the P–OH peak that is prominent in the bulk material at $\sim$950 cm^{-1} (see Fig. S4 and S5, ESI†), provides evidence for deprotonation of the phosphonic anchoring group and monolayer formation.

After spin-coating the SAM solution and heating the substrates at 100 °C for 10 min, the substrates are typically washed with the solvent that dissolves the molecules (here ethanol) to remove any molecules that did not bind to the oxide surface. The effect of this is visible in Fig. 2c. Here, the RAIR spectra are shown for ITO samples on which the different SAM solutions were spin-coated, with and without washing the substrates afterwards. For **V1036** (upmost curve), the intensity drops by a factor of $\sim$7 after the washing procedure, and the characteristic P–O absorption shoulder, *i.e.*, the monolayer fingerprint, appears at 1010 cm^{-1}. However, with **MeO-2PACz** and **2PACz**, we notice that the washing step only slightly decreases the intensity of the absorption bands and the monolayer fingerprint is already present without washing. Thus, we conclude that simply spin-coating **MeO-2PACz** and **2PACz** solution with a concentration of roughly 0.5–1 mmol l^{-1} and subsequent heating of the substrate is sufficient for obtaining a monolayer of the material. Indeed, a wide window of concentrations (at least between 0.5 mmol l^{-1} and 3 mmol l^{-1}, see Fig. S3, ESI†) of the solutions is found for which no extra rinsing step is required to obtain equivalently performing PSCs. This large processing window further adds to the simplicity of the here presented process strategy and highlights the robustness of monolayer formation with the new SAMs.

As another surface-sensitive technique, we utilized X-ray photoelectron spectroscopy (XPS) to detect the atomic species on the SAM-coated substrates. Fig. 2d shows the X-ray photoelectron spectra in the C1s binding energy region of the investigated SAMs on glass/ITO substrates. While the bare ITO substrate shows almost no signal in this region (see Fig. S14, ESI†), the SAM-coated substrates show characteristic signals that can be fitted with 4–5 peaks with a mixed Lorentzian/Gaussian lineshape and a linear background. The strongest peak can be assigned to aromatic carbon (C–C, C–H) with relative peak areas of 0.57, 0.38 and 0.42 compared to the area of the sum of all peaks for **2PACz**, **MeO-2PACz** and **V1036** respectively, each indicating the ratio of the atomic specie to the sum of atoms in the molecule structure. The second strongest peak arises from carbon atoms bonded to nitrogen (C–N), with relative peak areas of around 0.3, 0.27 and 0.28 for **2PACz**, **MeO-2PACz** and **V1036**, respectively. For **MeO-2PACz** and **V1036**, an additional peak is present compared to **2PACz** (0.21 relative peak area for **MeO-2PACz** and 0.16 for **V1036**), at an energy corresponding to ether functional groups.[75] In this case, it can be assigned to C atoms in C–O–C bonds, since methoxy groups are present only for **MeO-2PACz** and **V1036**. This is in conjunction with an additional analysis of the Oxygen specie in Fig. S12 of the ESI.† Regarding the peak between the respective C–O–C and C–P assignments, we hypothesize that it might stem from the C atoms bonded to three other C atoms in the carbazole fragment (4a and 4b positions). Overall, the trend of relative peak areas compared between the different SAMs is in line with the counts of atoms in the molecule structures depicted in Fig. 1c–e.

Perovskite solar cell performance

For comparing the performance and device-relevant characteristics of SAM-based solar cells, we chose to focus our analysis on the so called "triple cation" perovskite absorber[76] $Cs_5(MA_{17}FA_{83})_{95}Pb(I_{83}Br_{17})_3$ (CsMAFA), which is widely used due to its high reproducibility. The various hole-selective contacts (HSCs) are compared using the device design as shown in Fig. 1a. Since the polymeric hole transport material PTAA is currently being used in the highest-performing p–i–n PSCs,[27,34,36] we compare the SAM-based cells to PTAA-based PSCs and analyze the perovskite film and device properties. To keep the devices as simple as possible, the SAM and PTAA cells do not contain any interfacial compatibilizers, additives or doping. As such, our PTAA control cells are comparable to state-of-the art ones as found in literature.[27,77]

Fig. 3a shows *J–V* characteristics under simulated AM 1.5G illumination of best PSCs obtained on the respective HSCs in forward (J_{SC} to V_{OC}) and reverse scan (V_{OC} to J_{SC}) direction, with continuous maximum power point (MPP) tracks in the inset. Their photovoltaic parameters are summarized in Table 1. A statistical comparison of the PCEs is plotted in Fig. 3c with 41–53 solar cells per HSC (other device metrics in Fig. S7 in the ESI†). From the *J–V* curves, we obtain that hysteresis is overall negligible with MPP-tracked efficiencies close to the respective *J–V* scan values and the fill factor (FF) is overall comparable at around 80% between all PSCs. Fig. 3b displays the external quantum efficiencies (EQEs) of the best devices as well as the integrated product of EQE and AM 1.5G spectrum. The J_{SC} values from EQE integration have a negligible difference to the J_{SC} values obtained from the *J–V* scans ($\sim$1%). The most striking difference between the HSCs is visible in the open-circuit voltage (V_{OC}), with a difference of 63 mV between PTAA and **2PACz**. For the most efficient **2PACz** solar cell, a V_{OC} of $\sim$1.19 V is measured, which is among the highest for this perovskite composition and device architecture, and the

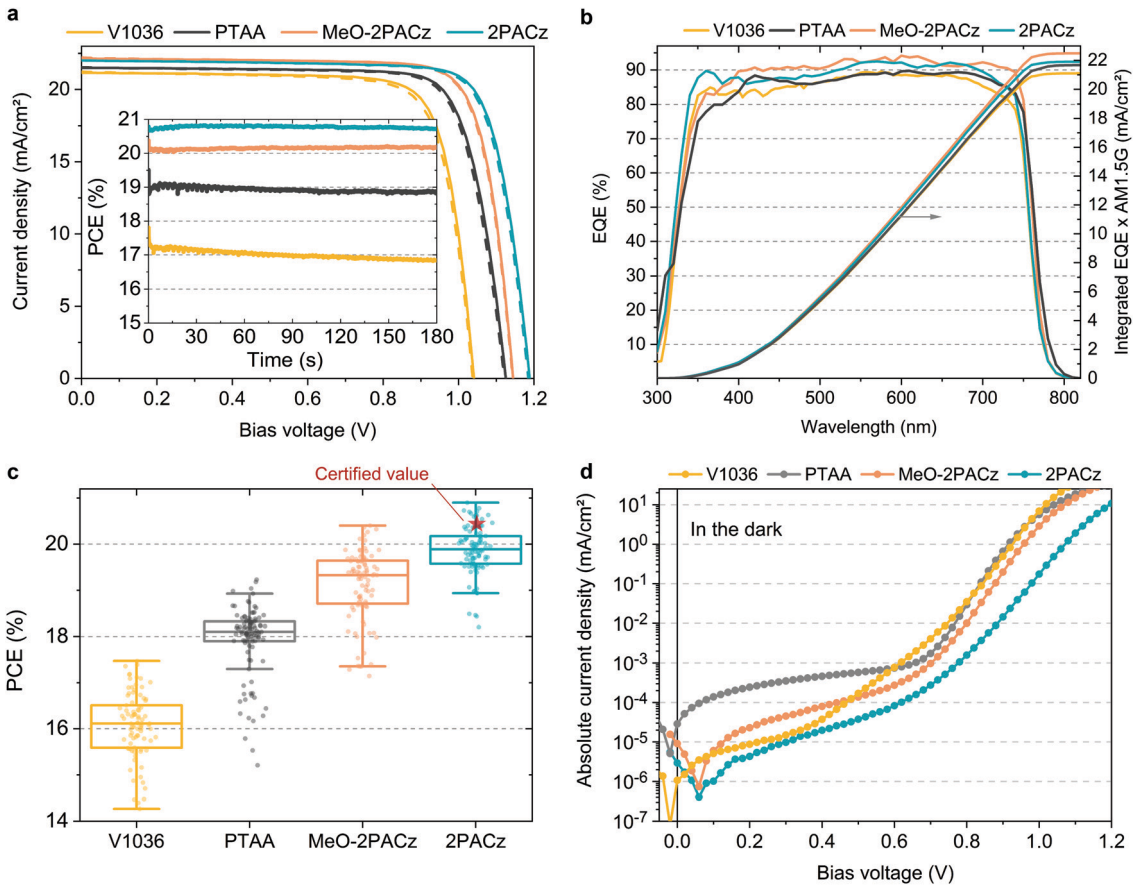

Fig. 3 Device-related analysis of SAM-based solar cells in comparison to state-of-the-art PTAA solar cells with triple cation perovskite absorber. (a) *J*–*V* curves under simulated AM 1.5G illumination at a scan rate of 250 mV s^{-1} in forward (J_{SC} to V_{OC}, dashed) and reverse scan (V_{OC} to J_{SC}, solid) with respective MPP tracks in the inset. (b) External quantum efficiency (EQE) spectra of best solar cells and corresponding integration of the product of EQE and AM 1.5G spectrum (right axis). (c) Box plot of power conversion efficiency (PCE) values for 41 **V1036**, 53 PTAA, 47 **MeO-2PACz** and 46 **2PACz** solar cells. (d) Typical *J*–*V* curves measured under dark conditions of the respective hole-selective contacts.

Table 1 Photovoltaic parameters from *J*–*V* scans under illumination in reverse scan direction together with the efficiency of MPP tracking of best CsMAFA perovskite solar cells based on the different investigated hole-selective contacts

HSC	J_{SC} (mA cm^{-2})	J_{SC}_EQE (mA cm^{-2})	V_{OC} (V)	FF (%)	PCE (*J*–*V*) (%)	PCE (MPP) (%)
V1036	21.2	21.1	1.041	79.3	17.5	16.9
PTAA	21.5	21.7	1.125	79.3	19.2	18.9
MeO-2PACz	22.2	22.5	1.144	80.5	20.4	20.2
2PACz	21.9	21.9	1.188	80.2	20.9	20.8

highest for CsMAFA cells without interlayers, dopants or additives. Overall, the PCE trend resembles the increase in V_{OC} and both **MeO-2PACz** and **2PACz** solar cells surpass the efficiency of PTAA cells, with **2PACz** yielding the highest efficiency of 20.9% in *J*–*V* scan and 20.8% in the maximum power point (MPP) track. One of the **2PACz** cells was masked, encapsulated and sent to Fraunhofer ISE for certification (see Fig. S23–S25 (ESI†) and red star in Fig. 3c). The certified MPP performance of 20.44% is close to our in-house measurement of 20.7% of that specific cell, validating our analysis. Interestingly, all SAM-based cells show a lower leakage current compared to a champion PTAA cell with a ~10 nm thick PTAA polymer film (see Fig. 3d). This finding demonstrates that the formed SAMs are dense enough (with regard to number of molecules per surface area) to provide efficient rectification, even though this is just one molecular layer covering the ITO surface.

Energetic alignment

As shown above, both **2PACz** and **MeO-2PACz** enable higher V_{OC} values in solar cells compared to PTAA. Changes in V_{OC} can have a variety of origins, most importantly changes of the bulk properties and of the non-radiative recombination velocities at one or both interfaces. The latter can be caused by either a higher selectivity due to more favorable energetic alignment and/or less defect states at one or both interfaces to the respective charge-selective contacts. Changes in the bulk properties (*e.g.*, density of trap states) could be caused by altered crystallization of the perovskite film. Since the perovskite film crystallizes on top of various HSCs here, the morphology of the perovskite is analyzed with scanning electron microscopy (SEM) images and X-ray diffraction (XRD) patterns (Fig. S9 and S10, ESI†). No obvious differences in the grain morphology and X-ray diffractograms are observed. Moreover, we estimate

the so-called Urbach energy, which is given by the slope of the exponential increase of the absorption edge,[2,78] to be around 16 ± 2 meV measured on PSCs based on all four HSCs (obtained from EQE, see Fig. S11, ESI†). The Urbach energy is a measure of electronic disorder in the absorber material, and has been associated with the crystalline quality of lead halide perovskite thin films.[79,80] Thus, since we observe neither significant differences in the Urbach energy, XRD, nor coarse grain morphology between the perovskites grown on the investigated HSCs, we conclude that the HSCs do not significantly alter the bulk film properties of the herein used CsMAFA perovskite.

To assess the energetic properties of the studied HSCs in relation to the perovskite absorber, we performed ultra-violet photoelectron spectroscopy (UPS) on ITO/HSC and on CsMAFA samples. We can thus compare the positions of the HSC's HOMO (highest occupied molecular orbital) to the perovskite's valence band maximum (VBM). Furthermore, adding the band gaps of the materials estimated from the absorption edge (Fig. 1b), we can also calculate the positions of the HSC's LUMO (lowest unoccupied molecular orbital) and compare it to the perovskite's conduction band minimum, CBM. The spectra are shown in Fig. S18 and S19 (ESI†) and a summary of the results is schematically displayed in Fig. 4a, referenced to the vacuum level. The valence band or HOMO onset values are given in the lowermost row and the work function (*i.e.*, difference between vacuum and Fermi level) values in the upmost row.

All SAMs show a p-type character in the energetic diagram. Comparing the valence band onset of the perovskite absorber to the HOMO levels of the HSC layers, it is apparent that **MeO-2PACz** and **2PACz** are energetically more hole-selective than PTAA, due to the higher energetic barrier for electrons,

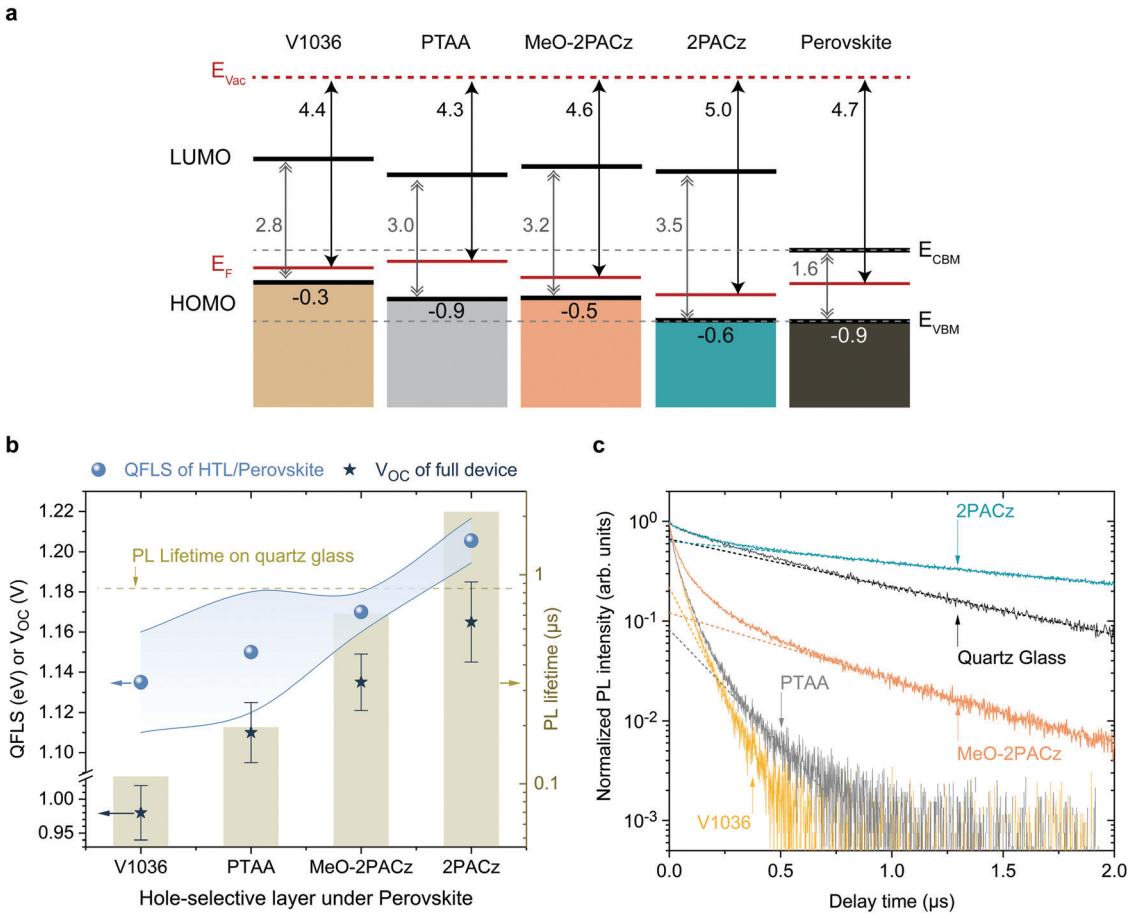

Fig. 4 Energetic alignment and Photoluminescence analysis on CsMAFA perovskite. (a) Schematic representation of the band edge positions of the investigated HSCs based on values from UPS measurements, referenced to the vacuum level. The lowermost numbers indicate the difference between Fermi level (E_F) of the ITO substrate and HOMO level or valence band maximum (E_{VBM}) (in eV, global error of ~0.1 eV). The energetic distance between conduction band minimum (E_{CBM}) or LUMO and E_{VBM} was estimated from the onset of optical absorption. The grey, dashed lines are guides to the eye that mark the CBM and VBM levels of the perovskite absorber. (b) Summary of absPL and TrPL measurements. Left axis: average V_{OC} values of solar cells (stars) based on the different HSCs, together with the average quasi Fermi level splitting values (QFLSs, blue spheres) obtained from perovskite films grown on the respective HSCs. The blue filling indicates the span between maximum and minimum QFLS values obtained from several samples (3 **V1036**, 5 PTAA, 8 **MeO-2PACz** and 9 **2PACz** samples). The V_{OC} error bars show the standard deviation from values of 38 **V1036** cells, 56 PTAA cells, 42 **MeO-2PACz** cells and 40 **2PACz** cells. Right axis: the light-green bars represent the highest obtained PL decay time; the decay time of the perovskite on quartz glass is indicated as a dashed line. (c) Photoluminescence transients of perovskite films deposited on the respective HSCs. The dotted lines are extrapolated fits to the mono-exponential tail of the transients, from which the PL decay time values are obtained.

while still allowing for an efficient extraction of holes (no barrier). **2PACz** shows the closest alignment to the valence band maximum (VBM) of the perovskite, whereas **V1036** shows the strongest offset. In this respect, **MeO-2PACz** is similar to PTAA, while the presence of methoxy groups in **MeO-2PACz** suggests a passivating function, as reported in earlier works.[81,82] Changes in ITO work function with PA-based SAMs have been thoroughly analyzed in literature.[71,83,84] In our case, the binding type between the studied SAMs is the same, thus differences between the work functions can be assigned to differences of the molecular dipole moments of the hole-selective fragments.[85,86] The shift in work function between bare ITO (4.6 eV, see Fig. S18a, ESI†) and the SAM-modified surface is higher for **2PACz** as compared to **MeO-2PACz**, being 5.0 and 4.6 eV, respectively. This is in line with the larger molecular dipole moment of **2PACz** of +2 D compared to +0.2 D for **MeO-2PACz** (calculated by DFT following a previously published procedure,[56] more details in the ESI†). **V1036** has a negative calculated dipole moment of −2.4 D, reducing the ITO work function to 4.4 eV. Judging from this energetic picture, the observed trend in V_{OC} could potentially be explained with how close the HOMO of the HSCs is aligned to the perovskite's VBM.[87] **V1036** devices show the smallest V_{OC} and **V1036** the largest offset in E_{VBM} (0.9 eV), whereas **2PACz** yields the highest V_{OC} and shows almost no offset to the perovskite's VBM.

Photoluminescence studies

The energetic alignment discussed above already provides a first hint to why PSCs based on the new SAMs outperform those on PTAA. However, it remains unclear how the bands align to each other at the buried interface between the HSC and perovskite itself. Recent reports also point to an insensitivity of the energetic difference in E_{VBM} between perovskite and HSC for moderate misalignment.[88] Thus, we further investigate the differences with photoluminescence (PL) studies, using time-resolved PL (trPL) to study the behavior of the charge carriers on short time scales and absolute PL (absPL) to estimate the "implied V_{OC}" or quasi Fermi level splitting (QFLS)[89] of the bare absorber computed by the high-energy tail fit method[27,90,91] for a temperature of 300 K. The PL measurements were conducted on glass/ITO/HSC/CsMAFA samples without the C_{60} overlayer. The QFLS was also determined from the full **2PACz** solar cell that is shown in Fig. 3a, with negligible difference to the eV_{OC} value obtained from a *J–V* scan (see Fig. S20, ESI†).

Fig. 4b shows a summary of the QFLS values from absPL (blue spheres) on the left axis, together with average values of measured V_{OC} (stars) of the full devices. The right axis presents PL decay times from TrPL (bars), calculated from Fig. 4c, in comparison to the PL decay time for a perovskite film on quartz glass (dashed line), which is known as a highly passivated surface.[27,92] The rising trend in average QFLS from **V1036** over PTAA to **MeO-2PACz** and **2PACz** fits to the trend in V_{OC}. Compared to **V1036** and PTAA, the spread of QFLS values is smaller with **MeO-2PACz** and **2PACz**. The TrPL transients are plotted in Fig. 4b and were recorded at an excitation fluence that is relevant for device operation at 1 sun illumination (fluence ∼15–30 nJ cm^{-2}, see PL section in ESI†). The PL measured on the perovskite film on glass decays mono-exponentially. The deviation from mono-molecular decay in the measurements with HSCs could be attributed to charge transfer effects.[93] **MeO-2PACz** allows for PL decay times of over 650 ns, which approaches the decay time of the same perovskite on quartz glass of ∼860 ns, a comparable value to the ones previously reported for the same perovskite in record-efficiency PSCs.[27] Interestingly, the decay time on **2PACz** with a value of 2 μs even surpasses the one on quartz glass by a factor of over 2. Since the **2PACz** PL transient shows signs of slow charge transfer, the significantly longer decay time cannot be attributed to a mere reduction of majority carriers at the interface. We thus conclude that the interface defect density must be negligibly low, highlighting that bare Carbazole is chemically compatible to the perovskite, forming a well-passivated surface. A direct comparison to **MeO-2PACz** with regard to interface defect density is not possible from the TrPL data alone, since an energetic offset can independently affect interfacial recombination.[94] However, the faster decay at early times suggests faster hole extraction. With the only difference between **MeO-2PACz** and **2PACz** being the termination with a methoxy group, it is interesting to observe such an intrinsically different behavior in the charge carrier dynamics.

Comparing the values obtained on PTAA and on **2PACz**, the decay times differ by an order of magnitude, and both the QFLS and V_{OC} values are around 60 mV higher with **2PACz**. This fits to the thermodynamically expected increase of 60 mV when increasing the photoluminescence yield by a factor of 10, with $kT\ln(10) \approx 60$ meV, where k is the Boltzmann constant and T the temperature (300 K).[95] We emphasize that the FF values of the full solar cells are comparable among all HSCs, suggesting similarly efficient charge extraction. Thus, we conclude that the trend in PL decay time is set by the non-radiative recombination velocity at the interface. Assuming that interface recombination is dominating, the recombination velocities can be estimated to range from 193 cm s^{-1} (**V1036**) to a lowest value of 12 cm s^{-1} for **2PACz** (upper estimate, see Section 8 for details, ESI†). The clear correlation between QFLS, PL decay time and V_{OC} provides a strong indication that the differences in V_{OC} of the solar cells are originating from differences in the compatibility of the HSC interface to the perovskite. This is either governed by the interface defect density, energetic alignment as addressed above, or a combination of both. It remains open whether the molecular dipole moments play a role other than the mentioned work function modifications. The energetic difference between QFLS and eV_{OC} with all HSCs is induced by non-radiative recombination at the perovskite/C_{60} interface (see also Fig. S20, ESI†). Previously it was identified that the perovskite/C_{60} interface limits the V_{OC} to a fixed value in the used PSC architecture, independent of the perovskite bulk quality.[27] Indeed, our PTAA devices achieve max. ∼1.13 V, even though the perovskite on PTAA can reach a QFLS of up to 1.18 eV. It is thus interesting that by increasing the hole-selectivity and decreasing the interface recombination velocity, the 1.13 V limitation can be overcome although the perovskite morphology stays the same. It is furthermore worth noting that

a recent study that compared a wide variety of typically used charge-selective layers identified that every single layer introduces non-radiative losses compared to the bare perovskite bulk, lowering the PL decay time and QFLS.[94] In sharp contrast, the herein introduced **2PACz** HSC is an important demonstration that the opposite is possible as well, rendering a "lossless" hole-selective interface. With SAM contacts, further enhancement of the V_{OC} to a level of the QFLS of the bare perovskite film or above is expected upon mitigating the losses introduced at the C_{60} interface.

To conclude our analysis, we identified several aspects as to why the herein introduced molecules lead to high-performance PSCs, besides the already discussed dense film-forming properties. Consequently, a clear guidance could be drawn from our findings to develop other lossless contact materials in the near future: on the one hand, the structure of these small molecules leads to a small density of interfacial trap states as seen by the comparison of quartz glass to **2PACz**-covered ITO and by the comparison of PTAA to **MeO-2PACz**. On the other hand, as shown by simulations of a similar device stack in a recent work,[94] our own energetic alignment data and other experimental studies,[96–100] energetic alignment for majority carrier extraction influences interfacial recombination losses and is a crucial factor for achieving high V_{OC} values. The strong correlation in our SAM model system (layers with similar carbazole chemistry and similar thickness, but different HOMO levels) indicates that by using carbazole derivatives and tuning the work function by dipole moment engineering, ideal hole-selective layers could be rationally designed for specific perovskite absorbers. Further investigations on the exact hole extraction mechanisms at a SAM interface might include simulations of the electric field in atomic scales,[84] tunneling of charge carriers and atomistic simulations on the interaction between dipole moment and perovskite interface.

Stability assessment

In addition to the increased efficiencies of both **MeO-2PACz** and **2PACz**-based solar cells compared to PTAA, we also observe an increased stability. Fig. 5a shows the time evolution of PCE under continuous MPP tracking for the investigated HSCs at simulated 1 sun AM 1.5G illumination without active sample cooling. The samples reach temperatures of at least 40 °C under operation. Only small differences are visible between cells with the investigated HSCs, while a slight advantage is evident for the **MeO-2PACz** and **2PACz**-based devices after 11 h of operation (<3% PCE loss with **2PACz** with a stable value after an initial drop, ~3% loss with **MeO-2PACz**, ~6% loss with PTAA and almost 12% loss with **V1036**). A stronger difference is visible when increasing the stress on the solar cells, which is done here by light soaking at open-circuit condition under 1 sun illumination, a condition at which a high average density of charge-carriers is present in the device that can induce a quick degradation of the PSC.[101] The most notable differences occur in the time evolution of V_{OC}, as displayed in Fig. 5b. PTAA-based solar cells show a substantial drop (60 mV amplitude) after two hours, while the V_{OC}s of all SAM-based cells remain virtually stable after an initial drop caused by increasing temperature. Interestingly, light soaking steadily improves the V_{OC} of **V1036**-based samples. The difference in stability between PTAA and SAMs under illumination cannot simply be explained with the differences in non-radiative recombination rates at the interface, since judging by QFLS and PL decay time, **V1036** should then show the weakest V_{OC} stability. We attribute the quick degradation of PTAA-based cells to be a material-specific characteristic of the CsMAFA/PTAA contact that occurs under conditions with a high number of excess charge carriers and direct illumination of the PTAA, as also observed in a recent work.[102] A previous study identified that a large number of excess charge carriers, as under illumination at open-circuit, leads to a lowered energetic threshold of ionic movement.[101] We hypothesize that the diffusion of iodine to the PTAA interface leads to structural damage of the PTAA, as recently argued by Sekimoto *et al.*[103] In contrast, a SAM, being a chemically robust electrode modification with virtually no volume, is

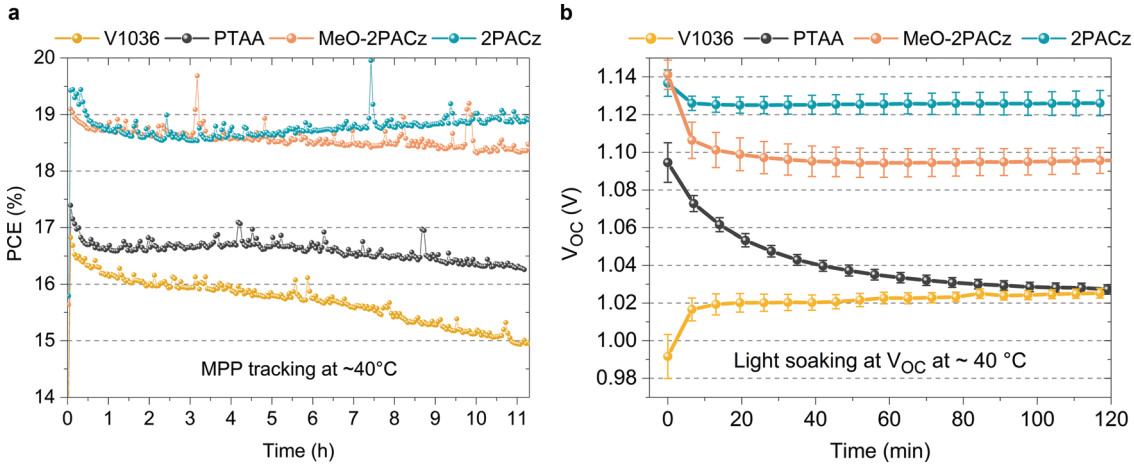

Fig. 5 Stability assessments of PSCs based on the investigated HSCs in N_2 atmosphere. (a) MPP tracking under continuous, simulated 1 sun AM 1.5G illumination of uncooled devices (reaching a temperature of ~40 °C in operation). (b) Time evolution of V_{OC} values of solar cells kept at open-circuit conditions under light-soaking at full sun illumination at ~40 °C cell temperature (no active cooling). The values were extracted from *J*–*V*-scans every 6–8 min. The error bars show the standard deviation of these values across the individual cells (4 **V1036**, 6 PTAA, 3 **MeO-2PACz** and 10 **2PACz** cells).

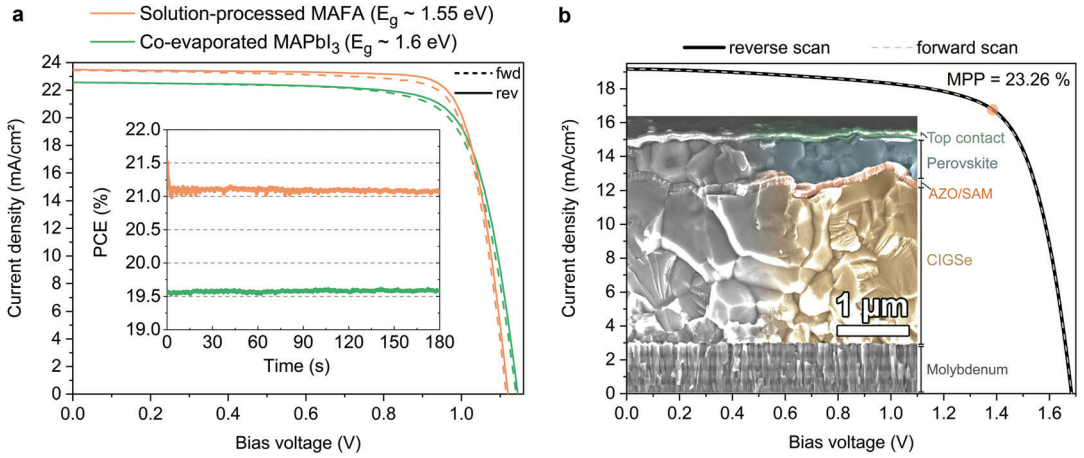

Fig. 6 Display of the versatility of SAM contacts and tandem solar cell integration. (a) *J–V* curves under illumination of solar cells based on a solution processed "double cation" perovskite absorber ($FA_{95}MA_5Pb(I_{95}Br_5)_3$, orange line) and co-evaporated perovskite absorber ($MAPbI_3$, green line). Inset: Continuous MPP tracks of these cells. (b) *J–V* curve of a monolithic CIGSe/perovskite tandem solar cell (active area of 1.034 cm^2), with **MeO-2PACz2PACz** as HSC conformally covering the rough CIGSe bottom cell. The orange circle indicates the MPP at 23.26% PCE (see certified MPP track by Fraunhofer ISE in Fig. S27, ESI†). Inset: SEM image of the cross-section of a representative tandem device. The recombination contact consists of aluminum-doped zinc oxide, sputtered onto the CIGSe surface and covered by **MeO-2PACz**.

neither susceptible to structural damages nor to an accumulation of ions.

Versatility of a SAM contact and tandem solar cell integration

In order to show versatility of the new HSC molecules, we demonstrate in Fig. 6 that the SAMs also yield highly efficient perovskite solar cells with perovskite compositions other than CsMAFA. In addition to the "triple cation" composition utilized for the analysis above, we investigate here a "double cation" $MA_5FA_{95}Pb(I_{95}Br_5)_3$ (MAFA)[8] absorber with a lower band gap of *ca.* 1.55 eV and a "single cation" ($MAPbI_3$) absorber layer that is fabricated by direct co-evaporation with an optical band gap of *ca.* 1.60 eV (see Fig. S26 for the absorption onset, ESI†). Table 2 shows the corresponding performance metrics. We noticed that on **MeO-2PACz**, the MAFA and $MAPbI_3$ perovskites tend to crystallize more reproducibly than on **2PACz**, thus we chose **MeO-2PACz** for the purpose of demonstrating that a SAM enables a broad spectrum of applications.

Perovskite processing by co-evaporation is highly attractive due to large-area compatibility and absence of potentially harmful solvents for fabrication. Utilizing **MeO-2PACz** as the HSC also works well with the co-evaporated $MAPbI_3$ perovskite absorber. The herein shown stabilized PCE of 19.6% with over 1.14 V V_{OC} is approaching the PCE of the best co-evaporated PSC to date and represents the highest reported value for p–i–n type devices utilizing co-evaporation for the perovskite absorber.[104,105]

Recently, highest PSC performances were reported for the MAFA double cation composition.[15,106] Compared to the CsMAFA solar cells shown before, the MAFA cell has an advantage in higher current density due to the lower bandgap of the composition, but still enables a relatively high V_{OC}. Without detailed optimization, the MAFA absorber enables a stabilized PCE of 21.1% when utilizing **MeO-2PACz** as the HSC. As seen in Table 2, for all three solar cells the J_{SC} values measured in the *J–V* curve closely fit to the values obtained by integrating the product of EQE measurement and AM 1.5G spectrum (Fig. S26a, ESI†). **2PACz** enables an over 21%-efficient MAFA PSC as well, as shown in Fig. S27 (ESI†).

Furthermore, we show in Fig. 6b that a SAM is also a suitable HSC for manufacturing PSCs on rough surfaces, which is essential for *e.g.*, CIGSe/perovskite tandem solar cells. All-thin-film tandem solar cells pose an attractive strategy for cheap, versatile and flexible high-efficiency solar cells and are a promising route for the introduction of halide perovskites into industrial production. CIGSe enables thin-film solar cells with a suitable bandgap for the use in perovskite-based tandem solar cells. However, the rough surface of the CIGSe makes it difficult to process the thin HSCs that currently enable efficient perovskite top cells. Recently, we demonstrated that the use of a NiO_x layer processed by atomic layer deposition (ALD) in combination with PTAA represents a CIGSe/perovskite-compatible hole-transport layer that prevents shunting caused by the CIGSe roughness, enabling a 21.6%-efficient tandem cell.[47] Here we now show that a SAM removes the need of an ALD step, since the self-assembly process works reliably even on rough surfaces, by dipping the CIGSe bottom cell into a **MeO-2PACz** solution. The perovskite layer was fabricated by solution-processing and the top contact layers by either evaporation or ALD/sputtering (see ESI† for details). The so prepared tandem solar cell, shown in Fig. 6b, shows a stabilized efficiency of 23.26% on an area of 1.03 cm^2 (certified by Fraunhofer ISE, see Fig. S30–S32, ESI†), while the bottom cell alone has a PCE of 15–16% (see Fig. S28, ESI†). The EQEs of both sub-cells measured in the tandem are shown in Fig. S29 (ESI†). Following the V_{OC} trend shown earlier, our SAM-based tandem shows an improved V_{OC} as compared to our previously published one (~90 mV increase from 1.59 to 1.68 V). However, the SAM-based tandem cell shows a lower FF (72% *vs.* 76% with the NiO_2/PTAA double layer), which here is mainly limited by the shunt resistance. Since the tandem current is limited

Table 2 Photovoltaic parameters from *J–V* scans under illumination in reverse scan direction as well as continuous MPP tracking. Presented are single cells with double cation MAFA and co-evaporated $MAPbI_3$ perovskite and a CIGSe/perovskite (triple cation) tandem solar cell. All cells are based on **MeO-2PACz** as the HSC

Perovskite	Device type	J_{SC} (mA cm^{-2})	J_{SC}_EQE (mA cm^{-2})	V_{OC} (V)	FF (%)	PCE (*J–V*) (%)	PCE (MPP) (%)
Co-evaporated $MAPbI_3$	Single	22.6	22.5	1.145	76.8	19.8	19.6
Double cation MAFA	Single	23.5	23.4	1.120	80.6	21.2	21.1
Triple cation CsMAFA	Monolithic Tandem	19.17 (certified)	20.2/19.1[a] (in-house)	1.68 (certified)	71.9 (certified)	23.16 (certified)	23.26 ± 0.75 (certified)

[a] First value corresponds to the perovskite top cell and second value to the CIGSe bottom cell.

here by the bottom cell, further optimization could be dedicated to developing a more robust stack design that prevents micro-shunts caused by processing and measuring (here we use the same design as in our previous work[47]). Nonetheless, the here presented tandem cell surpasses the previous record[46] (22.4%) in PCE and area (0.04 cm^2 *vs.* 1.03 cm^2 here). The simplicity of the tandem stack and the use of as-deposited CIGSe additionally suggests that our approach could be easily adopted in higher throughput fabrication.

In summary, the compatibility of the SAM to three different perovskite compositions, two different processing techniques (solution and vacuum process), two different oxides (ITO in the single junctions and Al-doped zinc oxide in the tandem) and two different substrate morphologies (rough and flat) strongly suggests that SAM hole-selective contacts represent a universal approach for perovskite-based photovoltaics.

Conclusion

Two new simple molecules that form self-assembling monolayers (SAMs), **MeO-2PACz** and **2PACz**, were synthesized and integrated into inverted perovskite solar cells, enabling hole-selective contacts with minimized non-radiative losses. The new SAMs can be deposited on transparent conductive oxides *via* spin-coating or by dipping the substrate into the solution, both yielding layers of comparable properties, combining high reproducibility and ease of fabrication. Both new SAMs outperform the polymer PTAA, the material that enabled the highest-performing p–i–n PSCs to date, in efficiency, stability and versatility. With a standard triple-cation absorber, a maximum power conversion efficiency of 20.9%, certified efficiency of 20.44% and a V_{OC} of up to 1.19 V were demonstrated. **MeO-2PACz** further enabled a 21.1%-efficient solar cell with a double-cation absorber, and a stabilized efficiency of 19.6% with a co-evaporated single-cation absorber. Photoelectron spectroscopy and photoluminescence (PL) investigations revealed a well-suited energetic alignment and strongly reduced non-radiative recombination at the interface between absorber and contact, leading to a PL decay time of 2 μs for a perovskite on **2PACz**. As deduced from a comparison between the PL transients of perovskite grown on **2PACz** *versus* on quartz glass, the interface defect density at the **2PACz**/perovskite interface is minimal. From the trend between surface recombination velocity, V_{OC} and offset between the SAM HOMO level and perovskite valence band edge, our model system provides experimental evidence for the energetic alignment and interface defect density being similarly important for mitigating non-radiative recombination losses. The results highlight that carbazole derivatives can combine all necessary features for lossless interfaces and are thus a compelling material class for future chemical engineering of high-performance hole-selective contacts. In a light-soaking stress test at open circuit conditions, SAM-based PSCs showed a higher stability compared to PTAA-based cells. Finally, by integrating a SAM contact into a monolithic CIGSe/perovskite tandem solar cell, the ability of conformally creating a hole-selective layer on a rough surface was demonstrated. This led to a stabilized, certified PCE of 23.26% with facile device design on an active area of 1.03 cm^2, surpassing the values achieved with a complex bilayer[47] or mechanical polishing.[46] Importantly, the herein demonstrated solar cells are fabricated without additional passivation layers, additives or dopants. Together with the minimal material consumption, manifold substrate compatibility and simplicity during fabrication, the SAM contacts might present a realistic way to further progress perovskite photovoltaics into a low-cost, wide-spread technology.

Author contributions

A. A. A., A. M., M. J. and S. A. coordinated the project and designed the experiments. A. M., Er. K. and T. M. designed, synthesized and characterized the SAM molecules. A. A. A. optimized the SAM formation procedures, carried out sample fabrication and solar cell characterization, coordinated data analysis and prepared the manuscript figures. M. T. recorded the RAIRS and FTIR spectra, and calculated the theoretical spectra; M. T., G. N., A. M. and A. A. A. analyzed the data. G. C. measured the UPS and XPS data; A. A. A., A. M. and G. C. analyzed the data. A. A. A. recorded the absolute PL data in a setup designed by J. A. M. and T. U., and, together with S. L., recorded the trPL data in a setup designed by C. J. H., S. L. and T. U. The PL data was analyzed by A. A. A., J. A. M, S. L. and T. U. Fabrication of the co-evaporated solar cell was carried out by M. R.; M. R. and L. G. E. optimized the co-evaporation process. A. A. A. and M. J. processed the CIGSe/perovskite tandem solar cell, with optimization of the top contact by Ei. K. The CIGSe bottom cell was fabricated by T. B. and C. K. All authors contributed to manuscript writing and scientific discussions. B. R., T. U., L. K., G. N., R. S., V. G. and S. A. supervised the project.

Conflicts of interest

There are no competing interests to declare.

Acknowledgements

The authors thank M. Gabernig, C. Ferber, T. Lußky, H. Heinz, C. Klimm and M. Muske at Institute for Silicon Photovoltaics (HZB), T. Hänel, B. Bunn, K. Mayer-Stillrich, M. Kirsch, S. Stutzke and J. Lauche at PVcomB (HZB) for technical assistance. For XPS and UPS measurements, the Energy Materials In-Situ Laboratory (EMIL), R. Wilks and J. Frisch are acknowledged. Funding was provided by German Federal Ministry for Education and Research (BMBF) (grant no. 03SF0540) within the project ''Materialforschung für die Energiewende'', (BMWi) project ''EFFCIS'' (grant no. 0324076B). A. M. and T. M. acknowledge funding by the Research Council of Lithuania under grant agreement no. S-MIP-19-5/SV3-1079 of the SAM project. G. N. gratefully acknowledges the Center of Spectroscopic Characterization of Materials and Electronic/Molecular Processes (SPECTROVERSUM Infrastructure) for use of their FTIR spectrometer. T. B. acknowledges funding from the BMWi project Speedcigs (grant no. 0324095D). The authors acknowledge the HyPerCells graduate school for support and the funding by the Helmholtz Foundation for the HySPRINT Innovation lab which was supported by the Helmholtz Energy Materials Foundry (HEMF). The research leading to these results has partly received funding from the European Union's Horizon 2020 research and innovation programme under grant agreement no. 763977 of the PerTPV project.

References

1 Web of Science search for 'perovskite' AND 'solar' AND 'cells' in the title.
2 S. de Wolf, J. Holovsky, S.-J. Moon, P. Löper, B. Niesen, M. Ledinsky, F. Haug, J. Yum and C. Ballif, *J. Phys. Chem. C*, 2014, **5**, 1035–1139.
3 W. J. Yin, T. Shi and Y. Yan, *Appl. Phys. Lett.*, 2014, **104**(6), 063903.
4 K. X. Steirer, P. Schulz, G. Teeter, V. Stevanovic, M. Yang, K. Zhu and J. J. Berry, *ACS Energy Lett.*, 2016, **1**, 360–366.
5 Z. Liu, L. Krückemeier, B. Krogmeier, B. Klingebiel, J. A. Márquez, S. Levcenko, S. Öz, S. Mathur, U. Rau, T. Unold and T. Kirchartz, *ACS Energy Lett.*, 2019, **4**, 110–117.
6 M. Liu, M. B. Johnston and H. J. Snaith, *Nature*, 2013, **501**, 395–398.
7 Z. Wei, H. Chen, K. Yan and S. Yang, *Angew. Chem., Int. Ed.*, 2014, **53**, 13239–13243.
8 N. J. Jeon, J. H. Noh, W. S. Yang, Y. C. Kim, S. Ryu, J. Seo and S. Il Seok, *Nature*, 2015, **517**, 476–480.
9 A. De Vos, *J. Phys. D: Appl. Phys.*, 1980, **13**, 839–846.
10 S. Albrecht, M. Saliba, J. P. Correa Baena, F. Lang, L. Kegelmann, M. Mews, L. Steier, A. Abate, J. Rappich, L. Korte, R. Schlatmann, M. K. Nazeeruddin, A. Hagfeldt, M. Grätzel and B. Rech, *Energy Environ. Sci.*, 2016, **9**, 81–88.
11 J. P. Mailoa, C. D. Bailie, E. C. Johlin, E. T. Hoke, A. J. Akey, W. H. Nguyen, M. D. McGehee and T. Buonassisi, *Appl. Phys. Lett.*, 2015, **106**(12), 121105.
12 T. Todorov, T. Gershon, O. Gunawan, Y. S. Lee, C. Sturdevant, L. Y. Chang and S. Guha, *Adv. Energy Mater.*, 2015, **5**, 1–6.
13 J. Luo, X. Wang, S. Li, J. Liu, Y. Guo, G. Niu, L. Yao, Y. Fu, L. Gao, Q. Dong, C. Zhao, M. Leng, F. Ma, W. Liang, L. Wang, S. Jin, J. Han, L. Zhang, J. Etheridge, J. Wang, Y. Yan, E. H. Sargent and J. Tang, *Nature*, 2018, **563**, 541–545.
14 G. E. Eperon, T. Leijtens, K. A. Bush, R. Prasanna, T. Green, J. T. W. Wang, D. P. McMeekin, G. Volonakis, R. L. Milot, R. May, A. Palmstrom, D. J. Slotcavage, R. A. Belisle, J. B. Patel, E. S. Parrott, R. J. Sutton, W. Ma, F. Moghadam, B. Conings, A. Babayigit, H. G. Boyen, S. Bent, F. Giustino, L. M. Herz, M. B. Johnston, M. D. McGehee and H. J. Snaith, *Science*, 2016, **354**, 861–865.
15 Q. Jiang, Y. Zhao, X. Zhang, X. Yang, Y. Chen, Z. Chu, Q. Ye, X. Li, Z. Yin and J. You, *Nat. Photonics*, 2019, **13**(7), 460–466.
16 K. Jäger, L. Korte, B. Rech and S. Albrecht, *Opt. Express*, 2017, **25**, A473.
17 K. Bush, A. F. Palmstrom, Z. J. Yu, M. Boccard, R. Cheacharoen, J. P. Mailoa, D. P. McMeekin, R. L. Z. Hoye, C. D. Bailie, T. Leijtens, I. M. Peters, M. C. Minichetti, N. Rolston, R. Prasanna, S. Sofia, D. Harwood, W. Ma, F. Moghadam, H. J. Snaith, T. Buonassisi, Z. C. Holman, S. F. Bent and M. D. McGehee, *Nat. Energy*, 2017, **2**, 1–7.
18 E. Köhnen, M. Jošt, A. B. Morales-Vilches, P. Tockhorn, A. Al-Ashouri, B. Macco, L. Kegelmann, L. Korte, B. Rech, R. Schlatmann, B. Stannowski and S. Albrecht, *Sustainable Energy Fuels*, 2019, **3**, 1995–2005.
19 J. Y. Jeng, Y. F. Chiang, M. H. Lee, S. R. Peng, T. F. Guo, P. Chen and T. C. Wen, *Adv. Mater.*, 2013, **25**, 3727–3732.
20 M. Saliba, M. Stolterfoht, C. M. Wolff, D. Neher and A. Abate, *Joule*, 2018, **2**, 1019–1024.
21 A. Magomedov, E. Kasparavičius, K. Rakstys, S. Paek, N. Gasilova, K. Genevičius, G. Juška, T. Malinauskas, M. K. Nazeeruddin and V. Getautis, *J. Mater. Chem. C*, 2018, **6**, 8874–8878.
22 F. Lamberti, T. Gatti, E. Cescon, R. Sorrentino, A. Rizzo, E. Menna, G. Meneghesso, M. Meneghetti, A. Petrozza and L. Franco, *Chem*, 2019, 1–12.
23 E. Kasparavicius, A. Magomedov, T. Malinauskas and V. Getautis, *Chem. – Eur. J.*, 2018, **24**, 9910–9918.
24 J. H. Heo, H. J. Han, D. Kim, T. K. Ahn and S. H. Im, *Energy Environ. Sci.*, 2015, **8**, 1602–1608.
25 P. Docampo, J. M. Ball, M. Darwich, G. E. Eperon and H. J. Snaith, *Nat. Commun.*, 2013, **4**, 1–6.
26 M. Kaltenbrunner, G. Adam, E. D. Głowacki, M. Drack, R. Schwödiauer, L. Leonat, D. H. Apaydin, H. Groiss, M. C. Scharber, M. S. White, N. S. Sariciftci and S. Bauer, *Nat. Mater.*, 2015, **14**, 1032–1039.
27 M. Stolterfoht, C. M. Wolff, J. A. Márquez, S. Zhang, C. J. Hages, D. Rothhardt, S. Albrecht, P. L. Burn, P. Meredith, T. Unold and D. Neher, *Nat. Energy*, 2018, **3**, 847–854.

28 J. Seo, S. Park, Y. Chan Kim, N. J. Jeon, J. H. Noh, S. C. Yoon and S. Il Seok, *Energy Environ. Sci.*, 2014, **7**, 2642–2646.
29 C. M. Wolff, F. Zu, A. Paulke, L. P. Toro, N. Koch and D. Neher, *Adv. Mater.*, 2017, **29**, 1–8.
30 Q. Wang, Q. Dong, T. Li, A. Gruverman and J. Huang, *Adv. Mater.*, 2016, **28**, 6734–6739.
31 X. Liu, Y. Zhang, L. Shi, Z. Liu, J. Huang, J. S. Yun, Y. Zeng, A. Pu, K. Sun, Z. Hameiri, J. A. Stride, J. Seidel, M. A. Green and X. Hao, *Adv. Energy Mater.*, 2018, 1800138.
32 J. Lee, H. Kang, G. Kim, H. Back, J. Kim, S. Hong, B. Park, E. Lee and K. Lee, *Adv. Mater.*, 2017, **29**, 1–8.
33 X. Zheng, B. Chen, J. Dai, Y. Fang, Y. Bai, Y. Lin, H. Wei, X. C. Zeng and J. Huang, *Nat. Energy*, 2017, **2**, 17102.
34 D. Luo, W. Yang, Z. Wang, A. Sadhanala, Q. Hu, R. Su, R. Shivanna, G. F. Trindade, J. F. Watts, Z. Xu, T. Liu, K. Chen, F. Ye, P. Wu, L. Zhao, J. Wu, Y. Tu, Y. Zhang, X. Yang, W. Zhang, R. H. Friend, Q. Gong, H. J. Snaith and R. Zhu, *Science*, 2018, **360**(6396), 1442–1446.
35 P. Caprioglio, F. Zu, C. M. Wolff, J. A. Márquez Prieto, M. Stolterfoht, P. Becker, N. Koch, T. Unold, B. Rech, S. Albrecht and D. Neher, *Sustainable Energy Fuels*, 2019, **3**, 550–563.
36 S. Yang, J. Dai, Z. Yu, Y. Shao, Y. Zhou, X. Xiao, X. C. Zeng and J. Huang, *J. Am. Chem. Soc.*, 2019, **141**(14), 5781–5787.
37 M. Halik and A. Hirsch, *Adv. Mater.*, 2011, **23**, 2689–2695.
38 A. Vilan, D. Aswal and D. Cahen, *Chem. Rev.*, 2017, **117**, 4248–4286.
39 W. C. Bigelow, D. L. Pickett and W. A. Zisman, *J. Colloid Sci.*, 1946, **1**, 513–538.
40 W. B. Russel, *Sci. Technol.*, 2001, **413**, 8257–8263.
41 B. Gothe, T. De Roo, J. Will, T. Unruh, S. Mecking and M. Halik, *Nanoscale*, 2017, **9**, 18584–18589.
42 L. Liu, A. Mei, T. Liu, P. Jiang, Y. Sheng, L. Zhang and H. Han, *J. Am. Chem. Soc.*, 2015, **137**, 1790–1793.
43 Z. Gu, L. Zuo, T. T. Larsen-Olsen, T. Ye, G. Wu, F. C. Krebs and H. Chen, *J. Mater. Chem. A*, 2015, **3**, 24254–24260.
44 A. Magomedov, A. Al-Ashouri, E. Kasparavičius, S. Strazdaite, G. Niaura, M. Jošt, T. Malinauskas, S. Albrecht and V. Getautis, *Adv. Energy Mater.*, 2018, **8**, 1801892.
45 E. Yalcin, M. Can, C. Rodriguez-Seco, E. Aktas, R. Pudi, W. Cambarau, S. Demic and E. Palomares, *Energy Environ. Sci.*, 2019, **12**, 230–237.
46 Q. Han, Y.-T. Hsieh, L. Meng, J.-L. Wu, P. Sun, E.-P. Yao, S.-Y. Chang, S.-H. Bae, T. Kato, V. Bermudez and Y. Yang, *Science*, 2018, **361**, 904–908.
47 M. Jošt, T. Bertram, D. Koushik, J. A. Marquez, M. A. Verheijen, M. D. Heinemann, E. Köhnen, A. Al-Ashouri, S. Braunger, F. Lang, B. Rech, T. Unold, M. Creatore, I. Lauermann, C. A. Kaufmann, R. Schlatmann and S. Albrecht, *ACS Energy Lett.*, 2019, **4**, 583–590.
48 H. Hoegl, *J. Phys. Chem.*, 1965, **69**, 755–766.
49 J. V. Grazulevicius, P. Strohriegl, J. Pielichowski and K. Pielichowski, *Prog. Polym. Sci.*, 2003, **28**, 1297–1353.
50 B. Wex and B. R. Kaafarani, *J. Mater. Chem. C*, 2017, **5**, 8622–8653.
51 M. S. Kang, S. Do Sung, I. T. Choi, H. Kim, M. Hong, J. Kim, W. I. Lee and H. K. Kim, *ACS Appl. Mater. Interfaces*, 2015, **7**, 22213–22217.
52 T. J. Gardner, C. D. Frisbie and M. S. Wrighton, *J. Am. Chem. Soc.*, 1995, **117**, 6927–6933.
53 E. L. Hanson, J. Guo, N. Koch, J. Schwartz and S. L. Bernasek, *J. Am. Chem. Soc.*, 2005, **127**, 10058–10062.
54 S. A. Paniagua, E. L. Li and S. R. Marder, *Phys. Chem. Chem. Phys.*, 2014, **16**, 2874–2881.
55 N. Metoki, L. Liu, E. Beilis, N. Eliaz and D. Mandler, *Langmuir*, 2014, **30**, 6791–6799.
56 I. Lange, S. Reiter, M. Pätzel, A. Zykov, A. Nefedov, J. Hildebrandt, S. Hecht, S. Kowarik, C. Wöll, G. Heimel and D. Neher, *Adv. Funct. Mater.*, 2014, **24**, 7014–7024.
57 R. Quiñones, A. Raman and E. S. Gawalt, *Thin Solid Films*, 2008, **516**, 8774–8781.
58 F. Ambrosio, N. Martsinovich and A. Troisi, *J. Phys. Chem. Lett.*, 2012, **3**, 1531–1535.
59 S. A. Paniagua, A. J. Giordano, O. L. Smith, S. Barlow, H. Li, N. R. Armstrong, J. E. Pemberton, J. L. Brédas, D. Ginger and S. R. Marder, *Chem. Rev.*, 2016, **116**, 7117–7158.
60 Y. Hou, X. Du, S. Scheiner, D. P. McMeekin, Z. Wang, N. Li, M. S. Killian, H. Chen, M. Richter, I. Levchuk, N. Schrenker, E. Spiecker, T. Stubhan, N. A. Luechinger, A. Hirsch, P. Schmuki, H. P. Steinrück, R. H. Fink, M. Halik, H. J. Snaith and C. J. Brabec, *Science*, 2017, **358**, 1192–1197.
61 H. Y. Nie, M. J. Walzak and N. S. McIntyre, *J. Phys. Chem. B*, 2006, **110**, 21101–21108.
62 S. Casalini, C. A. Bortolotti, F. Leonardi and F. Biscarini, *Chem. Soc. Rev.*, 2017, **46**, 40–71.
63 P. Xue, P. Wang, P. Chen, B. Yao, P. Gong, J. Sun, Z. Zhang and R. Lu, *Chem. Sci.*, 2017, **8**, 6060–6065.
64 R. F. Dou, X. C. Ma, L. Xi, H. L. Yip, K. Y. Wong, W. M. Lau, J. F. Jia, Q. K. Xue, W. S. Yang, H. Ma and A. K. Y. Jen, *Langmuir*, 2006, **22**, 3049–3056.
65 F. M. Hoffmann, *Surf. Sci. Rep.*, 1983, **3**, 107–192.
66 O. I. Negru and M. Grigoras, *J. Polym. Res.*, 2015, **22**, 1–11.
67 A. Botta, S. Pragliola, V. Venditto, A. Rubino, S. Aprano, A. De Girolamo Del Mauro, M. Grazia Maglione and C. Minarini, *Polym. Compos.*, 2015, **36**, 1110–1117.
68 O. Abbas, G. Compère, Y. Larondelle, D. Pompeu, H. Rogez and V. Baeten, *Vib. Spectrosc.*, 2017, **92**, 111–118.
69 I. Matulaitiene, Z. Kuodis, A. Matijoška, O. Eicher-Lorka and G. Niaura, *J. Phys. Chem. C*, 2015, **119**, 26481–26492.
70 S. Schneider, M. Füser, M. Bolte and A. Terfort, *Electrochim. Acta*, 2017, **246**, 853–863.
71 S. A. Paniagua, P. J. Hotchkiss, S. C. Jones, S. R. Marder, A. Mudalige, F. S. Marrikar, J. E. Pemberton and N. R. Armstrong, *J. Phys. Chem. C*, 2008, **112**, 7809–7817.
72 M. Bomers, A. Mezy, L. Cerutti, F. Barho, F. Gonzalez-Posada Flores, E. Tournié and T. Taliercio, *Appl. Surf. Sci.*, 2018, **451**, 241–249.
73 R. Quiñones, S. Garretson, G. Behnke, J. W. Fagan, K. T. Mueller, S. Agarwal and R. K. Gupta, *Thin Solid Films*, 2017, **642**, 195–206.

74 W. Zhang, W. Ju, X. Wu, Y. Wang, Q. Wang, H. Zhou, S. Wang and C. Hu, *Appl. Surf. Sci.*, 2016, **367**, 542–551.
75 J. F. Moulder, W. F. Stickle, P. E. Sobol and K. D. Bomben, *Handbook of X-ray Photoelectron Spectroscopy*, 1992.
76 M. Saliba, T. Matsui, J.-Y. Seo, K. Domanski, J.-P. Correa-Baena, M. K. Nazeeruddin, S. M. Zakeeruddin, W. Tress, A. Abate, A. Hagfeldt and M. Grätzel, *Energy Environ. Sci.*, 2016, **9**, 1989–1997.
77 X. Zheng, B. Chen, J. Dai, Y. Fang, Y. Bai, Y. Lin, H. Wei, X. C. C. Zeng and J. Huang, *Nat. Energy*, 2017, **2**, 17102.
78 F. Urbach, *Phys. Rev.*, 1953, **92**, 1324.
79 J. Kim, S. H. Lee, J. H. Lee and K. H. Hong, *J. Phys. Chem. Lett.*, 2014, **5**, 1312–1317.
80 A. Sadhanala, F. Deschler, T. H. Thomas, S. E. Dutton, K. C. Goedel, F. C. Hanusch, M. L. Lai, U. Steiner, T. Bein, P. Docampo, D. Cahen and R. H. Friend, *J. Phys. Chem. Lett.*, 2014, **5**, 2501–2505.
81 C. Huang, W. Fu, C. Z. Li, Z. Zhang, W. Qiu, M. Shi, P. Heremans, A. K. Y. Jen and H. Chen, *J. Am. Chem. Soc.*, 2016, **138**, 2528–2531.
82 S. J. Park, S. Jeon, I. K. Lee, J. Zhang, H. Jeong, J. Y. Park, J. Bang, T. K. Ahn, H. W. Shin, B. G. Kim and H. J. Park, *J. Mater. Chem. A*, 2017, **5**, 13220–13227.
83 P. J. Hotchkiss, H. Li, P. B. Paramonov, S. A. Paniagua, S. C. Jones, N. R. Armstrong, J. L. Brédas and S. R. Marder, *Adv. Mater.*, 2009, **21**, 4496–4501.
84 M. Timpel, H. Li, M. V. Nardi, B. Wegner, J. Frisch, P. J. Hotchkiss, S. R. Marder, S. Barlow, J. L. Brédas and N. Koch, *Adv. Funct. Mater.*, 2018, **28**, 1–12.
85 H. Li, P. Paramonov and J. L. Bredas, *J. Mater. Chem.*, 2010, **20**, 2630–2637.
86 J. Rittich, S. Jung, J. Siekmann and M. Wuttig, *Phys. Status Solidi B*, 2018, **255**, 27–29.
87 S. Ryu, J. H. Noh, N. J. Jeon, Y. Chan Kim, W. S. Yang, J. Seo and S. Il Seok, *Energy Environ. Sci.*, 2014, **7**, 2614–2618.
88 R. A. Belisle, P. Jain, R. Prasanna, T. Leijtens and M. D. McGehee, *ACS Energy Lett.*, 2016, **1**, 556–560.
89 K. Schick, E. Daub, S. Finkbeiner and P. Würfel, *Appl. Phys. A: Solids Surf.*, 1992, **54**, 109–114.
90 A. Delamarre, L. Lombez and J. F. Guillemoles, *Appl. Phys. Lett.*, 2012, **100**(13), 131108.
91 T. Unold and L. Gütay, *Advanced Characterization Techniques for Thin Film Solar Cells*, John Wiley & Sons, Ltd, 2011, pp. 151–175.
92 D. W. Dequilettes, S. Koch, S. Burke, R. K. Paranji, A. J. Shropshire, M. E. Ziffer and D. S. Ginger, *ACS Energy Lett.*, 2016, **1**, 438–444.
93 B. Krogmeier, F. Staub, D. Grabowski, U. Rau and T. Kirchartz, *Sustainable Energy Fuels*, 2018, **2**, 1027–1034.
94 M. Stolterfoht, P. Caprioglio, C. M. Wolff, J. A. Márquez, J. Nordmann, S. Zhang, D. Rothhardt, U. Hörmann, Y. Amir, A. Redinger, L. Kegelmann, F. Zu, S. Albrecht, N. Koch, T. Kirchartz, M. Saliba, T. Unold and D. Neher, *Energy Environ. Sci.*, 2019, **12**(9), 2778–2788.
95 R. T. Ross, *J. Chem. Phys.*, 1967, **46**, 4590–4593.
96 P. Schulz, L. L. Whittaker-Brooks, B. A. Macleod, D. C. Olson, Y. L. Loo and A. Kahn, *Adv. Mater. Interfaces*, 2015, **2**(7), 1400532.
97 J. P. Correa Baena, L. Steier, W. Tress, M. Saliba, S. Neutzner, T. Matsui, F. Giordano, T. J. Jacobsson, A. R. Srimath Kandada, S. M. Zakeeruddin, A. Petrozza, A. Abate, M. K. Nazeeruddin, M. Grätzel and A. Hagfeldt, *Energy Environ. Sci.*, 2015, **8**, 2928–2934.
98 P. Caprioglio, M. Stolterfoht, C. M. Wolff, T. Unold, B. Rech, S. Albrecht and D. Neher, *Adv. Energy Mater.*, 2019, 1901631.
99 P. Schulz, D. Cahen and A. Kahn, *Chem. Rev.*, 2019, **119**, 3349–3417.
100 P. Schulz, E. Edri, S. Kirmayer, G. Hodes, D. Cahen and A. Kahn, *Energy Environ. Sci.*, 2014, **7**, 1377–1381.
101 Y. Yan, P. N. Rudd, J. Zhao, Z. Yu, Y. Fang, Y. Lin, Y. Yuan, Y. Deng, J. Huang, B. Chen and C. Bao, *Nat. Commun.*, 2018, **9**, 1–9.
102 B. Chen, J. Song, X. Dai, Y. Liu, P. N. Rudd, X. Hong and J. Huang, *Adv. Mater.*, 2019, 1902413.
103 T. Sekimoto, T. Matsui, T. Nishihara, R. Uchida, T. Sekiguchi and T. Negami, *ACS Appl. Energy Mater.*, 2019, **2**, 5039–5049.
104 J. Avila, L. Gil-Escrig, P. P. Boix, M. Sessolo, S. Albrecht and H. J. Bolink, *Sustainable Energy Fuels*, 2018, **2**, 2429–2434.
105 C. Momblona, L. Gil-Escrig, E. Bandiello, E. M. Hutter, M. Sessolo, K. Lederer, J. Blochwitz-Nimoth and H. J. Bolink, *Energy Environ. Sci.*, 2016, **9**, 3456–3463.
106 N. J. Jeon, H. Na, E. H. Jung, T. Y. Yang, Y. G. Lee, G. Kim, H. W. Shin, S. Il Seok, J. Lee and J. Seo, *Nat. Energy*, 2018, **3**, 682–689.

Supporting Information

Conformal Monolayer Contacts with Lossless Interfaces for Perovskite Single Junction and Monolithic Tandem Solar Cells

Amran Al-Ashouri[1]*, Artiom Magomedov[2]*, Marcel Roß[1], Marko Jošt[1], Martynas Talaikis[3], Ganna Chistiakova[4], Tobias Bertram[5], José A. Márquez[5], Eike Köhnen[1], Ernestas Kasparavičius[2], Sergiu Levcenco[6], Lidón Gil-Escrig[1], Charles J. Hages[6], Rutger Schlatmann[5], Bernd Rech[4], Tadas Malinauskas[2], Thomas Unold[6], Christian A. Kaufmann[5], Lars Korte[4], Gediminas Niaura[3], Vytautas Getautis[2] and Steve Albrecht[1,7]*

[1]Young Investigator Group Perovskite Tandem Solar Cells, Helmholtz-Zentrum Berlin, Kekuléstraße 5, 12489 Berlin, Germany

[2]Department of Organic Chemistry, Kaunas University of Technology, Radvilenu pl. 19, Kaunas LT-50254, Lithuania

[3]Department of Organic Chemistry, Center for Physical Sciences and Technology, Sauletekio Ave. 3, Vilnius LT-10257, Lithuania

[4]Institute for Silicon Photovoltaics, Helmholtz-Zentrum Berlin, Kekuléstraße 5, 12489 Berlin, Germany

[5]PVcomB, Helmholtz Zentrum Berlin für Materialien und Energie GmbH, 12489 Berlin, Germany

[6]Department of Structure and Dynamics of Energy Materials, Helmholtz-Zentrum-Berlin für Materialien und Energie GmbH, Hahn-Meitner Platz 1, 14109 Berlin, Germany

[7]Faculty of Electrical Engineering and Computer Science, Technical University Berlin, Marchstraße 23, 10587 Berlin, Germany

* Corresponding authors: amran.al-ashouri@helmholtz-berlin.de, steve.albrecht@helmholtz-berlin.de, artiom.magomedov@ktu.lt

Table of Contents

1. Experimental Part

Device preparation

Patterned indium tin oxide (ITO) glass substrates (25x25 mm, resistivity = 15 Ω sq-1, nominal ITO thickness = 150 nm, patterned by Automatic Research GmbH) were cleaned sequentially for 15 min with a 2% Mucasol solution in water (Schülke), water, Acetone, and Isopropanol at ~ 40°C in an ultrasonic bath. After that, directly before HTM deposition, the substrates were treated in an UV-ozone cleaner for 15 min. UV treatment seemed crucial for achieving a high reproducibility. All subsequent procedures were done in a nitrogen-filled glovebox (MBRAUN). For the PTAA devices, PTAA dissolved in anhydrous Toulene (both by Sigma Aldrich) was spin-coated from a 2 mg/ml solution in at 5000 rpm (5 s acceleration) for 30 s and heated on a hot plate at 100°C for 10 min.

SAM powders were dissolved in anhydrous Ethanol at a concentration of 1 mmol/l and put into an ultrasonic bath for 15 min (30-40 °C) before using. 2PACz powder (molar weight 335.3 g/mol) was stored in a nitrogen glovebox, MeO-PACz (275.24 g/mol) was stored in ambient air. If stored otherwise before dissolving, penalties in performance were observed. The SAMs were prepared either by spin-coating or dipping. When spin-coating, 100 µl of the solution was uniformly released onto the middle of the substrate, the lid was closed and after ~ 5 s resting, the spin-coating program (30 s at 3000 rpm) was started. Alternatively, a lower concentration of 0.1 mmol/l can be used if dropping the solution 2-3 times dynamically during the spinning program. After spin-coating, the substrates were heated at 100 °C for 10 min. A washing step (with Ethanol) is possible but not necessary. For some perovskites, it might be beneficial to wash the substrates after heating, since it can change the contact angle of the perovskite (no significant performance differences were observed for all used perovskites in this work). SAMs by dipping were prepared by immersing the substrates into a 0.1 mmol/l solution for 2-12h, with subsequent heating at 100 °C for 10 min. After heating, the dipped substrates were washed dynamically during a 4000 rpm, 30 s spin-coating program by dripping 100-200 µl of Ethanol 2-3 times onto them.

Triple-cation $Cs_{0.05}(MA_{0.17}FA_{0.83})_{0.95}Pb(I_{0.83}Br_{0.17})_3$ (CsMAFA) perovskite film was formed according to our previously reported procedure[1]. 100 µl of the precursor was dripped onto the PTAA or SAM-covered substrates and the solution was spread with a pipette tip across the substrate before starting the spinning program (5s acceleration to 4000 rpm, 35s steady at 4000 rpm). On PTAA, 500 µl of Ethyl Acetate as the antisolvent was dripped onto the perovskite 25 s after starting the spin-coating program (closed spin-coater lid). On SAMs, either Ethyl Acetate, or, in later optimized stages, 200 µl of Chlorobenzene or Anisole[2] were used as the antisolvent (with open lid during the program), dripped 5-7 s before the end of the spinning program (with 3500 instead of 4000 rpm spinning speed). The SAMs are chemically robust and allow the use of more types of antisolvents than PTAA. Further, the perovskite was annealed at 100 °C for 30-60 min.

Double cation $MA_5FA_{95}Pb(I_{95}Br_5)_3$ (MAFA) perovskite was prepared similarly to the CsMAFA perovskite, with respectively changed ratio of mixing the $MAPbBr_3$ and $FAPbI_3$ precursor solutions and 60 min annealing. The final perovskite solution was mixed just before spin-coating. Additionally, a 1.24 mol/l MACl solution in DMSO was mixed with the perovskite solution in a 5:95 volume ratio. The same spin-coating program as for CsMAFA was used, with dripping 300 µl Chlorobenzene 5s before the end of the program.

Single cation $MAPbI_3$ was prepared by direct co-evaporation using a CreaPhys “PEROvap” deposition tool integrated into an inert glovebox (MBraun). The system includes a cooling shield inside the chamber, whose temperature was set to -25 °C for the entire process time. The rotation speed of the substrate holder was held constant at 10 rpm. Lead iodide and Methylammonium iodide were filled in two individual crucibles and the chamber was evacuated. At reaching a base pressure of 1E-6 mbar the sources where heated to 240 °C (PbI2) and 150 °C (MAI). Starting from this point the temperature was

slightly adjusted until a stable rate of 1.4 Å s^{-1} (PbI2) and 3.5 Å s^{-1} (MAI) were obtained. The ratio was monitored using individual quartz crystal microbalances (QCM, Inficon) for each material.

After perovskite deposition, 23 nm C60 and 8 nm BCP were thermally evaporated in a MBRAUN ProVap 3G at a base pressure of 1E-6 mbar with an evaporation rate of 0.1-0.18 Å/s. For completing the device, 100 nm Cu or Ag was thermally evaporated through a shadow mask. The overlap of the substrate's ITO with the Cu stripe defines the active area of 0.16 cm² (cross-checked with an optical microscope).

Some devices, such as the one sent for certification, were encapsulated with a cover glass and a two-component self-curing epoxy glue (5-min epoxy, R&G Faserverbundwerkstoffe GmbH). After encapsulation, an antireflective coating (100 nm NaF) was thermally evaporated onto the glass substrates, which increased the short-circuit current density distinctly stronger for 2PACz and MeO-2PACz devices than for PTAA and V1036 devices.

When employing SnO2 instead of BCP, we noticed better and more stable performance with MeO-2PACz than with 2PACz, possibly due to a faster hole-extraction with MeO-2PACz.

CIGSe/perovskite tandem solar cell

The CIGSe bottom cell was fabricated in a multi-step thermal evaporation on a glass substrate as described in the SI of our previous work[3], with RbF surface treatment. The p-type back contact is made of sputtered Molybdenum. The recombination contact consists of 10 nm sputtered i-ZnO and 140 nm ZnO:Al (AZO). After completion, the surface was rinsed with Ethanol and treated with UV-Ozone for 15 min, before submersing the CIGSe bottom cell into a 0.1 mmol/l MeO-PACz/Ethanol solution overnight. Spin-coating a 1 mmol/l MeO-PACz solution once or a 0.1 mmol/l solution three times also yielded >20 %-efficient tandem cells. Subsequently, the bottom cell was heated at 100 °C for 10 min in a N_2-filled glovebox, before proceeding the CsMAFA perovskite processing on top as described above.

After perovskite annealing, 20 nm C60 was thermally evaporated and 20 nm of SnO_2 processed on top at a substrate temperature of 80 °C via atomic layer deposition (ALD, Arradiance GEMStar) to form a buffer layer for the indium zinc oxide (IZO) sputtering, as optimized in another work[4]. SnO2 precursors were tetrakis(dimethylamino)tin(IV) (TDMASn) and water. The IZO top electrode was deposited by RF sputtering from a 10%wt ZnO and 90 %wt In_2O_3 target. For contacting the electrode, a 100 nm thick Ag frame was thermally evaporated through a shadow mask and 100 nm LiF as the anti-reflective coating. After device completion, the tandem cell was manually scribed around the Ag frame, since the AZO recombination and Molybdenum back contact were both processed on the full bottom cell area.

Materials

The molecules that form SAMs were synthesized (see next section). All other materials for the perovskite precursor and for evaporation were used as bought without further purification. Lead iodide and lead bromide were purchased from TCI (99.99%, trace metals basis) or Sigma Aldrich (99.999%, trace metals basis). FAI and MABr were purchased from Dyenamo (grade 99%), CsI from abcr GmbH (99.999%). Solvents (all anhydrous) DMF, DMSO and antisolvents ethyl acetate, chlorobenzene and anisole were from Sigma Aldrich, the SAM solvent ethanol was bought from VWR Chemicals. PTAA was by Sigma Aldrich.

Electron-selective contact and top electrode: C60 (99.99%) and BCP from Sigma Aldrich, Cu shots from Alfa Aesar.

For co-evaporated MAPbI3, lead iodide by TCI and Methylammonium iodide by Lumtec were used.

Analysis Methods

Molar extinction coefficient

The SAM or PTAA powders were dissolved in Chlorobenzene at a concentration of 1 mmol/l. The absorption spectra were recorded from the solution in a cuvette in a PerkinElmer Lambda 35 spectrometer.

Infrared spectroscopy (RAIRS and FTIR)

Reflection absorption infrared spectroscopy (RAIRS) data were recorded using Vertex 80v (Bruker Inc., Leipzig, Germany) spectrometer equipped with liquid nitrogen cooled narrow-band MCT detector. Samples were placed onto a horizontal accessory in evacuated (~2 mbar) spectrometer chamber. The bare ITO substrate was used as a reference. The spectra were taken with p-polarized incident light after incubation of the samples in vacuum for 180 s. Spectral resolution was set to 4 cm^{-1}, aperture to 4 mm, and spectra were acquired by averaging 256 scans. The spectra were taken in three steps: First, samples were measured as received. Next, they were rinsed with ethanol and incubated in chlorobenzene for 10 min in order to remove any possible multilayers and measured again. Lastly, measurements were repeated after one month to identify any changes occurring due a degradation of the samples (see fig. S6).

Fourier transform infrared (FTIR) spectra of bulk materials were taken from KBr pellet-pressed V1036 (**V1036)**, MeO-2PACz (**V1193)** and 2PACz (**V1194)** samples, using an Alpha (Bruker Inc., Leipzig, Germany) spectrometer equipped with a DLATGS detector in transmission mode. The resolution was set to 4 cm^{-1}. Geometry optimization and frequency calculations were performed using Gaussian 09W software with Becke three parameter functional, B3LYP, and def2-SVP basis set for V1036 and B3LYP functional with 6-311++g(2d,p) basis set for MeO-2PACz and 2PACz compounds. The scaling factor was applied for the theoretical results as described in a previous publication[5].

Solar cell characterization

Current-voltage (J-V) characteristics under 1 sun equivalent illumination were recorded using a Wavelabs Sinus-70 LED class AAA sun simulator in air, calibrated with a filtered KG3 Silicon reference solar cell certified by Fraunhofer ISE. J-V scans were performed as 2-point measurements with a Keithley 2400 SMU (4-point measurement with Keithley 2600 for the tandem cell), controlled by a measurement control program written in LabView. The single junctions were not masked during measurement (due to small differences between J_{SC} from integrated EQE and J-V). The voltage values are swept in 20 mV steps with an integration time of 40 ms per point and settling time of 20-40 ms after voltage application (maximum voltage sweep speed of 250 mV/s). EQE spectra were recorded with an Oriel Instruments QEPVSI-b system with a Newport 300 W xenon arc lamp, controlled by TracQ-Basic software. The white light filtered into monochromatic light by a Newport Cornerstone 260 monochromator with a 10 nm increment and chopped into a frequency of 78 Hz before being conducted to the solar cell surface via optical fibers. The system is calibrated using a Si reference cell with known spectral response before every measurement. The electrical response of the device under test is measured with a Stanford Research SR830 Lock-In amplifier (time constant of 0.3 s) and evaluated in TracQ. The typical short-circuit current mismatch between integrated external quantum efficiency (EQE) times AM1.5G irradiance and values from *J-V* scans is around 1%. For the Urbach energy estimation, the monochromator step size is reduced to 2 nm and Lock-In integration time increased to 1 s per increment.

The temperature during continuous MPP tracking was measured with a thermocouple attached to the samples's glass surface.

A spectral mismatch M[6] for the used solar simulator was calculated with typical CsMAFA and MAFA EQE spectra, the spectral response of the calibrated reference cell and the spectrum of the solar simulator. The small deviations from 1 (M = 0.997 for CsMAFA and 1.005 for MAFA) are within the measurement error margins during J-V characterizations, thus the measured J_{SC} values were not corrected by 1/M.

No pre-conditioning protocols were applied. For some cells, we observed a slight rising trend in V_{OC} upon multiple J-V scans (or some minutes of light-soaking until thermodynamic stabilization). Typically, the PCE value of the PSCs saturates at higher values a few days after perovskite processing.

Photoelectron spectroscopy

XPS measurements were conducted with a non-monochromated Mg Kα excitation source and a ScientaOmicron Argus CU electron analyzer in the Energy Materials In-Situ Laboratory (EMIL) of HZB. Core level peak fitting was performed with the free software fityk[7]. The number of Voigt peaks was determined by fitting all three datasets simultaneously with coupled width and shape parameters and increasing the number of peaks until the residuum was in the order of the background noise of the data. A linear background was included into the fit.

UPS measurements were conducted with the same equipment employing He I (21.22 eV) excitation. For measuring the secondary electron cutoff, a 10 V bias was applied to the substrate. The valence band onset was determined by the leading edge extrapolation method (see fig. S15).

The ITO substrates were prepared in the same manner as for the solar cells, in order to accurately reflect device-relevant ITO modification. The high V_{OC} values and low leakage currents obtained with the SAM-based PSCs, the constant PCE in dependence of the used solution concentration (Fig. S3) and the similarity in RAIRS of SAMs prepared by spin-coating vs. dipping ascertains that the studied SAMs are closely packed and that saturation of coverage is fulfilled. After preparation of the glass/ITO substrates in a nitrogen-filled glovebox, they were quickly transferred into the ultra-high vacuum UPS system without exposure to ambient air.

Absolute and transient photoluminescence

Time-resolved photoluminescence (trPL) measurements were carried out in a home-built setup using excitation at a 660 nm wavelength from a pulsed supercontinuum laser light source (SuperK) with a spot size of 25-35 μm in diameter. The repetition rate was set to 304 kHz and the sample's PL emission was collected panchromatically through a photomultiplier. Utilizing a time-correlated single photon counting technique (TCSPC), the PL decay was recorded with a time resolution of approximately 4 ns. The excitation power was varied with a linear ND filter, tracked with a power meter and chosen as follows, for injecting approximately the amount of charge carriers that is relevant for device operation under 1-sun conditions: If at a 1-sun equivalent excess charge-carrier density Δn the PL decay is dominated by monomolecular recombination, the recombination rate R can be approximated by $\Delta n/\tau$, where τ is the monomolecular recombination-limited PL lifetime. At quasi steady state, the generation rate G equals R. Thus, G is roughly the photon flux per penetration depth (approximated by the film thickness ~ 500 nm) divided by the steady-state PL lifetime (we assume 500 ns). This G is compared to the expected G under 1-sun equivalent excitation for an absorber with 1.63 eV band gap, which is given by the respective integration of the AM1.5G irradiance spectrum (1.5E+21 m^{-2} s^{-1}). Under these estimations, a fluence of ca. 10-30 nJ/cm² of pulsed excitation should create a 1-sun equivalent quasi-steady-state situation. The samples were excited on the perovskite side.

Absolute photoluminescence spectra and hyperspectral images were recorded with a custom setup described in another work[8]. Excitation was performed with two 450 nm LEDs, calibrated to ~ 1 sun equivalent fluence and PL emission was collected with a CCD camera. Wavelength-selectivity of the PL emission was achieved by coupling a tunable liquid crystal filter in front of the camera. The setup was calibrated to absolute photon numbers with light sources of known fluences[9], thus enabling to estimate the quasi fermi-level splitting from the generalized Planck law using the high-energy tail fit method.

XRD

X-ray diffraction patterns (only in SI) were recorded at room temperature using a Bruker D8 diffractometer in Bragg-Brentano geometry. For all measurements the Cu radiation from an X-ray tube operated at 40 mA and 40 kV acceleration voltage was used.

Synthesis of the SAM molecules

In brief, alkylation with dibromoethane of the respective carbazole derivatives was performed (compounds **1** and **2**), followed by an introduction of phosphonic acid ester groups via an Arbuzov reaction to yield the intermediate materials **3** and **4**. Finally, cleavage of the ethyl groups was performed with bromotrimethylsilane to produce the final products **2PACz** and **MeO-2PACz**. Further details are presented in the following

Chemicals, unless stated otherwise, were purchased from Sigma-Aldrich or TCI Europe and used as received without further purification. The ^{1}H and ^{13}C NMR spectra were taken on Bruker Avance III (400 MHz) spectrometer at RT. All the data are given as chemical shifts in δ (ppm). The course of the reactions products was monitored by TLC on ALUGRAM SIL G/UV254 plates and developed with UV light. Silica gel (grade 9385, 230–400 mesh, 60 Å, Aldrich) was used for column chromatography. Elemental analysis was performed with an Exeter Analytical CE-440 elemental analyzer, Model 440 C/H/N/. Electrothermal MELTEMP capillary melting point apparatus was used for determination of melting points.

UV/Vis spectra were recorded on a PerkinElmer Lambda 35 spectrometer.

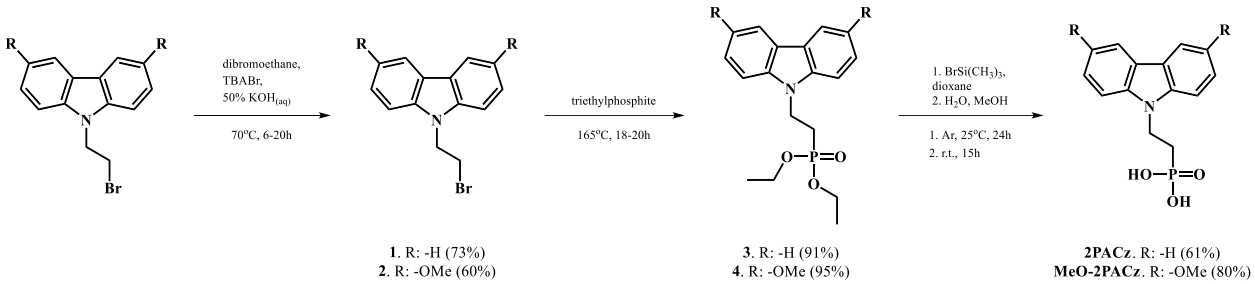

Figure S1 Synthesis scheme of the phosphonic acid functionalized carbazole derivatives **2PACz** and **MeO-2PACz**.

2PACz synthesis

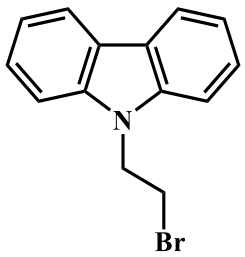

9-(2-bromoethyl)-9*H*-carbazole (1)

9*H*-carbazole (2 g, 12 mmol) was dissolved in 1,2-dibromoethane (20 ml), and tetrabutylammonium bromide (0.08 g, 0.25 mmol) with 50% KOH aqueous solution (7.2 ml) were added subsequently. Reaction was stirred at 70°C for 6 h (TLC, acetone:n-hexane, 3:22, v:v). After completion of the reaction, extraction was done with ethyl acetate. The organic layer was dried over anhydrous Na_2SO_4 and the solvent was distilled off under reduced pressure. The crude product was directly used for the further synthesis. 2.4 g (73 %) of white crystalline material was isolated– compound **1**.

Anal. calcd for $C_{14}H_{12}NBr$, %: C 61.33; H 4.41; N 5.11; found, %: C 61.39; H 4.37; N 5.03.

^{1}H NMR (400 MHz, $CDCl_3$) δ 8.08 (d, J = 7.7 Hz, 2H), 7.51 – 7.36 (m, 4H), 7.29-7.20 (m, 2H), 4.66 (t, J = 7.5 Hz, 2H), 3.64 (t, J = 7.5 Hz, 2H).

^{13}C NMR (101 MHz, CDCl3) δ 140.05, 126.07, 123.25, 120.66, 119.70, 108.55, 44.77, 28.23.

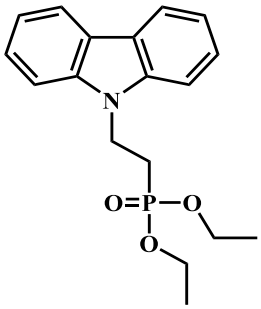

diethyl [2-(9*H*-carbazol-9-yl)ethyl]phosphonate (3)

Compound **1** (1.14 g, 4.16 mmol) was dissolved in triethylphosphite (14 ml) and the reaction mixture was heated at reflux for 20 h. After reaction completion (TLC, acetone:*n*-hexane, 7:18, v:v) the solvent was distilled off under reduced pressure. The crude product was purified by column chromatography using n-hexane as eluent, with the gradual change of the eluent to acetone:*n*-hexane, 1:4, v:v, to give 1.25 g (91%) of clear liquid – compound **3**.

Anal. calculated for $C_{18}H_{22}NO_3P$, %: C 65.25; H 6.69; N 4.23; found, %: C 64.99; H 6.60; N 4.16.

^{1}H NMR (400 MHz, DMSO-d6) δ 8.15 (dd, J = 7.9, 1.9 Hz, 2H), 7.58 (d, J = 8.2 Hz, 2H), 7.52 – 7.43 (m, 2H), 7.26 – 7.17 (m, 2H), 4.65 – 4.54 (m, 2H), 3.94 – 3.85 (m, 4H), 2.35 – 2.21 (m, 2H), 1.23 (t, J = 7.0 Hz, 16H).

^{13}C NMR (101 MHz, DMSO) δ 139.49, 125.71, 122.34, 120.26, 118.96, 109.20, 61.22, 61.16, 36.59, 24.95, 23.59, 15.97.

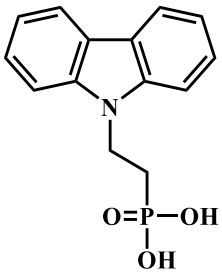

[2-(9H-carbazol-9-yl)ethyl]phosphonic acid (2PACz)

Compound **3** (1 g, 3.02 mmol) was dissolved in dry 1,4-dioxane (30 ml) under argon. Afterwards, bromotrimethylsilane (4 ml) was added dropwise. Reaction was kept for 24 h at 25 °C under argon atmosphere. Afterwards solvent was distilled off under reduced pressure, solid residue was dissolved in methanol (30 ml) and distilled water was added dropwise (150 ml), until solution became opaque, and was stirred for 24 h. The solution was concentrated under vacuum and the product was filtered off and washed with water to give 0.510 g (61 %) of pale-blue solid – **2PACz**.

Anal. calculated for $C_{14}H_{14}NO_3P$, %: C 61.09; H 5.13; N 5.09, found, %: C 60.64; H 5.22; N 5.02.

^{1}H NMR (400 MHz, DMSO-d6) δ 8.15 (d, J = 7.8 Hz, 2H), 7.54 (d, J = 8.2 Hz, 2H), 7.51 – 7.42 (m, 2H), 7.21 (t, J = 7.4 Hz, 2H), 4.62 – 4.49 (m, 2H), 2.12 – 1.96 (m, 2H).

^{13}C NMR (101 MHz, DMSO) δ 139.40, 125.85, 122.29, 120.41, 118.96, 108.93, 37.37, 27.94, 26.64.

MeO-2PACz synthesis

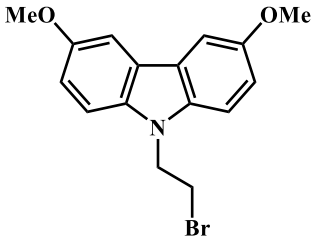

9-(2-bromoethyl)-3,6-dimethoxy-9*H*-carbazole (2)

3,6-dimethoxycarbazole (0.534 g, 2.35 mmol) was dissolved in 1,2-dibromoethane (8 ml), and tetrabuthylammonium bromide (0.08 g, 0.25 mmol) with 50% KOH aqueous solution (6.9 ml) were added subsequently. Reaction was stirred at 70°C for 20 h (TLC, acetone:n-hexane, 3:22, v:v). After completion of the reaction, extraction was done with ethylacetate. The organic layer was dried over anhydrous Na_2SO_4 and the solvent was distilled off under reduced pressure. The crude product was purified by column chromatography using acetone:n-hexane, 1:49, v:v as eluent to give 0.352 g (60 %) of white crystalline material – compound **2**.

Anal. calcd for $C_{16}H_{16}O_2NBr$, %: C 57.50; H 4.83; N 4.19; found, %: C 57.39; H 4.86; N 4.15.

^{1}H NMR (400 MHz, CDCl3) δ 7.51 (d, J = 2.5 Hz, 2H), 7.29 (d, J = 8.8 Hz, 2H), 7.10 (dd, J = 8.8, 2.5 Hz, 2H), 4.62 (t, J = 7.5 Hz, 2H), 3.93 (s, 6H), 3.62 (t, J = 7.5 Hz, 2H).

^{13}C NMR (101 MHz, CDCl3) δ 153.85, 135.65, 123.39, 115.30, 109.41, 103.45, 56.27, 45.07, 28.55.

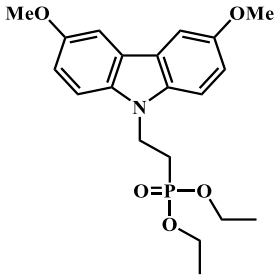

diethyl [2-(3,6-dimethoxy-9*H*-carbazol-9-yl)ethyl]phosphonate (4)

Compound **2** (0.316 g, 0.95 mmol) was dissolved in triethylphosphite (2.7 ml) and the reaction mixture was heated at reflux for 18 h. After reaction completion (TLC, acetone:*n*-hexane, 1:4, v:v) the solvent was distilled off under reduced pressure. The crude product was purified by column chromatography using acetone:*n*-hexane, 1:1, v:v as eluent to give 0.353 g (95%) of clear liquid – compound **4**.

Anal. calculated for $C_{20}H_{26}NO_5P$, %: C 61.37; H 6.70; N 3.58; found, %: C 61.32; H 6.73; N 3.55.

^{1}H NMR (400 MHz, $CDCl_3$) δ 7.52 (d, *J* = 2.5 Hz, 2H), 7.30 (d, *J* = 8.8 Hz, 2H), 7.10 (dd, *J* = 8.8, 2.5 Hz, 2H), 4.60 – 4.49 (m, 2H), 4.09 – 4.03 (m, 4H), 3.93 (s, 6H), 2.29 – 2.15 (m, 2H), 1.28 (t, *J* = 7.1 Hz, 6H).

^{13}C NMR (101 MHz, $CDCl_3$) δ 153.67, 135.46, 123.37, 115.20, 109.49, 103.46, 62.02, 61.96, 56.28, 37.31, 26.15, 24.79, 16.56, 16.50.

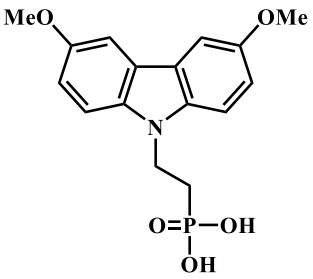

[2-(3,6-dimethoxy-9*H*-carbazol-9-yl)ethyl]phosphonic acid (MeO-2PACz)

Compound **4** (0.335 g, 0.86 mmol) was dissolved in dry 1,4-dioxane (25 ml) under argon. Afterwards, bromotrimethylsilane (1.12 ml) was added dropwise. Reaction was kept for 24 h at 25°C under argon atmosphere. Afterwards solvent was distilled off under reduced pressure, solid residue was dissolved in methanol (15 ml) and distilled water was added dropwise (30 ml), until solution became opaque, and was stirred for 15 h. Product was filtered off and washed with water to give 0.230 g (80 %) of beige solid – **MeO-2PACz**.

Anal. calculated for $C_{16}H_{18}NO_5P$, %: C 57.32; H 5.41; N 4.18, found, %: C 57.19; H 5.53; N 4.11.

^{1}H NMR (400 MHz, MeOD) δ 7.57 (d, *J* = 2.5 Hz, 2H), 7.34 (d, *J* = 8.8 Hz, 2H), 7.05 (dd, *J* = 8.8, 2.5 Hz, 2H), 4.58 – 4.48 (m, 2H), 3.87 (s, 6H), 2.20 – 2.06 (m, 2H).

^{13}C NMR (101 MHz, MeOD) δ 154.97, 136.71, 124.61, 116.03, 110.37, 104.29, 56.46, 38.47.

2. Comparison of spin-coating, dipping and different SAM solution concentrations

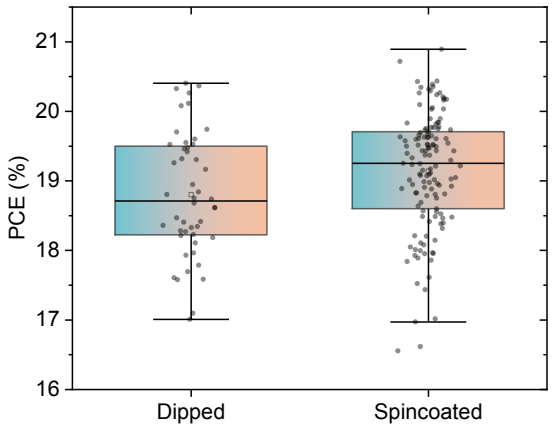

Figure S2 Statistical comparison between SAMs from spin-coating (no washing) and dipping (with subsequent washing), with triple cation perovskite absorber. The ITO substrates were either dipped into SAM solutions (0.1 mmol/l concentration in Ethanol, both MeO-2PACz and 2PACz are shown here) for several hours at room temperature with subsequent washing, or were prepared by spin-coating a 1 mmol/l SAM solution at 3000 rpm for 30s with subsequent heating at 100°C for 10 min. When spin-coating the SAM solution, subsequent washing of the substrates is optional and shows no PCE difference. Both preparation techniques yield similar efficiencies. The slightly higher average PCE obtained by SAMs from spin-coating is due to the fact that process optimization started with dipping and later stages predominantly spin-coating was used for single junction cells.

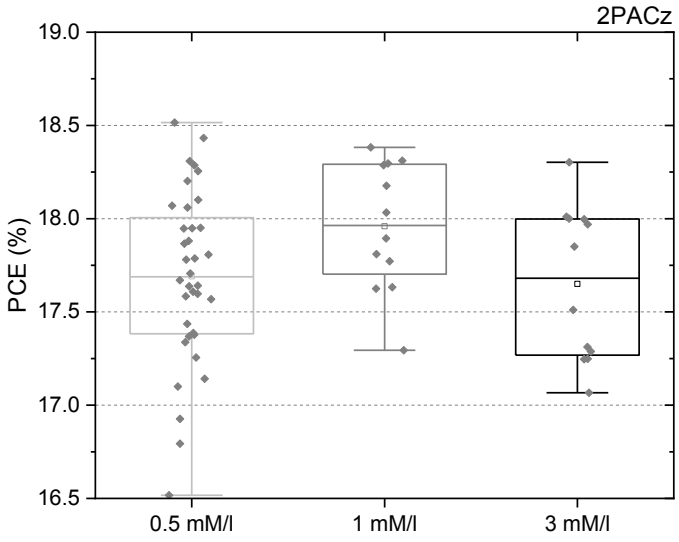

Figure S3 Power conversion efficiency of CsMAFA solar cells based on 2PACz, spin-coated from different concentrations in Ethanol.

3. Additional information to the RAIRS measurements

V1036: The high frequency feature at 1585 cm^{-1} was assigned to the asymmetric stretching vibrations of carbazole and p-methoxy-phenyl rings. 1484-cm^{-1} band was associated with carbazole ring stretching vibrations. Slightly lower frequency shoulder near 1441−1465 cm^{-1} has highest contribution from deformation vibrations of CH_3 groups. In-plane deformation vibrations of ring C−H bonds are visible at 1182 cm^{-1}. The broad band near 1010 cm^{-1} belongs to stretching vibration of phosphate group.[10,11]

MeO-2PACz: Pair of well-defined bands of compound MeO-2PACz near 1164 and 1211 cm^{-1} are related with rings C−H in-plane deformation vibrations coupled with C−O stretching mode. Two carbazole ring stretching modes of compound 2PACz are visible at 1242 and 1347 cm^{-1}. Presence of phosphonic acid group can be recognized from the broad band at 1010, 1021, and 1017 cm^{-1} for V1036, MeO-2PACz, and 2PACz monolayers, respectively.

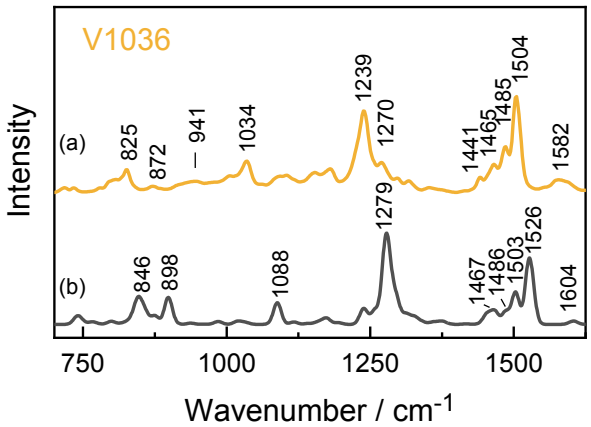

Figure S4 Comparison of FTIR spectrum of V1036 compound pressed into KBr pellet (a) and calculated spectrum at DEF2-SVP level of theory (b). The broad feature at 941 cm^{-1} for the bulk spectrum stems from P-OH species that are not present in monolayers.

Figure S4 shows the bulk spectrum of V1036 and the theoretical spectrum calculated by density functional theory (DFT), and figure S5 shows the same for MeO-2PACz and 2PACz. For V1036, the spectrum can be almost fully replicated by the calculation. For MeO-2PACz and 2PACz, prominent features can be replicated as well, although not all peaks expected by the DFT calculation can be found in the experimental spectra and vice versa, which we contribute to intermolecular interactions in the SAM, which are not present in the calculation that was conducted for a free-floating molecule in vacuum.

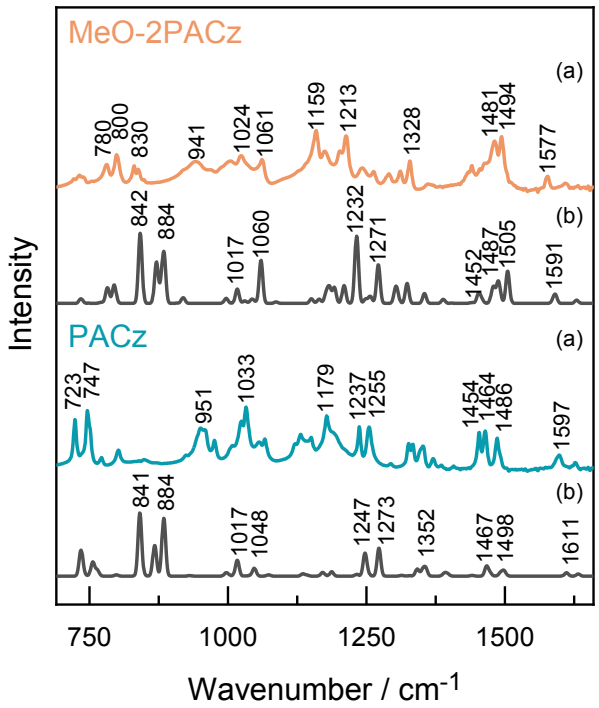

Figure S5 Comparison of FTIR spectrum of 2PACz and MeO-2PACz compounds pressed into KBr pellet (a) and calculated spectra at DEF2-SVP level of theory (b). The broad features at 941 cm^{-1} and 951 cm^{-1} stem from P-OH species[10–13] that are not present in the monolayer spectra.

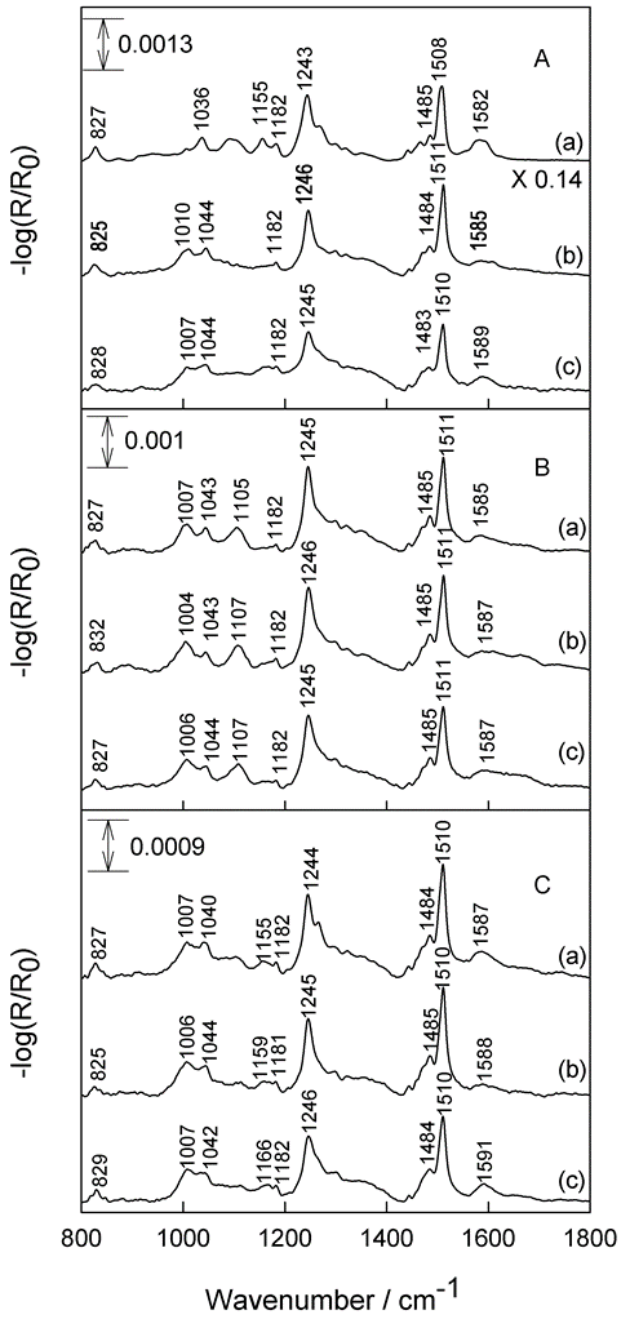

Figure S6 RAIRS spectra of different preparations of V1036 self-assembled monolayers on an ITO substrate. Spectra are shown of spin-coated (A) and formed from dipping (B, C, respectively) samples solutions before (a), after rinsing with ethanol and chlorobenzene (b) and after being kept in a lab environment for one month (c).

4. Additional device metrics

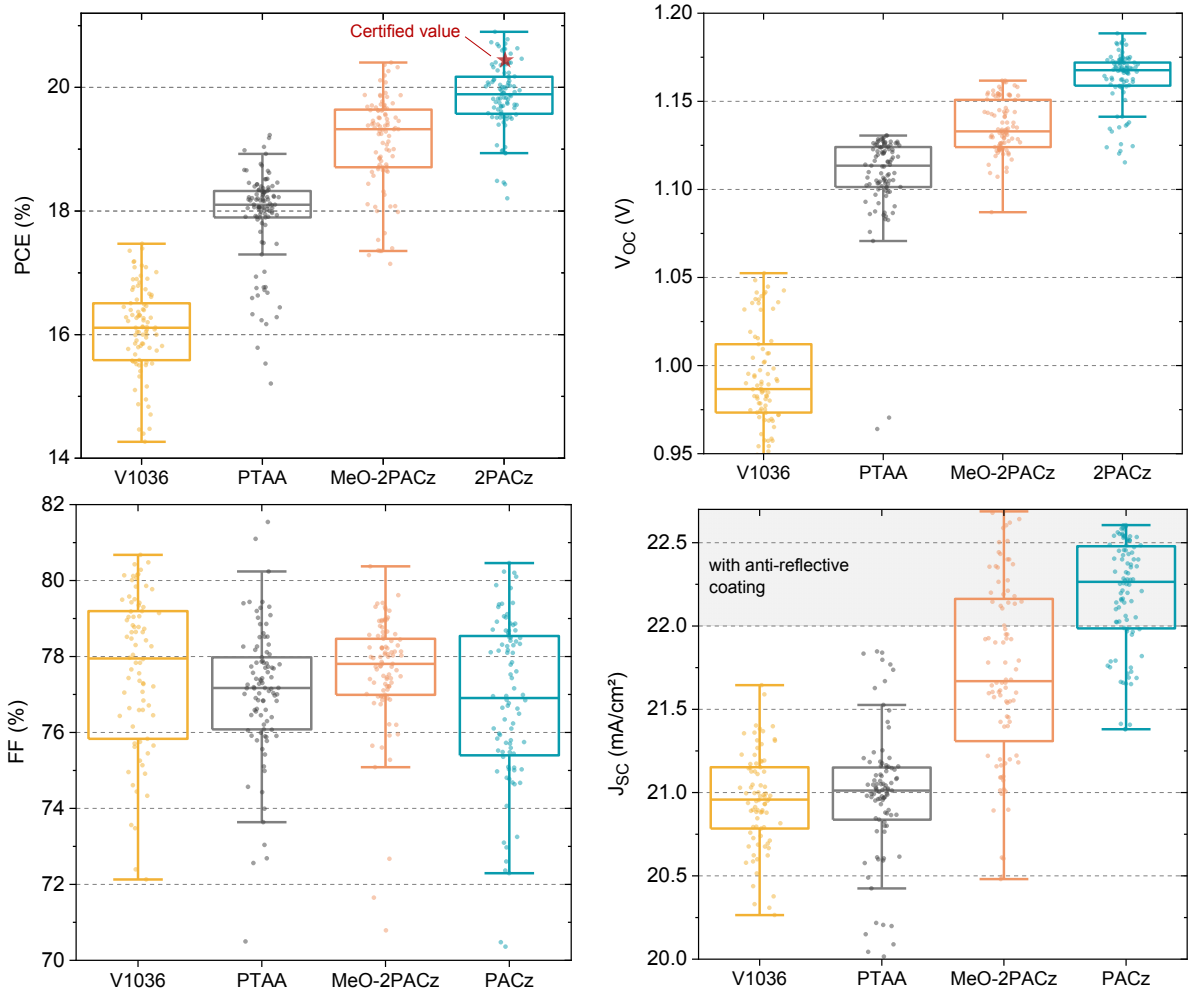

Figure S7 Solar cell device metrics for all investigated HTMs with CsMAFA "triple cation" perovskite absorber with 1.63 eV optical bandgap, on devices with area of 0.16 cm² (1:1 aspect ratio). The high J_{SC} values over 22 mA/cm² with both new SAMs are only achieved with a NaF antireflective (AR) coating. We notice that the AR coating is not as beneficial for PTAA-based devices, but adding 0.3 – 0.6 mA/cm² current density to 2PACz and MeO-2PACz devices. Note that, despite enabling a higher *Jsc*, the FF values of the (MeO-)2PACz devices are comparable to the ones of the PTAA devices, pointing to a higher extraction efficiency with (MeO-)2PACz.

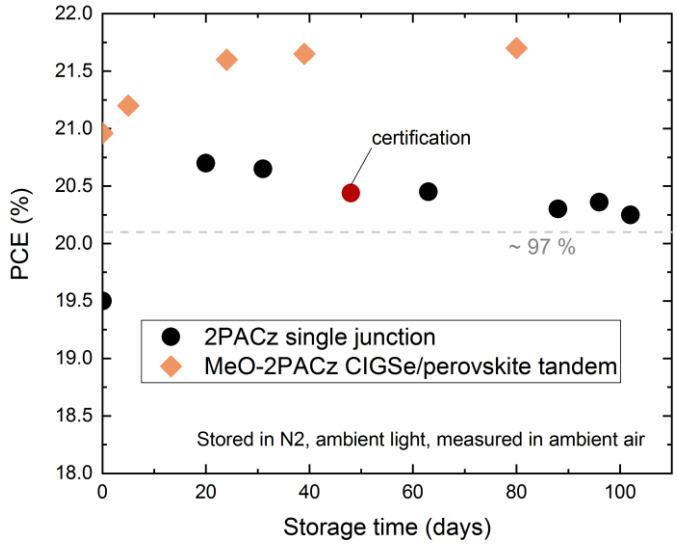

Figure S8 Initial stability assessment of SAM-based solar cells. The plot shows the time evolution of stabilized PCE of the single junction cell that was sent for certification. This cell was repeatedly handled and measured in ambient air (RH 30-60 %) and was stored in a nitrogen-filled glovebox in between the measurements. The orange points show the same for a representative CIGSe/perovskite tandem solar cell (same device stack as for the cell in the main text). The cell was measured in ambient air and was stored in nitrogen in between the measurement days. We expect that SAMs are suitable for the integration into PSC architectures that are specialized for high stability.

5. X-Ray Diffraction patterns and SEM pictures

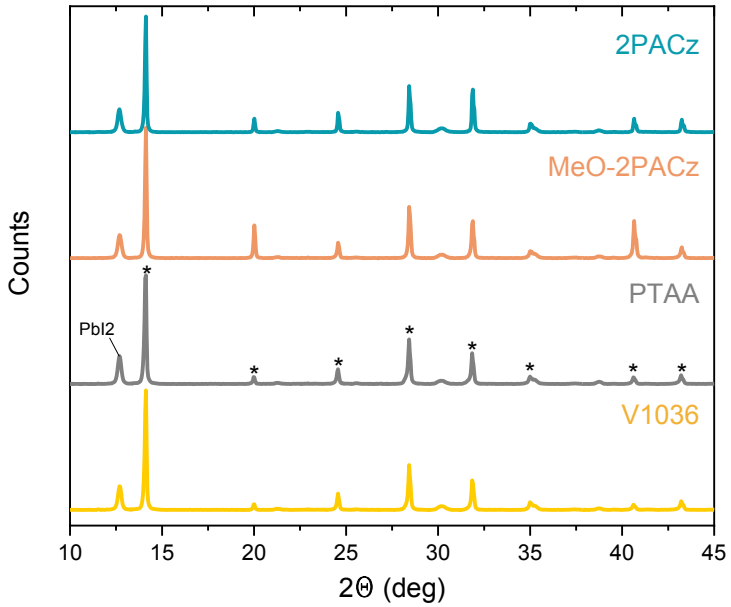

Figure S9 X-ray diffractograms of CsMAFA Perovskite films grown on the investigated HTMs (stack is glass/ITO/HTM/Perovskite). The stars on the PTAA case indicate the expected positions of perovskite crystal diffraction peaks.

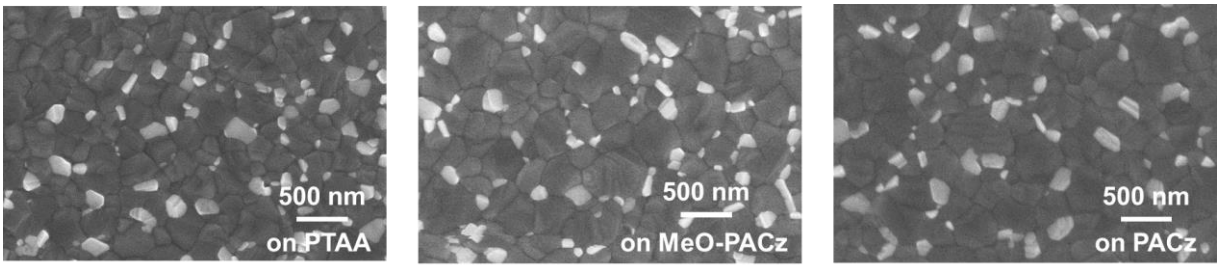

Figure S10 Scanning electron microscopy images of CsMAFA perovskite grown on PTAA, MeO-PACz and PACz. SEM pictures of the same perovskite on V1036 was previously published[1].

6. Photocurrent Spectra to determine the Urbach Energy

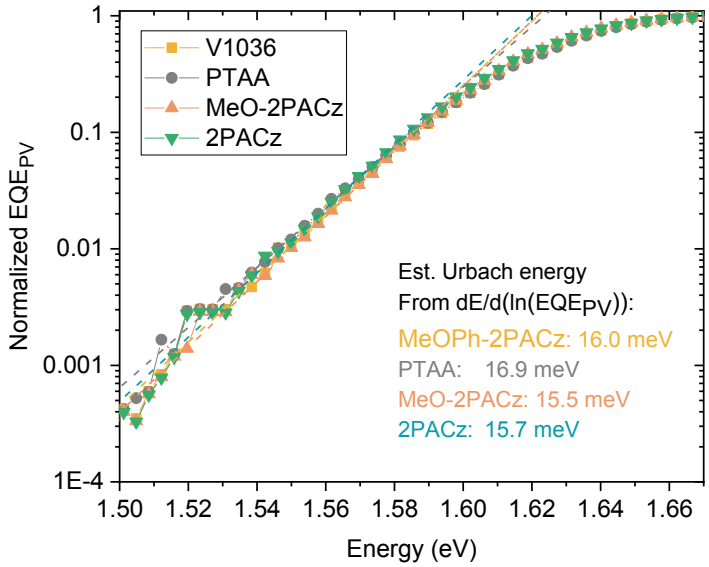

Figure S11 Normalized EQE of Perovskite solar cells based on the investigated HTMs, measured by a lock-in amplified current signal of the solar cell under modulated, monochromatic light (step size 2 nm & 1 second integration time). The slope in the "Urbach regime" gives an estimate of the energy of tail states ("Urbach energy"), which is likely to be overestimated by this method, but still gives a comparable value to the ones determined by a sophisticated full-fit.[14] The kink at 1.52-1.53 eV might stem from the low spectral response of the reference cell used for calibration.

7. Additional information to Photoelectron spectroscopy

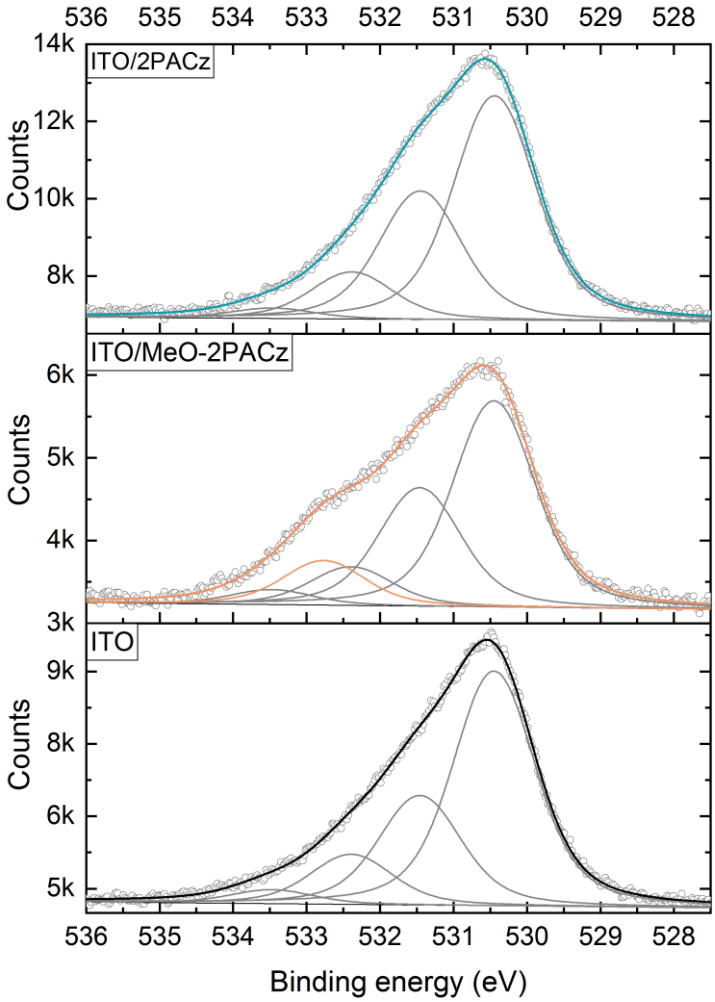

Figure S12 X-ray photoelectron spectroscopy (XPS) spectra in the O1s region of cleaned and O3-treated ITO (lower panel), ITO covered with MeO-2PACz (middle) and covered with 2PACz (top panel). After heating, the SAM-treated samples were washed with Ethanol. The number of necessary peaks for the fit was determined as for the C1s fitting in the main text (with linear background included into the fit). The peak shape parameters (Voigt curves) are the same for all shown peaks. For the (MeO-)2PACz fits, the relative distances between the peaks were locked to the same values as determined from the bare ITO fit, in order to unambiguously determine whether additional peaks are needed. Only the MeO-2PACz fit needed an additional peak (orange) that is here assigned to C-O-C species[15], in conjunction with the C1s study of the main text. The largest peak at 530.5 eV is assigned to oxygen in In_2O_3 in both bulk and surface of the ITO[16]. In this case, a possible tin-oxygen bond coincides in binding energy with In-O bonds[17]. The second largest peak at 531.5 eV is assigned to metal hydroxide species[15]. The area ratio between this peak and the largest one is 0.47 for the bare ITO sample. Upon SAM treatment, this ratio rises to 0.57 for both MeO-2PACz and 2PACz, pointing either to an increased concentration of O-H groups[18] on the surface or that less signal from the ITO bulk is collected. The remaining two peaks at higher binding energies might be assigned to other hydroxides and adventitious contaminants, like H_2O[15,16]. We assume that P-O species cannot be resolved here due to limited sensitivity and possible overlap with the contaminant peaks.

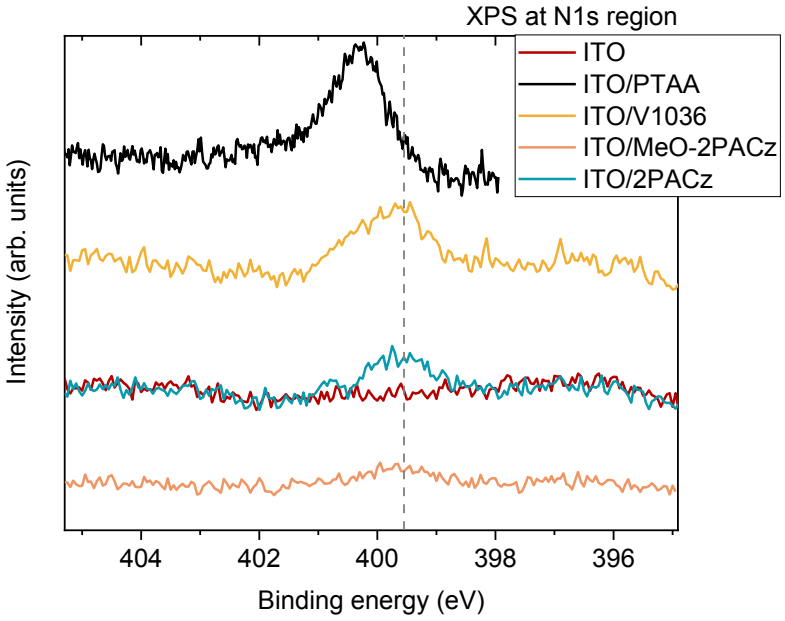

Figure S13 X-ray photoelectron spectroscopy on the studied substrates at the N1s region. Both MeO-2PACz and 2PACz share the same peak position, whereas V1036 shows a broader peak due to the presence of an additional N species in the diphenylamine group. A more detailed peak analysis would require a higher signal-to-noise ratio.

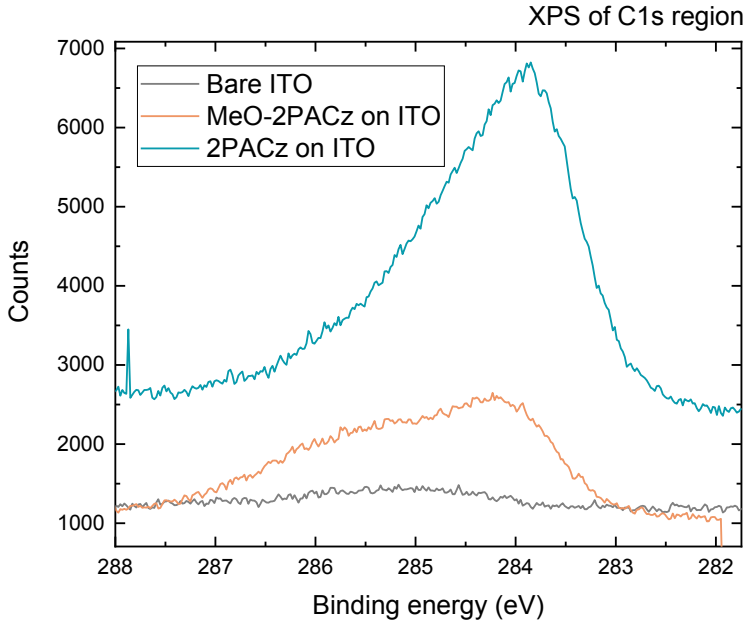

Figure S14 X-ray photoelectron spectroscopy at the C1s region of ITO glass, with and without SAM spin-coated on top (from 1 mmol/l solution, with subsequent heating to 100°C for 10 min). The residual small signal of the bare ITO sample is probably caused by adventitious carbon of the e. g. the sample storage boxes or glovebox.

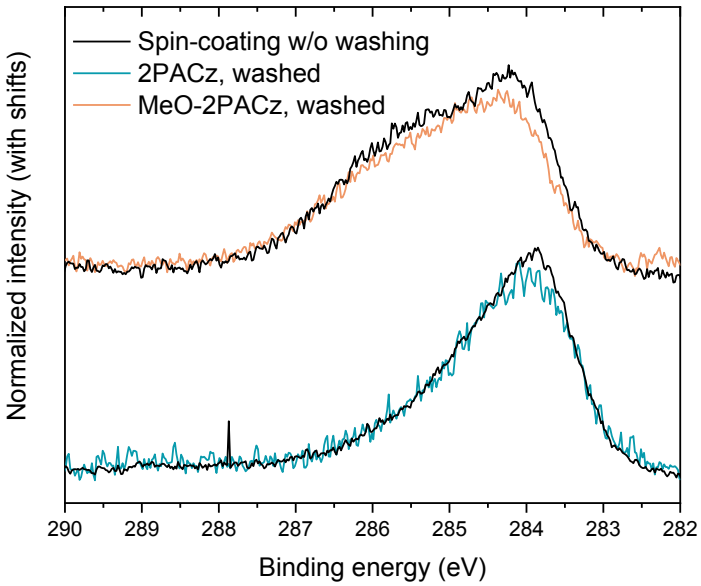

Figure S15 X-ray photoelectron spectroscopy at the C1s region for samples on which the SAM solution (1 mmol/l in Ethanol) was spin-coated (with subsequent heating to 100°C for 10 min), with and without washing the substrates subsequently.

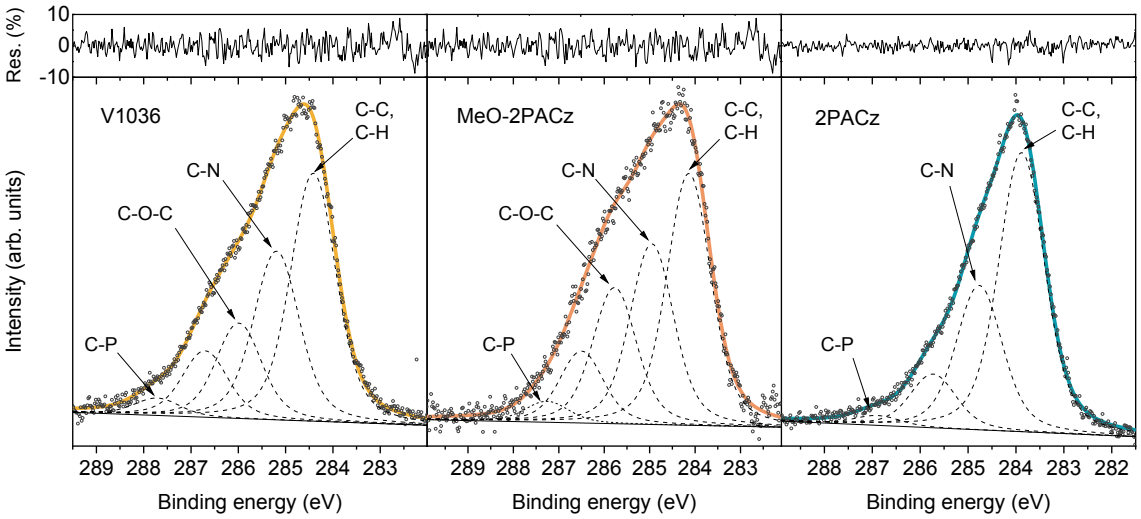

Figure S16 Same XPS measurement as in the main text, with the additional graph on top of each plot showing the relative residuum of each fit. The number of peaks was determined by fitting all three datasets globally with the same width and shape parameters and increasing the number of peaks until the residuum was in the order of the background noise of the data.

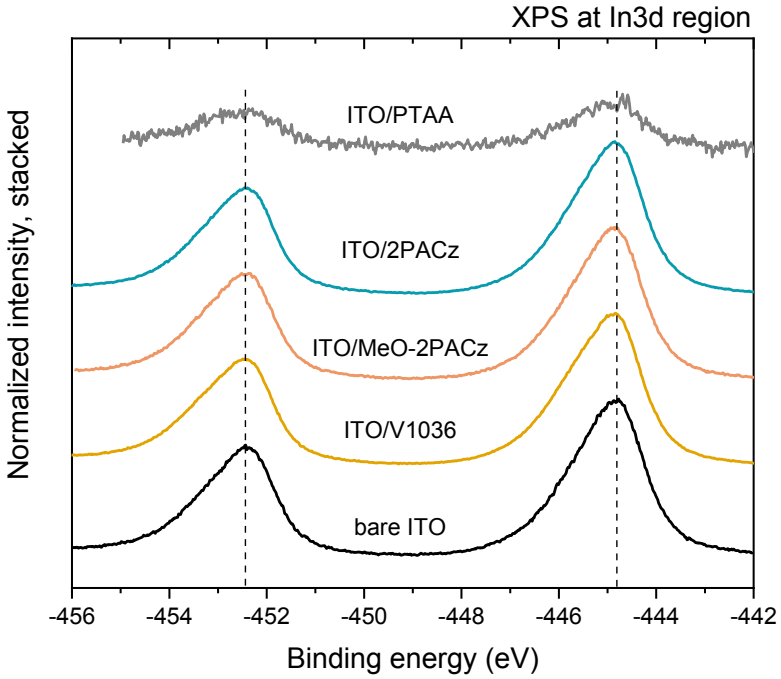

Figure S17 X-ray photoelectron spectra of the substrates on which UPS for the energy band edge diagram in fig. 4 of the main text (except for the perovskite values) has been conducted. The XPS measurement was recorded directly after the UPS measurement and shows the In peaks of the ITO substrate. All peaks are aligned, showing that no sample charging effects might have altered the energetic values.

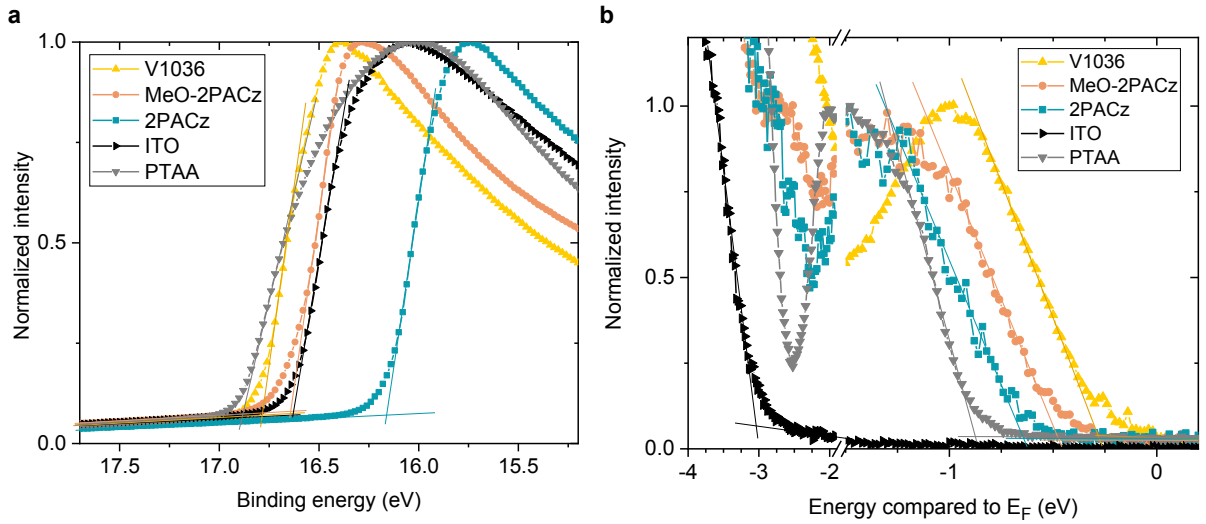

Figure S18 Ultra-violet photoelectron spectra (UPS) from which the work function (a) and valence band onset values (b) were extracted for the energy band edge diagram in fig. 4 of the main text (excitation energy is 21.22 eV). The excitation energy was 21.22 eV. After every UPS measurement, an XPS measurement was recorded to check for any charging effects of the substrates that could cause any shifts of the spectra (see comparisons of the substrates' In peaks in fig. S14).

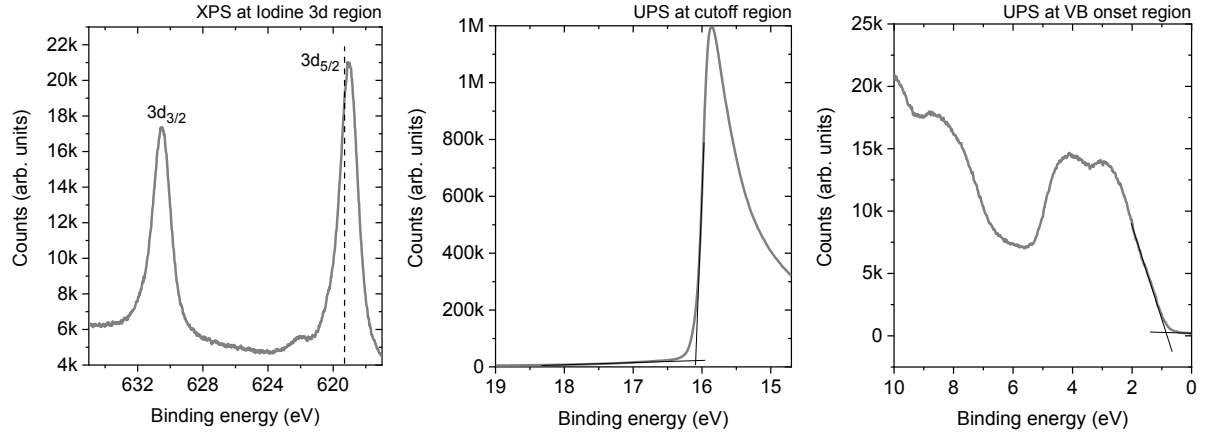

Figure S19 X-ray and UV Photoelectron spectroscopy of CsMAFA perovskite grown on PTAA (glass/ITO substrate). The dashed line in the XPS measurement (left) marks the expected position of the Iodine $3d_{5/2}$ peak[19]. The black lines in the UPS measurements (middle and right plot) are linear extrapolations of the leading edges.

Calculation of the dipole moment

The dipole moment was calculate following the previously published procedure[20]. In brief, as the hole-selective fragment is electronically decoupled from the phosphonic acid group due to the non-conjugated linking ethylene fragment, the contribution of the PA fragment to the final dipole moment can be excluded (following the assumption that the binding to the ITO surface is roughly the same for all three SAMs). Therefore, for the calculations the phosphonic acid group was replaced by hydrogen. DFT calculations were performed using TURBOMOLE version 7.0 software[21], with Becke's three parameter functional, B3LYP[22,23], and def2-SVP[24,25] basis set in vacuum. Note that the mentioned dipole moments do not necessarily contribute in the relative same magnitude for all different SAMs, since the orientation relative to the ITO surface is not known for the individual SAMs.

8. Further PL measurements

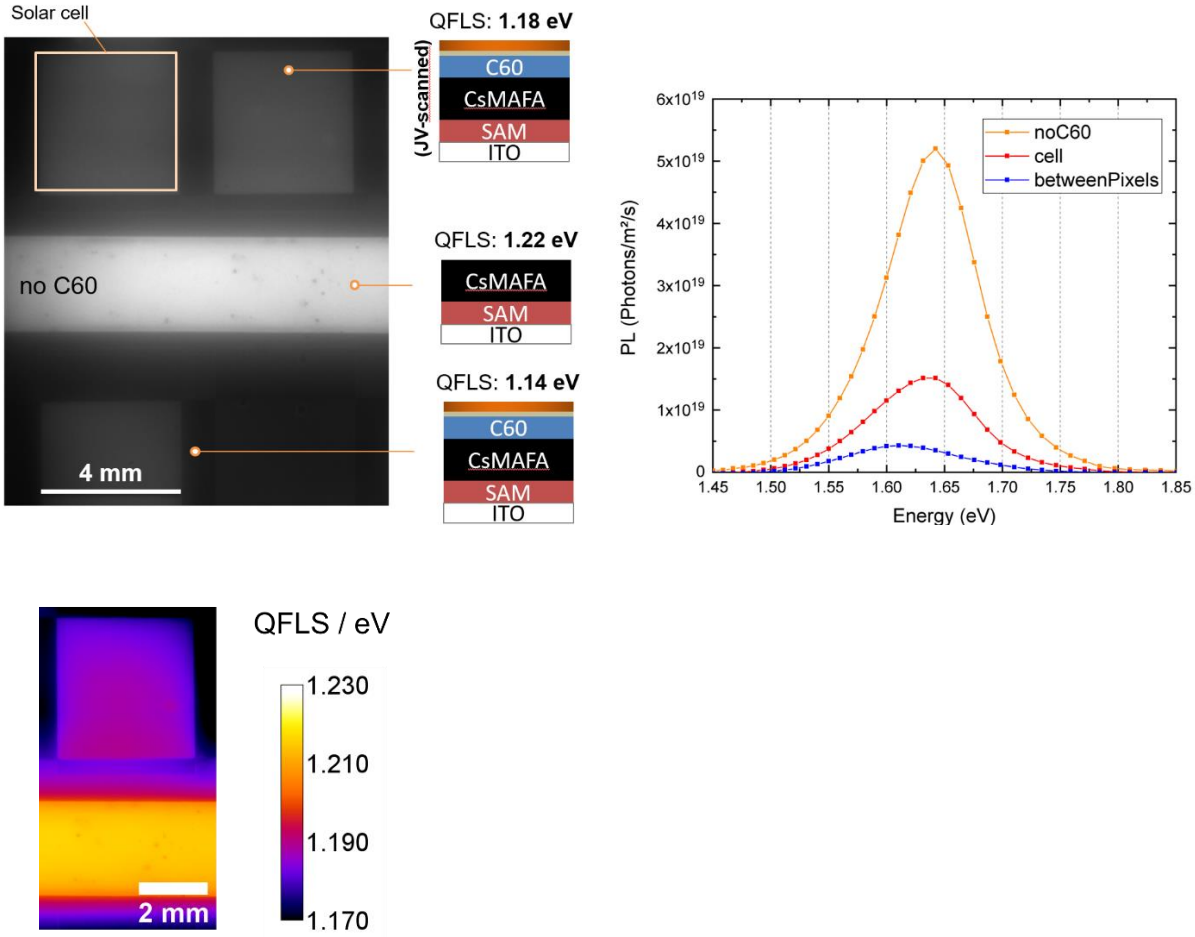

Figure S20 Absolute photoluminescence imaging of a sample with solar cells (bright squares, champion 2PACz device of the main text), recorded under an equivalent 1-sun intense fluence. By recording the photon-count calibrated PL spectra (displayed on the right for this sample) and applying the high-energy tail slope method as previously described for the same setup on perovskites,[8] the quasi fermi-level splitting (QFLS) values are obtained. The solar cell pixel shows a QFLS of 1.18 eV, while the same solar cell shows 1.188 V V_{OC} in the *J-V* scan. The bright stripe in the middle of the image shows an area without C60 evaporated on the perovskite. The QFLS of 1.22 eV (PL quantum yield of ~ 0.4 %) represents the maximum possible V_{OC} with this perovskite on 2PACz and the comparison to the solar cell shows that the C60 interface is leading to a loss of ~ 40 meV. This, interestingly, is lower than for the same perovskite grown on PTAA.[8] The lower panel shows a 2D plot of the QFLS of the upper part of the upper image (calculated from the difference of PL quantum yield to radiative limit[26], with same results as obtained with the high-energy tail slope fit).

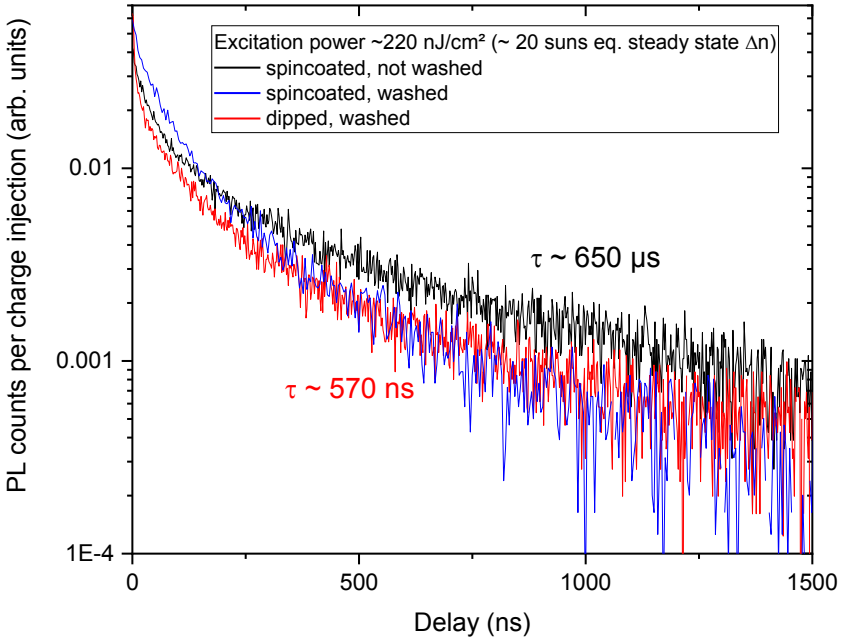

Figure S21 TrPL transients of CsMAFA perovskite film to investigate possible differences between spin-coating and dip-coating of the SAM solution (exemplary for MeO-2PACz). The non-significant difference is in line with the initially presented conclusions made with the RAIRS analysis.

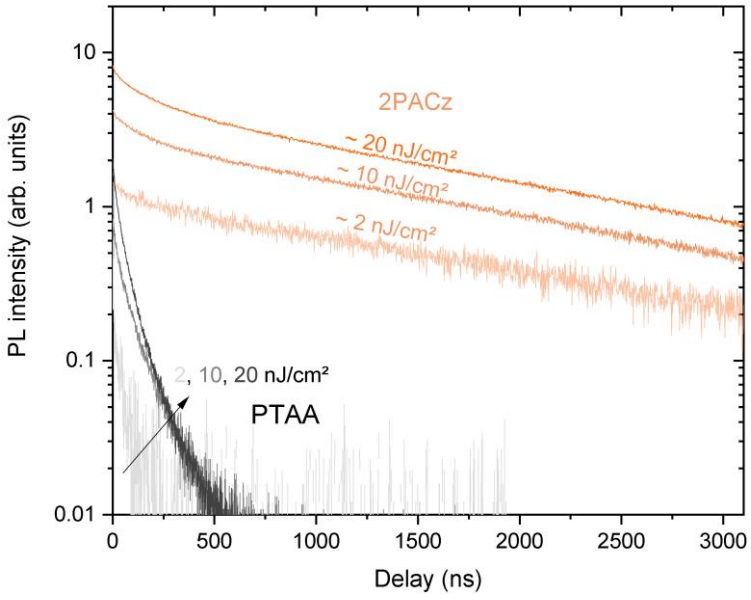

Figure S22a TrPL transients of CsMAFA perovskite films on 2PACz and PTAA for different excitation intensities.

Estimation of the interface recombination velocity

Assuming one-sided surface recombination (thus over-estimating S, since the CsMAFA top side is not passivated), we calculate the interface recombination velocity S through

$$\tau_2/2 = \frac{d}{S} + \frac{4}{D}\left(\frac{d^2}{\pi^2}\right),$$

with sample thickness d (~ 500 nm) and diffusivity D (~ 0.5). The calculated values for CsMAFA perovskite on the different HSCs are listed in the following table. Here, the two lifetimes were obtained from a bi-exponential fit, τ_2 corresponds to the value reported in the main text (which is roughly the same as obtained from a linear fit of the long tail), τ_1 was not used for the calculation:

	τ_1(ns)	$\tau_2/2$ (ns)	S (cm/s)
Quartz glass	0	708	35
V1036	60	130	193
PTAA	60	200	125
MeO-2PACz	109	641	39
2PACz	161	2041	12

9. Certification Results

Seite 3/6
Page

Fraunhofer ISE

10001090HMI059

CalLab PV Cells

Die Rückführung der Spektralmessung auf SI-Einheiten erfolgte über den Vergleich mit einer Standardlampe.
The traceability of the measurement of the spectral distribution to SI-Units is achieved using a standard lamp for the calibration of the spectroradiometer.

Identitäts-Nr. / *Identity-Nr.* :	Kalibrierschein-Nr./ *Certificate-Nr.* :	Rückführung/ *Traceability* :
BN-9101-451	40002-14-PTB	PTB

3. Messbedingungen
Measurement conditions

Standardtestbedingungen (STC) / *Standard Testing Conditions (STC)* :

Absolute Bestrahlungsstärke / *Total irradiance* :	1000	W/m²
Temperatur des Messobjektes / *Temperature of the DUT* :	25	°C
Spektrale Bestrahlungsstärke / *Spectral irradiance distribution* :	AM1.5G Ed.2 (2008)	

Die Messung der IV-Kennlinie (Strom-Spannungs-Kennlinie) des Messobjektes erfolgt mit Hilfe eines Vierquadranten-Netzteiles und eines Kalibrierwiderstandes.
The measurement of the IV-curve is performed with a 4-quadrant power amplifier and a calibration resistor.

4. Messergebnis
Measurement results

Fläche / *Area* (da)[1]: = (0.108 ± 0.003) cm²

[1] : *(t) = total area, (ap) = aperture area, (da) = designated illumination area /7/*

Kennlinienparameter des Messobjektes unter Standardtestbedingungen (STC) / *IV-curve parameter under Standard Testing Conditions (STC)* :

		Vorwärtsrichtung / *forwards scan direction*	Rückwärtsrichtung / *reverse scan direction*	MPP-Tracking / *MPP-Tracking*
V_{oc}	=	(1156.7 ± 7.8) mV	(1158.3 ± 7.8) mV	
I_{SC} (Ed.2 - 2008)	=	(2.34 ± 0.04) mA	(2.34 ± 0.04) mA	
I_{MPP}	=	2.19 mA	2.18 mA	(2.20 ± 0.07) mA
V_{MPP}	=	999.6 mV	1004.3 mV	(1002.7 ± 24.2) mV
P_{MPP}	=	2.19 mW	2.19 mW	(2.21 ± 0.06) mW
FF	=	80.95 %	80.91 %	
η	=	20.29 %	20.28 %	(20.44 ± 0.82) %

Figure S23 Fraunhofer ISE certificate of a representative 2PACz solar cell with a CsMAFA perovskite absorber. The cell was masked from a 0.16 cm² area to ~ 0.108 cm² and then sent to the calibration laboratory.

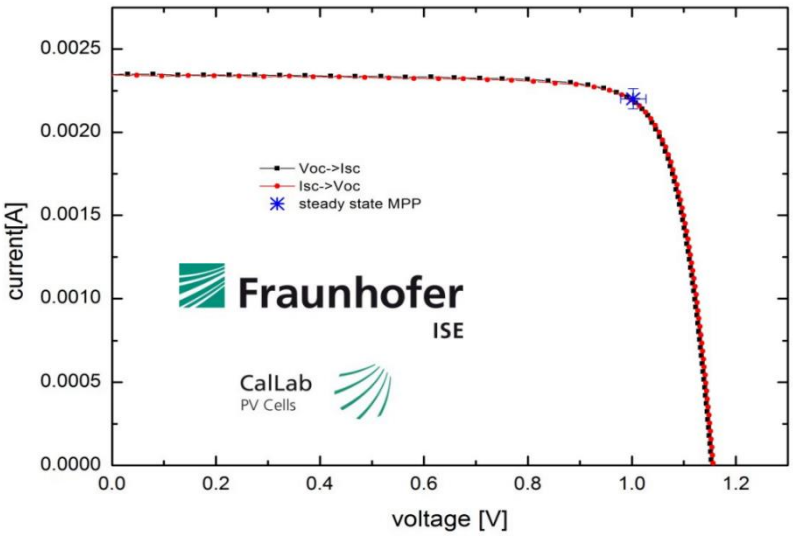

Figure S24 JV measurement by Fraunhofer ISE of a representative 2PACz solar cell with a CsMAFA perovskite absorber.

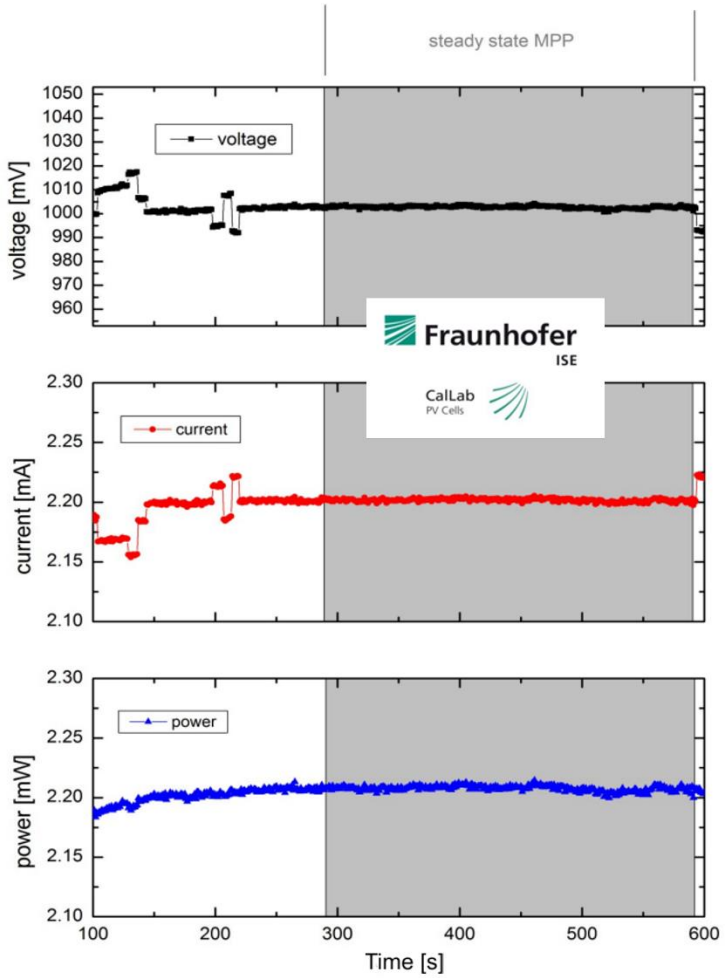

Figure S25 MPP tracking measurement by Fraunhofer ISE of a representative 2PACz solar cell with a CsMAFA perovskite absorber. The certified PCE value of 20.44 % is drawn from this measurement. The in-house MPP measurement of this device was 20.7 % 2 weeks prior to certification (with an in-house measured area of 0.107 cm², *FF* of 81.6% and V_{OC} of 1.15 V).

10. Additional results with the other perovskite absorbers

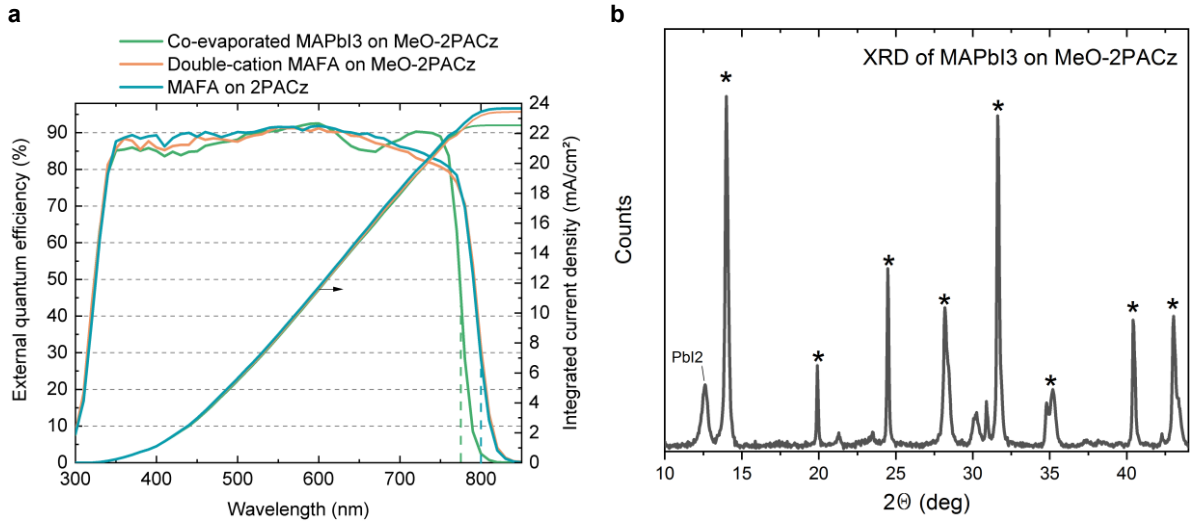

Figure S26 a, External quantum efficiency measurements of the "double" and "single" cation perovskite solar cells shown in fig. 7a of the main text, and corresponding integration of the product of EQE and AM1.5G spectrum (right axis). The JV-curve of the 2PACz/MAFA cell is shown in fig. S23. The vertical dashed lines indicated the position of the maximum of the curve's derivative (for estimation of the optical band gap, 775 nm for $MAPbI_3$ and 800 nm for MAFA). **b**, XRD of a representative $MAPbI_3$ perovskite prepared by co-evaporation on MeO-2PACz. The asterisks indicate the expected perovskite crystal diffraction peaks.

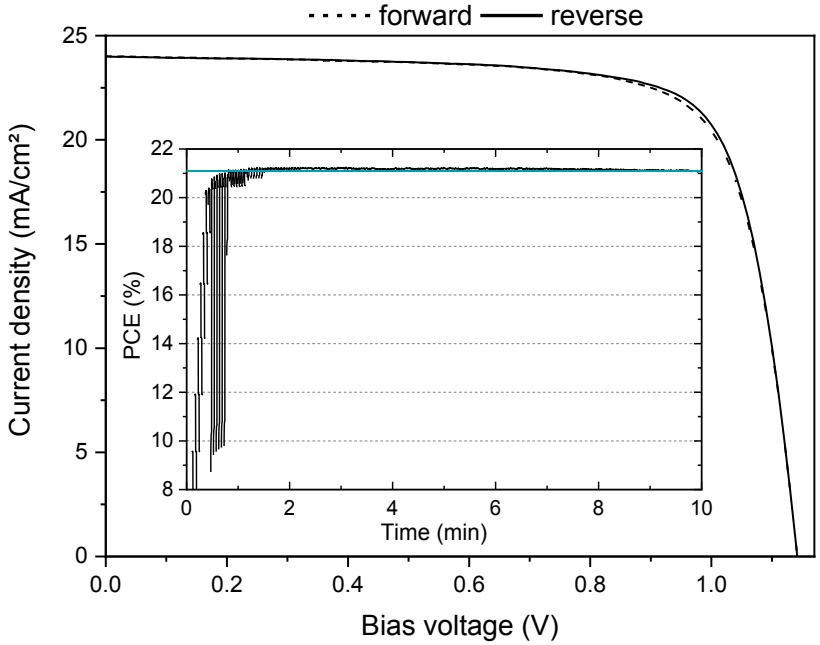

Figure S27 J-V scan (250 mV/s scan rate) at standard measurement conditions and MPP tracking in the inset of a PSC based on "double-cation" MAFA perovskite on 2PACz. Compared to MeO-2PACz, the V_{OC} is slightly higher, following the trend presented with CsMAFA in the main text. Device metrics are (reverse scan parameters): PCE = 21.0 %, V_{OC} = 1.142 V, FF = 76.7 %, J_{SC} = 24.0 mA/cm² (integrated EQE x AM1.5G = 23.7 mA/cm²). The blue line in the MPPT inset marks the 21.1 % value.

11. Additional results to the Perovskite/CIGSe Tandem

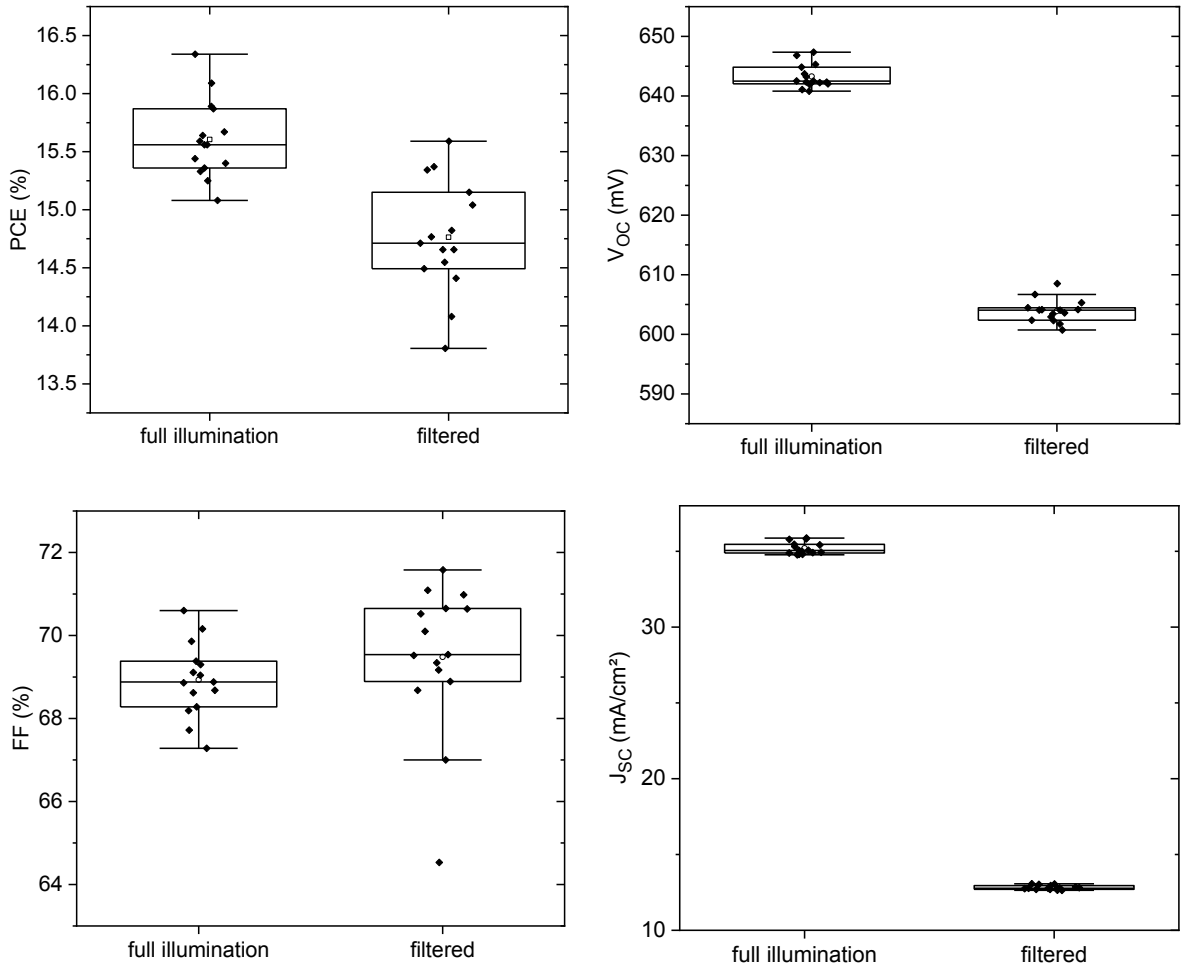

Figure S28 Solar cell device metrics of representative CIGSe bottom cells, similar to the one used for the tandem cell, under full 1-sun illumination and filtered for visible range absorption (as absorbed by the perovskite). The PCE values for the filtered case have been adjusted for the smaller illumination intensity.

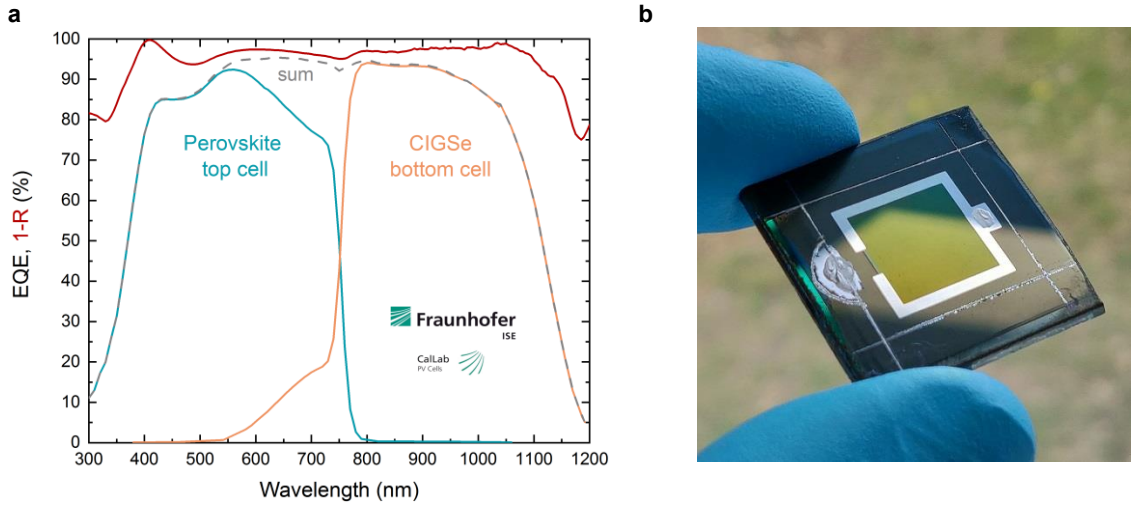

Figure S29 **a**, External quantum efficiency measurement (provided by Fraunhofer ISE, CalLab) of the CIGSe/perovskite monolithic tandem solar cell shown in figure 6b of the main text. The red line shows a 1-reflection measurement of the certified cell measured in-house. **b**, photograph of a representative CIGSe/perovskite monolithic tandem solar cell with ~ 1 cm² active area (surrounded by a silver frame).

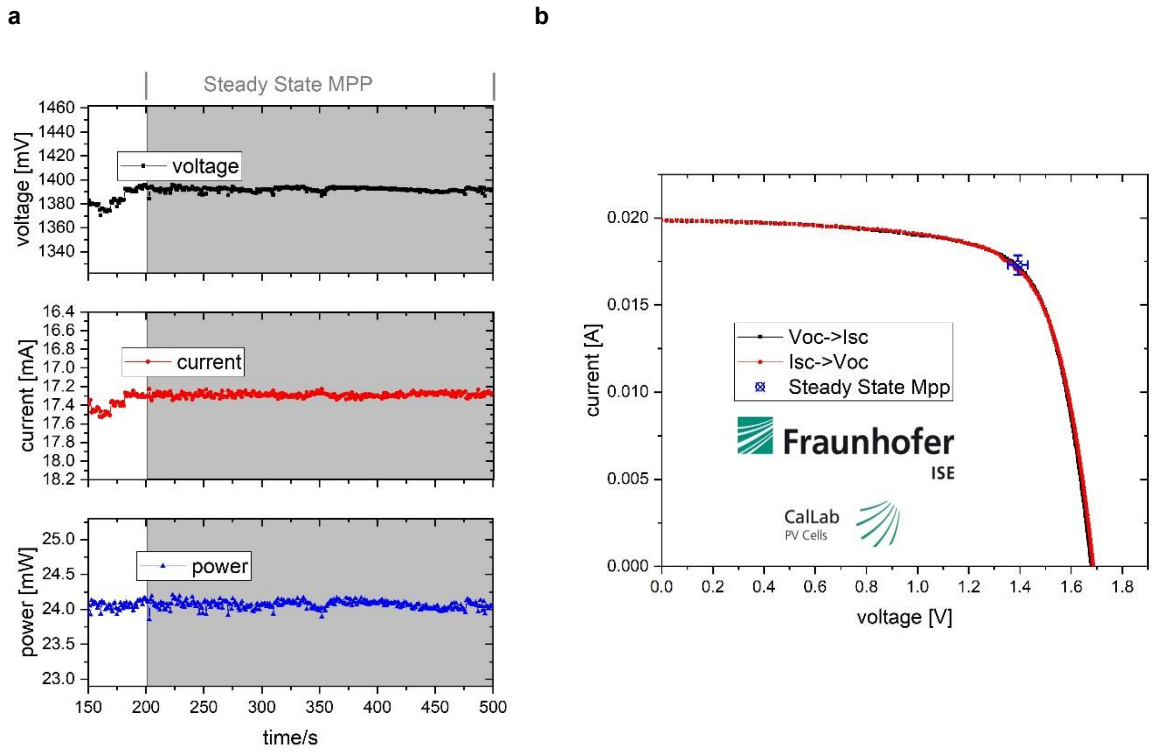

Figure S30 Certification results by Fraunhofer ISE of the CIGSe/Perovskite tandem solar cell (area ~ 1.035 cm²). **a**, maximum power point tracking from which the steady-state MPP value was extracted (in-house measurement was 23.2 %, fitting to the certified 23.26 %). **b**, J-V curve.

Fraunhofer ISE

CalLab PV Cells

10005085HMI0418

1. Beschreibung des Kalibriergegenstandes

Description of the calibrated object

Das Messobjekt ist eine Tandem-Solarzelle . Typ: Perowskit/CIGSe.

The device under test is a perovskite-CIGSe tandem solar cell.

2. Messverfahren

Measurement procedure

Die Kalibrierung des Kalibrierobjektes wird gemäß /1/ mit einem Zweilampen-DC-Sonnensimulator durchgeführt. Die Einstrahlung wird mit Hilfe einer Monitorzelle während der gesamten Messdauer aufgenommen und deren Schwankungen bezüglich der Messung korrigiert. Die Divergenz der Randstrahlen ist < 5°. Die Solarzelle wird auf einem Vakuumprobentisch thermisch stabilisiert.

The calibration of the test sample was performed at Standard Testing Conditions (STC) with a dual light steady-state solar simulator according to /1/. The irradiance is controlled with a monitor cell during the measurement in order to correct fluctuations. The divergence of the peripheral beams is < 5°. The solar cell is kept at a constant temperature

Rückführung der Referenzsolarzellen/*Traceability of the reference solar cells* :

Identitäts-Nr. / *Identity-Nr.* :	Kalibrierschein-Nr./ *Certificate-Nr.* :	Rückführung/ *Traceability* :
007-2012	47149-PTB-17	PTB
022-2018	47114-PTB-18	PTB

Die Korrektur der spektralen Fehlanpassung (Mismatch), die durch die Abweichung der spektralen Verteilung des Sonnen Simulators vom Standard-Spektrum AM1.5G /3/ in Kombination mit den verschiedenen spektralen Empfindlichkeiten von Referenzzelle und Messobjekt entsteht /4/, wurde durch eine erweiterte Mismatchberechnung /4/ - wie in /2/ beschrieben - korrigiert.

Dazu wurde die spektrale Verteilung der Bestrahlung (Sonnensimulator) mit einem Spektralradiometer und die spektrale Empfindlichkeit des Messobjektes mit einem laserbasierten Messplatz /5/ gemessen (s. Kalibrierschein Nr: 9005085HMI0418).

The spectral mismatch - caused by the deviation of the simulator spectrum from the standard spectrum AM1.5G /3/ in combination with the difference between the spectral response of the reference cell and that of the device under test (DUT) – is calculated by a generalized mismatch correction /3/ as described in /2/.

For the spectral mismatch correction the spectral distribution of the solar simulator is measured with a spectroradiometer, the spectral response of the DUT is measured with a laser-based setup according to /5/ (cf.

Der P_{MPP} wurde durch MPP-Tracking über 500s bestimmt. Der angegebene P_{MPP} ist der Mittelwert der letzten 300s dieser stabilisierten Messung. Anschließend wurde die IV-Kennlinie in zwei Richtungen (V_{OC} -> I_{SC} und I_{SC} -> V_{OC}) aufgenommen.

The P_{MPP} was determined by MPP-Tracking for 500s. The reported P_{MPP} represents the average value of the last 300s of this stabilized measurement. Afterwards, the IV-curve was determined with a scan in both directions (V_{OC} -> I_{SC} and I_{SC} -> V_{OC}).

Figure S31 Certification sheet for the CIGSe/perovskite tandem, description of the measurement procedure and type of solar cell.

Fraunhofer ISE

10005085HMI0418

CalLab PV Cells

Die Rückführung der Spektralmessung auf SI-Einheiten erfolgte über den Vergleich mit einer Standardlampe.
The traceability of the measurement of the spectral distribution to SI-Units is achieved using a standard lamp for the calibration of the spectroradiometer.

Identitäts-Nr. / *Identity-Nr.* :	Kalibrierschein-Nr./ *Certificate-Nr.* :	Rückführung/ *Traceability* :
BN-9101-451	40006-17-PTB	PTB

3. Messbedingungen

Measurement conditions

Standardtestbedingungen (STC) / *Standard Testing Conditions (STC)* :

Absolute Bestrahlungsstärke / *Total irradiance* :	1000	W/m²
Temperatur des Messobjektes / *Temperature of the DUT* :	25	°C
Spektrale Bestrahlungsstärke / *Spectral irradiance distribution* :	AM1.5G Ed.4 (2019)	

Die Messung der IV-Kennlinie (Strom-Spannungs-Kennlinie) des Messobjektes erfolgt mit Hilfe eines Vierquadranten-Netzteiles und eines Kalibrierwiderstandes.
The measurement of the IV-curve is performed with a 4-quadrant power amplifier and a calibration resistor.

4. Messergebnis

Measurement results

Fläche / *Area* (da)[1]: = (1.0347 ± 0.0099) cm²

[1] : *(t) = total area, (ap) = aperture area, (da) = designated illumination area /7/*

Kennlinienparameter des Messobjektes unter Standardtestbedingungen (STC) / *IV-curve parameter under Standard Testing Conditions (STC)* :

		Vorwärtsrichtung / *forwards scan direction*	Rückwärtsrichtung / *reverse scan direction*	MPP-Tracking / *MPP-Tracking*
V_{OC}	=	(1686.6 ± 11.3) mV	(1680.0 ± 11.3) mV	
I_{SC} (Ed.2 - 2008)	=	(19.85 ± 0.38) mA	(19.83 ± 0.38) mA	
I_{MPP}	=	17.21 mA	17.29 mA	(17.29 ± 0.57) mA
V_{MPP}	=	1379.7 mV	1385.9 mV	(1391.9 ± 38.2) mV
P_{MPP}	=	23.74 mW	23.96 mW	(24.06 ± 0.76) mW
FF	=	70.94 %	71.91 %	
η	=	22.95 %	23.16 %	(23.26 ± 0.75) %

Figure 32 Certification sheet for the CIGSe/perovskite tandem, performance parameters, measurement conditions and active area (designated area, defined by an evaporated silver ring, while the rest of the cell was masked).

Supporting Information References

1 A. Magomedov, A. Al-Ashouri, E. Kasparavičius, S. Strazdaite, G. Niaura, M. Jošt, T. Malinauskas, S. Albrecht and V. Getautis, *Adv. Energy Mater.*, 2018, **8**, 1801892.

2 P. Zhao, B. J. Kim, X. Ren, D. G. Lee, G. J. Bang, J. B. Jeon, W. Bin Kim and H. S. Jung, *Adv. Mater.*, 2018, **1802763**, 1–8.

3 M. Jošt, T. Bertram, D. Koushik, J. A. Marquez, M. A. Verheijen, M. D. Heinemann, E. Köhnen, A. Al-Ashouri, S. Braunger, F. Lang, B. Rech, T. Unold, M. Creatore, I. Lauermann, C. A. Kaufmann, R. Schlatmann and S. Albrecht, *ACS Energy Lett.*, 2019, **4**, 583–590.

4 E. Köhnen, M. Jošt, A. B. Morales-Vilches, P. Tockhorn, A. Al-Ashouri, B. Macco, L. Kegelmann, L. Korte, B. Rech, R. Schlatmann, B. Stannowski and S. Albrecht, *Sustain. Energy Fuels*, , DOI:10.1039/c9se00120d.

5 M. Talaikis, O. Eicher-Lorka, G. Valincius and G. Niaura, *J. Phys. Chem. C*, 2016, **120**, 22489–22499.

6 V. Shrotriya, G. Li, Y. Yao, T. Moriarty, K. Emery and Y. Yang, *Adv. Funct. Mater.*, 2006, **16**, 2016–2023.

7 M. Wojdyr, *J. Appl. Crystallogr.*, 2010, **43**, 1126–1128.

8 M. Stolterfoht, C. M. Wolff, J. A. Márquez, S. Zhang, C. J. Hages, D. Rothhardt, S. Albrecht, P. L. Burn, P. Meredith, T. Unold and D. Neher, *Nat. Energy*, 2018, **3**, 847–854.

9 A. Delamarre, L. Lombez and J. F. Guillemoles, *Appl. Phys. Lett.*, 2012, **100**, 2012–2015.

10 S. A. Paniagua, P. J. Hotchkiss, S. C. Jones, S. R. Marder, A. Mudalige, F. S. Marrikar, J. E. Pemberton and N. R. Armstrong, *J. Phys. Chem. C*, 2008, **112**, 7809–7817.

11 M. Bomers, A. Mezy, L. Cerutti, F. Barho, F. Gonzalez-Posada Flores, E. Tournié and T. Taliercio, *Appl. Surf. Sci.*, 2018, **451**, 241–249.

12 W. Zhang, W. Ju, X. Wu, Y. Wang, Q. Wang, H. Zhou, S. Wang and C. Hu, *Appl. Surf. Sci.*, 2016, **367**, 542–551.

13 R. Quiñones, S. Garretson, G. Behnke, J. W. Fagan, K. T. Mueller, S. Agarwal and R. K. Gupta, *Thin Solid Films*, 2017, 642, 195–206.

14 J. A. Guerra, A. Tejada, L. Korte, L. Kegelmann, J. A. Töfflinger, S. Albrecht, B. Rech and R. Weingärtner, *J. Appl. Phys.*, 2017, **121**, 173104.

15 J. S. Kim, P. K. H. Ho, D. S. Thomas, R. H. Friend, F. Cacialli, G. W. Bao and S. F. Y. Li, *Chem. Phys. Lett.*, 1999, **315**, 307–312.

16 C. Donley, D. Dunphy, D. Paine, C. Carter, K. Nebesny, P. Lee, D. Alloway and N. R. Armstrong, *Langmuir*, 2002, **18**, 450–457.

17 A. W. C. Lin, N. R. Armstrong and T. Kuwana, *Anal. Chem.*, 1977, **49**, 1228–1235.

18 P. J. Hotchkiss, S. C. Jones, S. A. Paniagua, A. Sharma, B. Kippelen, N. R. Armstrong and S. R. Marder, *Acc. Chem. Res.*, 2012, **45**, 337–346.

19 J. F. Moulder, W. F. Stickle, P. E. Sobol and K. D. Bomben, *Handbook of X-ray Photoelectron Spectroscopy*, 1992.

20 I. Lange, S. Reiter, M. Pätzel, A. Zykov, A. Nefedov, J. Hildebrandt, S. Hecht, S. Kowarik, C. Wöll, G. Heimel and D. Neher, *Adv. Funct. Mater.*, 2014, **24**, 7014–7024.

21 R. Ahlrichs, M. Bär, M. Häser, H. Horn and C. Kölmel, *Chem. Phys. Lett.*, 1989, **162**, 165–169.

22 C. Lee, W. Yang and R. G. Parr, *Phys. Rev. B*, 1988, **37**, 785–789.

23 A. D. Becke, *J. Chem. Phys.*, 1993, **98**, 5648–5652.

24 A. Schäfer, H. Horn and R. Ahlrichs, *J. Chem. Phys.*, 1992, **97**, 2571–2577.

25 F. Weigend and R. Ahlrichs, 2005, 3297–3305.

26 R. T. Ross, *J. Chem. Phys.*, 1967, **46**, 4590–4593.

7.5 Publication to chapter 5

The *accepted version* of the paper text with published versions of the figures are reprinted here with permission (lic. no. 4984121212048) – Published by The AAAS [209] (formatted and edited version by *Science* available online)

Title: Monolithic Perovskite/Silicon Tandem Solar Cell with >29% Efficiency by Enhanced Hole Extraction

Authors: Amran Al-Ashouri*[,a], Eike Köhnen*[,a], Bor Li[a], Artiom Magomedov[b], Hannes Hempel[c], Pietro Caprioglio[a,f], José A. Márquez[c], Anna Belen Morales-Vilches[e], Ernestas Kasparavicius[b], Joel A. Smith[g,j], Nga Phung[g], Dorothee Menzel[a], Max Grischek[a,f], Lukas Kegelmann[a], Dieter Skroblin[h], Christian Gollwitzer[h], Tadas Malinauskas[b], Marko Jošt[a,i], Gašper Matič[i], Bernd Rech[d,k], Rutger Schlatmann[e,k], Marko Topič[i], Lars Korte[a], Antonio Abate[g], Bernd Stannowski[e], Dieter Neher[f], Martin Stolterfoht[f], Thomas Unold[c], Vytautas Getautis[b], Steve Albrecht[a,l,§]

Affiliations:
a Young Investigator Group Perovskite Tandem Solar Cells, Helmholtz-Zentrum Berlin, Kekuléstraße 5, 12489 Berlin, Germany.
b Department of Organic Chemistry, Kaunas University of Technology, Radvilenu pl. 19, Kaunas LT-50254, Lithuania.
c Department of Structure and Dynamics of Energy Materials, Helmholtz-Zentrum-Berlin für Materialien und Energie GmbH, Hahn-Meitner Platz 1, 14109 Berlin, Germany
d Helmholtz-Zentrum Berlin, Scientific Management, 12489 Berlin, Germany
e PVcomB, Helmholtz Zentrum Berlin, Schwarzschildstr. 3, 12489 Berlin, Germany
f Institute of Physics and Astronomy, University of Potsdam, 14476 Potsdam, Germany
g Young Investigator Group Active Materials and Interfaces for Stable Perovskite Solar Cells, Kekuléstraße 5, 12489 Berlin, Germany
h Physikalisch-Technische Bundesanstalt (PTB), Abbestraße 2-12, 10587 Berlin, Germany
i University of Ljubljana, Faculty of Electrical Engineering, Tržaška 25, 1000 Ljubljana, Slovenia
j Department of Physics & Astronomy, University of Sheffield, Hicks Building, Hounsfield Road, Sheffield, S3 7RH, U.K.
k HTW Berlin – University of Applied Sciences, Wilhelminenhofstr. 75a, 12459 Berlin, Germany
l Faculty of Electrical Engineering and Computer Science, Technical University Berlin, Marchstraße 23, 10587 Berlin, Germany
** contributed equally, § corresponding author*

Abstract

Tandem solar cells that pair silicon with metal-halide perovskite are a promising option for surpassing the single-cell efficiency limit. We report a certified record monolithic perovskite/silicon tandem with a power conversion efficiency of 29.15%. The perovskite absorber with 1.68 eV bandgap remained phase-stable under illumination through a combination of fast hole extraction and minimized non-radiative recombination at the hole-selective interface. Key was a self-assembled, methyl-substituted carbazole monolayer as hole-selective layer in the perovskite cell. The accelerated hole extraction was linked to a low ideality factor of 1.26 and single-junction fill factors of up to 84%, while enabling the yet highest tandem open-circuit voltage of up to 1.92 volts. In air, without encapsulation, a tandem retained 95% of its initial efficiency after 300 hours of operation.

One Sentence Summary: Combining interface passivation with fast charge extraction for stable, highly efficient perovskite/silicon tandem solar cells

Main text:

A tandem solar cell with a silicon cell overlaid by a perovskite solar cell (PSC) (*1*) could increase efficiencies of commercial mass market photovoltaics beyond the single-junction cell limit (*1*, *2*) without adding substantial costs (*3*, *4*). The power conversion efficiency (PCE) of PSCs has reached up to 25.2% for single-junction solar cells (at an area of ~0.1 cm²) (*5*), 24.2% for perovskite/CIGSe (copper-indium-gallium-selenide) tandem cells (~1 cm²) (*5*–*7*), 24.8% for all-perovskite tandem cells (0.05 cm²) (*8*, *9*) and 26.2% for the highest openly published perovskite/silicon tandem efficiency (~1 cm^2) (*10*, *11*). Perovskite/silicon tandem cells have additionally undergone technological advances in both stability

and compatibility with textured silicon substrates (*11–13*). However, there is still room for improvement for these perovskite-based tandem solar cells, as practical limits for all these tandem technologies are well above 30% (*14*, *15*).

The increase in PSC efficiency has been driven in part by advances in physical and chemical understanding of the defect and recombination mechanisms. Some reports presented near-perfect passivation of surfaces and grain boundaries with photoluminescence quantum yields (PLQYs) approaching theoretical limits (*16–18*). Consequently, PSCs were reported with open-circuit voltage (V_{OC}) values of only a few 10 meV below their radiative limit (*19–23*). These values surpass those reached with crystalline silicon absorbers and are comparable with solar cells based on epitaxially grown GaAs (*23*, *24*). However, perovskite compositions with a wider bandgap that are needed for high-efficiency tandem solar cells still show considerable V_{OC} losses (*14*, *25*). The main reasons include comparably low PLQYs of the absorber material itself, an unsuitable choice of selective contacts and phase instabilities. Even state-of-the-art perovskite/silicon tandem cells still have V_{OC}s well below 1.9 V.

We present a strategy to overcome these issues simultaneously, demonstrated on a 1.68 eV bandgap triple-cation perovskite composition, which enables photostable tandem devices with a V_{OC} of 1.92 V. We note that the charge extraction efficiency, and with that, the fill factor (FF) of PSCs, is still poorly understood. Although reported PSCs usually feature a small active area (~0.1 cm²) with small absolute photocurrents (a few milliamperes), and thus small series resistance losses at the contacts, usual FFs of high-efficiency devices generally range from 79 to 82%. However, based on the detailed balance limit, PSCs should be able to deliver a FF of 90.6% at a bandgap of 1.6 eV. Wider bandgap perovskite compositions near 1.7 eV seem especially prone to low FFs, resulting in tandem cell FF values commonly below 77%, near current-matching conditions (*11*, *12*, *26*). In optimized perovskite single-junction devices, the FFs only recently exceeded 80%, with a maximum value of 84.8% (*27*).

One reason for the low FF might be that there are only few techniques for quantifying and analyzing the FF losses in PSCs. We show that intensity-dependent transient and absolute photoluminescence is a viable technique. A main FF limitation of high-efficiency PSCs is the ideality factor n_{ID}, with typical values of 1.4 to 1.8 for high-V_{OC} devices (*28*), while established solar cell technologies reach values of 1 to 1.3 (*29*). Thus, an important goal for perovskite photovoltaics is to lower the ideality factor while minimizing nonradiative interface recombination to achieve a high V_{OC} (*28*). We designed a self-assembled monolayer (SAM) with methyl group substitution as a hole-selective layer, dubbed Me-4PACz ([4-(3,6-dimethyl-9H-carbazol-9-yl)butyl]phosphonic acid) and show that a fast hole extraction led to a lower ideality factor. Thus, FFs of up to 84% in *p-i-n* single-junction PSCs and >80% in tandem devices were achieved.

The SAM provided both fast extraction and efficient passivation at the hole-selective interface. This combination slowed down light-induced halide segregation of a tandem-relevant perovskite composition with 1.68 eV bandgap, allowed a PLQY as high as on quartz glass and led to high single-junction device V_{OC}s > 1.23 V. The single-junction improvements transferred into tandem devices, which allowed us to fabricate perovskite/silicon tandem solar cells with a certified PCE of 29.15%. This value surpasses the best silicon single-junction cell (26.7%) and is comparable to the best GaAs solar cell (*27*) at the same area of 1 cm². Under maximum power point tracking (MPP) in ambient air without encapsulation, a Me-4PACz tandem cell retained 95% of its initial efficiency after 300 h. Furthermore, we used injection-dependent, absolute electroluminescence spectroscopy to reconstruct the individual subcell current-voltage curves without the influence of series resistance (pseudo-*J-V* curves), demonstrating that the tandem device design that features only a standard perovskite film without additional bulk passivation could in principle realize PCE values up to 32.4%.

Stabilization of wide-bandgap perovskite with the hole-selective layer

The ideal top cell bandgap for perovskite absorbers in conjunction with CIGSe and Si bottom cells is ~1.68 eV (*30–32*). These wider bandgap compositions often feature a Br to I ratio >20%, which can lead to phase instabilities caused by light-induced halide segregation, most strikingly evident from photoluminescence (PL) spectra that show a double-peak formation under continuous illumination (*33*, *34*). Upon generation of charge carriers in the perovskite film, iodide-rich clusters can form that are highly luminescent as they serve as charge carrier sinks given their lower bandgap compared to the surrounding material (*35*). As quantified by Mahesh et al., although some portion of the V_{OC} loss is related to halide segregation, the dominant source of V_{OC} loss is likely the generally low optoelectronic quality of the Br-rich mixed halide perovskite absorbers itself, or high non-radiative recombination rates at their interfaces (*35*). Hence, in order to unambiguously determine the limitations and potentials of wide bandgap compositions, it is necessary to find suitable charge-selective contacts that do not introduce further losses or instabilities.

We show that fast charge extraction paired with surface passivation can effectively suppress the formation of a double-peak emission in the PL, indicative of phase stabilization, and simultaneously enable a high quasi Fermi level splitting (QFLS) and device performance. Rather than optimizing the perovskite composition or passivating the film, we chose a variant of the widely used Cs-, FA- and MA-containing "triple-cation" perovskite (*36*) that is highly reproducible and focused on preparing an optimal charge-selective contact on which the perovskite film was deposited. We shifted the bandgap upward by increasing of the Br to I ratio to obtain a 1.68 eV (23% Br) absorber instead of the commonly used 1.6-1.63 eV (~17% Br), yielding a nominal precursor composition of $Cs_{0.05}(FA_{0.77}MA_{0.23})_{0.95}Pb(I_{0.77}Br_{0.23})_3$.

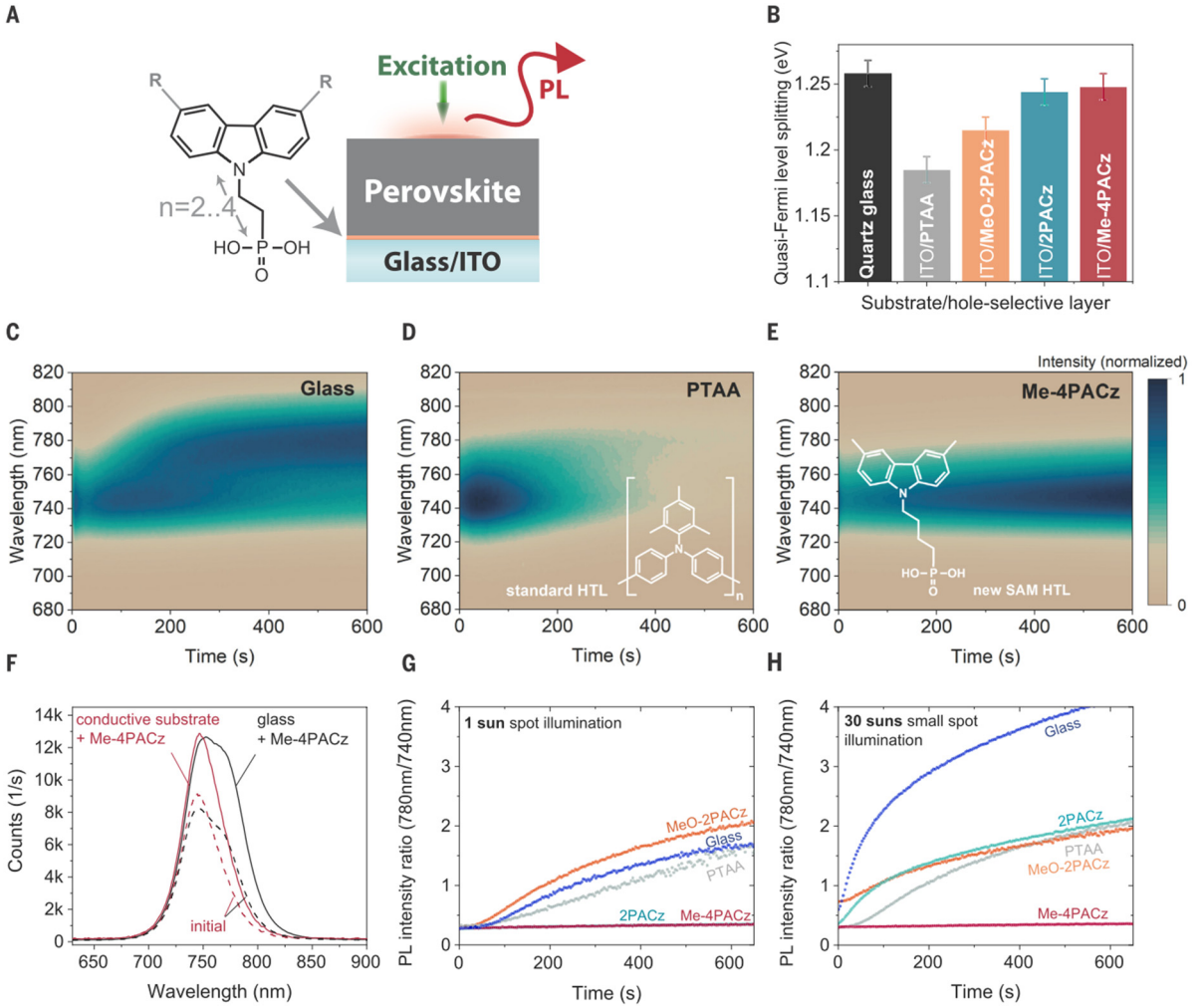

Fig. 1 Photoluminescence properties and stability assessment of perovskite films on different substrates. (**A**) schematic description of the photoluminescence (PL) experiment and chemical structure of a general carbazole-based SAM, with R denoting a substitution (or "termination"), which in this work is either nothing (2PACz), a methoxy group (MeO-2PACz) or a methyl group (Me-4PACz). The number 2 or 4 denotes the number of the linear C-atoms between the phosphonic acid anchor group and the conjugated carbazole main fragment. (**B**) Quasi Fermi level splitting (QFLS) values of non-segregated 1.68 eV bandgap perovskite films on a bare glass substrate and different hole-selective layers on the transparent and conductive indium tin oxide (ITO). (**C-E**), Time-dependent photoluminescence spectra analyzing phase stability of perovskite absorbers with 1.68 eV bandgap. The perovskite films were deposited either on glass (C) or on ITO substrates with different hole-selective layers (D, E). (**F**) PL spectra before (dashed lines) and after 600 s of light-soaking (solid lines) under 1-sun equivalent illumination flux in air, comparing the perovskite grown on Me-4PACz that was deposited on either a glass substrate or conductive ITO substrate. (**G**) As figure of merit for stability, the ratio of PL intensities at 780 nm and 740 nm is shown, from the PL evolutions in (C), (D), (E), and two other hole-selective layers (shown in SI, illumination spot size ~0.12 cm²). (**H**) Same as for (G), but at higher illumination intensity through decrease of the excitation spot size to 0.4 mm².

A schematic of the device stack and the used hole-selective layers (commonly abbreviated as HTLs, "hole transporting layers") used for PL measurements is shown in **Fig. 1**. We first compared the QFLS measured by absolute PL and then the PL stability of this perovskite composition prepared on indium tin oxide (ITO) substrates covered by the HTLs. In recently published high-PCE p-i-n ("inverted") single-junction and tandem PSCs, the polymer bis(4-phenyl)(2,4,6-trime-thylphenyl)amine] (PTAA) or the comparable Poly(N,N'-bis-4-butylphenyl-N,N'-bisphenyl)benzidine (polyTPD) are standardly used (*10*, *11*, *37*, *38*). Alternatively, self-assembled monolayers (SAMs) based on carbazole such as MeO-2PACz and 2PACz can form passivated interfaces while allowing for low transport losses due to their ultrathin thickness (<1 nm) (*7*). The introduction of a methyl-group substitution to the "lossless" hole-selective interface created by 2PACz (*7*) lead to a more optimized alignment with the perovskite valence band edge (see energetic band edge diagram in Figure S1) with a similar dipole moment (~1.7 D) and resulted in faster charge extraction. The supplementary materials contain the synthesis scheme of the herein used SAMs. In literature of the n-i-p configuration of PSCs, methoxy substituents were prevalently used in HTLs, with some works reporting a possible passivation function at the perovskite

interface (*39–42*). For the p-i-n configuration however, the standard high-performance HTLs PTAA and polyTPD contain alkyl substituents. In the present study, we directly compared methoxy and methyl substituents in p-i-n cells with MeO-2PACz and Me-4PACz, with the results showing advantages for the methyl substitution regarding both passivation and hole extraction. We tested the influence of the aliphatic chain length (n) in carbazole SAMs without (nPACz) and with methyl substitution (Me-nPACz) on PSC performance and found an optimum FF at n = 2 for nPACz and at n = 4 for Me-nPACz (see Figure S23). For n = 6, both SAMs lead to current-voltage hysteresis.

The QFLS values of bare perovskite films (**Fig. 1B**) deposited on 2PACz and Me-4PACz were similar to that on quartz glass, commonly regarded as a perfectly passivated substrate (*16*). Perovskite compositions with high Br content typically segregate into I-rich phases indicated by increased PL intensity at lower photon energies, here at a wavelength of 780 nm (*33*). Pristine regions of the non-segregated perovskite film emitted photons at a peak wavelength of around 740 nm for perovskite deposited on glass (**Fig. 1C**) or ITO/PTAA (**Fig. 1D**), and a similar response was seen for the SAM MeO-2PACz (Figure S3) on ITO. However, the perovskite emission was more stable over time on ITO/2PACz and ITO/Me-4PACz substrates (**Fig. 1E** and Figure S3). The raw spectra are shown in Figure S4.

Among the studied HTLs, phase segregation was only inhibited if the perovskite was grown on a substrate that fulfilled the requirements of both fast charge extraction and good passivation; **Fig. 1F** demonstrates that passivation alone was insufficient. The black curve shows a PL spectrum of the perovskite film on an insulating glass substrate that was covered by Me-4PACz, after 10 min of continuous spot illumination with 1-sun equivalent photon flux. The illuminated film showed signs of I-rich phases emitting at a center wavelength of ~780 nm. The glass substrate ensured that no hole transfer out of the perovskite bulk occurred. In contrast, a conductive ITO substrate that allowed hole transmission in combination with Me-4PACz increased the PL stability, as evidenced by the sharp peak with emission centered at ~740 nm even after 10 min of spot illumination.

A bare ITO substrate seemed to prevent charge accumulation as well, allowing a stable PL peak position at 1-sun intensity (0.12 cm^2 spot size, see Figure S6). The connection between charge accumulation in the perovskite and phase instability was reported in previous studies in which a reduced density of carriers increased the activation energy of mobile ion species and allowed the film to remain in its initial form (*43*, *44*). Spot illumination (0.12 cm^2 with 1-sun photon flux) represented increased stress testing on phase stability compared to full illumination because it created an outward driving force for ions from the illuminated area (*45*). Consequently, a smaller illumination spot (i.e., larger edge-to-area ratio) at the same illumination intensity showed a faster PL redshift (see Figure S5 & Figure S6). To compare the degree of PL redshift and double-peak formation, we evaluated the ratio of the two emission center intensities at 740 and 780 nm for two different excitation fluences equivalent to 1-sun and 30-suns illumination, in **Fig. 1G** and **H,** respectively. At 1-sun-equivalent intensity, only 2PACz and Me-4PACz on ITO had a stable ratio. However, upon increasing the intensity and thus charge carrier generation rate 30-fold, a Me-4PACz-covered ITO substrate differed from the 2PACz-covered by still displaying a similarly stable PL intensity ratio.

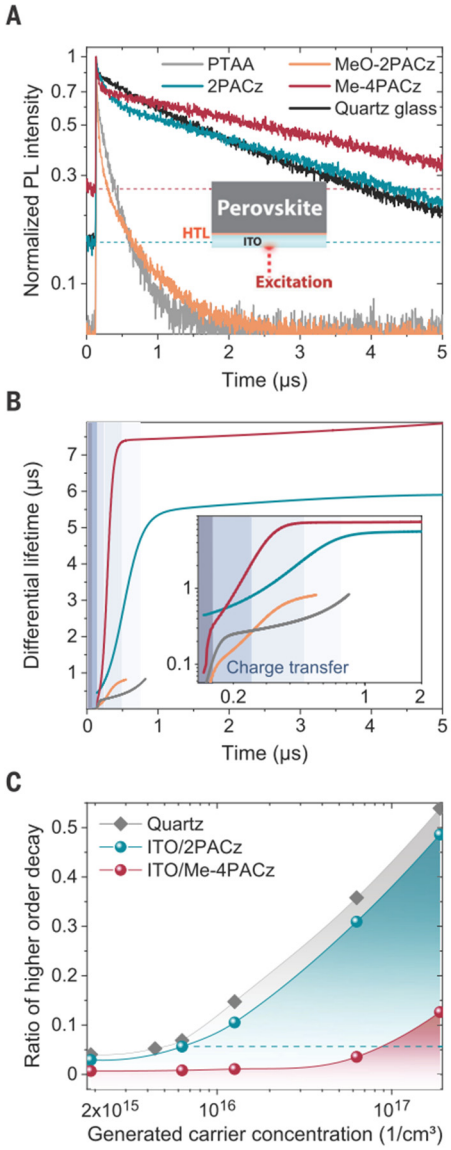

Fig. 2 Role of charge transfer on transient photoluminescence (TrPL). (**A**) PL transients of perovskite on ITO/hole-selective layer substrates. The dashed lines indicate the background levels. (**B**) Computed differential lifetimes from fits to the transients in (A), showing the single-exponential decay time at each time of the transient, with early times shown in the inset. The inset highlights the region of the Me-4PACz and 2PACz transients that is governed by hole transfer into the ITO. Excitation density is similar to 1-sun conditions (fluence of ~30 nJ/cm², 2-3 x 10^{15} cm^{-3}). (**C**) Ratio of higher-order processes to mono-exponential decay in the TrPL transients, revealing that Me-4PACz not only extracts holes faster (inset in B), but also with a ~10 times higher efficiency compared to 2PACz, since the Me-4PACz transient shows the same magnitude of radiative recombination only at a ~10 times higher charge carrier generation (comparison along the dashed line, see Figure S10 for details).

We used transient photoluminescence (TrPL) to analyze charge carrier transfer into adjacent charge-selective layers (*46*). The full decay is governed by non-radiative, trap-assisted surface/bulk recombination (mostly mono-exponential decay), radiative recombination ("bimolecular", second-order differential equation) and charge transfer effects, which can be disentangled if these time constants differ sufficiently from each other (*18*). **Fig. 2A** presents PL transients of 1.68 eV-bandgap perovskite films on ITO/HTL substrates. With MeO-2PACz and PTAA, it is not possible to clearly differentiate between charge extraction and trap-assisted recombination because both the nonradiative recombination is high (as evidenced by lower QFLS values compared to quartz glass, **Fig. 1B**) and the transients did not saturate towards one process. In contrast, the PL transients for 2PACz and Me-4PACz showed a clear mono-exponential decay at later times, indicating Shockley-Read-Hall recombination (*47*). Fits to the TrPL transients (Figure S8) were used to compute the differential lifetime $\tau = -\left(d\ln\left(\phi(t)\right)/dt\right)^{-1}$ (**Fig. 2B**), with $\phi(t)$ being the time-dependent PL photon flux. In this representation, the processes that reduce the PL counts over time are separable and the transient decay time (or "lifetime") is directly readable at each time point (*46*).

The high, asymptotically reached TrPL lifetimes of >5 µs for both 2PACz and Me-4PACz suggested that there were minimal non-radiative recombination losses at the SAM interfaces. The charge transfer process at early times (until ~1 µs) led to a sharp rise of τ, resembling simulated curves by Krogmeier

et al. (*46*). The transition from increasing lifetime to the plateau marks when the charge transfer ends, and non-radiative first-order recombination becomes dominant. Because PLQY measurements of films on 2PACz and Me-4PACz indicated a similar level of interface recombination and charge generation conditions are the same (see also Figure S9), the steepness of this rise was influenced by the charge transfer speed. The observed gradient for Me-4PACz implied a faster hole transfer to the underlying ITO compared to 2PACz, with the saturation starting after ~300 ns as compared to ~1 µs.

In the charge carrier generation regime of this experiment (~1-sun, $\sim 3 \cdot 10^{15}$ cm^{-3}), trap-assisted recombination dominated with the PL flux scaling proportionally to the density of photogenerated carriers n, as evidenced by intensity-dependent TrPL shown in Figure S9. Figure S9 further demonstrates that at higher generation conditions, the PL flux scaled proportionally to n^2, where transients usually show a multi-exponential signature, as seen with 2PACz and quartz (see Figure S10). Nevertheless, in this regime the Me-4PACz transients remained mono-exponential until generation densities exceeded ~35-suns-equivalent. We interpret this as a consequence of a large hole-extraction flux, which causes first-order recombination to dominate even in this injection regime.

We quantified this phenomenon of persisting domination of first-order recombination in **Fig. 2C** by displaying the ratio of higher-order to first-order recombination for the different generation conditions (see supplementary text for the evaluation method). The comparison of Me-4PACz to 2PACz indicated that Me-4PACz had a >10 times larger hole-extraction flux, because the curvature of the TrPL transient only began to resemble that of 2PACz at a >10 times higher generation density (indicated by the blue dashed line in **Fig. 2C**).

The carrier mobilities determined by optical-pump-terahertz-probe measurements (Figure S12) were similar between perovskite films grown on the different HTLs. To also exclude differences in perovskite composition and crystal orientation due to possible growth differences, we probed the effect of the HTL on these properties by grazing-incidence wide-angle x-ray scattering (GIWAXS) at the four crystal monochromator beamline of the Physikalisch-Technische Bundesanstalt (*48*). Azimuthally integrated diffraction patterns collected on a movable PILATUS detector module (*49*) showed comparable composition in each case (Figure S13), with marginally increased PbI_2 scattering intensity on PTAA as we observed in our previous work (*7*). Comparing azimuthal intensity profiles for perovskite scattering features (Figure S14), we found negligible difference in crystallographic orientation between the samples.

Our complete solar cells were capped by C_{60} as the electron-selective contact. The electron extraction speed was not limiting the cell operation, as demonstrated by a time-resolved Terahertz photoconductivity measurement combined with TrPL on a quartz/perovskite/C_{60} sample (Figure S11). We compared the decays of free charge carriers after interface-near carrier generation on both sample sides and found an electron transfer time constant of roughly 1 ns, significantly faster than hole transfer at the hole-selective layer (~100 ns range). The extraction velocity into the C_{60} in our model was $1.6 \cdot 10^4$ cm/s (see Figure S11 for details), a similar value to earlier reported velocities (*46*).

Performance of perovskite single-junction solar cells

For the analysis on solar cell level, we focused on the simple single-junction device stack glass/ITO/HTL/perovskite/C_{60}/SnO_2/Ag, with the SnO_2 serving as a buffer layer for indium zinc oxide (IZO) sputtering in the fabrication of tandem solar cells (*50*). We show that the combination of fast charge extraction and passivated interface not only mitigated phase instability (re **Fig. 1**) but was also linked to an increased FF of solar cell devices, mainly by a decreased diode ideality factor of the PSCs. The FF is the major remaining parameter for which PSCs have not yet come close to the values of established solar cell technologies (*24*, *51*) (see Figure S16 for FF comparisons), with the ideality factor being one of the main properties that limit high-efficiency PSCs (*29*). MeO-2PACz and 2PACz lead to FFs of up to 82% (**Fig. 3A**), while with Me-4PACz, the values ranged to up to 84%, representing ~93% of the radiative limit.

Fig. 3B shows *J-V* curves recorded at simulated AM1.5G illumination conditions, comparing champion PTAA and Me-4PACz cells of the same batch and showing the superior performance of the SAM. The ideality factors n_{ID} for PSCs with different HTLs (**Fig. 3C**) were about 1.26 for Me-4PACz, 1.42 for 2PACz, 1.51 for MeO-2PACz, and 1.55 for PTAA cells. Figure S20 compares the V_{OC} values achieved with the different HTLs. Despite the large differences in passivation at the hole-selective interface, the differences in V_{OC} were not as large (average difference of 30 mV between PTAA and Me-4PACz), due to the limiting non-radiative recombination at the C_{60} interface. However, as reasoned above, the C_{60} layer did not limit charge extraction, thus the different extraction speeds invoked by the HTLs directly influenced the FF values. The high FF with Me-4PACz was accompanied by high V_{OC} values of up to 1.16 V and up to 1.234 V with a LiF interlayer between the perovskite and C_{60} (*52*, *53*) (see **Fig. 3D** and Figure S20). The combination of a high V_{OC} with low n_{ID} was previously considered as challenging for PSCs (*28*) and it allowed us to fabricate a perovskite single-junction with a PCE of 20.8% with Me-4PACz (Figure S18) at 1.68 eV bandgap.

To investigate the FF values without the influence of series resistance losses, we measured intensity-dependent absolute PL spectra and computed the QFLS values (or implied V_{OC}, iV_{OC}) at each carrier generation condition. The derived data pairs of generation currents and iV_{OC} values allowed the reconstruction of hypothetical, so-called pseudo-*J-V* curves, as recently shown in ref. (*54*) (**Fig. 3D)**. The extracted FF and pseudo-FF values (FF in absence of transport losses) of bare perovskite films grown on different HTLs are summarized in **Table 1**, line 1. Both 2PACz and Me-4PACz enabled high "pseudo-FF" values of ~88%, which is 96.8% of the detailed balance limit and similar to the value achieved on a bare quartz substrate. PTAA allowed for a pFF of only 85.6%.

This analysis highlights how the SAMs formed a practically lossless interface between ITO and perovskite. Interestingly, when including a C_{60} layer on top of the perovskite film, no differences between the studied HTLs for the iV_{OC} and pseudo-FF were apparent (dashed lines in **Fig. 3D, Table 1**, line 2), as the C_{60} layer sets a iV_{OC} limitation through high non-radiative recombination rates (*53*). This limitation was only overcome with a counter electrode on the C_{60} (**Fig. 3E** and full devices), which underlines the role of the dipoles that Me-4PACz and 2PACz created at the ITO surface. The calculated molecular dipole value of the hole-transporting fragment is ~0.2 D for MeO-2PACz, ~1.7 D for Me-4PACz and ~2 D for 2PACz. The positive dipoles shifted the work function of the ITO towards higher absolute numbers (Figure S2a), which presumably resulted in a higher built-in potential throughout the device (*55*, *56*). A well-defined built-in potential can exist with the presence of a second electrode countering the ITO; in this case Ag or Cu. Thus, when reconstructing the *J-V*s from the suns-V_{OC} measurement on full devices in **Fig. 3C** to extract the pFF (**Table 1**, line 3), both 2PACz and Me-4PACz overcame the pFF and iV_{OC} limitations imposed by the C_{60} layer (**Fig. 3E**).

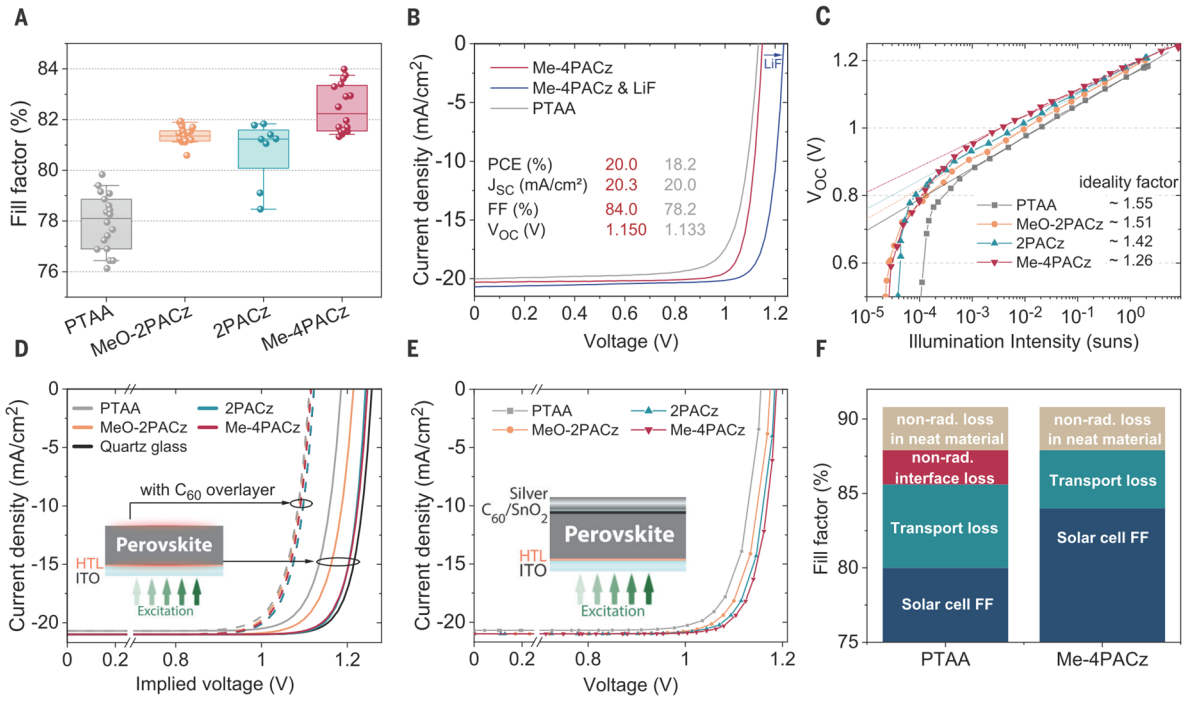

Fig. 3 Performance and fill factor loss analysis of *p-i-n* solar cells with different hole-selective layers. (**A**) Comparison of fill factor values of PSCs with the stack glass/ITO/HTL/perovskite/C_{60}/SnO_2/Ag, triple-cation perovskite absorber with 1.68 eV bandgap. All shown cells are made from the same perovskite precursor and contact processing batch. (**B**) *J-V* curves of the best cells of the batch in (A), and a *J-V* curve of a Me-4PACz cell from another batch with LiF interlayer between C_{60} and perovskite, reaching a V_{OC} of 1.234 V. (**C**) Intensity-dependent open-circuit voltage with linear fits (dashed lines). (**D**) Pseudo-*J-V* curves reconstructed from intensity-dependent absolute PL measurements on the illustrated sample stack. The 2PACz and Me-4PACz curves almost coincide; the dashed lines represent pseudo-*J-V* curves from the sample variations including the electron-selective C_{60} layer, with which all curves are comparable due to the limiting non-radiative recombination at the C_{60} interface. (**E**) Pseudo-*J-V* curves reconstructed from the measurements in (C). Table 1 summarizes the FF values extracted from the pseudo-*J-V* curves. (**F**) Repartition of loss mechanisms lowering the cell's FF below the detailed balance limit, comparing PTAA and Me-4PACz cells.

Table 1 Comparison of "pseudo" fill factors (pFF) and implied open-circuit voltages (*iV*$_{OC}$). The values were derived from suns-PL and suns-V_{OC} measurements for our perovskite film on all studied hole-selective layers and on quartz glass. The table also shows the maximum FF attained in *J-V* measurements (max FF) (see also **Fig. 3**). "Half cell" refers to substrate/HTM/absorber, whereas "full cell" denotes the complete solar cell including C_{60}, SnO_2 and Ag metal electrode.

	Quartz	PTAA	MeO-2PACz	2PACz	Me-4PACz
pFF (%), half cell (suns-PL)	87.9	85.6	85.5	88.3	87.5
pFF (%), half cell + C_{60} (suns-PL)	85.3	85.3	85.3	85.3	85.3
pFF (%), full cell (suns-Voc)		85.8	85.9	86.9	87.9
max FF (%), full cell (*J-V*)		79.8	81.9	81.8	84.0
***iV*$_{OC}$ (V)**, half cell (absolute PL)	1.258	1.185	1.215	1.244	1.248
n_{ID}, full cell (suns-V_{OC})		1.55	1.51	1.42	1.26

The differences between the electrical *J-V* curves (max. FF 84%) in **Fig. 3B** and pseudo-*J-V* curves (max. FF ~88%) arose from transport losses caused by the finite mobility of the C_{60}, non-optimized sample design, ITO sheet resistance and from the measurement setup. **Fig. 3F** summarizes a comparison of the different contributions to FF losses for PTAA and Me-4PACz, derived from comparisons of the pseudo-*J-V* curves to the electrical ones and radiative limits, as previously reported by Stolterfoht *et al.* (*54*). In addition to non-radiative losses at the PTAA interface (red), the film thickness (~10 nm as

compared to <1 nm with a SAM) and low conductivity of the PTAA led to greater transport losses than with Me-4PACz.

Integration into monolithic perovskite/silicon tandem solar cells

Efficient passivation in combination with fast hole extraction of Me-4PACz in perovskite single-junctions transferred into monolithic tandem solar cells, which led to significantly higher FF, V_{OC} and stability. A schematic stack of this solar cell is shown in **Fig. 4A**. We use a silicon heterojunction (SHJ) solar cell as the bottom cell (*26*), based on a 260 µm thick n-type float-zone Si wafer processed as described in the methods. The textured rear side enhanced the near-infrared absorption, whereas the polished front side enabled the deposition of spin-coated perovskite. The 20 nm ITO recombination layer also served as the anchoring oxide for the SAMs (*7*). The top cell, with the same 1.68 eV perovskite band gap and nominal precursor composition $Cs_{0.05}(FA_{0.77}MA_{0.23})_{0.95}Pb(I_{0.77}Br_{0.23})_3$ as analyzed above, resembled the single-junction stack of ITO/HTL/Perovskite/(LiF)/C_{60}/SnO_2/IZO/Ag/LiF. **Fig. 4B** shows a scanning electron microscope cross-section image of a part of the tandem solar cell; no obvious differences were observed between perovskite films on the different HTLs (Figure S24). The molecular SAM cannot be resolved with the SEM. A photograph and layout of the tandem device is shown in Figure S25.

Fig. 4C compares the PCE of tandem solar cells based on PTAA, MeO-2PACz, 2PACz and Me-4PACz, with and without a LiF interlayer at the perovskite/C_{60} interface. With PTAA, the LiF interlayer lead to rapid degradation of the cells (see Figure S26 for individual parameters). Without the interlayer, we achieved an average PCE of 25.25%. In contrast, the average efficiency of MeO-2PACz and 2PACz was 26.21% and 26.56%, respectively. The utilization of a LiF interlayer for Me-4PACz cells increased the V_{OC} but reduced the FF. Thus, both configurations reached a similar average PCE of 26.25% and 26.41%, respectively. However, with Me-4PACz the maximum PCEs are with >29% higher than cells with 2PACz, mainly because of higher FF of up to 81%. These high FF were achieved despite almost all cells being perovskite limited (Table S1). The statistics of all photovoltaic parameters are shown in Figure S26. The *J-V* measurements of the champion cells of each configuration are shown in Figure S27 and the PV parameters are summarized in Table S2.

The tandem solar cells did not reach FF values as in single-junction cells due to the larger active area (1 cm^2) and a TCO without grid fingers, leading to increased series resistance. The cells showed very high V_{OC}s of up to 1.92 V (Figure S28). With a V_{OC} of ~715 mV from the bottom cell at half illumination (Figure S29), the contribution of the perovskite subcell was ~1.2 V. **Fig. 4D** shows a direct comparison between champion PTAA and Me-4PACz tandem cells, emphasizing that besides the 50 mV improvement in V_{OC}, the enhanced hole extraction boosted the FF by ~4% absolute.

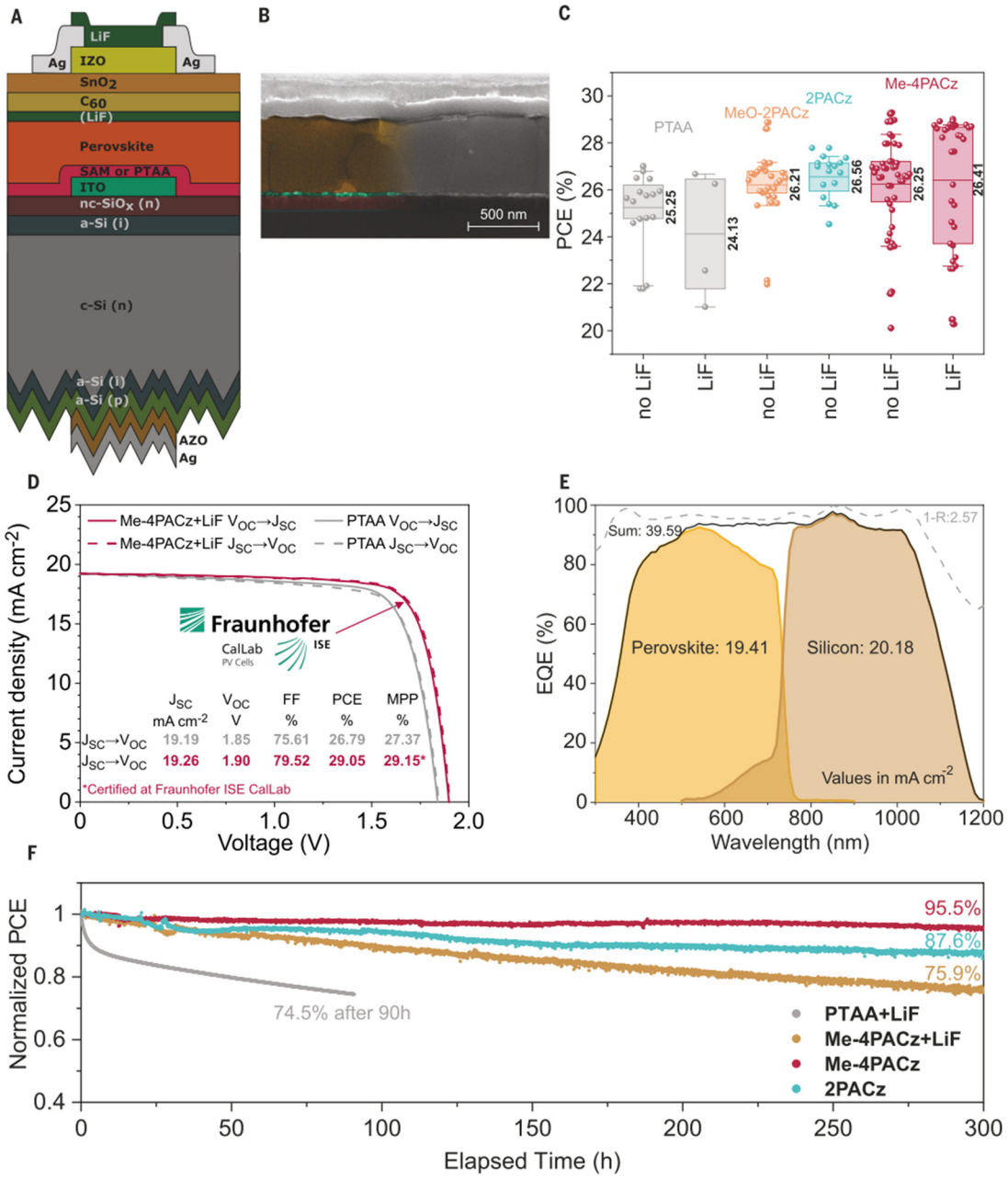

Fig. 4: **Characteristics of monolithic perovskite/silicon tandem solar cells utilizing various HTLs.** (**A**) Schematic stack of the monolithic perovskite/silicon tandem solar cell. (**B**) Scanning electron microscope (SEM) image of a tandem cross-section with Me-4PACz as HTL. (**C**) Statistics of the PCE of several PTAA, MeO-2PACz, 2PACz and Me-4PACz tandem solar cells from *J-V*-scan. (**D**) Certified *J-V* curve conducted at Fraunhofer ISE including the MPP and the device parameters (red) in comparison to a tandem cell with PTAA (gray) as HTL measured in-house. (**E**) External quantum efficiency (EQE) and 1-reflection of the certified tandem cell measured in-house. The AM1.5G-equivalent current densities are given in the legend in mA cm^{-2}. (**F**) Long term MPP-track using a dichromatic LED illumination of non-encapsulated solar cells in air at a controlled temperature of 25°C and relative humidity of 30 to 40%. The data are normalized to the MPP average of the first 60 minutes of each individual track to account for measurement noise. Due to the fast degradation, the MPP-track of the PTAA + LiF cell is normalized to the first recorded value. The legend shows which HTL and whether the LiF interlayer was used.

We sent a tandem cell with Me-4PACz and LiF interlayer to Fraunhofer ISE CalLab for independent certification (**Fig. 4D**; see Figure S30 for certificate). With a V_{OC} of 1.90 V, FF of 79.4% and J_{SC} of 19.23 mA cm^{-2}, the cell had a PCE of 29.01% when measuring from J_{SC} to V_{OC}, similar to our in-house measurement (Figure S31), and was certified at the MPP with a PCE of 29.15% with a designated area of 1.064 cm^2. This PCE surpasses other monolithic (*10*, *27*) and four-terminal perovskite-based tandem solar cells (*57*), and is on par with the best GaAs single cell at the same active area (*27*).

Fig. 4E shows the external quantum efficiency (EQE) of the certified tandem cell. Under AM1.5G-equivalent illumination conditions, the photogenerated current density J_{ph} in the perovskite and silicon subcells were 19.41 mA cm^{-2} and 20.18 mA cm^{-2}, respectively, which agreed with the measured J_{SC} of 19.23 mA cm^{-2}. The tandem solar cell exhibited a non-ideal current mismatch of 0.77 mA cm^{-2}, and although the perovskite cell sets the tandem shunt resistance, the cell reached an FF of 79.5%. The cumulative photogenerated current density and loss caused by reflection were 39.59 mA cm^{-2} and 2.57 mA cm^{-2}, respectively. A comparison of EQEs and reflection losses between a cell of this work (planar front side) and a fully textured cell by Sahli *et al.* is shown in Figure S32.

After the certification, we fabricated more Me-4PACz tandem solar cells without LiF interlayer (Figure S26), which showed similar average performance as with LiF. The champion cell showed a higher FF of 81% and lower V_{OC} of 1.87 V than without LiF. Together with a J_{SC} of 19.37 mA cm^{-2} this lead to a PCE of 29.29% and a stabilized efficiency of 29.32% (Figure S33).

We measured the stability of different non-encapsulated tandem solar cells (**Fig. 4F**). To track the degradation induced by either the top- or the bottom cell more carefully, we developed a dichromatic LED setup using LEDs with 470 nm and 940 nm center emission wavelengths (Figure S34) and independent intensity calibration and recording. We adjusted the mismatch so that the J_{ph} in the individual subcells was equal to that measured under AM1.5G-equivalent illumination to maintain proper stability tracking of monolithic tandem solar cells (see below and supplementary text). The devices were measured under continuous MPP load (using voltage perturbation), at 25 °C and in ambient air with 30-40% relative humidity. The photogenerated current densities of the subcells are given in Table S3 and set which subcell is limiting. The degradation for a perovskite-limited tandem cell with Me-4PACz+LiF showed 75.9% of its initial efficiency (29.13%) after 300 hours. Substituting the Me-4PACz with PTAA (perovskite-limited), the PCE decreased to 74.5% of its initial PCE (25.9%) after only 90 hours.
We additionally tracked a cell with Me-4PACz as HTL without a LiF interlayer to test the intrinsic stability of the HTL/perovskite combination. After 300 hours, the cell still operated at 95.5% of its initial PCE. Although the cells were current-matched, this track monitored a degradation of the perovskite as it directly translates into the performance of the tandem cell and no degradation of the Silicon subcell is expected within these timescales. Our comparison strongly suggests that the utilization of a LiF interlayer reduced the stability. As described in other works (*58–61*), the decrease in stability might be caused by deterioration of the electrodes and C_{60} interface upon migration of Li^+ and F^- ions. We would like to note that it is important to declare the mismatch-conditions because the utilization of a NIR-poor spectrum would lead to a silicon limited cell and thus to a higher stability (see supplementary text). Comparing this result to state-of-the-art stability tests of non-encapsulated tandem solar cells in ambient conditions, where the cells retained and 90% after 61 hours (*62*) and 92% after 100 hours (*13*), our Me-4PACz tandem solar cell showed a superior operational stability.

Beside the long-term stability measurements at 25°C, we conducted an MPP track of a Me-4PACz tandem cell at elevated temperatures. Following the procedure of Jost *et al.*, the temperature was successively increased from 25°C to 85°C and back to 25°C (*63*). There was no loss in PCE after this 200 minutes procedure, despite the increased methylammonium and Br amount of the herein used wide band gap perovskite (Figure S35).

Subcell *J-V* characteristics of a monolithic tandem solar cell

One downside of monolithic multijunction solar cells is that the subcell characteristics are barely accessible. External quantum efficiency measurements are the only subcell-resolved measurements presented in almost all publications reporting multijunction solar cells. Here, we used absolute photoluminescence measurements in each subcell of a representative tandem solar cell (Me-4PACz + LiF). With this, we could estimate the QFLS, and thus the V_{OC} was accessible for both subcells independently. Instead of local excitation and evaluation, we used hyperspectral imaging under 1-sun equivalent excitation fluence (spectra and images shown in **Fig. 5A**).

From the high-energy slope of the absolute PL spectra of the subcells, the individual implied V_{OC}s were calculated, 1.18 V and 0.72 V for the perovskite and silicon subcell, respectively (*18*, *64*). From the PL spectra, we calculated the PLQY of both subcells yielding values of 1.5% for Si and 0.02% for the perovskite. PLQY values exceeding 5% have been already demonstrated in perovskite single-junction devices for lower band gaps (*19*).

To estimate the pseudo-*J*-*V* curves of the subcells, we performed absolute electroluminescence (EL) imaging, where the excess charge carriers are generated electrically to access the subcell characteristics (*65–68*). For each injected current, an EL image was recorded, from which the voltage of the subcells can be calculated from an average over the active area (Figure S36). With the reconstructed pseudo-*J*-*V* curves from injection current-dependent EL imaging, we analyzed the maximum possible efficiency of this cell stack with minimized charge transport losses (see methods and supplementary text for more details). We reconstructed both subcell *J*-*V* curves by calculating the implied voltage at each injected current, yielding a "pseudo" light-*J*-*V* (JV_{EL}) for each subcell after shifting it by the respective photogenerated current density J_{ph} being calculated from EQE measurements and amount to 18.7 and 20.6 mA cm^{-2} for the top and bottom cell, respectively. The open symbols in **Fig. 5B** show the measured EL data points averaged over the perovskite and silicon subcell and shifted by their respective J_{ph}.

For the perovskite, we additionally fitted the data with a single-diode model to display the *J*-*V* curve in the whole range, which was otherwise not accessible during the EL measurement. To obtain the tandem JV_{EL}, the voltages of the subcells were summed up for each current density. The dashed line shows the result. The reconstructed curve deviated from the electrically measured *J*-*V* curve under a solar simulator. This is mainly because EL gave access only to the internal voltage, whereas an electrical *J*-*V* curve displayed the current density versus external voltage (which is the internal voltage minus the voltage lost at series resistances); more details can be found in the supplementary text. Hence, a high FF (87.8%) of the JV_{EL} can be regarded as the maximum achievable value for this particular tandem cell if the electrodes and all charge selective layers would pose zero series resistance losses. This would give a PCE of 31.7%, surpassing the theoretical PCE maximum of a silicon single cell (29.4%) (*69*). Thus, this cell stack has the capacity to overcome the 30% barrier through technical optimization of the contacts alone. However, by adjusting the mismatch conditions, even higher efficiencies are achievable.

To find the requirements for the highest efficiency, we fit the silicon subcell with a single-diode model. We conducted SPICE simulations to sweep the photogenerated current densities in the subcell. The single-diode models of the silicon and perovskite subcells were connected in series (schematically shown in Figure S37a) and the cumulative current density was fixed to 39.3 mA cm^{-2} (as it is for AM1.5G-equivalent illumination). Figure S37b shows the photovoltaic parameters as a function of the mismatch ($J_{ph,Si}$-$J_{ph,Pero}$). As shown in a previous publication, the V_{oc} is almost independent of the mismatch, whereas the FF is affected by it (*26*). A minimum FF occurs when the $J_{ph,Si}$ is 0.7 mA cm^{-2} below the $J_{ph,Pero}$. However, simultaneously the J_{SC} is highest under this condition. Here, the highest efficiency is 32.43% in a current matching situation.

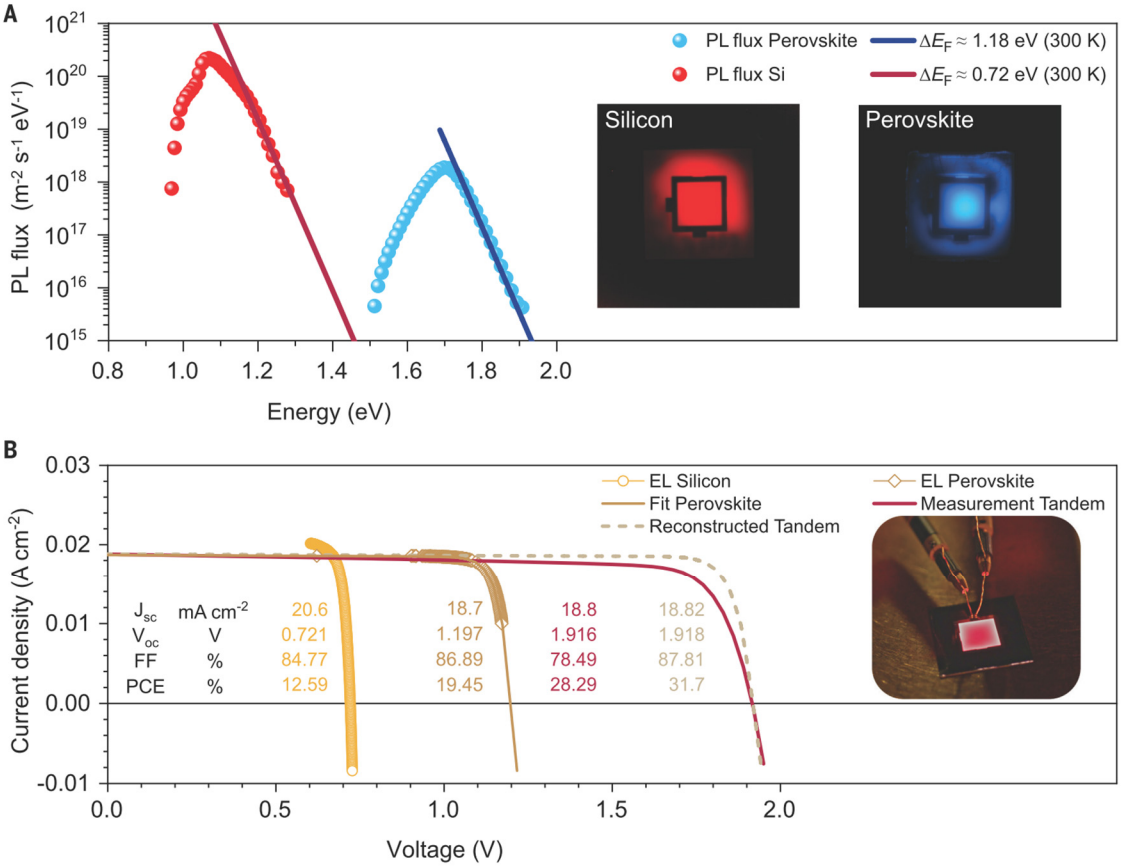

Fig. 5 Luminescence subcell analysis of a tandem solar cell with Me-4PACz and LiF interlayer. (**A**) Absolute PL spectra of the subcells recorded under 1-sun equivalent illumination. The exciting wavelength are 455 nm and 850 nm for the perovskite and silicon subcell, respectively. Additionally, PL images, constructed of the integrated PL fluxes are shown. (**B**) Reconstructed *J-V* curves calculated from injection-dependent electroluminescence measurements (open symbols) and shifting by the photogenerated current density. Furthermore, the perovskite subcell is fitted with a single diode model (solid brown line). The reconstructed tandem *J-V* (dashed line) was calculated by adding the voltages of the subcells for each current density. The *J-V* measurement under simulated 1-sun illumination of this cell is shown as a solid red line. Furthermore, a photo of the tandem solar cell at high injection current is shown. Due to a bandgap of 1.68 eV, the subcell emits light in the visible wavelength range and thus, the emission is visible by eye and with a regular digital camera.

Conclusion

We have demonstrated monolithic perovskite/silicon tandem solar cells with a certified record power conversion efficiency of 29.15%. We elucidated that the combination of efficient passivation at the hole-selective interface and enhanced hole-extraction speed stabilize a perovskite absorber with tandem-relevant bandgap of 1.68 eV. This was revealed by accelerated tests investigating light-induced phase segregation via spot-illumination at 30-suns excitation intensity. Although the electron-selective C_{60} layer in solar cell devices limited the open-circuit voltage, the fill factor was limited by the hole-selective interface. Improved fill factors and photostability were achieved by a new methyl-substituted, carbazole-based self-assembled monolayer (Me-4PACz) that bonds to the transparent conductive oxide of the perovskite cell. With intensity-dependent transient photoluminescence analysis we presented a method to assess charge transfer effects that are relevant for device operation. The faster hole extraction was linked to a low ideality factor of 1.26 for the perovskite subcell, while allowing a high V_{OC} of up to 1.23 V. Fill factors of up to 84% were achieved, and a maximum pseudo-fill factor of 88% was measured by intensity-dependent absolute PL (suns-PL) and suns-V_{OC} measurements. A non-encapsulated tandem cell with Me-4PACz retained 95.5% of its initial efficiency after 300 h of continuous maximum power point tracking in ambient air, under precise control of the subcell photocurrents to match 1-sun-equivalent conditions. Furthermore, we examined the subcell characteristics without the influence of parasitic resistances by measuring injection-dependent electroluminescence, allowing us to reconstruct

the subcell-*J-V* curves. We thereby estimated that upon technical improvements a maximum efficiency of 32.4% for the presented device stack is possible.

Materials and Methods

Single-junction perovskite solar cells were fabricated on glass/ITO substrates. First, the hole-selective layer (PTAA, MeO-2PACz, 2PACz or Me-4PACz) was deposited by spin-coating followed by the one-step spin-coating deposition of the perovskite precursor solution using the antisolvent method. The precursor had a nominal concentration of 1.24 mol/l. Afterwards, layers of C_{60} and SnO_2 were deposited via thermal evaporation and atomic layer deposition. Finally, a layer of silver was deposited via thermal evaporation.

To analyze the quasi-fermi-level splitting, glass/ITO/HTL/perovskite samples were fabricated. The samples were illuminated from the perovskite site with a photon flux equivalent to 1-sun illumination.

Transient photoluminescence was measured by pulsed excitation with 660 nm wavelength and time-correlated single photon counting. The fluence was set to 1-sun equivalent charge generation.

Suns-V_{OC} was measured by illuminating solar cells with varying intensities. For each intensity the stabilized open-circuit voltage was measured. Similarly, suns-PL is measured by illuminating the indicated sample stacks with different intensities. For each intensity (corresponding to a "pseudo" injection current) the quasi-fermi level splitting was calculated.

Tandem solar cells were fabricated by depositing the p-i-n perovskite top cell with various hole-selective layers on a silicon heterojunction solar cell with a textured rear side and polished front side. *J-V* measurements were conducted at simulated AM1.5G illumination in air at 25°C. For long term stability measurements, a custom-built setup with an LED array emitting at 470 nm and 940 nm was designed. This enabled a stable illumination at simulated AM1.5G-equivalent charge carrier generation conditions of the solar cells, which were tracked in air at 25°C. For analyzing the subcells of the tandem solar cell we measured hyperspectral absolute photoluminescence by illuminating the tandem cell with 450 nm light for excitation of the perovskite subcell and an 850 nm wavelength source for the excitation of the silicon subcell. To reconstruct the subcell *J-V*, absolute electroluminescence imaging was conducted at scanned bias voltage.

A detailed description of the fabrication and measurement techniques can be found in the Supplementary Materials.

Acknowledgements

Acknowledgements: The authors thank M. Gabernig, C. Ferber, T. Lußky, H. Heinz, C. Klimm and M. Muske at Institute for silicon Photovoltaics (HZB), T. Hänel, T. Henschel, M. Zelt, H. Rhein, K. Meyer-Stillrich and M. Hartig at PVcomB (HZB) for technical assistance. A.A.A. thanks Aboma Merdasa for his expertise during construction of the steady-state PL setup. E.K. and S.A. thank Christian Wolff (Uni. Potsdam) and Kai Brinkmann (Uni. Wuppertal) for fruitful discussion at the beginning of the project. AM acknowledges Aida Drevilkauskaite for help with the synthesis of 4PACz and 6PACz materials. **Funding:** Funding was provided by the German Federal Ministry for Education and Research (BMBF) (grant no. 03SF0540) within the project "Materialforschung für die Energiewende". Parts of this work received funding by the BMWi funded project ProTandem (no. 0324288C). The authors acknowledge the HyPerCells graduate school for support and the funding by the Helmholtz Association within the HySPRINT Innovation lab project and TAPAS project. M.G., P.C., S.A., and D.N. acknowledge funding from the Helmholtz Association via HI-SCORE (Helmholtz International Research School). The research has partly received funding from the European Union's Horizon 2020 research and innovation programme under grant agreement No. 763977 of the PerTPV project. A.M. and TM acknowledges funding by the Research Council of Lithuania under grant agreement no. S-MIP-19-5/SV3-1079 of the SAM project. M.J., G.M and M.T. thank Slovene Research Agency (ARRS) for funding through

research programs P2-0197 and J2-1727. M.S., D.N. and S.A. further acknowledge the Deutsche Forschungsgemeinschaft (DFG, German Research Foundation) - project number 423749265 and 03EE1017C - SPP 2196 (SURPRISE and HIPSTER) for funding. J.A.S. thanks EPSRC and Prof. David Lidzey for Ph.D. studentship funding via CDT-PV (EP/L01551X/1) and Erasmus+ for funding. **Author Contributions** A.A.A., E.K., B.L., and S.A. planned the experiments, coordinated the work and prepared the figures. Er.K., A.M. and T.M. designed and synthesized the Me-4PACz SAM and the (Me-)nPACz series. A.A.A. and B.L. processed the single-junction cells and optimized the SAM deposition. E.K. and B.L. processed the tandem cells. A.B.M.-V. processed the Si bottom cells. A.A.A., H.H. and J.A.M conducted and analyzed the PL experiments. J.A.M., A.A.A. and E.K. performed the EL studies. H.H. recorded the Terahertz measurements and performed the data analysis. P.C., M.G. and M.S. conducted the pseudo-*J-V* and FF-V_{OC} loss analysis (intensity-dep. V_{OC} and QFLS). D.M. performed the photoelectron spectroscopy. J.A.S., D.S. and N.P. performed crystallographic analysis. G.M., M.J., B.L. and E.K. designed and built the tandem aging setup and recorded the long-term MPP tracks. S.A., V.G., M.S., T.U., T.M., C.G., R.S., M.T., La.K., A.A., D.N., B.S. and B.R. supervised the projects. All authors contributed to data interpretation and manuscript writing. **Competing interests:** HZB and KTU filed patents for the herein used SAM molecules and their use in tandem solar cells. **Data and materials availability:** All data is available in the main text or the supplementary materials.

Supplementary Materials:

Materials, Processing and Methods

Figures S1-S43

Table S1-3

Supplementary text

References (70 - 85)

References

1. A. De Vos, Detailed balance limit of the efficiency of tandem solar cells. *J. Phys. D. Appl. Phys.* **13**, 839–846 (1980).

2. W. Shockley, H. J. Queisser, Detailed Balance Limit of Efficiency of p-n Junction Solar Cells. *J. Appl. Phys.* **32**, 510–519 (1961).

3. S. E. Sofia, H. Wang, A. Bruno, J. L. Cruz-Campa, T. Buonassisi, I. M. Peters, Roadmap for cost-effective, commercially-viable perovskite silicon tandems for the current and future PV market. *Sustain. Energy Fuels*. **4**, 852–862 (2020).

4. Z. Li, Y. Zhao, X. Wang, Y. Sun, Z. Zhao, Y. Li, H. Zhou, Q. Chen, Cost Analysis of Perovskite Tandem Photovoltaics. *Joule*. **2**, 1559–1572 (2018).

5. National Renewable Energy Laboratory, "Best Research-Cell Efficiency Chart" (2020), (available at www.nrel.gov/pv/cell-efficiency.html).

6. T. Todorov, T. Gershon, O. Gunawan, Y. S. Lee, C. Sturdevant, L.-Y. Chang, S. Guha, Monolithic Perovskite-CIGS Tandem Solar Cells via In Situ Band Gap Engineering. *Adv. Energy Mater.* **5**, 1500799 (2015).

7. A. Al-Ashouri, A. Magomedov, M. Roß, M. Jošt, M. Talaikis, G. Chistiakova, T. Bertram, J. A. Márquez, E. Köhnen, E. Kasparavičius, S. Levcenco, L. Gil-Escrig, C. J. Hages, R. Schlatmann, B. Rech, T. Malinauskas, T. Unold, C. A. Kaufmann, L. Korte, G. Niaura, V. Getautis, S. Albrecht, Conformal monolayer contacts with lossless interfaces for perovskite single junction and monolithic tandem solar cells. *Energy Environ. Sci.* **12**, 3356–3369 (2019).

8. R. Lin, K. Xiao, Z. Qin, Q. Han, C. Zhang, M. Wei, M. I. Saidaminov, Y. Gao, J. Xu, M. Xiao, A. Li, J. Zhu, E. H. Sargent, H. Tan, Monolithic all-perovskite tandem solar cells with 24.8% efficiency exploiting comproportionation to suppress Sn(ii) oxidation in precursor ink. *Nat. Energy*. **4**, 864–873 (2019).

9. G. E. Eperon, T. Leijtens, K. A. Bush, R. Prasanna, T. Green, J. T.-W. Wang, D. P. McMeekin, G. Volonakis, R. L. Milot, R. May, A. Palmstrom, D. J. Slotcavage, R. A. Belisle, J. B. Patel, E. S. Parrott, R. J. Sutton, W. Ma, F. Moghadam, B. Conings, A. Babayigit, H.-G. Boyen, S. Bent, F. Giustino, L. M. Herz, M. B. Johnston, M. D. McGehee, H. J. Snaith, Perovskite-perovskite tandem photovoltaics with optimized band gaps. *Science (80-.).* **354**, 861–865 (2016).

10. D. Kim, H. J. Jung, I. J. Park, B. W. Larson, S. P. Dunfield, C. Xiao, J. Kim, J. Tong, P. Boonmongkolras, S. G. Ji, F. Zhang, S. R. Pae, M. Kim, S. B. Kang, V. Dravid, J. J. Berry, J. Y. Kim, K. Zhu, D. H. Kim, B. Shin, Efficient, stable silicon tandem cells enabled by anion-engineered wide-bandgap perovskites. *Science (80-.).* **368**, 155–160 (2020).

11. J. Xu, C. C. Boyd, Z. J. Yu, A. F. Palmstrom, D. J. Witter, B. W. Larson, R. M. France, J. Werner, S. P. Harvey, E. J. Wolf, W. Weigand, S. Manzoor, M. F. A. M. van Hest, J. J. Berry, J. M. Luther, Z. C. Holman, M. D. McGehee, Triple-halide wide–band gap perovskites with suppressed phase segregation for efficient tandems. *Science (80-.).* **367**, 1097–1104 (2020).

12. Y. Hou, E. Aydin, M. De Bastiani, C. Xiao, F. H. Isikgor, D.-J. Xue, B. Chen, H. Chen, B. Bahrami, A. H. Chowdhury, A. Johnston, S.-W. Baek, Z. Huang, M. Wei, Y. Dong, J. Troughton, R. Jalmood, A. J. Mirabelli, T. G. Allen, E. Van Kerschaver, M. I. Saidaminov, D. Baran, Q. Qiao, K. Zhu, S. De Wolf, E. H. Sargent, Efficient tandem solar cells with solution-processed perovskite on textured crystalline silicon. *Science (80-.).* **367**, 1135–1140 (2020).

13. B. Chen, Z. J. Yu, S. Manzoor, S. Wang, W. Weigand, Z. Yu, G. Yang, Z. Ni, X. Dai, Z. C. Holman, J. Huang, Blade-Coated Perovskites on Textured Silicon for 26%-Efficient

Monolithic Perovskite/Silicon Tandem Solar Cells. *Joule*. **4**, 850–864 (2020).

14. M. Jošt, L. Kegelmann, L. Korte, S. Albrecht, Monolithic Perovskite Tandem Solar Cells: A Review of the Present Status and Advanced Characterization Methods Toward 30% Efficiency. *Adv. Energy Mater.* **10**, 1904102 (2020).

15. Y. Jiang, I. Almansouri, S. Huang, T. Young, Y. Li, Y. Peng, Q. Hou, L. Spiccia, U. Bach, Y.-B. Cheng, M. A. Green, A. Ho-Baillie, Optical analysis of perovskite/silicon tandem solar cells. *J. Mater. Chem. C*. **4**, 5679–5689 (2016).

16. I. L. Braly, D. W. DeQuilettes, L. M. Pazos-Outón, S. Burke, M. E. Ziffer, D. S. Ginger, H. W. Hillhouse, Hybrid perovskite films approaching the radiative limit with over 90% photoluminescence quantum efficiency. *Nat. Photonics*. **12**, 355–361 (2018).

17. D. W. deQuilettes, S. Koch, S. Burke, R. K. Paranji, A. J. Shropshire, M. E. Ziffer, D. S. Ginger, Photoluminescence Lifetimes Exceeding 8 μs and Quantum Yields Exceeding 30% in Hybrid Perovskite Thin Films by Ligand Passivation. *ACS Energy Lett.* **1**, 438–444 (2016).

18. T. Kirchartz, J. A. Márquez, M. Stolterfoht, T. Unold, Photoluminescence-Based Characterization of Halide Perovskites for Photovoltaics. *Adv. Energy Mater.* **10**, 1904134 (2020).

19. Z. Liu, L. Krückemeier, B. Krogmeier, B. Klingebiel, J. A. Márquez, S. Levcenko, S. Öz, S. Mathur, U. Rau, T. Unold, T. Kirchartz, Open-Circuit Voltages Exceeding 1.26 V in Planar Methylammonium Lead Iodide Perovskite Solar Cells. *ACS Energy Lett.* **4**, 110–117 (2019).

20. P. Caprioglio, F. Zu, C. M. Wolff, J. A. Márquez Prieto, M. Stolterfoht, P. Becker, N. Koch, T. Unold, B. Rech, S. Albrecht, D. Neher, High open circuit voltages in pin-type perovskite solar cells through strontium addition. *Sustain. Energy Fuels*. **3**, 550–563 (2019).

21. Q. Jiang, Y. Zhao, X. Zhang, X. Yang, Y. Chen, Z. Chu, Q. Ye, X. Li, Z. Yin, J. You, Surface passivation of perovskite film for efficient solar cells. *Nat. Photonics*. **13**, 460–466 (2019).

22. S. Yang, J. Dai, Z. Yu, Y. Shao, Y. Zhou, X. Xiao, X. C. Zeng, J. Huang, Tailoring Passivation Molecular Structures for Extremely Small Open-Circuit Voltage Loss in Perovskite Solar Cells. *J. Am. Chem. Soc.* **141**, 5781–5787 (2019).

23. L. Krückemeier, U. Rau, M. Stolterfoht, T. Kirchartz, How to Report Record Open-Circuit Voltages in Lead-Halide Perovskite Solar Cells. *Adv. Energy Mater.* **10**, 1902573 (2020).

24. P. K. Nayak, S. Mahesh, H. J. Snaith, D. Cahen, Photovoltaic solar cell technologies: analysing the state of the art. *Nat. Rev. Mater.* **4**, 269–285 (2019).

25. A. Rajagopal, R. J. Stoddard, S. B. Jo, H. W. Hillhouse, A. K. Y. Jen, Overcoming the Photovoltage Plateau in Large Bandgap Perovskite Photovoltaics. *Nano Lett.* **18**, 3985–3993 (2018).

26. E. Köhnen, M. Jošt, A. B. Morales-Vilches, P. Tockhorn, A. Al-Ashouri, B. Macco, L. Kegelmann, L. Korte, B. Rech, R. Schlatmann, B. Stannowski, S. Albrecht, Highly efficient monolithic perovskite silicon tandem solar cells: analyzing the influence of current mismatch on device performance. *Sustain. Energy Fuels*. **3**, 1995–2005 (2019).

27. M. A. Green, E. D. Dunlop, J. Hohl-Ebinger, M. Yoshita, N. Kopidakis, A. W. Y. Ho-Baillie, Solar cell efficiency tables (Version 55). *Prog. Photovoltaics Res. Appl.* **28**, 3–15 (2020).

28. P. Caprioglio, C. M. Wolff, O. J. Sandberg, A. Armin, B. Rech, S. Albrecht, D. Neher, M. Stolterfoht, On the Origin of the Ideality Factor in Perovskite Solar Cells. *Adv. Energy Mater.* **10**, 2000502 (2020).

29. M. A. Green, A. W. Y. Ho-Baillie, Pushing to the Limit: Radiative Efficiencies of Recent Mainstream and Emerging Solar Cells. *ACS Energy Lett.* **4**, 1639–1644 (2019).

30. K. Jäger, L. Korte, B. Rech, S. Albrecht, Numerical optical optimization of monolithic planar perovskite-silicon tandem solar cells with regular and inverted device architectures. *Opt. Express*. **25**, A473 (2017).

31. M. Jošt, E. Köhnen, A. B. Morales-Vilches, B. Lipovšek, K. Jäger, B. Macco, A. Al-Ashouri, J. Krč, L. Korte, B. Rech, R. Schlatmann, M. Topič, B. Stannowski, S. Albrecht, Textured interfaces in monolithic perovskite/silicon tandem solar cells: advanced light management for improved efficiency and energy yield. *Energy Environ. Sci.* **11**, 3511–3523 (2018).

32. T. Leijtens, K. A. Bush, R. Prasanna, M. D. McGehee, Opportunities and challenges for tandem solar cells using metal halide perovskite semiconductors. *Nat. Energy*. **3**, 828–838 (2018).

33. E. T. Hoke, D. J. Slotcavage, E. R. Dohner, A. R. Bowring, H. I. Karunadasa, M. D. McGehee, Reversible photo-induced trap formation in mixed-halide hybrid perovskites for photovoltaics. *Chem. Sci.* **6**, 613–617 (2015).

34. D. J. Slotcavage, H. I. Karunadasa, M. D. McGehee, Light-Induced Phase Segregation in Halide-Perovskite Absorbers. *ACS Energy Lett.* **1**, 1199–1205 (2016).

35. S. Mahesh, J. M. Ball, R. D. J. Oliver, D. P. McMeekin, P. K. Nayak, M. B. Johnston, H. J. Snaith, Revealing the origin of voltage loss in mixed-halide perovskite solar cells. *Energy Environ. Sci.* **13**, 258–267 (2020).

36. M. Saliba, T. Matsui, J.-Y. Seo, K. Domanski, J.-P. Correa-Baena, M. K. Nazeeruddin, S. M. Zakeeruddin, W. Tress, A. Abate, A. Hagfeldt, M. Grätzel, Cesium-containing triple cation perovskite solar cells: improved stability, reproducibility and high efficiency. *Energy Environ. Sci.* **9**, 1989–1997 (2016).

37. M. Stolterfoht, P. Caprioglio, C. M. Wolff, J. A. Márquez, J. Nordmann, S. Zhang, D. Rothhardt, U. Hörmann, Y. Amir, A. Redinger, L. Kegelmann, F. Zu, S. Albrecht, N. Koch, T. Kirchartz, M. Saliba, T. Unold, D. Neher, The impact of energy alignment and interfacial recombination on the internal and external open-circuit voltage of perovskite solar cells. *Energy Environ. Sci.* **12**, 2778–2788 (2019).

38. D. Luo, W. Yang, Z. Wang, A. Sadhanala, Q. Hu, R. Su, R. Shivanna, G. F. Trindade, J. F. Watts, Z. Xu, T. Liu, K. Chen, F. Ye, P. Wu, L. Zhao, J. Wu, Y. Tu, Y. Zhang, X. Yang, W. Zhang, R. H. Friend, Q. Gong, H. J. Snaith, R. Zhu, Enhanced photovoltage for inverted planar heterojunction perovskite solar cells. *Science (80-.).* **360**, 1442–1446 (2018).

39. Q. Wang, E. Mosconi, C. Wolff, J. Li, D. Neher, F. De Angelis, G. P. Suranna, R. Grisorio, A. Abate, Rationalizing the Molecular Design of Hole-Selective Contacts to Improve Charge Extraction in Perovskite Solar Cells. *Adv. Energy Mater.* **9**, 1900990 (2019).

40. C. Huang, W. Fu, C.-Z. Li, Z. Zhang, W. Qiu, M. Shi, P. Heremans, A. K. Y. Jen, H. Chen, Dopant-Free Hole-Transporting Material with a C 3 h Symmetrical Truxene Core for Highly Efficient Perovskite Solar Cells. *J. Am. Chem. Soc.* **138**, 2528–2531 (2016).

41. A. Torres, L. G. C. Rego, Surface Effects and Adsorption of Methoxy Anchors on Hybrid Lead Iodide Perovskites: Insights for Spiro-MeOTAD Attachment. *J. Phys. Chem. C*. **118**, 26947–26954 (2014).

42. M. Saliba, S. Orlandi, T. Matsui, S. Aghazada, M. Cavazzini, J.-P. Correa-Baena, P. Gao, R. Scopelliti, E. Mosconi, K.-H. Dahmen, F. De Angelis, A. Abate, A. Hagfeldt, G. Pozzi, M. Graetzel, M. K. Nazeeruddin, A molecularly engineered hole-transporting material for efficient perovskite solar cells. *Nat. Energy*. **1**, 15017 (2016).

43. Y. Lin, B. Chen, Y. Fang, J. Zhao, C. Bao, Z. Yu, Y. Deng, P. N. Rudd, Y. Yan, Y. Yuan, J. Huang, Excess charge-carrier induced instability of hybrid perovskites. *Nat. Commun.* **9**, 4981 (2018).

44. B. Chen, J. Song, X. Dai, Y. Liu, P. N. Rudd, X. Hong, J. Huang, Synergistic Effect of Elevated Device Temperature and Excess Charge Carriers on the Rapid Light-Induced Degradation of Perovskite Solar Cells. *Adv. Mater.* **31**, 1902413 (2019).

45. N. Phung, A. Al-Ashouri, S. Meloni, A. Mattoni, S. Albrecht, E. L. Unger, A. Merdasa, A. Abate, The Role of Grain Boundaries on Ionic Defect Migration in Metal Halide Perovskites. *Adv. Energy Mater.* **10**, 1903735 (2020).

46. B. Krogmeier, F. Staub, D. Grabowski, U. Rau, T. Kirchartz, Quantitative analysis of the transient photoluminescence of CH 3 NH 3 PbI 3 /PC 61 BM heterojunctions by numerical simulations. *Sustain. Energy Fuels*. **2**, 1027–1034 (2018).

47. F. Staub, H. Hempel, J.-C. Hebig, J. Mock, U. W. Paetzold, U. Rau, T. Unold, T. Kirchartz, Beyond Bulk Lifetimes: Insights into Lead Halide Perovskite Films from Time-Resolved Photoluminescence. *Phys. Rev. Appl.* **6**, 044017 (2016).

48. M. Krumrey, G. Ulm, High-accuracy detector calibration at the PTB four-crystal monochromator beamline. *Nucl. Instruments Methods Phys. Res. Sect. A Accel. Spectrometers, Detect. Assoc. Equip.* **467**–**468**, 1175–1178 (2001).

49. D. Skroblin, A. Schavkan, M. Pflüger, N. Pilet, B. Lüthi, M. Krumrey, Vacuum-compatible photon-counting hybrid pixel detector for wide-angle x-ray scattering, x-ray diffraction, and x-ray reflectometry in the tender x-ray range. *Rev. Sci. Instrum.* **91**, 023102 (2020).

50. K. A. Bush, A. F. Palmstrom, Z. J. Yu, M. Boccard, R. Cheacharoen, J. P. Mailoa, D. P. McMeekin, R. L. Z. Z. Hoye, C. D. Bailie, T. Leijtens, I. M. Peters, M. C. Minichetti, N. Rolston, R. Prasanna, S. Sofia, D. Harwood, W. Ma, F. Moghadam, H. J. Snaith, T. Buonassisi, Z. C. Holman, S. F. Bent, M. D. McGehee, 23.6%-efficient monolithic perovskite/silicon tandem solar cells with improved stability. *Nat. Energy*. **2**, 17009 (2017).

51. J.-F. Guillemoles, T. Kirchartz, D. Cahen, U. Rau, Guide for the perplexed to the Shockley–Queisser model for solar cells. *Nat. Photonics*. **13**, 501–505 (2019).

52. J. Seo, S. Park, Y. Chan Kim, N. J. Jeon, J. H. Noh, S. C. Yoon, S. Il Seok, Benefits of very thin PCBM and LiF layers for solution-processed p-i-n perovskite solar cells. *Energy Environ. Sci.* **7**, 2642–2646 (2014).

53. M. Stolterfoht, C. M. Wolff, J. A. Márquez, S. Zhang, C. J. Hages, D. Rothhardt, S. Albrecht, P. L. Burn, P. Meredith, T. Unold, D. Neher, Visualization and suppression of interfacial recombination for high-efficiency large-area pin perovskite solar cells. *Nat. Energy*. **3**, 847–854 (2018).

54. M. Stolterfoht, M. Grischek, P. Caprioglio, C. M. Wolff, E. Gutierrez-Partida, F. Peña-Camargo, D. Rothhardt, S. Zhang, M. Raoufi, J. Wolansky, M. Abdi-Jalebi, S. D. Stranks, S. Albrecht, T. Kirchartz, D. Neher, How To Quantify the Efficiency Potential of Neat Perovskite Films: Perovskite Semiconductors with an Implied Efficiency Exceeding 28%. *Adv. Mater.* **32**, 2000080 (2020).

55. N. Tessler, Y. Vaynzof, Insights from Device Modeling of Perovskite Solar Cells. *ACS Energy Lett.* **5**, 1260–1270 (2020).

56. W. Wang, P. Chen, C. Chiang, T. Guo, C. Wu, S. Feng, Synergistic Reinforcement of Built-In Electric Fields for Highly Efficient and Stable Perovskite Photovoltaics. *Adv. Funct. Mater.* **30**, 1909755 (2020).

57. B. Chen, S.-W. Baek, Y. Hou, E. Aydin, M. De Bastiani, B. Scheffel, A. Proppe, Z. Huang, M. Wei, Y.-K. Wang, E.-H. Jung, T. G. Allen, E. Van Kerschaver, F. P. García de Arquer, M. I. Saidaminov, S. Hoogland, S. De Wolf, E. H. Sargent, Enhanced optical path and electron diffusion length enable high-efficiency perovskite tandems. *Nat. Commun.* **11**, 1257 (2020).

58. R. Quintero-Bermudez, J. Kirman, D. Ma, E. H. Sargent, R. Quintero-Torres, Mechanisms of

LiF Interlayer Enhancements of Perovskite Light-Emitting Diodes. *J. Phys. Chem. Lett.* **11**, 4213–4220 (2020).

59. Z. Li, C. Xiao, Y. Yang, S. P. Harvey, D. H. Kim, J. A. Christians, M. Yang, P. Schulz, S. U. Nanayakkara, C.-S. Jiang, J. M. Luther, J. J. Berry, M. C. Beard, M. M. Al-Jassim, K. Zhu, Extrinsic ion migration in perovskite solar cells. *Energy Environ. Sci.* **10**, 1234–1242 (2017).

60. S.-M. Bang, S. S. Shin, N. J. Jeon, Y. Y. Kim, G. Kim, T.-Y. Yang, J. Seo, Defect-Tolerant Sodium-Based Dopant in Charge Transport Layers for Highly Efficient and Stable Perovskite Solar Cells. *ACS Energy Lett.* **5**, 1198–1205 (2020).

61. S. N. Habisreutinger, T. Leijtens, G. E. Eperon, S. D. Stranks, R. J. Nicholas, H. J. Snaith, Carbon Nanotube/Polymer Composites as a Highly Stable Hole Collection Layer in Perovskite Solar Cells. *Nano Lett.* **14**, 5561–5568 (2014).

62. F. Sahli, J. Werner, B. A. Kamino, M. Bräuninger, R. Monnard, B. Paviet-Salomon, L. Barraud, L. Ding, J. J. Diaz Leon, D. Sacchetto, G. Cattaneo, M. Despeisse, M. Boccard, S. Nicolay, Q. Jeangros, B. Niesen, C. Ballif, Fully textured monolithic perovskite/silicon tandem solar cells with 25.2% power conversion efficiency. *Nat. Mater.* **17**, 820–826 (2018).

63. M. Jošt, B. Lipovšek, B. Glažar, A. Al-Ashouri, K. Brecl, G. Matič, A. Magomedov, V. Getautis, M. Topič, S. Albrecht, Perovskite Solar Cells go Outdoors: Field Testing and Temperature Effects on Energy Yield. *Adv. Energy Mater.* **10**, 2000454 (2020).

64. T. Unold, L. Gütay, in *Advanced Characterization Techniques for Thin Film Solar Cells* (Wiley-VCH Verlag GmbH & Co. KGaA, Weinheim, Germany, 2011), pp. 151–175.

65. S. Chen, L. Zhu, M. Yoshita, T. Mochizuki, C. Kim, H. Akiyama, M. Imaizumi, Y. Kanemitsu, Thorough subcells diagnosis in a multi-junction solar cell via absolute electroluminescence-efficiency measurements. *Sci. Rep.* **5**, 7836 (2015).

66. D. Alonso-Alvarez, N. Ekins-Daukes, Photoluminescence-Based Current–Voltage Characterization of Individual Subcells in Multijunction Devices. *IEEE J. Photovoltaics*. **6**, 1004–1011 (2016).

67. S. Roensch, R. Hoheisel, F. Dimroth, A. W. Bett, Subcell I-V characteristic analysis of GaInP/GaInAs/Ge solar cells using electroluminescence measurements. *Appl. Phys. Lett.* **98**, 251113 (2011).

68. D. Hinken, K. Ramspeck, K. Bothe, B. Fischer, R. Brendel, Series resistance imaging of solar cells by voltage dependent electroluminescence. *Appl. Phys. Lett.* **91**, 182104 (2007).

69. A. Richter, M. Hermle, S. W. Glunz, Reassessment of the Limiting Efficiency for Crystalline Silicon Solar Cells. *IEEE J. Photovoltaics*. **3**, 1184–1191 (2013).

70. L. Mazzarella, Y. Lin, S. Kirner, A. B. Morales-Vilches, L. Korte, S. Albrecht, E. Crossland, B. Stannowski, C. Case, H. J. Snaith, R. Schlatmann, Infrared Light Management Using a Nanocrystalline Silicon Oxide Interlayer in Monolithic Perovskite/Silicon Heterojunction Tandem Solar Cells with Efficiency above 25%. *Adv. Energy Mater.* **9**, 1803241 (2019).

71. U. Rau, Reciprocity relation between photovoltaic quantum efficiency and electroluminescent emission of solar cells. *Phys. Rev. B*. **76**, 085303 (2007).

72. H. Hempel, T. Unold, R. Eichberger, Measurement of charge carrier mobilities in thin films on metal substrates by reflection time resolved terahertz spectroscopy. *Opt. Express*. **25**, 17227 (2017).

73. M. Meusel, R. Adelhelm, F. Dimroth, A. W. Bett, W. Warta, Spectral mismatch correction and spectrometric characterization of monolithic III-V multi-junction solar cells. *Prog. Photovoltaics Res. Appl.* **10**, 243–255 (2002).

74. G. Ashiotis, A. Deschildre, Z. Nawaz, J. P. Wright, D. Karkoulis, F. E. Picca, J. Kieffer, The

fast azimuthal integration Python library: pyFAI. *J. Appl. Crystallogr.* **48**, 510–519 (2015).

75. Z. Ni, C. Bao, Y. Liu, Q. Jiang, W.-Q. Wu, S. Chen, X. Dai, B. Chen, B. Hartweg, Z. Yu, Z. Holman, J. Huang, Resolving spatial and energetic distributions of trap states in metal halide perovskite solar cells. *Science (80-.).* **367**, 1352–1358 (2020).

76. C. M. Wolff, F. Zu, A. Paulke, L. P. Toro, N. Koch, D. Neher, Reduced Interface-Mediated Recombination for High Open-Circuit Voltages in CH 3 NH 3 PbI 3 Solar Cells. *Adv. Mater.* **29**, 1700159 (2017).

77. H. Hempel, C. J. Hages, R. Eichberger, I. Repins, T. Unold, Minority and Majority Charge Carrier Mobility in Cu2ZnSnSe4 revealed by Terahertz Spectroscopy. *Sci. Rep.* **8**, 14476 (2018).

78. H. Hempel, A. Redinger, I. Repins, C. Moisan, G. Larramona, G. Dennler, M. Handwerg, S. F. Fischer, R. Eichberger, T. Unold, Intragrain charge transport in kesterite thin films—Limits arising from carrier localization. *J. Appl. Phys.* **120**, 175302 (2016).

79. F. Peña-Camargo, P. Caprioglio, F. Zu, E. Gutierrez-Partida, C. M. Wolff, K. Brinkmann, S. Albrecht, T. Riedl, N. Koch, D. Neher, M. Stolterfoht, Halide Segregation versus Interfacial Recombination in Bromide-Rich Wide-Gap Perovskite Solar Cells. *ACS Energy Lett.* **5**, 2728–2736 (2020).

80. J. A. Bardecker, H. Ma, T. Kim, F. Huang, M. S. Liu, Y.-J. Cheng, G. Ting, A. K.-Y. Jen, Self-assembled Electroactive Phosphonic Acids on ITO: Maximizing Hole-Injection in Polymer Light-Emitting Diodes. *Adv. Funct. Mater.* **18**, 3964–3971 (2008).

81. P. N. Dickerson, A. M. Hibberd, N. Oncel, S. L. Bernasek, Hydrogen-Bonding versus van der Waals Interactions in Self-Assembled Monolayers of Substituted Isophthalic Acids. *Langmuir*. **26**, 18155–18161 (2010).

82. N. Nerngchamnong, L. Yuan, D.-C. Qi, J. Li, D. Thompson, C. A. Nijhuis, The role of van der Waals forces in the performance of molecular diodes. *Nat. Nanotechnol.* **8**, 113–118 (2013).

83. R.-F. Dou, X.-C. Ma, L. Xi, H. L. Yip, K. Y. Wong, W. M. Lau, J.-F. Jia, Q.-K. Xue, W.-S. Yang, H. Ma, A. K. Y. Jen, Self-Assembled Monolayers of Aromatic Thiols Stabilized by Parallel-Displaced π−π Stacking Interactions. *Langmuir*. **22**, 3049–3056 (2006).

84. M. Boccard, C. Ballif, Influence of the Subcell Properties on the Fill Factor of Two-Terminal Perovskite–Silicon Tandem Solar Cells. *ACS Energy Lett.* **5**, 1077–1082 (2020).

85. P. Caprioglio, M. Stolterfoht, C. M. Wolff, T. Unold, B. Rech, S. Albrecht, D. Neher, On the Relation between the Open-Circuit Voltage and Quasi-Fermi Level Splitting in Efficient Perovskite Solar Cells. *Adv. Energy Mater.* **9**, 1901631 (2019).

Supplementary Materials

Contents

Materials and Methods

Materials for perovskite cell preparation

Anhydrous DMSO (dimethyl sulfoxide), anh. DMF (dimethylformamide), anh. Anisole, PTAA (poly [bis (4-phenyl) (2,5,6-trimentlyphenyl) amine]) and lithium fluoride (purity ≥ 99.99 %) were purchased from Sigma Aldrich. C_{60} (sublimed) was bought from CreaPhys GmbH. FAI (formamidinium iodide) and MABr (methylammonium bromide) were purchased from Dyenamo. PbI_2 and $PbBr_2$ were bought from TCI. CsI was purchased from abcr GmbH. The ceramic 2-inch IZO target was purchased from FHR Anlagenbau GmbH. The SAMs MeO-2PACz and 2PACz were synthesized by TCI. The synthesis of Me-4PACz and the (Me-)nPACz series by us is described in the synthesis section at the end of this document. Ethanol (anh.) for the SAMs was bought from VWR (no difference was observed when using Ethanol from other suppliers, independent of the water content).

Perovskite single-junction preparation

The perovskite solar cell has an inverted (*p-i-n*) planar structure and is deposited on ITO-covered glass (Automated Research GmbH, both 7 Ohm/sq and 15 Ohm/sq sheet conductivities were used in this study), which was cleaned with Mucasol (2% in DI-water, substrates were brushed), DI-water, acetone and isopropanol, each for 15 minutes in an ultrasonic bath. Afterwards the surface was "activated" for 10-15 minutes in an UV-O_3 cleaner (FHR UVOH 150 Lab), which is a crucial step before SAM functionalization (for the tandem cells as well). The single-junction cell configuration is ITO/HTL/Perovskite/(LiF)/C_{60}/SnO_2/Ag, where the HTL is PTAA, MeO-2PACz, 2PACz or Me-4PACz. All the spin-coating layer deposition steps were conducted in a nitrogen atmosphere. The hole transport material PTAA (2 mg ml^{-1} in toluene) was deposited using spin-coating (5000 rpm for 30 s, 5 s acceleration), followed by heating for 10 min at 100 °C. The rotation was reduced for the SAM-solutions to 3000 rpm (used concentration of the SAM solutions = 1 mmol/l, or ~0.3 mg/ml). The perovskite was prepared following the typical triple cation process. In short, 1.5 M nominal PbI_2 and $PbBr_2$ in DMF:DMSO = 4:1 volume were first prepared as stock solutions (shaken overnight at 60 °C) and then added to FAI and MABr with 9 % PbX_2 excess, respectively (X = I or Br) (typical amounts were 0.3 g FAI and 0.06 g of MABr). The so obtained $FAPbI_3$ and $MAPbBr_3$ were then mixed in 77:23

volume ratio to obtain the "double cation" perovskite. Finally, 5 vol-% of 1.5 M nominal CsI in DMSO was added to the perovskite precursor (stock solution prepared one day before, typically ~50 mg powder). 100 µl of perovskite solution was then spread on the substrate and spun using one step spin-coating process (3500 for 35 s, 5 s acceleration). 10-13 s before the end of the program, 300 µl of Anisole as the anti-solvent was dripped on the film. The films were then annealed at 100 °C for 15-30 min. Afterwards, 20 nm of C_{60} was thermally evaporated at a rate of 0.15 Å s^{-1} onto the perovskite film. Optionally, as indicated, a 1 nm-thick LiF interlayer was deposited between C_{60} and perovskite, evaporated at a rate of 0.05 Å s^{-1}, within the same vacuum run as the C_{60} layer. 20 nm of SnO_2 were then deposited by thermal ALD in an Arradiance GEMStar reactor. Tetrakis(dimethylamino)tin(IV) (TDMASn) was used as the Sn precursor and was held at 60 °C in a stainless-steel container. Water was used as oxidant, and was delivered from a stainless-steel container without active heating, whereas the precursor delivery manifold was heated to 115 °C. For the deposition at 80 °C, the TDMASn/purge1/H_2O/purge2 times were 1s/10s/0.2s/15s with corresponding nitrogen flows of 30sccm/90sccm/90sccm/90sccm. With this, 140 cycles lead to 20 nm tin oxide. More details can be found in a previous publication (*26*). We noticed a beneficial effect when letting the TDMASn bottle cool down to room temperature when not in use. Finally, 100 nm Ag were deposited by thermal evaporation at a rate of 1 Å s^{-1}.

Silicon solar cell preparation

The silicon heterojunction (SHJ)-bottom cell was fabricated from a 260 µm thick, ~3 Ω cm^{-1} polished FZ <100> n-type crystalline silicon (c-Si) wafer in a rear junction configuration. The front surface of the wafer was left polished by capping with a PECVD deposited SiO_2 prior to wet texturing to obtain random pyramids with <111> facets. After removal of the capping in HF another final RCA clean and HF dip (1 % dilution in water) were done and an approx. 5 nm thick, intrinsic (i) amorphous silicon (a-Si:H) layer stack was grown on both sides of the c-Si wafer in order to passivate the c-Si surface. On the textured rear-side, an approx. -5-nm thick, p-doped a-Si:H layer stack was deposited to form the hole contact (junction). On the polished front-side, a 95-nm thick (20-nm thick for single-junction reference cells), n-doped nanocrystalline silicon oxide layer (nc-SiO_x:H) with a refractive index, n, of 2.7 at 633 nm was used as the electron contact of the SHJ bottom cell and the optical intermediate layer between the top and the bottom cells (*70*). The a- and nc-Si layers were deposited with an Applied Materials (AKT1600) plasma enhanced chemical vapor deposition (PECVD) cluster tool. In order to contact the bottom cell a ZnO:Al/Ag layer stack was deposited on the textured rear-side and a 20 nm (70-nm thick for single-junction references) thick ITO layer was deposited on the polished front-side on top of the nc-SiO_x:H interlayer. Both depositions were DC-sputtered in an in-line sputter tool from Leybold Optics using Ar/O_2 gas mixtures. For the ITO a tube target with 95/5 doping ratio and for the AZO a tube target with 1% Al_2O_3 in ZnO was used. Both contact-layer stack of the silicon were deposited using aligned shadow masks with an opening of 1.13 x 1.13 cm^2 (2 x 2 cm^2 for single-junction reference). For single-junction reference cells with an aperture area of 2 x 2 cm^2, an Ag grid was screen-printed on top of the front ITO.

Preparation of tandem solar cells

The bottom cells were blown clean with N_2 and UV-O_3-treated for 15 minutes. The same HTL, perovskite, (LiF), C_{60} and SnO_2 deposition as described above was conducted on the silicon bottom cells. Subsequently, 100 nm IZO (Roth&Rau MicroSys 200 PVD, ceramic target purchased from FHR Anlagenbau GmbH) are deposited by sputtering. The 2-inch ceramic target consisted of 90 %wt. In_2O_3 and 10 %wt. ZnO. At a RF-power of 70 W the cells oscillated under the target to have a uniform deposition. 0.2%$_{vol}$ O_2 was added to the chamber. The previously optimized layer (*26*) has a mobility, carrier density and resistivity of 43.5 cm^2 V^{-1} s^{-1}, $3.4 \cdot 10^{20}$ cm^{-3} and $4.2 \cdot 10^{-4}$ Ω cm, respectively. A 100 nm silver frame was thermally evaporated through a shadow mask to collect the charge carriers without a need of grid fingers. Lastly, 100 nm LiF is evaporated as an antireflective coating by thermal

evaporation. The active area is defined by the metal frame and is slightly larger than 1 cm^2. A photo and schematic of a monolithic tandem solar cell is shown in Figure S25.

Luminescence spectroscopy techniques

Time-dependent steady-state photoluminescence

Time-dependent steady state absolute photoluminescence measurements were performed on a home-built setup using an integrating sphere, where the samples were placed at the edge of the sphere. The PL was collected with a fiber connected to a CCD-array spectrometer (Ocean Optics). The samples were excited with a continuous-wave laser at 532 nm emission wavelength, a photon flux of ~1.2E16 photons/s and a spot size on the sample of 0.12 cm^2 (around 1-sun-equivalent excitation fluence, calibrated with a certified silicon reference cell). The 30-suns case was realized by a focusing lens to reduce the spot size to 0.4 mm^2. The spot size was measured by fitting a Gaussian curve to the beam profile extracted from CCD imaging the laser spot. The 1-sun 0.4 mm^2 case was realized by a focusing lens and appropriate ND filters. Non-absorbed laser light and emitted photoluminescence fluxes were simultaneously detected by the spectrometer, of which the spectral sensitivity was calibrated using a NIST-traceable halogen lamp. The spectral time evolutions of the perovskite films were recorded with an integration time of 300 ms and delay of 2-3 s between each recording. Measurements were carried out in air; the samples were measured promptly after they were taken out from the N2-filled glovebox.

Absolute PL and pseudo-*J-V*s

Excitation for the PL imaging measurements was performed with a 520 nm CW laser (Insaneware) through an optical fibre into an integrating sphere. The intensity of the laser was adjusted to a 1 sun equivalent intensity by illuminating a 1 cm^2-sized perovskite solar cell under short-circuit and matching the current density to the J_{SC} under the sun simulator (e.g. ~22.0 mA cm^{-2} at 100 mW cm^{-2}, or $1.375x10^{21}$ photons m^{-2} s^{-1}). A second optical fiber was used from the output of the integrating sphere to an Andor SR393i-B spectrometer equipped with a silicon CCD camera (DU420A-BR-DD, iDus). The system was calibrated by using a halogen lamp with known spectral irradiance, which was shone into to integrating sphere. A spectral correction factor was established to match the spectral output of the detector to the calibrated spectral irradiance of the lamp. The spectral photon density was obtained from the corrected detector signal (spectral irradiance) by division through the photon energy (hf), and the photon numbers of the excitation and emission were obtained from numerical integration using Matlab. In a last step, three fluorescent test samples with high specified PLQY supplied from Hamamatsu Photonics where measured where the specified value could be accurately reproduced within a small relative error of less than 5%.

The samples were illuminated in the integrating sphere using the same 520 nm CW laser (Insaneware) as described above. A continuously variable neutral density filter wheel (ThorLabs) was used to attenuate the laser power to measure at different intensities which was monitored using an additional Si photodetector. The samples were illuminated at a given intensity for a variable illumination time using an electrical shutter. After an illumination time of 1 second, the PL spectra were recorded by averaging 30 spectra taken using a detector exposure time of 30 µs. The electrical shutter was then closed and the filter wheel was moved to the next position and the steps were repeated. A custom-built Labview code was written to automate the measurement, and a Matlab code to automate the data evaluation.

Pseudo-*J-V*s

The pseudo-*J-V*s were deduced from the intensity-dependent QFLS or V_{OC} measurements as recently demonstrated in ref. (*54*). This was done by calculating the dark-current density from the generated current density at a given light intensity in equivalent suns. E.g. 1 sun corresponds to 22.0 mA cm^{-2}, 1% of a sun to 0.220 mA cm^{-2}. The obtained dark current was then plotted against the measured QFLS or

V_{OC} at the given light intensity to create a transport/series resistance-free dark *J-V*-curve. This curve was then shifted to the J_{SC} in the *J-V*-measurement to create the pseudo-*J-V* curve allowing to read of the pseudo- (or implied) FF and V_{OC} of the measured partial cell stack (e.g. the neat film, or perovskite/transport layer junction) or the complete cell. We note, that the implied FF is only impacted by the non-radiative (and radiative) recombination processes in the studied sample but not by charge transport or resistive losses that are induced by the active layer or the transport layers, and resistances (e.g. the ITO sheet resistance).

Intensity-dependent V_{OC} measurements

Steady-state intensity dependent V_{OC} measurements were obtained with a 520 nm continuous wave laser (Insaneware) providing a power of 1 W. A continuously variable neutral density filterwheel (ThorLabs) was used to attenuate the laser power (up to OD 6). The light intensity was thereby simultaneously measured with a silicon photodetector and a Keithley 485 to improve the accuracy of the measurement. The measurement was performed by measuring the V_{OC} after a 1 second illumination at a given light intensity and then the J_{SC} after 1 second illumination before the filterwheel rotated to the next position. A custom-built LabView code was written to automate the measurement.

Transient photoluminescence

TrPL measurements were carried out in a home-built setup using 660 nm excitation laser light from a supercontinuum light source (SuperK) with a 25-35 µm spot size. The samples were excited from the glass side to avoid increased reflection stray light, however, no significant difference in decay times was observed between excitation from both sides. We chose the longer wavelength excitation to avoid effects of charge diffusion from a high to low carrier density region. The excitation pulse had a repetition rate of 150 kHz and the PL emission was collected panchromatically through a photomultiplier and time-correlated single photon counting technique. The fluence was controlled with a tuneable neutral density filter and monitored with a power meter.

Absolute photo and electroluminescence imaging of tandems

Absolute PL imaging measurements were performed with two 450 nm LEDs for the perovskite subcell and with an 850 nm LED for the excitation of the silicon subcell. The excitation intensities for both measurements was set to 1.4×10^{21} photons m^{-2} s^{-1}. The photoluminescence image detection was performed with a charge-coupled device (CCD) camera (Allied Vision) for the perovskite subcell and with an InGaAs based camera for the Si subcell. Both cameras were coupled with a liquid crystal tunable filter unit. The systems were calibrated to absolute photon numbers.

Quantitative electroluminescence imaging was performed by sweeping a voltage between 1.4 and 2.0 V with a 2 mV voltage step and 0.5 s dwell time. The dark current J_{dark} was recorded for the sweeps. To avoid large data collection a luminescence image at every step for every subcell was recorded at the maximum energy of the luminescence. The intensity of the images was scaled to absolute photon numbers with a full hyperspectral image collected at a given injection. This results in a data set containing the electroluminescence yield of each subcell (*j*) $Y_{EL}^{j}(J_{dark})$ as a function of the injected current J_{dark}. The radiative current of every subcell J_{rad}^{j} is calculated by multiplying the $Y_{EL}^{j}(J_{dark})$ by the elementary charge. Finally, the voltage of the subcells V^{j} is calculated with:

$$V^{j} = kT \ln\left(\frac{J_{rad}^{j}+J_{0,rad}^{j}}{J_{0,rad}^{j}}\right).$$

Here, $J_{0,rad}^{j}$ is calculated from the EQE of the individual subcells following the reciprocity theorem (*71*):

$$J_{0,rad}^{j} = q \int EQE^{j}(E)\phi_{bb}(E)dE.$$

Terahertz-Probe (OPTP) spectroscopy

Optical-Pump Terahertz-Probe (OPTP) spectroscopy can measure the transient photo-excited sheet conductivity $\Delta\sigma_S$ and sum mobility $\mu_\Sigma = \mu_e + \mu_h$ of the electron mobility μ_e and the hole mobility μ_h. The terahertz pulses are generated by optical rectification of 800 nm pulses in a ZnTe crystal. These terahertz pulses are guided through the perovskite sample and the transmitted terahertz field T is measured by electro-optical sampling in a second ZnTe crystal. Additionally, the perovskite samples can be photo-excited by pump pulses with a wavelength of 400 nm and a pulse length of ≈150 fs. These charge carriers alter the transmission of the terahertz probe pulse by ΔT, which is also detected. The derived pump-induced change in THz transmission $\Delta T/T$ is analyzed by the thin-film approximation in equation (S5) for the photo-excited sheet conductivity $\Delta\sigma_S$, which is the integral of the induced photoconductivity Δσ over the sample thickness d. The parameters are the speed of light c, the permittivity of the vacuum ε_0, and the terahertz refractive index of the substrates n_{sub}, which is 1.95 for the used quartz glass substrate.

$$\Delta\sigma_s = \int_{x=0}^{d} \Delta\sigma dx = -\varepsilon_0 c(1 + n_{sub}) \frac{\frac{\Delta T}{T}}{1 + \frac{\Delta T}{T}} \quad (1)$$

The transient of the photo-excited sheet conductivity is measured by scanning the delay of the pump pulse by an optical delay line. In this case, the terahertz pulse is sampled at its maximum. Additionally, the full terahertz pulse was scanned by a second delay line at a pump delay time of 10 ps. After both ΔT and T are Fourier-transformed, the photo-excited sheet conductivity spectrum is derived by Equation (1). The sum mobility spectrum is obtained by Equation (2) from the photo-excited sheet conductivity, the flux of the pump beam of 7 x 10^{11} photons/pulse/cm^2, and the reflectance of the pump beam at 400 nm of 25%. The quantum yield of exciton dissociation in such mixed halide perovskites is approximately 1 at room temperature.

$$\Sigma\mu = \mu_e(f,t) + \mu_h(f,t) = \frac{\Delta\sigma_s}{q\varphi_{pump}(1-R)} \quad (2)$$

The gained sum mobility is a spectrum at the frequencies from 0.5 to 3 THz, which constitute the terahertz probe pulse. The observed flat frequency-dependence in fig. 1 indicates no significant difference between the measured terahertz mobilities and the DC-value, which is relevant for the device operation or carrier diffusion.

Further details on the OPTP measurement can be found in (*72*).

Single junction solar cell characterization (Current-Voltage curves, EQE)

The *J-V* curves of single-junction cells were recorded in nitrogen atmosphere with a solar simulator (Oriel LCS-100) and Keithley 2400 source-measure unit, controlled by a custom LabView program. The intensity was calibrated to AM1.5G 1-sun-equivalent with a filtered KG3 Silicon reference solar cell, calibrated by Fraunhofer ISE (spectral mismatch is around 0.997, within the measurement error, thus no correction was applied). *J-V* scans were as performed in a 2-point-probe configuration. The typical step size was 20 mV, with an integration time of 20 ms and settling time of 20 ms (250 mV/s). The cells did not experience any preconditioning. Shunted or partially shunted devices (mostly due to scratches and not perfectly clean substrates) were not considered in the analysis.

EQE spectra were recorded with an Oriel Instruments QEPVSI-b system with a Newport 300 W xenon arc lamp, controlled by TracQ-Basic software. The system is calibrated using a Si reference cell with known spectral response before every measurement. The electrical response of the device under test is measured with a Stanford Research SR830 Lock-In amplifier (time constant of 0.3 s) and evaluated in TracQ. The typical short-circuit current mismatch between integrated external quantum efficiency (EQE) times AM1.5G irradiance and values from *J-V* scans is around 1% if the area of the cell precisely known (considering shadowing through the mask during metal evaporation).

Tandem solar cell characterization (Current-Voltage curves, EQE)

The tandem solar cells were measured in air under AM1.5G (1 sun) equivalent illumination with a Wavelabs Sinus-70 LED class AAA sun simulator. The cells did not experience any preconditioning. For calibration we used a slightly modified calibration route compared to Meusel *et al.* (*73*). We adjusted the spectrum such that for both subcells it led to the photogenerated current densities obtained by EQE measurements. Thus, for a perovskite-limited cell, we first increased the intensity of the blue light in order to get a silicon-limited cell. Subsequently, the NIR region was adjusted until the J_{SC} of the silicon-limited tandem solar cell was equal to the $J_{ph,Si}$ (calculated from EQE and AM1.5G spectrum). Finally, the intensity of the blue light was decreased until the tandem solar cell was perovskite-limited again and the J_{SC} was equal to the $J_{ph,Pero}$. For a silicon-limited cell it is done vice versa. The backside of the cell was contacted with a metal vacuum chuck at 25°C, whereas the front side was contacted with two Au probes. A black laser-cut aperture mask covered the substrate outside of the active area. The *J-V* measurements and MPP tracks were recorded using a home-built LabView software. The EQE spectra were recorded with a home-built setup using chopped (79 Hz) monochromatic light from a Xe and He lamp, respectively. To measure the EQE of the perovskite subcell, the silicon subcell was saturated using an LED with 850 nm peak emission. To maintain short circuit conditions, a bias voltage of 0.6 V was applied. The silicon subcell was measured by saturating the perovskite subcell with blue light from a LED (455 nm) and applying a bias voltage of 1 V.

The boxes in the PV parameter boxplots indicate the 25/75 percentiles and the whiskers mark the 10/90 percentiles. The line in the plots mark the respective average value.

Helium Ultra-Violet Photoelectron Spectroscopy

Helium ultra-violet photoelectron spectroscopy (He-UPS) with an excitation energy of 21.2 eV was applied to investigate the secondary electron cutoff (SECO) and the valence band onset. Four different layer stacks were investigated: i) ITO-covered glass substrate, two different SAMs ii) Me-4PACz and iii) 2PACz on an ITO-covered substrate and iv) ITO/PTAA/Perovskite (1.68 eV band gap). All samples were transferred from the glovebox to the vacuum system in a portable chamber in nitrogen atmosphere. The measurements were conducted using a step width of 0.05 eV and a dwell time of 3 seconds. Between the sample, contacted via the ITO, and the electron analyzer a bias voltage of 7 V was applied. Both, the SECO and the valence band onset (E_F-E_V), were determined by the intersection of the linear fit of the data with the linear background. Considering the excitation energy of He I, (21.2 eV - SECO) leads directly to the work function (E_{Vak}-E_F) of the material.

X-ray diffraction

Grazing-incidence wide-angle X-ray scattering (GIWAXS) data were acquired at the four crystal monochromator beamline of the Physikalisch-Technische Bundesanstalt at the synchrotron radiation facility BESSY II (*48*). Under high vacuum, X-rays with 8 keV photon energy (λ = 1.5498 Å) were incident on 1 cm^2 samples prepared with stack silicon/ITO/HTL/perovskite/C_{60} to mimic growth conditions in devices, and with C_{60} to prevent any material changes under vacuum. Grazing incidence angles from 1.5° to 6.5° were used to probe different depths in the film and at high angles the broadening due to the beam footprint on the sample is reduced. Scattering was detected with a vacuum-compatible version of the PILATUS3 X 100K hybrid photon-counting detector (DECTRIS) (*49*). This detector was rotated around the sample center in 4.5° steps through 16 positions at a sample-to-detector distance of 206 mm with 30 s acquisition at each detector angle. The photon flux was approximately 1.82 x 10^8 s^{-1} with 80 μm beam height. Data was reduced and corrected using *PyFAI* (*74*).

Further 1D X-ray diffraction measurements were acquired using a PANalytical X'Pert Pro MPD (multi-purpose diffractometer) in grazing incidence geometry (GI-XRD). Diffraction patterns were collected with a step size of 0.02 degree, for 6 seconds at each step and at a grazing angle of 1°, with the measurement conducted in air.

Long term stability measurement

Monolithic tandem solar cells were tracked over 300 h at the maximum power point (MPP) with a self-constructed ageing setup in collaboration with the University of Ljubljana (with them providing the LED-array and measurement components). To guarantee homogenous illumination the LED-array consists of 193 LEDs, 144 of which are blue LEDs and 49 are near-infrared LEDs with a wavelength of 470 nm and 940 nm, respectively. The normalized spectra are given in Figure S34. With an independent tunability of both intensities via two potentiometers, the photocurrent of the top and bottom cell can be adjusted to increase or decrease the current mismatch as intended. The bottom cell is electrically connected to a copper block on the backside, whereas the top cell is connected with 2 pogo-pins. Under ambient conditions (relative humidity of 30-40%, measured with a calibrated humidity tracker) the measurement took place in a closed housing at a stable 25°C, while the cells were kept in place with a diaphragm pump. While monitoring the current and voltage of each cell at MPP (using voltage perturbation) the intensity of a blue and infrared reference diode was logged to account for any drops/fluctuation of illumination.

Ultraviolet photoelectron spectroscopy

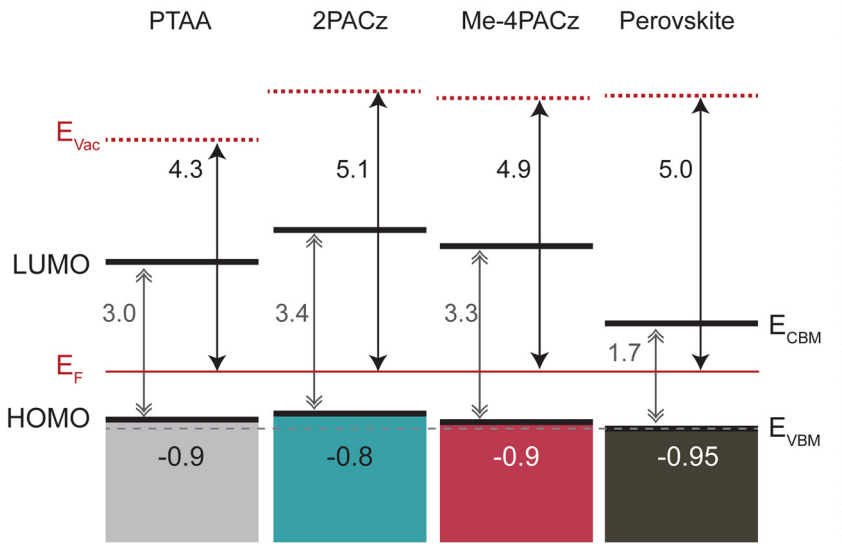

Figure S1 Energetic diagram comparing the alignment between perovskite valence band edge and the HOMO levels of the studied hole-selective layers. A correlation is apparent between fill factor and how close the alignment between perovskite valence band edge and HOMO level of the hole-selective layers is; considering that PTAA has a low conductivity but significant thickness (~10 nm), which adds series resistance that influences the FF as well. The absorption onset in Figure S38 was used to estimate the “bandgap” of the SAMs. The data for PTAA is from ref. (*7*) (this and the following citations refer to the numbers of the main paper), measured at another UPS setup.

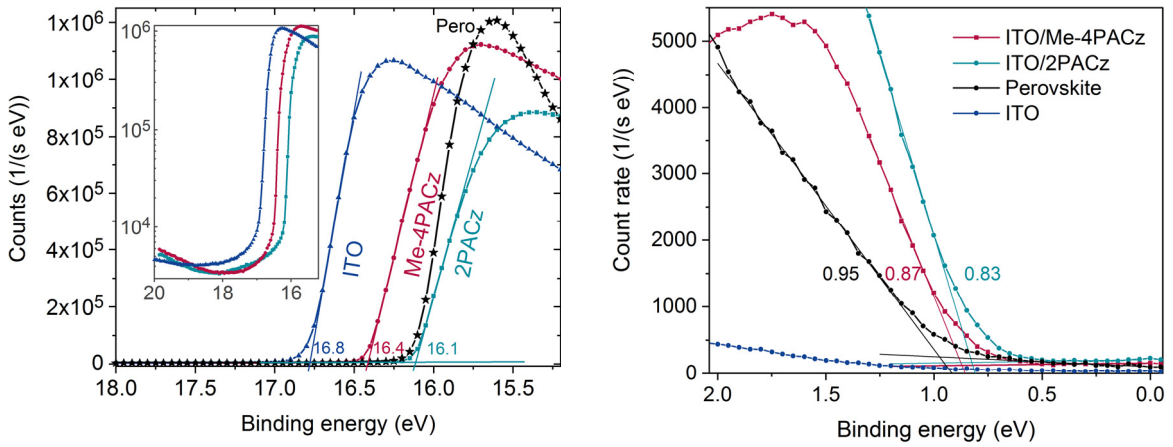

Figure S2 ITO work function shift by the HTLs. Helium ultra-violet photoelectron spectroscopy comparing ITO substrates covered by Me-4PACz or 2PACz, or PTAA/Perovskite (1.68 eV bandgap). The energy scale is relative to the Fermi level. The left panel shows the secondary electron cutoff region and the right panel shows the valence band onset. Both were fitted with a linear function and the intersection with the linear background was read as the work function and the valence band onset, respectively.

Additional photoluminescence data

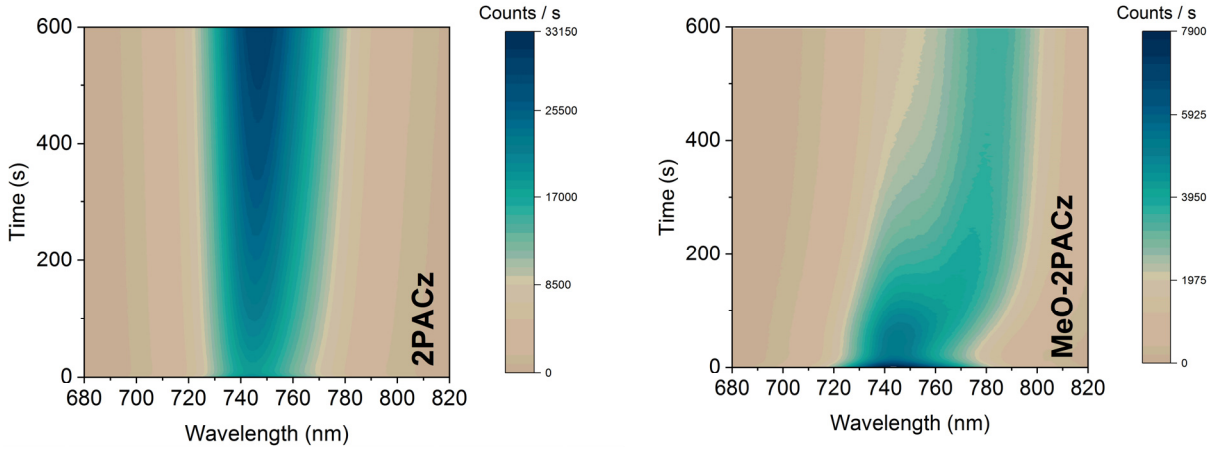

Figure S3 Photoluminescence time evolution of 1.68 eV bandgap perovskite on ITO/2PACz and ITO/MeO-2PACz, complementing Figure 1 of the main text.

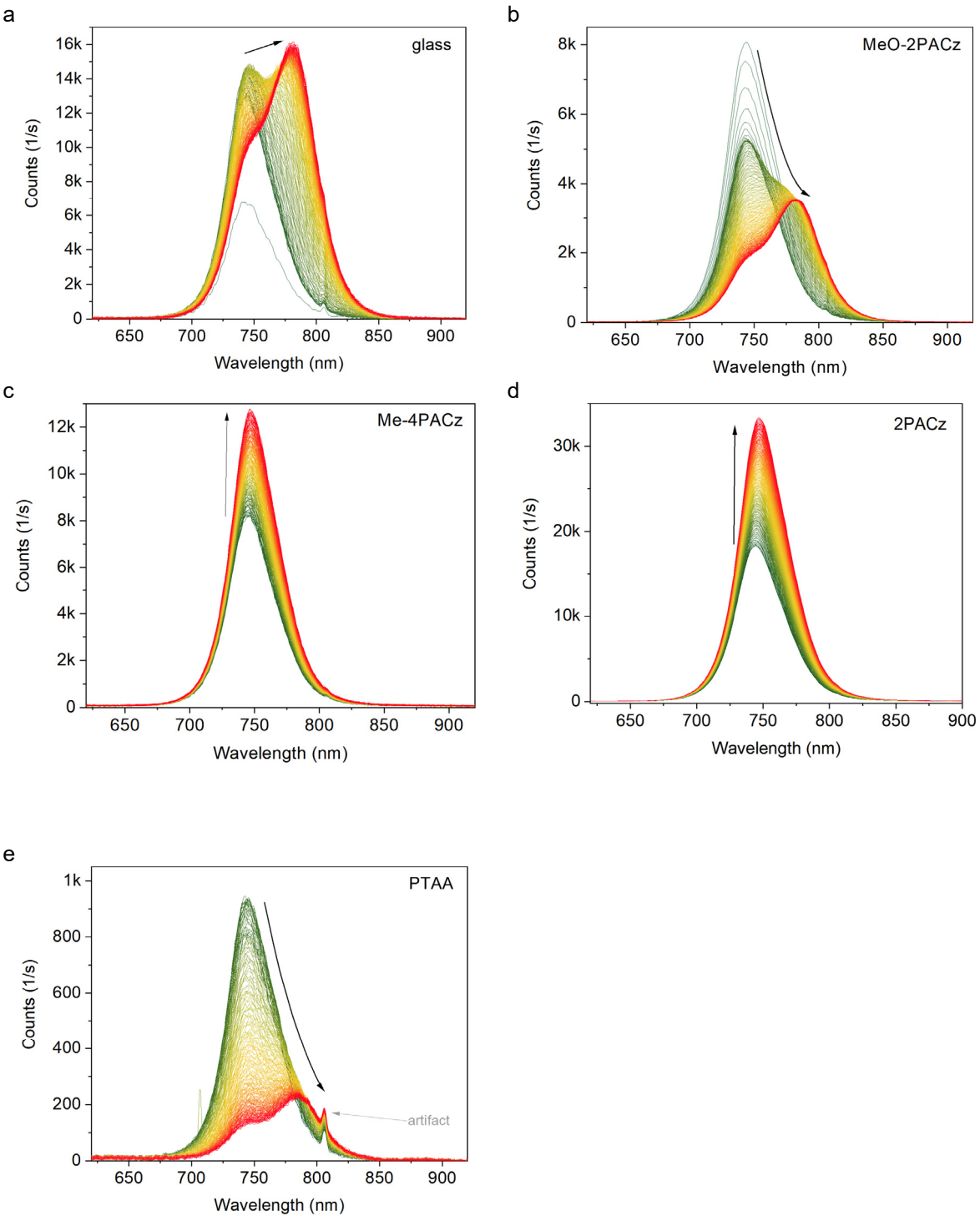
a
glass
Counts (1/s)
Wavelength (nm)
b
MeO-2PACz
Counts (1/s)
Wavelength (nm)
c
Me-4PACz
Counts (1/s)
Wavelength (nm)
d
2PACz
Counts (1/s)
Wavelength (nm)
e
PTAA
artifact
Counts (1/s)
Wavelength (nm)

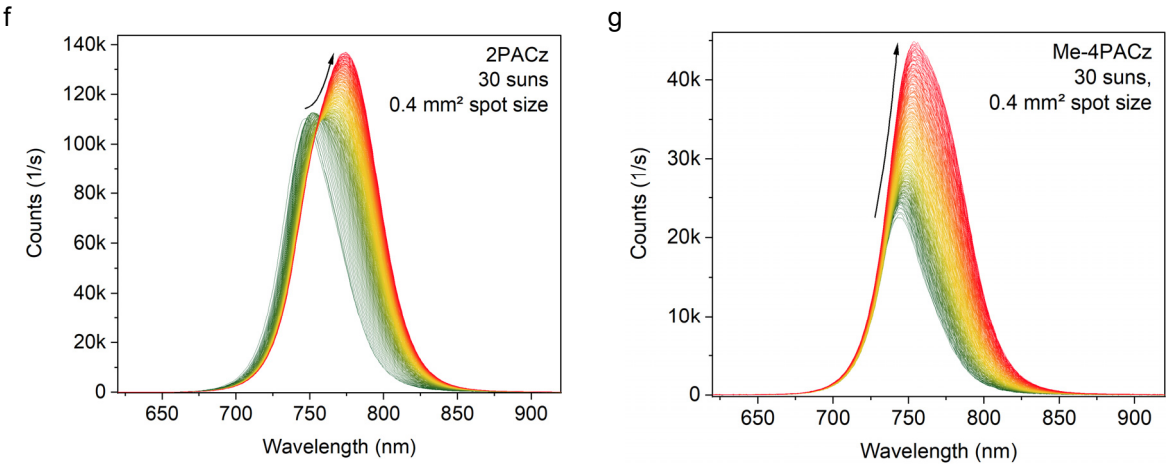

Figure S4 Photoluminescence spectra over time (10 min) under spot-illumination at 1-sun-equivalent excitation fluence. **a-e** show the spectra used for the plots Fig. 1 and Fig. S3. **f-g** show the spectra upon 30-suns fluence and smaller spot illumination.

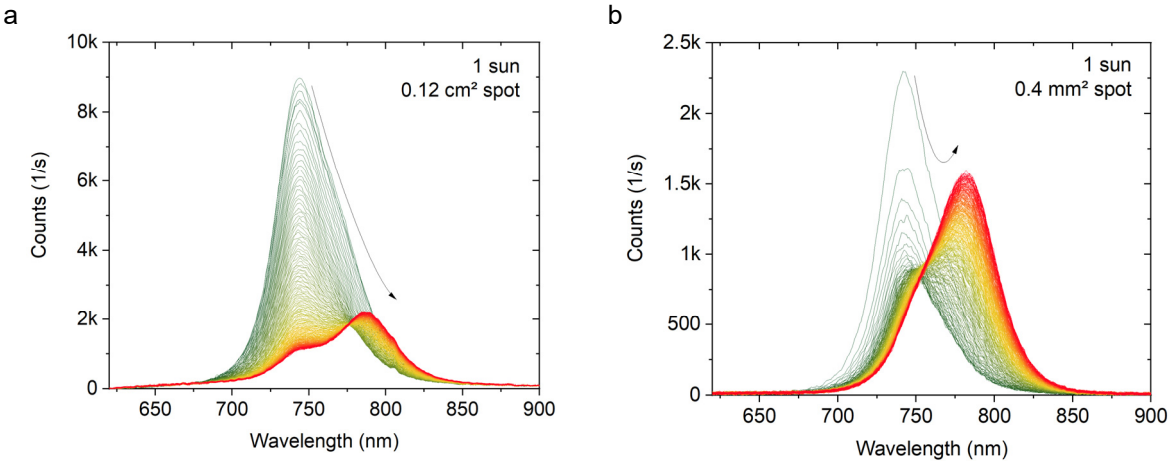

Figure S5 Photoluminescence spectra over time (10 min) of a perovskite film on ITO/MeO-2PACz. The same sample was measured with two different spot sizes: 0.12 cm² (a) and 0.4 mm² (b), each at different positions on the sample – but the excitation fluence was kept the same by placing additional ND1+ND0.4 filters into the beam for the 0.4 mm² case. This demonstrates that a smaller spot, i.e. steeper charge carrier gradient and larger spot edge-to-area ratio, causes a quicker rise of PL of segregated low-bandgap regions (*45*) (which are more emissive than Br-rich phases). The same behavior was observed for all studied substrate/HTL configurations.

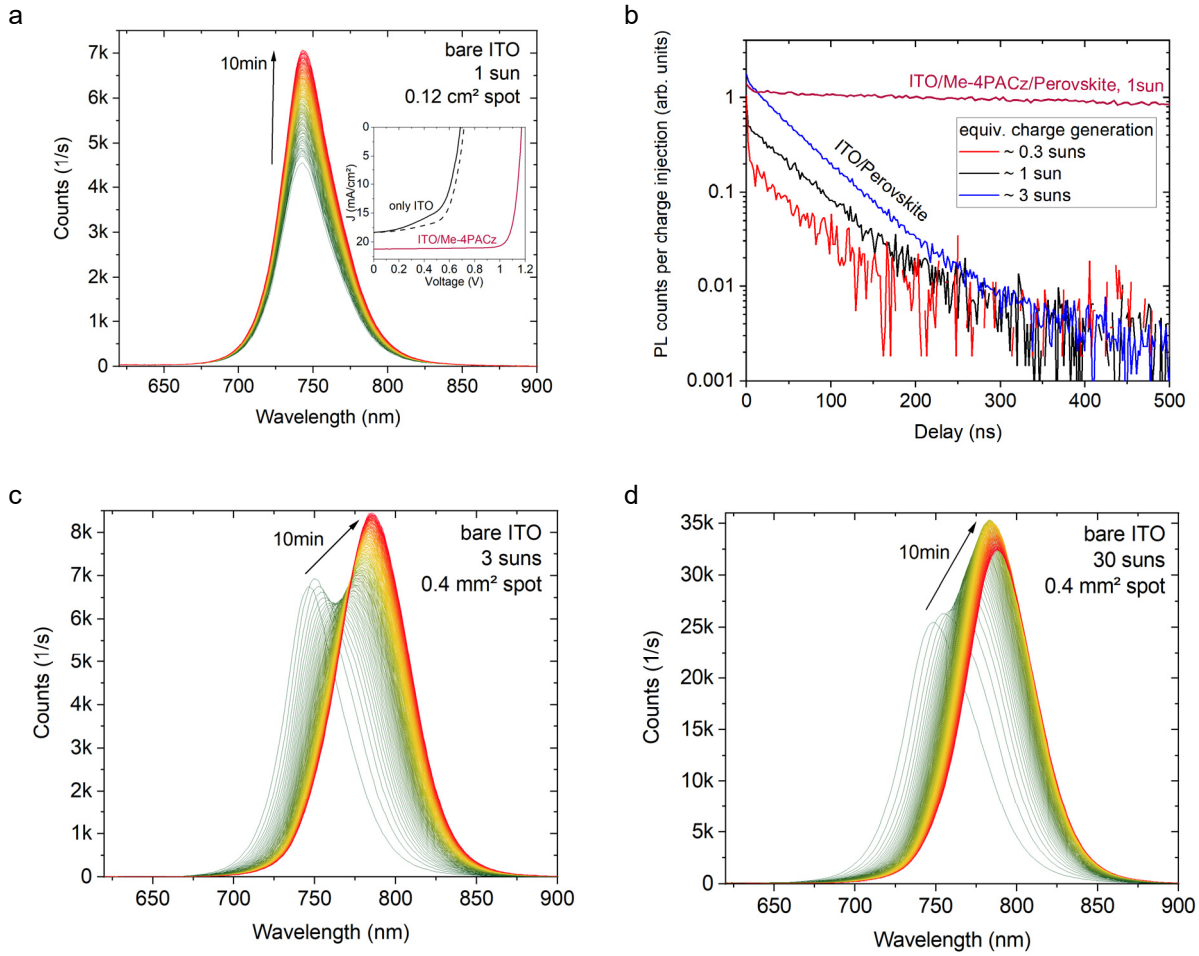

Figure S6 PL on a bare glass/ITO substrate (cleaned and O3-treated like the HTL-covered substrates). **a**, PL evolution in the same experiment as for Figure S4, showing that the conductive substrate could mitigate charge accumulation and thus suppress a double-peak formation. However, due to the ITO being not hole-selective enough, it is not suitable for efficient device operation with the herein used perovskite (inset). **b**, TrPL transients on a bare ITO/perovskite sample for three different excitation fluences. A mono-exponential fit to the 1-sun transient between 50 and 150 ns yielded a decay time of 70 ns. For comparison, the Me-4PACz transient as shown in the main text is included. **c**, Same experiment as in a, but with a smaller illumination spot size. **d**, same spot size as in c, but with 10-times higher intensity.

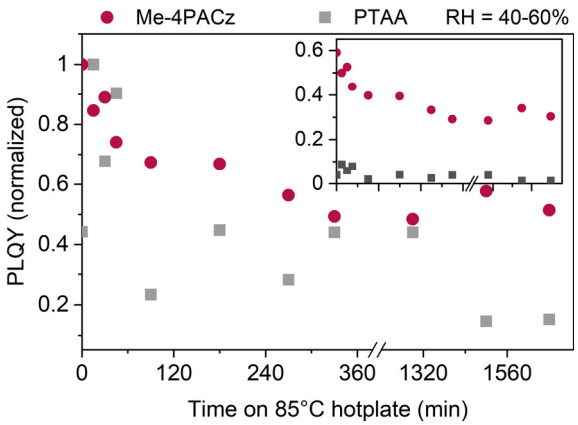

Figure S7 Photoluminescence quantum yield under 85°C in air of perovskite films on Si substrates covered with PTAA and Me-4PACz. The inset shows the non-normalized values. The samples were left on a hotplate in air (relative humidity 40-60 %) and cooled to room temperature before every PL measurement. The PLQY of the PTAA sample fell to almost background-noise level after 90 min. The PL was measured in air under 1-sun equivalent generation with spot illumination (532 nm excitation, 0.12 cm² spot size).

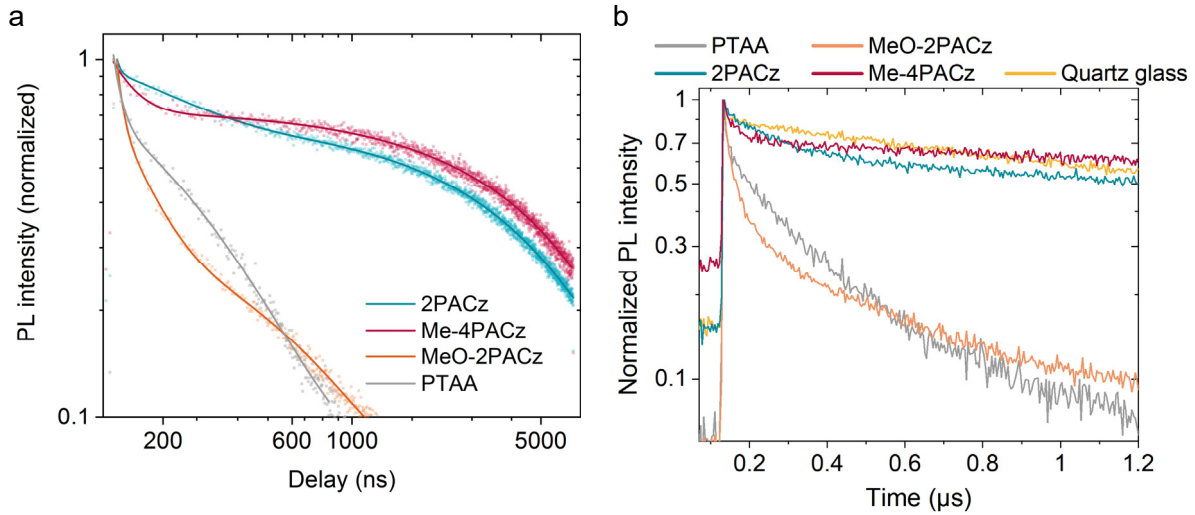

Figure S8 a, Fits to the TrPL transients shown in Figure 2 of the main text. The fits are triple-exponential functions (no physical model, arbitrary choice to fit the data to help with the differential lifetime evaluation) with offsets and are used to compute the derivative of the transients (or differential lifetimes) to avoid high noise levels arising from differentiating the raw experimental data. **b**, Zoom-in to Fig. 2A of the main text.

Supplementary text: Amount of higher order recombination estimated from the TrPL transient

The ratio of higher-order to first-order recombination from the TrPL transients was extracted by first fitting a mono-exponential function to the linear part in logarithmic scale and extrapolating it until t=0. Thus, we could identify the part of the transient corresponding to higher order processes, including radiative recombination (see Figure S10). Integrating the higher-order part of the transient and dividing it by the total area under the transient gives the ratio. Doing this for all investigated generation conditions yielded Figure 2C of the main text.

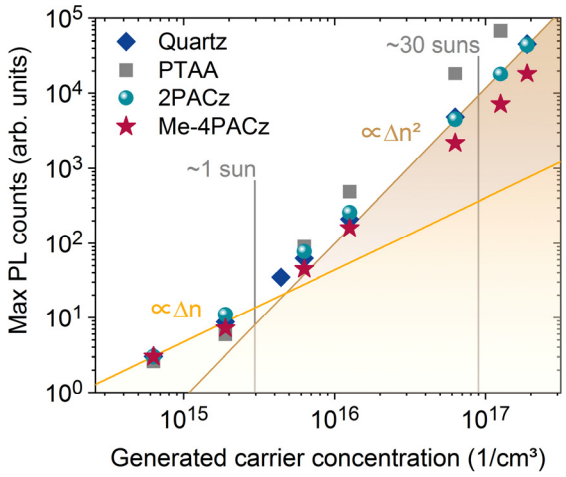

Figure S9 Charge generation regimes in TrPL. Maximum PL intensity for a series of excitation conditions. The transition from linear to quadratic dependence marks the carrier concentration above the background concentration or at which radiative recombination dominates. Although above 1-sun-equivalent carrier generation, Me-4PACz and 2PACz are in this regime, the Me-4PACz transients still showed mostly mono-exponential decay (Figure S10).

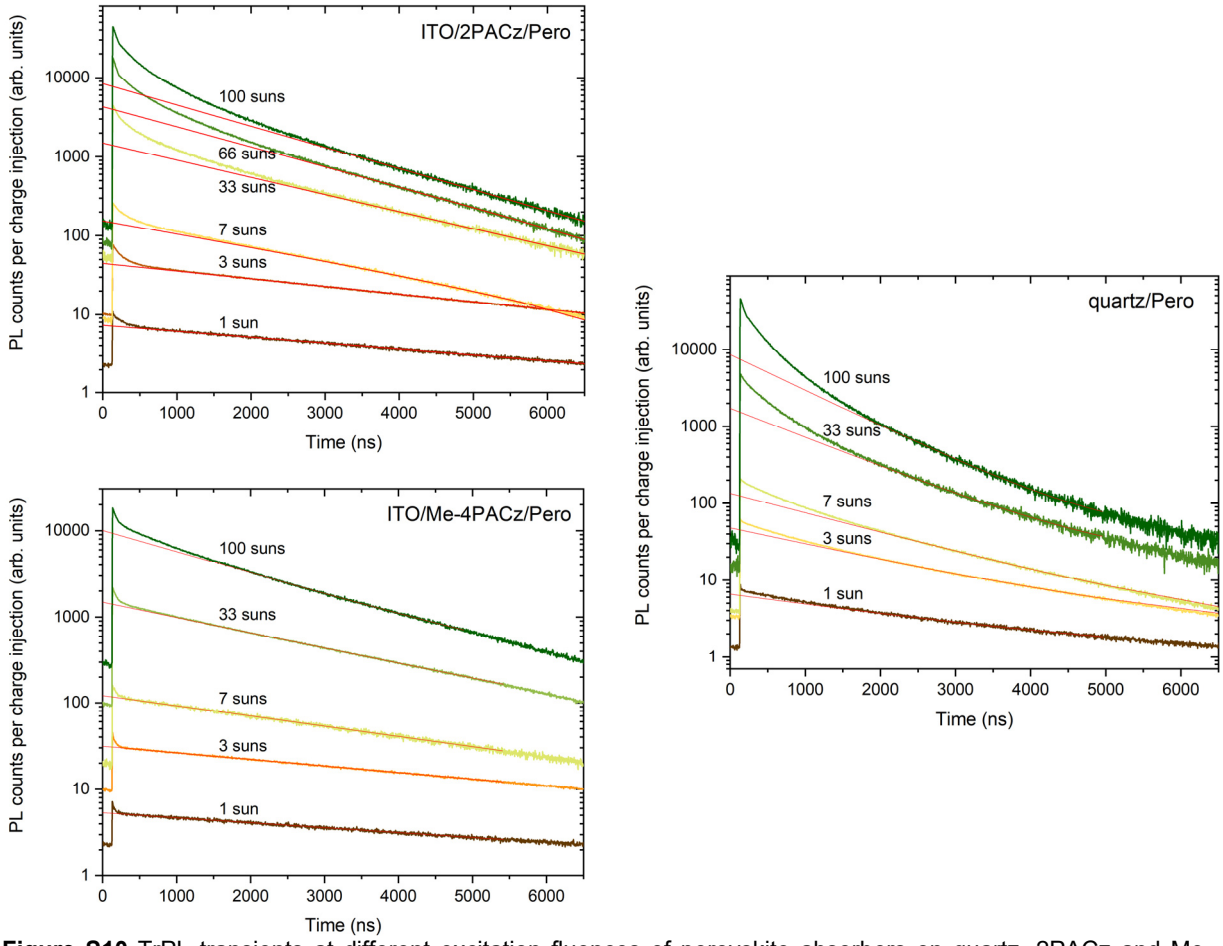

Figure S10 TrPL transients at different excitation fluences of perovskite absorbers on quartz, 2PACz and Me-4PACz. The red lines are linear fits to the mono-exponential tails of the transients. The area under the transients, the area under the linear fit and between linear fit and transient were used for the calculation of Figure 2C of the main text. Only the Me-4PACz transient shows little to no deviation from mono-exponential decay after the charge transfer process.

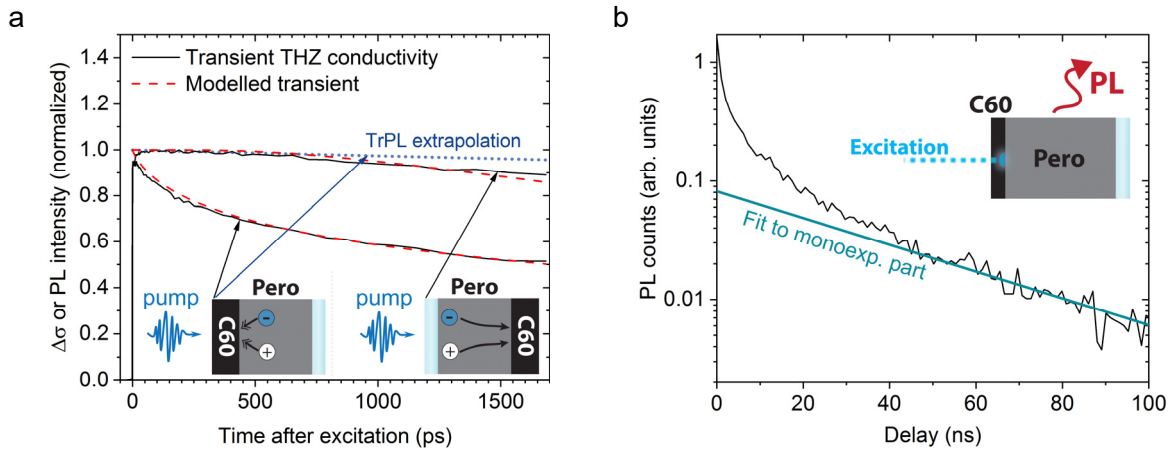

Figure S11 Speed of electron extraction into the C60 layer. a, Terahertz conductivity transients of perovskite films on quartz glass covered by the electron-selective C60 layer. Notably, the decay is considerably slower when the pump pulse hits the quartz side first. A fast decay is visible when the blue pump pulse hits the C_{60} side first since the majority of charge carriers are excited at the C_{60}-near perovskite surface and fast extraction to the C_{60} layer or non-radiative recombination occurs at/in the C_{60} layer (*53*, *75*, *76*). Assuming negligible non-radiative

recombination at the quartz interface, the comparison to the C60-side illumination hints that charge carriers diffuse through the perovskite film with a transition time of ~2.3 ns (eq-S1). In order to differentiate whether electron extraction or non-radiative recombination decays the transient, the plot shows an extrapolation of the mono-exponential part of a TrPL transient on the same sample (b), where trap-assisted recombination dominates, showing that trap-assisted non-radiative recombination would be too slow to be assigned as the underlying cause of the fast decay. Hence, it can be assigned to electron transfer into the C60, happening with a time constant of roughly 1 ns, significantly faster than hole transfer as indicated in Figure 2B (~300 ns). The C60 transients can be modeled by the ambipolar diffusion of the charge carriers to the contact layers with an ambipolar diffusion coefficient D_{am} of 0.5 cm^2/s and their extraction with an extraction velocity S of 1.6 x 10^4cm/s. To this end, the continuity equation with S as a boundary condition is used (eq-S2 & eq-S3).

$$\tau_{\text{Transition}} \approx \frac{d^2}{\pi^2 D_{am}} + \frac{d}{2S} \qquad \text{(eq-S1)}$$

$$\frac{d}{dt}\Delta n = D_{am}\frac{d^2}{dx^2}\Delta n \qquad \text{(eq-S2)}$$

$$D_{am}\frac{d}{dx}\Delta n|_{x=0} = -S\Delta n \qquad \text{(eq-S3)}$$

$$D_{am} = 2\frac{k_B T}{e}\frac{\mu_e \mu_h}{\mu_e + \mu_h} \qquad \text{(eq-S4)}$$

Equation (eq-S2) describes diffusion through the perovskite film, with d being the film thickness and D_{am} denoting the ambipolar diffusion coefficient. (eq-S3) describes recombination at the surface with a recombination velocity S. The ambipolar diffusion coefficient is connected in high injection to the individual mobilities of electrons and holes by (eq-S4). The combination of the ambipolar diffusion coefficient and the sum mobility $\mu_\Sigma = \mu_e + \mu_h$ can be used to gain to the individual mobilities of electrons and holes (*77*). For the sum mobility μ_Σ of 30 cm^2/Vs, electron and hole mobilities of 6 cm^2/Vs and 24 cm^2/Vs are derived. However, it cannot be clarified whether electrons or holes have the higher value.

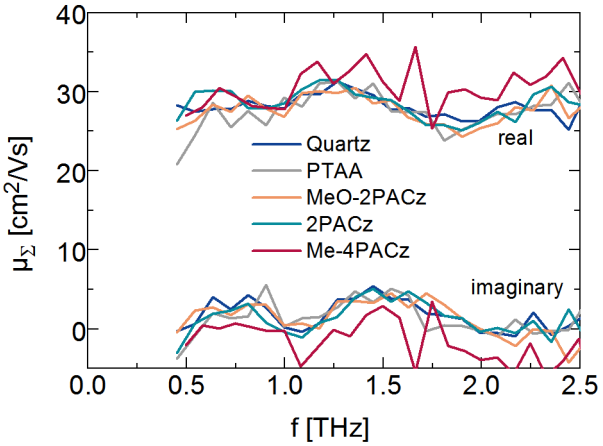

Figure S12 Terahertz (intragrain) mobilities of perovskite films deposited on the studies hole-selective layers and quartz. Growing perovskite on quartz, PTAA, MeO-2PACz, 2PACz or Me-4PACz has no effect on the terahertz mobility in the perovskite film. Such mobilities can be attributed to intra-grain transport for grain sizes above >100 nm (*78*). Therefore, we conclude that the intra-grain transport in the perovskite thin films is not altered by growing on SAMs and that the gain in fill factor is not caused by improved intra-grain transport.

X-ray diffraction study

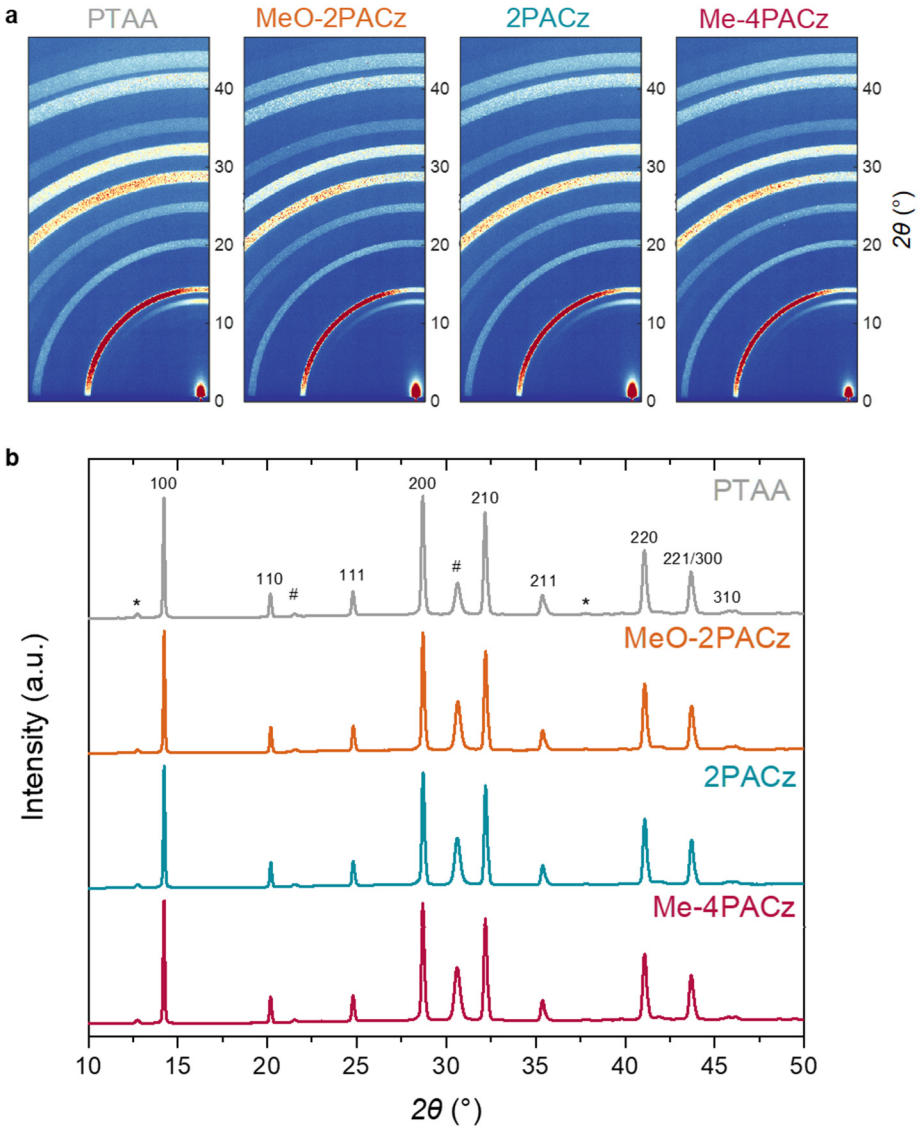

Figure S13 Absence of an effect of HTL on perovskite crystal orientation. a, Combined GIWAXS detector images at a grazing incidence angle of 0.5° and **b**, X-ray diffraction patterns generated by azimuthal integration of GIWAXS images acquired at 6.5° for perovskite grown on the four HTLs (with stack glass/ITO/HTL/Perovskite). Reflections from the pseudo-cubic perovskite are denoted by their Miller index and additional marked scattering features are reflections from ITO (#) and PbI_2 (*). Scattering data shown in part a) are uncorrected images with the scale indicating the detector rotation about the sample.

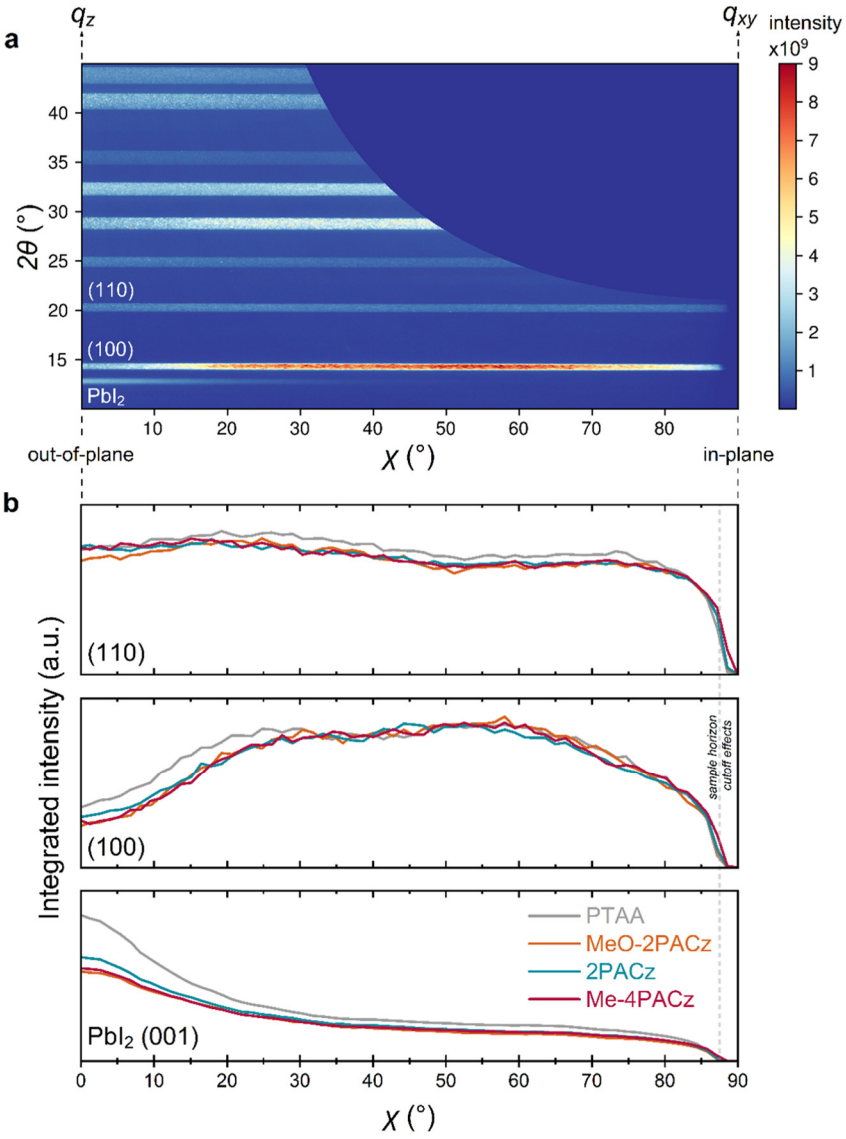

Figure S14 a) Typical remapped 2D scattering intensity data (Me-4PACz shown), plotted as χ (azimuthal scattering angle) vs. 2θ, with (100) and (110) perovskite reflections and PbI_2 marked. b) Azimuthal intensity profiles showing orientation distribution for the radially integrated (100) and (110) scattering features and PbI_2 for all samples. All data was acquired at a grazing incidence angle of 0.5°.

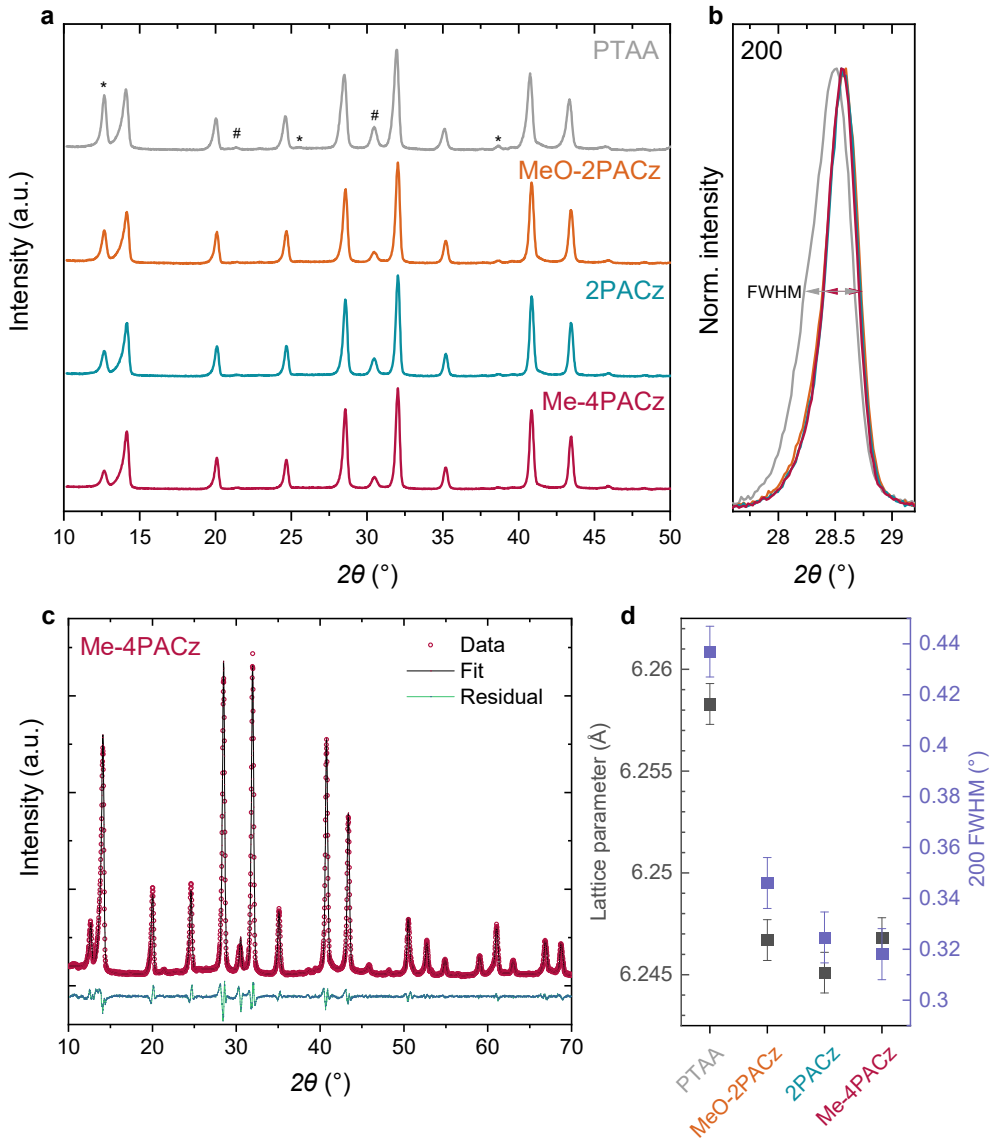

Figure S15 Grazing-incidence X-ray diffraction acquired with a rotating 1D detector (GI-XRD) at an incidence angle of 1°. Prior to measurement, samples were stored for ~2 weeks under N2 and measured in air, so may have undergone partial degradation. **a,** Diffraction patterns from the perovskite thin films with additional marked scattering features from ITO (#) and PbI_2 (*). Here the PbI2 scattering intensity is exaggerated with respect to the perovskite by the 1D detector geometry and out-of-plane texture of this phase, as observed in the GIWAXS measurements (Figure S13). **b**, Highlighted perovskite 200 reflection, showing shift and broadening of the scattering for the PTAA sample. **c**, Example Le Bail structural refinement of the Me-4PACz pattern with cubic Pm-3m perovskite, PbI2 and ITO phases present. **d**, Le Bail refined cubic perovskite lattice parameters and Pseudo-Voigt fitted full width at half maximum (FWHM) of the 200 reflections shown in part b). The differences in peak broadening between SAMs and PTAA might be over-estimated due to possible degradation of the PTAA sample (increased PbI2 peak), which was less pronounced in the 1D scans extracted from the GIWAXS data.

Additional single-junction device data

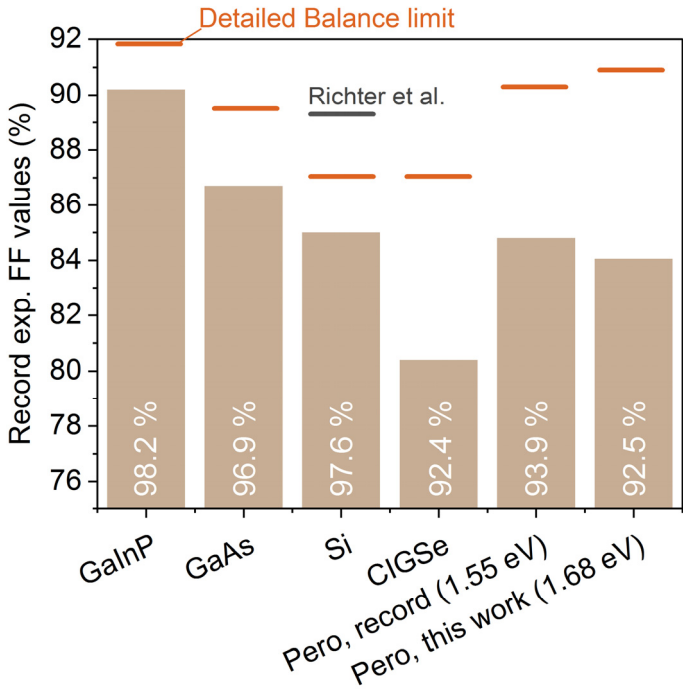

Figure S16 Comparison of experimentally achieved FF values of single-junction cells with different solar materials (*27*). The numbers inside the bars are the percentages with regard to the respective detailed balance limit. For Silicon, the large Auger recombination rate reduces the ideality factor to below 1, thus higher FFs than the detailed balance limit are possible (*69*).

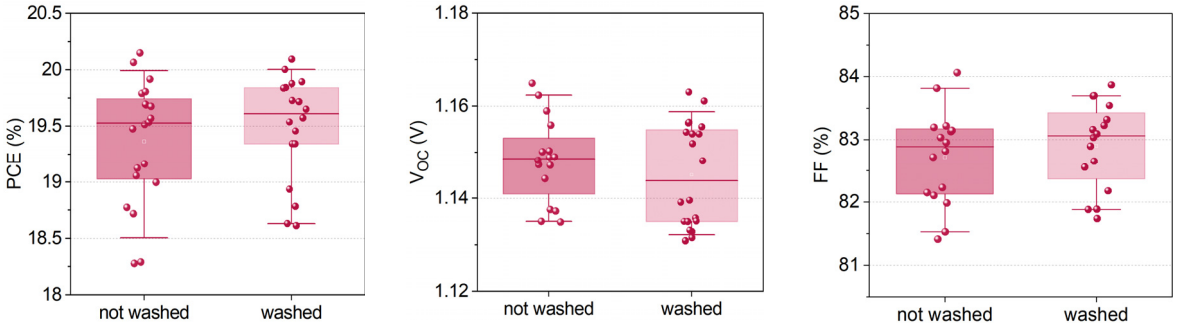

Figure S17 Influence of SAM washing on devices. Performance parameters of single-junction devices (without LiF interlayer) in which the ITO substrate was washed with EtOH after Me-4PACz spin-coating or not. The absence of a difference is characteristic for SAM-covered ITO substrates and in line with our previous findings demonstrating with 2PACz that spin-coating of a dilute solution (~0.3 mg/ml) already yielded a substrate-covering monolayer (*7*).

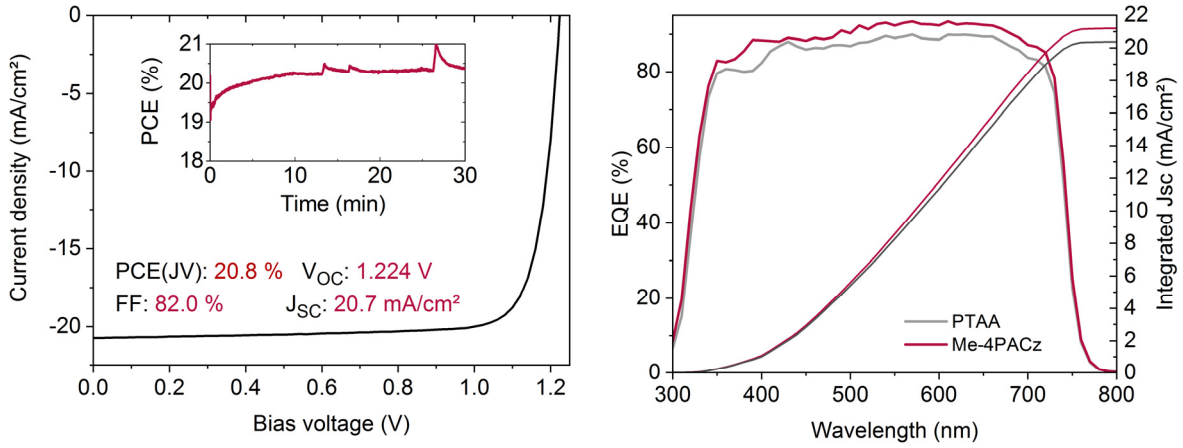

Figure S18 Left: *J-V* curve of the champion single-junction cell based on Me-4PACz as the hole-selective layer and LiF/C_{60}/SnO_2 on the electron-selective side, with the perovskite absorber bandgap being 1.68 eV. The inset shows a MPP track of that cell (spikes are from the unstable halogen lamp). Right: Representative EQE spectra of Me-4PACz and PTAA cells.

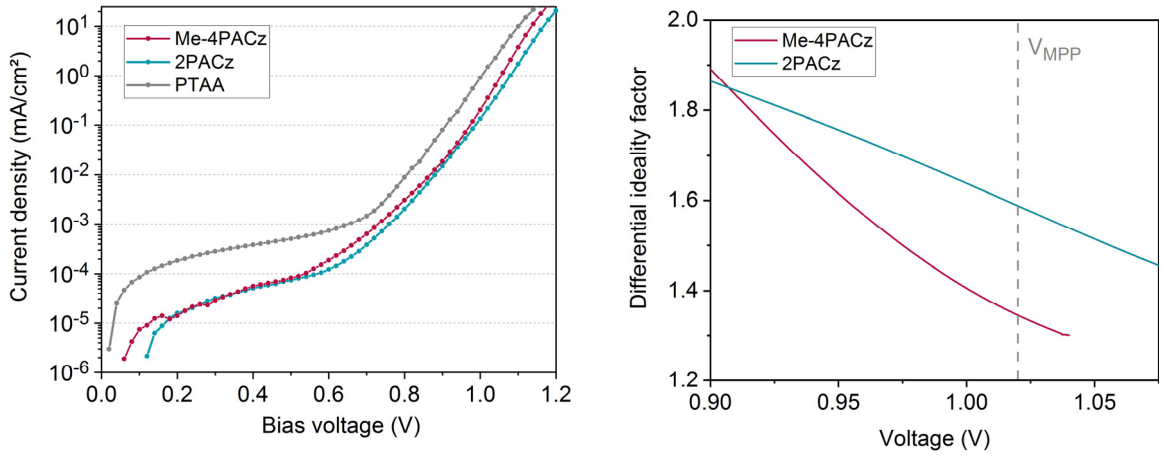

Figure S19 Difference in ideality factor from dark-*J-V* curves. Representative dark-*J-V* curves (left) of single-junction cells (no LiF) and ideality factor extracted from a fit on the data, of which the inverse of the derivative of the logarithm, divided by the thermal energy (25.8 meV) is plotted on the right. In line with the previous findings, the lower ideality factor with Me-4PACz is also visible in the dark curve as a steeper slope of the dark current. However, the suns-Voc method as shown in the main text is the more accurate way of determining the value of the ideality factor.

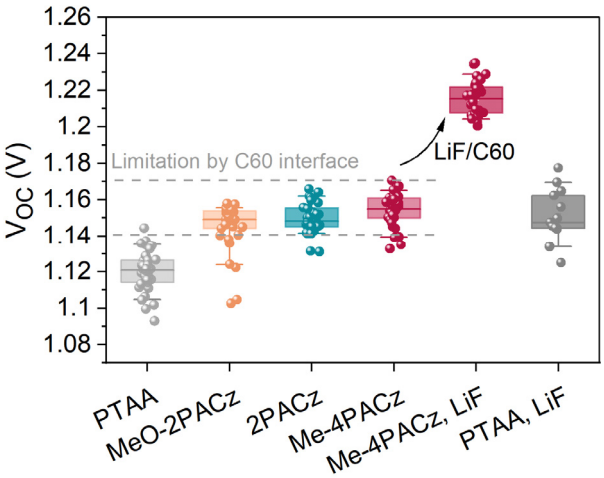

Figure S20 Open-circuit voltages of perovskite solar cells (single-junctions) with the studied hole-selective layers, with and without LiF interlayer between the perovskite and C60 layer. The full V_{OC} potential is only visible upon suppression of non-radiative recombination at the C60 interface, which we here demonstrated by an LiF interlayer. PTAA-based devices are limited by the PTAA interface to ~1.18 V (fitting to the QFLS of bare perovskite on PTAA).

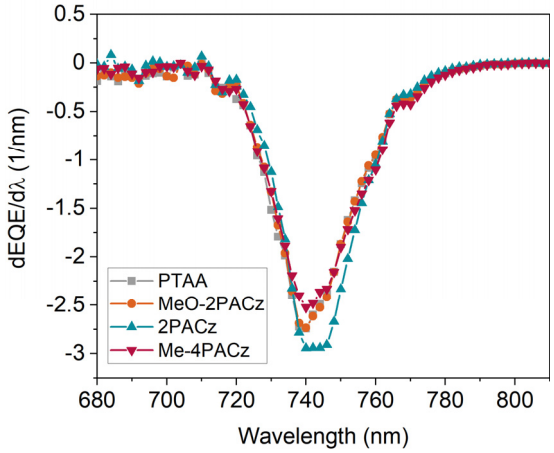

Figure S21 Derivative of the external quantum efficiency of single-junction PSCs based on the compared hole-selective layers. The derivative, or inflection point (*23*), lies at 740 nm, the same wavelength as the PL peaks of pristine perovskite films.

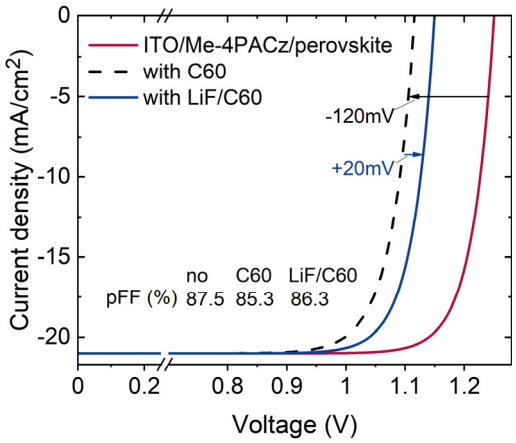

Figure S22 Addition to Figure 3D of the main text, showing the influence of LiF between perovskite and C60 on the intensity-dependent PL measurements for determination of the pFF values. The passivation effect of LiF on the perovskite surface is only minor (20 meV gain in QFLS), hinting that the large gain in V_{OC} by introduction of the LiF interlayer (see Figure S20) cannot be explained by surface passivation alone. We speculate that it might again be connected to differences in built-in potential across the full device and a hole-blocking nature of LiF (*79*).

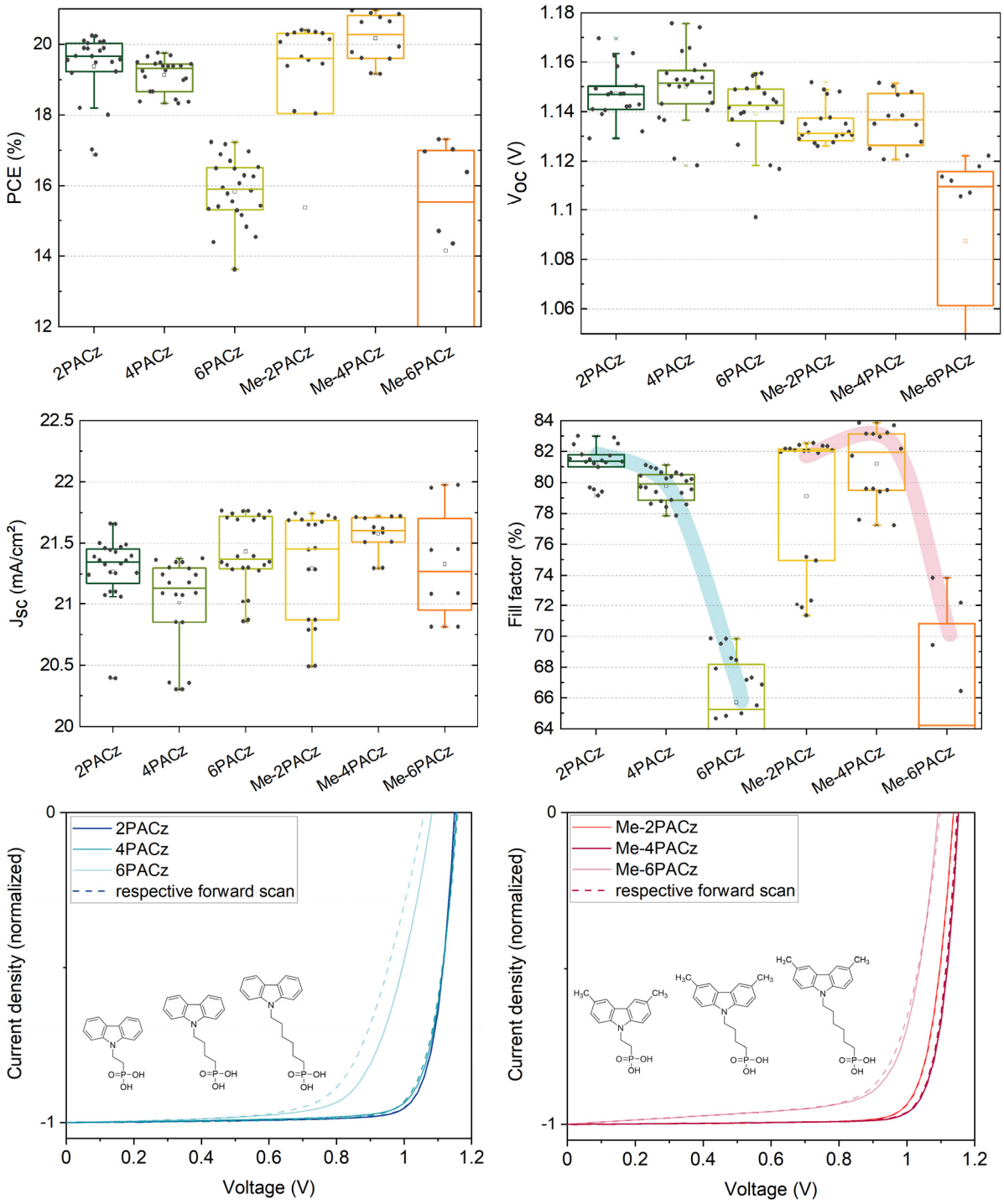

Figure S23 Influence of aliphatic chain length with bare and methyl-substituted carbazole SAMs on perovskite single-junction performance (no LiF). Mainly the FF was affected (J_{SC} values are likely slightly over-estimated, compared to EQE in **Figure S18**). The bottom panels show normalized *J-V* curves of the best-FF devices of each variation. For larger lengths of the isolating, non-conjugated SAM part (aliphatic chains containing 4 and 6 hydrocarbon segments), the fill factor decreases due to higher series resistance and ideality factor. The hampered hole extraction lead to current-voltage hysteresis in n=6 devices. For the methyl-substituted SAM, the optimum FF was reached with a chain length of n=4, while for nPACz, the highest FF was enabled by n=2. Possibly, self-assembly of the bare carbazole SAM nPACz is stabilized by pi-pi interactions of the carbazole fragments, whereas for the Me-substituted SAM an interplay between steric repulsion between the methyl fragments and van der Waals interaction between the hydrocarbon chains controls the SAM ordering and thus interface quality (*80–83*). This might cause the different optimum aliphatic chain lengths for the two different SAM types. Further investigations are needed to clarify the exact role of molecular orientation and effective dipole moment.

a

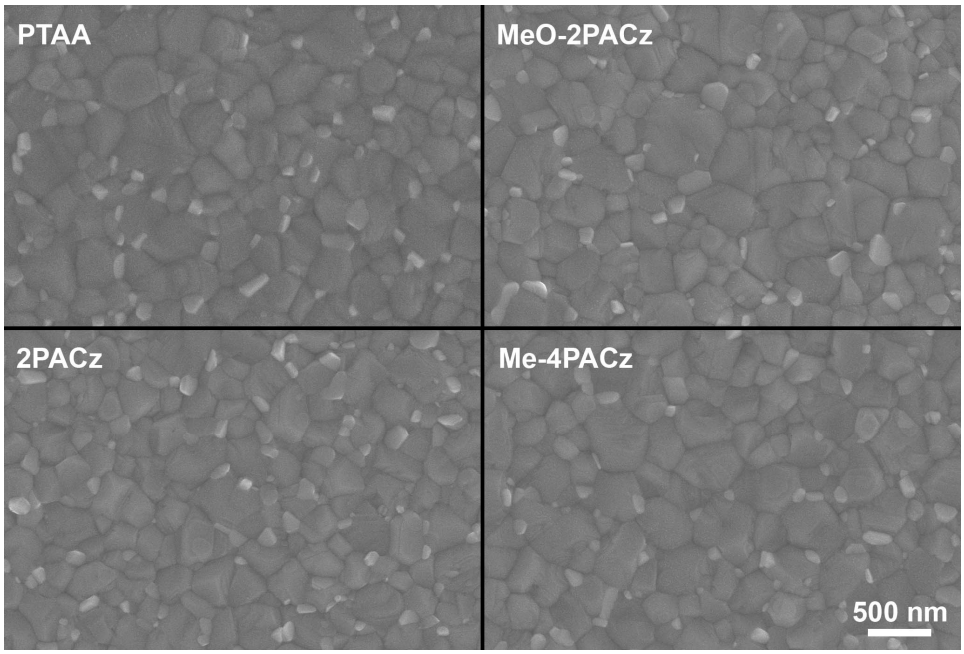

b

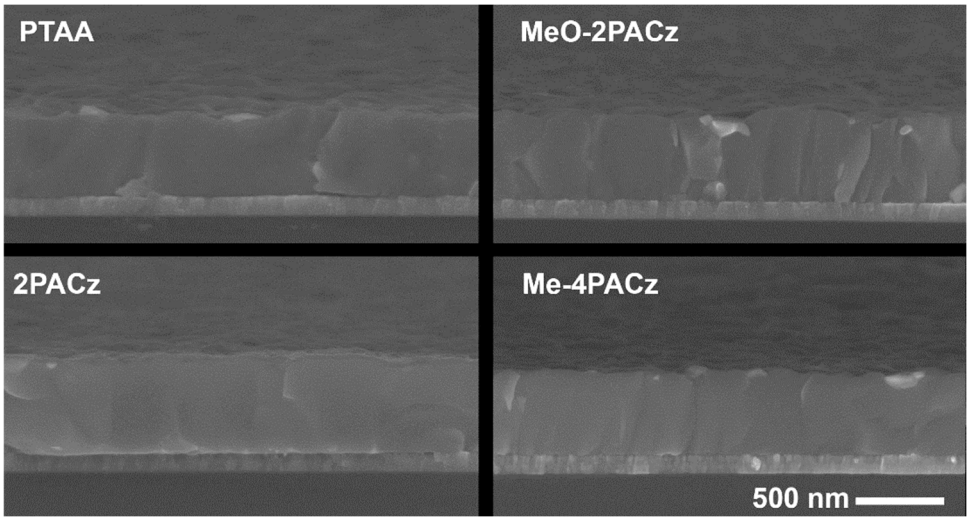

Figure S24 Scanning electron microscopy images of perovskite films on the studied hole-selective layers. **a**, top view. **b**, cross-section.

Additional data on tandem devices

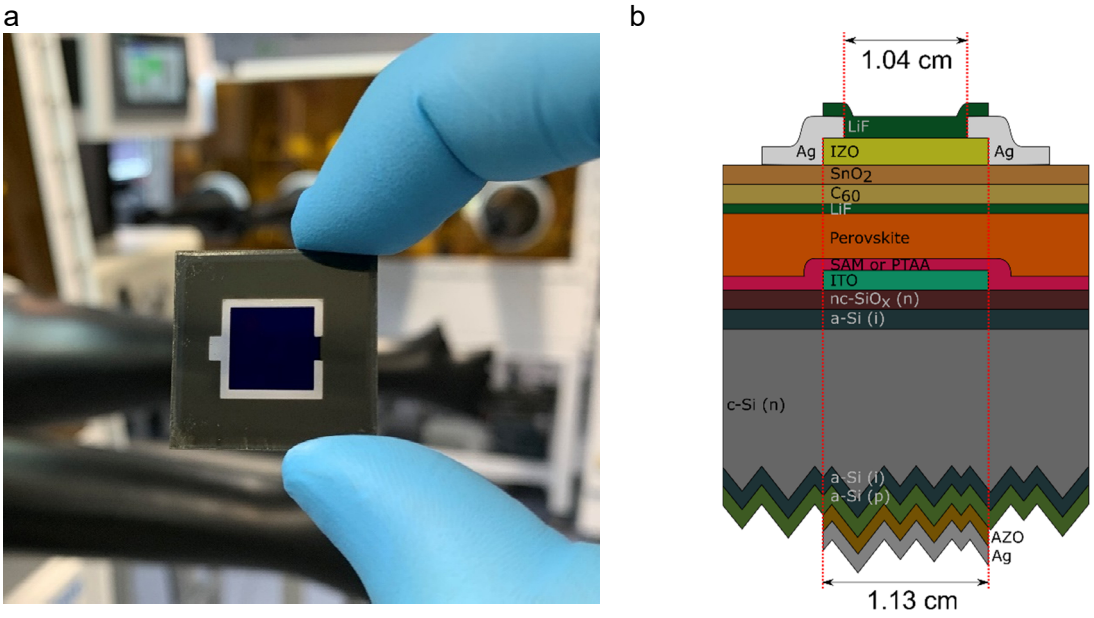

Figure S25 a) Photograph of a monolithic perovskite/silicon tandem solar cell. b) Layout of the tandem solar cells used in this work.

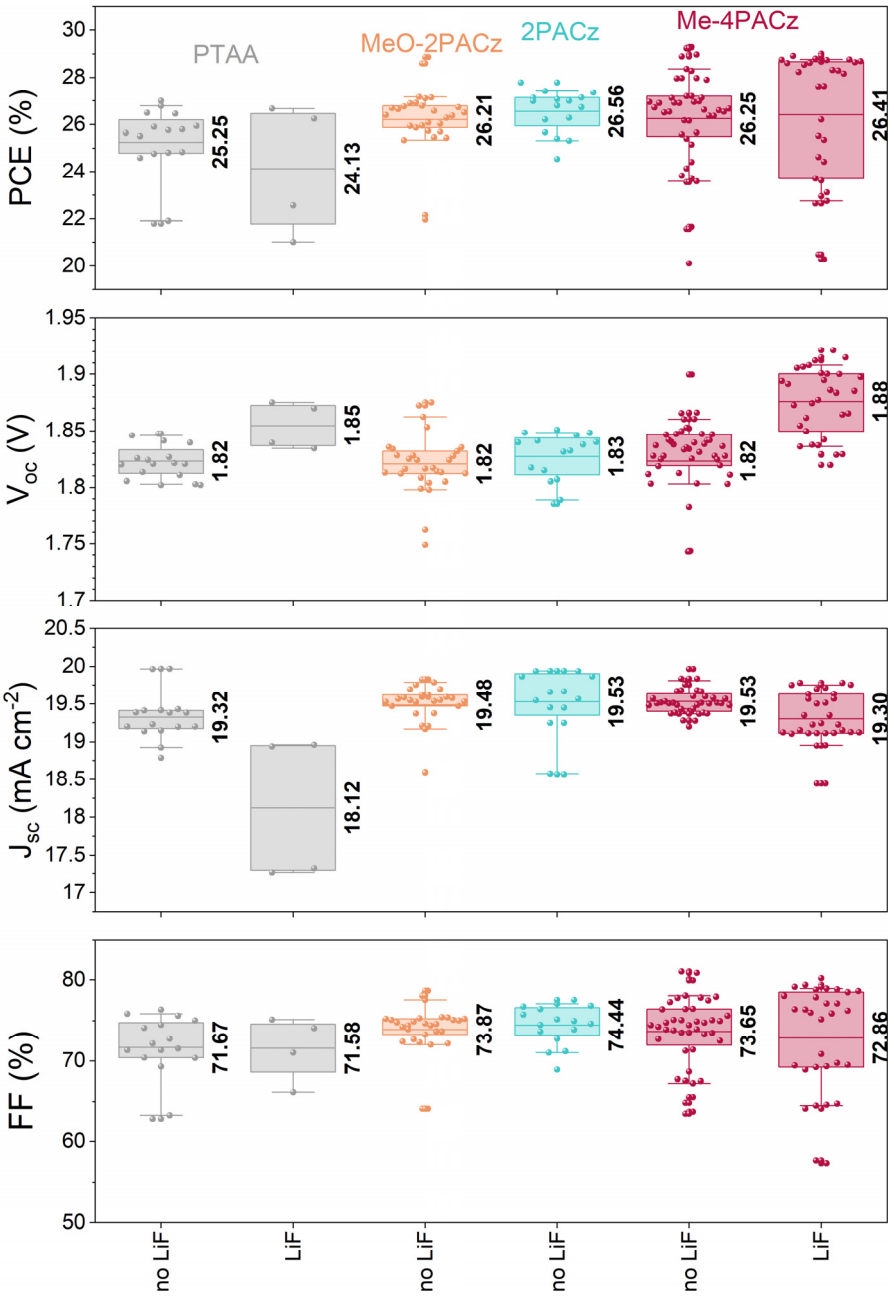

Figure S26 Tandem cell performance parameters from *J-V* curves under 1-sun equivalent illumination, comparing the different hole-selective layers with and without a 1 nm LiF interlayer between C_{60} and perovskite. The arithmetic mean is given for each parameter and HTL.

Table S1 Subcell photogenerated current densities (J_{ph}) values of the tandem cells with Me-4PACz presented in Figure S26 showing that for almost all cells, the perovskite top cell was limiting. This table includes cells with and without LiF interlayer where EQE data was available.

Silicon J_{ph} (mA/cm²)	Perovskite J_{ph} (mA/cm²)	Mismatch: $J_{ph,Silicon}$-$J_{ph,Perovskite}$ (mA/cm²)
19.87	19.42	0.45
19.63	19.39	0.24
20.18	19.58	0.6
19.94	19.51	0.43
20.2	19.51	0.69
20.22	19.52	0.7
19.89	19.05	0.84
20.18	19.41	0.77
20.73	18.76	1.97
20.6	18.7	1.9
20.47	18.98	1.49
19.94	19.24	0.7
19.56	19.31	0.25
19.38	19.41	-0.03
19.6	19.63	-0.03

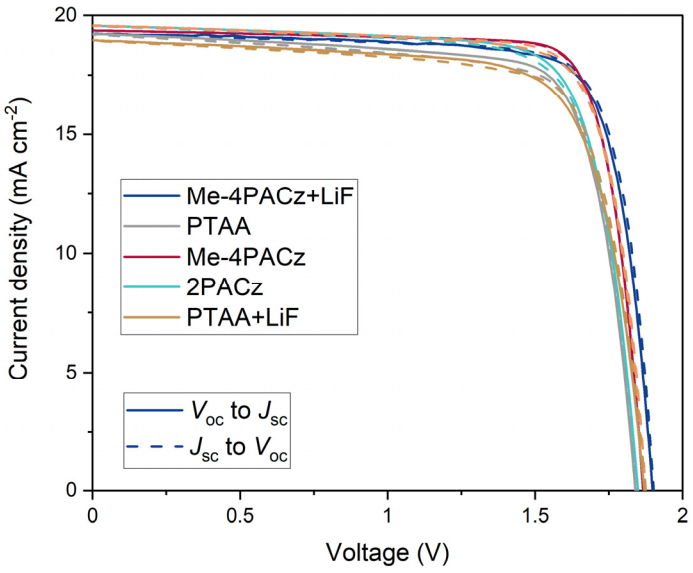

Figure S27 *J-V* curves of the champion tandem solar cells with various HTLs. The parameters are given in Table S2.

Table S2 Photovoltaic parameters of the champion cells using PTAA, MeO-2PACz, 2PACz and Me-4PACz as HTL. Additionally, we distinguished between cells with and without LiF interlayer.

Configuration	Direction	J_{sc} in mA cm^{-2}	V_{oc} in V	FF in %	PCE in %
PTAA	J_{sc} to V_{oc}	19.19	1.85	75.6	26.79
PTAA	V_{oc} to J_{sc}	19.23	1.84	76.3	27.00
PTAA - LiF	J_{sc} to V_{oc}	18.94	1.88	75.10	26.67
PTAA - LiF	V_{oc} to J_{sc}	18.96	1.87	74.04	26.25
MeO-2PACz	J_{sc} to V_{oc}	19.57	1.88	78.07	28.60
MeO-2PACz	V_{oc} to J_{sc}	19.58	1.88	78.66	28.88
2PACz	J_{sc} to V_{oc}	19.55	1.85	75.73	27.36
2PACz	V_{oc} to J_{sc}	19.57	1.85	76.83	27.79
Me-4PACz	J_{sc} to V_{oc}	19.37	1.87	80.89	29.23
Me-4PACz	V_{oc} to J_{sc}	19.37	1.87	81.06	29.29
Me-4PACz – LiF (certified values)	J_{sc} to V_{oc}	19.23	1.90	79.40	29.00
Me-4PACz – LiF (certified values)	V_{oc} to J_{sc}	19.24	1.89	78.85	28.75

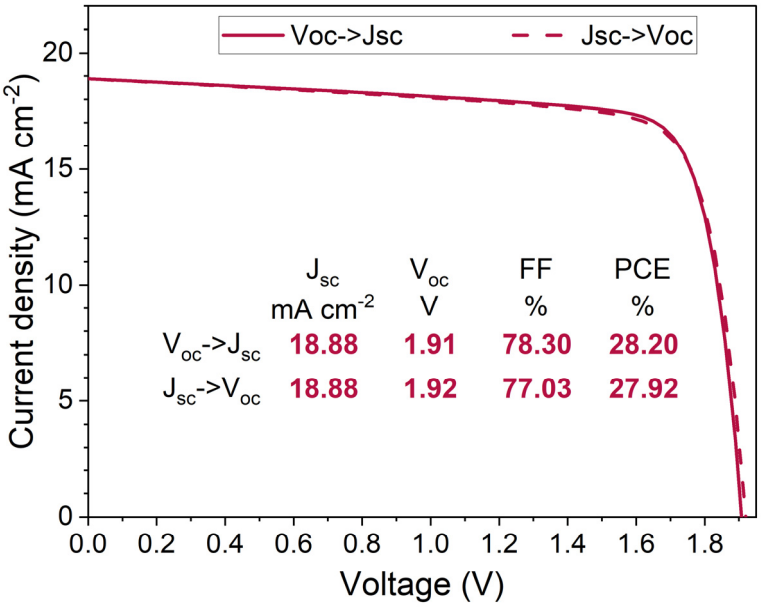

Figure S28 *J-V* of the monolithic perovskite silicon tandem solar cell with the new HTL Me-4PACz and LiF interlayer, showing a record V_{OC} of 1.92 eV, featuring a 1.68 eV bandgap perovskite absorber.

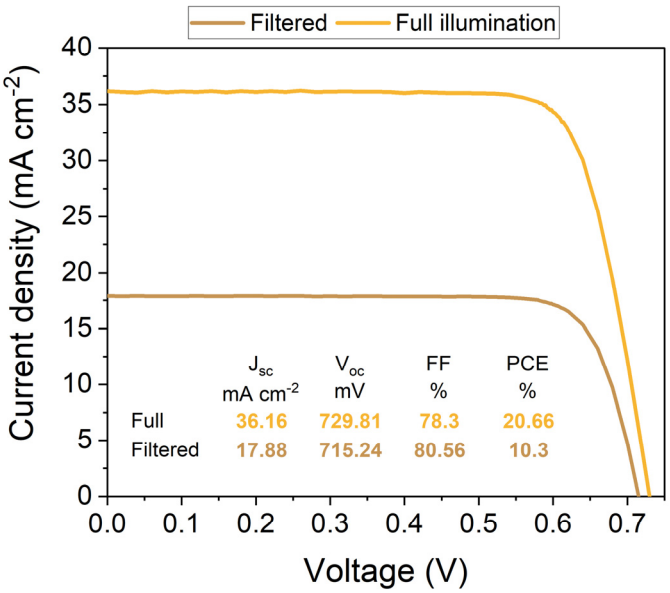

Figure S29 *J-V* curves of a representative silicon single-junction reference cell measured under full 1-sun-equivalent illumination and under filtered light, roughly as transmitted by a perovskite cell. As described in the methods, instead of 95 nm nc-SiO_x:H and 20 nm ITO on the front side (which becomes the recombination layer in a tandem solar cell), this reference cell comprises 20 nm nc-SiO_x:H and 70 nm ITO. To extract the charges from the 2 x 2 cm^2 active area, a screen-printed Ag grid is used.

Fraunhofer ISE

CalLab PV Cells

10003155HMI0919

Die Rückführung der Spektralmessung auf SI-Einheiten erfolgte über den Vergleich mit einer Standardlampe.
The traceability of the measurement of the spectral distribution to SI-Units is achieved using a standard lamp for the calibration of the spectroradiometer.

Identitäts-Nr. / *Identity-Nr.* :	Kalibrierschein-Nr./ *Certificate-Nr.* :	Rückführung/ *Traceability* :
BN-9101-451	40002-14-PTB	PTB

3. Messbedingungen
Measurement conditions

Standardtestbedingungen (STC) / *Standard Testing Conditions (STC)* :

Absolute Bestrahlungsstärke / *Total irradiance* :	1000	W/m²
Temperatur des Messobjektes / *Temperature of the DUT* :	25	°C
Spektrale Bestrahlungsstärke / *Spectral irradiance distribution* :	AM1.5G Ed.2 (2008)	

Die Messung der IV-Kennlinie (Strom-Spannungs-Kennlinie) des Messobjektes erfolgt mit Hilfe eines Vierquadranten-Netzteiles und eines Kalibrierwiderstandes.
The measurement of the IV-curve is performed with a 4-quadrant power amplifier and a calibration resistor.

4. Messergebnis
Measurement results

Fläche / *Area* (da)[1]: = (1.0599 ± 0.0066) cm²

[1] : *(t) = total area, (ap) = aperture area, (da) = designated illumination area /7/*

Kennlinienparameter des Messobjektes unter Standardtestbedingungen (STC) / *IV-curve parameter under Standard Testing Conditions (STC)* :

		Vorwärtsrichtung / *forwards scan direction*	Rückwärtsrichtung / *reverse scan direction*	steady state MPP
V_{oc}	=	(1900.3 ± 12.7) mV	(1894.6 ± 12.7) mV	
I_{sc} (Ed.2 - 2008)	=	(20.38 ± 0.39) mA	(20.40 ± 0.39) mA	
I_{MPP}	=	18.83 mA	18.75 mA	(19.11 ± 0.40) mA
V_{MPP}	=	1633.0 mV	1625.3 mV	(1616.6 ± 36.6) mV
P_{MPP}	=	30.74 mW	30.47 mW	(30.90 ± 0.85) mW
FF	=	79.40 %	78.85 %	
η	=			(29.15 ± 0.82) %

Fraunhofer ISE

CalLab PV Cells

10003155HMI0919

Angegeben ist jeweils die erweiterte Messunsicherheit, die sich aus der Standardmessunsicherheit durch Multiplikation mit dem Faktor *k*=2 ergibt. Sie wurde gemäß dem "Guide to the expression of Uncertainty in Measurement" ermittelt. Sie entspricht bei einer Normalverteilung der Abweichungen vom Messwert einer Überdeckungswahrscheinlichkeit von 95%.
The expanded measurement uncertainty resulting from the standard measurement uncertainty multiplied with a factor k=2 is specified. The calculation was carried out according to the "Guide to the expression of Uncertainty in Measurement". The value corresponds to a Gaussian distribution denoting the deviations of the measurement value within a probability of 95%.

5. Zusatzinformationen

Additional information

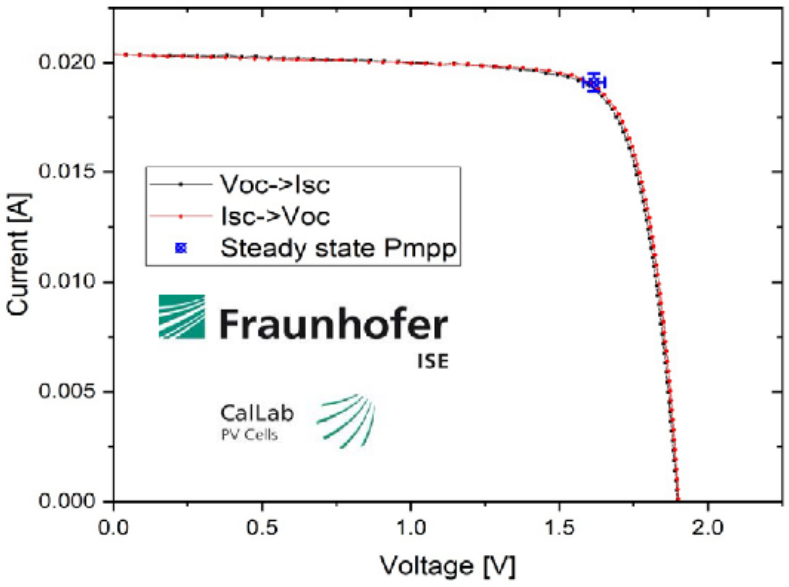

Fraunhofer ISE

CalLab PV Cells

10003155HMI0919

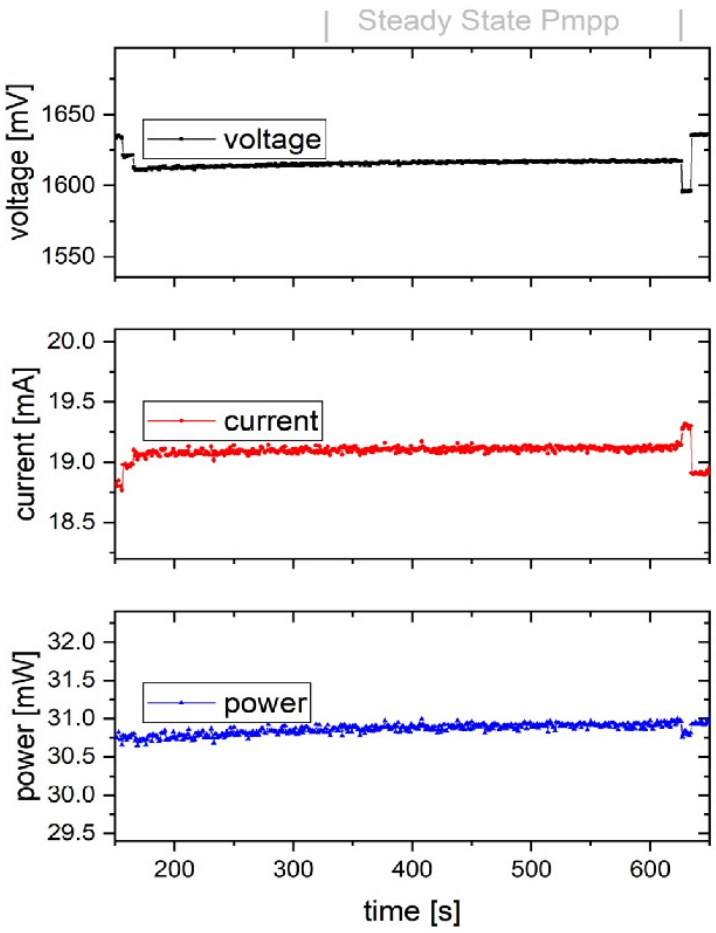

Figure S30: Certification report from Fraunhofer ISE for a monolithic perovskite silicon tandem solar cell with Me-4PACz as HTL and LiF interlayer.

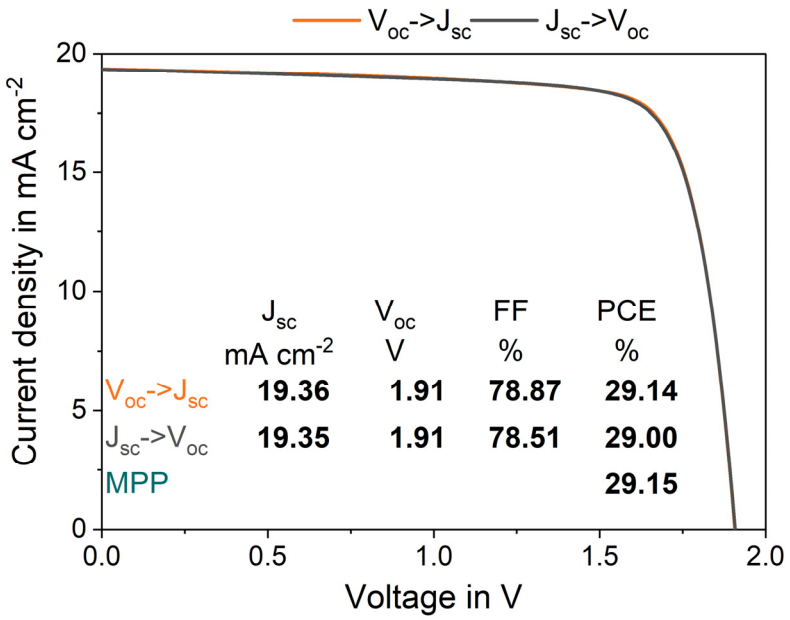

Figure S31 *J-V* curve under 1-sun-equivalent illumination of the certified Me-4PACz+LiF tandem solar cell, measured in-house, yielding almost the same results as the certified measurement shown in the main text.

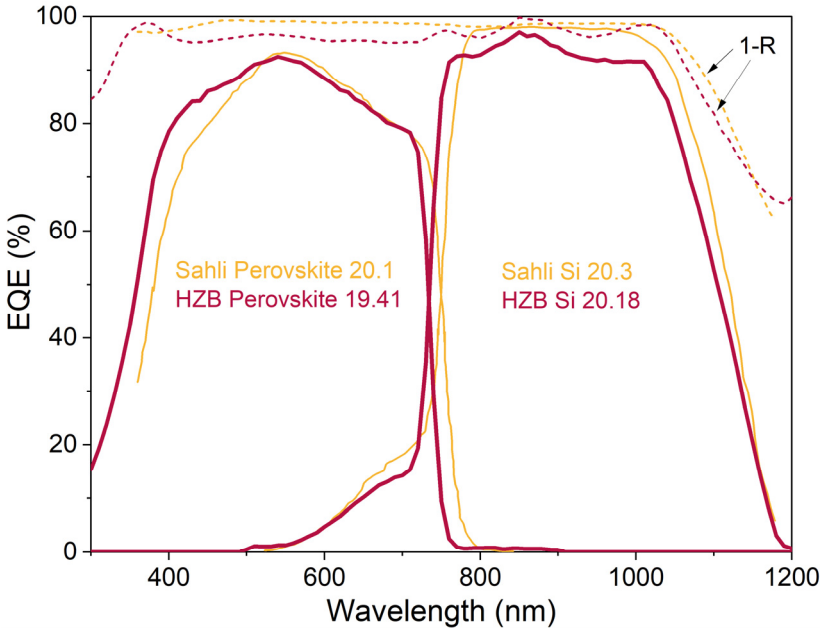

Figure S32 External quantum efficiencies of the certified champion device in this publication (measured in-house) and of the publication from Sahli *et al.* (*62*). The latter shows that the textured front side can increase the photogenerated current density by reduced reflection. This led to a cumulative current density of 40.4 mA cm^{-2}, whereas the flat front side of this publication led to 39.59 mA cm^{-2}. Additionally, the dashed lines show the reflection (1-R) of the respective cell.

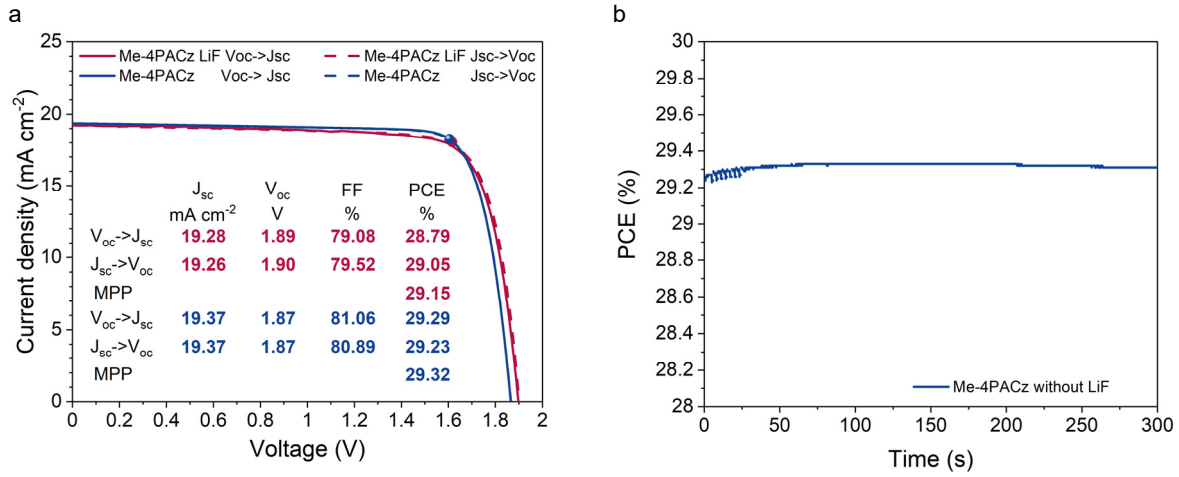

Figure S33 a) Comparison of champion monolithic perovskite silicon tandem solar cells (Me-4PACz) with and without LiF interlayer. The *J-V* of the cell with LiF interlayer was certified at Fraunhofer ISE. The higher V_{oc} but lower FF for cells with LiF interlayer is clearly visible. b) 5 minutes MPP-track of the champion cell withouf LiF interlayer with an average value of 29.32%

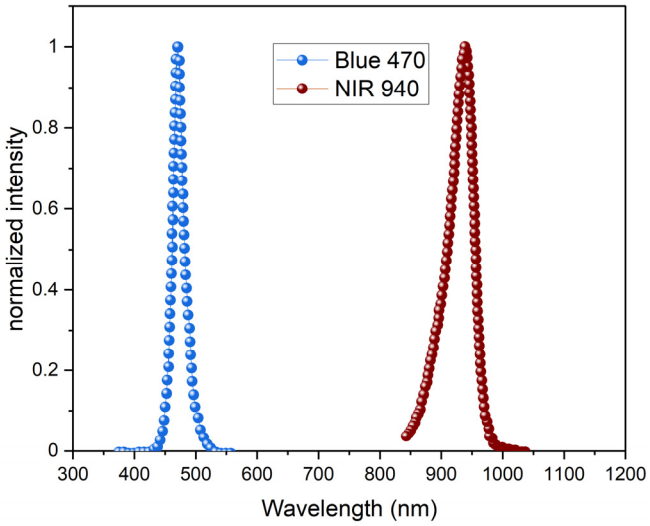

Figure S34 Normalized spectra of the LEDs used for long term MPP-tracks of tandem solar cells. The spectra are given by the manufacturer. For the MPP-tracks, the intensities were adjusted such that in the subcells the same charge carrier densities are generated as derived from the respective EQE measurements.

Supplementary text: Light sources for long term stability tests of tandem solar cells

Typically, low-class lamp spectra provide less NIR light and thus the photogenerated current density of the silicon bottom cell will be reduced, leading potentially to a silicon-limited tandem solar cell. Silicon-limited tandem solar cells would show higher stability as the degradation of the perovskite subcell barely affects the performance of the tandem until a certain threshold is reached. Therefore, the subcell limitation will also affect operational stability, depending on the degree of mismatch and type of degradation. A detailed analysis of the influence of the subcell properties on the tandem solar cell is given by Boccard and Ballif (*84*).

Table S3 Photogenerated current of tandem solar cells. The photogenerated current densities were extracted by measuring the short circuit current under one or the other limitation. We assume that the short circuit current is equal to the photogenerated current of the limiting subcell. The limitation is artificially created by enhancing the sun simulator intensity in the spectral region that only the non-limiting cell absorbs (i.e., increased NIR intensity for perovskite limitation and increased blue intensity for silicon limitation).

	$I_{ph,Pero}$ (mA)	$I_{ph,Si}$ (mA)
PTAA LiF	18.88	20.05
Me-4PACz LiF	19.57	19.86
2PACz	19.04	19.5
Me-4PACz	20.10	20.06

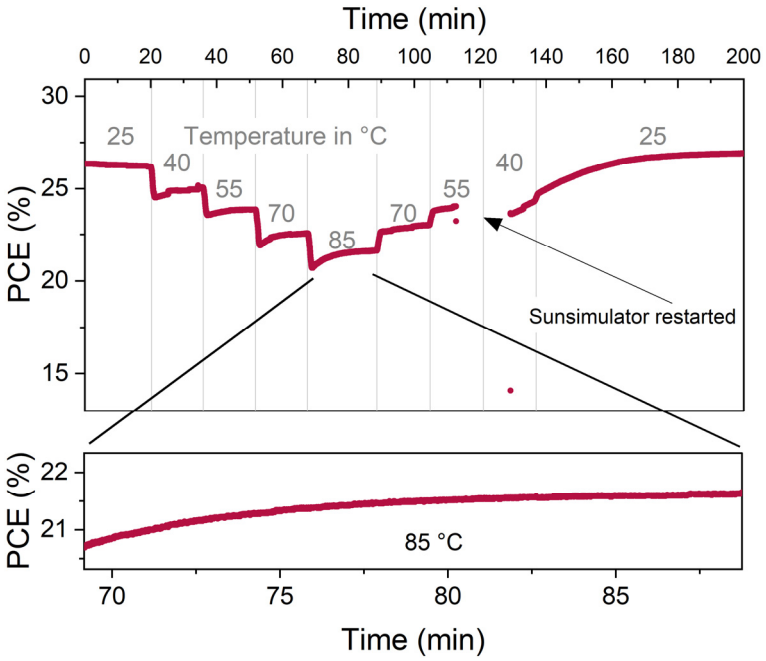

Figure S35 MPP track of a tandem solar cell with Me-4PACz as HTL (without LiF interlayer). The cell was illuminated with an AM1.5G spectrum (calibrated with a KG-3 filtered silicon reference cell, certified at Fraunhofer ISE). Following the procedure of Jošt *et al.*(*63*), the cell was held for 15 minutes at 40 °C, 55 °C and 70 °C and for 20 minutes at 85 °C. Due to a technical issue, the sun simulator needed to be restarted. However, the cell was still exposed to the elevated temperature.

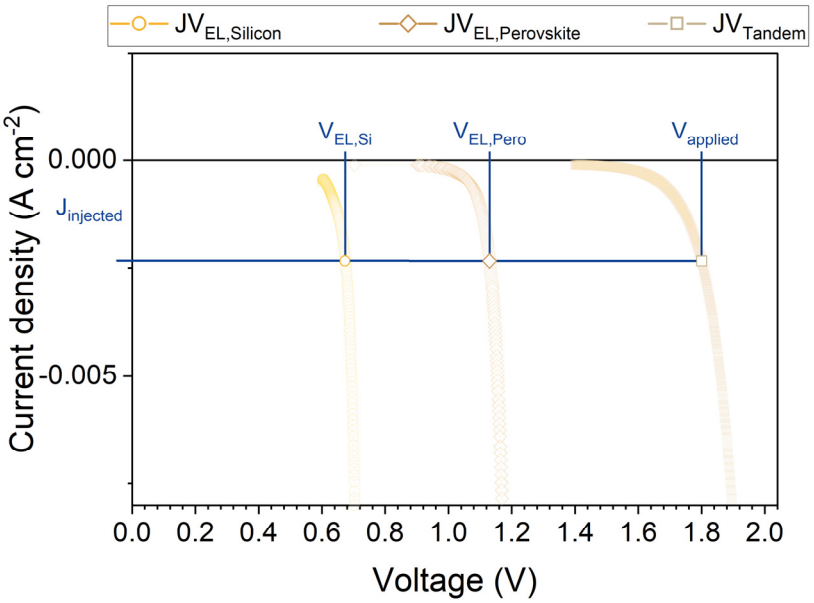

Figure S36 Injection dependent EL measurements of a monolithic tandem solar cell using Me-4PACz as HTL and LiF interlayer. By applying a voltage to the solar cell, we inject a current, which flows through both subcells. From the EL measurement, we extract the QFLS at each injected current and can reconstruct a dark *J-V*.

Supplementary text: *J-V* reconstructed from EL measurements

When comparing the reconstructed *J-V* obtained from EL measurements (JV_{EL}) to the *J-V* measured under a solar simulator (JV_{Sunsim}), we first notice a slightly higher shunt resistance R_{Sh} for the $JV_{EL,Tandem}$. We attribute this to pinholes in the perovskite top cell (e.g., direct contact between C_{60} and ITO), which are electrically active and lead to leakage currents in the JV_{Sunsim}. However, these pinholes are not visible in the EL images due to limited camera resolution and pixel bleeding of the luminescence intensity. Thus, the reconstructed perovskite subcell $JV_{EL,Pero}$ is a representation of a top cell processed under perfect substrate and precursor cleanliness, pinhole-free wetting etc. Secondly, the reconstructed JV_{EL} curve does not feature any series resistance, because the EL gives access only to the *internal* voltage, whereas an electrical *J-V* curve displays the current density versus *external* voltage. The external voltage at a given current is smaller than the internal one for example due to voltage drops at series resistances (*85*). Additionally, in the EL reconstruction, a larger current is flowing at the reconstructed V_{OC} as compared to the reconstructed V_{MPP}, since 1-sun equivalent electrical current injection corresponds to the reconstructed V_{OC}. In contrast, under electrical *J-V*-sweeping, a higher net current flows at V_{MPP} compared to V_{OC}. Since in a solar cell diode equation the series resistance appears in the product $R_s \times I$, the JV_{EL} thus simulates a *J-V* curve under small net current flow.

a

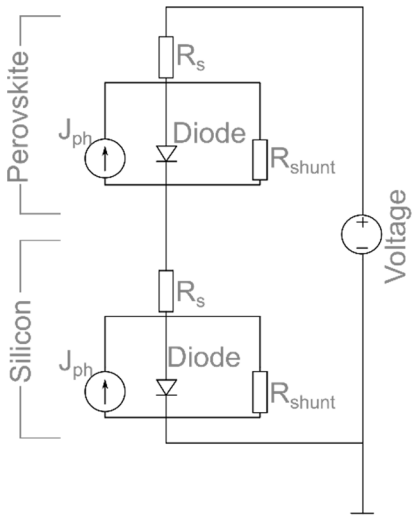

b

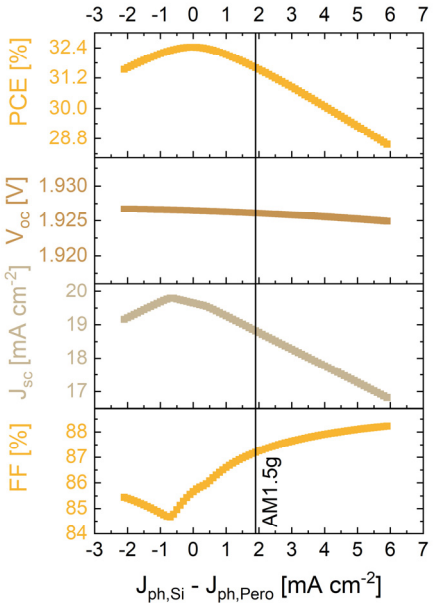

Figure S37 a, Schematic of the SPICE simulation. For the top and bottom cell a single diode model is used consisting of a current source J_{ph}, series resistance R_s, parallel resistance R_{shunt} and the diode. In this case, the Rs was set to 0. **b**, result of the simulation using the parameter extracted from the JV_{EL} of the individual subcells. The J_{ph} of the subcells were changed while maintaining a constant cumulative current density of 39.3 mA cm^{-2} as it is the case for AM1.5G-equivalent illumination (calculated by EQE). Thus, the individual parameters are a function of the mismatch of the subcells. A FF minimum occurs at a mismatch of -0.7 mA cm^{-2}, whereas it is simultaneously the point of maximum J_{sc}. Thus, a tradeoff needs to be done. Here, the maximum PCE of 32.43% is reached when both subcells have the same J_{ph} (i.e. mismatch=0).

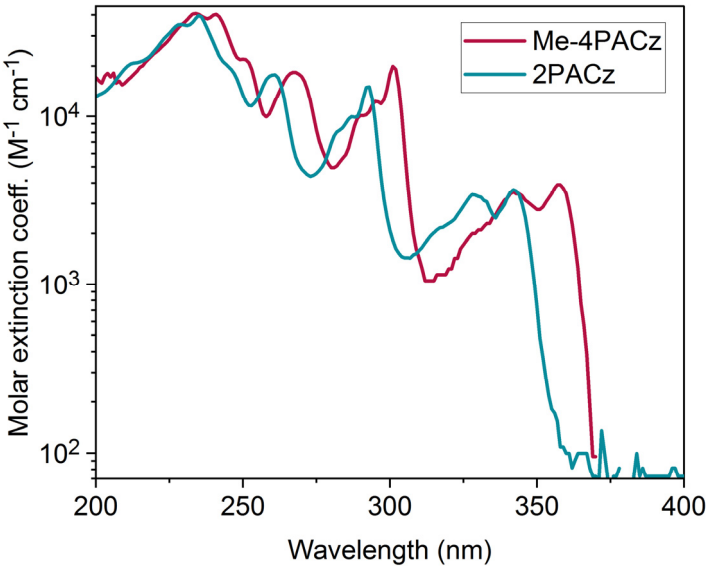

Figure S38 Molar extinction coefficient of 2PACz and Me-4PACz dissolved in THF (10^{-4} M). UV/Vis spectra were recorded on a PerkinElmer Lambda 35 spectrometer.

Me-nPACz (n = 2,4,6)

Materials used for the synthesis were purchased from Sigma-Aldrich or TCI Europe and were used as received without further purification.

The ^{1}H and ^{13}C NMR spectra were taken on Bruker Avance III (400 MHz) spectrometer at room temperature. Chemical shifts are reported in parts per million (δ, ppm) downfield from tetramethylsilane standard and are referenced to residual signal of the solvent. The course of the reactions products was monitored by TLC on ALUGRAM SIL G/UV254 plates and developed with UV light. Silica gel (grade 9385, 230–400 mesh, 60 Å, Aldrich) was used for column chromatography. Elemental analysis was performed with an Exeter Analytical CE-440 elemental analyzer, Model 440 C/H/N/.

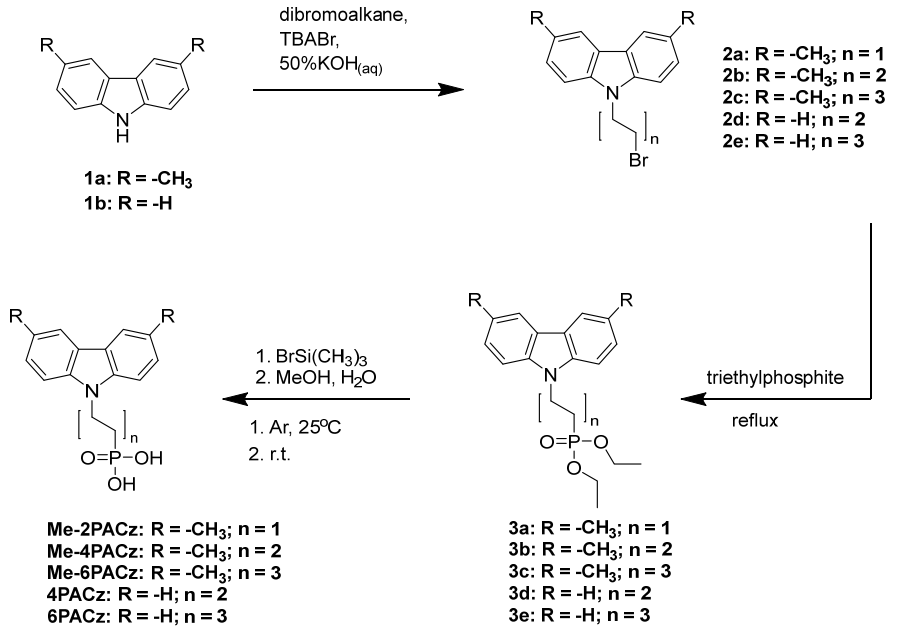

Figure S39 Synthesis scheme of the new materials **(Me)-nPACz** (n = 2, 4, 6).

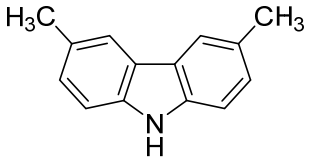

(3,6-Dimethyl-9*H*-carbazole) (1a). 3,6-Dibromocarbazole (10 g, 30.77 mmol) and 1,3-bis-(diphenylphosphino)dichloronickel(II) ($Ni(dppp)_2Cl_2$) (2.5g, 4.62 mmol) were dissolved in 700 ml of absolute diethyl ether under argon atmosphere. After 15 min, 40.9 mL of a 3 M CH_3MgBr solution in diethyl ether (123.08 mmol) was added over a period of 60 min to the purple red suspension, yielding a brown and clear solution. Afterwards reaction mixture was refluxed for 5 h, cooled to room temperature, and quenched with 100 mL of saturated aqueous NH_4Cl solution. Organic phase was separated and extracted three times with 200 mL of saturated aqueous Na_2CO_3 solution, three times with 200 mL of water, and finally three times with 200 mL of saturated aqueous NaCl solution. The organic layer was dried over anhydrous Na_2SO_4 and the solvent was distilled off under reduced pressure. The crude product was purified by column chromatography (acetone *n*-hexane 1:24 v/v) to give 3.5 g (58 %) of white crystalline powder.

^{1}H NMR (400 MHz, $(CD_3)_2SO$): δ 10.95 (s, 1H), 7.84 (s, 2H), 7.35 (d, J = 8.1 Hz, 2H), 7.18 (d, J = 8.0 Hz, 2H), 2.46 (s, 6H).

^{13}C NMR (100 MHz, $(CD_3)_2SO$): δ 138.3, 126.8, 126.6, 122.4, 119.8, 110.6, 21.1.

Anal. calcd for $C_{14}H_{13}N$, %: C 86.12, H 6.71, N 7.17, found, %: C 85.91, H 6.82, N 7.27.

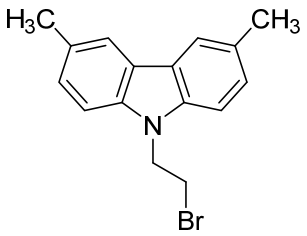

9-(2-Bromoethyl)-3,6-dimethyl-9*H*-carbazole (2a): **1a** (0.6 g, 3.07 mmol) was dissolved in 1,2-dibromoethane (7 ml, 81.23 mmol), tetrabuthylammonium bromide (0.148 g, 0.46 mmol) and 50% KOH aqueous solution (0.86 ml, 15.35 mmol) were added subsequently. Reaction was stirred at 50°C for two days (TLC, acetone: *n*-hexane 2:23 *v/v*) after each 24h tetrabuthylammonium bromide (0.1 g, 0,31 mmol) and 0.5 ml of 50% aqueous KOH solution were added. After completion of the reaction, extraction was done with dichloromethane. The organic layer was dried over anhydrous Na_2SO_4 and the solvent was distilled off under reduced pressure. The crude product was purified by column chromatography (acetone: *n*-hexane 1:23 *v/v*) to give 0.52 g (47%) of colourless solid.

^{1}H NMR (400 MHz, $CDCl_3$): δ 7.82 (s, 2H), 7.27 – 7.22 (m, 4H), 4.57 (t, *J* = 7.5 Hz, 2H), 3.58 (t, J = 7.5 Hz, 2H), 2.50 (s, 6H).

^{13}C NMR (100 MHz, $CDCl_3$): δ 138.6, 128.8, 127.2, 123.2, 120.6, 108.2, 44.8, 28.4, 21.5.

Anal. calcd for $C_{16}H_{16}BrN$, %: C 63.59, H 5.34, N 4.63, found, %: C 63.72, H 5.52, N 4.77.

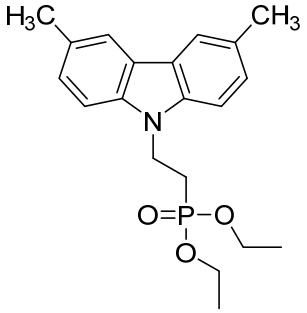

Diethyl [2-(3,6-dimethyl-9*H*-carbazol-9-yl)ethyl]phosphonate (3a): **2a** (0.4 g, 1.32 mmol) was dissolved in triethyl phosphite (6 ml, 34.99 mmol) and the reaction mixture was heated at reflux for 19 h. After reaction completion (TLC, acetone: *n*-hexane 8:17 *v/v*) the solvent was distilled off under reduced pressure. The crude product was purified by column chromatography (acetone: *n*-hexane 1:4 *v/v*) to give 0.46g (97%) of yellowish resin.

^{1}H NMR (400 MHz, $CDCl_3$): δ 7.84 (s, 2H), 7.30 – 7.23 (m, 4H), 4.55 (q, *J* = 8.5 Hz, 2H), 4.08 (quint, *J* = 7.1 Hz, 4H), 2.52 (s, 6H), 2.28 – 2.16 (m, 2H), 1.28 (t, *J* = 7.0 Hz, 6H).

^{13}C NMR (100 MHz, $CDCl_3$): δ 138.3, 128.4, 127.1, 123.2, 120.5, 108.2, 62.0, 61.9, 37.1, 26.0, 24.6, 21.5, 16.54, 16.48.

Anal. calcd for $C_{20}H_{26}NO_3P$, %: C 66.84, H 7.29, N 3.90, found, %: C 67.01, H 7.09, N 4.08.

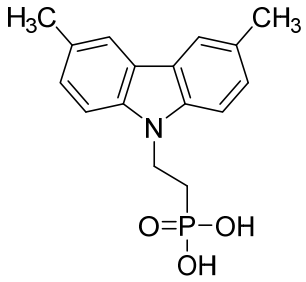

[2-(3,6-dimethyl-9*H*-carbazol-9-yl)ethyl]phosphonic acid (Me-2PACz): **3a** (0.47 g, 1.31 mmol) was dissolved in anhydrous 1,4-dioxane (15 ml) under argon atmosphere and bromotrimethylsilane (1.73 ml, 13.07 mmol) was added dropwise. Reaction was stirred for 22 h at 25 °C under argon atmosphere. Afterwards, methanol (3 ml) was added and stirring continued for 3h. Finally, distilled water was added dropwise (10 ml), until solution became opaque, and it was stirred overnight. Product was filtered off, washed with water, dissolved in tetrahydrofuran (1 ml) and precipitated into *n*-hexane (12 ml). The product was filtered off and washed with *n*-hexane, to give 0.360 g (91 %) of white powder.

^{1}H NMR (400 MHz, $(CD_3)_2SO$): δ 9.59 (br s, 2H), 7.88 (s, 2H), 7.38 (d, J = 8.3 Hz, 2H), 7.25 (d, J = 8.3 Hz, 2H), 4.59 – 4.40 (m, 2H), 2.46 (s, 6H), 2.09 – 1.90 (m, 2H).

^{13}C NMR (100 MHz, $(CD_3)_2SO$): δ 138.0, 127.4, 126.9, 122.3, 120.2, 108.6, 37.4, 28.0, 26.7, 21.0.

Anal. calcd for $C_{16}H_{18}NO_3P$, %: C 63.36, H 5.98, N 4.62, found, %: C 63.53, H 5.81, N 4.76.

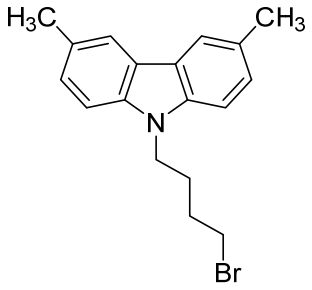

9-(4-bromobutyl)-3,6-dimethyl-9*H*-carbazole (2b): 1a (0.6 g, 3.07 mmol) was dissolved in 1,4-dibromobutane (9.1 ml, 76.75 mmol), tetrabuthylammonium bromide (0.148 g, 0.46 mmol) and 50% KOH aqueous solution (0.86 ml, 15.35 mmol) were added subsequently. Reaction was stirred at 60°C overnight (TLC, acetone:*n*-hexane, 1:24, v:v). After completion of the reaction, extraction was done with dichloromethane. The organic layer was dried over anhydrous Na_2SO_4 and the solvent was distilled off under reduced pressure. The crude product was purified by column chromatography (acetone *n*-hexane 1:124 v/v) to give 0.91 g (90 %) of white crystalline solid.

^{1}H NMR (400 MHz, $CDCl_3$): δ 7.85 (s, 2H), 7.29 – 7.20 (m, 4H), 4.27 (t, J = 6.8 Hz, 2H), 3.33 (t, J = 6.5 Hz, 2H), 2.52 (s, 6H), 2.01 (quint, J = 7.1 Hz, 2H), 1.86 (quint, J = 6.4 Hz, 2H).

^{13}C NMR (100 MHz, $CDCl_3$): δ 139.0, 128.1, 127.0, 123.0, 120.5, 108.3, 42.3, 33.4, 30.4, 27.8, 21.5.

Anal. calcd for $C_{18}H_{20}BrN$, %: C 65.46, H 6.10, N 4.24, found, %: C 65.31, H 6.34, N 4.39.

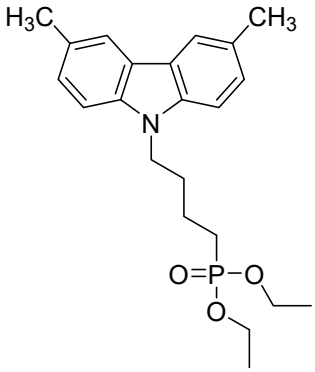

Diethyl [4-(3,6-dimethyl-9*H*-carbazol-9-yl)butyl]phosphonate (3b): **2b** (0.8 g, 2.42 mmol) was dissolved in triethyl phosphite (9 ml, 52.49 mmol) and the reaction mixture was heated at reflux overnight. After reaction completion (TLC, acetone: *n*-hexane, 6:19, v:v) the solvent was distilled off under reduced pressure. The crude product was purified by column chromatography (acetone/*n*-hexane 1:4 v/v) to give 0.89g (95%) of yellowish resin.

^{1}H NMR (400 MHz, $CDCl_3$): δ 7.84 (s, 2H), 7.25 – 7.22 (m, 4H), 4.24 (t, *J* = 7.0 Hz, 2H), 4.00 (quint, *J* = 7.3 Hz, 4H), 2.51 (s, 6H), 1.93 (quint, *J* = 7.5 Hz, 2H), 1.75 – 1.58 (m, 4H), 1.24 (t, *J* = 7.0 Hz, 6H).

^{13}C NMR (100 MHz, $CDCl_3$): δ 139.0, 127.9, 126.9, 122.9, 120.4, 108.3, 61.62, 61.56, 42.6, 29.92, 29.77, 26.2, 24.8, 21.5, 20.54, 20.49, 16.53, 16.47.

Anal. calcd for $C_{22}H_{30}NO_3P$, %: C 68.20, H 7.80, N 3.62, found, %: C 68.03, H 7.98, N 3.79.

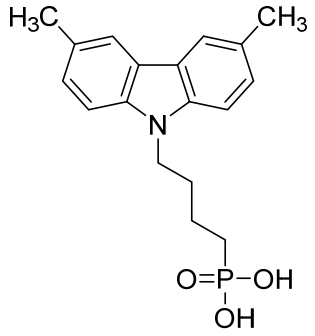

[4-(3,6-dimethyl-9*H*-carbazol-9-yl)butyl]phosphonic acid (Me-4PACz): **3b** (0.6 g, 1.55 mmol) was dissolved in anhydrous 1,4-dioxane (20 ml) under argon atmosphere and bromotrimethylsilane (2.12 ml, 15.59 mmol) was added dropwise. Reaction was stirred for 22 h at 25°C under argon atmosphere. Afterwards, methanol (3 ml) was added and stirring continued for 3h. Finally, distilled water was added dropwise (15 ml), until solution became opaque, and it was stirred overnight. Product was filtered off, washed with water, dissolved in tetrahydrofuran (1 ml) and precipitated into *n*-hexane (15 ml). The product was filtered off and washed with *n*-hexane, to give 0.460 g (91 %) of white powder.

^{1}H NMR (400 MHz, $(CD_3)_2SO$): δ 7.88 (s, 2H), 7.45 (d, *J* = 8.3 Hz, 2H), 7.23 (d, *J* = 8.3 Hz, 2H), 4.34 – 4.27 (m, 2H), 2.47 (s, 6H), 1.85 – 1.76 (m, 2H), 1.58 – 1.45 (m, 4H).

^{13}C NMR (100 MHz, $(CD_3)_2SO$): δ 138.6, 127.0, 126.8, 122.0, 112.0, 109.0, 42.0, 29.71, 29.56, 28.1, 26.8, 21.1, 20.49, 20.45.

Anal. calcd for $C_{18}H_{22}NO_3P$, %: C 65.25, H 6.69, N 4.23, found, %: C 65.38, H 6.51, N 4.29.

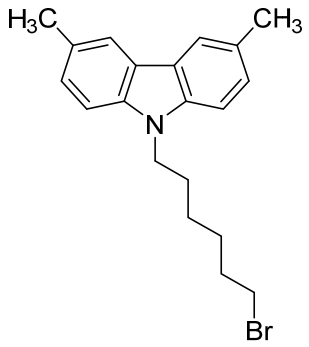

9-(6-Bromohexyl)-3,6-dimethyl-9*H*-carbazole (**2c**): **1a** (0.6 g, 3.07 mmol) was dissolved in 1,6-dibromohexane (9 ml, 58.51 mmol), tetrabuthylammonium bromide (0.148 g, 0.46 mmol) and 50% KOH aqueous solution (0.86 ml, 15.35 mmol) were added subsequently. Reaction was stirred at 60°C overnight (TLC, acetone: *n*-hexane 1:24 *v/v*). After completion of the reaction, extraction was done with dichloromethane. The organic layer was dried over anhydrous Na_2SO_4 and the solvent was distilled off under reduced pressure. The crude product was purified by column chromatography (acetone: *n*-hexane 1:249 *v/v*) to give 1.04 g (95 %) of colourless compound

^{1}H NMR (400 MHz, $CDCl_3$): δ 7.85 (s, 2H), 7.25 – 7.23 (m, 4H), 4.22 (t, *J* = 7.0 Hz), 3.32 (t, *J* = 6.7 Hz, 2H), 2.52 (s, 6H), 1.88 – 1.80 (m, 2H), 1.80 – 1.72 (m, 2H), 1.47 – 1.39 (m, 2H), 1.38 – 1.29 (m, 2H).

^{13}C NMR (100 MHz, $CDCl_3$): δ 139.1, 127.9, 126.9, 122.9, 120.4, 108.4, 43.0, 33.9, 32.7, 29.0, 28.1, 26.6, 21.5.

Anal. calcd for $C_{20}H_{24}BrN$, %: C 67.04, H 6.75, N 3.91, found, %: C 67.18, H 6.62, N 4.10.

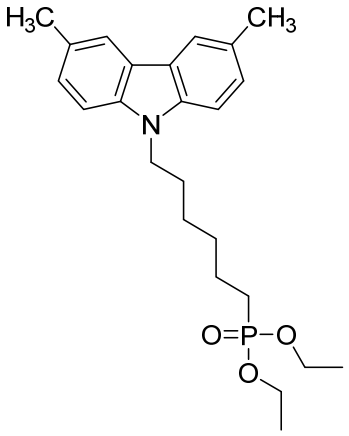

Diethyl [6-(3,6-dimethyl-9*H*-carbazol-9-yl)hexyl]phosphonate (3c): **2c** (1 g, 2.79 mmol) was dissolved in triethyl phosphite (10 ml, 58.32 mmol) and the reaction mixture was heated at reflux overnight. After reaction completion (TLC, acetone: *n*-hexane 6:19 *v/v*) the solvent was distilled off under reduced pressure. The crude product was purified by column chromatography (acetone: *n*-hexane 4:21 *v/v*) to give 0.96g (82%) of yellowish resin.

^{1}H NMR (400 MHz, $CDCl_3$): δ 7.84 (s, 2H), 7.25 – 7.22 (m, 4H), 4.22 (t, *J* = 7.0 Hz, 2H), 4.10 – 3.99 (m, 4H), 2.52 (s, 6H), 1.82 (p, *J* = 7.0 Hz, 2H), 1.70 – 1.59 (m, 2H), 1.59 – 1.48 (m, 2H), 1.40 – 1.31 (m, 4H), 1.28 (t, *J* = 7.0 Hz, 6H).

^{13}C NMR (100 MHz, $CDCl_3$): δ 139.0, 127.8, 126.8, 122.8, 120.3, 108.3, 61.50, 61.44, 43.0, 30.52, 30.36, 28.9, 26.9, 26.4, 25.0, 22.45, 22.40, 21.5, 16.6, 16.5.

Anal. calcd for $C_{24}H_{34}NO_3P$, %: C 69.37, H 8.25, N 3.37, found, %: C 69.56, H 8.13, N 3.50.

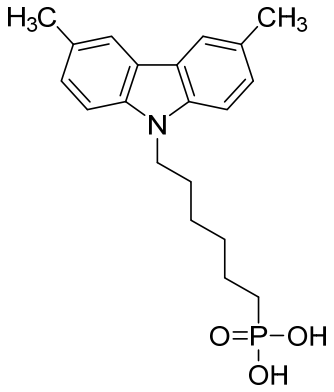

[6-(3,6-Dimethyl-9*H*-carbazol-9-yl)hexyl]phosphonic acid (Me-6PACz): **3c** (0.8 g, 1.92 mmol) was dissolved in anhydrous 1,4-dioxane (20 ml) under argon atmosphere and bromotrimethylsilane (2.5 ml, 19.25 mmol) was added dropwise. Reaction was stirred for 22 h at 25 ºC under argon atmosphere. Afterwards, methanol (3 ml) was added and stirring continued for 3h. Finally, distilled water was added dropwise (15 ml), until solution became opaque, and it was stirred overnight. Product was filtered off, washed with water, dissolved in tetrahydrofuran (2 ml) and precipitated into *n*-hexane (25 ml). The product was filtered off and washed with *n*-hexane, to give 0.580 g (84 %) of white powder.

^{1}H NMR (400 MHz, $(CD_3)_2SO$): δ 8.44 (br s, 2H), 7.84 (s, 2H), 7.38 (d, *J* = 8.4 Hz, 2H), 7.20 (d, *J* = 8.2 Hz, 2H), 4.25 (t, *J* = 6.9 Hz, 2H), 2.43 (s, 6H), 1.72 – 1.63 (m, 2H), 1.46 – 1.17 (m, 8H).

^{13}C NMR (100 MHz, $(CD_3)_2SO$): δ 138.6, 127.0, 126.8, 122.0, 120.0, 108.8, 42.2, 31.0, 29.9, 29.7, 28.4, 26.2, 22.7, 22.1, 21.0, 14.0.

Anal. calcd for $C_{20}H_{26}NO_3P$, %: C 66.84, H 7.29, N 3.90, found, %: C 66.73, H 7.47, N 3.76.

nPACz (n = 2,4,6)

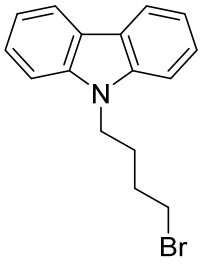

9-(4-Bromobutyl)-9*H*-carbazole (2d): **1b** (1 g, 5.98 mmol) was dispersed in toluene (13 ml). Afterwards, catalytic amount of tetrabutylammonium bromide, 50% KOH aqueous solution (13 ml) and 1,4-dibromobutane (1.428 ml, 11.96 mmol) were added. After 24h of stirring at room temperature, additional amount of 1,4-dibromobutane (1.428 ml, 11.96 mmol) was added, and the mixture was stirred at room temperature for additional 24h. After completion of the reaction (TLC, acetone:n-hexane, 3:22, v:v)., extraction was done with ethyl acetate. The organic layer was dried over anhydrous Na_2SO_4 and the solvent was distilled off under reduced pressure. The product was purified by column chromatography (*n*-hexane), to give 1.31 g (73 %) of white crystalline solid.

^{1}H NMR (400 MHz, $(CD_3)_2SO$): δ 8.15 (d, *J* = 7.7 Hz, 2H), 7.62 (d, *J* = 8.2 Hz, 2H), 7.45 (t, *J* = 7.7 Hz, 2H), 7.19 (t, *J* = 7.4 Hz, 2H), 4.44 (t, *J* = 6.6 Hz, 2H), 3.54 (t, *J* = 6.3 Hz, 2H), 2.00 – 1.70 (m, 4H).

^{13}C NMR (101 MHz, $(CD_3)_2SO$): δ 139.9, 125.7, 122.0, 120.3, 118.7, 109.2, 41.3, 34.7, 29.8, 27.2.

Anal. calcd for $C_{16}H_{16}BrN$, %: C 63.59, H 5.34, N 4.63, found, %: C 63.64, H 5.40, N 4.67.

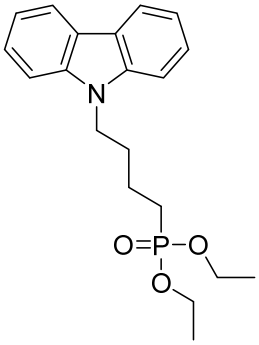

Diethyl [4-(9*H*-carbazol-9-yl)butyl]phosphonate (3d): **2d** (1.3 g, 4.3 mmol) was dissolved in triethyl phosphite (13 ml, 76 mmol) and the reaction mixture was heated at reflux for 24 h. After reaction completion (TLC, acetone:*n*-hexane, 7:18, v:v) the solvent was distilled off under reduced pressure. The crude product was purified by column chromatography (*n*-hexane; acetone:*n*-hexane, 1:4, v:v) to give 1.46 g (95%) of clear liquid.

^{1}H NMR (400 MHz, $(CD_3)_2SO$): δ 8.14 (d, *J* = 7.7 Hz, 2H), 7.62 (d, *J* = 8.2 Hz, 2H), 7.44 (t, *J* = 7.7 Hz, 2H), 7.19 (t, *J* = 7.4 Hz, 2H), 4.41 (t, *J* = 7.0 Hz, 2H), 3.89 (quint, *J* = 7.4 Hz, 4H), 1.96 – 1.63 (m, 4H), 1.58 – 1.39 (m, 2H), 1.13 (t, *J* = 7.0 Hz, 6H).

^{13}C NMR (101 MHz, $(CD_3)_2SO$): δ 140.4, 126.1, 122.5, 120.7, 119.1, 109.8, 61.24, 61.18, 42.2, 29.76, 29.60, 25.4, 24.0, 20.26, 20.21, 16.71, 16.66.

Anal. calcd for $C_{20}H_{26}NO_3P$, %: C 66.84, H 7.29, N 3.90, found, %: C 66.58, H 7.21, N 3.82.

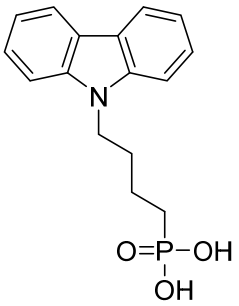

[4-(9*H*-carbazol-9-yl)butyl]phosphonic acid (4PACz): **3d** (1 g, 2.78 mmol) was dissolved in anhydrous 1,4-dioxane (30 ml) under argon atmosphere and bromotrimethylsilane (3 ml, 22.73 mmol) was added dropwise. Reaction was stirred for 24 h at 25 °C under argon atmosphere. Afterwards solvent was partially distilled off under reduced pressure, and the liquid residue was dissolved in methanol (30 ml). Next, distilled water was added dropwise (30 ml), until solution became opaque. Product was filtered off and washed with water to give 0.47 g (56 %) of white solid.

^{1}H NMR (400 MHz, $(CD_3)_2SO$): δ 8.14 (d, *J* = 7.7 Hz, 2H), 7.61 (d, *J* = 8.2 Hz, 2H), 7.44 (t, *J* = 7.6 Hz, 2H), 7.19 (t, *J* = 7.4 Hz, 2H), 4.39 (t, *J* = 6.9 Hz, 2H), 1.85 (quint, *J* = 7.2 Hz, 2H), 1.64 – 1.42 (m, 4H).

^{13}C NMR (101 MHz, $(CD_3)_2SO$): δ 140.2, 125.9, 122.2, 120.4, 118.8, 109.5, 42.2, 29.9, 29.7, 28.3, 26.9, 20.72, 20.67.

Anal. calcd for $C_{16}H_{18}NO_3P$, %: C 63.36, H 5.98, N 4.62, found, %: C 63.25, H 6.11, N 4.54.

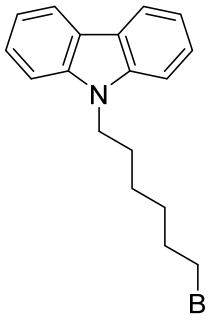

9-(6-bromohexyl)-9*H*-carbazole (2e): **1b** (1 g, 5.98 mmol) was dispersed in toluene (13 ml). Afterwards, catalytic amount of tetrabutylammonium bromide, 50% KOH aqueous solution (13 ml) and 1,6-dibromohexane (1.84 ml, 11.96 mmol) were added. After 24h of stirring at room temperature, additional amount of 1,6-dibromohexane (1 ml, 6.5 mmol) was added, and the mixture was stirred at room temperature for additional 24h. After completion of the reaction (TLC, acetone:*n*-hexane, 3:22, v:v)., extraction was done with ethyl acetate. The organic layer was dried over anhydrous Na_2SO_4 and the solvent was distilled off under reduced pressure. The product was purified using column chromatography (*n*-hexane), to give 1.38 g (70 %) of white crystalline solid.

^{1}H NMR (400 MHz, $(CD_3)_2SO$): δ 8.14 (d, *J* = 7.7 Hz, 2H), 7.59 (d, *J* = 8.2 Hz, 2H), 7.44 (t, *J* = 7.6 Hz, 2H), 7.19 (t, *J* = 7.4 Hz, 2H), 4.37 (t, *J* = 7.1 Hz, 2H), 3.46 (t, *J* = 6.6 Hz, 2H), 1.86 – 1.64 (m, 4H), 1.47 – 1.22 (m, 4H).

^{13}C NMR (101 MHz, $(CD_3)_2SO$) δ 139.7, 125.4, 121.8, 120.0, 118.4, 109.0, 41.9, 34.8, 31.9, 28.1, 27.0, 25.4.

Anal. calcd for $C_{18}H_{20}BrN$, %: C 65.46, H 6.10, N 4.24, found, %: C 65.52, H 6.09, N 4.26.

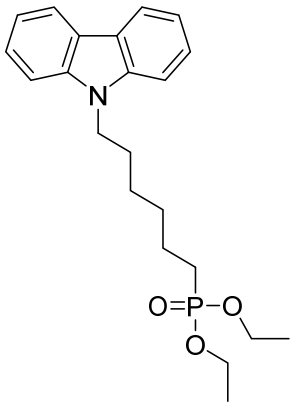

diethyl [6-(9*H*-carbazol-9-yl)hexyl]phosphonate (3e): **2e** (1.18 g, 3.59 mmol) was dissolved in triethyl phosphite (12 ml, 69.98 mmol) and the reaction mixture was heated at reflux for 24 h. After reaction completion (TLC, acetone:*n*-hexane, 7:18, *v/v*) the solvent was distilled off under reduced pressure. The crude product was purified by column chromatography (*n*-hexane; acetone:*n*-hexane, 1:4, *v/v*), to give 1.39 g (99%) of clear yellowish liquid.

^{1}H NMR (400 MHz, $(CD_3)_2SO$): δ 8.14 (d, *J* = 7.7 Hz, 2H), 7.59 (d, *J* = 8.2 Hz, 2H), 7.44 (t, *J* = 7.6 Hz, 2H), 7.19 (t, *J* = 7.4 Hz, 2H), 4.38 (t, *J* = 7.0 Hz, 2H), 4.07 – 3.94 (m, 4H), 1.79 – 1.57 (m, 6H), 1.43 – 1.23 (m, 10H).

^{13}C NMR (101 MHz, $(CD_3)_2SO$): δ 140.0, 125.6, 122.0, 120.2, 118.6, 109.2, 60.73, 60.67, 42.1, 29.43, 29.27, 28.2, 25.9, 25.0, 23.6, 21.95, 21.90, 16.30, 16.24.

Anal. calcd for $C_{22}H_{30}NO_3P$, %: C 68.20, H 7.80, N 3.62, found, %: C 68.33, H 7.84, N 3.68.

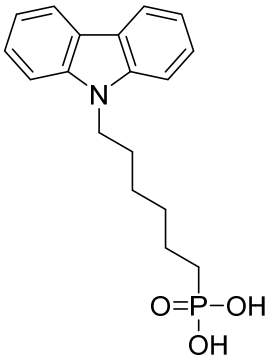

[6-(9*H*-carbazol-9-yl)hexyl]phosphonic acid (6PACz): **3e** (1.4 g, 3.16 mmol) was dissolved in dry 1,4-dioxane (30 ml) under argon and bromotrimethylsilane (3 ml, 22.73 mmol) was added dropwise. Reaction was stirred for 24 h at 25 °C under argon atmosphere. Afterwards solvent was partially distilled off under reduced pressure, and the liquid residue was dissolved in methanol (30 ml). Next, distilled water was added dropwise (40 ml), until solution became opaque. Product was filtered off and washed with water to give 0.33 g (25 %) of white solid.

^{1}H NMR (400 MHz, $(CD_3)_2SO$): δ 8.15 (d, *J* = 7.7 Hz, 2H), 7.59 (d, *J* = 8.2 Hz, 2H), 7.45 (t, *J* = 7.6 Hz, 2H), 7.19 (t, *J* = 7.4 Hz, 2H), 4.37 (t, *J* = 7.1 Hz, 2H), 1.75 (quint, *J* = 7.2 Hz, 2H), 1.52 – 1.20 (m, 8H).

^{13}C NMR (101 MHz, $(CD_3)_2SO$): δ 140.0, 125.7, 122.0, 120.3, 118.6, 109.2, 42.2, 29.80, 29.64, 28.34, 28.10, 26.75, 26.15, 22.69, 22.64.

Anal. calcd for $C_{18}H_{22}NO_3P$, %: C 65.25, H 6.69, N 4.23, found, %: C 65.40, H 6.62, N 4.17.

Nomenclature

J_{SC}	Short-circuit current density
n_{ID}	Ideality factor
V_{OC}	Open-circuit voltage
J_0	Dark saturation current density
n	Charge carrier density
2PACz	[2-(9H-carbazol-9-yl)ethyl]phosphonic acid
FF	Fill factor
AFM	Atomic force microscopy
ALD	Atomic layer deposition
AM1.5G	Air mass 1.5G
AZO	Al-doped zinc oxide
CIGSe	Copper Indium Gallium Selenide
DMF	dimethylformamide
DMSO	dimethyl sulfoxide
EA	Electron affinity
EQE	External quantum efficiency
ETL	Electron transport layer
FAI	Formamidinium iodide
GIWAXS	Grazing incidence wide-angle x-ray scattering
HTL	Hole transport layer
I_p	Ionization potential
ITO	Indium tin oxide
IZO	Indium zinc oxide
LiF	Lithium fluoride
MABr	Methylammonium bromide
Me-4PACz	[4-(3,6-dimethyl-9H-carbazol-9-yl)butyl]phosphonic acid
MeO-2PACz	[2-(3,6-dimethoxy-9H-carbazol-9-yl)ethyl]phosphonic acid

MPP	Maximum power point
NaF	Sodium fluoride
PCE	Power conversion efficiency
PCE	Power
PL	Photoluminescence
PLQY	Photoluminescence quantum yield
PSC	Perovskite solar cell
PTAA	Polytriarylamine
QFLS	Quasi-Fermi level splitting
SAM	Self-assembled monolayer
SEM	Scanning electron microscopy
SMU	Source measure unit
SPV	Surface photovoltage
SRH	Shockley-Read-Hall
TrPL	Transient photoluminescence
UPS	Ultraviolet photoelectron spectroscopy
V1036	(2-{3,6- bis[bis(4-methoxyphenyl)amino]-9H-carbazol-9-yl}ethyl)phosphonic acid
WF	Work function
XPS	X-ray photoelectron spectroscopy
XRD	X-ray diffraction

Acknowledgments

This thesis and my time at HZB has shown me once again how working in an open, supportive and diligent team is absolutely crucial for the success of any project. I hereby want to express my gratitude to all my colleagues and collaborators, on whose support I could rely during my work. First, I greatly thank Steve Albrecht for adding me to his young group at HZB in 2017, for all his efforts in setting up highly equipped and organized laboratories and for creating the supportive and calm atmosphere in our group. From him I have learned important aspects about motivating people and about being ambitious while staying ordered and relaxed. Further, I'd like to thank him for the freedom in choosing projects, while still providing guidance where necessary. I am also grateful to Bernd Rech, who had the vision of setting up perovskite competence in Adlershof and for taking time in providing ideas and discussions. I am also grateful to Lars Korte, Thomas Dittrich, Eva Unger, Antonio Abate and Thomas Unold for their inspiring inputs.

For his guidance, tutorials in the beginning and important advices, I sincerely thank Marko Jošt, who has introduced me to solar cell processing and has given me valuable guides during the thesis - I wish him all the best and further good ideas during his work in Ljubljana.

Special thanks go to Artiom Magomedov, who gave the inital idea of SAM-based solar cells, which at the time seemed too challenging, but after seeing the potential then became the main theme of my work. Without his ongoing support and sendings of high-quality materials together with Tadas Malinauskas and Ernestas Kasparavicius, many aspects of this work and the progress in our labs would not have been possible.

The generation and interpretation of results would probably not have been even half as efficient without the help of my group members and people in the shared HySPRINT laboratory. I owe huge thanks to Philipp, Lukas, Marcel, Max and Bor for always being supportive and keeping the fun aspects of life even when lab work sometimes didn't work out as wished for. I also feel privileged to have shared the lab with so many talented researchers, which are impossible to name all, but I want to especially thank Nga, Jorge, Diego, Joel, Weiwei, Aboma, Janardan, Gopi and Doro for the interesting projects, for sweetening the lab work even in stressful times and also for the fun times outside of work. To my office mate Eike I'm also very thankful for his open ears (even when wearing headphones), for sharing the philosophy that being open with tips & tricks in the lab is a standard and for all the enjoyable collaborative work.

I express further gratitude to the group of Thomas Unold for the inspiring and informative discussions. To him, José A. Marquez (Pepe) and Charles Hages (Chuck) I am very thankful for entrusting me with their precious PL setups since the start of my

thesis. Also big thanks to Pepe and Hannes Hempel for their guidance in the physics of charge carrier recombination. Many thanks to our colleagues in Potsdam as well, Martin, Christian and Pietro, for providing support during the establishment of our perovskite solar cell baseline and for always interesting discussions.

I owe further thanks for the reliable supply of CIGSe bottom cells by Tobias Betram and Christian Kaufmann, and silicon bottom cells by Anna Morales-Vilches and Bernd Stannowski, as well as for their support and advice in our projects, to which I also valued the contributions by Rutger Schlatmann. I'd also like to express my gratitude to all the colleagues, the "hidden heros", who kept the laboratories running and supported the researchers with their technical expertise: Carola Ferber, Thomas Lußky, Martin Muske, Tobias Hänel, Hagen Heinz, Monika Gabernig, Mona Wittig, Kerstin Jacob and Carola Klimm. And great thanks to Marion Krusche and Antonia Tallarek, who always looked out for every single one of us, reliably took care of organizational and bureaucratic tasks and were unfailingly supportive. Furthermore, I really appreciated the memorable moments during the PhD retreats, a big Thanks to the PhD representatives and organization teams, and thanks to the PhD coordinators for organizing the valuable workshops, as well as to the HyPerCells graduate school for the meetings/retreats that established a collaborative network among the many researchers.

Finally, sincere thanks to my dearest Maike for her exceptional patience, empathy, support and positive energy that enriched my life in uncountable ways. Similarly, I owe immeasurable gratitude to my family for all their strenuous efforts to enable me to grow up and study smoothly in Germany, and for their unconditional backup in all situations.

Thank you.